Fatigue Analysis and Testing of Wind Turbine Blades

GREAVES, PETER,ROBERT

How to cite:

GREAVES, PETER,ROBERT (2013) *Fatigue Analysis and Testing of Wind Turbine Blades*, Durham theses, Durham University. Available at Durham E-Theses Online: http://etheses.dur.ac.uk/7303/

Fatigue Analysis and Testing of Wind Turbine Blades

Peter Greaves

A thesis presented for the degree of
Doctor of Philosophy

Durham
University

School of Engineering and Computer Sciences

May 2013

Dedicated to

Jo and my family

Fatigue Analysis and Testing of Wind Turbine Blades

Peter Robert Greaves

Submitted for the degree of Doctor of Philosophy

May 2013

Abstract

This thesis focuses on fatigue analysis and testing of large, multi MW wind turbine blades. The blades are one of the most expensive components of a wind turbine, and their mass has cost implications for the hub, nacelle, tower and foundations of the turbine so it is important that they are not unnecessarily strong. Fatigue is often an important design driver, but fatigue of composites is poorly understood and so large safety factors are often applied to the loads. This has implications for the weight of the blade.

Full scale fatigue testing of blades is required by the design standards, and provides manufacturers with confidence that the blade will be able to survive its service life. This testing is usually performed by resonating the blade in the flapwise and edgewise directions separately, but in service these two loads occur at the same time. A fatigue testing method developed at Narec (the National Renewable Energy Centre) in the UK in which the flapwise and edgewise directions are excited simultaneously has been evaluated by comparing the Palmgren-Miner damage sum around the blade cross section after testing with the damage distribution caused by the service life.

A method to obtain the resonant test configuration that will result in the optimum mode shapes for the flapwise and edgewise directions was then developed, and simulation software was designed to allow the blade test to be simulated so that realistic comparisons between the damage distributions after different test types could be obtained.

During the course of this work the shortcomings with conventional fatigue analysis methods became apparent, and a novel method of fatigue analysis based on multi-continuum theory and the kinetic theory of fracture was developed. This method was benchmarked using physical test data from the OPTIDAT database and was applied to the analysis of a complete blade. A full scale fatigue test method based on this new analysis approach is also discussed.

Declaration

No part of this thesis has been submitted elsewhere for any other degree or qualification. The content of this thesis is all my own work unless referenced to the contrary in the text.

Acknowledgements

Over the three years since January 2010 many people have assisted me in completing the work described in this thesis, and I am grateful to them all. In particular, I would like to thank the following people:

- My primary PhD supervisor Dr. Rob Dominy, whose academic guidance has been invaluable.
- My secondary supervisors Dr. Grant Ingram, Dr. Hui Long and Dr. Tomek Koziara have all been very helpful in reviewing my work and making suggestions during the course of my PhD.
- Prof. Peter Tavner at Durham University and Stephen Wilson at Narec were invaluable in securing the funding for this research.
- Richard Court, Shona Ridley, Sally Poxon and Harry Jones at Narec have all provided useful information about blade testing.
- Richard McSherry performed CFD calculations at Narec which were extremely helpful in understanding the flow around the blade.
- Longhuan Du developed the vortex element program used to predict the forces on the blade due to unsteady aerodynamic effects.
- The technicians at Durham University, particularly Colin Wintrip, Stephen Richardson, Ian Hutchinson and Kevan Longley who all helped with the small scale test rig, and Tony McFarlane who has assisted with computer issues.
- Cornelis van Beveren at LM Wind Power has provided vast quantities of data without which much of this research would have been impossible.
- Jesper Thinggaard Jensen and Torben Lindby at LM Wind Power have also provided valuable data.
- Douglas Kenik at Firehole Composites has made many valuable suggestions which have helped with the alternative fatigue analysis method developed in this work.
- Dr. Tim Camp at GL Garrad Hassan for his assistance in getting a copy of Bladed.

Contents

Figures

Nomenclature

A	Swept area, Curve fitting parameter, Characteristic area
a	Axial induction factor, Amplitude
$[\boldsymbol{A}]$	Pre-calculated matrix to avoid matrix inversions during time stepping scheme, Laminate extensional stiffness matrix, Multi-continuum convenience matrix
$\boldsymbol{a}$	Multi-continuum theory convenience vector
B	Curve fitting parameter
$[\boldsymbol{B}]$	Laminate coupling matrix
B_t, B_{s1}, B_{s2}	Transverse effective stress weighting coefficients
C_p	Power coefficient
C	Curve fitting parameter
c	Chord length, Linear intercept
C_D	Drag coefficient
$[\boldsymbol{C}]$	Stiffness matrix in ply coordinate system, Damping matrix
$[\bar{\boldsymbol{C}}]$	Stiffness matrix in laminate coordinate system
C_x, C_y	Element centroid coordinates
C_{ex}, C_{ey}	Section neutral axis coordinates
C_{mx}, C_{my}	Section mass centre coordinates
D	Drag force, Damage sum, Domain
$[\boldsymbol{D}]$	Laminate bending matrix
d	Low stress correction cut off point
E	Young's Modulus, Energy dissipated as heat
$\hat{E}_x$	Equivalent extensional Young's modulus of laminate
F_x, F_y, F_z	Beam stress shear forces and axial force
f	Constant amplitude test frequency
f_F, f_E	Flapwise frequency/ Edgewise frequency
$\boldsymbol{F}$	Force vector
$\boldsymbol{f}$	Element internal forces

g	Gravitational acceleration
G	Shear modulus
$\hat{G}_{xy}$	Equivalent transverse shear modulus of laminate
h	Laminate thickness, Planck's constant
I_{xx}, I_{yy}, I_{xy}	Second moments of area and product moment of area
I_t, I_{s1}, I_{s2}, I_h	Transverse effective stress convenience variables
J''	Polymer loss compliance
k	Boltzmann constant, Saddle thickness, Newton cooling constant
$[\boldsymbol{K_E}]$	Beam element stiffness matrix
$[\boldsymbol{K}]$	Stiffness matrix
$\boldsymbol{k}$	Laminate mid-plane curvatures
K_B	Bond rupture rate
L	Lift force, Beam element length
l	Distance saddle protrudes from blade, Distance eccentric mass is mounted from neutral axis, Cross section element length
$M_x,\ M_y, M_z$	Beam stress bending and torsional moments
M_F, M_E	Flapwise and edgewise bending moments
M_T, M_A	Target and achieved bending moments
m	Mass, Mass per unit length of beam, Linear gradient
$[\boldsymbol{M_E}]$	Beam element mass matrix
m_d	Dynamic mass of excitation equipment
m_s	Static mass of excitation equipment
$[\boldsymbol{M}]$	Mass matrix
$\boldsymbol{M}$	Moment flow vector
M_{xx}, M_{yy}	First moment of area about x and y axes
N	Number of cycles to failure
n	Number of cycles, Number of CRMs mounted to blade, Kinetic theory damage parameter
$\boldsymbol{N}$	Force flow vector
P	Power, Probability

$P_R(V)$	Probability that 10 minute average wind speed is less than V
P_B	Probability of bond breaking
P_H	Probability of bond healing
$\boldsymbol{Q}$, $Q_{\boldsymbol{i}}$	Generalised force vector/ Component of generalised force vector
$\boldsymbol{q}$, q_i	Modal participation vector/ Component of modal participation vector
q_o	Open section shear flow
q_c	Closing shear flow
q_t	Torsional shear flow
r	Radius
R	R-value of fatigue cycle
S	Strength (fatigue or ultimate), fatigue cycle stress, strain or load
S_r	Residual strength
S_u	Initial strength
s	Mass per unit length of saddle frame, Curvilinear section coordinate
$[\boldsymbol{S}]$	Compliance matrix in ply coordinate system
$[\overline{\boldsymbol{S}}]$	Compliance matrix in laminate coordinate system
SC_x, SC_y	Coordinates of shear centre
T	Absolute temperature
t	Time, Blade thickness as proportion of chord
$[\mathbf{T}]$	Transformation matrix
U_∞	Upstream wind velocity
U	Activation energy
v	Wind velocity
V	10 minute average wind velocity, Volume
V_{Hub}	Hub height 10 minute average wind velocity
V_{Ave}	Annual average wind speed
V_{In}	Cut-in wind speed
V_{Out}	Cut-out wind speed
W	Apparent wind velocity

w	Distributed gravitational load
x, y	Beam cross section coordinates
$[\boldsymbol{X}]$	Eigenvector matrix
$\boldsymbol{x}$, x_i	Displacement vector / Displacement vector components
$\dot{\boldsymbol{x}}$, $\dot{x}_i$	Velocity vector/ Velocity vector components
$\ddot{\boldsymbol{x}}$, $\ddot{x}_i$	Acceleration vector / Acceleration vector components
z_{Hub}	Hub height
z	Height above ground, Beam axial coordinate, distance from laminate mid-plane
α	Wind shear exponent, angle of attack, Rayleigh damping mass coefficient, Newmark coefficient
$\boldsymbol{\alpha}$	Thermal expansion coefficient vector
β	Blade set angle, Rayleigh damping stiffness coefficient, Newmark coefficient
γ	Activation volume, Shear strain
ε_{zz}	Axial strain in beam
ε_m, ε_a	Strain cycle mean value/strain cycle amplitude
$\boldsymbol{\varepsilon_0}$	Laminate mid-plane strains
$\boldsymbol{\varepsilon}$	Strain tensor
ζ_i	Damping of mode i
θ	Ply angle, Blade angular twist
λ	Slope parameter of damage evolution equation
ν	Poisson’s ratio
ν_0	Atomic vibration frequency approximation
ρ	Density of air, Equivalent density of element
ρ_s	Saddle material density
σ	Stress level
$\boldsymbol{\sigma}$	Stress tensor
σ_{eff}	Kinetic theory effective stress
σ_{SVM}	Signed Von Mises stress
σ_{Ref}	Intercept of power law to approximate low stress behaviour

τ	Kinetic theory time to failure
τ_0	Period of atomic vibration
τ_d	Time at which kinetic theory behaviour diverges from log-linear
ϕ	Angle of apparent wind to rotor plane, Bending axes rotation angle, Volume fraction
φ	Phase angle
ψ	Hysteretic heating constant
Ω	Rotor angular speed, Area enclosed by median line of cell
ω	Natural frequency, Angular velocity

Subscripts

A_1, A_2, A_3	Property in ply coordinate system
A_a	Amplitude
A_C	Composite property
A_F	Fibre property
A_i	Vector component (row or column), Identifier
A_{ij}	Matrix component (row, column)
A_k	Laminate layer number
A_M	Mean value, Matrix property
A_{min}, A_{max}	Minimum and maximum value
A_x, A_y, A_z	Property in laminate coordinate system, Property in blade coordinate system

1 Introduction

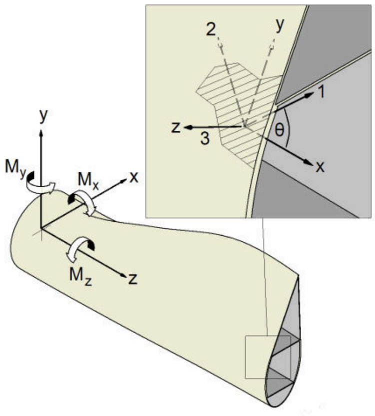

The wind has been harnessed by humankind for thousands of years. Long before the industrial revolution, the attraction of getting something for nothing encouraged us to create machines that allow the kinetic energy of moving air to be put to work. The energy was used to move boats, pump water, saw wood and, of course, mill grain [1].

With the advent of steam power in the late 1700s, the use of wind power began to dwindle [1]. The use of fossil fuels grew exponentially; with their high energy density and constant availability they represented a much more attractive way of generating power than the mercurial wind.

A temporary reduction in fossil fuel use occurred during the oil crisis in the 1970s. US intervention in the Yom Kippur war in 1973 prompted many countries in the Middle East to withhold oil supplies from Western countries, and this increased the price of oil considerably for several years [1]. Around the same time, climate change also began to make its way onto the political agenda. However, it would be several decades before it started to have any real influence on policy and the interest in renewable energy sources in the 70s can be attributed mainly to the high price of oil.

Due to these issues many countries began to invest in wind energy research, some of which have given continued support until the present day. These countries, in particular Denmark and Germany, are now the world leaders in wind energy.

The resultant increase in understanding of the aerodynamics and structural dynamics of wind turbines quickly led to turbines which, to the untrained eye, look very similar to the gigantic machines which are becoming commonplace today.

The design standards put in place during these early years are now highly developed and have led to a very low incidence of catastrophic failures. This is no accident; the standards require that turbines are certified in the field before they become commercially available and full scale testing of the rotor blades is required. Full scale test facilities for the drivetrain are also becoming available although they are not yet mandatory.

This introductory chapter will begin with a background of why wind energy is of interest; climate change, fossil fuel dependency and energy security will all be addressed. It will then give a brief introduction to wind turbine design and testing before finishing with a declaration of the original contribution of this work.

1.1 Climate Change

In 1824 Joseph Fourier calculated that given the amount of incoming solar radiation the earth should be considerably colder than it is. He originally thought that the discrepancy might be due to interstellar radiation, but he eventually realised that the earth's atmosphere acts as insulation and traps some of the incoming heat; the so called 'greenhouse effect' [2].

John Tyndall successfully established the importance of water vapour and carbon dioxide using some simple experiments [2]. The Swedish physicist Svante Arrhenius then built on this work and came to the realisation that there is a balance between the high frequency radiation that penetrates the atmosphere and heats the earth and the infrared heat energy leaving the atmosphere. The main point of his 'hothouse law' was that that some of the infrared energy that is emitted back into space is absorbed by carbon dioxide in the atmosphere and reemitted back towards the ground, although he also predicted the importance of the oceans in absorbing carbon dioxide [2]. Perhaps because he was from one of the colder parts of the world, he was of the opinion that global warming was a positive effect that would benefit humankind by allowing increased crop production and preventing ice ages; an opinion that is still popular today.

Since the industrial revolution the concentration of atmospheric carbon dioxide has been increasing steadily due to the burning of fossil fuels [2]. The consensus among climate scientists is that the global average surface temperature has already increased as a result, and much greater increases are predicted during this century if carbon emissions are not drastically reduced during the next few decades. There is great uncertainty about the temperature rises that can be expected because of various feedback mechanisms (such as the loss of arctic ice resulting in large quantities of methane being released from what used to be permafrost, greater temperatures increasing the amount of water vapour in the atmosphere and the loss of sea ice reducing the albedo of the earth's surface [3]) and the general complexity of the system but even the most conservative increases would have far reaching implications for humankind [4].

The burning of fossil fuels currently accounts for around 57% of carbon emissions worldwide [5], and this fact has prompted the European Union to create binding targets for renewable energy production of 20% by 2020 [6]. Wind power is predicted to account for around 40% of the renewable electricity production [6].

1.2 Energy Security and Fossil Fuel Dependency

Fossil fuels are an extremely important part of the global economy, and as such any disruption in supply can have extremely far reaching consequences. Many governments seek to isolate themselves from these effects by creating home grown sources of energy, either through the use of renewable energy or by exploiting harder-to-reach fossil fuel reserves that are within their own borders. Examples of this approach include the renewable energy boom in Europe in the 1970s, the exploitation of North Sea oil and gas and biofuel production in the United States [7].

Another factor is that much of the world's remaining oil reserves are located in the Middle East, a region with the potential for conflicts that could disrupt oil supplies. This means that there is no guarantee that the price of oil will not fluctuate even in the short term.

Even if climate change and energy security are neglected as a driver for a move away from fossil fuels, there are still compelling arguments for renewable energy sources. As fossil fuel reserves are depleted, the remaining reserves become more difficult and expensive to exploit which increases the competitiveness of renewable energy sources.

1.3 Wind Turbine Design

The current prevalent design of large wind turbines (three bladed, horizontal axis, variable speed and pitch with an upwind rotor) has evolved over the last 30 or 40 years. It has been designed for onshore conditions where noise and visual intrusion are design drivers so it is thought that different designs of turbine may be better optimized for offshore applications [8]. Onshore, three bladed turbines were selected as a compromise between increased speed of rotation (which decreases the torque for a given power output so the rating of the gearbox can be reduced) and reduced noise (noise increases dramatically as tip speed increases). Three bladed turbines have improved fatigue life compared to two bladed turbines as the loads on the hub are more balanced because tower shadow and maximum wind shear effects do not occur at the same time [9]. Research has also shown that 3 bladed turbines are less visually intrusive [9]. Upwind turbines were chosen so that the effects of tower shadow were less severe, both from a fatigue point of view and because the blade passing the tower is a major source of aerodynamic noise [9]. It is thought that turbines designed specifically for offshore use could be two bladed and downwind, as this would allow a higher rotor speed and thus reduce the cost of the gearbox and generator. Blade stiffness would cease to be such an important design driver because collision with the tower would no longer be a concern and so the blades could also become cheaper. It would also be easier to transport and install two bladed turbines [8].

The power that a turbine can capture from the wind is given by equation (1.1), in which ρ is the density of the air, A is the area swept out by the blades, v is the wind speed and C_p is the power coefficient [9].

$$P = \frac{1}{2}\rho \mathrm{A} \mathrm{v}^3 \mathrm{C_p} \tag{1.1}$$

Of these variables, the turbine designer has control over A and C_p. There is an increasing trend, particularly for offshore turbines, to install fewer large turbines rather than more small turbines in order to reduce the cost of installation and grid connection. This means that the swept area (and therefore the blade length) must increase as C_p is limited to a maximum theoretical value of 0.59 (the Betz limit) and in practice 0.45 is more realistic (the reduction is due to tip losses, stall losses, drag, and the need to balance structural and aerodynamic design drivers) [9]. The cost of the blade and the consequences of failure both become greater as the length of the blade is increased, so it is becoming ever more important to have a full understanding of the loads, the materials and the analysis methods in order to drive down the blade weight (and therefore the cost of energy from the wind turbine) whilst ensuring that the blade performs as intended.

There are several different design standards for wind turbines used around the world. Some of these are national standards, and some apply internationally. The international standards include the IEC standard [10] and the Germanischer-Lloyd guidelines [11]. These are the standards that have been used in this work.

1.3.1 The wind resource

The power available from the wind varies with the cube of the wind speed. This means that it is extremely important to understand the wind resource at a potential site, both from a financial perspective (in order to determine how much energy can be obtained from the wind turbine over the course of its life) and from a loading perspective (in order to understand whether the turbine will be operating within its design margins once installed). In view of this second point, the design standards for wind turbines specify a relatively harsh site compared to what would be encountered in practice. A typical wind farm in the UK would have an annual average wind speed of 7 or 8 m/s at most, and the design standards specify that an average of 10m/s must be used [10, 11] for class I wind turbines. Given that the wind loads vary with the square of the wind speed this is significant. The wind resource at a given site can be characterised statistically, and it has been found that 10 minute average wind speed fits a Weibull distribution well in many places, although seasonal variations sometimes dictate that separate parameters are used for winter and summer [9]. However, the standards [10, 11] recommend that a Rayleigh distribution is used (this is a special case of the Weibull distribution with a shape factor of 2, which is typical of a lot of wind sites).

The wind speed also varies with height in the region in which wind turbines operate because of the boundary layer effect. The standards [10, 11] recommend using a power law to calculate wind speed V at different heights z, given by equation (1.2).

$$V(z) = V_{Hub}\left(\frac{z}{z_{Hub}}\right)^{\alpha} \tag{1.2}$$

The exponent α is the surface roughness. A rougher surface, such as forest, will have a higher value, increasing the wind shear effect whereas a smooth surface like ice or water will have less variation of wind speed with height. Both the GL standard and the IEC standards use 0.2 as the design value for wind turbines in standard classes [10, 11]. Söker et al. investigated the effects of varying the exponent α and found that 0.2 is a fairly high value, resulting in differences between the maximum and minimum root flapwise bending moment being increased by 1.5 times when compared to a site specific value for α of 0.05 [12].

Superimposed on this deterministic wind field is a stochastic component of wind velocity known as turbulence, as shown in Figure 1.1. This component has a zero mean but it cannot be ignored as it is a major source of fatigue loading. Several different models can be used to generate turbulent wind fields, but both standards recommend the use of the Mann model [10, 11].

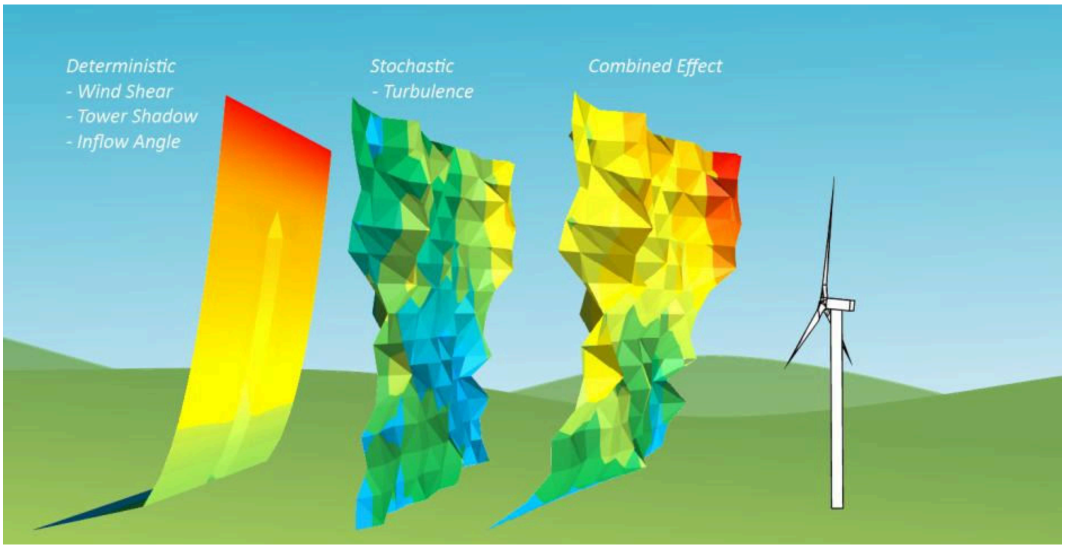

Figure 1.1 - Components of Wind Velocity

The design standards give all the parameters required to model the wind field at different average wind speeds.

1.3.2 Wind turbine blade loading

Wind turbine blades operate in a similar way to an aeroplane wing. Rather than using drag as the driving force, as old fashioned windmills such as those used to pump water on American farms do, they use the lift generated by an aerofoil to create torque. Figure 1.2 and Figure 1.3 show an element of a wind turbine blade [9]. The turbine is rotating about an axis that runs vertically down the page.

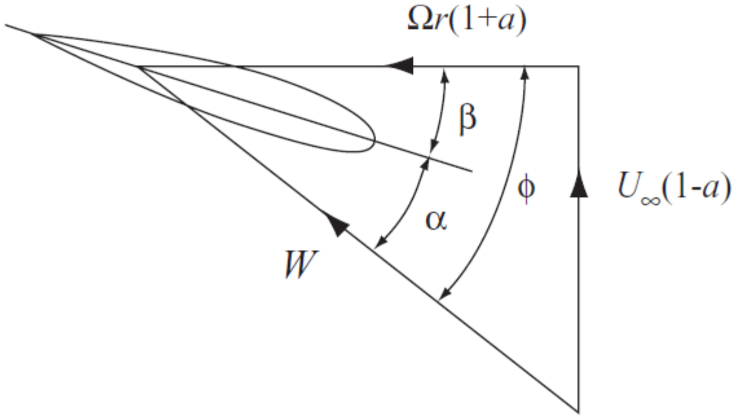

Figure 1.2 - Components of Wind at Rotor [9]

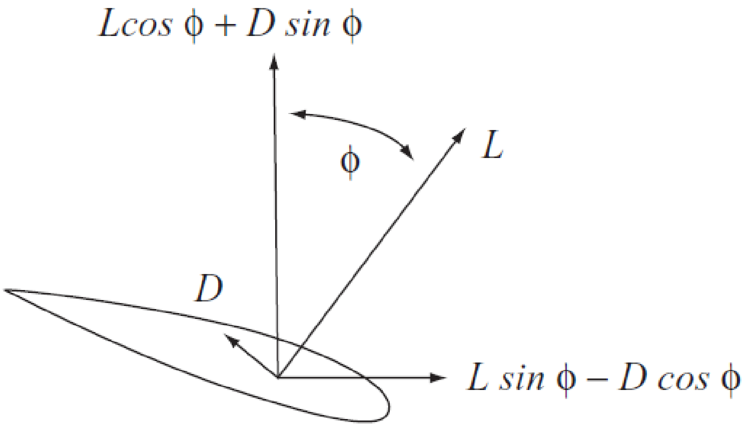

Figure 1.3 - Lift and Drag Forces [9]

Ωr is the speed of the blade due to rotation (r is the distance from the centre of the blade to the element). U_∞ is the wind velocity upstream, W is the apparent wind and a is the axial induction factor, which is defined as the fractional decrease in wind velocity between the free stream and the rotor plane. The angle of attack is denoted by α, and β is the initial set angle of the airfoil (this varies along the length of the blade to maintain an efficient angle of attack, as the tip will have a much higher speed due to the blade rotation than the root). As the angle of attack is varied, the lift and drag forces change. The lift and drag forces can be resolved so they are coherent with the hub coordinate system of the wind turbine (so that they can be used for torque and thrust calculations on the input shaft of the nacelle) or into edgewise and flapwise loads on the blade. The blade element momentum model is usually used to calculate the loads on the blade. A full discussion of the model can be found in [9].

As well as the aerodynamic loads, the blade is also loaded by its own weight and by inertial loads. The whole wind turbine system also has resonant frequencies that will be excited at different levels by turbulence, the blades passing the tower and the effects of wind shear. This must be taken account of when loading calculations are performed.

The complexity of the wind turbine system means that it is not feasible to perform simple hand calculations to assess the loads, and there are several software packages that can simulate a wind field and a wind turbine in order to derive the loads. These will be discussed in section 1.3.4 and section 2.1.

1.3.3 Blade structure

Many materials have been used for wind turbine blade construction. In the early days of the industry, steel was used because of its high stiffness and well understood processing techniques. However, its specific strength (Yield strength/density) is too low and it is too difficult to form twist optimised blades [13]. Aluminium was also used but it was found to be too fatigue sensitive and insufficiently stiff [13]. Wood is widely used on smaller turbines but its properties are generally too variable to produce reliable designs, so although it has excellent fatigue properties it is rarely used in significant quantity for modern wind turbine blades [13].

The prevailing materials for modern wind turbines are composites. They have been selected for their high specific stiffness, good fatigue properties, low density and the ability to tailor the material properties in different directions [9, 13, 14]. E-glass is the most commonly used reinforcement material. Carbon fibre is also occasionally used as reinforcement but although it is stronger, stiffer, more fatigue resistant and less dense than E glass it costs significantly more so its use on commercial wind turbines so far has been limited to local reinforcement and the blade spar [14].

A typical composite wind turbine blade is composed of two mouldings for the suction and the pressure face that make the aerodynamic shape of the blade. These are made as a sandwich structure, with a low density foam or balsa wood core to separate the composite skins which increases the panel’s second moment of area and thus the resistance to buckling [14].

A separate load bearing spar is used to resist the aerodynamic loads, as the blade is thin in the direction that this load is being applied in. This is composed of two spar caps held apart by a shear web, to create an I-beam shape (or sometimes a box shape if two shear webs are used). The spar caps must take high tensile stresses on the pressure side and compressive stresses on the suction side, so they are predominantly composed of unidirectional fibres to resist these forces (some off axis fibres will be used so that the spar caps can take the shear loads caused by the blades self weight) [9, 13, 14]. The shear webs are typically made up of fibres at ±45 to transfer the shear loads and keep the spar caps from moving relative to each other [14].

The whole blade is then finished by adhesively bonding the suction and pressure mouldings to the spar cap, and to each other at the leading and trailing edge [14]. Figure 1.4 illustrates this blade architecture.

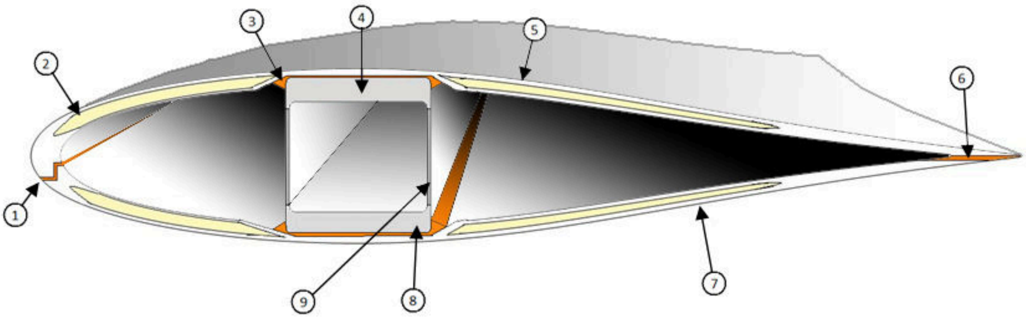

1. *Leading edge adhesive joint*
2. *Sandwich structure with foam core between multidirectional laminates to give good strength in all directions*
3. *Adhesive joint between spar and suction side moulding*
4. *Suction side spar cap, large proportion of 0° fibres to give good properties in compression*
5. *Suction side moulding*
6. *Trailing edge adhesive joint*
7. *Pressure side moulding*
8. *Pressure side spar cap, large proportion of 0° fibres to give high strength in tension*
9. *Shear web, Multidirectional fibres to transmit load between spar caps and resist shear loads*

Figure 1.4 - Typical Blade Structure

The blades are twisted and tapered along their length to maintain an optimum angle of attack and chord length along the length of the blade, and the material thickness varies. This is done in order to keep the strain level along the blade reasonably constant [14] as the forces and moments near the tip are far smaller than those near the root.

1.3.4 Modelling wind turbine blades

The loads that a wind turbine blade will see are not solely down to the blade itself. They are dependent on the design of the whole turbine. For instance, the power electronics and control can have a big influence on the blade loading in the event of a grid loss. With the load removed, the turbine will start to accelerate, meaning that when the grid comes back online (effectively acting as a brake on the shaft) the inertia of the blades causes huge edgewise bending loads.

As such the design procedure for blades starts with the production of a set of load cases produced by aero-elastic software that takes account of the aerodynamic and dynamic structural behaviour of the blades themselves, the inertia of the rotating components in the nacelle, the structural dynamic behaviour of the tower and foundations, the electrical dynamics of the generator, power electronics and the grid, the control system behaviour and the environment (the wind field onshore and wind, waves and tides offshore). This procedure is necessary because the blades will twist and bend under the forces from the wind, thus altering their aerodynamic properties. The load cases are usually derived from time domain simulations of the wind turbine for a sufficient period of time to represent the statistical variation of turbulence. The relevant loads are output as time histories.

Several wind turbine analysis codes are now available, and they are discussed in more depth in chapter 2. Generally they model the turbine structural dynamics using a multi-body formulation or a finite element/ modal analysis approach. The aerodynamic modelling is usually performed using blade element momentum theory, with some codes allowing for a generalised dynamic wake. For offshore devices waves and tides can excite the foundations of the turbine causing additional blade loads. Hydrodynamic loading is usually modelled using the Morison equations [15].

For static stress analyses, finite element analysis is usually used, although a beam stress analysis can be used as a less computationally expensive alternative.

1.3.5 Introduction to fatigue terminology

Once the loads have been calculated using the simulation software described above, the resulting stresses or strains can be calculated using beam theory or a finite element analysis and a fatigue analysis can be performed. This section introduces some basic fatigue terminology which is used later on.

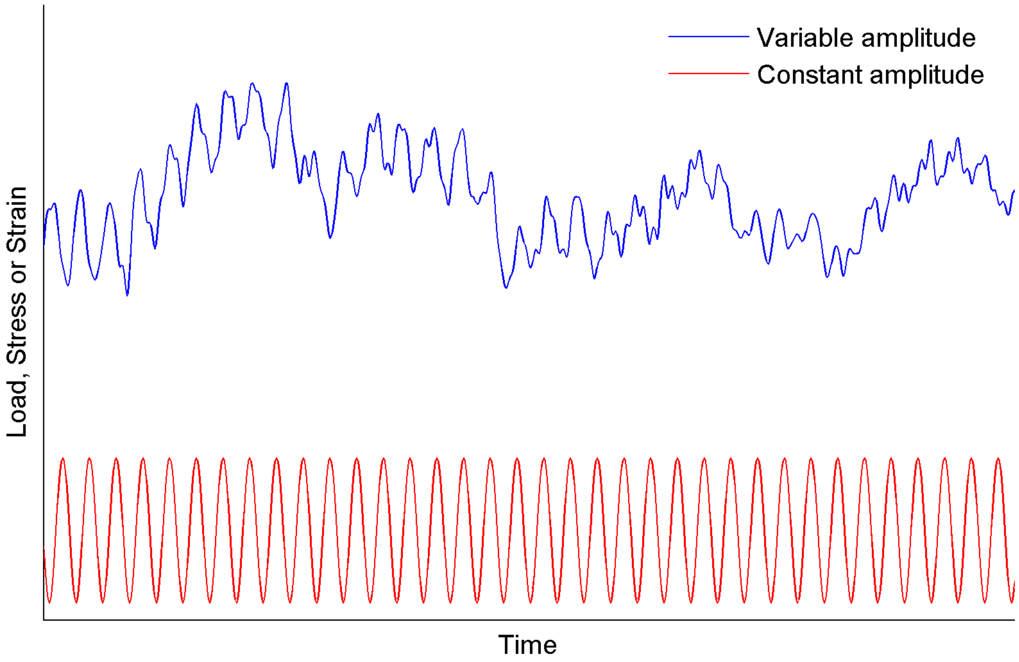

Figure 1.5 – Comparison of variable amplitude and constant amplitude fatigue

Figure 1.5 shows the difference between constant amplitude and variable amplitude fatigue. The variable amplitude time history can be considered as a series of constant amplitude cycles characterised by their amplitude, mean value and frequency. A fatigue analysis is usually based on constant amplitude fatigue test data generated by cycling small coupons of the material until they fail. Typical coupons are shown in Figure 1.6 and a fatigue test rig is shown in Figure 1.7.

Figure 1.6- Fatigue test coupons [16]

Figure 1.7 - Fatigue testing machine [17]

These tests are characterised using the terminology shown in Figure 1.8. The fatigue testing machine may be either load controlled or displacement controlled, resulting in constant stress throughout the test or constant strain respectively (as the stiffness of composites tends to degrade as they are cycled the choice of stress or strain control is important). The stress, strain or load is generally termed ‘S’ and the number of cycles to failure is termed ‘N’. The ratio of the minimum value of ‘S’ in a cycle to the maximum is termed the R-value, as defined in equation (1.3).

$$R = \frac{S_{min}}{S_{max}} \tag{1.3}$$

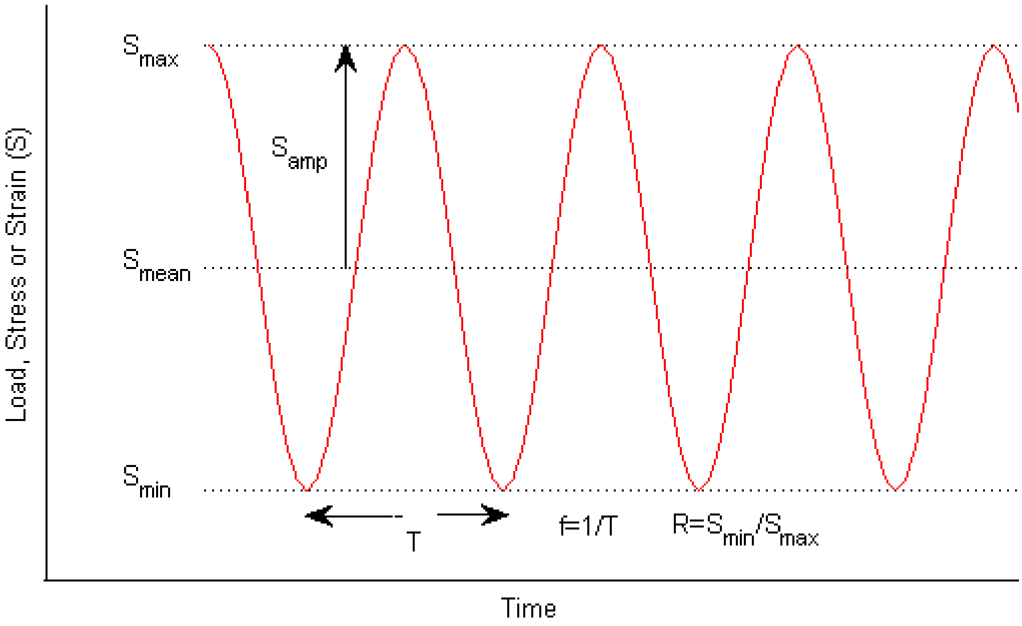

Figure 1.8 - Constant amplitude fatigue terminology

The constant amplitude test conditions can therefore be completely characterised by the R-value, some characteristic of 'S' cycle (the maximum value, the mean value or the amplitude) and the test frequency. Test data from fatigue tests of this type are presented on SN curves.

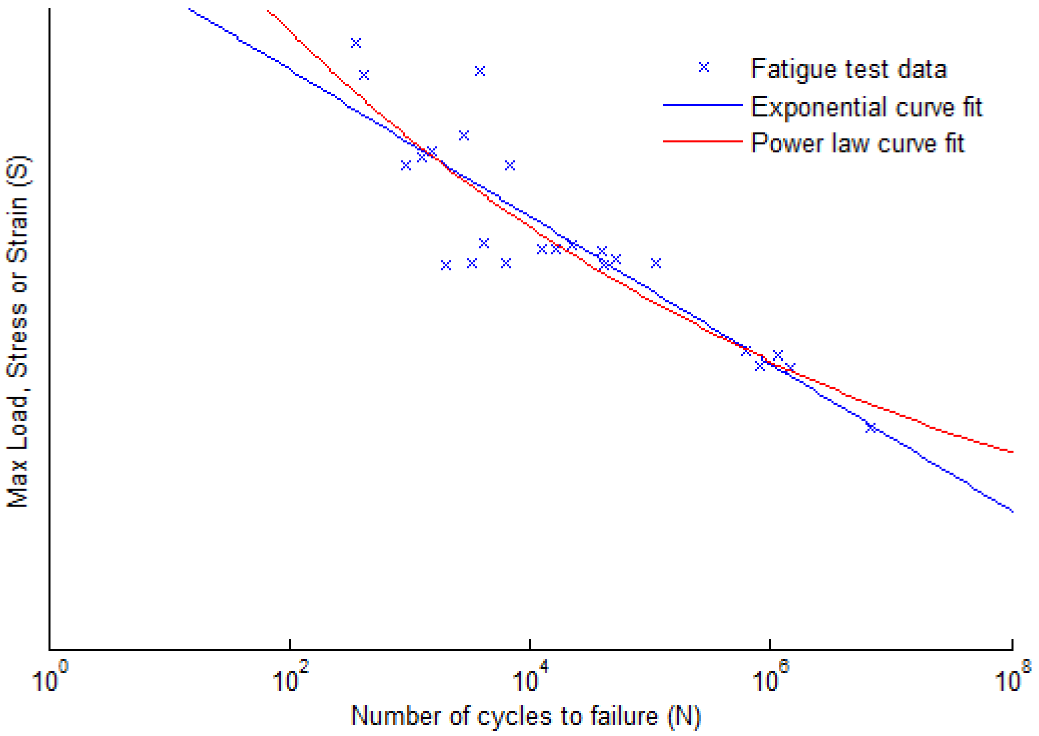

Figure 1.9 - SN curve

As the fatigue data is discrete it is usual to fit a curve to it so that values can be interpolated at loads between those for which test data is available. Figure 1.9 illustrates the exponential curve fit and the power law curve fit, which are the most commonly used. The form of the power law curve fit is given in equation (1.4) and the exponential fit is given in equation (1.5). These are discussed in detail in chapter 3. In both equations, S is the stress, strain or load parameter, N is the number of cycles to failure and A and B are curve fitting parameters. Although in both cases A defines the intercept and B defines the slope they would not be expected to take the same value for both curve fits.

$$S = AN^{-B} \tag{1.4}$$

$$S = A - B\ln N \tag{1.5}$$

Composite materials exhibit very different characteristics depending on whether the applied load is tensile, compressive or some combination of the two. In order to account for this, SN curves are generated for a range of different R-values and the results are presented in a Goodman diagram. The Goodman diagram allows the effect of the mean stress to be considered as shown in Figure 1.10. Goodman diagrams are sometimes referred to as constant life diagrams, as they are defined by isolines of a certain number of cycles to failure. For example in Figure 1.10, the third line in from the outside represents 100 cycles to failure.

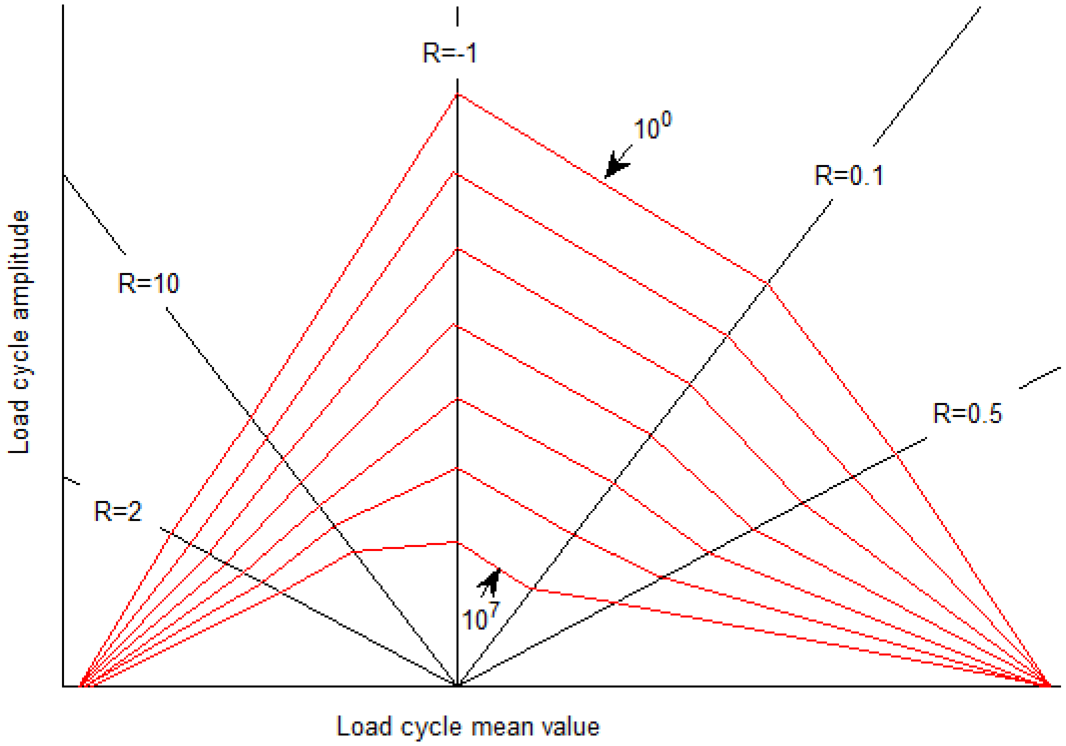

Figure 1.10 - Goodman diagram

The relationship between the Goodman diagram and the SN curves from which it is generated is shown in Figure 1.11.

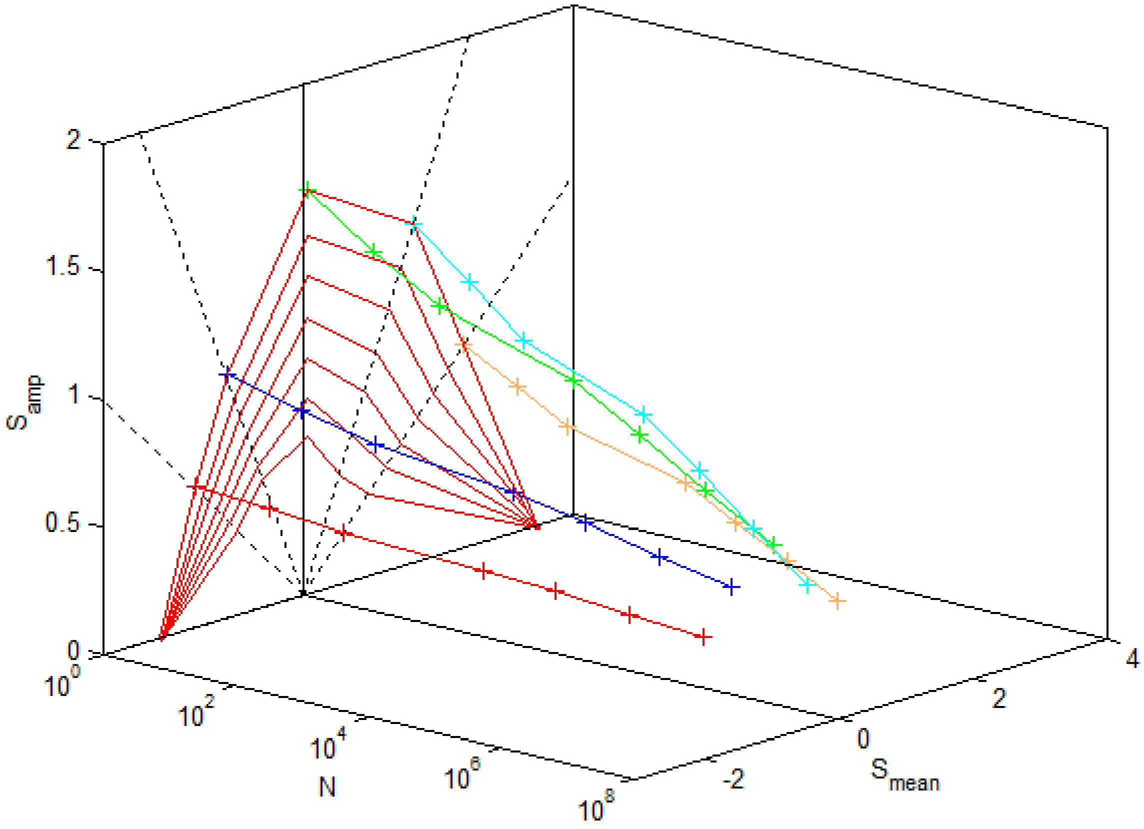

Figure 1.11 - Relation of Goodman diagram to SN curves

When the raw data is plotted on a SN curve, information about the test frequency is lost and when a curve fit is made to the SN plot to create the Goodman diagram further information about the true values of the test loads and cycles to failure is lost. Care must be taken to ensure that the scatter is not so great that the Goodman diagram is meaningless.

A damage accumulation rule is then used to calculate how much damage each cycle does in a variable amplitude time history. Damage accumulation models are discussed in more depth in chapter 2. For full scale testing, the test loads are calculated by finding the constant amplitude load that causes the same amount of damage as the variable amplitude simulated service after a given number of cycles.

1.4 Testing of Wind Turbine Blades

The blades are undoubtedly one of the most critical components of a wind turbine. A catastrophic failure of one blade can lead to the whole turbine being destroyed and widespread damage to the turbine’s surroundings. For this reason, full scale tests are performed on all new designs of turbine blade as part of the certification process to ensure that they are fit to survive the loading that they will encounter in service [10, 18]. These tests involve mounting a production standard blade horizontally from its root and applying appropriate loads to it.

Static tests are generally performed by attaching wooden saddles to the blade at several points along its length. These saddles are shaped so that they fit snugly around the blade profile. Winches attached to the saddles are then used to load the blade such that the bending moment distribution matches as closely as possible the extreme loads that the blade sees in service.

A fatigue test is also performed. During the course of their design lives of 20 years or more, modern multi-MW wind turbines can undergo more than 100 million revolutions. It is impractical to take the blade through this many cycles in a test because even the fastest methods of testing are usually limited to the first natural frequency of the blade, which may only be a few times higher than the blade passing frequency. This means that the test would take several years to complete. To overcome this issue the loads are increased so that an equivalent amount of damage accumulates after around a million cycles, allowing tests to be performed in just a few weeks.

Tests are usually performed in the flapwise (wind excited) and edgewise (gravity excited) directions separately, but in service the two loads occur at the same time. To overcome this issue, multi-axial loading can be used so that the flapwise and edgewise tests are performed simultaneously.

Fatigue tests can be performed in several ways but only two approaches have been adopted widely. Forced displacement testing was the first method to be developed [19] which involves using hydraulic cylinders attached to a fixed structure to cycle the blade back and forth as shown in Figure 1.12. It has the advantage that precise control of the phase angle between the flapwise and edgewise loads is possible if testing both axes simultaneously, but as blades have grown in size it has fallen out of favour because the required forces and displacements make hydraulic systems impractical. Another disadvantage of this test method is that it is often only practical to adopt a single point loading for each axis which achieves an unrealistic linear bending moment distribution.

Figure 1.12 - Dual axis forced displacement testing

The second popular test method is resonant testing, shown in a flapwise configuration in Figure 1.13, which involves using a moving mass that is mounted on the blade to excite it at its resonant frequency. The mass can be moved by hydraulic cylinders or a rotating eccentric mass can be used, usually powered by an electric motor.

Figure 1.13 - Single axis resonant fatigue test

The response of the blade can be tuned by adjusting the amplitude of the motion of the mass if reciprocating motion is used, or by moving the excitation frequency away from or nearer to the blade resonant frequency if the rotating eccentric mass is used. Resonant testing has several advantages over forced displacement testing; it requires far less energy and capital investment, the bending moment distribution can be tuned by adding static masses to the blade to adjust its mode shape and it can be scaled for larger blades. A hybrid resonant/forced displacement dual axis test method was developed at NREL in which the flap loading was imparted using resonance and the edge direction was forced using a hydraulic cylinder driving a bell crank [20]. This method has the advantage of allowing the phase angle between the two loads to be controlled, but it will be difficult to scale for large blades and the edgewise bending moment distribution can only be linear.

The National Renewable Energy Centre in the UK (Narec) has pioneered dual axis resonant testing of blades by exciting the first flapwise mode and first edgewise mode of the blade simultaneously [21] and this approach is now being pursued by others. Desmond and White [22, 23] have performed scaling studies and dynamic analysis on the method, although no fatigue analysis has been published.

The purpose of this work is to build on the work performed by White [20] in order to establish whether or not dual axis testing using resonant excitation represents an improvement over single axis testing.

1.5 Structure of Thesis

This thesis brings together the work performed since January 2010 to investigate fatigue of wind turbine blades. The chapters reflect the different areas of research.

In chapter 1 the motivations for exploiting wind energy are discussed. The reader is introduced to wind turbine design, and more specifically the considerations that are necessary when designing a blade. The different methods of full scale blade testing are also discussed. In chapter 2 a more in-depth review of composite fatigue analysis and testing is performed.

Before it is possible to perform comparisons between different methods of full scale testing it is necessary to understand the damage that is done to the blade by its service life. Chapter 3 explains the approach taken in the present work and draws conclusions about the effect of choosing various different fatigue analysis methods.

Chapter 4 uses the optimal test loads obtained in chapter 3 and details the development of software to optimise blade tests so that the bending moment distribution along the blade length during a test causes damage to the blade that matches as closely as possible the damage caused by the blade service life.

In chapter 5 the test configurations designed in chapter 4 are simulated using a more thorough time-stepping method to ensure that the effects of air resistance and blade twist are properly accounted for. The feasibility of improving the dual axis results by altering the edgewise natural frequency is also investigated.

Chapter 6 investigates an alternative method of fatigue analysis that addresses several of the issues with current fatigue analysis methods that became apparent during the course of the work.

The seventh and final chapter draws conclusions from this work and makes suggestions for future areas of investigation.

There are several appendices containing more detailed information on blades for which data has been used, complete equations, extra results and published papers.

1.6 Original Contribution

Fatigue analysis of wind turbine blades is not simple. The nature of the loading and the complex behaviour of the materials involved mean that there is a lot of uncertainty in the results obtained from both fatigue analyses and full scale testing.

This work has reduced the uncertainty involved in testing the blades by further developing a test method that has been shown to be more representative of what occurs in service than the current approach. The analysis methods used and modelling techniques developed are more advanced than those used in previous analyses, so it is possible to place more confidence in the results obtained.

The kinetic theory of fracture has been shown to address many of the issues with current fatigue analysis methods. Prior to this work there were several aspects of the theory that meant it was not possible to apply it to wind turbine blade analysis, and these have either been addressed or suggestions have been made about how they could be addressed in future.

In summary, the author believes that the work has made a significant contribution to wind turbine blade fatigue analysis and testing.

2 Literature Review

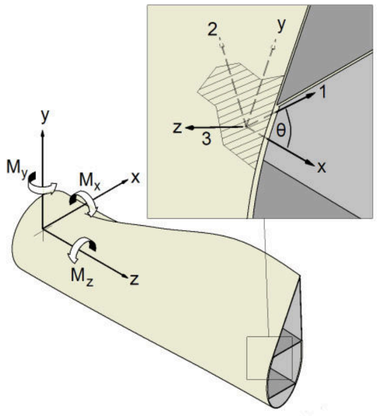

Full scale testing of wind turbine blades is a multi-disciplinary exercise, and it is an area that has not attracted much research.

In order to design the fatigue test it is first necessary to calculate the service life loads. Simulations must be performed using dedicated wind turbine analysis software which has been developed over several decades. There is a great deal of literature on the development of these tools, but as simulation is not the focus of the present work this literature has not been reviewed in-depth, and the reader is directed to established, thorough literature reviews on the subject rather than individual papers. Similarly, the calculation of the fatigue life involves an understanding of fatigue of composites. Again, there is a vast amount of literature in this area, so the focus is on research that is relevant to wind turbine blade analysis and the classic papers.

This literature review is divided into sections according to the process that is followed when designing a fatigue test.

2.1 Wind turbine simulation

Wind turbine simulation is an essential part of the design process for many system components. The analysis methods used have massively increased in complexity since the 1970s, which allows the designer to have more confidence in the results obtained. This increases the competitiveness of wind energy by reducing the size of the design margins.

There are now several commercial and open source wind turbine simulation codes, which have grown out of research performed over the last few decades. These are summarised in Table 2.1.

Code	**Bladed**	**HAWC**	**HAWC 2**	**BHAWC**	**FLEX 5**	**FAST**	**ADAMS**
Licensing	Commercial	Open source	Commercial	In house	Commercial	Open source	Commercial
Aerodynamics	BEM, GDW	BEM, GDW	BEM, GDW	BEM	BEM	BEM, GDW	BEM, GDW
Structural	MBS, FEM	FEM	MBS, FEM	FEM	Modal, FEM	Modal, MBS	MBS
Offshore loads	ME	ME	ME	ME	ME	ME, PFT	ME, PFT

BEM – Blade element momentum theory, GDW – Generalised dynamic wake
FEM – Finite element method, MBS – Multi body simulation
ME – Morison equations, PFT – Potential flow theory

Table 2.1 - Wind turbine simulation tools, simplified from [15]

Bladed is a commercial code with a user interface which is widely used in the wind industry. The structural model has recently been completely overhauled and it now uses a multibody simulation approach [24]. It was used in the present work because it is freely available for academic use and is widely used within the wind industry.

HAWC was originally developed by Petersen [25], and because the formulation is described in full as part of his thesis it forms the basis of many in-house codes. The model assumes linear behavior of the rotor, so nonlinear effects such as centrifugal stiffening (where the axial force developed due to blade rotating acts to reduce the bending moment on the blade) are neglected. Petersen summarised the early (pre 1990) work on wind turbine aero-elasticity, much of which focused on a single blade or the rotor only [25]. His work on a full finite element model of the entire turbine laid the foundations for HAWC, HAWC 2 and BHAWC [26]. HAWC 2 completely overhauled the structural model and it now uses a very general multibody formulation which allows completely arbitrary wind turbine architectures to be modeled. The formulation represents the blade as several connected bodies, so highly nonlinear behavior (for example downwind turbines with very flexible blades) can be modeled [26]. However, the improved modeling capability increases the computational cost.

NREL developed AeroDyn [26], an aerodynamic load calculation tool that interfaces with the multi body simulation software ADAMS [27], and FAST [28], a simulation tool using a similar method to the representation of flexible elements in ADAMS. In FAST, a multibody approach is used with a modal representation of the blades. Only the first two flapwise modes and the first edgewise mode are included, so although the model runs very fast this comes at the cost of accuracy.

Quarton reviewed the evolution of simulation tools over the first 20 years of the industry [29] and concluded that the drivers for the improvement of simulation tools are the increasing power of computers, the trend towards large scale machines and the requirements of the design standards. The research areas identified in [29] are still relevant today; improvements to the understanding of the turbulent wind field, rotor aerodynamics, structural dynamics and power train and control dynamics are all ongoing areas of research [30]. The complexity of shell finite element models of a full blade means that it is rare to obtain loads and perform stress analysis with one model, although this has been done [31].

2.2 Wind turbine blade stress analysis

Once the ultimate and fatigue loads for the blade design in question have been determined using one of the simulation tools described above, a more in-depth stress analysis must then be performed to check whether the blade will be able to survive the service loads. The shell like structure of wind turbine blades described in the previous chapter means that analysis is usually performed using a finite element model, eg. [20, 32-35]. The models are usually built up from shell elements, although it is possible to use brick elements to represent the thicker parts of the blade and the glue eg. [33].

Shell elements are used when the thickness of the structure is much smaller than the other two dimensions. Typically it is not possible to calculate through-thickness stresses, although continuum shell elements do allow these stresses to be calculated at the expense of increasing the complexity of the model. This has implications when modeling composites because delamination (separation of the layers of the composite) occurs due to out of plane stresses.

Brick elements are useful where a structure has to be modeled and it cannot be considered as a shell. In a wind turbine blade this condition may occur at the trailing edge or where there is a thick build up of glue. The benefits of this class of element are increased model sophistication, but this comes at the expense of difficulty in modeling (all that is required for a shell element is a reference surface, for example the blade aerodynamic faces and shear webs). This is problematic for wind turbine blades as the thickness of the laminate changes in steps when plies are dropped or added meaning that very thin elements are required.

There are many pieces of software for streamlining the time consuming process of calculating the laminate properties and building up the blade model. Some of these are independent eg. [36-38], and some have been developed by the blade companies themselves eg. [39, 40]. Stress and strain analysis can also be performed using beam theory to reduce computation time, although the design standards then require additional safety factors [10].

2.3 Composite fatigue analysis

As stated earlier, wind turbine blades are usually constructed from composite materials (predominantly glass fibre reinforced plastic, although blades are becoming available that use carbon fibre reinforced plastic). Fatigue analysis of composite materials is a complicated problem due to their anisotropic strength and stiffness characteristics. If plastic is used as a matrix material then the composite will also be sensitive to changes in the temperature and the test frequency.

Although several reviews on the literature related to composite fatigue modelling are available (see for example [41, 42]), the models will be discussed in detail here as composite fatigue forms a cornerstone of the present work. Composite fatigue models can be broadly categorised as damage accumulation or residual strength models. Micro-mechanics type models form a third category, but they have not been considered here. This is because these models attempt to understand fatigue processes by modeling individual plies down to the level of the matrix and fibre system, and as such are far too computationally expensive to apply to complete wind turbine blades. Also, models which monitor the health of composite structures by looking at the stiffness degradation are not considered as they cannot be used for design purposes.

2.3.1 Constant amplitude fatigue

Constant amplitude fatigue data is characterised by the load amplitude, mean value and frequency [41]. The load can be given as a stress or strain, but for practical reasons the tests are usually controlled in such a manner that the stress remains constant throughout the test [41]. Nijssen [41] performed a thorough and very useful review of the literature on constant amplitude fatigue, and drew interesting conclusions on curve fitting, test frequency, the existence (or non existence) of a fatigue limit, load rate, data scatter and the inclusion of static test data when generating S-N curves. These conclusions are summarised here as they are relevant to the present work.

The choice of fit between exponential (lin-log) and power law (log-log) curve fit was found to be important, with one study finding an increase of 30% in the final design mass when an exponential curve fit is used instead of a power law fit [41]. This is because the low stress cycles have much greater influence if the exponential fit is used. Nijssen found examples of work in which both types of curve fit were said to be the most appropriate [41], but no firm conclusion was drawn on which approach is best. Nijssen generally used a power law curve fit in his own work [41]. In order for data to be fitted in any manner, it is important that the test frequency and the temperature of the coupons are held constant across all load levels. This is rarely achieved in practice.

Nijssen concluded that if the load amplitude was low enough for hysteretic heating to be negligible at elevated test frequencies then an increase in frequency increased the number of cycles to failure (which is consistent with strain rate effects in static testing) [41]. However, if the load amplitude is high then increasing the frequency decreases the life because the coupon fails due to overheating [41].

Nijssen also concluded that a fatigue limit has not been proven to exist for composite materials [41]. However, in order for the exponential curve fit to be used, it is necessary to assume the life increases at low stress, otherwise a finite life will be predicted even at zero load. Nijssen argued that because composites are structures rather than materials, the non-existence of a fatigue limit is sensible [41]. He cites the fact that a fatigue limit exists in steels because failure initiates due to dislocation movement which requires a minimum force to occur, but in a steel structure no fatigue limit is assumed. However, fatigue of composites begins in the matrix which can be considered to be material rather than a structure, and hence may exhibit a fatigue limit. Certainly, a fatigue limit has been said to exist for two commonly used wind turbine composite matrix materials, polyethylene (PE) and epoxy (EP) [43].

There is debate about whether or not to include static failure data when constructing S-N curves. This is because the static test is actually usually only a quarter of a cycle rather than a full cycle, and static tests are generally performed at very different strain rates to fatigue tests [41]. Nijssen concluded that it is unnecessary to include the static data [41].

The constant life diagram (sometimes known as the Goodman diagram) is a method of displaying the effect of mean stress on the number of cycles to failure. The effect of the formulation of the Goodman diagram has been studied by several authors in relation to wind turbine blade materials [41, 44-49].

The consensus is that the linear Goodman diagram recommended by the GL design guidelines [11] does not provide sufficient information to properly characterise the fatigue response and results in life predictions that are grossly inaccurate. Sutherland and Mandell [47] analysed fatigue lives for the WISPER spectrum using Goodman diagrams constructed from various different numbers of R-values, and concluded that a Goodman diagram constructed from R=-2, R=-1, R=-0.5, R=0.1 and R=0.5 was the optimum. This reflects the fact that tensile cycles tend to be more damaging.

There is discussion about how the behaviour at low amplitudes and high mean stresses (creep behaviour) should be represented on the Goodman diagram, as the usual method of tapering all of the constant life lines towards the ultimate tensile stress and the ultimate compressive stress does not allow creep to be accounted for [41, 47, 48].

In summary, the S-N curves and Goodman diagram can have a huge effect on the predicted lifetime, and care must be taken when formulating them.

The variable amplitude load time history is converted to a series of constant amplitude cycles which can be analysed with a Goodman diagram using some kind of cycle counting algorithm. This can be achieved using range-mean counting or rainflow counting (as developed by Matsuiski and Endo [50]). Nijssen studied the effect of cycle counting method, and concluded that rainflow counting was the most appropriate method if it could be used with the chosen damage accumulation model.

The algorithm that is usually used in the rainflow counting approach was developed by Downing and Socie [51]. It is used to reduce a variable amplitude load time history into a series of constant amplitude cycles. The advantage of rainflow counting over range-mean counting (which simply involves moving through a time history of peaks and troughs and looking at the range of each cycle and its mean value) is that it does not miss the large amplitude cycles. Consider a sine wave with noise superimposed on it. Range-mean counting would pick up a series of low amplitude cycles with a varying mean, whereas rainflow counting would see a large amplitude cycle and many small amplitude cycles. The name 'rainflow' comes from considering a time history as a Pagoda roof with rain running down it [50].

2.3.2 Damage accumulation

The simplest and most commonly used composite fatigue analysis methods are derived from methods used for homogeneous materials. A comprehensive review of cumulative fatigue analysis methods for homogeneous materials was presented by Fatemi and Yang [52].

The most commonly used damage accumulation rule is the Palmgren-Miner rule [53, 54]. It states that the accumulated damage of a block of cycles is the number of cycles that occur divided by the number of cycles that would fail the material.

$$D = \sum_i \frac{n_i}{N_i} \tag{2.1}$$

Failure is considered to occur when the value of the accumulated damage (damage sum) is equal to 1. It has been shown to be both non-conservative and conservative when applied to spectrum loading [45], so although it is widely used in the wind industry reasonably large safety factors are required. It can be used with a constant life diagram (sometimes referred to as a Goodman or Haigh diagram) to characterise uni-axial fatigue behaviour for any R-value. The Palmgren-Miner rule is a laminate level method; fatigue testing must be undertaken for every significantly different ply stack in the wind turbine blade if the results are to be useful. It has been used in the present work because it is the method defined in the design standards [10, 11].

Various other damage accumulation models have been proposed since the Palmgren-Miner rule. Marco and Starkey [55] proposed the form:

$$D = \left(\frac{n}{N}\right)^C \tag{2.2}$$

where the parameter C is a function of stress level and R-value. This means that this model is non linear and load order dependent [45]. Extra test work is required to find the value of C.

Owen and Howe [56] suggested the following form of damage equation for glass reinforced polymer composites:

$$D = \sum_i \left[A\left(\frac{n_i}{N_i}\right) + (1 - A)\left(\frac{n_i}{N_i}\right)^2 \right] \tag{2.3}$$

where A is a curve fitting parameter which can be found by fitting variable amplitude fatigue data [45]. This model is load order independent.

Bond and Farrow [57] generalized Owen and Howe's model.

$$D = \sum_i \left[A\left(\frac{n_i}{N_i}\right) + B\left(\frac{n_i}{N_i}\right)^C \right] \tag{2.4}$$

A, B and C are calculated from formulae which use the initial strength and stiffness values. They obtained slightly conservative values compared to Miner's rule for matrix dominated plies, but the results were overly conservative in fibre dominated plies such as those used in wind turbine blades.

The additional complexity of the models with additional curve fitting parameters means that they are rarely used instead of the Palmgren-Miner rule.

2.3.3 Residual strength models

Residual strength models have the benefit that they are linked to a physical property of the material, its strength. The strength of the material degrades by some rule as stress is applied to it, and the material fails in fatigue when a load cycle occurs that causes a stress higher than the residual strength [41, 42]. All residual strength models assume that initial residual strength is equal to the static strength, and that the residual strength is a monotonically decreasing function of the cycles applied. Under constant amplitude fatigue, the residual strength at failure is equal to the applied stress [42].

The first residual strength model for composites was developed by Broutman and Sahu [58]. They proposed a linear reduction in residual strength as shown in equation (2.5) in which S_u is the initial strength, S_r is the residual strength and σ_i is the stress level of the ith cycle. It was found to produce much better results than the Palmgren-Miner rule for two block loading.

$$S_r = S_u - \sum_i (S_u - \sigma_i)\frac{n_i}{N_i} \tag{2.5}$$

The model has the advantage that no further parameters are required beyond those used for the Palmgren-Miner rule.

Hahn and Kim [59] were the first to assume that the specimens with a higher static strength would have a higher fatigue life, and this was referred to as the strength-life equal rank assumption (SLERA) by Chou and Croman [60]. Many residual strength models make use of this assumed property to draw conclusions about the statistical fatigue properties of a material. The SLERA cannot be shown to be true, because it is impossible to perform both a static test and a fatigue test on a specimen.

Sarkani et al [61] generalised residual strength models by using the fact that in many models the rate of change of the residual strength is a monotonically decreasing function of the cycles applied. Wahl [49] used a variant of this generalised non-linear model in his extensive study of the material DD16 from the DOE/MSU composite materials database [62]. Schaff and Davidson used a two parameter Weibull distribution to represent the life distribution and strength distribution after a constant amplitude load history [63].

Nijssen [41] used the generalised model adapted to deal with compressive and tensile stresses. It was assumed that the tensile strength degradation had no impact on the compressive strength degradation. He concluded that residual strength models did not represent a significant improvement over linear damage accumulation and efforts should be focused on characterising the material at a broad range of R-values.

The phenomenological approaches described above ignore the physical processes that cause fatigue. Reifsnider and co-workers have investigated the microscopic effects that result in macroscopic property degradation [64]. The model developed as a result is based on a critical element approach [65]. The critical element is the one that fails last, typically this would be the 0° layer for tensile fatigue. Failure of the non critical layers has the effect of increasing the stress carried by the critical layer. Subramanian et al [66] extended the critical element model to account for the fibre-matrix interphase region. They obtained good results for the data set used. Song and Otani [67] modelled failure of cross ply laminates using a critical element approach. The model agreed well with experimental results.

Philippidis and Passipoularidis reviewed several different residual strength models and concluded that the simplicity and reduced amount of experimental data required by the Broutman-Sahu model meant that it was preferable [68]. More recently, they have developed and validated a piece of software called FADAS [69] that could predict failure of multidirectional laminates from unidirectional lamina results. The software performed well when applied to spectrum loading.

Post reviewed a wide array of damage accumulation, residual strength and micro mechanics based fatigue models [42]. He later developed his own phenomenological model that accounted for the fact that failure mechanisms are different in tension and compression, and also that compression and tension loading can interact (compressive damage can increase the rate of tensile residual strength degradation). It required laminate level characterisation.

2.3.4 Kinetic theory of fracture

Recently, a method has been developed that must be considered as separate to damage accumulation and residual strength. Fertig and Kenik [70] presented a fatigue model based on the kinetic theory of fracture. They used multi-continuum theory to break the composite stress in the material down into the matrix stress and the fibre stress, arguing that most of the time in composite fatigue is spent developing cracks in the matrix, with the fibres only failing when the matrix is no longer able to distribute the load between them. For this reason the matrix stress was used as the relevant quantity, with the stress tensor resolved into an effective scalar stress based on the static failure envelope. The kinetic theory of fracture is then used to calculate when the matrix cracks will cause failure.

This approach has several advantages over a conventional fatigue analysis. It allows creep, temperature and test frequency effects to be accounted for, and fatigue and static results can be considered together. Also, as the approach is ply level rather than laminate level less physical testing is required to characterise a material and multi-axial stress states can be analysed without extra testing [71].

The earliest physical theory for fracture was the Griffith equation [72], which is applicable only to brittle materials, and over-predicts the strength of ductile materials. Experimental results based on, for example, the emission of free radicals [73], show that degradation is not instantaneous but that in fact molecular defects develop with time. Aleksandrov [74] and Gurevich [75] introduced time dependency to describe the viscoelastic properties of liquids and solids. Tobolsky and Eyring [76] must also be credited with work which eventually contributed to the kinetic theory of fracture developed by Zhurkov and co-workers [73, 77-80]. The theory is usually presented in the form shown in equation (2.6) in which τ is the time to failure, σ is the applied stress, T is the absolute temperature and k is the Boltzmann constant. The remaining variables in the equation have simple physical meanings; τ_0 is the period of the atomic vibration, U is an activation energy (of the order of, but generally smaller than, the disassociation energy), and $\gamma\sigma$ is the induced decrease in the activation energy due to the mechanical load.

$$\tau = \tau_0 \exp\left(-\frac{U - \gamma\sigma}{kT}\right) \tag{2.6}$$

A huge volume of work on the kinetic theory of fracture was built up in Soviet Russia during the latter part of the 20th century, and the reader can refer to review papers such as Regel et al [81] for more details. Zhurkov's major accomplishments include showing that equation (2.6) is valid at the macroscopic level as well as the microscopic level (it is thought that γ accounts for the average correlation between the overall stress and the local stress on the molecule being broken [82]). This explains why γ is different depending on the state of the material (e.g. annealed, rolled etc.) whereas U remains constant [81]. Zhurkov also performed experiments to show that τ_0 corresponds to the period of atomic vibration for a wide range of materials [73], and performed experiments at different temperatures to establish the effect of temperature [73]. Fatigue has been addressed using the kinetic theory of fracture before the work of Fertig and Kenik [71]. Regel used static time-to-fail material properties to predict fatigue life, and found that the theory predicted fatigue well if the temperature was maintained [83]. The theory has also been applied to wind turbine blade materials by Mishnaevsky and Brøndsted [84], although the effective stress was assumed to be the overall composite stress rather than the matrix stress, resulting in rather poor results that could not be used other than to draw conclusions about frequency effects.

Although equation (2.6) applies for a wide range of conditions, there are still unresolved issues with the kinetic theory of fracture [81]. At low stresses, recombination and material instability mean that the log of the time to failure does not appear to be linear with stress [73, 81]. Von Schmeling attempted to describe this behaviour whilst still maintaining the physical basis of the kinetic theory, but his approach still required time to failure data at low stresses to be available in order to perform curve fitting [85]. This means that the experiments can be very time consuming.

2.4 Full scale blade testing

Full scale testing of blades is a relatively new field, so the literature is somewhat limited. However, since 1990 reports have been published from various test houses which allow an understanding of how the current methods have been arrived at.

Forced displacement testing was developed independently at NREL in the United States, CRES in Greece and ECN in the Netherlands [19, 86, 87]. Resonant testing was mainly developed in Denmark [88].

During the oil crisis of the 1970s wind power became very popular in Denmark. The movement was characterised by "self builders" who built turbines from scratch, although the blades were often purchased from established manufacturers [89]. In the very early days of the industry static testing was performed by placing sandbags along the blade length to mimic the bending moment distribution seen in service as shown in Figure 2.1.

Figure 2.1- Static blade tests using sandbags, 1978 and 1981 [89]

As the industry grew, it was recognised that fatigue was an issue. AeroForm blades built a fatigue test facility at Sparkær in Denmark which is still in operation today, and still using the same rotating eccentric mass resonant excitation system [88]. Figure 2.2 shows a fatigue test in progress. The black boxes in the blade contain the rotating eccentric masses. The tests were monitored by a microphone connected to loudspeakers in the owner's bedroom!

Figure 2.2 - Fatigue tests at Sparkær, 1984 [89]

The rotating eccentric mass resonant excitation system is by far the most energy efficient method of testing blades because the motion is rotary rather than reciprocating, which is one of the reasons that its use has continued for such a long time. However, it does tend to introduce unwanted local bending moments at the load introduction point as the axis of rotation is offset from the neutral axis of the blade.

Jensen et al [90] published fatigue testing results of an 8.5m blade and detailed the calculation of the test loads.

Since 1990 blades have been tested at the National Renewable Energy Laboratory (NREL) in Golden, Colorado [87]. Fatigue tests have been performed since 1993 [86].

Musial and Allread [86] published their test methodology for single axis forced displacement tests of an 8m blade and a 7.2m blade. The tests were performed after static testing, and the loading was designed to match the bending moment distribution over the first 40% of the blades as this was the region that was determined to be fatigue critical. They encountered several issues that are not present when testing is performed at the coupon level such as choosing the correct load introduction point, dynamic effects, test control, data acquisition and failure monitoring. Musial et al [87] later published a summary of their blade test software development which addressed many of these problems. The knowledge gained from these early tests at NREL allowed them to develop a dual-axis forced displacement rig in 1999 [91]. The dual axis forced displacement rig at NREL has produced some interesting results; a direct comparison between fatigue tests of two blades of the same design was made for single axis testing and dual axis testing [92]. The single axis test (in which the flapwise and edgewise loads were applied in phase by a single actuator) resulted in the blade failing an order of magnitude earlier than in a test in which the edgewise and flapwise loads were applied separately with a realistic phase angle between them. Unfortunately, the flapwise and edgewise loads were never applied separately for comparison.

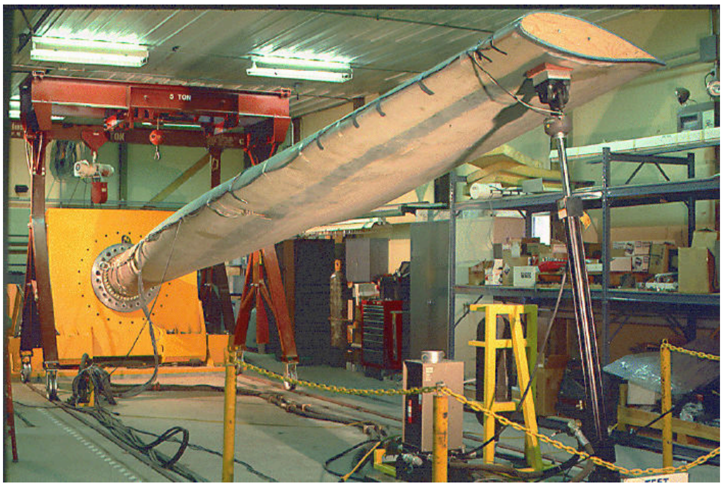

Figure 2.3 – Single point forced displacement testing at NREL, USA [18]

Figure 2.4 - Forced displacement testing with multi point loading at CRES, Greece [18]

The full scale blade test standard [18] was developed to ensure that different test houses around the world adhered to best practice when testing blades. The standard was written in 2002 at a time when there were only a few test houses, and several different blade test methods were in use. In order that the standard is not unfair to any one test house it does not specify which test method to use, and instead summarises the strengths and weaknesses of the different approaches. The standard assumes that horizontal axis blades are being tested for which the equivalent loads are already known.

For fatigue, the standard requires that safety factors be applied to account for errors in the fatigue formulation, blade to blade variation and consequences of failure. Combined together, these result in an increase over the design equivalent load of 1.33.

The standard also recommends that the fatigue test or tests be performed after the static tests. A residual strength test is then performed after the fatigue tests. This has implications for predicting the fatigue response, as the static test will cause damage which will reduce the stiffness of the blade. It is also acknowledged that unless edgewise tests are performed together with flapwise tests then the results will not be representative of what is seen in service.

Figure 2.5 - Resonant testing using rotating eccentric mass at Sparkær [93]

Kristansen and Jørgensen performed accelerated fatigue testing of three different 19.1m blades manufactured by LM Glasfiber [93]. On one of the blades the loads were increased by almost 50% over that which would be used for a 5 million cycle test; the patterns of damage over the blade were monitored using thermal imaging equipment and the damage occurred in the same places as in a conventional test. The authors concluded that greatly accelerating tests was reasonable if it is done in blocks so that it is possible to check that hotspots occur in the same places as the load is increased.

Several authors have attempted to model blade fatigue tests. The key factors that must be considered when performing a blade test simulation include the structural modelling of the blade itself, the modelling of the actuators, structural damping and aerodynamic damping.

White et al [94] performed analysis on simulated load time histories to obtain the distribution of the phase angle between the flapwise and edgewise loads. They then used simple fatigue analysis methods to obtain equivalent alternating strains around the blade cross sections, and performed damage analysis using these data. It was found that the phase angle between the flapwise and edgewise loads had a major effect on the amount of damage that accumulates around the blade. This finding was consistent with the dual axis forced displacement physical tests at NREL [91]. The simplicity of the fatigue analysis performed by White et al [94] was justified as the study was only meant to return general trends. However, subsequent research has identified that it is very important to properly take account of the R-value (minimum strain/maximum strain) for each cycle. Nijssen [41] and Sutherland et. al [47, 48] both performed material testing that showed that the Goodman diagram must characterise the damage behaviour at a properly representative range of R-values if reliable predictions of fatigue failure are to be made.

As part of his research at NREL, White developed a hybrid resonant and forced displacement actuation system [20]. The flapwise loads were applied by a hydraulic resonant mass and the edgewise loads were applied using a hydraulic cylinder driving a bell crank. The phase angle between the two loads could be controlled [20]. He also developed an optimisation routine to match the bending moment distribution seen in service as closely as possible by adding static masses to the blade.

The National Renewable Energy (Narec) in the UK originally licensed the NREL hybrid excitation method when it was first set up in 2003 [32]. This method was developed by Narec by reducing the size of the exciting equipment and mounting it in-line with the neutral axis of the blade. This reduces the local moment induced by the excitation equipment and allows dual axis resonant testing to be performed because the test equipment is balanced on either side of the blade.

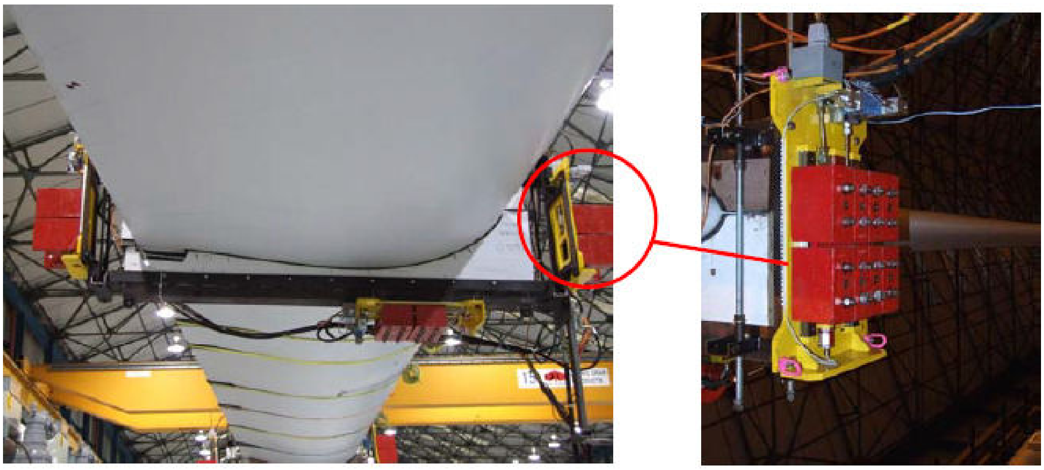

Figure 2.6 - Dual axis compact resonant mass set up at Narec, UK [32]

Court et al [32] performed a simulation of dual axis resonant testing using a shell element model developed by the Rutherford-Appleton laboratory (RAL). The simulation results were compared to a physical test and the general behaviour was seen to be the same. Structural damping was represented using Rayleigh damping, and the damping due to air resistance was ignored which is a major flaw with this study. The blade was not of the same design as the finite element model so firm conclusions could not be drawn from the modelling exercise, but the fact that the blade tip traces out a Lissajous curve dictated by the blade twist, the amplitude of the flapwise and edgewise motion and the two natural frequencies was confirmed. Also, the fact that a full brick and shell element model was used and that the excitation equipment was properly modelled means that this is still a very relevant piece of work. The authors also noted that an implicit linear analysis yielded identical results to more complicated simulations.

Ridley [95] simulated a single axis flapwise test of a 40m blade using a multi-body simulation. Air resistance was accounted for, but unfortunately sectional data was not available for the blade for which physical test data was available. However, by adjusting the structural characteristics of the blade to match the physical test data she was able to perform scaling studies.

Desmond and White [23] performed scaling studies to predict the tip displacements that would need to be accommodated in the design of a future blade test facility for large turbines. They used a finite element model of the blade and found good agreement with historical data. They predicted tip deflections of around 5m for a 100m blade fatigue test.

They also used a finite element model and multi-body simulation to investigate dual axis resonant fatigue testing [22]. The beam finite element model analysed flap and edge separately, so the results were not as good as those obtained with the multi-body simulation. The results were compared to a physical test using accelerometers to check the mode shape and were found to be in reasonable agreement. A similar damage analysis was used to [20], so it was rather simplified.

More recently, Malhotra [96] presented a review of current blade test systems and proposed a new design of edgewise actuation system that eliminates some of the problems with the NREL hybrid dual axis excitation system by actively positioning the edgewise actuator so that it is always level with the load introduction point. This has both capital and energy cost implications and would probably not be feasible for very large blades.

White et al [97] attempted to model the effect of increasing the flapwise stiffness through the use of a spring attaching the blade to the floor located around the mid-span of the blade. The spring stiffness needed to be so great that the blade was effectively built in at the point at which the spring was added, so this method was ruled out. Forcing the blade in the edgewise direction at the flapwise frequency was also considered but the hydraulic requirements were found to be very high.

2.5 Summary and Conclusions

Fatigue of wind turbine blades has been identified as a multi-disciplinary problem. The literature on wind turbine simulation and wind turbine blade stress analysis has been reviewed as these areas are both relevant to the current work.

The literature related to fatigue of composites has been reviewed in some depth, and it is clear that there are shortcomings with the methods of fatigue analysis that are currently recommended by the design standards.

Full scale testing of blades is a relatively new field but published work on the subject does exist and this literature has been reviewed. The most promising method of fatigue testing for the next generation of very large blades appears to be resonant testing as it is much more scalable than forced displacement testing. However, dual axis resonant fatigue testing has not been studied in any depth.

3 Wind Turbine Blade Fatigue Analysis

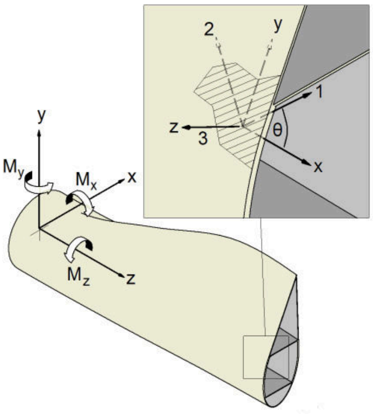

3.1 Introduction

In order to draw conclusions on the performance of different methods of wind turbine blade fatigue testing it is first necessary to understand the damage that is done to the blade during its service life. To this end, fatigue analysis performed according to the design standards [10, 11] is presented here. The results have then been compared with predicted results from different fatigue test methods.

Fatigue analysis has been recognised as a critical part of the design process for wind turbine blades since the middle of the 1980s [98]. In the current dominant design of wind turbine (three bladed, upwind rotor, variable speed/ variable pitch device) the blades are often not fatigue critical due to the high stiffness required to stop them clipping the tower during an extreme gust. However, this cannot be taken for granted, particularly as the size and weight of blades increases. Furthermore, the move to place turbines offshore means that the turbine designer is able to consider turbine designs that would not be able to be installed on land due to visual and noise design drivers; if these constraints are removed, then the rotor can be two bladed and downwind of the tower. Although this may result in a lower cost of energy, it does make the blades much more fatigue critical – they will complete more revolutions, have higher loads, be heavier, and the effect of tower shadow and wind shear will be greater. The blades could also be less stiff than they currently are as they will not be able to clip the tower. Fatigue analysis of blades is therefore more important than ever before.

3.2 Method

The fatigue analysis methodology is dictated by the UK and international design standards [10, 11], and is described below. The basic procedure used is as follows:

- Define turbine and blade properties in wind turbine simulation software.
- Simulate fatigue load cases required by the design standards.
- Use cross-sectional loads obtained to perform a beam strain analysis at 36 points around the blade section.
- Rainflow count strain time histories.
- Look up number of cycles to failure for each strain cycle.
- Calculate damage caused by each cycle using the Palmgren-Miner linear damage assumption.

The test loads are then calculated and the predicted damage caused by the service life was compared to the predicted damage caused by various different full scale fatigue test methods. The procedure is described in more detail below.

3.2.1 Load cases

In this analysis BS EN61400-1: Wind Turbines – Design Requirements was used to define the wind conditions and fatigue analysis methodology [10]. Where necessary, additional information was obtained from the Germanischer-Lloyd Guidelines for the Certification of Wind Turbines [11].

The basic parameters for wind turbine classes are shown in Table 3.1. The parameter V_{Ref} is the reference wind speed for each class, which is the maximum 10 minute average wind speed expected during 50 years of operation for the given class. The expected value of the turbulence intensity at 15m/s is given by I_{Ref} [10]. The turbulence intensity is the ratio of the wind speed standard deviation to the mean wind speed, determined from the same set of measured data samples of wind speed, and taken over a specified period of time [10].

Wind turbine class	**I**	**II**	**III**
V_{Ref} (m/s)	50	42.5	37.5
A - I_{Ref} (15m/s)	0.16		
B- I_{Ref} (15m/s)	0.14		
C- I_{Ref} (15m/s)	0.12		

Table 3.1-Wind turbine classes [10, 11]

The turbine used in this analysis was in the wind class 1A. This means that the reference wind speed was 50m/s, the turbulence intensity was 0.16 and the annual average wind speed was 10m/s [10].

The first step in the analysis is to derive load time histories for all the load cases required by the design standards for fatigue; these are defined in Table 3.2 (NWP stands for normal wind profile and NTM stands for normal turbulence model, V_{In} is the cut-in wind speed, V_{Out} is the cut-out wind speed and V_{Hub} is the 10 minute average wind speed at hub height) [10, 11].

Load case	**Wind conditions**	**Germanischer-Lloyd load case number**	**BS EN61400-1 load case number**
Normal power production	NTM $V_{In}< V_{Hub}<V_{Out}$	1.2	1.2
Normal power production plus fault occurrence	NTM $V_{In}< V_{Hub}<V_{Out}$	2.3	2.4
Normal start-up	NWP $V_{In}< V_{Hub}<V_{Out}$	3.1	3.1
Normal shut-down	NWP $V_{In}< V_{Hub}<V_{Out}$	3.1	3.1
Parked	NTM $V_{Hub}<0.7V_{Ref}$	6.4	6.4

Table 3.2 - Fatigue load cases [10, 11]

The standards assume a wind speed distribution, and the life of the turbine can be represented by simulating the turbine’s operation at mean wind speeds and then calculating how often each load case will occur using this wind speed distribution, which is referred to as ‘binning’ the load cases. For fatigue analysis it is required that the wind speed bins are no larger than 2m/s [10]; for this analysis a bin size of 1m/s was used to increase the accuracy. The highest wind speed for a fatigue load case is 35m/s, as this is $0.7V_{Ref}$ (for a class IA turbine) as shown in Table 3.2. This means that in total 35 normal power production and parked simulations are required, plus the start-up and shut-down simulations. The Mann turbulence model was used in the Bladed wind turbine simulation software package [24] to generate 35 3D turbulent wind fields, with average wind speeds ranging from 1m/s to 35m/s. All parameters were those defined in [10].

Simulations one hour in length were used so that turbulence events that would be missed in a shorter analysis are accounted for. The turbine model control strategy resulted in the turbine being operational in wind speeds above 4m/s and below 25m/s inclusive, and parked otherwise. The azimuth angle of the rotor in the parked simulations was randomly selected. As no information about the turbine control strategy was available, no simulations of fault occurrences could be performed. This also meant that the number of starts and stops per year could not be calculated. The Germanischer-Lloyd design guidelines [11] specify 1000 start-up and shut-down events at the cut in wind speed, 50 start up and shut downs at the rated wind speed and 50 at the cut out wind speed if the number of start-up and shut-down events cannot be predicted.

A Rayleigh wind speed distribution with a mean wind speed of 10m/s was assumed as specified in [10]. The probability that the turbine is operating in each wind speed bin was calculated using equation (3.1) [10], in which V_{Ave} is the annual average wind speed and V_{Hub} is the 10 minute average wind speed.

$$P_R(V_{Hub}) = 1 - \exp\left(-\pi\left(\frac{V_{Hub}}{2V_{Ave}}\right)^2\right) \tag{3.1}$$

A 25 year design life was assumed as the standards specify at least a 20 year life [10, 11], and most manufacturers design for a 25 year life. This means that the number of occurrences of each load case (35 1 hour parked and power production load cases and 6 start-up and shut-down load cases) can easily be calculated by multiplying the probability that the wind speed lies within a bin by the total turbine design life in hours. Figure 3.1 shows the number of occurrences of each load case. The first 35 load cases represent 1 hour of operation at wind speeds ranging from 0.5m/s to 34.5m/s, and the final 6 load cases represent start up and shut down operations at the cut-in wind speed, rated wind speed, and cut-out wind speed.

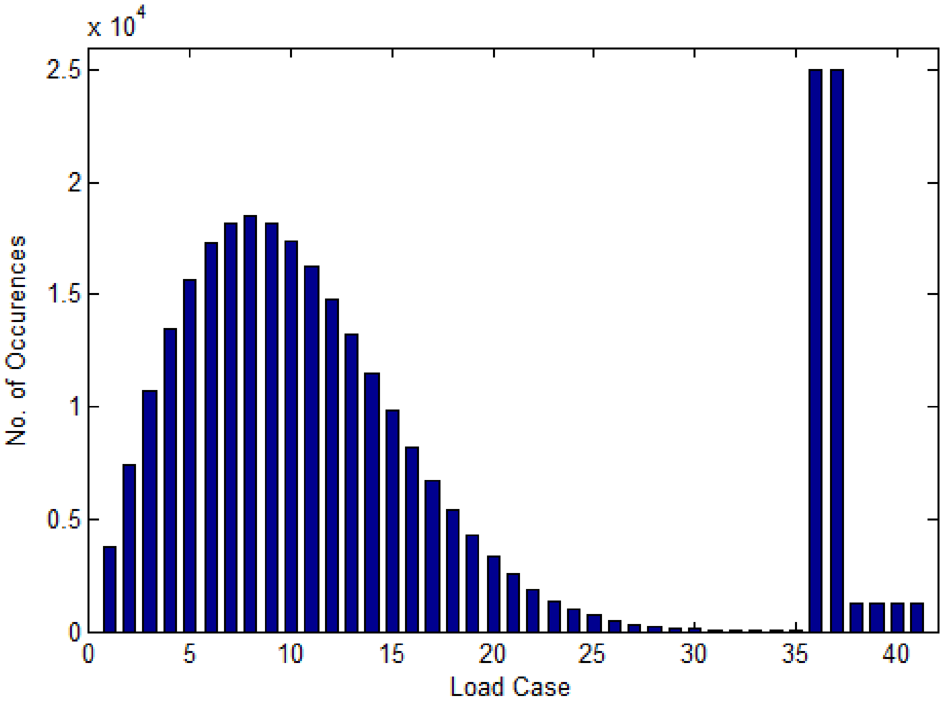

Figure 3.1 – Load Case Distribution

3.2.2 Turbine Model

The Bladed software developed by Garrad Hassan [24] comes with a 2MW demonstration turbine and this was used as the basis for the calculations. In depth detail of the turbine model is given in appendix A. As the blade properties are of the most interest these are summarised in Table 3.3. The blade planform is shown in Figure 3.2.

Distance from root (m)	Chord length (m)	Aerodynamic twist (°)	Thickness (% chord)	Pitch axis (% chord)	Neutral axis (% chord)	Mass/unit length (kg/m)	Flapwise EI (Nm^2)	Edgewise EI (Nm^2)
0	2.07	0	100	50	50	1084.77	7.47e9	7.47e9
1.15	2.07	0	100	50	50	369.81	2.61e9	2.43e9
3.44	2.76	9	64	38	38	277.36	2.09e9	1.41e9
5.74	3.44	13	40	29	29	234.21	1.43e9	8.34e8
9.19	3.44	11	30	29	29	209.56	1.29e9	5.56e8
16.07	2.76	7.8	22	29	29	172.58	5.65e8	2.09e8
26.41	1.84	3.3	15	29	29	103.55	1.22e8	2.95e7
35.59	1.15	0.3	13	29	29	55.47	2.43e7	2.26e6
38.23	0.69	2.75	13	29	29	40.68	4.52e6	1.14e5
38.75	0.03	4	13	29	29	24.65	8.17e3	3.13e3

Table 3.3 – Bladed demonstration turbine blade properties [24]

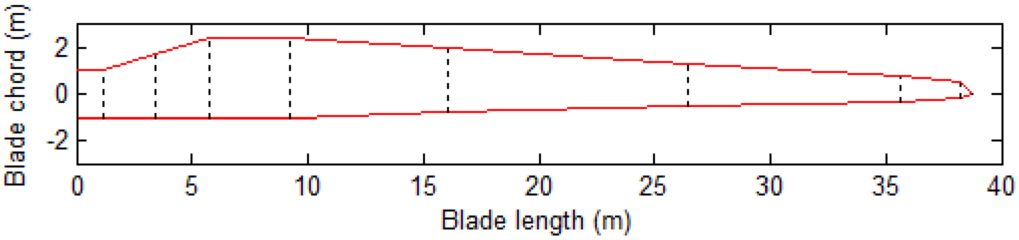

Figure 3.2 – Blade planform

Coordinate data for the aerofoil used on this turbine was obtained from [99] and used to generate a series of 36 points around each of the 8 blade cross sections shown by dotted lines in Figure 3.2, which are ordered from root to tip. A circle was used for the first cross section as shown in Figure 3.3, with the remaining sections being calculated from the original cross section data by scaling the chord and thickness as shown in Figure 3.4 and Figure 3.5. The neutral axis of the section was used as the origin in each case. No design information for the blade beyond the data given in Table 3.3 was available, so the internal structure of the blade is not known. However, because the method of fatigue analysis defined in the design standards [10, 11] specifies that only the axial strain due to the bending and axial loads needs to be considered this is not a problem because the greatest strains occur on the blade surface.

Bladed represents the blade using a beam element model, and so it is possible to output a time history of the forces and moments acting on each blade cross section. The flapwise and edgewise bending moments, flapwise and edgewise shear forces, axial force and torsional moment were output for each of the 41 load cases and 8 blade cross sections (the tip has no forces or moments acting on it so it was disregarded, and the root will have substantially different fatigue properties to the rest of the blade because of the root bolting arrangement). The design standards [10] specify a value of 1 for the partial load safety factor for fatigue so the loads are unchanged.

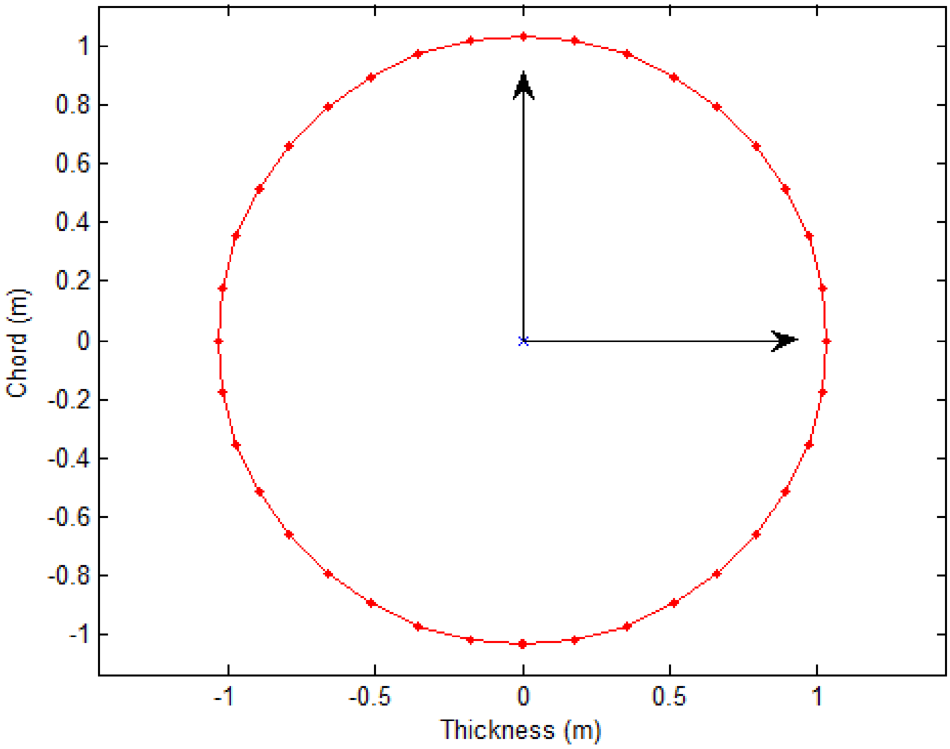

Figure 3.3 – Analysis points at 1.15m from root

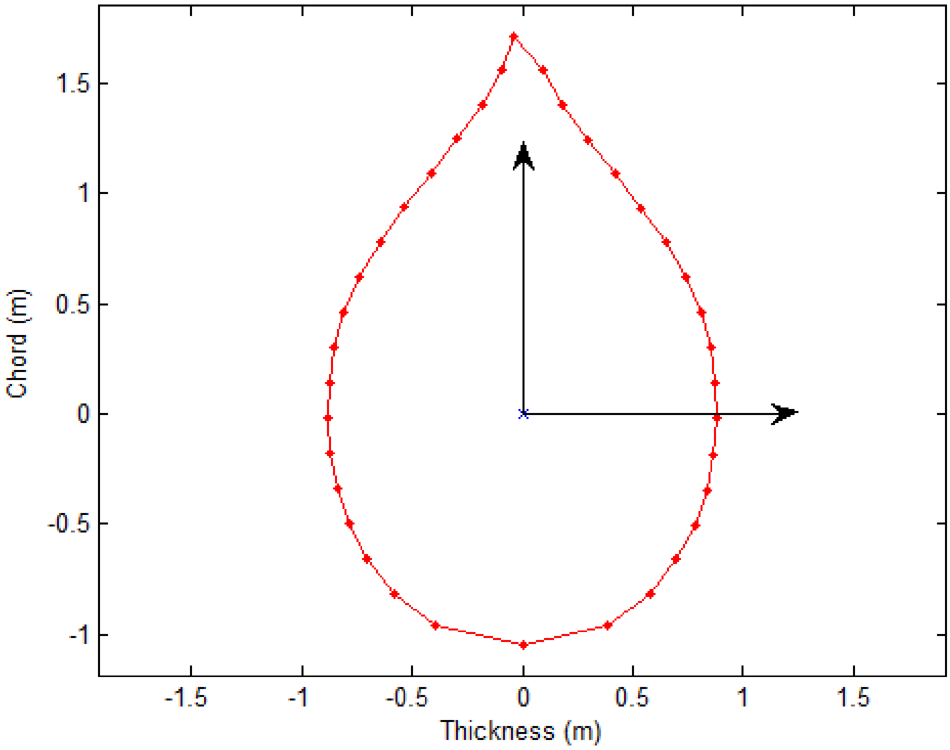

Figure 3.4 – Analysis points at 3.44m from root

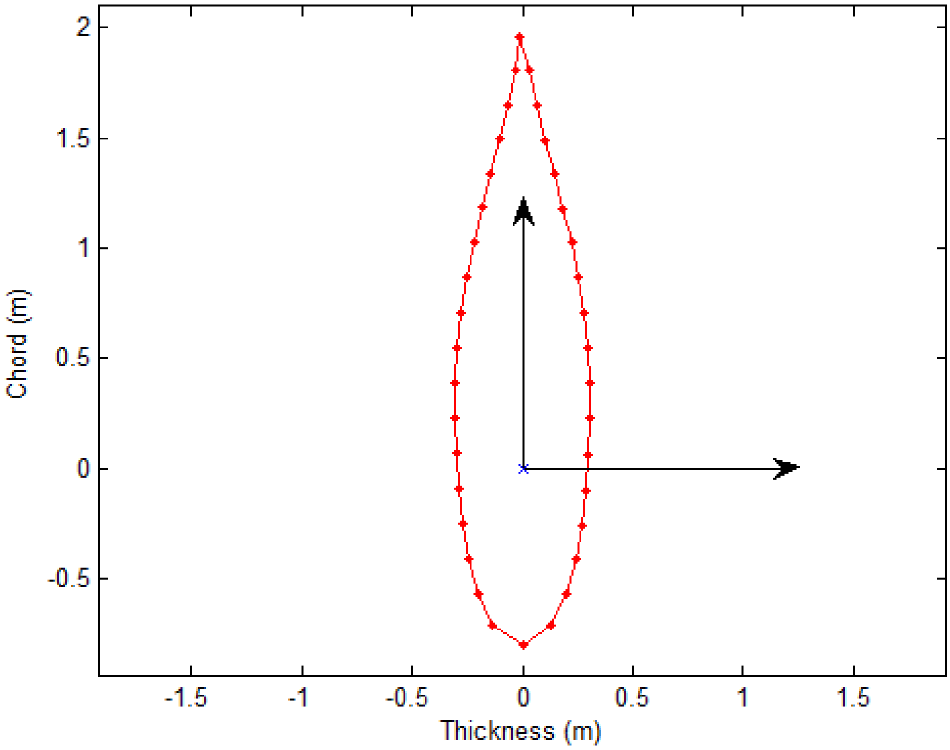

Figure 3.5 – Analysis points at 16.07m from root

3.2.3 Strain Analysis

A strength of materials approach was used to perform strain analysis on the blade. For the initial fatigue analysis, only the longitudinal strains were of interest. Very little information about the blade is required to perform these analyses, and results for long time histories can be obtained very quickly. The longitudinal normal strain can be calculated using equation (3.2) [100]. This equation assumes that the blade is prismatic, long and slender and that plane sections remain plane after deformation.

$$\varepsilon_{zz} = \left[\frac{F_z}{EA} + \frac{1}{k_{xy}}\left[\left(-M_y EI_{xx} + M_x EI_{xy}\right)x + \left(M_x EI_{yy} + M_y EI_{xy}\right)y\right]\right] \tag{3.2}$$

where

$$k_{xy} = EI_{xx}EI_{yy} - \left(EI_{xy}\right)^2$$

If the blade shape and its lay-up are assumed to be symmetrical about the chord line, strain rather than stress is of interest and the axial loads are neglected then equation (3.2) can be simplified to equation (3.3).

$$\varepsilon_{zz} = \frac{M_x y}{EI_{xx}} - \frac{M_y x}{EI_{yy}} \tag{3.3}$$

The blade root coordinate system used in this study is shown in Figure 3.6.

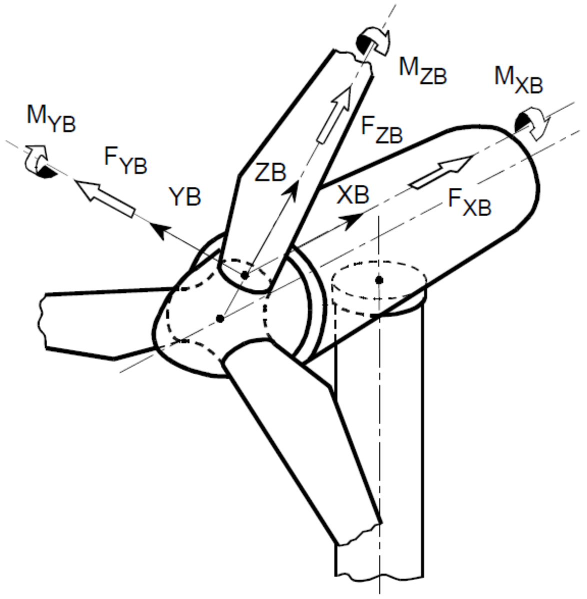

XB in direction of the rotor axis
ZB radially
YB so that XB, YB, ZB rotate clockwise

Figure 3.6 - GL coordinate system [11]

If simulation results are available for a beam element model of a blade for which a full shell/ brick element finite element model is also available, then it is possible to do a more in depth analysis. The full finite element model is divided up into sections corresponding to the elements in the beam element model. Simulations are then performed for each section with a unit load applied in the x-direction (flapwise) and y-direction (edgewise). A centrifugal load case can also be performed. The results from the beam element model can then be analysed to obtain the flapwise and edgewise loads on each section by subtracting the shear forces from adjacent sections. If linear behaviour is assumed, superposition can be used to obtain the combined effect of all the loads for the full model. This is done by multiplying the unit load results by the force on each section and summing across all sections. This method is shown in Figure 3.7. The yellow arrows on the shell element model represent a flapwise body load of 1N applied between the 23m and 26m stations. The multiplying factor for this load is calculated for a given time step by subtracting the x-direction shear force at section i ($F_{x\,i}$) from the shear force at the previous section ($F_{x\,i-1}$). This method is much less computationally expensive than the alternatives, such as using shell elements for the simulation, or even just applying the sectional loads as time histories which would involve solving the finite element model perhaps 6000 times for a ten minute simulation. In the example in Figure 3.7, there are 20 sections so the model only has to be solved 41 times (20 x-direction loads, 20 y-direction loads and a centrifugal load case).

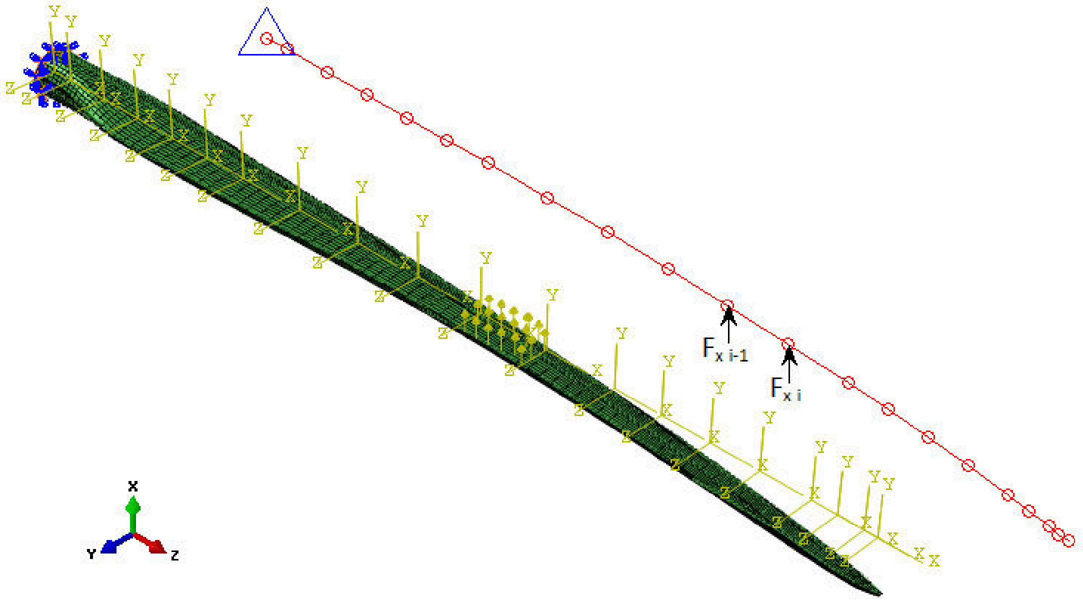

Figure 3.7 - Abaqus/CAE blade model showing loads for shell and beam models (blade model courtesy of LM Wind Power)

This method of performing strain analysis can be implemented in the fatigue analysis software FE-Safe [101].

3.2.4 Rainflow Counting

Once the strain time histories have been generated they are rainflow counted so that they can be treated as a series of constant amplitude strain cycles defined by their range and mean values.

Before rainflow counting can proceed the strain data must be filtered so that only the peaks and valleys remain. This process was performed by checking if the adjacent points in the history were both higher than the point of interest (meaning the point is a valley) or both lower (meaning the point is a peak). The rainflow algorithm also requires that the peak/valley data is then reordered so that it starts and ends with the highest peak or lowest valley.

The rainflow counting algorithm developed by Downing and Socie [51] was used to process the data. The output of the rainflow counting algorithm is a list of the amplitude and mean values of strains. These values can then be used with a Goodman Diagram to assess the amount of damage caused by each cycle. The MatLab implementation of the rainflow counting algorithm developed by Neislony [102] was used for this work.

3.2.5 Goodman Diagram

The quality of the Goodman diagram has been shown to be critical for fatigue predictions [41, 46-48]. However, due to the cost of testing large numbers of samples it is usual to use a Goodman diagram with R values of -1, 0.1 and 10 to capture fully reversed, tension-tension and compression-compression fatigue. The Goodman diagrams used for the fatigue analysis process in this instance were obtained from [49] and are typical for a laminate used in the shell of wind turbine blades. They were chosen because they offered the possibility of analysing the effects of the data fit method (exponential or power law) and the effects of including or excluding static test data.

In order to determine the number of load cycles the portion of the blade will survive at a given strain range and mean it is necessary to look up the values from a Goodman diagram.

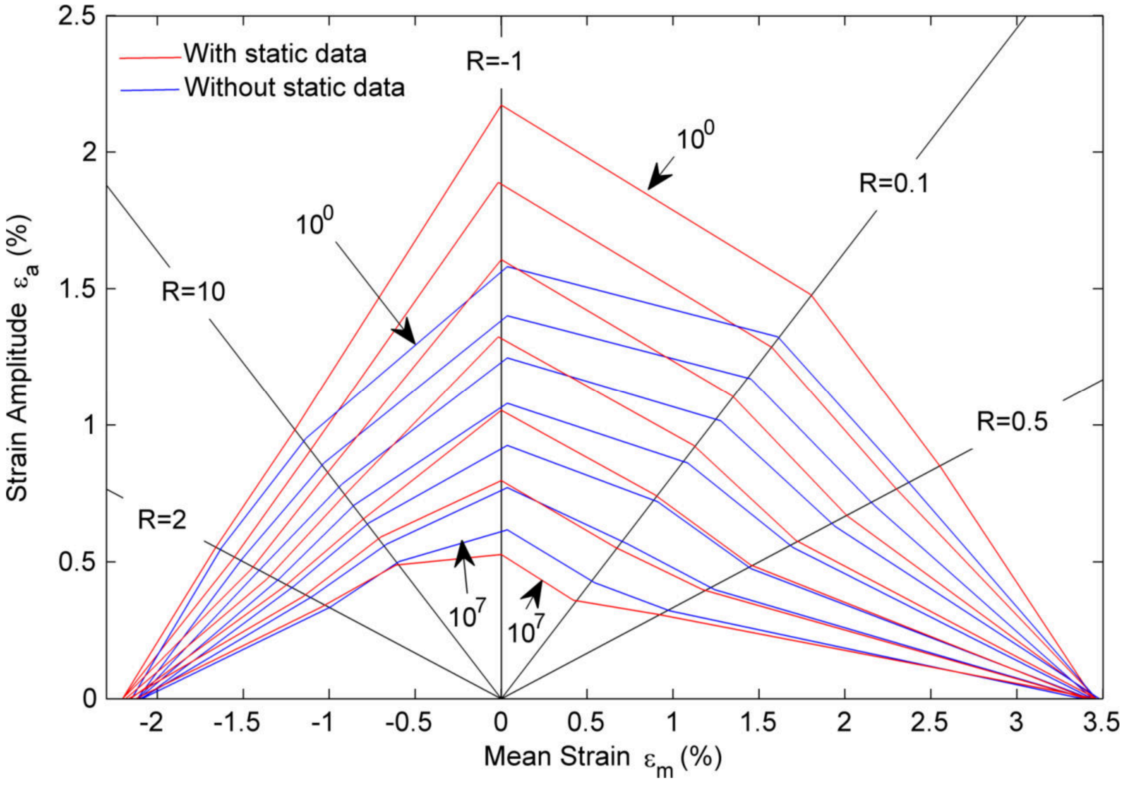

Figure 3.8 – DD16 Goodman diagram exponential curve fits [49]

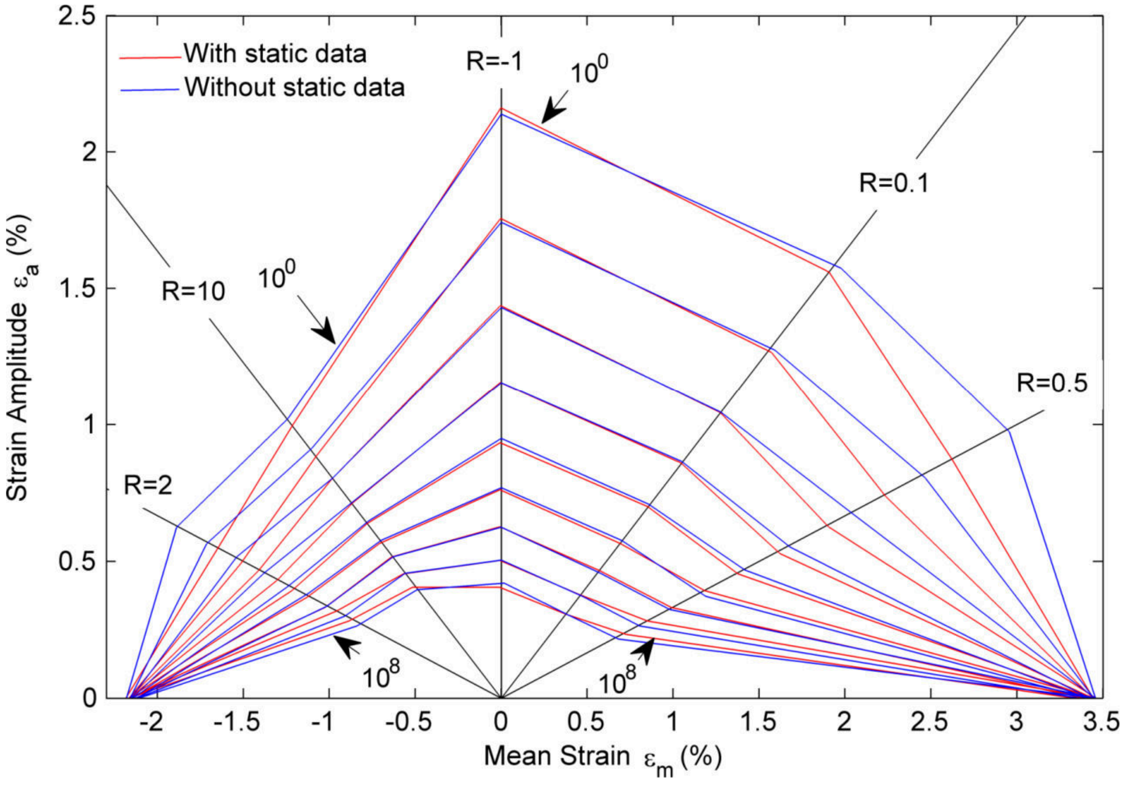

Figure 3.9 - DD16 Goodman diagram power law curve fits [49]

A Goodman diagram defined by tests at 3 different R-values and static tests in compression and tension might have a series of lines corresponding to the number of cycles to failure at each strain range and mean value as shown in Figure 3.8 and Figure 3.9.

Each point in each line can be defined by the strain range, mean and number of cycles to failure. For example, the outermost line corresponding to 1 cycle to failure is defined by the data in Table 3.4.

Cycles	Strain Mean (%)	Strain Amplitude (%)
1	-2.185	0
	-1.888	0.624
	-1.241	1.021
	0	2.138
	1.975	1.573
	2.955	0.973
	3.462	0

Table 3.4 – Example Goodman diagram definition data

More R-values could be used by adding extra coordinates if required. The Goodman diagram in this example has 6 sectors, with boundaries defined by the angles of the R value line. Given a strain cycle range and mean value, it is possible to plot its R-value using simple trigonometry, and then decide which sector it lies in based on the angle it makes with the x-axis (measured anticlockwise, with 0° as the positive x-axis). For example, if the cycle of interest has an R-value of -0.4, then it makes an angle of 66.6° with the positive x-axis. This places it in the third sector which is between R=-1 at 90° and R=0.1 at 39.28°. With this fact, it is possible to calculate the x-y coordinates of each intersection with a line on the Goodman diagram.

The formula for the corresponding line on the Goodman diagram can be found from the coordinates of its end points. In the example above the R-value is in the third sector so the coordinates used are the third and fourth lines in the Table 3.4. The equation of the line segment is given by equation (3.4).

$$\varepsilon_a = \frac{(\varepsilon_{a1} - \varepsilon_{a0})}{(\varepsilon_{m1} - \varepsilon_{m0})}\varepsilon_m + \varepsilon_{a1} - \frac{(\varepsilon_{a1} - \varepsilon_{a0})}{(\varepsilon_{m1} - \varepsilon_{m0})}\varepsilon_{m1} \tag{3.4}$$

Equation (3.6) can then be used to solve for the intersection of each line segment with the R-value line, which is defined by equation (3.5).

$$\varepsilon_a = \left(\frac{1-R}{1+R}\right)\varepsilon_m \tag{3.5}$$

$$\varepsilon_m = \left[\varepsilon_{a1} - \frac{(\varepsilon_{a1} - \varepsilon_{a0})}{(\varepsilon_{m1} - \varepsilon_{m0})}\varepsilon_{m1}\right] \Big/ \left[\left(\frac{1-R}{1+R}\right) - \frac{(\varepsilon_{a1} - \varepsilon_{a0})}{(\varepsilon_{m1} - \varepsilon_{m0})}\right] \tag{3.6}$$

By solving for the intersection of the R value line with each of the constant life lines on the Goodman diagram it is possible to build up a complete picture of the relationship between the strain amplitude at any given R value and the number of cycles to failure. This is enough information to populate an SN curve for the R-value in question as shown in Figure 3.10.

A curve fit is then made to the points on the SN curve using linear regression. This fit can be of the form shown in equation (3.7) if a power law fit is being used or the form shown in equation (3.8) if an exponential fit is being used.

$$S = AN^{-B} \tag{3.7}$$

$$S = A - B \ln N \tag{3.8}$$

These equations can then be rearranged to obtain N, the number of cycles to failure, for the strain cycle amplitude in question.

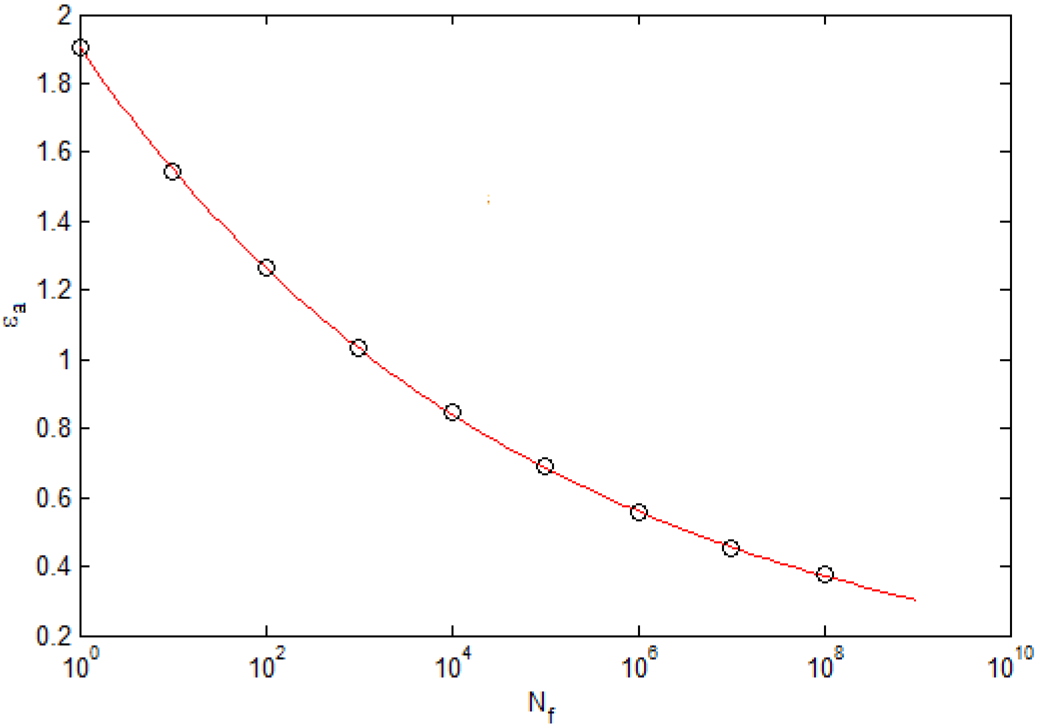

Figure 3.10 - SN curve with power law curve fit

Analysis was also performed using the simpler method suggested by the Germanischer-Lloyd standard, for the same material. This was to allow comparison between the different methods of formulating a Goodman diagram. The linear Goodman diagram described in the Germanischer-Lloyd standard is shown in Figure 3.11 [11] .

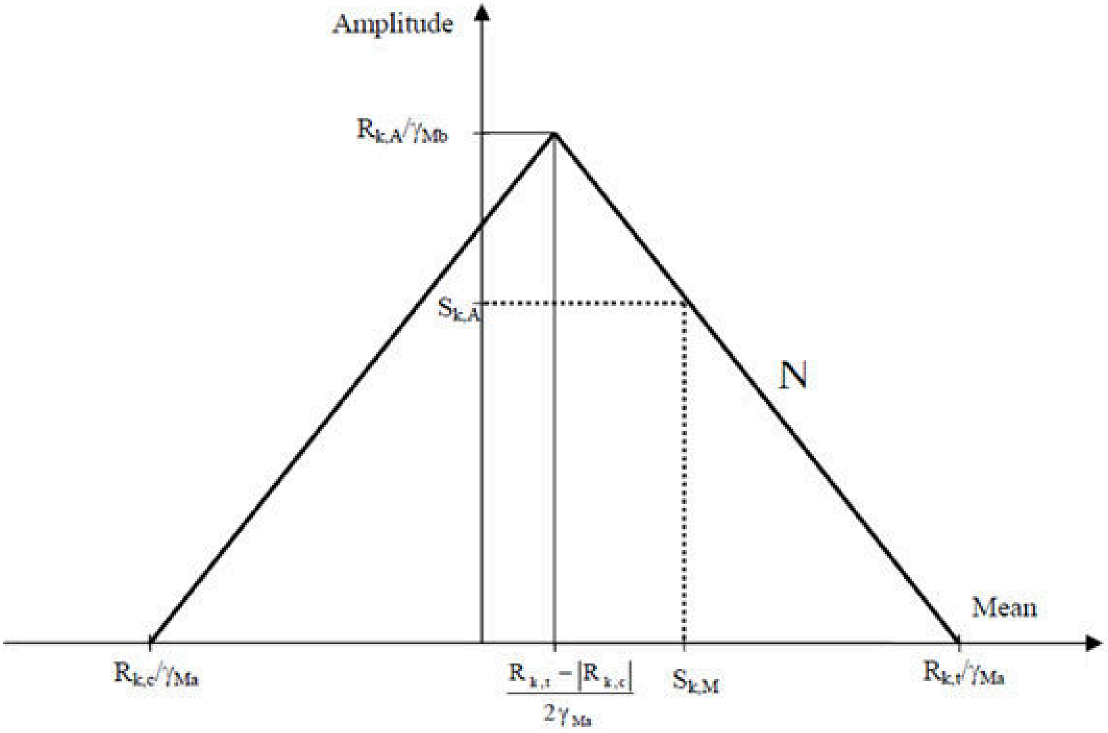

$$N = \left[\frac{R_{k,t} + |R_{k,c}| - |2 \cdot \gamma_{Ma} \cdot S_{k,M} - R_{k,t} + |R_{k,c}||}{2 \cdot (\gamma_{Mb}/C_{1b}) \cdot S_{k,A}} \right]^m$$

where:

$S_{k,M}$ = mean value of the characteristic actions

$S_{k,A}$ = amplitude of the characteristic actions ($|S_{k,max} - S_{k,min}|/2$)

$R_{k,t}$ = characteristic short-term structural member resistance for tension

$R_{k,c}$ = characteristic short-term structural member resistance for compression

m = slope parameter m of the S/N curve

$R_{k,A}$ = amplitude of the characteristic structural member resistances for load cycle number N=1.

The auxiliary variables m and $R_{k,A}$ are laid down through an analysis (S/N curve) to be agreed with GL Wind. For simplified assumptions, see Sections 5.5.4 and 5.5.5.

N = permissible load cycle number

Figure 3.11 – Linear Goodman diagram [11]

The damage calculation can then be made using the Palmgren-Miner linear damage assumption [53, 54]. It is common practice in fatigue analysis to sort the cycles into bins by their mean value and amplitude, and use the number of cycles in each bin as the numerator in equation (3.9).

However, in the present work the cycles are not binned as it was found that binning reduced the speed and accuracy of the simulation. Each cycle therefore occurs once in the load case and equation (3.9) can be used to calculate the damage done to a point on the blade by a load case. In equation (3.9) n is the same for every cycle and is the number of occurrences of the load case, found from the load case distribution shown in Figure 3.1.

$$D = \sum \frac{n}{N} \tag{3.9}$$

The total damage for each load case at each node is then recorded in a matrix for each blade cross section as shown in Table 3.5, so that the total damage at each node can be summed while still retaining key information about which load cases are causing the most damage.

	Node						
Load Case	1	2	3		34	35	36
1	1.56E-30	6.45E-29	2.77E-31	…	2.72E-46	1.59E-40	5.72E-35
2	4.3E-187	3.4E-185	7.5E-184	…	1.3E-196	6.1E-223	1.1E-220
3	5.03E-51	7.31E-50	7.68E-49	…	3.12E-58	6.31E-54	2.3E-52
…	…	…	…	…	…	…	…
39	7.07E-08	8.61E-08	8.5E-08	…	1.3E-08	3.86E-08	7.14E-08
40	3.63E-07	3.99E-07	4.27E-07	…	2.82E-07	3.23E-07	4.96E-07
41	1.55E-08	1.04E-08	1.38E-08	…	6.89E-09	1.08E-08	1.62E-08
Sum	0.000403	0.000737	0.000918	…	0.000239	0.000324	0.000443

Table 3.5 – Damage Matrix

The R-value of each cycle is also recorded and binned so that analysis can be performed to see which areas of the blade see the most occurrences of a given R-value.

3.2.6 Test Target Bending Moment Amplitude Calculation

The test target bending moment amplitude calculation is performed separately for the flapwise and edgewise directions for each section. In reality the blade twist will result in coupling between the flapwise and edgewise directions, but the twist angle is generally small enough for this to be neglected. This assumption has been checked for the blade analysed here in section 5.3.3.

On the flapwise neutral axis the flapwise bending moment does not cause any damage. Therefore at this point on the blade, all of the damage can be assumed to have been caused by the edgewise bending moment (using the assumptions of equation (3.3)). The same is true for the edgewise neutral axis. The damage is matched at the most damaged point on each neutral axis, which will be referred to as the control points henceforth.

For the edgewise neutral axis this is generally on the pressure side because this side tends to be subjected to predominantly tensile loading, which is more damaging for the material used in this study. The flapwise neutral axis tends to be most damaged at the trailing edge. This is partly because the turbine is producing torque so the trailing edge has a tensile mean strain, and partly because it tends to be further from the neutral axis than the leading edge (for typical blade architectures where the spar caps are located at the thickest part of the section) which results in higher strain amplitudes.

If the service life damage at a control points takes the value D and n is the number of cycles in the fatigue test (5 million cycles is usually used in the wind industry because accelerating the test further can cause the blade to fail due to overheating [93]), then using the Palmgren-Miner rule [53, 54] the number of cycles N that would fail the blade can be calculated using equation (3.10).

$$N = \frac{n}{D} \tag{3.10}$$

The Goodman diagram is piecewise linear so the SN curve varies with the R-value of the cycle. This means that there is no simple formula to calculate what bending moment amplitude will result in N cycles to failure (the calculation of N is described in section 3.2.5). In the present work, this issue has been addressed by searching for the strain amplitude ε_a that will result in the correct number of cycles to failure numerically using a bisection search. This works as follows:

1. Lower and upper boundaries for the strain amplitude are chosen and the midpoint between the two boundaries is calculated.
2. Either the lower boundary and the midpoint or the midpoint and the upper boundary will bracket a value of the strain amplitude that will result in a correct value for N.
3. Redefine the boundaries as the midpoint and whichever of the two boundaries brackets the solution and calculate a new midpoint.
4. Repeat 2-3 until the difference between the two boundaries is less than 1e-6.

This is a very simple root finding algorithm that is highly robust and although it is quite slow that is not an issue in the present application [103], as results are typically obtained in less than 1s.

The bending moment amplitude which will result in a given strain amplitude is calculated using equation (3.11), where ε_a is the strain amplitude (calculated using the procedure described above), EI is the bending stiffness in the direction in question and y is the distance to the neutral axis.

$$M_a = \frac{\varepsilon_a EI}{y} \tag{3.11}$$

A further issue stems from the fact that the mean bending moment distribution and ratio between the two natural frequencies under test conditions is unknown initially. This can be resolved as follows:

1. Calculate the mean (self weight) bending moment at each section and first flapwise and edgewise natural frequencies of the blade without any test equipment mounted on it using a beam finite element model of the blade. The ratio between the flapwise and edgewise natural frequencies is important because it dictates how many edgewise cycles will be performed for a given number of flapwise cycles in a dual axis test.
2. Calculate the target bending moment amplitude in the flapwise and edgewise directions at each cross section for the blade with no equipment mounted on it using the bisection search described above.
3. Use experience or the method described in chapter 4 to obtain the position and mass of the test equipment to be mounted on the blade to achieve the bending moment amplitude distribution obtained in step 2.
4. Recalculate the bending moment amplitude distribution using the natural frequency ratio and mean bending moment distribution obtained when the test equipment is mounted on the blade.
5. If the required bending moment amplitude distribution can still be achieved using the test equipment selected in step 3 then the process is complete. It is rarely necessary to perform another design loop but it can be done if necessary.

The bending moment amplitude that causes the same amount of damage as the service life at each control point will be referred to as the target bending moment amplitude from this point onwards. The bending moment range is twice the bending moment amplitude. With the target bending moment amplitudes at each section calculated for the flapwise and edgewise directions it is possible to simulate test load time histories and thus compare the damage caused by the service life to the damage caused by different types of testing.

3.2.7 Test Load Generation

For the initial assessment of how dual axis testing compared to single axis testing the loads were generated as simple sine waves. The flapwise and edgewise frequencies and mean bending moments were obtained by modelling the blade using beam elements with additional mass added at the relevant nodes to represent the excitation equipment. Equations (3.12) and (3.13) are used to calculate the flapwise and edgewise bending moment time histories respectively. In these equations M refers to the bending moment, f is the test frequency and φ is the phase angle. The subscripts F and E refer to the flapwise and edgewise directions respectively and a and m refer to the amplitude and mean value of the bending moment waveform respectively.

$$M_F(t) = M_{F\,a}\cos(2\pi f_F t + \varphi) + M_{F\,m} \tag{3.12}$$

$$M_E(t) = M_{E\,a}\cos(2\pi f_E t + \varphi) + M_{E\,m} \tag{3.13}$$

3.3 Results and Discussion

There are several different approaches to the fatigue analysis of wind turbine blades. The difference in the results when each of these approaches is adopted is evaluated in order to draw conclusions about which approach is the more robust.

3.3.1 Comparison of beam theory with FEA results

The beam model used in the present work has been validated by comparing the results obtained with those found when using a more sophisticated shell finite element model of the LM 40.3 P2 blade.

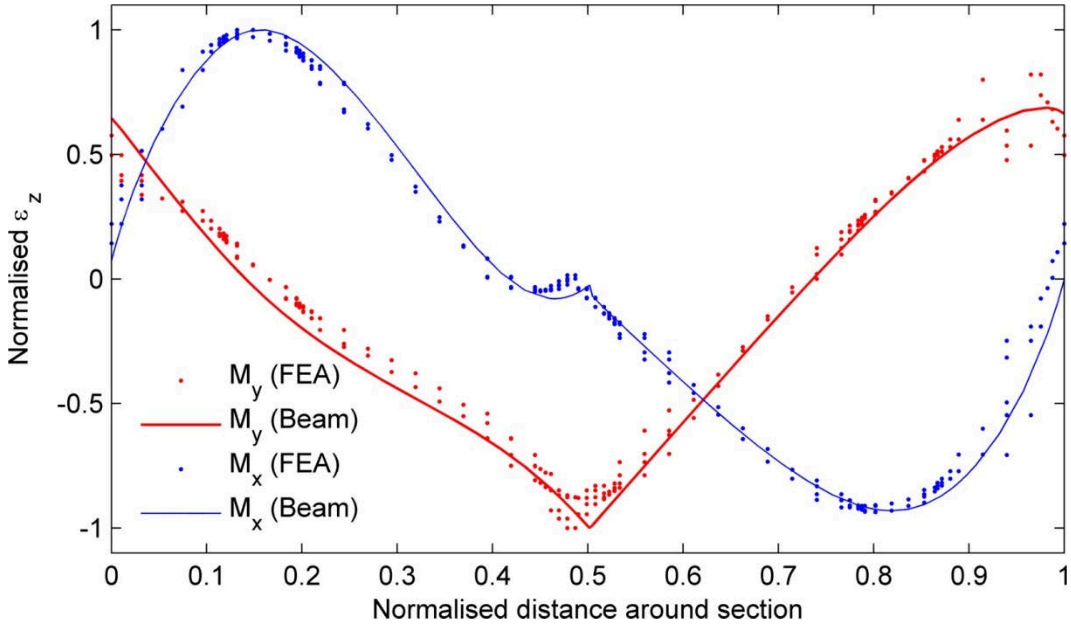

Figure 3.12 – Comparison of beam theory and FEA results

For the comparison, a unit load was applied to the tip of the finite element model in the flapwise and edgewise directions. The strains in the longitudinal direction of the blade were obtained at a section for the flapwise and edgewise loading and compared to the results obtained using beam theory in order to validate the model. The results are shown in Figure 3.12.

The LM 40.3 P2 blade has a complex asymmetrical cross section at the section for which results are shown in Figure 3.12 so it appears that the use of beam theory is justified. It can therefore be used for the 2MW blade used in this study, which is not commercially sensitive.

3.3.2 Piecewise linear Goodman diagram

The way that damage accumulates around the blade is highly dependent on the Goodman diagram used and the choice of curve fit. In Figure 3.14 to Figure 3.17 the node labels LE, PS, TE and SS refer to the leading edge, pressure side, trailing edge and suction side as shown in Figure 3.13.

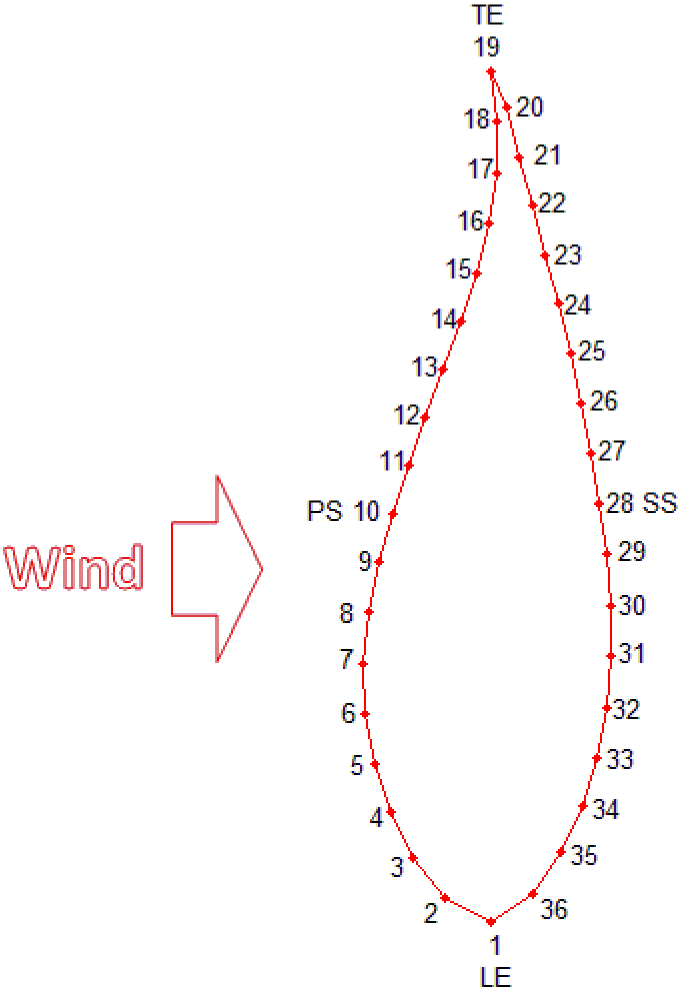

Figure 3.13 – Node numbering for a general section

Load cases 1-35 refer to the average wind speed in m/s, and 36 to 41 refer to start-up and shut-down at the cut-in wind speed, start-up and shut-down at the rated wind speed and start-up and shut-down at the cut-out wind speed. The frequency of occurrences of the load cases is taken into account.

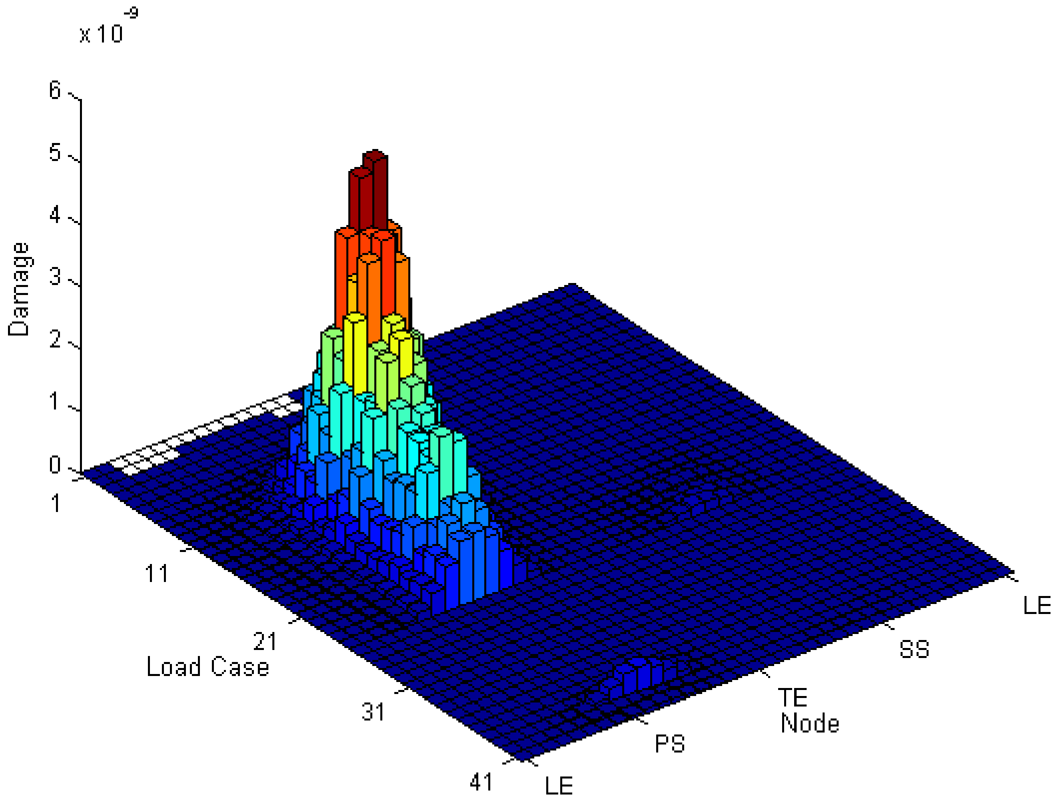

Figure 3.14 – Damage accumulation at the 1.15m section (power law)

Figure 3.14 shows that the damage at the root is located mainly on the pressure side towards the trailing edge, as this is the part of the blade that sees the highest proportion of tensile loading. This is because this part of the blade is upwind, and also because the turbine is producing torque so the trailing edge has a tensile mean strain. Tensile loading is more damaging than compressive loading for the blade material in question and also generally for composites. There is a small but significant amount of damage caused by shut-downs at the rated wind speed, and there is also a small amount of damage on the suction side at high wind speeds. This is attributable to the fact that the blades are pitched in high winds which results in the gravity loads fatiguing this area.

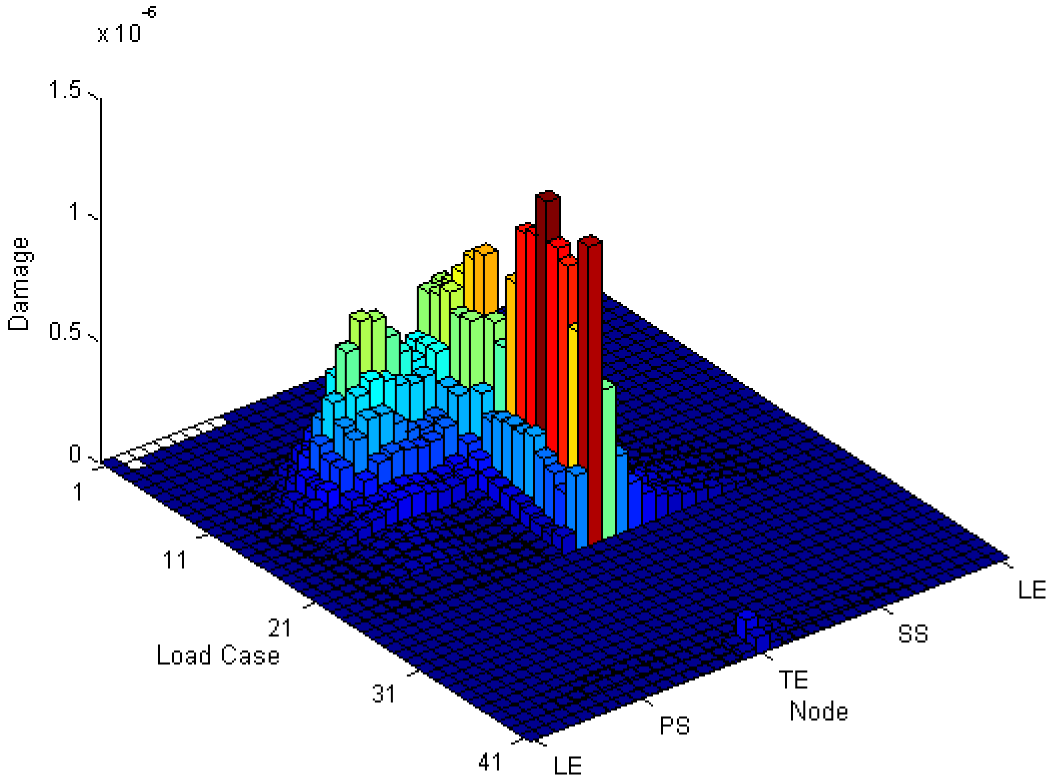

Figure 3.15 – Damage accumulation at the 16.05m section (power law)

Figure 3.15 shows the damage accumulation at a mid-span section of the blade if a power law curve fit is used for the fatigue data. The majority of the damage is concentrated around the trailing edge, although there is also a significant amount on the pressure side as well. Again, this is because this area of the blade experiences the highest tensile strains due to the large distance to the trailing edge from the neutral axis and the fact that the blade is producing torque. The suction side is hardly damaged at all because the slope of the fatigue curves for compression is very shallow.

When an exponential fit is used to the coupon fatigue test data the results are very different; there is a factor of almost 10 million between the maximum values found using a power law curve fit in Figure 3.14 and an exponential curve fit in Figure 3.16. The reason for this is that the exponential curve fit continues to cause damage even at extremely low strain amplitudes. Indeed, although the method used ignores cycles with amplitudes extremely close to 0 (R=1) the exponential curve fit shown in equation (1.5) will still predict that the material will fail if the strain amplitude is zero.

The effect of this can be mitigated by allowing for an endurance limit as is used with steels, although this has not been done in the present work.

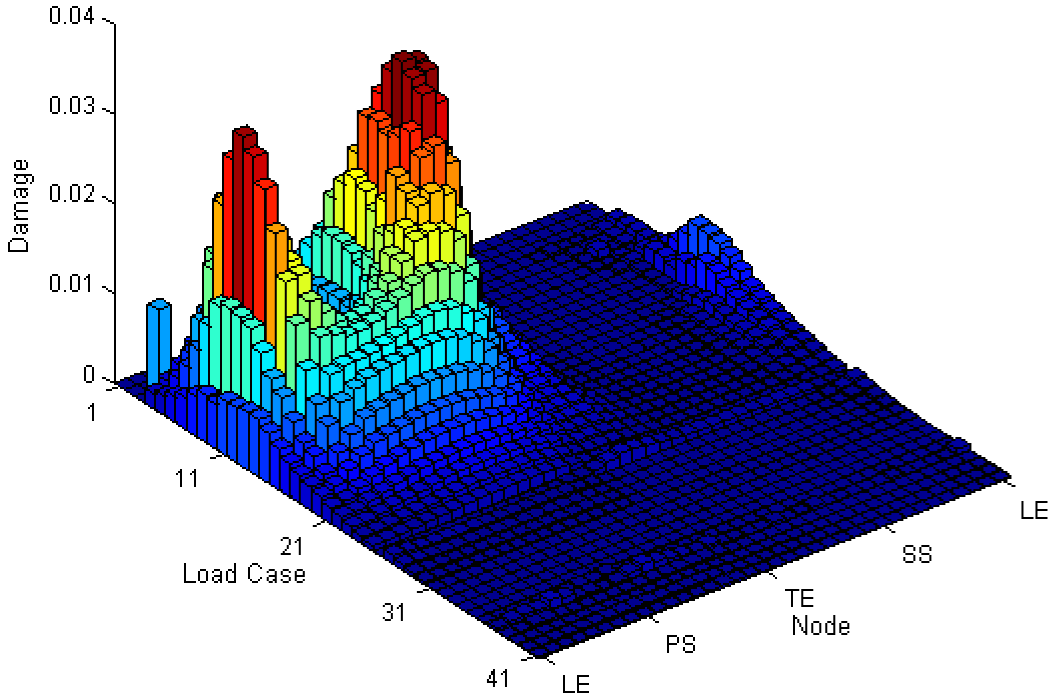

Figure 3.16 – Damage accumulation at 1.15m section (exponential)

In Figure 3.16 the effect of the turbine producing torque, which alters the behaviour on the pressure side, is seen to be much less pronounced with exponential curve fitting than it is with power law fitting. This is because the low amplitude cycles are having much more of an effect. However, the damage is still very much concentrated on the pressure side. The start-up at the cut-in wind speed (a frequently occurring but fairly light duty load case) is the most damaging of the start up and shut down load cases.

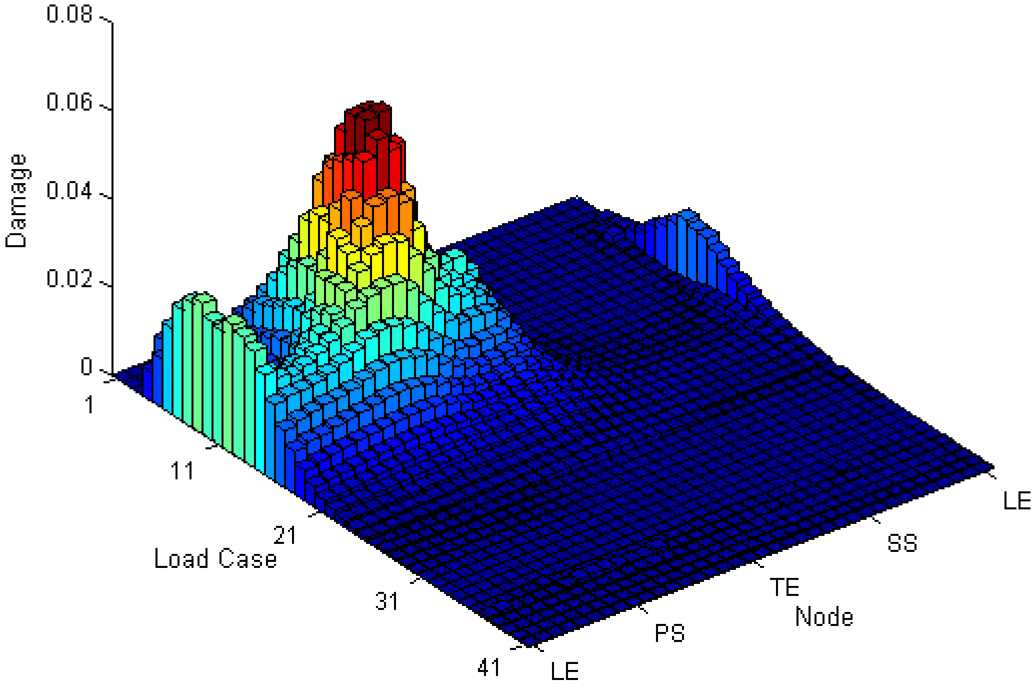

Figure 3.17 – Damage accumulation at 16.05m section (exponential)

Figure 3.17 shows the damage accumulation at the mid-span section using an exponential fit to the curve data. The trailing edge is not the most damaged part of the blade as it is when a power law fit is used for the curve data. The explanation for this behaviour is that the pressure side is exposed to frequently occurring low amplitude cycles due to turbulence, while at the trailing edge the higher amplitude but relatively rare cycles that arise from gravity loading are not as significant as they are when a power law curve fit is used.

Figure 3.18 shows the number of occurrences of different strain levels during a 10 minute simulation at the rated wind speed. Clearly, very low strain amplitudes dominate. This explains the completely different behaviour when the damage is calculated using a power law curve fit (Figure 3.14 and Figure 3.15) as opposed to when it is calculated using an exponential curve fit (Figure 3.16 and Figure 3.17). With the power law curve fit, these very low amplitude cycles cause almost no damage. However, with the exponential curve fit they still have an effect.

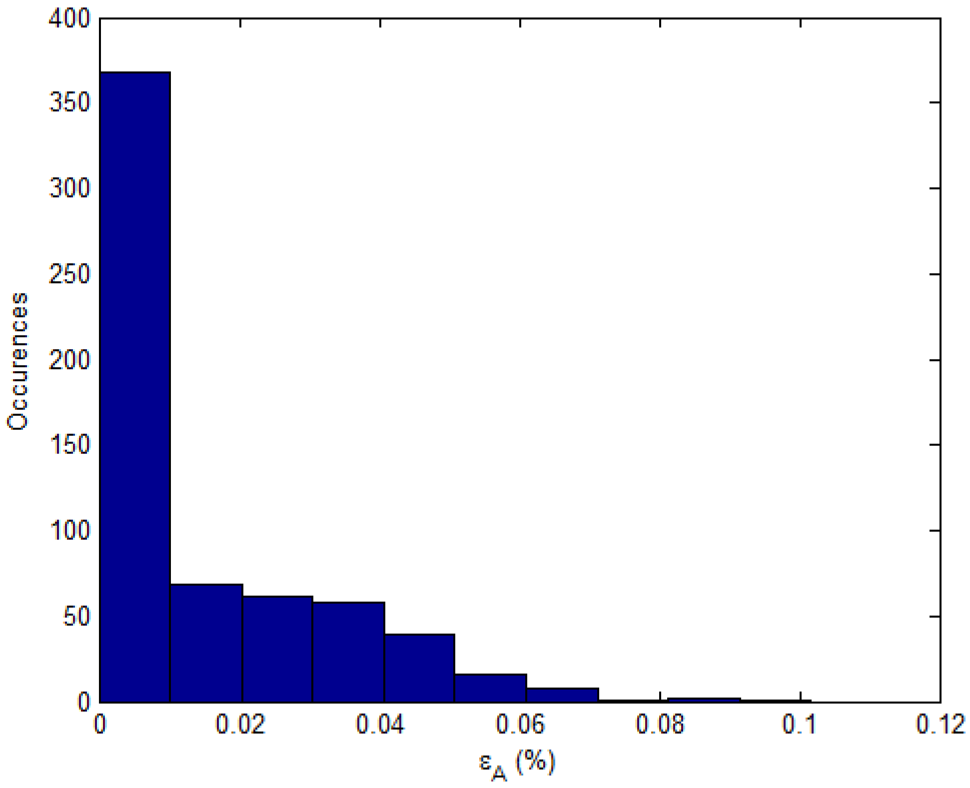

Figure 3.18 – Histogram of strain amplitudes on pressure side at rated wind speed

The cumulative effect of all the load cases at each blade cross section studied when using the exponential curve fitting method is shown in Figure 3.19. The outer edges of the blade, which are very lightly loaded, still show a significant amount of damage. This is again a result of the exponential curve fitting method causing damage at very low load levels.

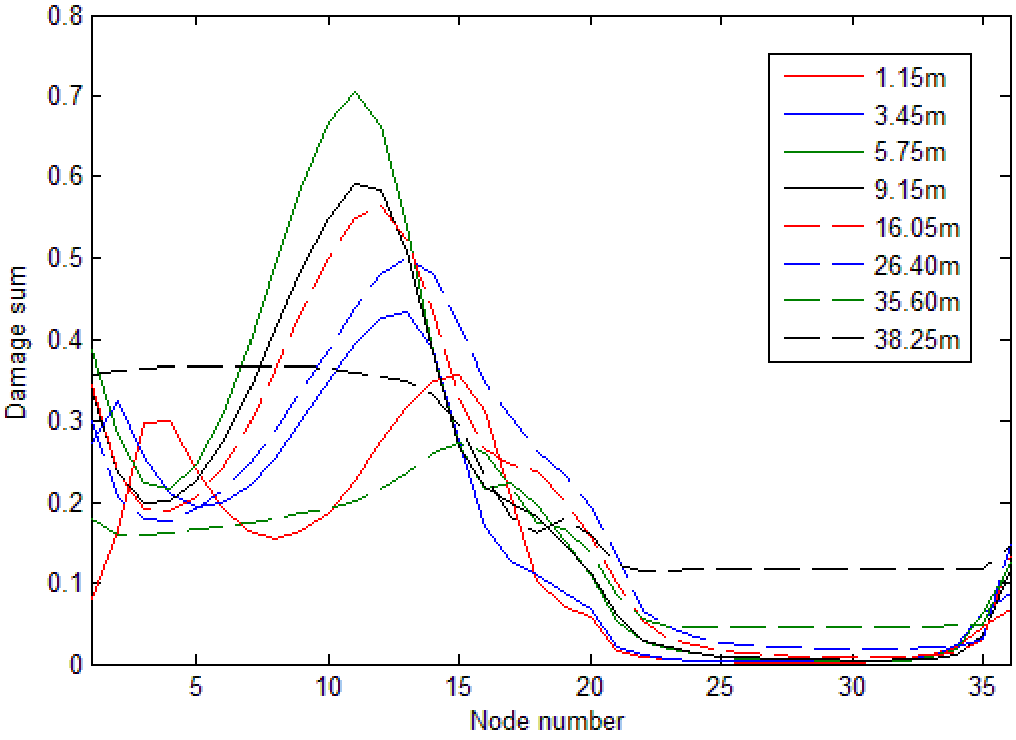

Figure 3.19 – Damage sum at all blade cross sections for service life (exponential)

The total damage sum at each blade section for all load cases when a power law curve fit is used is shown in Figure 3.20. The outermost two blade sections are not shown as the damage sums there are negligible. Note the damage sum is shown on a logarithmic scale; this was necessary because the variation in damage across the blade is much greater than when an exponential curve fit is used to the Goodman diagram.

The damage is still concentrated on the pressure side, but because the effect of small amplitude cycles has diminished the trailing edge at the maximum chord section is now the most damaged point on the blade. This section is also the most damaged when an exponential fit is used, but the damage accumulates more on the trailing edge with the power law because the higher amplitude cycles from the blade passing frequency have more effect there.

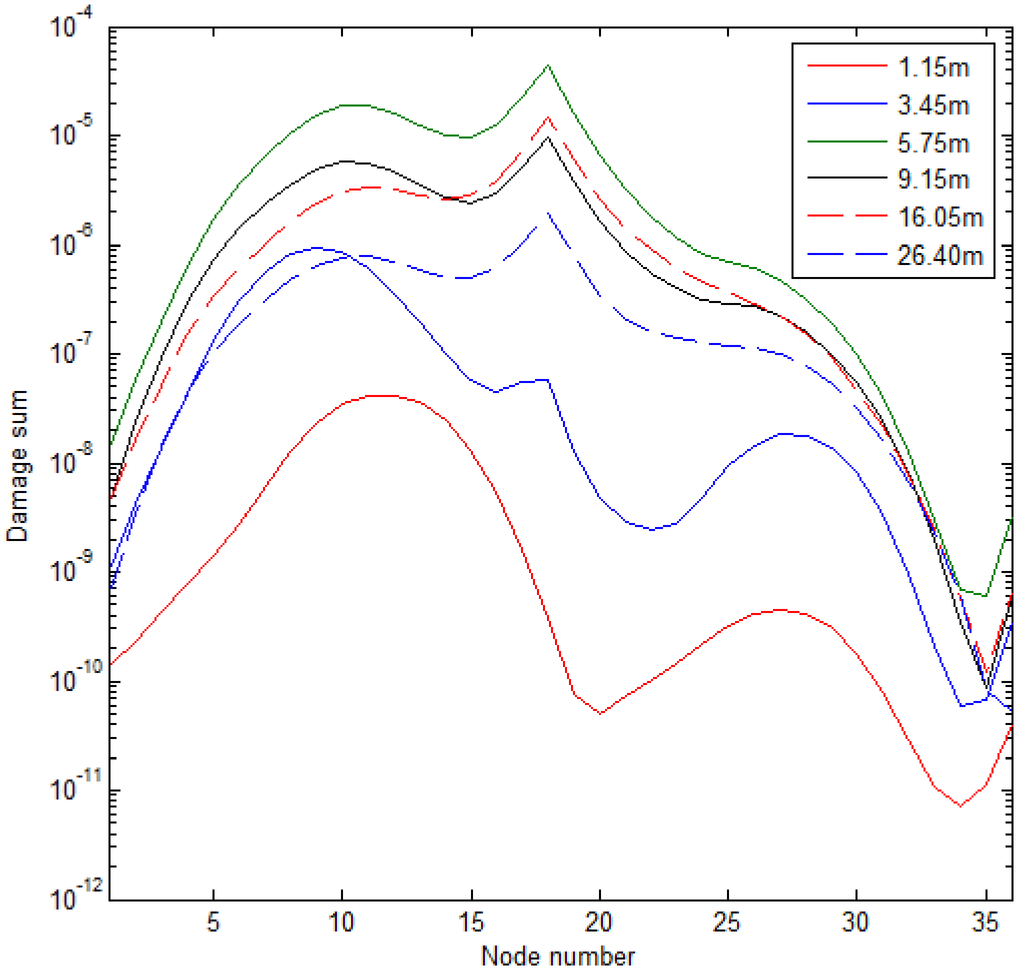

Figure 3.20 - Damage sum at all blade cross sections for service life (power law)

For all of the above results the Goodman diagram neglected static data. For the power law curve fit, this had very little effect on the results, but for the exponential curve fit the damage increased considerably when the static data was included. The reason for this is that the static data skews the fatigue data and increases the slope of the SN-curve. This has the effect of making infrequent high strain amplitude cycles less damaging, but the low amplitude cycles are more damaging. Indeed, the only case in which the blade in question fails the fatigue analysis is when the exponential fit is used and static data are included, as shown in Figure 3.21.

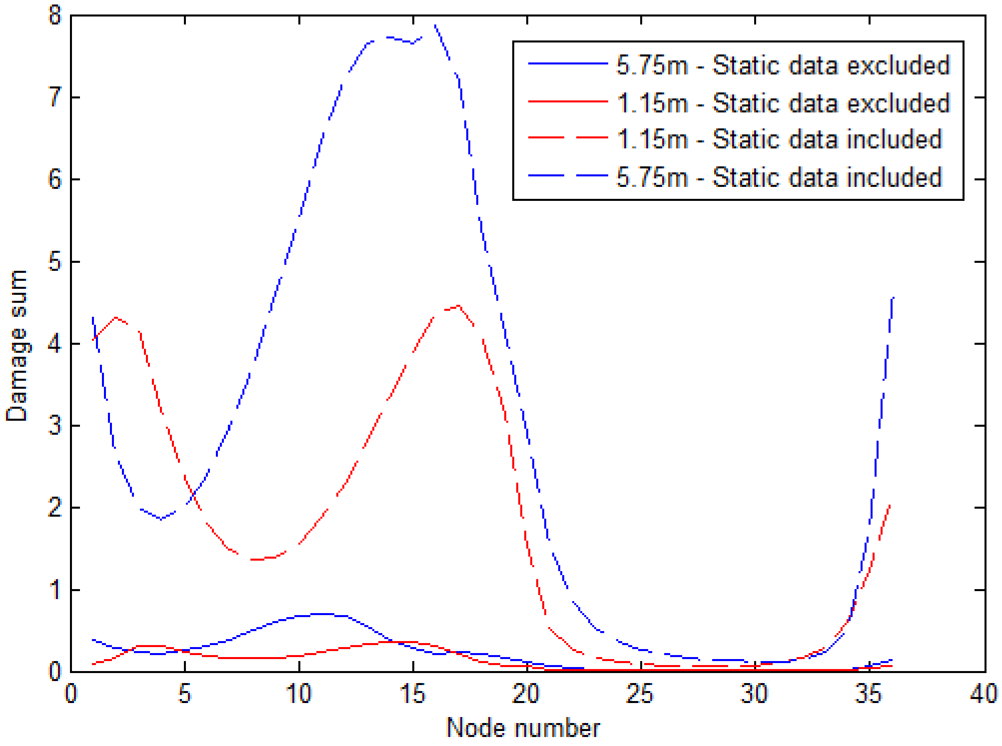

Figure 3.21 – Effect of including static data

Nijssen [41] reviewed several articles which discussed whether or not to include static data in the formulation of the SN curve and concluded that there are ‘fundamental and practical obstacles preventing the inclusion of static data’. Although there are arguments in favour of including the data, the fact that low amplitude loads dominate so overwhelmingly suggests that if there is any doubt that including the data is beneficial then it should not be used.

In the current fatigue analysis the highest amplitude strain in the rainflow count of any load case was 0.31%, and the highest mean value of the strain was 0.3085%. These values, even if taken together, correspond to around 10^8 cycles on the Goodman diagram, a region for which experimental data is not readily available.

3.3.3 Linear Goodman diagram

The Germanischer-Lloyd design guidelines suggest performing fatigue analysis using a linear Goodman diagram [11] as shown in Figure 3.11, which simplifies the behavior under different loading conditions by only using data for R=-1 to calculate the fatigue. Although fatigue analysis using the procedure described in section 3.2 is a significant improvement over this method, analysis using the linear Goodman diagram was performed using the same material data as a comparison.

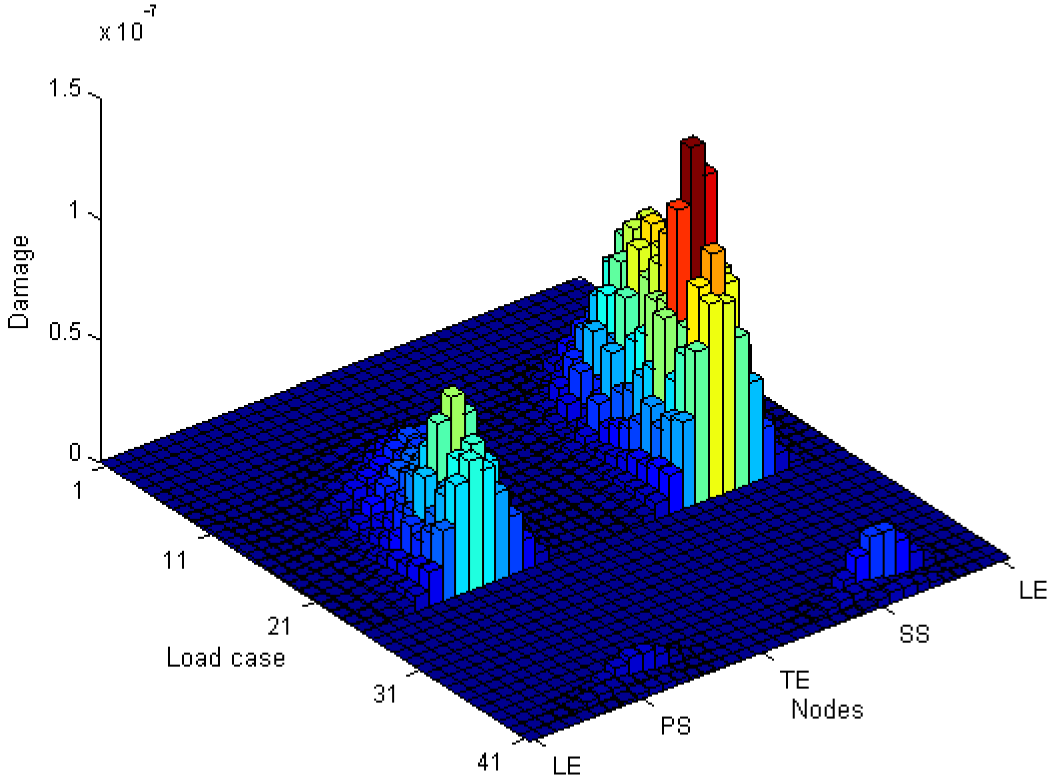

Figure 3.22 – Damage accumulation at 1.15m section (GL Goodman diagram)

Results for the blade root are shown in Figure 3.22, and the damage accumulation on the pressure side is of the order of that seen when the piecewise linear Goodman diagram was used with a power law fit (shown in Figure 3.14). However, by far the most damage accumulates on the suction side. The reason for this is that no account is taken of the fact that the slope of the SN curve for compression is less severe with the GL Goodman diagram (although it allows for different slope factors to be specified depending on the R-value, this is not mandatory). As the static compressive strength is used to define the power law and this is lower than the tensile strength, the compressive cycles are more damaging.

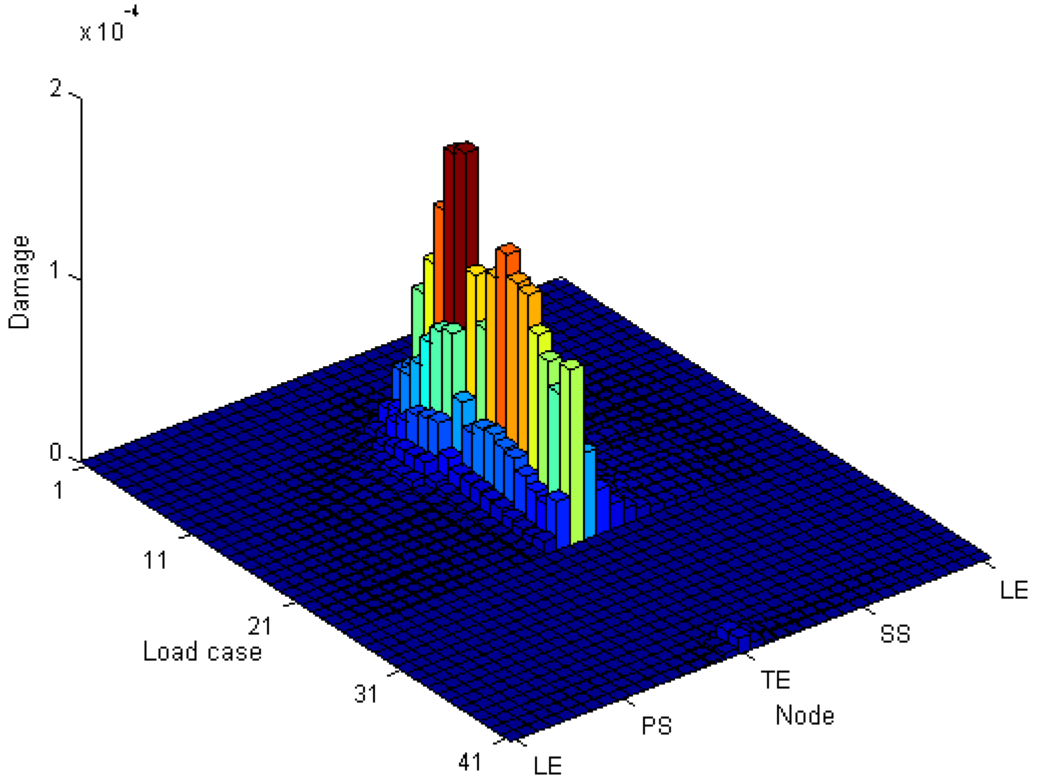

Figure 3.23 – Damage accumulation at 16.05m section (GL Goodman diagram)

For a mid-span section, the damage accumulation is more similar to what was seen in Figure 3.15, albeit with a very large difference in the peak damage sum. This can be attributed to the fact that the trailing edge is much more fatigue critical than the pressure side and suction side in this case.

The linear Goodman diagram is not generally regarded as being sufficient for a proper fatigue analysis. Sutherland and Mandell [48] studied the effect of mean stress on variable amplitude fatigue predictions and found that ideally at least 5 R-values should be used to construct the Goodman diagram. In practice, three values are usually used; R=10 (compression-compression), R=-1 (compression-tension) and R=0.1 (tension-tension).

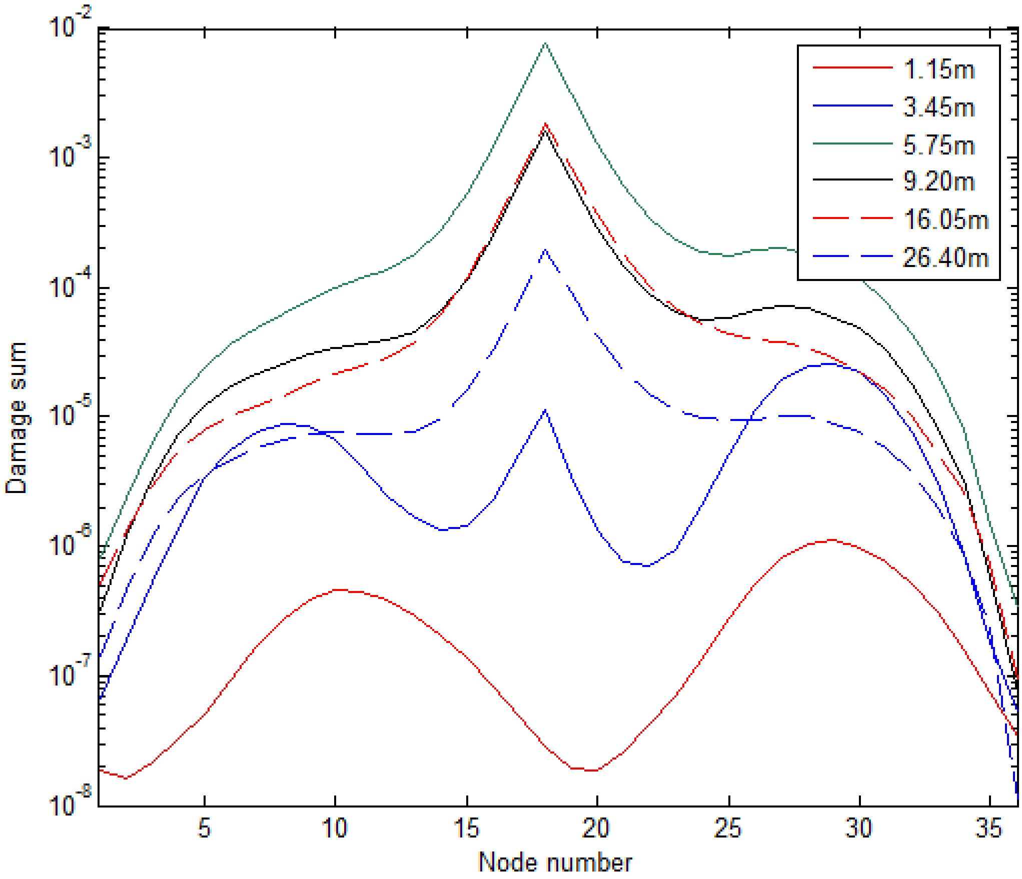

Figure 3.24 – Damage sum at all blade cross sections for service life (GL Goodman diagram)

The damage sums at all of the blade stations are shown in Figure 3.24. The pressure side is consistently less damaged than the suction side. The 5.75m section was the most damaged by the service life, as was the case with all of the other Goodman diagrams.

3.3.4 Analysis of damage by R-value

When performing fatigue testing it is desirable to have an understanding of which types of fatigue loading produce the most damage so that time and effort can be focused on the most important R-values. To this end, during the time history fatigue analysis procedure described in section 3.2 the number of occurrences, the strain amplitude and the damage caused by each cycle are binned by R-value and node. As the Goodman diagram used characterises the material at a fairly broad range of R-values (R=2, R=10, R=-1, R=0.1 and R=0.5) it is possible to perform a fairly in-depth study into which R-values are the most damaging and where they occur. For this analysis, the power law relationship was used so that the low amplitude cycles were not disproportionately represented.

In Figure 3.25, Figure 3.26 and Figure 3.27 the R-values are divided according to the type of loading. Fully tensile cycles are labeled T-T, tension dominated cycles are labeled T-C, compression dominated cycles are labeled C-T and fully compressive cycles are labeled C-C.

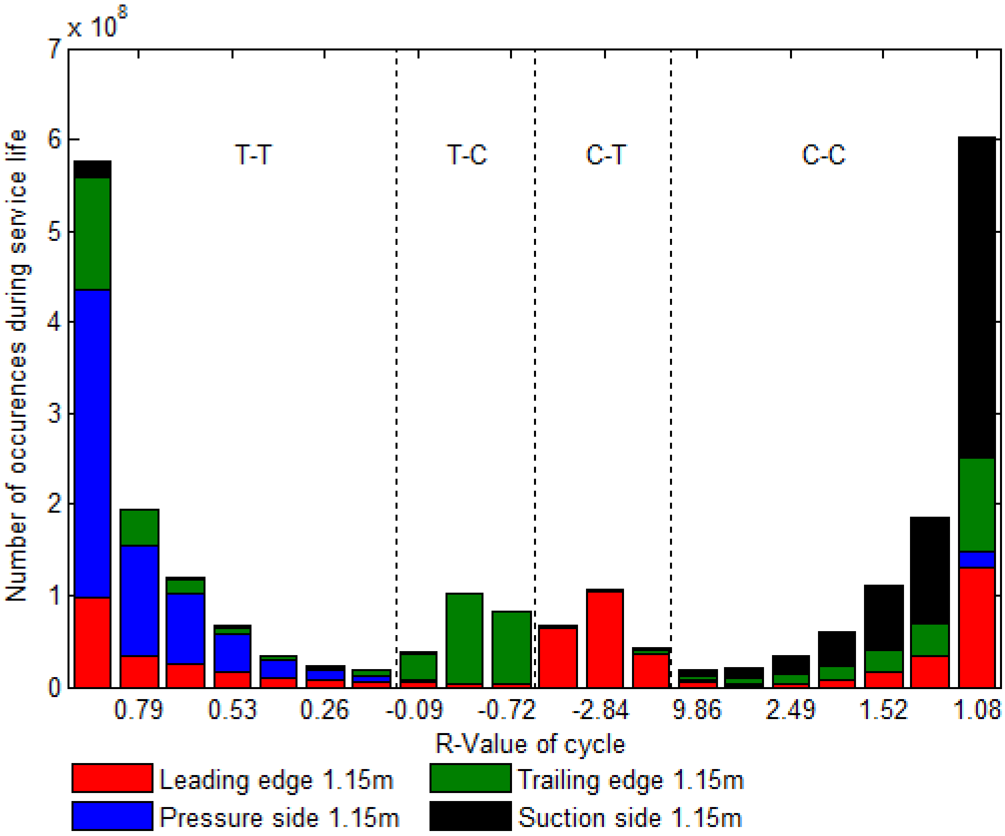

Figure 3.25 – Number of occurrences of cycle by R-value and position at 1.15m

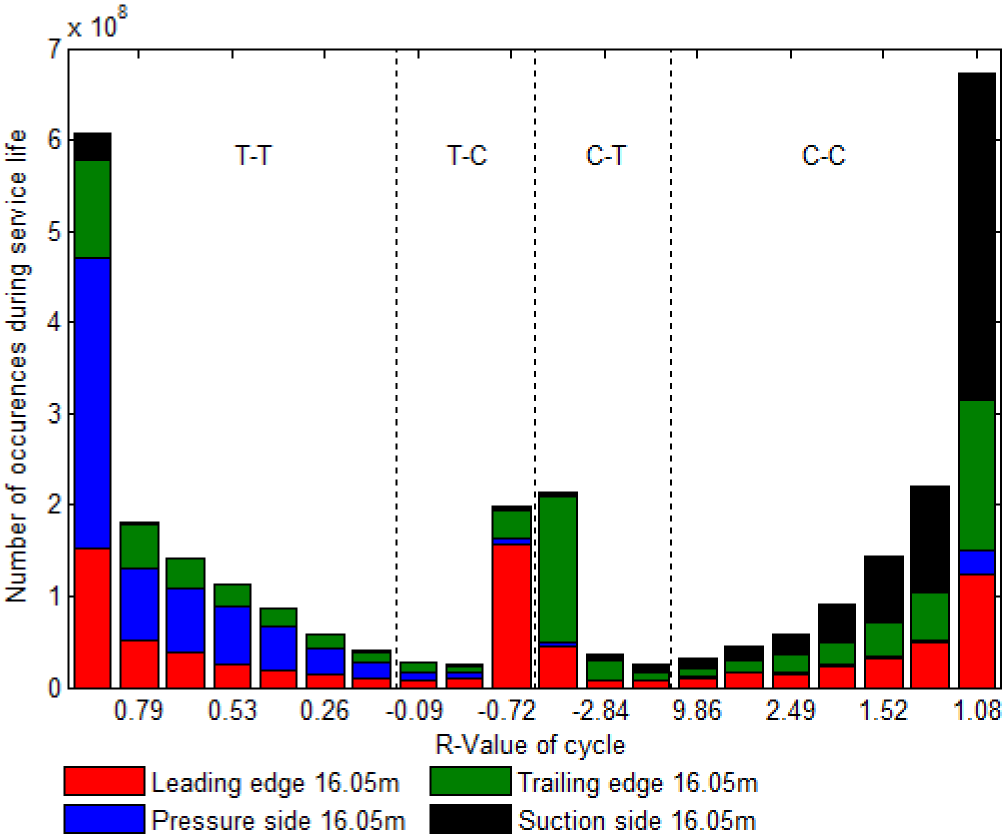

Figure 3.26 - Number of occurrences of cycle by R-value and position at 16.05m

Figure 3.25 and Figure 3.26 show the number of occurrences of cycles that fall into each bin at the 1.15m section and the 16.05m section respectively. On the pressure side, very low amplitude tensile cycles dominate (R-value is close to but less than 1). On the suction side, very low amplitude compressive cycles are the most commonly occurring (R-value is close to but greater than 1). At the leading edge there are a similar number of compressive and tensile low amplitude cycles, but most of the cycles are concentrated around fully reversed loading (R=-1). In Figure 3.25 it can be seen that near the root the leading edge loads are reversing with a compressive bias and the trailing edge loads are reversing with a tensile bias (because the turbine is producing torque). At the mid-span section (Figure 3.26) the leading edge cycles are mainly reversing with a tensile bias, and the trailing edge cycles are reversing with a compressive bias. Although the turbine is producing torque, the blade twist at this section means that the trailing edge cycles are not tensile dominated.

Another result that was obtained was the sum of the amplitudes of every cycle that occurs in each R-value bin at each node on the blade. This is instructive because it is possible to see which parts of the blade are being fatigued most severely.

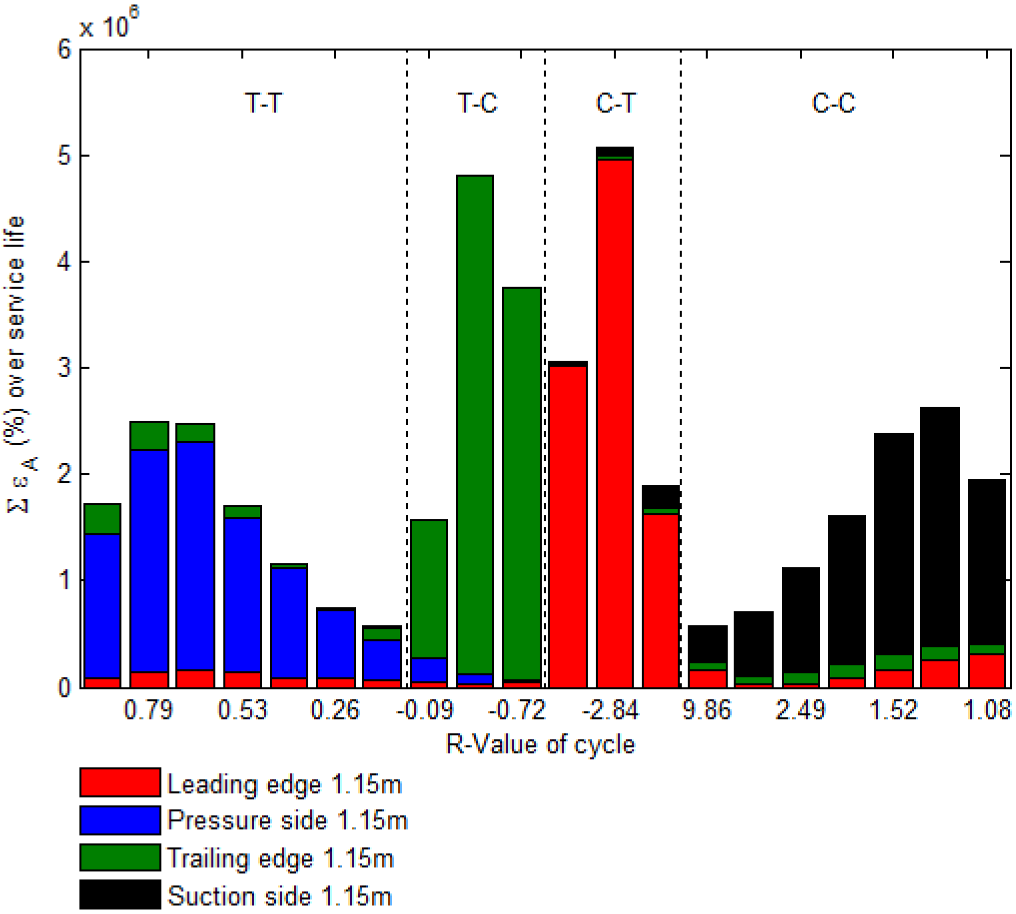

Figure 3.27 – Sum of amplitudes for all cycles in each R-value bin by position at 1.15m from root

Figure 3.27 shows the sum of all cycles binned by R-value at the blade root (1.15m section). The pressure side is again dominated by tensile cycles, the leading edge by compression-tension cycles, the trailing edge by tension-compression cycles and the suction side by compression cycles. However, the cycles near R=1 have a much lower amplitude sum despite the high number of occurrences which can be seen in Figure 3.25. This is because the amplitudes are very low here.

Perhaps a more interesting result is the sum of the cycle amplitudes at different points around the entire blade cross section for all R-values. Figure 3.28 shows the sum of all the amplitudes of strain cycles. It is easy to see why the 5.75m section is the most damaged; this portion of the blade sees the highest strains of the sections examined. Similarly, the strain amplitudes at the tip are smaller by an order of magnitude or more which explains why the damage sums at this part of the blade are very low.

Also of interest is the fact that at the circular root section neither the pressure side nor the trailing edge is the most damaged. The area that sees the highest average strain amplitude is between the two and is due to the combined effect of the flapwise and edgewise bending moments.

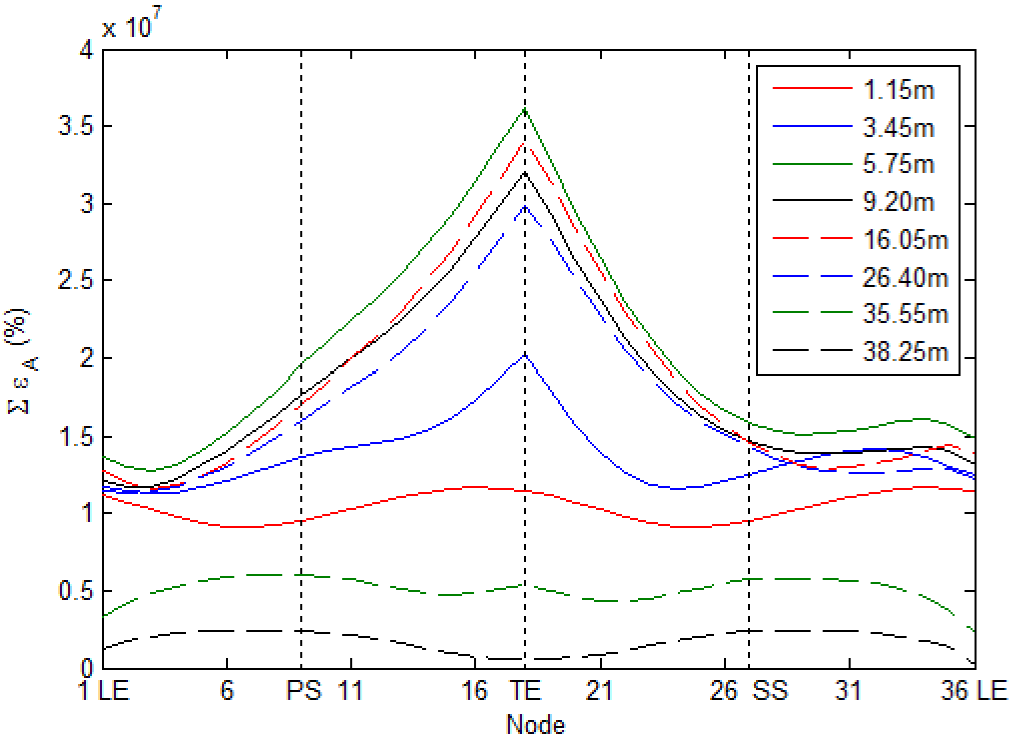

Figure 3.28 – Sum of strain amplitudes for all cycles in service life

The R-values that cause the most damage during the service life can also be analysed. Figure 3.29 shows the sum of the damage at every analysis node and blade section. No account has been made for the average amplitude of the cycles in each R-value bin or the frequency of occurrence. However, it may be argued that if an R-value is causing the most damage (even if this is because it occurs more frequently) then testing should be performed in this region. Very little fatigue data is available for these low amplitude regions and there is discussion about whether or not the assumption that the fatigue data can be combined with the static data at low amplitudes is valid [41]. In this region, the conditions are more akin to creep than fatigue cycling so further testing needs to be done to understand these fatigue conditions. In particular, because the isolines on the Goodman diagram are bunched very closely together in the low amplitude regions the slope of the resulting SN-Curve tends to be very shallow. Despite this, damage can still accumulate because the strain amplitude that defines the intercept of the SN-curve is small.

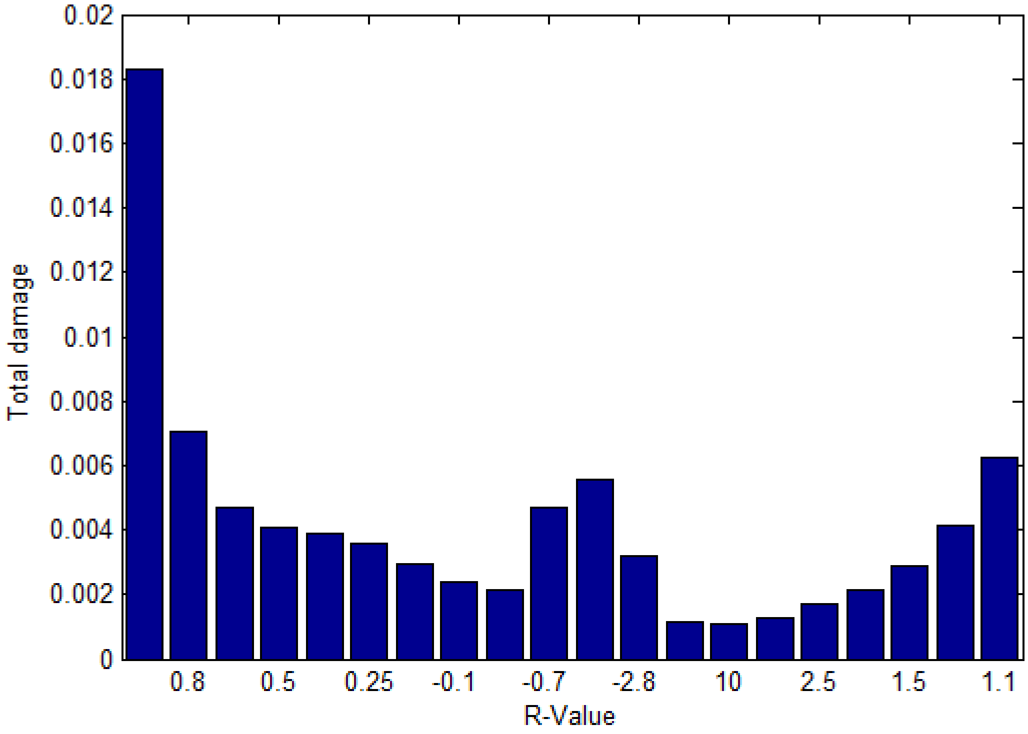

Figure 3.29 – Sum of damage at every analysis node by R-value (power law)

This analysis was also performed for a damage analysis conducted using an exponential curve fit. The two results are compared in Figure 3.30. The y-axis is normalised as the damage sums for the exponential fit are much higher. Notice that the power law fit results in a much larger proportion of damage in the region of R=-1; this is because the large amplitude cycles account for a much larger proportion of the accumulated damage, despite occurring in lower numbers.

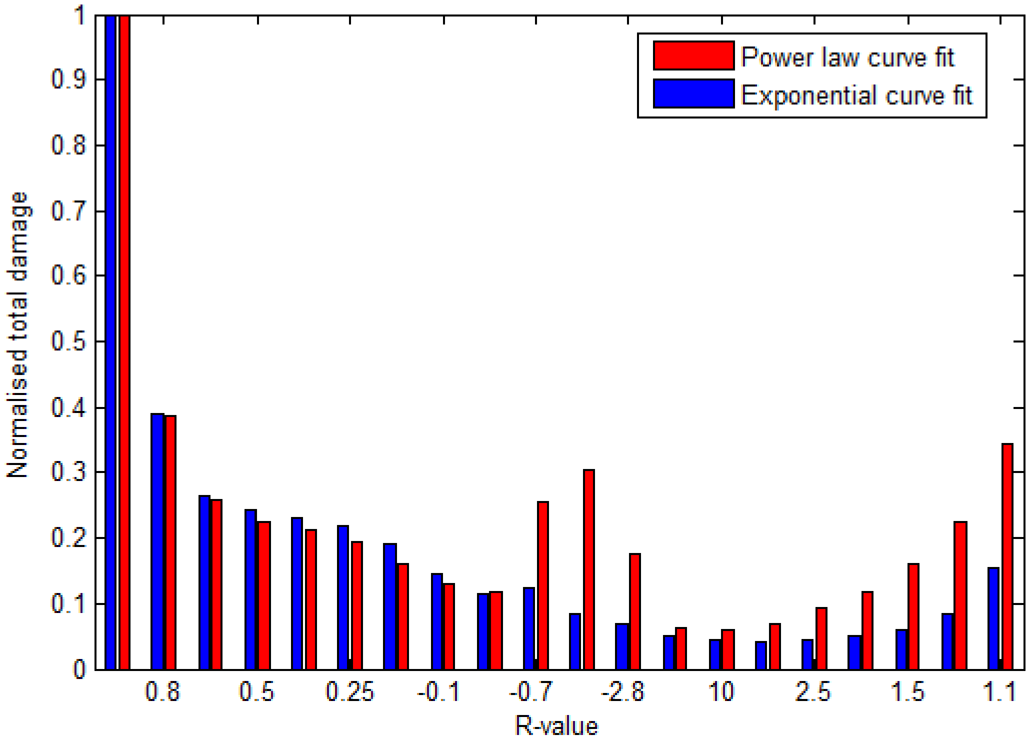

Figure 3.30 – Comparison of total damage sums for power law and exponential fits

The data can be further processed to analyse the average damage resulting from an occurrence of a cycle by R-value. When this correction is performed the fully reversed cycles are again the most damaging, as shown in Figure 3.31.

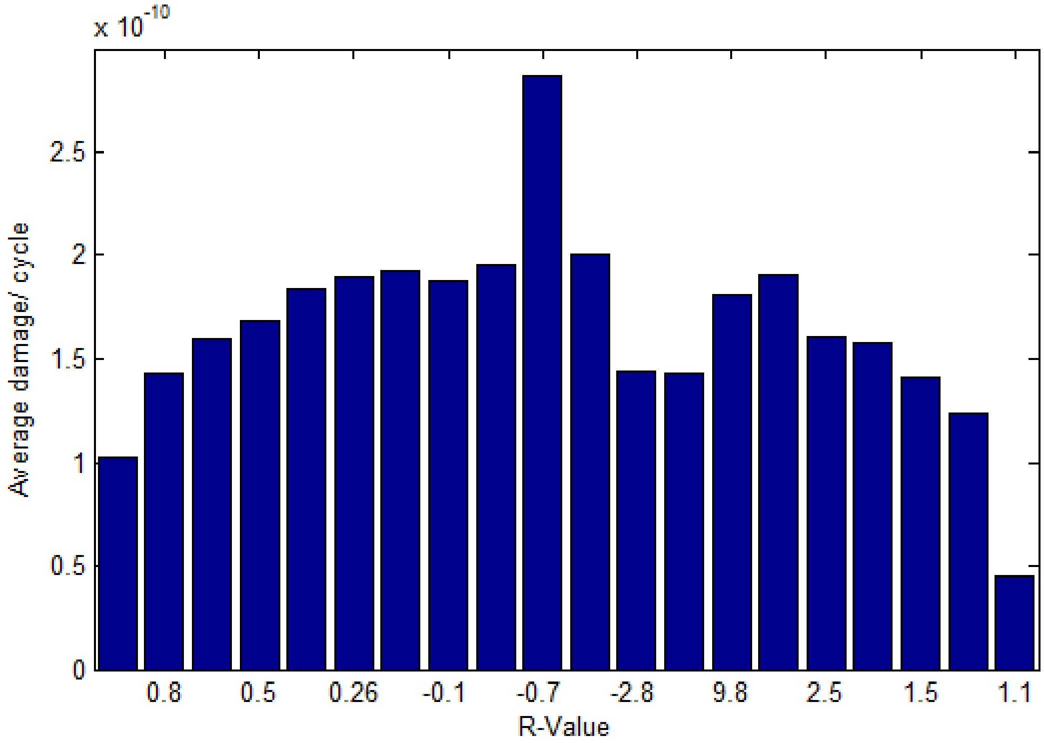

Figure 3.31 – Average damage per cycle by R-value(power law)

However, other R-values are still exhibiting similar damage levels. Also, no account has been made for the fact that different R-values have different average amplitudes. The distribution of average amplitude by R-value over all of the analysed blade sections is shown in Figure 3.32.

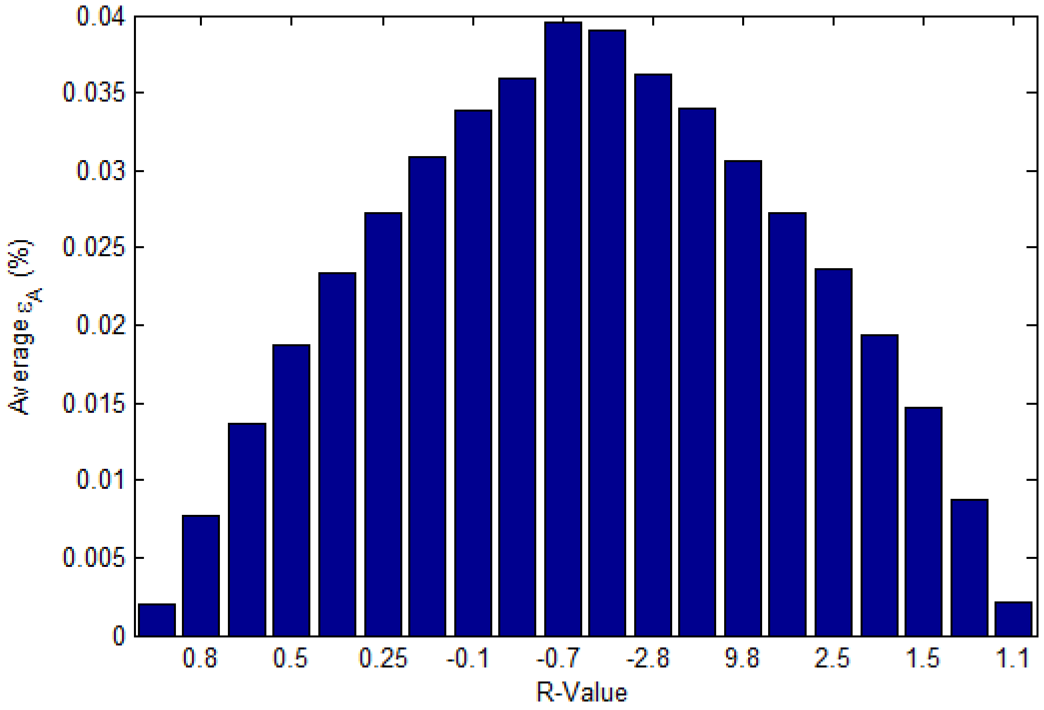

Figure 3.32 – Average strain amplitude by R-value

If the data is processed to reflect the average amplitude in each R-value bin then the low amplitude cycles can be seen to be much more damaging than other cycles, as shown in Figure 3.33. This is a reflection of the fact that these cycles have low amplitudes on average, so the damage per average amplitude is higher. As discussed earlier, the fatigue results projected from a combination of static data and fatigue data at low amplitudes are not trustworthy, and further research is required to understand what is happening under these conditions.

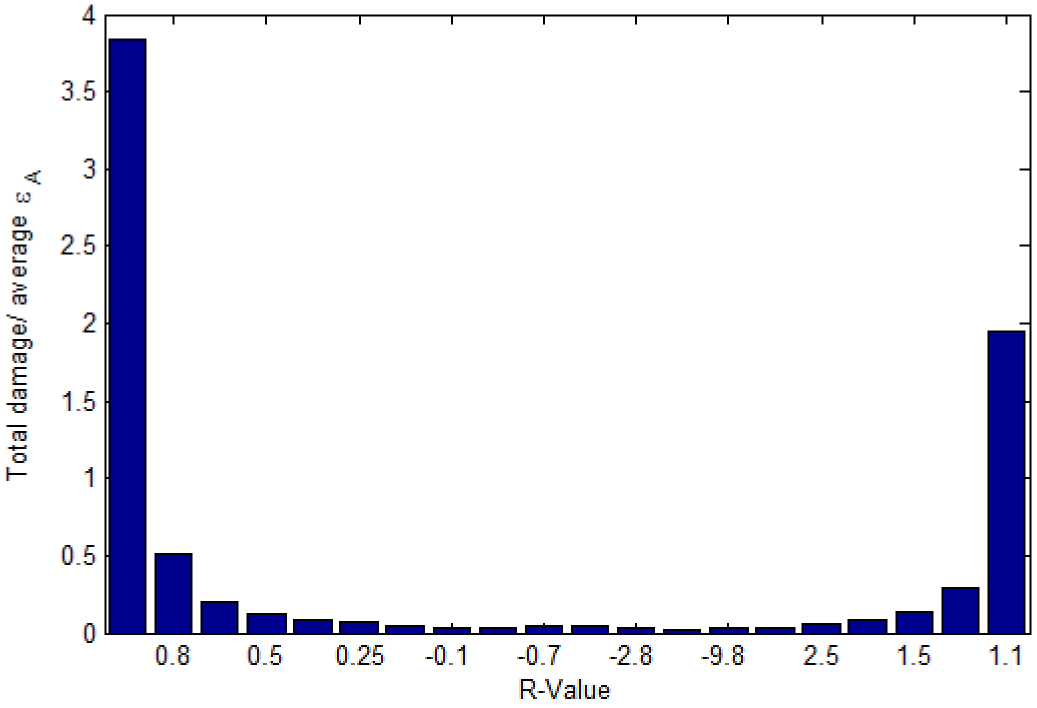

Figure 3.33 – Damage per average amplitude by R-value (power law)

Analysis of this type is instructive because it shows that the low amplitude cycles for which little research exists appear to have a significant impact on the fatigue life. Passipoularidis et al [69] suggest that in the region of R=1 either S-N curves should be derived to verify what is happening or the lines should not converge at the UTS and UCS and should instead meet the x-axis at some point dictated by the creep behaviour.

3.3.5 Comparison of blade fatigue test methods

In order to judge the effectiveness of different methods of blade fatigue testing, the damage caused by the simulated service life is compared to the damage caused by simulated fatigue tests of different types. The method used to describe the service life simulation is described in section 3.2, the calculation of the test load amplitudes is described in section 3.2.6, and the method used to derive the test load time histories is described in section 3.2.7.

The first comparison is a simple comparison of single axis testing, dual axis testing and forced displacement dual axis testing. The comparison is made at the root section, transition section, the most damaged section and a mid-span section. A typical test set up for this size of blade has been used to find the test frequencies and bending moment distribution. The power law curve fit has been used for these analyses.

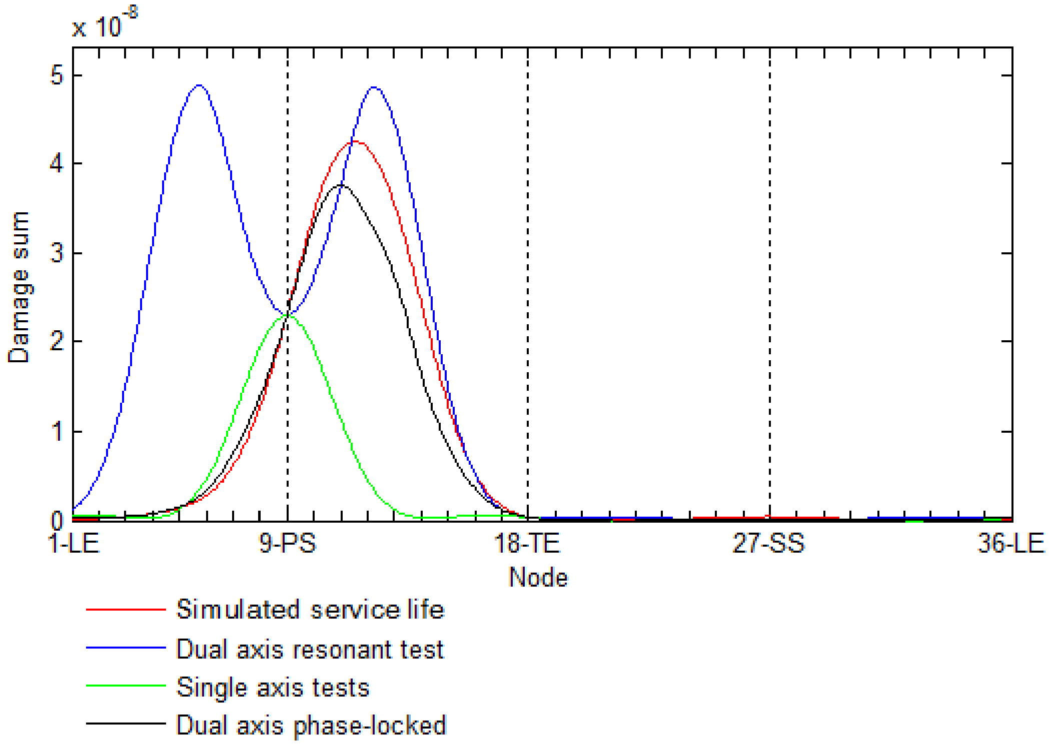

Figure 3.34 – Damage accumulation by test type at 1.15m (root section, power law)

At the blade root, it is clear that the combination of flapwise and edgewise single axis tests is seriously under-testing the blade at the critical area due to the service life. The dual axis resonant test damages the pressure side leading edge more than it should but it is still an improvement over the single axis tests. The best option is a phase-locked test, in which the edgewise and flapwise loads cycle at the same frequency with a realistic phase angle between them. This is difficult to achieve in practice without the use of forced displacement testing, but it allows the blade to be moved in a manner that is closer to field conditions. The phase angle between the flapwise and edgewise loads is very important. White [20] studied simulated load time histories to find the mean and standard distribution of the angle by which the peak edgewise bending moment lags the peak flapwise bending moment and concluded that if the phase angle is to be held constant then a value of 72° is the optimal value for fatigue testing. In this instance, this results in slight under-testing of the blade as shown in Figure 3.34. For the current blade, a phase-locked dual axis test with a phase angle of 66° obtained the closest match to the service life damage at the root.

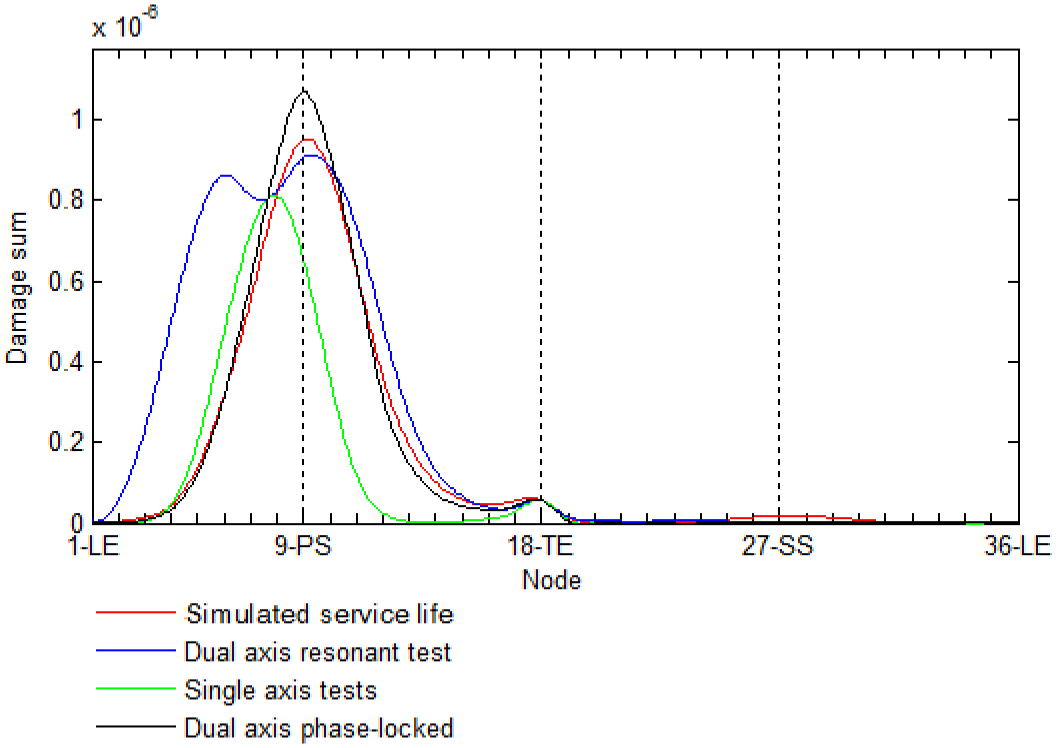

Figure 3.35– Damage accumulation by test type at 3.45m (transition section, power law)

Figure 3.35 shows the damage accumulation by test type at the transition from the root to the aerofoil profile. The trailing edge damage peak is beginning to be more pronounced here, but most of the damage is still focused on the pressure side. The single axis tests are failing to match the damage profile at this section although the issue is less severe than at the root. The over testing due to the dual axis resonant tests is qualitatively less severe than at the root, and the best test method is still the phase-locked dual axis test.

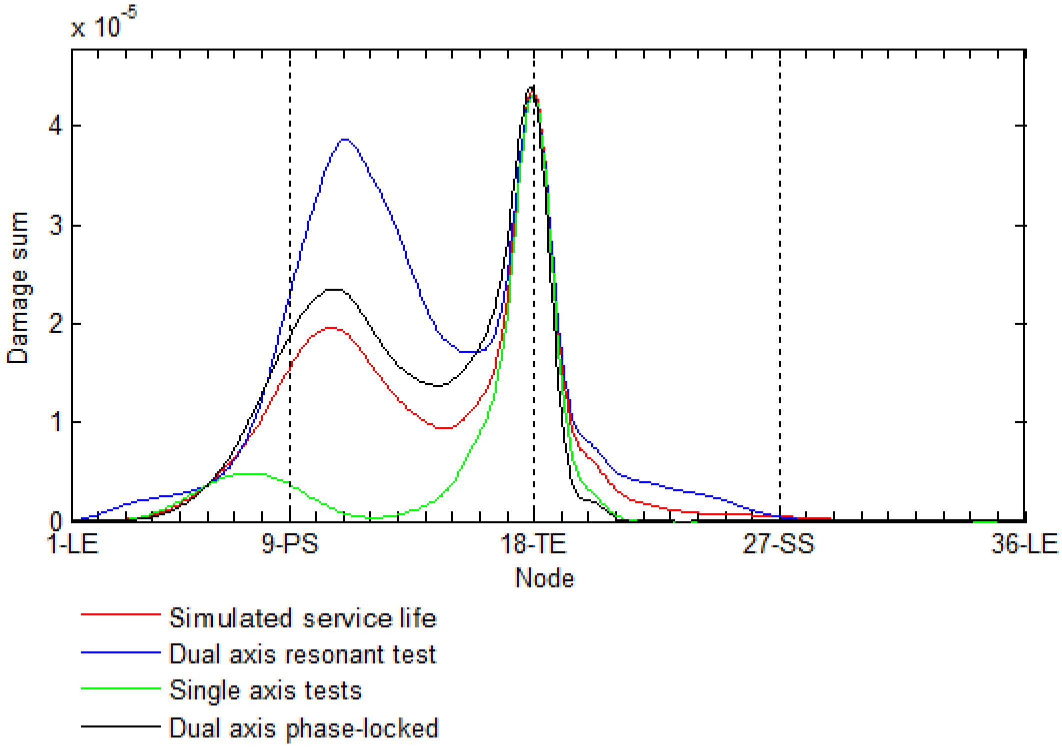

Figure 3.36 - Damage accumulation by test type at 5.75m (most damaged section, power law)

For all of the scenarios considered during the fatigue analysis of the blade service life the 5.75m section was the most damaged. Figure 3.36 shows the damage accumulation at this section due to the service life and different types of testing. The trailing edge service life damage is matched by all of the different test types but the pressure side continues to be over tested by dual axis resonant testing and under tested by single axis testing. Phase-locked dual axis testing is the most effective overall although it is under-testing the suction side compared to dual axis-resonant testing.

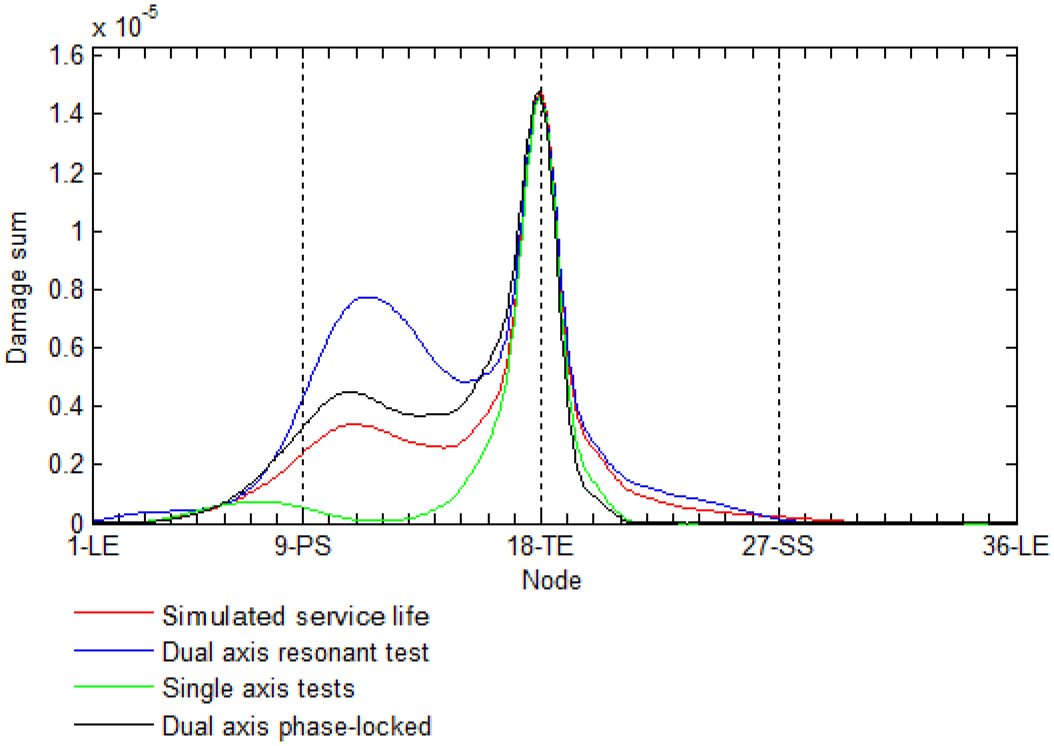

Figure 3.37 - Damage accumulation by test type at 16.05m (mid-span section, power law)

The damage accumulation at the mid-span section shows much less damage accumulation due to the service life on the pressure side, and the dual axis resonant test is quite effective at this section compared to the other test methods as it performs well on the suction side. This is due to the mean bending moment due to the blade self weight being favourable compared to the mean aerodynamic load during the service life.

3.3.6 Effect of Goodman diagram on full scale testing

The analysis of different full scale testing methods above was performed using a power law fit to the fatigue data. If an exponential curve fit is used with the Goodman diagram, the results are very different. This phenomenon was discussed for the service life in section 3.3.2. The calculation of the target bending moment amplitudes for each blade cross section was described in section 3.2.6. As the strains induced by full scale testing are much higher than those seen during the service life and the exponential fit causes much of the damage to be induced by low amplitude cycles, the test results look very different indeed. The target bending moments are also much higher. Target bending moment amplitudes are shown in Table 3.6 for dual axis tests.

	Power law fit BM amplitude		Exponential fit BM amplitude	
Blade section	**Flap (MNm)**	**Edge (MNm)**	**Flap (MNm)**	**Edge (MNm)**
1.15m	2.22e6	1.91e6	8.25e6	8.21e6
3.45m	2.10e6	1.44e6	5.97e6	4.50e6
5.75m	1.87e6	1.24e6	4.70e6	2.15e6
16.05m	9.26e5	5.59e5	2.64e6	1.10e6

Table 3.6 – Comparison of flap and edge bending moment amplitudes for power law and exponential fit

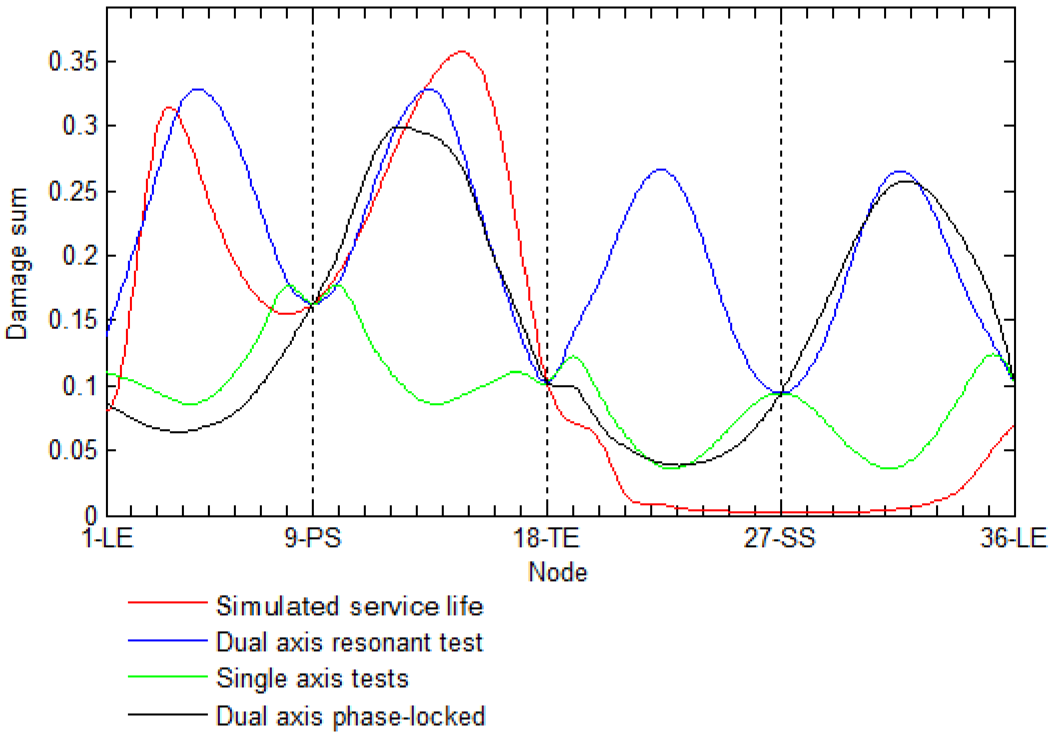

Figure 3.38 – Damage accumulation at 1.15m section (exponential curve fit)

As discussed previously, the exponential fit gives much more weight to the frequently occurring very low amplitude cycles than the power law fit. This results in the pressure side being much more damaged as turbulence plays a greater role. The damage on the suction side is difficult to match because in order to perform accelerated life testing it is necessary to increase the strain amplitude. The self weight of the blade when it is bolted to the test stand results in a mean tensile strain on the top face of the blade (usually this would be the pressure side so that the self weight acts to represent the mean aerodynamic loading). As the amplitude of the test is increased, the R-value of the cycles experienced by the top and bottom faces converges to R=-1. The very high amplitudes required to match the damage on the pressure face when an exponential fit to the fatigue coupon data has been used results in similar fatigue conditions on the top and bottom faces of the blade. This effect is diminished as the number of test cycles is increased, thus reducing the amplitude. Even at 5 million fatigue cycles (which is a reasonably long fatigue test), it can be seen in Figure 3.38 that both the pressure side and suction side accumulate a similar amount of damage compared to what was seen in Figure 3.34, when a power law fit was used. The phase-locked test does not outperform dual axis resonant testing when an exponential fit is used, because the pressure side leading edge is not as highly loaded as it is when resonant testing is used. Dual axis resonant testing better simulates the small amplitude cycles due to turbulence that are so damaging when the exponential fit is used.

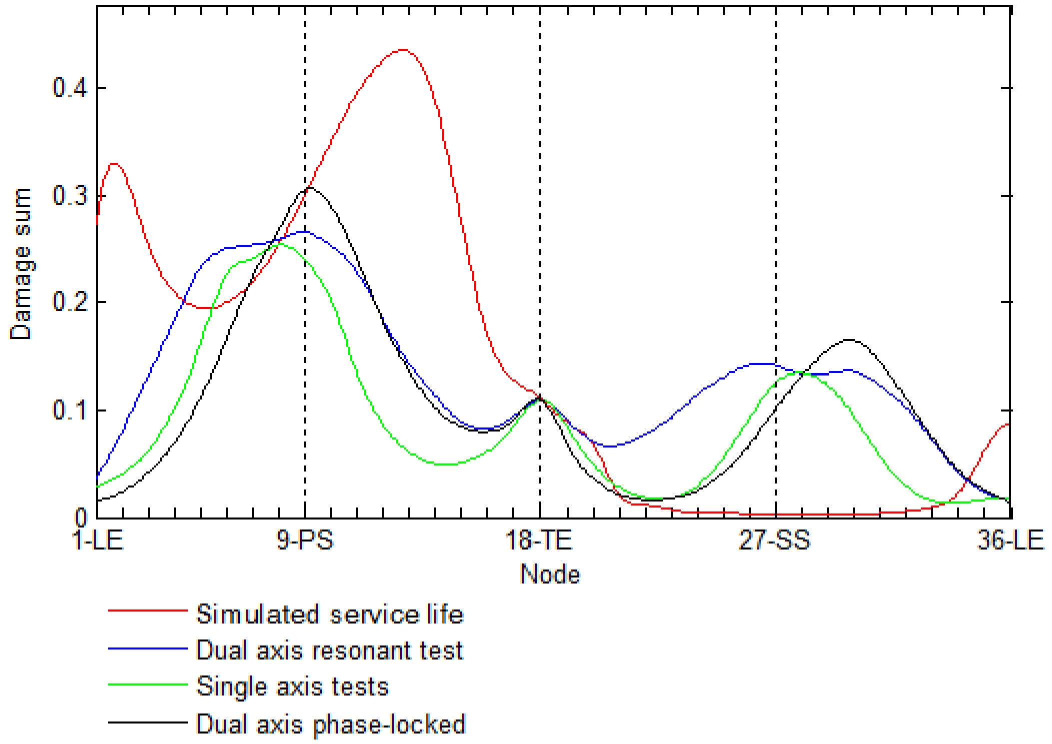

Figure 3.39 – Damage accumulation at 3.45m section (exponential curve fit)

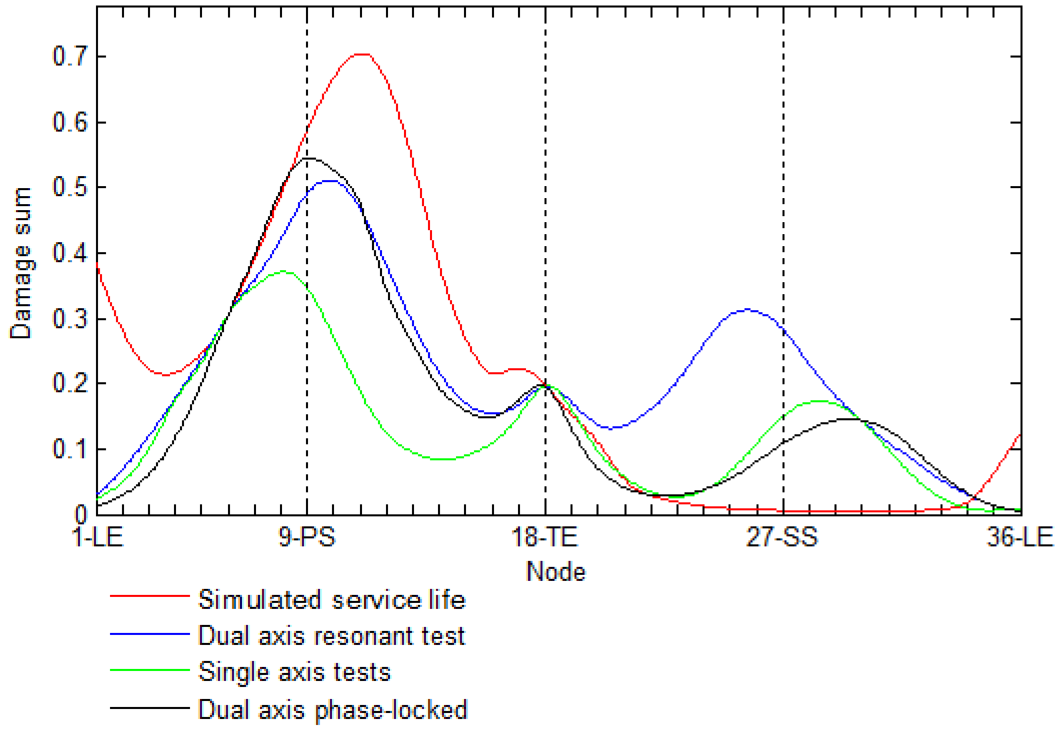

Figure 3.40 – Damage accumulation at 5.75m section (exponential curve fit)

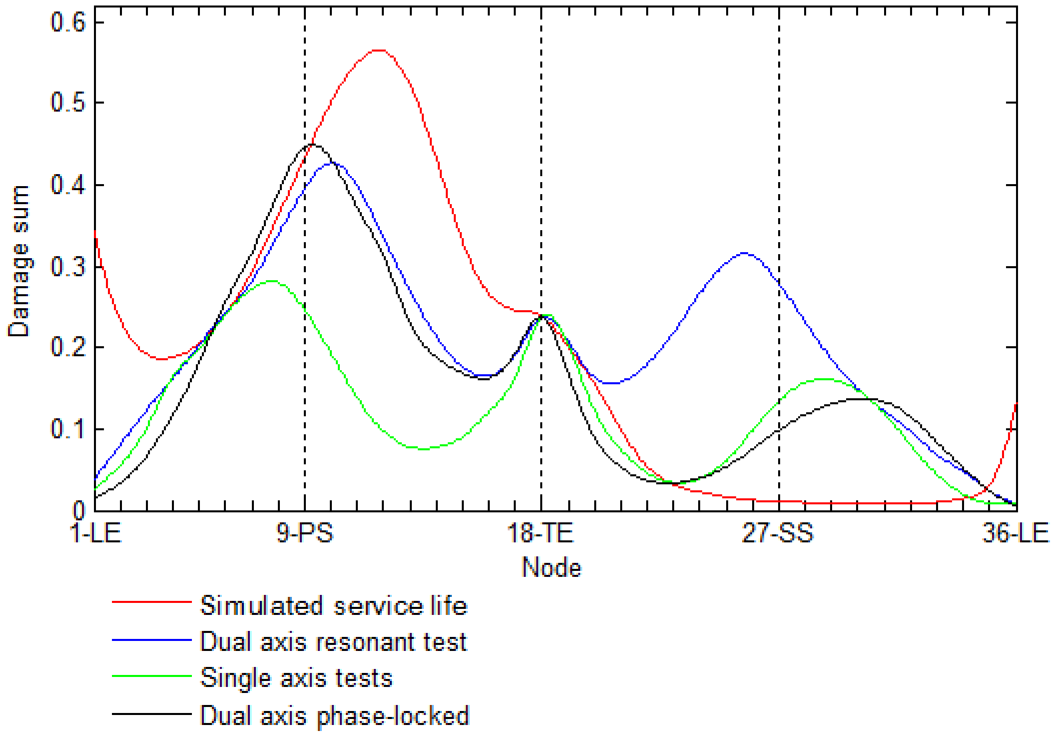

Figure 3.41 – Damage accumulation at 16.05m section (exponential curve fit)

Figure 3.39, Figure 3.40 and Figure 3.41 show the damage sums for testing at the 3.45m section, the 5.75m section and the 16.05m section. These points represent a transition section, the most damaged section and a mid-span section. The main feature to note on these plots is the absence of a pronounced peak at the trailing edge; the small amplitude cycles have such a large effect that the damage caused by the large amplitude reversing cycles is much less significant. The test conditions (high strain amplitude relative to the mean strain) are again causing an increased amount of damage on the suction side.

Using an Exponential fit to fatigue data is more conservative, but the greater influence of the low amplitude cycles is difficult to ignore and could result in an overly short fatigue life. The full scale test loads required when the exponential curve fit is used are much larger than for a power law curve fit.

3.3.7 Influence of test equipment on test results

The test equipment mounted on the blade will modify the mean bending moment along the blade length, and also alter the natural frequency of the blade. These effects need to be understood, as changing the mean bending moment will alter the R-value of the strain cycles and thus change the amount of damage that will accumulate. The ratio of the first flapwise and first edgewise natural frequencies is also important, because it affects the number of edgewise cycles that will be completed in a resonant dual axis test. These effects have been studied by comparing the target bending moment amplitudes and the natural frequencies of a bare blade and a blade loaded with test equipment, using the method described in section 3.2.6.

The mean bending moment and flapwise and edgewise first natural frequencies have been calculated using a beam finite element model. The results are shown in Table 3.7

Section (m)	Dual axis (Nm)	Flapwise test (Nm)	Edgewise test (Nm)	Bare blade (Nm)
1.15	1.74e06	1.62e06	1.39e06	7.56e05
3.45	1.50e06	1.41e06	1.12e06	6.34e05
5.75	1.28e06	1.22e06	8.66e05	5.29e05
9.20	9.60e05	9.60e05	5.12e05	3.95e05
16.05	4.01e05	5.05e05	1.97e05	1.97e05
26.40	4.32e04	1.07e05	4.32e04	4.32e04

Table 3.7 – Mean bending moment with different test set ups

	Dual axis test		Flapwise test		Edgewise test		Bare blade	
	Flap	Edge	Flap	Edge	Flap	Edge	Flap	Edge
Frequency (Hz)	0.81	1.17	0.67	1	1.01	1.5	1.03	1.56
Moment (Nm)								
1.15m	1.68e6	1.59e6	1.72e6	1.58e6	1.78e6	1.58e6	1.97e6	1.58e6
3.45m	1.61e6	1.20e6	1.63e6	1.19e6	1.72e6	1.19e6	1.86e6	1.19e6
5.75m	1.44e6	1.03e6	1.46e6	1.03e6	1.56e6	1.03e6	1.66e6	1.02e6
9.20m	1.19e6	8.15e5	1.19e6	8.13e5	1.33e6	8.13e5	1.36e6	8.12e5
16.05m	7.59e5	4.63e5	7.28e5	4.62e5	8.18e5	4.62e5	8.18e5	4.62e5
26.40m	2.26e5	1.25e5	2.07e5	1.24e5	2.26e5	1.24e5	2.26e5	1.24e5

Table 3.8 – Comparison of natural frequencies and target bending moment amplitudes

Table 3.8 compares the target bending moment distribution for a bare blade with three substantially different test configurations. The edgewise test has less test equipment mounted on the blade than the flapwise test and the dual axis test. As the mean bending moment decreases, the target amplitude increases in order to cause the same amount of damage. The ratio between the natural frequencies remains fairly constant at around 1.5. The difference between the dual axis test and the edgewise test is around 10%, so this means that it is advisable to have some idea before target bending moment amplitudes are calculated what the mean bending moment distribution will be. As the largest difference between the calculated target test amplitudes is around 10%, this is unlikely to require more than one of the design loops described in section 3.2.6.

3.4 Conclusions

The fatigue analysis performed here has provided insights that are highly relevant for blade fatigue analysis.

Fatigue analysis was performed according to the design standards, and the effect of the type of Goodman diagram (linear, as defined in the Germanischer-Lloyd standard, or piecewise linear) and the choice of curve fit to the data (exponential or power law) was studied.

The first and perhaps the most important result is the vast difference in the magnitude of the damage sums obtained when a power law relationship is used to fit a curve to the fatigue test data compared to the results obtained when an exponential fit is used. This is a result of the fact that the very low amplitude cycles contribute much more to the damage sum when an exponential fit is used, and it can result in vastly different damage levels around the blade. For instance, when a power law fit is used the trailing edge tends to be the most damaged area because the strain cycles which occur in this area are generally higher amplitude. However, if an exponential fit is used the turbulence cycles on the pressure side tend to have a much greater effect because they occur in greater numbers. The choice of curve fit is therefore critical; the exponential fit is far more conservative, but it leads to counter-intuitive damage distributions around the blade cross section. Real material behaviour tends to indicate exponential behaviour that tends towards infinite life at low stresses as described by Zhurkov [73].

The analysis of the R-values which occur during the service life of a blade also provided several instructive results. Even when a power law fit is used, the tensile R-values very close to R=1 (low amplitude compared to the mean stress) are still the most damaging by far. This is an important result, as very little fatigue data is available in this regime.

Analysis of the damage caused by full scale fatigue tests shows that single axis tests are prone to under test large areas of the blade when compared to dual axis forced displacement testing and dual axis resonant testing.

The choice of curve fit was again critical; the target bending moment amplitudes calculated when the exponential fit was used were up to 4 times higher when the exponential curve fit was used.

The target bending moment amplitudes for each section were calculated with a variety of mean bending moment distributions along the length of the blade. It was found that although the ratio between the natural frequencies remains close enough to be neglected, the required bending moment amplitude is highly dependent on the mean bending moment. For this reason, test design should be an iterative process; the approximate amount of test equipment to achieve a given bending moment amplitude distribution should be calculated and the target bending moment amplitude should then be recalculated using the mean bending moment distribution from this test set up.

4 Blade Test Optimisation

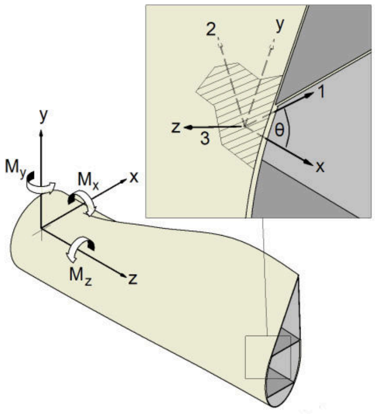

4.1 Introduction

Although there will always be one particularly fatigue critical area on the blade, it is still desirable to obtain the correct bending moment distribution over as much of the length of the blade as possible. By optimising the mass and position of the excitation equipment it is possible to design a test that will result in a similar amount of damage to the service life over a large part of the span of the blade.

White [20] developed an optimisation routine for resonant fatigue testing for use at the NREL test facility. He used the method of steepest descent to optimise the position of static masses attached to the blade. The normalised target bending moment amplitude distribution was used as a target, and the obtained bending moment distribution was found using a finite element model of the blade. The method has the drawback that it can produce test designs that are not feasible in practice. It was also designed solely for the flap direction, as at that time NREL was using a hybrid resonant/ forced actuation system.

The test optimisation routine described below has several advantages; it can optimise a dual axis resonant test, it takes account of air resistance (a major source of damping), and it only produces solutions that are practicable with the test equipment available.

4.2 Background

Any resonant testing system can broadly be described as a mass mounted on the blade that moves at the resonant frequency of the blade.

Figure 4.1 - NREL load frame (courtesy of Narec)

Originally Narec licensed the technology developed by White whilst working at NREL [95]. However, although this design of load frame is reasonably effective for flapwise testing it has several limitations.

The dynamic mass is located at a significant distance from the neutral axis of the blade (see Figure 4.1), which introduces an unwanted moment at the attachment point when the blade is not level which can lead to local failures of the blade [95]. Furthermore, if an edgewise test is to be performed then the mounting arrangements are rather precarious [95]. Figure 4.1 also shows the mounting arrangement common to most methods of excitation. Profiles with a cut out that is the same shape as the local blade cross section at the point at which the equipment will be mounted are created, and then they are clamped together by steel frames. These profiles are typically made from plywood, and the same profiles used to perform a static test are often reused for fatigue tests.

In order to remedy the problems with the NREL excitation equipment, Narec developed an improved method of excitation known as the compact resonant mass (CRM). This was designed in such a way that it would be mounted as close to the blade neutral axis as possible, and with one CRM mounted on each side of the blade the loads are balanced. An edgewise test also becomes much easier and safer with this type of equipment because the system is more stable.

Figure 4.2 shows a CRM of the type used at Narec.

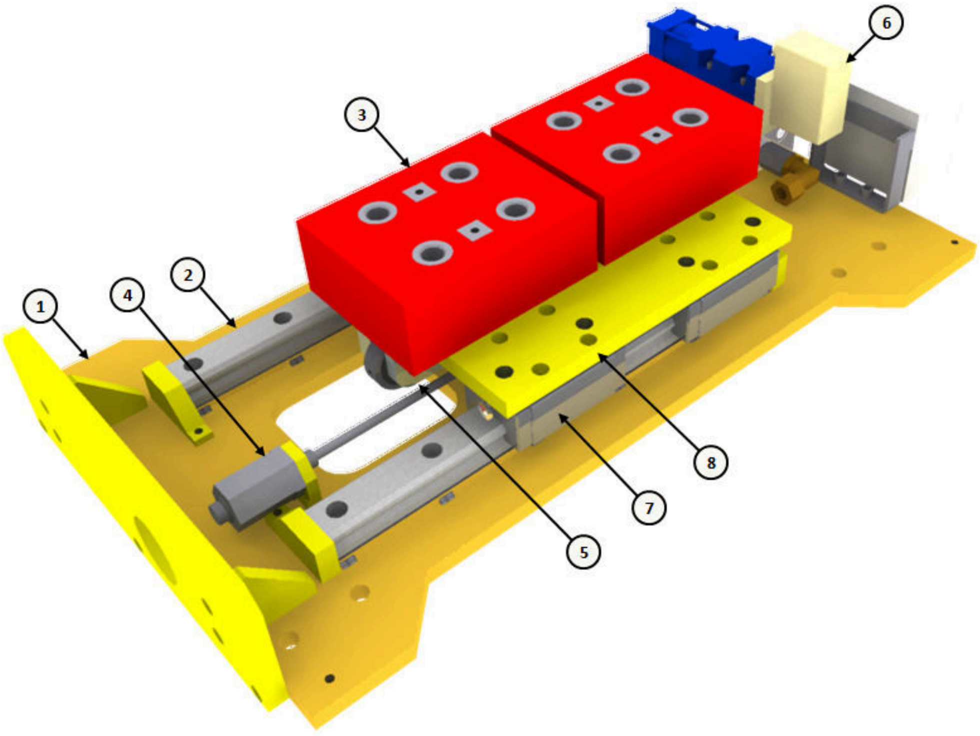

Figure 4.2 - Compact resonant mass (CRM). Courtesy of Narec.

The numbered items in Figure 4.2 are:

1. Mounting frame (static)
2. Rails (static)
3. Adjustable masses (dynamic)
4. Displacement transducer (static)
5. Hydraulic cylinder (assumed static)
6. Servo valve (static)
7. Slides (dynamic)
8. Carriage (dynamic)

4.3 Method

The test optimisation routine developed here uses a finite element model of the blade to find the steady state response of the blade to excitation. The model is used by a genetic algorithm to test how good prospective test configurations are by comparing the flapwise and edgewise bending moment distribution obtained with a given test set up to the target bending moment amplitude distribution.

4.3.1 Finite element model blade and test parameters

Modal superposition was used to find the damped steady state response of the blade to excitation. In order to do this, it is first necessary to develop the stiffness and mass matrices for the blade. The first step is to input information about the blade at ‘stations’ along its length. This information includes:

- Distance of station from root (m)
- Mass per unit length at station (kg/m)
- Flapwise bending stiffness (Nm^2)
- Edgewise bending stiffness (Nm^2)
- Chord length (m)
- Thickness (% of chord length)

Information about the compact resonant masses (CRMs) attached to the blade is then defined. This information includes:

- Distance of CRMs from the root (m)
- Flapwise excitation mass (kg)
- Edgewise excitation mass (kg)
- Flapwise excitation amplitude (m)
- Edgewise excitation amplitude (m)

The blade properties at the positions at which CRMs are to be mounted are then interpolated using a cubic spline and added to the list of blade stations at the appropriate point. The static mass of the saddle is determined by its position on the blade; clearly a saddle mounted at the maximum chord will have a larger mass than a saddle mounted near the tip.

4.3.2 Static mass of excitation equipment

The carriage, slides, adjustable masses and the rod of the cylinder are considered “dynamic mass”. For the Narec system, the minimum mass of this part of a CRM is 47kg. Around 330kg of adjustable mass can be added. The rest of the parts are considered static and have a mass of 85kg [95]. The hydraulic cylinder drives the carriage with a sinusoidal motion (with amplitude up to 0.095m) [95], and a closed loop control system controls the frequency and amplitude of this motion so that the strain amplitude on a critical strain gauge is maintained at a target level defined in the test specification [95].

The approximate static mass of the saddles and mounting frames can be calculated using equation (4.1).

$$m = \rho_s k[(c + 2l)(tc + 2l) - 0.685tc^2] + s[2c(t + 1) + 8l] + nm_s \tag{4.1}$$

Where m is the total static mass of the test equipment, c is the chord length at the mounting point, t is the thickness of the blade (as a proportion of the chord), l is the length that the saddle protrudes past the end of the blade profile, s is the mass per unit length of the clamping frame, ρ_s is the density of the saddle material, k is the thickness of the saddle material, n is the number of CRMs (2 for a single axis test or 4 for a dual axis test) and m_s is the mass of the static parts of a CRM. The factor 0.685 was found by integrating the equation for a NACA 4 digit symmetrical aerofoil, and can be adjusted for different types of aerofoil.

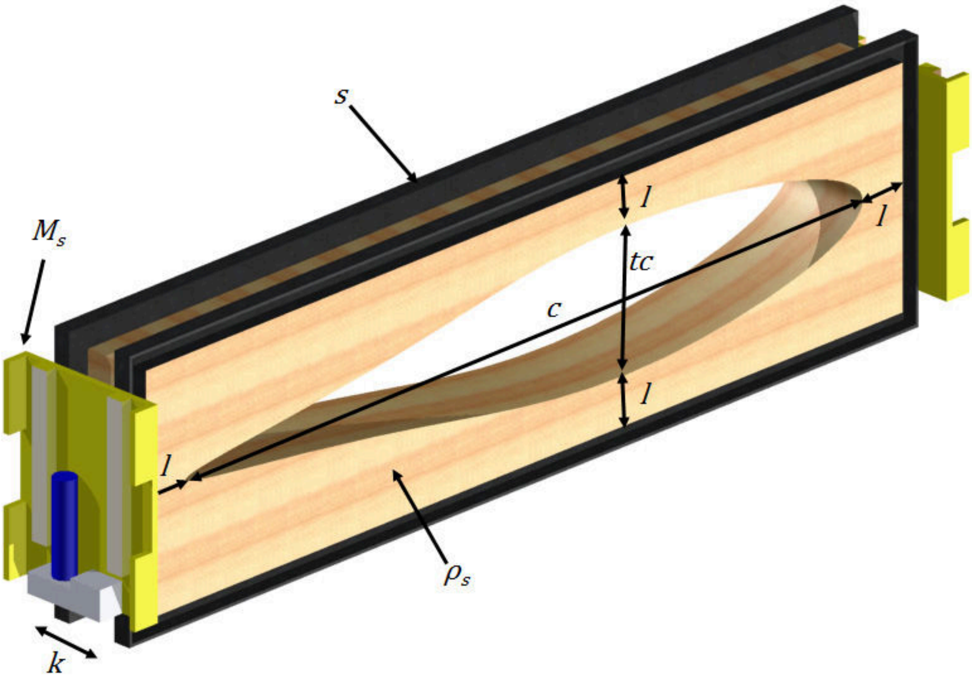

Figure 4.3 - Saddle static mass calculation parameters

4.3.3 Beam element

A simple 1D linear beam element was used, in which each node is free to move vertically and rotate. This made the optimisation process quicker, and also increased its stability. The stiffness and mass matrices are assembled for each element and added to the global stiffness and mass matrices.

$$[\boldsymbol{K_E}] = \frac{EI}{L^3}\begin{bmatrix} 12 & 6L & -12 & 6L \\ 6L & 4L^2 & -6L & 2L^2 \\ -12 & -6L & 12 & -6L \\ 6L & 2L^2 & -6L & 4L^2 \end{bmatrix}$$

$$[\boldsymbol{M_E}] = \frac{mL}{6}\begin{bmatrix} 3 & 0 & 0 & 0 \\ 0 & L^2 & 0 & 0 \\ 0 & 0 & 3 & 0 \\ 0 & 0 & 0 & L^2 \end{bmatrix} \tag{4.2}$$

In equation (4.2) $[\boldsymbol{K_E}]$ is the element stiffness matrix, $[\boldsymbol{M_E}]$ is the element mass matrix, EI is the bending stiffness, L is the element length and m is the blade mass/ unit length at the start of the element [104].

Once the global stiffness and mass matrices have been assembled the mass of the excitation equipment is added to the appropriate nodes and boundary conditions at the hub are imposed by removing the rotational and translational degrees of freedom at the hub node.

4.3.4 Steady state response

The eigenvalues and orthonormalised eigenvectors are then found using the ‘eig’ function in MatLab. The method described by Rao was used to find the steady state response of the system [104]. Firstly, the generalised force vector is found using equation (4.3).

$$\boldsymbol{Q} = [\boldsymbol{X}]^{\boldsymbol{T}}\boldsymbol{F} \tag{4.3}$$

In equation (4.3), $\boldsymbol{Q}$ is the generalised force vector, $[\boldsymbol{X}]$ is the matrix containing the eigenvectors of the system and $\boldsymbol{F}$ is the force vector. If the modal participation factors are denoted by $\boldsymbol{q}$ then the decoupled equations of motion of the system can be written as shown in equation (4.4) for each mode.

$$\ddot{q}_i(t) + 2\zeta_i\omega_i\dot{q}_i(t) + \omega_i^2 q_i(t) = Q_i(t), i = 1,2 \dots n \tag{4.4}$$

In equation (4.4), q_i is the modal participation factor for mode i, ω_i is the natural frequency of the mode (determined from the eigenvalues) and ζ_i is the damping coefficient for the mode, determined by testing as described in section 4.3.6. Chortis et al [105] predicted the damping coefficients for the first 3 flapwise and edgewise modes of a composite blade. They found that the damping coefficients for the flapwise modes were approximately equal and the same was true for the edgewise modes. This suggests that it is a reasonable approximation to assign the same damping coefficient to all modes. As the flapwise case is analysed separately to the edgewise case in the present work this is easily achieved.

The steady state solution of equation (4.4) can be calculated using equation (4.5), which can be used to calculate each component of the modal participation vector $\boldsymbol{q}$.

$$q_i(t) = q_{i0}\cos(\omega t - \varphi)\,, i = 1,2 \dots n$$

where

$$q_{i0} = \frac{Q_{i0}}{\omega_i^2}\frac{1}{\sqrt{\left[\left\{1-\left(\frac{\omega}{\omega_i}\right)^2\right\}^2 + \left(2\zeta_i\frac{\omega}{\omega_i}\right)^2\right]}} \tag{4.5}$$

The steady state response can then be found from equation (4.6).

$$\boldsymbol{x} = [\boldsymbol{X}]\boldsymbol{q} \tag{4.6}$$

The boundary conditions are then reinserted (hub node displacement and rotation set to 0) and the x-displacements, $\boldsymbol{x_i}$ are substituted into equation (4.7) to find the internal forces and moments, $\boldsymbol{f_i}$ in element i.

$$\boldsymbol{f_i} = [\boldsymbol{K_E}]_{\boldsymbol{i}}\boldsymbol{x_i} \tag{4.7}$$

The bending moment distribution can then be compared to the target bending moment distribution obtained using the method described in section 3.2.6 and used as a scoring criterion.

4.3.5 Forces

The force vector $\boldsymbol{F}$ is composed of aerodynamic forces as well as the forces from the CRMs. The CRM forces are easy to find, as the motion of the reciprocating mass is sinusoidal. The force amplitude can therefore be found from equation (4.8) for each CRM. This force is added to the relevant part of the force vector.

$$F_{CRM} = m_d a\omega^2 \tag{4.8}$$

In equation (4.8), m_d is the total dynamic mass of a pair of CRMs (static and dynamic mass are defined in Figure 4.2), a is the amplitude of the CRM motion and ω is the angular velocity of the excitation.

The aerodynamic forces are much more complicated. Although the maximum velocity of each node can easily be calculated using equation (4.9) if the amplitude is known, the forces are related to the velocity of the blade, which is found from the amplitude of the oscillation and the frequency of oscillation, which in turn requires knowledge of the forces.

$$\dot{x}_{i\,max} = x_{i\,max}\omega \tag{4.9}$$

This means that there is a circular reference. Also, because the motion of the blade is unsteady the aerodynamic force on a node i of the blade cannot strictly be calculated using equation (4.10). This is because of several factors. The blade encounters its own wake, meaning the relative velocity is higher than if the flow was steady. It also pulls a volume of air with it that must be accelerated, and generates leading and trailing edge vortices that interact with the blade.

$$F_{D\,i} = -\frac{1}{2}\rho A_i C_{D\,i}|\dot{x}_i|\dot{x}_i \tag{4.10}$$

In equation (4.10) $F_{D\,i}$ is the drag force acting on node i, ρ is the air density, A_i is the characteristic area associated with node i and x_i is the translational velocity of the blade. $C_{D\,i}$ is a dimensionless constant that quantifies the air resistance of the 2-D blade cross section node i under steady conditions.

The unsteady effects have been checked by computational fluid dynamics work performed at Narec. As the mesh updates at each time step the solution is very time consuming. The mesh sensitivity was checked, and the results were found to be the same for both course and fine meshes and time steps so the results are considered to be reliable. As can be seen in Figure 4.4 the domain was very large compared to the blade, so the effect of the floor and walls in the blade test facility is not accounted for.

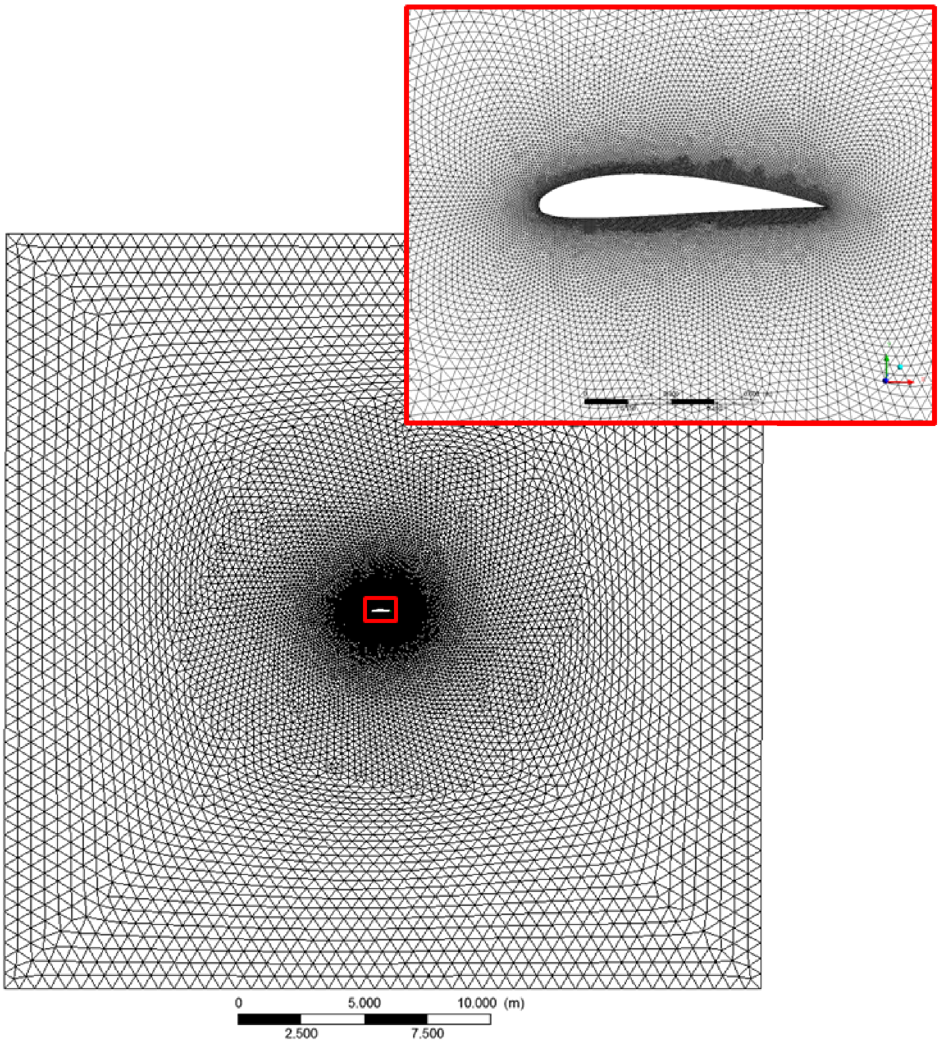

Figure 4.4 - CFD mesh. Courtesy of Narec.

There is currently work being performed at Durham University to investigate if a meshless vortex method developed for flapping wing micro aircraft can be adapted to model the air resistance during blade tests as this will reduce the simulation time very significantly [106]. It may eventually be combined with the structural simulation described in chapter 5.

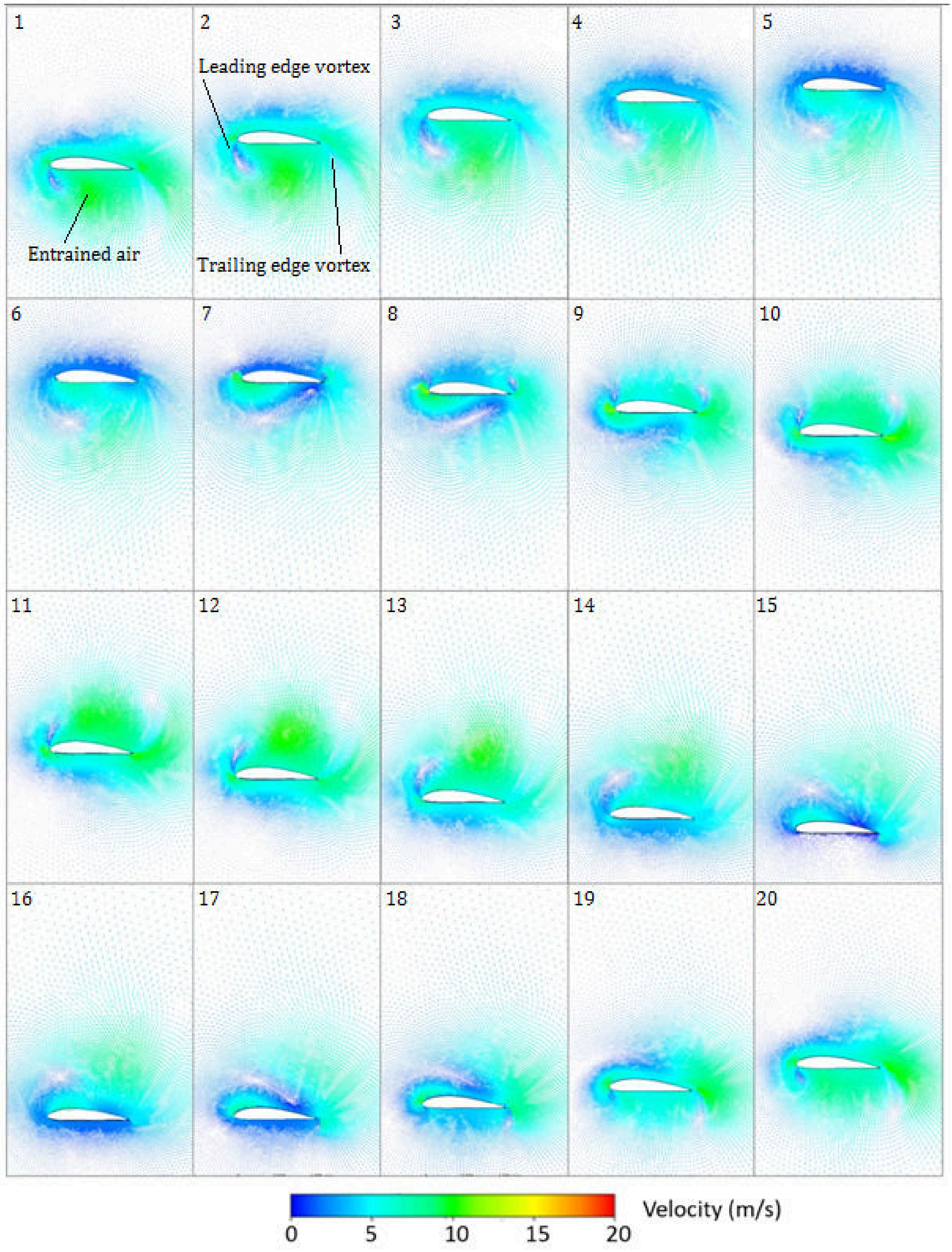

Figure 4.5 - Air velocity around blade for 1 cycle. Courtesy of Narec.

Figure 4.5 shows velocity vectors around the blade as it undergoes one cycle and clearly shows the shed vortices, entrained air and wake interaction that result in the higher than expected drag forces acting on the blade.

The force predicted if the problem is considered to be quasi-steady is compared to the CFD results in Figure 4.6. The large increase in drag coefficient is attributed to the blade interacting with its wake and the shed vortices, and the phase shift is assumed to be due to the blade having to accelerate the entrained air. Unfortunately, as the computational cost of performing the simulations was so high simulations were only performed in the flapwise direction for a 1m chord length oscillating with 1m amplitude and 2m amplitude. This means it is not possible to draw conclusions about the relationship between frequency and amplitude. The 1m oscillations resulted in an effective drag coefficient of 5.3 and the 2m oscillations resulted in a value of 4.45. As such, an effective drag coefficient for use in equation (4.10) has been assumed to be 5 for all points on the blade. No simulations were performed for the edgewise direction but the drag coefficient has assumed to be the same for this as well (this assumption is not as coarse as it may seem, as the blade twist will increase the edgewise drag coefficient). The thickness of the blade has been used to calculate the area for the edgewise direction and the chord for the flapwise direction.

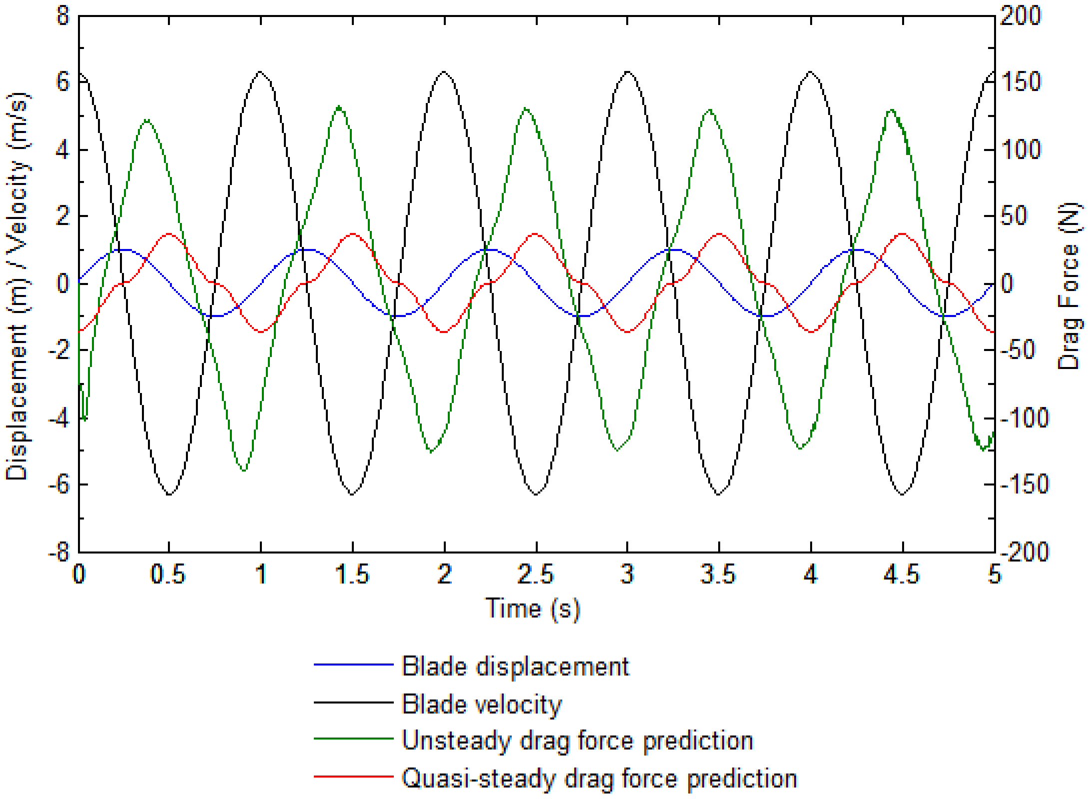

Figure 4.6 –Quasi-steady drag and unsteady drag at 1m amplitude, 1Hz frequency

A fairly simple way of improving the results would be to build up a look-up table for the drag coefficient based on the amplitude and frequency. This would become very difficult for a dual axis test, but for single axis tests it would not be too hard.

With the unsteady effects accounted for by increasing $C_{D\,i}$ in equation (4.10) it can be used to calculate the drag force at each node. As the aerodynamic force is due to the velocity of the blade, it is out of phase with the excitation force by π radians. It can also be approximated as a sinusoid, so it can be represented in the force vector as a harmonic force.

To solve the problem of the circular reference when calculating the aerodynamic drag force, the blades displacement was assumed to be the first mode shape multiplied by a scaling factor. This assumption holds true because the system is being excited at its first natural frequency (the modal participation factor of the first mode is very high, typically accounting for over 99.9% of the total). For a given scaling factor, the peak velocity of each node can be calculated from the natural frequency and the displacement of the node. The parameters involved in calculating the aerodynamic drag are shown in Figure 4.7 (the characteristic area A_i for each node is calculated from the chord (or thickness for the edgewise case) and the distance to the adjacent nodes.

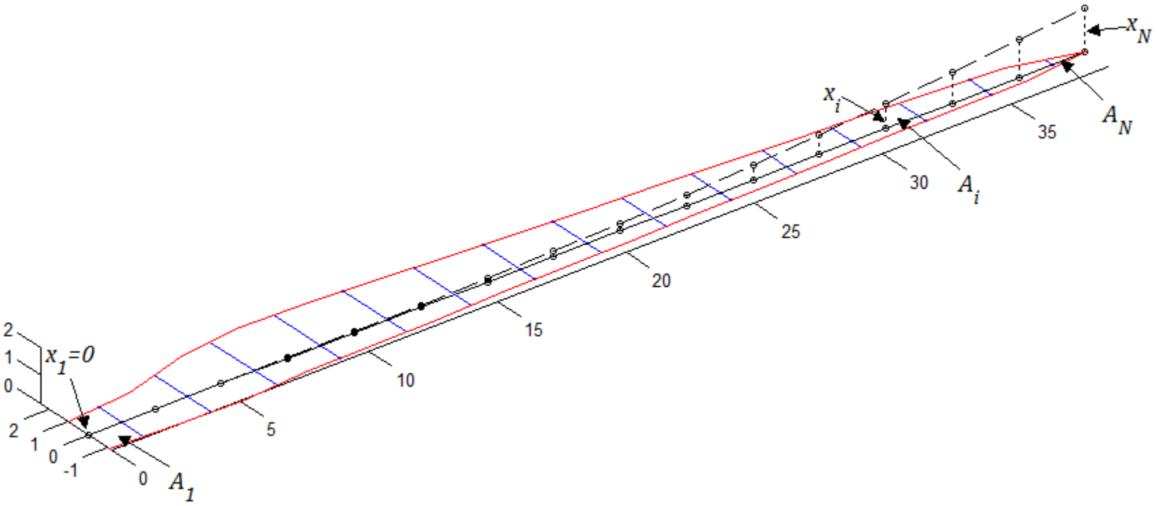

Figure 4.7 - Drag force calculation parameters

A bisection search was used to find a scaling factor for the mode shape that resulted in a tolerable difference between the displacements of the scaled mode shape (x_{sms}) and the displacements of the calculated response (x_{cr}) when the aerodynamic force is calculated using the scaled mode shape.

$$\sum_{i=1}^{i=n} x_{sms\,i} - \sum_{i=1}^{i=n} x_{cr\,i} \le tol \tag{4.11}$$

A bisection search works by bracketing the solution by two values, one which results in a positive solution and one in a negative solution [103]. The midpoint of the two values is then found and two new brackets are created. The pair which brackets the root is chosen, and the process is repeated until the difference between the negative and positive values is smaller than a predefined tolerance. It is a very robust method [103], but it is quite slow. However, this part of the code does not represent a significant part of the overall solution time so this is not a concern.

4.3.6 Structural damping

The structural damping in equation (4.5) can easily be found by experimentation. During the set-up process for the test, the blade can be excited and then left to vibrate freely. Strain gauge or tip displacement time histories can be used to find the damping coefficient either by curve fitting or from the logarithmic decrement.

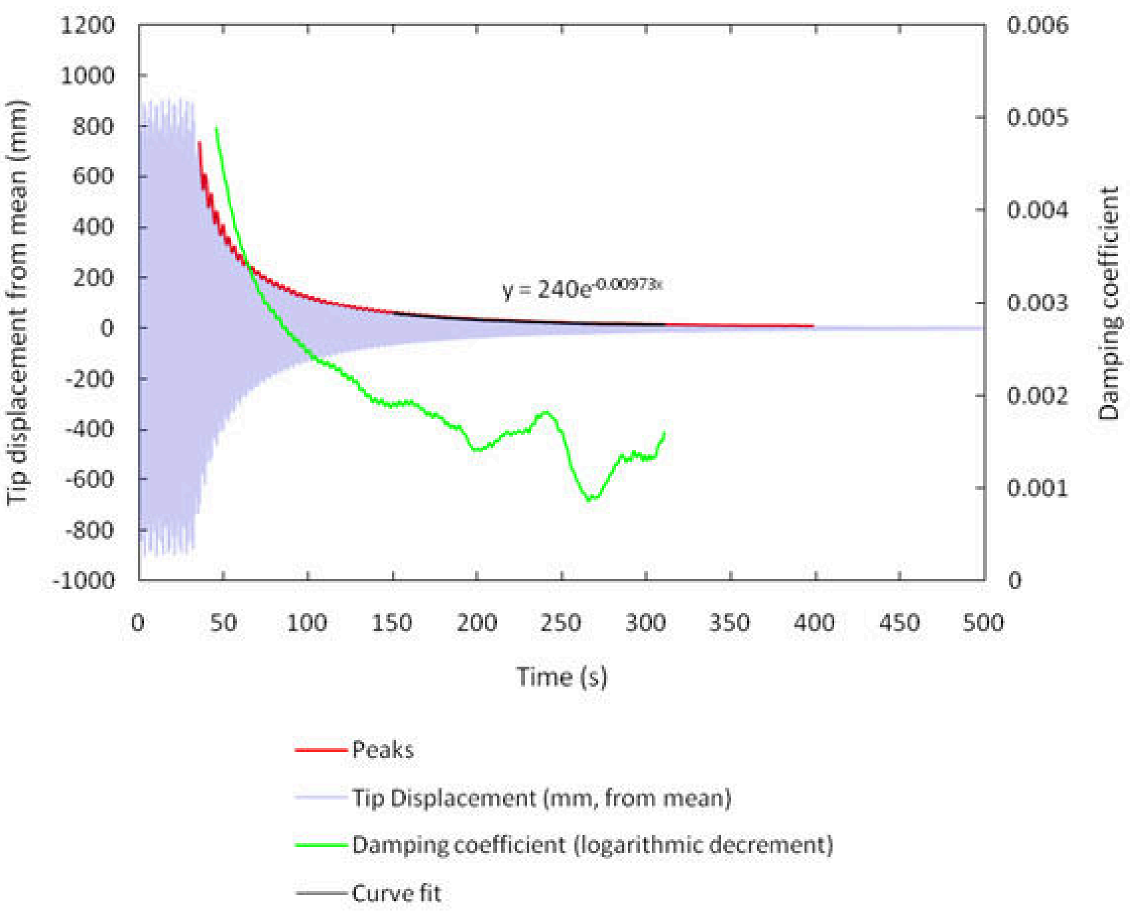

Figure 4.8 - Calculation of structural damping coefficient

Figure 4.8 shows a time history of the mean tip displacement of a blade of similar size to the one investigated in this work after excitation has stopped. The influence of the air resistance can be seen in the damping coefficient calculated by logarithmic decrement. It falls steadily until around 150 seconds, when it starts to level out before the resolution of the test equipment and interaction between the flap and edge vibrations starts to cause it to become unsteady. The structural damping coefficient must be determined from data obtained after the air resistance has ceased to be a significant factor. The curve fit is of the form of equation (4.12).

$$y = a\exp(-\zeta\omega t) \tag{4.12}$$

The damping coefficient for this data calculated using the curve fit and equation (4.12) is 0.001549. By taking the average of the damping coefficient calculated from the logarithmic decrement over the same time period we obtain a value of 0.001506. This low value means the system is extremely lightly damped, and most of the damping comes from air resistance so the 3% discrepancy between these values is not worrying.

The high modal participation factor of the first mode discussed earlier means that it is reasonable to use this damping value for all the modes. The edgewise damping can be found in a similar way.

4.3.7 Flap and edge

The process is the same for both flap and edge loading. If both the flapwise and edgewise bending moment distributions are of interest then the process is performed for both directions (the same mass matrix is used for flap and edge, but the stiffness matrix is rebuilt for each analysis).

Performing these analyses separately has the disadvantage that the blade twist is not taken account of, but it is much quicker and more robust method than a 3D analysis. The effect of blade twist is checked subsequently with a transient analysis, as described in chapter 5.

4.3.8 CRM capability

The hydraulic cylinder pull force is a limiting factor on the performance of a CRM. The cylinder force required to maintain the motion is found from equation (4.13).

$$F_{CRM} = m_d(a_{CRM} + a_{Blade})\omega^2 + \ m_d g \tag{4.13}$$

In equation (4.13) m_d is the dynamic mass, a_{CRM} is the CRM amplitude, a_{Blade} is the amplitude of the blades motion at the point at which the CRM is mounted and ω is the angular velocity of the excitation. If the CRM is mounted horizontally then the gravity term can be neglected. The program checks if this value exceeds the pull force of the cylinder that drives the CRM and returns a flag if any of the CRMs are operating beyond their capabilities. This results in the test set up artificially being assigned a very poor score in the optimisation routine.

4.3.9 Frequency alteration feasibility study

As described in chapter 3, the results of a dual axis test are considerably improved if the flapwise and edgewise loads are cycled at the same frequency with the edgewise loads lagging the flapwise loads by a pre-determined angle. Studies performed by White [20] showed that the optimal value for this angle is 72°, and this was found to be effective for the present work as well. The B-Rex hybrid forced displacement/ resonant excitation system employed at NREL was found to be an effective test method for smaller blades. However, as blades increase in size it is not practicable. It is worthwhile to consider the effect of altering the edgewise frequency so that the loads cycle at the same frequency so that resonant testing can be used for both axes.

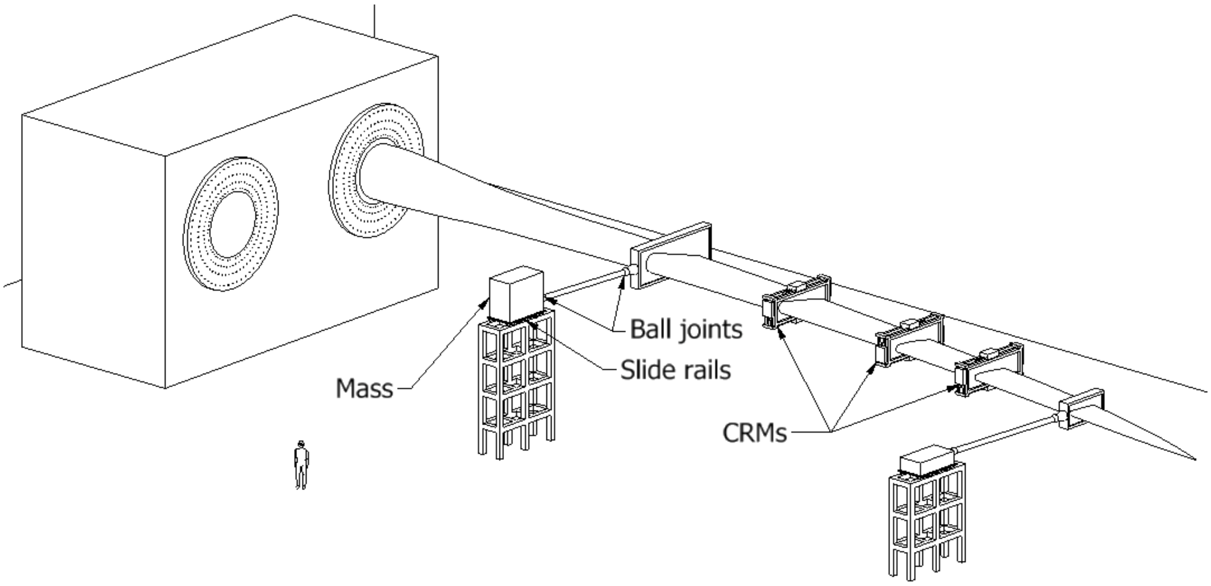

Figure 4.9 - Possible method of edgewise frequency reduction

This could possibly be achieved by adding mass to the edgewise direction only as shown in Figure 4.9. The push rods connecting the blade to the sliding mass would need to be as long and as light as possible so that they do not affect the flapwise direction too much. Ideally, these sliding masses would be distributed over the entire length of the blade, but in practice this is not realistic. Given that setting up large blade tests is already a challenging task, it is not feasible to use more than two of these tuning masses, so this approach has been adopted in the present work.

The finite element model was altered slightly in order to allow a feasibility study into reducing the edgewise frequency of the blade by adding extra mass to the edge direction only. The mass was treated as a saddle which was only added to the mass matrix for the edgewise direction.

4.3.10 Test Configuration Optimisation

A genetic algorithm was used to optimise the position, dynamic mass and amplitude of the CRMs. This approach was taken because genetic algorithms are better at finding global minima than, for example, steepest descent methods [107].

Genetic algorithms mimic the process of natural evolution [107]. The variables (or 'genes') of a particular solution to the problem are contained in a vector called a 'chromosome'. An initial 'population' of individuals is generated by randomly selecting values for each variable in the chromosome between predefined bounds. A 'fitness' is assigned to each individual by comparing the bending moment amplitude distribution along the length of the blade obtained with the solution to the target bending moment amplitude distribution. A new population is then created by selecting pairs of individuals from the old population and adding them to the new population. Fitter members of the population are more likely to be selected, and the pair may have their 'genes' swapped over at a random point in the chromosome. A random mutation may also be applied to a single gene in the chromosome of one or both of the pairs. This process is repeated until the new population is the same size as the old, at which point it replaces it and the cycle repeats. The process continues for a predefined number of generations, or until the average fitness of the whole population converges towards the fitness of the fittest individual. A flow chart of the process is shown in Figure 4.10.

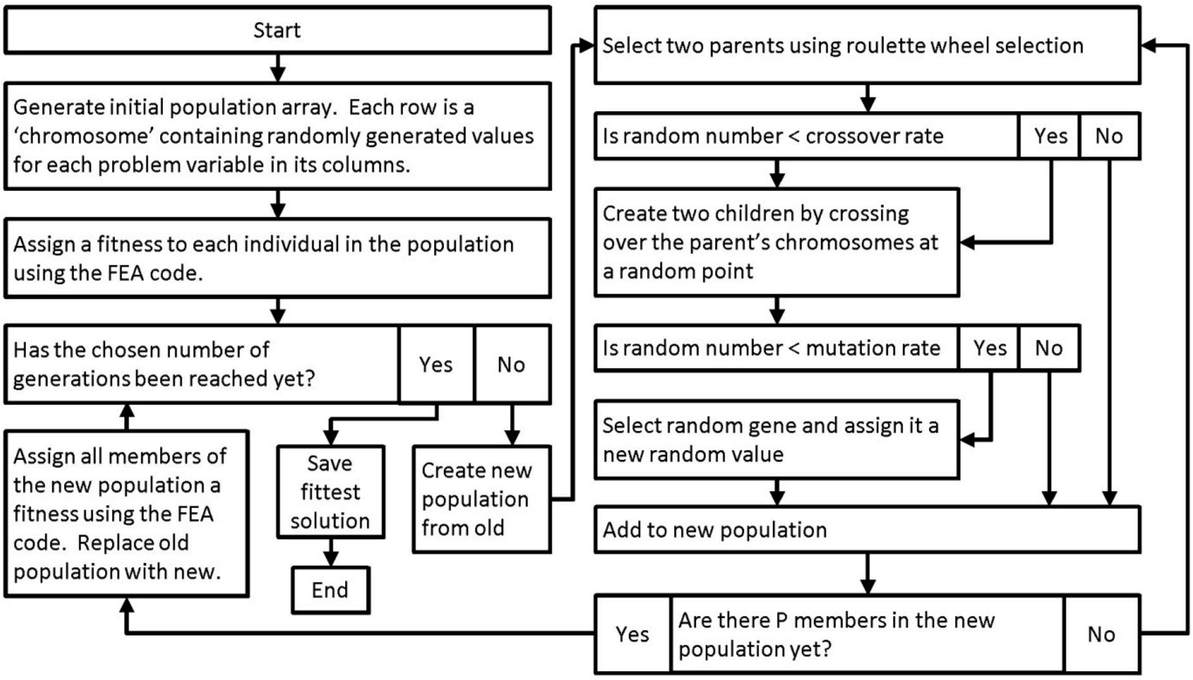

Figure 4.10 - Genetic algorithm flowchart

4.3.11 Chromosomes

There are two possible scenarios for the blade test optimisation problem. Either the blade test customer is willing to pay to have separate CRM mounting saddles made up for the test, or they would like to use saddles made up previously for a static test to save time and reduce cost. Naturally choosing to use saddles at predefined points reduces the quality of the bending moment distribution.

If the customer is willing to pay to have saddles made then the chromosome is of the form shown in Table 4.1. The first 3 cells will be repeated as many times as there are CRMs. The static mass of the excitation equipment is based on the position along the blade, and whether one pair or two pairs of CRMs will be attached to the saddle. If the test is only being performed in one axis then the CRM dynamic mass and amplitude for the redundant axis can be set to have a maximum of a very low value.

Position (m)	Flap dynamic mass (kg)	Edge dynamic mass (kg)	Flap amplitude (m)	Edge amplitude (m)

Table 4.1 - Chromosome for undefined saddle positions

If the customer is using pre made saddles then the chromosome is of the form shown in Table 4.2. The first 3 cells will be repeated as many times as there are pre made saddles.

Flap dynamic mass (kg)	Edge dynamic mass (kg)	CRM switch	Flap amplitude (m)	Edge amplitude (m)

Table 4.2 - Chromosome for predefined saddle positions

CRM switch is a randomly generated number between 0 and 1. If it is greater than 0.5 then the CRM is ‘on’. If it is less, then the CRM is considered ‘off’ and the saddle mass, and flap and edge dynamic masses are set to 0. This allows the best saddles from a pool to be used, and as the saddle masses are already known it is not necessary to calculate them. The chromosome is converted to a form that is recognisable by the finite element code so that its fitness can be evaluated.

The variables are stored in a row vector rather than binary form, which makes the code easier to implement in MATLAB. The entire population is therefore a matrix, with n rows and m columns, where n is the population size and m is the number of variables.

4.3.12 Fitness criteria

The fitness criteria chosen was the difference between the bending moment distribution obtained with a given test set up and the target bending moment distribution. Several criteria were assessed; it was found that if the equation (4.14) was used as a criteria then too much weight was given to the stations near the tip which are rarely fatigue critical.

$$Error = S_F \sum_{i=1}^{i=n} \left| 1 - \frac{M_{F\,T\,i}}{M_{F\,A\,i}} \right| + S_E \sum_{i=1}^{i=n} \left| 1 - \frac{M_{E\,T\,i}}{M_{E\,A\,i}} \right| \tag{4.14}$$

If equation (4.15) was used, then more weight was given to the part of the blade near the root as the bending moments are much higher there.

$$Error = S_F \sum_{i=1}^{i=n} (M_{F\,T\,i} - M_{F\,A\,i})^2 + S_E \sum_{i=1}^{i=n} (M_{E\,T\,i} - M_{E\,A\,i})^2 \tag{4.15}$$

Equation (4.16) was found to be a good compromise between the two approaches.

$$Error = S_F \sum_{i=1}^{i=n} \left|1 - \frac{M_{F\,T\,i}}{M_{F\,A\,i}}\right| (M_{F\,T\,i} - M_{F\,A\,i})^2 + S_E \sum_{i=1}^{i=n} \left|1 - \frac{M_{E\,T\,i}}{M_{E\,A}\,i}\right| (M_{E\,T\,i} - M_{E\,A})^2 \tag{4.16}$$

In equations (4.14) to (4.16), M_i refers to the bending moment at point i and S is a switch for which is 1 or 0 depending on whether flapwise bending moment amplitude distribution, edgewise bending moment amplitude distribution or both are of interest. The subscripts F and E refer to the flap and edge directions respectively, and T and A refer to the target and achieved bending moment distributions. The fitness is found from the error using equation (4.17), so that smaller errors result in high fitness.

$$Fitness = \frac{1}{Error} \tag{4.17}$$

For the special case of the feasibility study into reducing the edgewise natural frequency to the same level as the flapwise frequency (see section 4.3.9) a fitness function was defined which combined the bending moment amplitude distribution and the difference between the flapwise and edgewise natural frequencies as shown in equation (4.18) . Multiplying the two components of the error together (the bending moment part and the frequency part) is not a conventional approach for a fitness function. The reason this method was used in this case is because the difference between the two frequencies is several orders of magnitude less than the error in the bending moment distribution, so if they are added together then the frequency part will have no effect. This could be remedied by normalising the bending moments in future.

$$Fitness = \frac{1}{\left[\sum_{i=1}^{i=n} (M_{F\,T\,i} - M_{F\,A\,i})^2 + \sum_{i=1}^{i=n} (M_{E\,T\,i} - M_{E\,A\,i})^2\right] \times |f_E - f_F|} \tag{4.18}$$

This equation was found to be effective if the bending moment amplitude distributions were normalized by the value at the root.

4.3.13 Selection process

Roulette wheel selection was used to choose which population members will be added to the new population. Consider a pie chart of the fitness of all the members of the population as a roulette wheel; the ball would be most likely to stop on the fittest member of the population. However, it is not a certainty, which helps to keep the program from becoming stuck on local optima.

This was implemented by taking the cumulative sum of the fitness through the population. A random number is then chosen between 0 and the sum of the fitness for all population members, and the first row in the cumulative table that is greater than this value is selected.

Two chromosomes are selected in this way and then a decision is made on whether or not to add them to the new population unaltered, or cross their genes over at a random point in the chromosome.

4.3.14 Crossover

A crossover rate of 70% was chosen for this problem. This rate strikes a balance between avoiding the loss of good solutions and having a stagnant population [107]. This was implemented by comparing a random number between 0 and 1 to 0.7. If it is less, crossover occurs, and if it is more the pair is added to the new population unaltered. Crossover was implemented by choosing a random gene in the chromosome and then creating two new chromosomes, as shown in Figure 4.11. A single point crossover was used for simplicity.

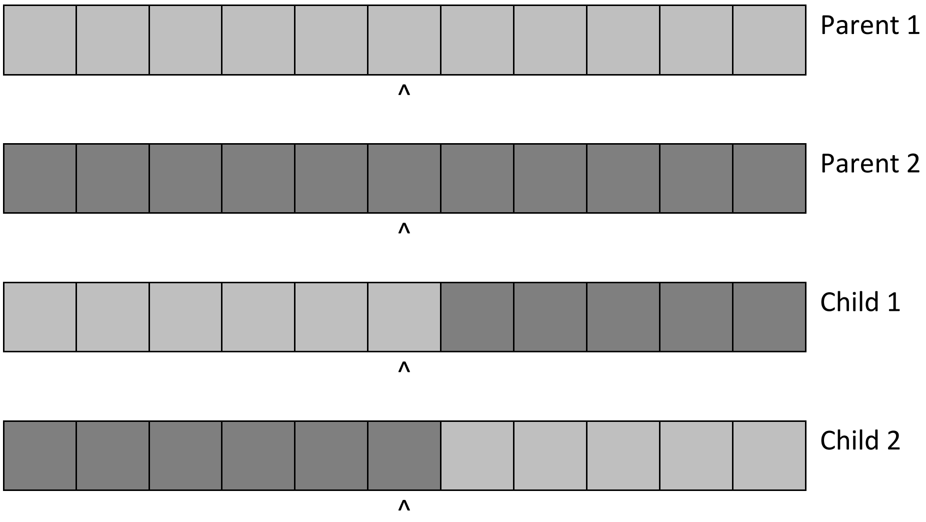

Figure 4.11 – Crossover

If no crossover occurs, then the parents are added to the new population.

4.3.15 Mutation

A mutation rate of 0.1% was used for this problem. If a random number between 0 and 1 was less than 0.001 then a random variable in the chromosome was selected and assigned a new random value between predefined bounds. This also helps in stopping the code from finding local optima [107].

4.3.16 Frequency alteration feasibility study

For the frequency alteration feasibility study mentioned in section 4.3.9, the genetic algorithm worked in exactly the same way except extra variables were added to the end of the chromosome that represented the position and magnitude of the additional edgewise static masses.

The bending moment was normalised to the value at the blade root to allow solutions which had the correct mode shape but were over or under excited to succeed. This has the disadvantage of allowing test configurations that are not feasible with the equipment currently available at Narec, but it was necessary because the difference in the flapwise and edgewise natural frequencies was also an optimisation target. If the bending moment was used without being normalised, the difference in the natural frequencies was completely insignificant in the error and the routine did not find solutions with the same natural frequency in the flap and edge directions.

4.4 Graphical User Interface

A graphical user interface was created for the software so that anyone at Narec could perform optimisation studies for blade tests without needing knowledge of MatLab or even having it installed on their computer. It is divided into a front end, a results screen and a blade editor.

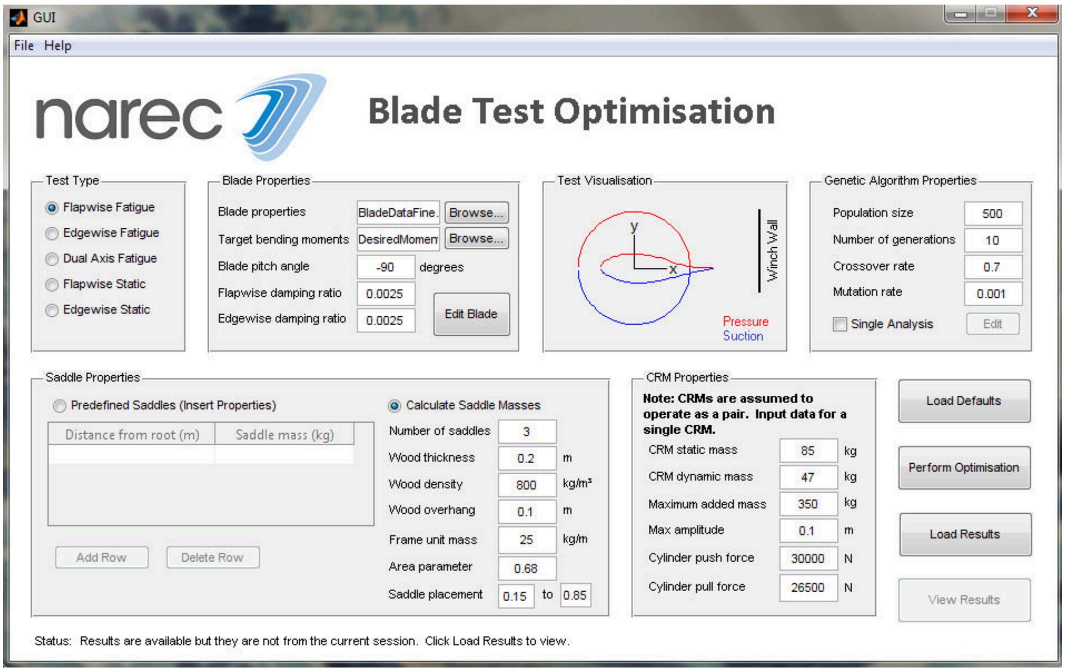

Test Type:
- ● Flapwise Fatigue
- ○ Edgewise Fatigue
- ○ Dual Axis Fatigue
- ○ Flapwise Static
- ○ Edgewise Static

Blade Properties:
- Blade properties: BladeDataFine.
- Target bending moments: DesiredMomen
- Blade pitch angle: -90 degrees
- Flapwise damping ratio: 0.0025
- Edgewise damping ratio: 0.0025

Genetic Algorithm Properties:
- Population size: 500
- Number of generations: 10
- Crossover rate: 0.7
- Mutation rate: 0.001
- ☐ Single Analysis

Saddle Properties:

○ Predefined Saddles (Insert Properties)

Distance from root (m)	Saddle mass (kg)

● Calculate Saddle Masses
- Number of saddles: 3
- Wood thickness: 0.2 m
- Wood density: 800 kg/m³
- Wood overhang: 0.1 m
- Frame unit mass: 25 kg/m
- Area parameter: 0.68
- Saddle placement: 0.15 to 0.85

CRM Properties:

Note: CRMs are assumed to operate as a pair. Input data for a single CRM.
- CRM static mass: 85 kg
- CRM dynamic mass: 47 kg
- Maximum added mass: 350 kg
- Max amplitude: 0.1 m
- Cylinder push force: 30000 N
- Cylinder pull force: 26500 N

Status: Results are available but they are not from the current session. Click Load Results to view.

Figure 4.12 - User interface main screen

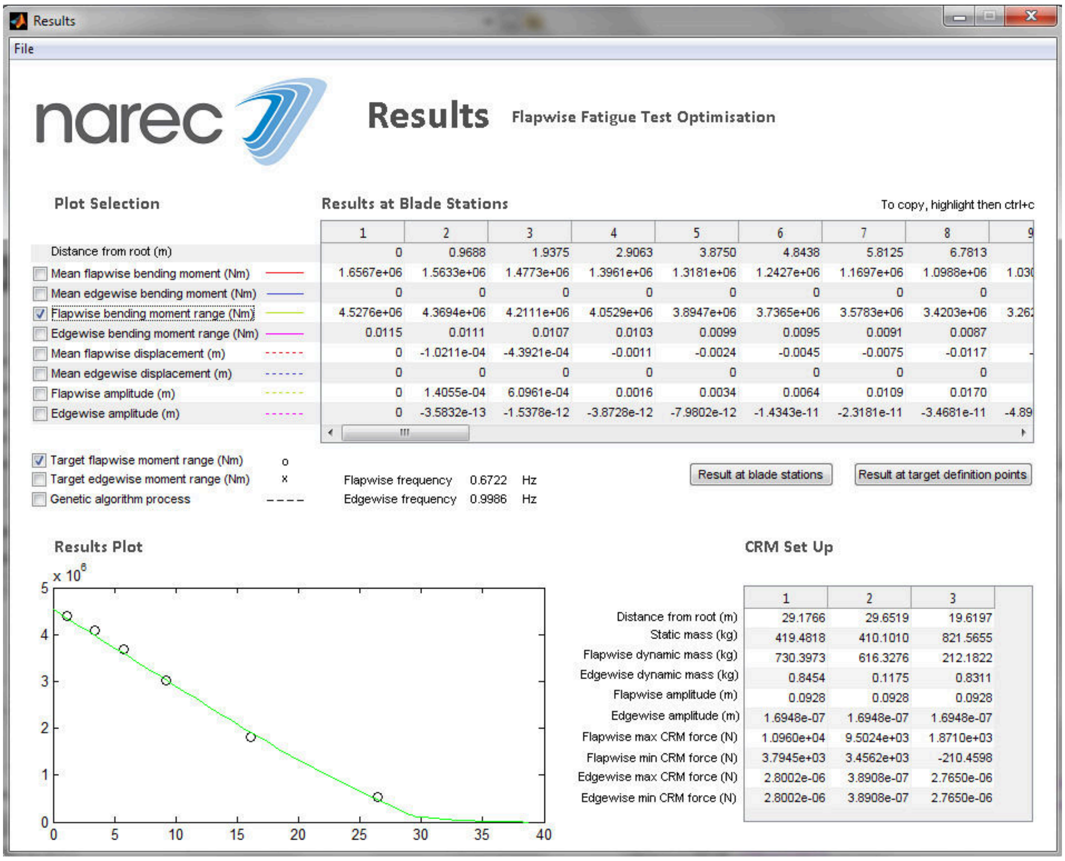

Results at Blade Stations

	1	2	3	4	5	6	7	8
Distance from root (m)	0	0.9688	1.9375	2.9063	3.8750	4.8438	5.8125	6.7813
☐ Mean flapwise bending moment (Nm)	1.6567e+06	1.5633e+06	1.4773e+06	1.3961e+06	1.3181e+06	1.2427e+06	1.1697e+06	1.0988e+06
☐ Mean edgewise bending moment (Nm)	0	0	0	0	0	0	0	0
☑ Flapwise bending moment range (Nm)	4.5276e+06	4.3694e+06	4.2111e+06	4.0529e+06	3.8947e+06	3.7365e+06	3.5783e+06	3.4203e+06
☐ Edgewise bending moment range (Nm)	0.0115	0.0111	0.0107	0.0103	0.0099	0.0095	0.0091	0.0087
☐ Mean flapwise displacement (m)	0	-1.0211e-04	-4.3921e-04	-0.0011	-0.0024	-0.0045	-0.0075	-0.0117
☐ Mean edgewise displacement (m)	0	0	0	0	0	0	0	0
☐ Flapwise amplitude (m)	0	1.4055e-04	6.0961e-04	0.0016	0.0034	0.0064	0.0109	0.0170
☐ Edgewise amplitude (m)	0	-3.5832e-13	-1.5378e-12	-3.8728e-12	-7.9802e-12	-1.4343e-11	-2.3181e-11	-3.4681e-11

- ☑ Target flapwise moment range (Nm) o
- ☐ Target edgewise moment range (Nm) x
- ☐ Genetic algorithm process – – – –

Flapwise frequency 0.6722 Hz
Edgewise frequency 0.9986 Hz

CRM Set Up

	1	2	3
Distance from root (m)	29.1766	29.6519	19.6197
Static mass (kg)	419.4818	410.1010	821.5655
Flapwise dynamic mass (kg)	730.3973	616.3276	212.1822
Edgewise dynamic mass (kg)	0.8454	0.1175	0.8311
Flapwise amplitude (m)	0.0928	0.0928	0.0928
Edgewise amplitude (m)	1.6948e-07	1.6948e-07	1.6948e-07
Flapwise max CRM force (N)	1.0960e+04	9.5024e+03	1.8710e+03
Flapwise min CRM force (N)	3.7945e+03	3.4562e+03	-210.4598
Edgewise max CRM force (N)	2.8002e-06	3.8908e-07	2.7650e-06
Edgewise min CRM force (N)	2.8002e-06	3.8908e-07	2.7650e-06

Figure 4.13 - User interface results screen

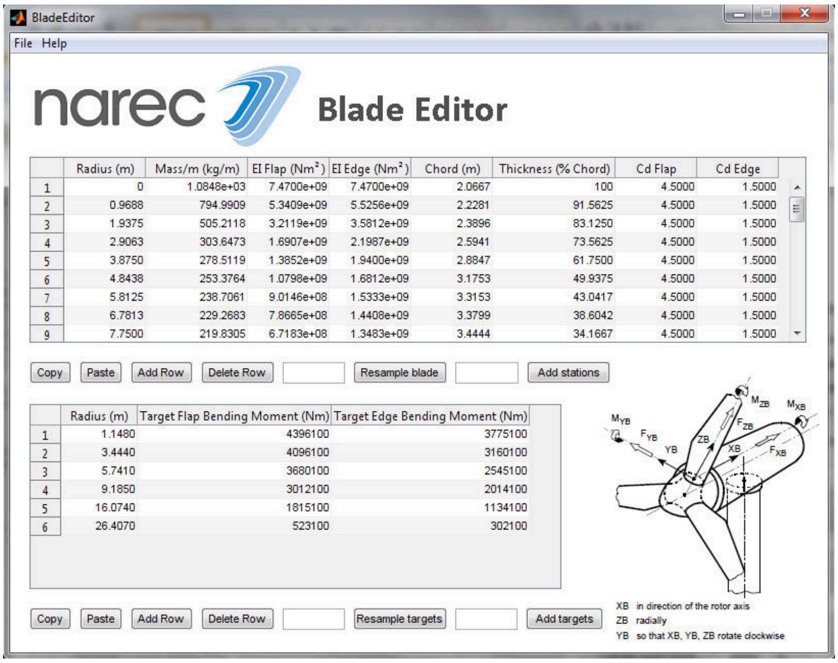

	Radius (m)	Mass/m (kg/m)	EI Flap (Nm²)	EI Edge (Nm²)	Chord (m)	Thickness (% Chord)	Cd Flap	Cd Edge
1	0	1.0848e+03	7.4700e+09	7.4700e+09	2.0667	100	4.5000	1.5000
2	0.9688	794.9909	5.3409e+09	5.5256e+09	2.2281	91.5625	4.5000	1.5000
3	1.9375	505.2118	3.2119e+09	3.5812e+09	2.3896	83.1250	4.5000	1.5000
4	2.9063	303.6473	1.6907e+09	2.1987e+09	2.5941	73.5625	4.5000	1.5000
5	3.8750	278.5119	1.3852e+09	1.9400e+09	2.8847	61.7500	4.5000	1.5000
6	4.8438	253.3764	1.0798e+09	1.6812e+09	3.1753	49.9375	4.5000	1.5000
7	5.8125	238.7061	9.0146e+08	1.5333e+09	3.3153	43.0417	4.5000	1.5000
8	6.7813	229.2683	7.8665e+08	1.4408e+09	3.3799	38.6042	4.5000	1.5000
9	7.7500	219.8305	6.7183e+08	1.3483e+09	3.4444	34.1667	4.5000	1.5000

	Radius (m)	Target Flap Bending Moment (Nm)	Target Edge Bending Moment (Nm)
1	1.1480	4396100	3775100
2	3.4440	4096100	3160100
3	5.7410	3680100	2545100
4	9.1850	3012100	2014100
5	16.0740	1815100	1134100
6	26.4070	523100	302100

XB in direction of the rotor axis
ZB radially
YB so that XB, YB, ZB rotate clockwise

Figure 4.14 - User interface blade editor screen

The user interface has been successful in encouraging people who are unfamiliar with programming to perform blade optimisation studies.

4.5 Results and Discussion

The blade test optimisation routine has been used to produce test set-ups for a variety of scenarios. These include tests of the baseline blade described in chapter 3, and tests of a 100m blade, the design and fatigue loads for which were taken from [108] and [109]. The alternative test method described in section 4.3.9 is also optimised. The performance of the genetic algorithm is also assessed.

4.5.1 Genetic algorithm performance

The genetic algorithm was not the primary focus of the present work, so the values chosen for parameters such as the crossover rate and the mutation rate are based on those recommended by others [107]. The size of the population chosen is also not an issue, as the program is very fast. This means that large populations can be used without a significant time penalty. Although large populations increase the time to convergence, they also increase the likelihood that an initial guess is in the right part of the search space [107]. As the program is fast (convergence is typically reached within 2 minutes for a population of 100 on a standard modern PC), the time to converge is acceptable even for large populations. Convergence was said to have occurred when the average fitness was greater than 90% of the maximum fitness.

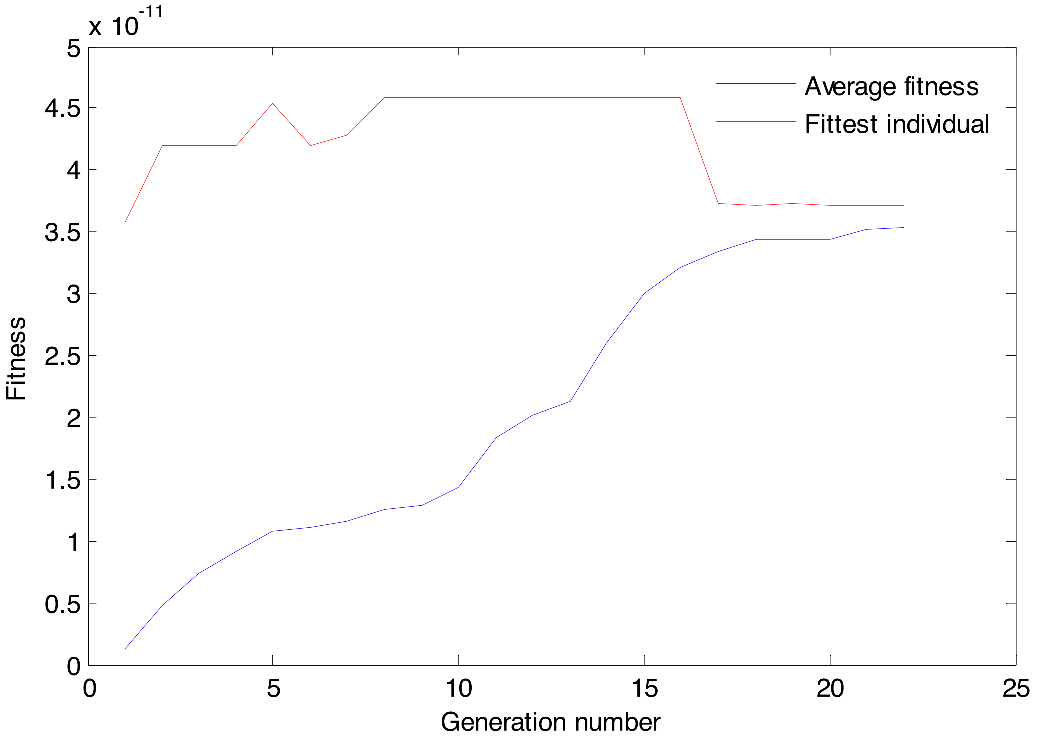

Figure 4.15 - Genetic algorithm convergence

A typical plot of the convergence of the average fitness and the fittest individual by generation is shown in Figure 4.15. Clearly, the fittest individual does not occur in the final generation. However, the program stores the fittest individual in every generation so that the fittest overall solution found in the process is used.

4.5.2 Test optimisation for 2MW baseline turbine blade

The performance of the test optimisation algorithm was assessed by using it to set up tests for the baseline 38.75m blade which was analysed for fatigue in chapter 3. Flapwise, edgewise and dual axis test optimisations were performed and the optimisation routine was also tested for the case when the saddle positions are predefined.

The target bending moment amplitudes are given in Table 4.3 for different test types. The first analysis performed is a comparison of all three test types on a bare blade to allow comparison of the bending moment range distributions obtained. The target bending moment amplitudes are all calculated using the method described in section 3.2.6.

	Dual axis test		Flapwise test		Edgewise test		Bare blade	
	Flap	**Edge**	**Flap**	**Edge**	**Flap**	**Edge**	**Flap**	**Edge**
Frequency (Hz)	0.81	1.17	0.67	1	1.01	1.5	1.03	1.56
Moment range (Nm)								
1.15m	1.68e6	1.59e6	1.72e6	1.58e6	1.78e6	1.58e6	1.97e6	1.58e6
3.45m	1.61e6	1.20e6	1.63e6	1.19e6	1.72e6	1.19e6	1.86e6	1.19e6
5.75m	1.44e6	1.03e6	1.46e6	1.03e6	1.56e6	1.03e6	1.66e6	1.02e6
9.20m	1.19e6	8.15e5	1.19e6	8.13e5	1.33e6	8.13e5	1.36e6	8.12e5
16.05m	7.59e5	4.63e5	7.28e5	4.62e5	8.18e5	4.62e5	8.18e5	4.62e5
26.40m	2.26e5	1.25e5	2.07e5	1.24e5	2.26e5	1.24e5	2.26e5	1.24e5

Table 4.3 - Target bending moment amplitudes for different test types

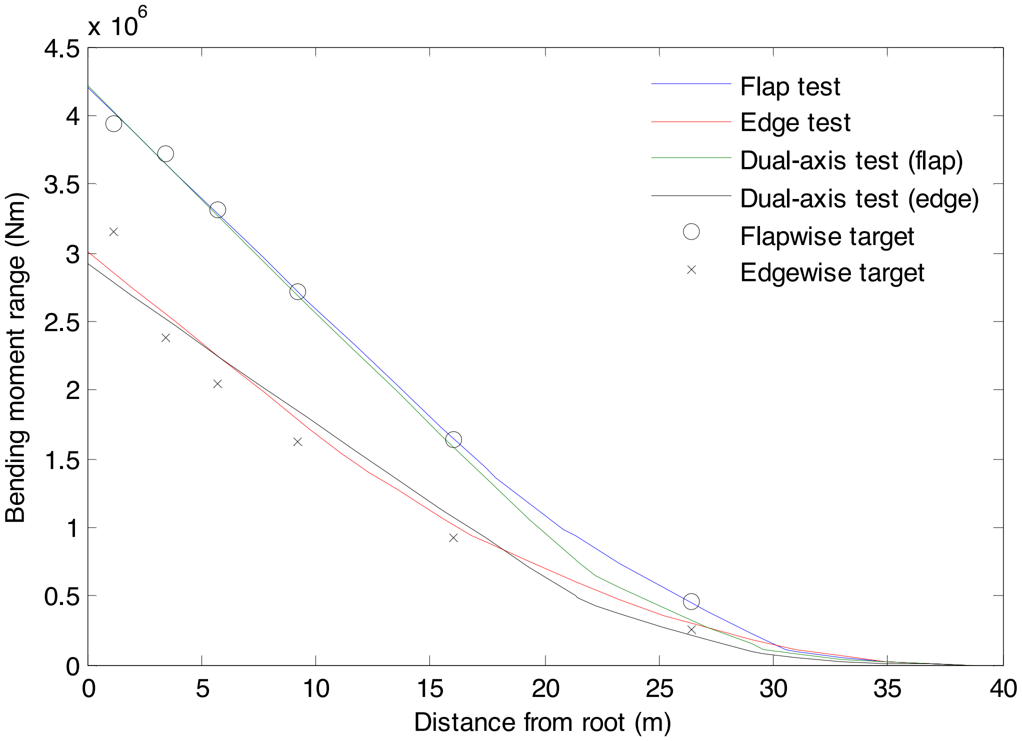

Figure 4.16 - Optimised bending moment distributions

Figure 4.16 shows the optimised bending moment distributions for a flapwise test, an edgewise test and a dual-axis test with the same target bending moments. It is clear that the dual axis test does not match the target bending moment distributions as well as the single axis tests, but if the damage distributions around the blade cross-section are improved then dual-axis testing would still represent an improvement over single axis testing. This will be studied in chapter 5 for the optimal tests described below. The test set-ups and natural frequencies are shown in Table 4.4.

	Flapwise test			**Edgewise test**			**Dual-axis test**		
Saddle Number	1	2	3	1	2	3	1	2	3
Distance from root (m)	20.8	17.9	30.5	11.2	12.3	16.8	29.6	22.2	21.4
Static mass (kg)	648.3	814.4	365.8	1548.8	1383.9	891.0	550.4	755.1	788.1
Flapwise dynamic mass (kg)	545.8	740.8	553.8	0	0	0	228.3	681.5	687.5
Edgewise dynamic mass (kg)	0	0	0	459.8	143.1	240.3	151.9	628.1	217.9
Flapwise CRM amplitude (m)	0.094	0.094	0.094	0	0	0	0.079	0.079	0.079
Edgewise CRM amplitude (m)	0	0	0	0.018	0.018	0.018	0.006	0.006	0.006
Flapwise frequency (Hz)	0.79			1.04			0.76		
Edgewise frequency (Hz)	1.16			1.54			1.09		

Table 4.4 - Optimal test set-ups for bare blade

The edgewise test places the equipment as near to the root as possible, while the flapwise and dual axis-tests have the equipment mounted nearer to the tip. The dual-axis test frequency is not much lower than the flapwise frequency, so in this direct comparison the single axis tests would be completed in 110 days (assuming no time for swapping the test equipment over) while the dual axis test would complete in 77 days. This is a significant time saving.

Test set-ups for the target bending moment amplitudes given in Table 4.3 were found using the optimisation routine. The resulting bending moment distributions are shown in Figure 4.17.

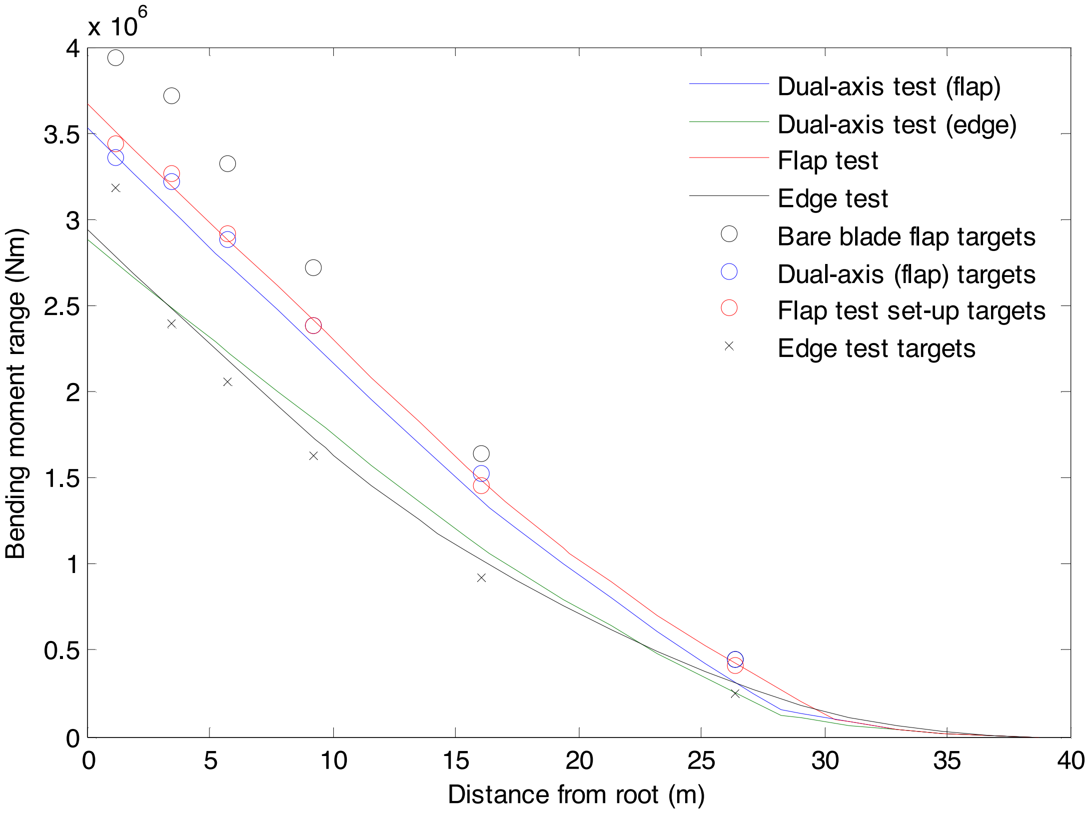

Figure 4.17 - Target and optimised bending moment range distributions

It is clear that there is a large difference between the distribution of the range of the target bending moment for the bare blade and for a blade on which the mean bending moment distribution is affected by the test equipment. This is because the cycles with a higher mean stress are more damaging, and it means that at least one design loop should be used when calculating the test target bending moment amplitudes.

	Flapwise test			Edgewise test			Dual-axis test		
Saddle Number	1	2	3	1	2	3	1	2	3
Distance from root (m)	19.6	30.4	17.1	14.3	9.3	10	28.2	5.3	16.4
Static mass (kg)	709.5	367.2	871.1	1130.6	1843.7	1730.1	574.5	2413.4	1095.0
Flapwise dynamic mass (kg)	230.9	745.9	464.7	0	0	0	572.9	652.7	580.6
Edgewise dynamic mass (kg)	0	0	0	397.7	523.3	751.2	356.1	197.9	412.1
Flapwise CRM amplitude (m)	0.078	0.078	0.078	0	0	0	0.094	0.094	0.094
Edgewise CRM amplitude (m)	0	0	0	0.014	0.014	0.014	0.008	0.008	0.008

Table 4.5 – Test set ups for comparison of single and dual axis testing

The test set-ups produced by the optimisation routine are given in Table 4.5 and are analysed in chapter 5.

The optimisation routine was also used to find a test set-up for the case when the saddle positions are predefined. This scenario is not uncommon; blade manufacturers frequently wish to save time and money by reusing saddles from static testing during the fatigue test.

Saddle location and mass data for a static test of a similar sized blade was obtained from Narec and is shown below in Table 4.6.

Distance from root (m)	Saddle mass (kg)
13.7	670
17.9	600
22.1	550
26.4	421
31.6	321
35.9	365

Table 4.6 - Predefined saddle position and mass

Using these saddles, the optimisation routine was used to find test configurations with the best possible bending moment distribution. The achievable bending moment distributions for the flapwise test, edgewise test and dual axis test are shown in Figure 4.18.

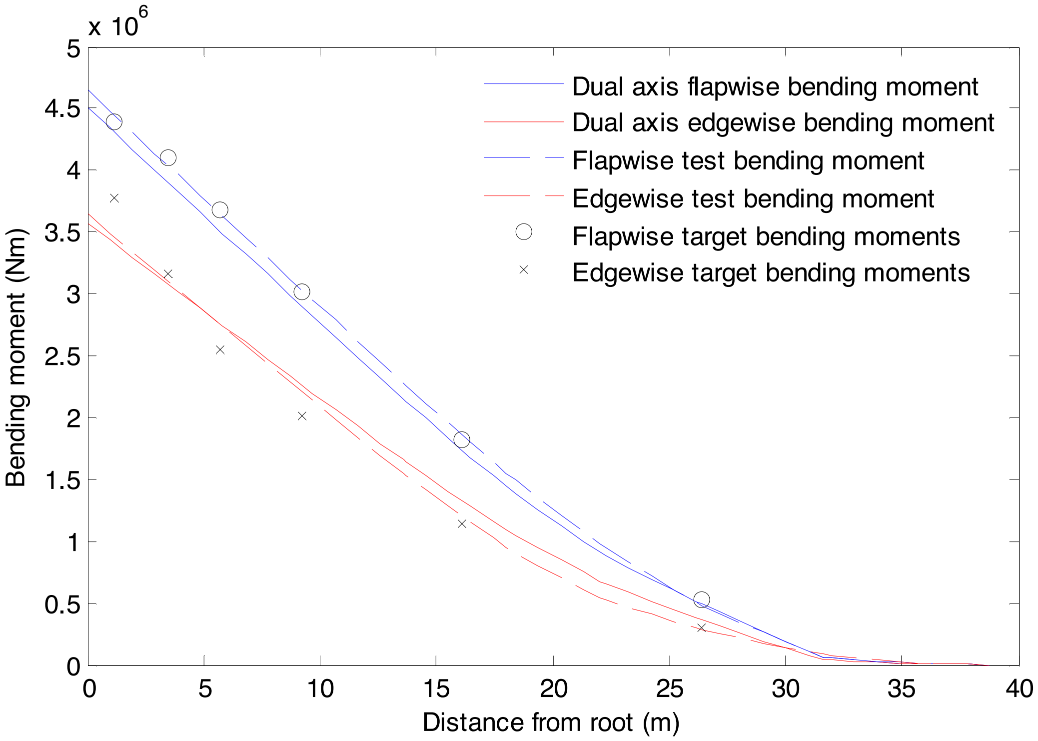

Figure 4.18- Bending moment distribution with predefined saddles

As before, the optimal results for single axis tests perform better than those for dual axis tests. This is expected as the optimal flap configuration tends to have the saddles located towards the tip whereas the optimal edgewise configuration tends to have the saddles nearer the root, as shown in Table 4.7. A dual axis test must balance both of these requirements and so it inevitably cannot fit the target distribution as well as a single axis test. The governing natural frequency for the flapwise test is 0.64Hz, for the edgewise test it is 1.37Hz and for the dual axis test it is 0.62Hz, so the dual axis test will be substantially quicker.

Another interesting point to note is that the optimal flapwise test configuration uses 5 saddles; this enables the curve of the bending moment distribution to better match the targets, and the result actually represents an improvement over the solution where the saddles can be placed anywhere (although this is at the expense of a lower natural frequency than if fewer saddles were used).

	Flapwise					**Edgewise**			**Dual axis**			
Saddle Number	1	2	3	4	5	1	2	3	1	2	3	4
Radius (m)	13.7	18.0	22.0	26.4	31.6	13.7	18.0	22.0	13.7	18.0	22.0	31.6
Static mass (kg)	840	770	720	591	491	840	770	720	1010	940	890	661
Flap dyn. mass (kg)	336	623	734	105	761	0	0	0	724	735	425	735
Edge dyn. mass (kg)	0	0	0	0	0	148	634	357	519	693	751	118.34
Flap CRM amp. (m)	0.088	0.088	0.088	0.088	0.088	0	0	0	0.09	0.09	0.09	0.09
Edge CRM amp. (m)	0	0	0	0	0	0.01	0.01	0.01	0.01	0.01	0.01	0.01

Table 4.7 - Predefined saddle test set-ups

The predefined saddle optimisation tool has been shown to work, and is actually used more often by Narec engineers than the tool for optimising saddle placement.

4.5.3 Test optimisation and feasibility study for 100m blade

The 100m all glass fibre blade design developed by Griffith and Ashwill [109] was used to study the test facility requirements for a very large blade. The blade is suitable for this study because a fatigue analysis has already been performed on it, the results of which are available [109]. The blade cross-sectional properties are also available [108], and are shown in appendix B.

The blade parameters are given in Table 4.8. Note that the blade mass is very high; this is a result of the all GFRP construction. The high mass results in a blade design that is dominated by the edgewise fatigue loads. The low natural frequency of the blade means that a fatigue test will inevitably be time consuming.

Parameter	**Value**
Blade Designation	SNL100-00
Wind Speed Class	IB
Blade Length (m)	100
Blade Weight (kg)	114,172
Span-wise CG location (m)	33.6
Maximum chord (m)	7.628 (19.5% span)
Flapwise frequency (Hz)	0.42

Table 4.8 - Blade parameters

Fatigue data is available for the blade, and is shown in Table 4.9. The cycles to failure that will result in an equivalent amount of damage after 5 million test cycles is calculated using the Palmgren-Miner linear damage rule. The stress, σ, that will result in this number of cycles to failure for the material in question (E-LT-5500-EP from the DOE/MSU composites database [62]) is calculated from equation (4.19), in which A is the stress axis intercept of the curve fit to the fatigue data (1000MPa), N is the cycles to failure and B is the slope factor, which takes the value of 9. The fatigue analysis performed in [109] is very simplistic as all cycles are assumed to use the same SN-curve. However, this makes calculation of test target bending moment amplitudes easier.

$$\sigma = AN^{-\frac{1}{B}} \tag{4.19}$$

The strain can then be calculated from the Young's modulus of E-LT-5500-EP, which is 29.38GPa. The Euler-Bernoulli beam equation is then used to calculate the bending moment, with the test bending moment calculated by including the safety factors from the blade test standard [18].

Distance from root (m)	Damage sum	Cycles to failure	Stress (MPa)	Strain (%)	Neutral axis y (m)	Bending stiffness GNm^2	Test bending moment range (Nm)	Bending moment range with safety factors (Nm)
Edgewise fatigue								
0.00	1.25E-07	4.00E+13	30.81	0.10%	2.85	322.00	1.19E+08	1.58E+08
11.11	1.55E-02	3.23E+08	113.40	0.39%	3.83	84.57	8.52E+07	1.13E+08
15.22	2.25E-03	2.22E+09	91.51	0.31%	4.33	91.55	6.59E+07	8.76E+07
19.50	6.33E-04	7.90E+09	79.48	0.27%	4.73	105.10	6.01E+07	7.99E+07
24.28	1.06E-03	4.72E+09	84.17	0.29%	4.68	100.04	6.13E+07	8.14E+07
50.00	1.72E-08	2.91E+14	24.71	0.08%	3.78	24.70	5.50E+06	7.31E+06
Flapwise fatigue								
0.00	1.38E-10	3.62E+16	14.46	0.05%	2.85	322.00	5.57E+07	7.39E+07
11.11	4.88E-05	1.02E+11	59.79	0.20%	2.07	57.45	5.64E+07	7.50E+07
15.22	3.23E-05	1.55E+11	57.11	0.19%	1.81	48.94	5.27E+07	7.00E+07
19.50	3.13E-05	1.60E+11	56.91	0.19%	1.55	38.76	4.86E+07	6.45E+07
24.28	3.25E-05	1.54E+11	57.15	0.19%	1.37	29.68	4.21E+07	5.60E+07
50.00	3.50E-05	1.43E+11	57.62	0.20%	0.72	6.26	1.71E+07	2.27E+07

Table 4.9 - Fatigue data for SNL100-00 blade

The fatigue analysis performed for this blade in [109] is rather simplistic, as the fatigue data is for R=0.1 regardless of the individual cycle R-value. This could explain why the target bending moment distributions are not monotonically decreasing along the blade length as would be expected which makes a good fit to the targets impossible. However, the flapwise and edgewise fatigue loads are of the order which would be predicted from a simple scaling of the 2MW turbine used in this work based on the laws presented by Griffith and Ashwill [109] so they can be considered to be representative. A blade of this size would be likely to use a CFRP spar, which would decrease the edgewise gravity loads significantly and thus reduce the edgewise test target bending moment amplitudes.

The low frequency and high amplitude of the flapwise oscillations means that the unsteady aerodynamic effects are likely to be reduced because the wake has more time to dissipate before the blade re-enters it. In order to provide a conservative estimate of the facility requirements, the drag coefficient has been assumed to take a value of 4 in both the flapwise and edgewise directions.

The optimisation for a flapwise test uses 5 saddles along the blade length. A blade of this size would require larger CRMs than the ones currently in use at Narec. For this reason, the CRMs were scaled by a factor of 2 (masses are multiplied by 8, cylinder areas are multiplied by 4). The cylinder stroke was multiplied by 5.

The excitation required for a flapwise fatigue test is shown in Table 4.10, and the resulting bending moment distribution is shown in Figure 4.19. The flapwise test frequency is 0.27445 Hz, so a 5 million cycle test would take around 211 days.

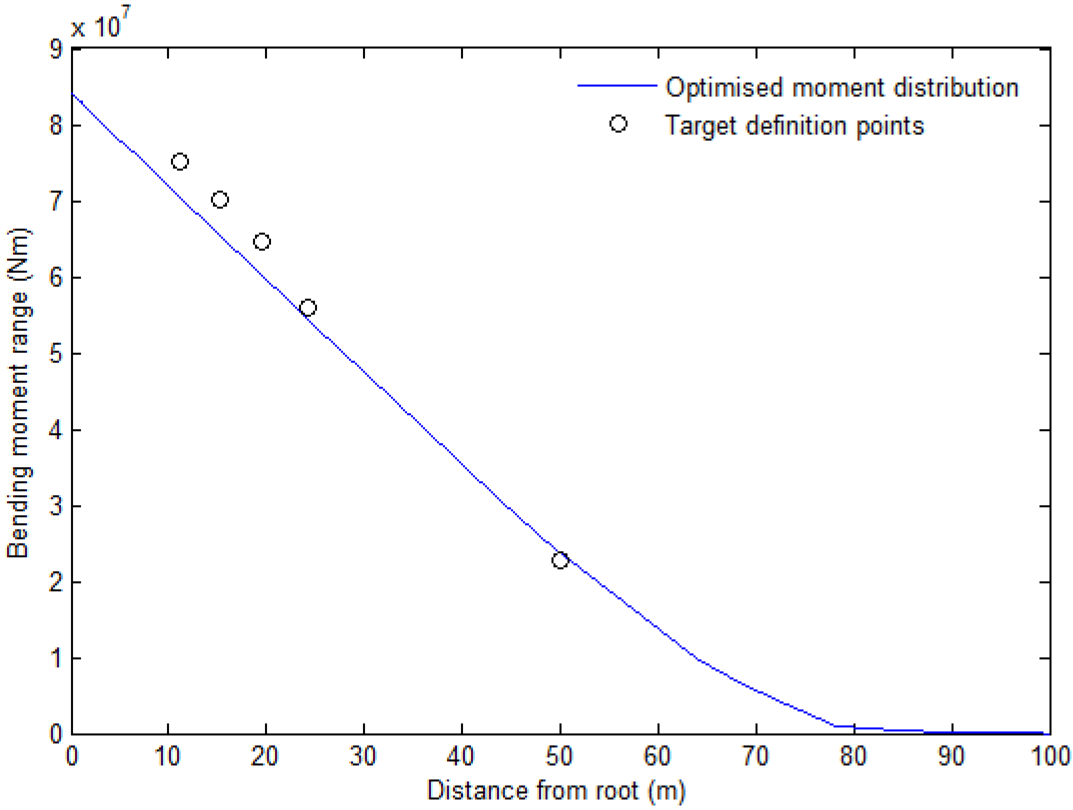

Figure 4.19 - SNL100-00 blade flapwise bending moment distribution

	Saddle 1	Saddle 2	Saddle 3	Saddle 4	Saddle 5
Distance from root (m)	49.6	63.9	67.1	78.3	78.3
Static mass (kg)	16289	11134	10161	7387	7372
Dynamic mass (kg)	5115	1860	3552	5741	4167
Cylinder amplitude (m)	0.34	0.34	0.34	0.34	0.34
Saddle amplitude (m)	0.8047	1.5985	1.8231	2.7573	2.7637
Max force (N)	33821.49	14492.34	28867.11	54631.85	39694.66

Table 4.10 - Flapwise fatigue test set-up

The edgewise test would be very demanding for the hub of the test stand, but would require much less test equipment to be mounted on the blade, so a test using 3 saddles was assumed. The edgewise frequency is 0.43365 Hz meaning that the test would take around 134 days.

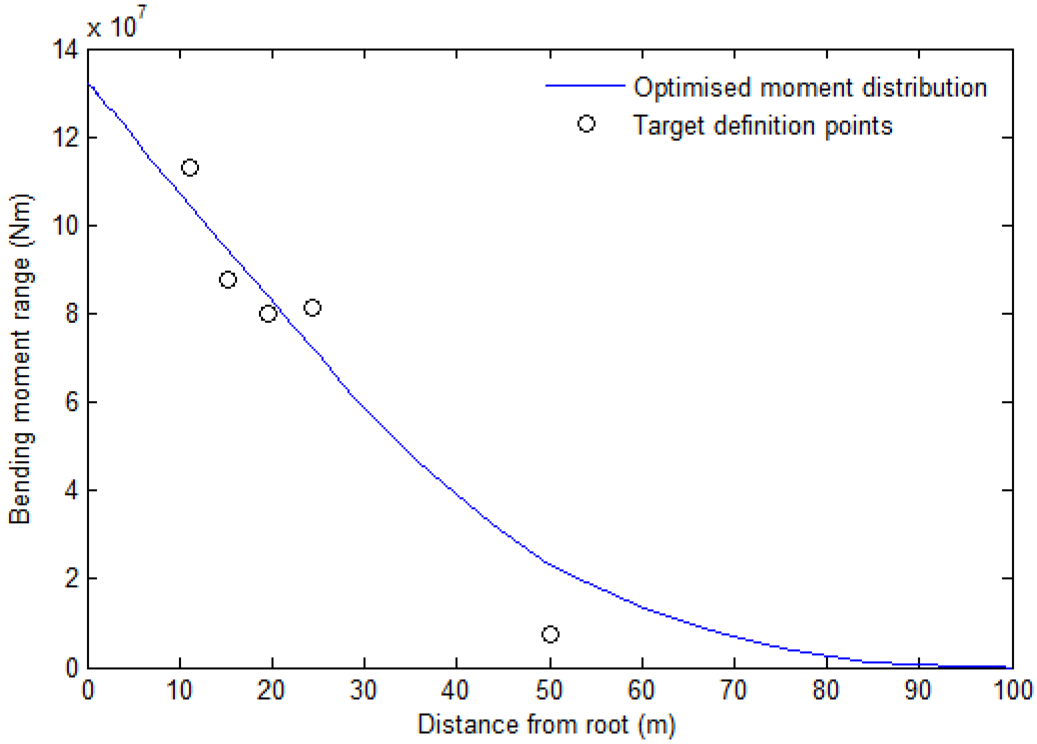

Figure 4.20 - SNL100-00 blade edgewise bending moment distribution

	Saddle 1	Saddle 2	Saddle 3
Distance from root (m)	29.2	37.0	49.8
Static mass (kg)	33299	24426	16186
Dynamic mass (kg)	1973	802	3684
Cylinder amplitude (m)	0.17	0.17	0.17
Saddle amplitude (m)	0.20	0.32	0.56
Max force (N)	5428.66	2903.16	19972.65

Table 4.11 – Edgewise fatigue test set-up

Finally, a dual axis test has been optimised for the SNL100-00 blade. Again, 5 CRMs are required to deliver sufficient force to overcome the air resistance. The results are shown in Figure 4.21, and the test set-up is described in Table 4.1. The flapwise frequency was 0.3549 Hz and the edgewise frequency was 0.5237 Hz, meaning the test will be complete in 163 days.

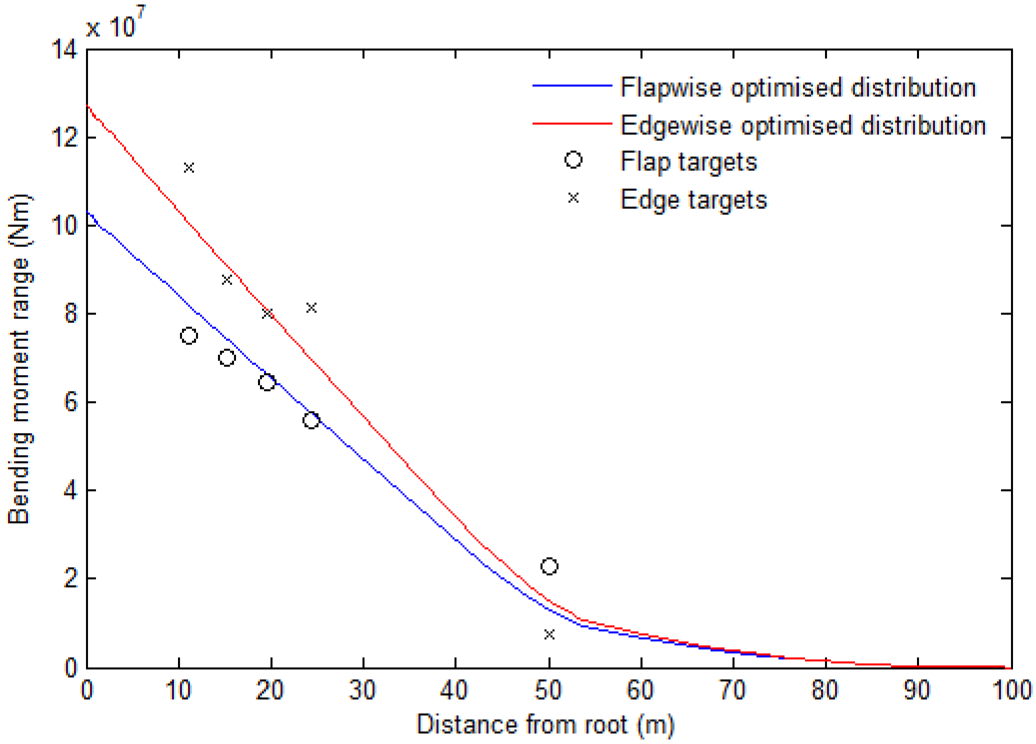

Figure 4.21 - SNL100-00 dual axis bending moment distributions

	Saddle 1	Saddle 2	Saddle 3	Saddle 4	Saddle 5
Distance from root (m)	42.9	53.7	47.6	50.5	53.5
Static mass (kg)	21016	15967	18519	17232	16036
Flapwise dynamic mass (kg)	3637	5666	3822	5126	3970
Edgewise dynamic Mass (kg)	4849	3347	3735	2376	1894
Flapwise cylinder amplitude (m)	0.45	0.45	0.45	0.45	0.45
Edgewise cylinder amplitude (m)	0.06	0.06	0.06	0.06	0.06
Flapwise saddle amplitude (m)	0.60	1.02	0.77	0.89	1.01
Edgewise saddle amplitude (m)	0.40	0.61	0.49	0.54	0.61
Max flapwise force (N)	55274.41	98406.22	61424.19	85444.59	68775.78
Max edgewise force (N)	24694.05	24845.05	22652.79	15918.5	13976.35

Table 4.12 - Dual axis fatigue test set-up

The optimisation routine tends to place saddles around the mid-span of the blade for dual axis tests, towards the tip of the blade for flapwise tests and towards the root for edgewise tests. This means that higher actuator forces are required for dual axis testing than for flapwise tests, but it does have the benefit of higher test frequencies. The lower air resistance in the edgewise direction means that although the excitation equipment is placed nearer the root, the CRMs do not need to be driven at particularly high amplitudes.

With a blade of this size the tip displacements will be of interest. Figure 4.22 shows the extreme displacement from the equilibrium position during the test described above if the test stand has a tilt angle of 1°. These displacements are reasonable and are within the capabilities of the new facilities being developed by Narec.

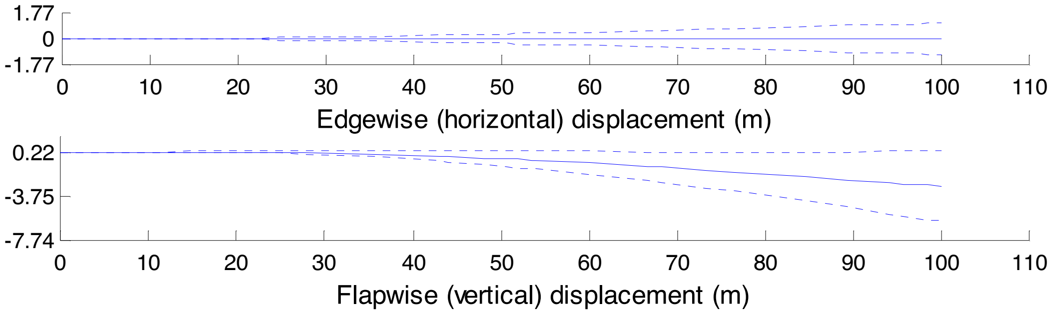

Figure 4.22 - Blade displacement

Although the loads required are very high, they do not make the fatigue test unfeasible. Resonant testing is probably the only realistic method of testing a blade of this size, given the magnitudes of the loads involved, and the frequency alteration discussed in section 4.3.9 would simply not be viable.

4.5.4 2MW Blade frequency alteration feasibility study results

In section 3.3.5 it was seen that the best results were obtained by cycling the flapwise and edgewise loads at the same frequency with a constant, realistic, phase angle between them. This is impossible to achieve in practice with dual axis resonant testing unless the two natural frequencies are the same, which is unlikely to be the case for any real blade. A way in which this problem could be overcome was described in section 4.3.9 of this chapter.

The optimisation routine described in section 4.3.16 was used to find the best placement for two tuning masses. The aim was to have a reasonable bending moment distribution along the whole length of the blade, whilst making the two natural frequencies the same. The results are shown in Figure 4.23. The isolated edgewise masses are located 28.9m and 11.27m from the root, and have a masses of 1.9Te and 29.5Te respectively. The configuration of the flapwise equipment is shown in Table 4.13.

Saddle number	**1**	**2**	**3**
Distance from root (m)	20.0	8.3	9.7
Flapwise static mass (kg)	689.7	2000.4	1772.6
Edgewise static mass (kg)	587.3	121.4	231.5

Table 4.13 - Flapwise test configuration

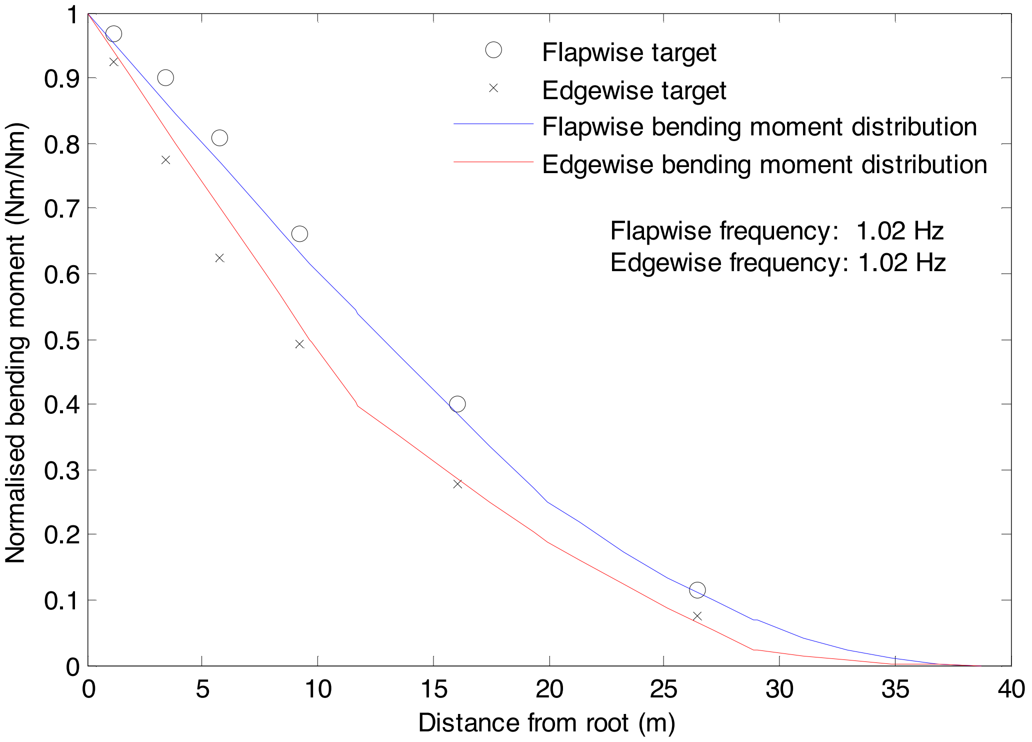

Figure 4.23 - Edgewise frequency reduction

The achieved bending moment distribution is acceptable, but the additional mass required to bring the frequencies together is very large. If the requirement to have the frequencies the same is removed, then the bending moment distribution can be improved by adding the edgewise static masses, as shown in Figure 4.24. In this case the optimal solution involved adding a 27 Te mass at 6.6m and a 29 Te mass at 8.9m, which is unrealistic in practice. The flapwise test configuration for this case is given in Table 4.14. The edgewise excitation would need to be achieved by forcing the isolated static masses because adding excitation mass to the edgewise direction would upset the flapwise bending moment distribution. This would also allow control of the phase angle between the two loads.

Saddle number	**1**	**2**	**3**
Distance from root (m)	5.4	23.6	5.0
Static mass (kg)	2252.9	527.0	2226.5
Flapwise dynamic mass (kg)	241.3	107.7	361.4

Table 4.14 - Flapwise test configuration

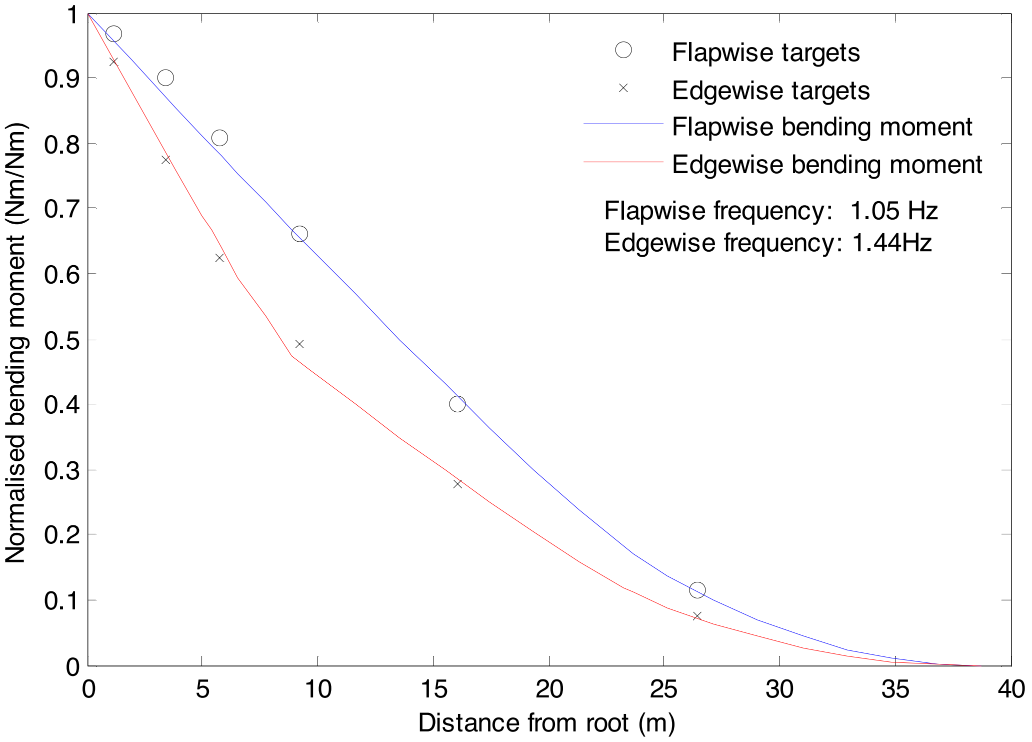

Figure 4.24 - Additional edgewise static masses with no frequency reduction

Although the additional mass required to make the edgewise frequency the same as the flapwise frequency is very large (even for this relatively small 38.75m blade), the benefits in terms of fatigue distribution around the blade mean that the approach is worth investigating further. There are likely to be interactions between the flapwise and edgewise directions arising from the blade twist, so the issues involved will be investigated further in the following chapter.

4.6 Conclusions

The method of finding optimal test configurations described in this chapter has been shown to work effectively under a wide range of conditions. The main advantage of calculating the frequency response of a finite element model of the blade rather than trying to optimise the mode shape is that this optimisation routine does not produce results that are impracticable.

The model also accounts for air resistance, which is important because this is the most significant cause of energy loss from the system. Work performed to support this project has shown that the drag force cannot be calculated based on steady state conditions because the shed vortices and the fact that the blade re-enters its wake account for a large part of the drag force. The drag force is dependent on the square of the blade velocity, so it cannot be represented as part of the damping matrix. The iterative method used to find the point at which the drag was in equilibrium with the forces due to strain, structural damping and the inertial loads allowed this problem to be overcome.

The genetic algorithm used to find optimal solutions was shown to work, and several different variants were tested allowing single and dual axis tests with both predefined and free saddle placement to be optimised. The optimisation routine was used to design a test for a 100m blade, and the results will inform the design of test equipment for the large blades of the future.

The method of reducing the edgewise frequency by adding isolated masses could be feasible, although several issues will need to be investigated that cannot be covered using the 1-D beam element used for the optimisation routine. These will be covered in the following chapter.

5 Blade Test Simulation

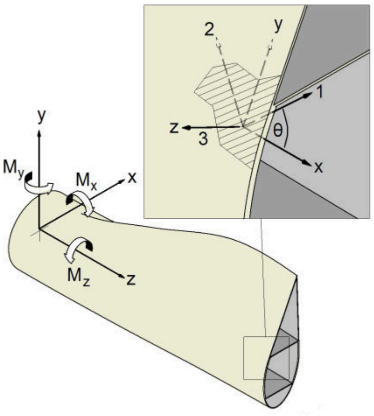

5.1 Introduction

The simulation of full scale blade tests is important for several reasons. As blades grow in size it is necessary to have an understanding of the magnitude of the forces that the test equipment will be required to deliver and the blade displacements that will be required when testing the next generation of offshore wind turbine blades. Also, the size of modern wind turbine blades means that setting up a test is a time consuming operation. If the natural frequencies can be predicted and the optimal position of test equipment can be found so that the bending moment amplitude distribution matches the target distribution found using the method described in section 3.2.6 then this can save a substantial amount of time and money over a ‘trial and error’ approach.

The blade test optimisation software developed during the course of this work is both useful and instructive, but there are limitations which mean that it is necessary to perform more in-depth analyses before the results can be deemed trustworthy. The effect of air resistance is taken into account using a simple approximation in the blade test optimisation code, and the blade twist is not modelled. This means that coupling effects between the flapwise and edgewise directions which occur in practice are not simulated. For these reasons it was decided that a transient analysis should be performed with a more representative blade model.

The approach used in the present work is detailed here. Results are then presented for the analysis of the 2MW blade model as well as several case studies in which the simulation predictions are compared to full scale test results and small scale test results.

5.2 Blade Test Simulation Methodology

The model used in the present work uses beam elements with an implicit time stepping solver. The various different aspects of the model are discussed in the following sections.

5.2.1 Blade data

The first step in the analysis is to read in information about the blade sectional properties at each station. This is stored in a comma separated text file. The sectional properties include:

- Distance from the root
- Coordinates of the shear centre relative to the root
- Structural twist angle
- Mass per unit length
- Bending stiffness about the local x and y axes

- Extensional stiffness
- Shear stiffness in the local x and y directions
- Torsional stiffness
- Chord length
- Thickness
- Aerodynamic twist
- Drag coefficient in flapwise and edgewise directions

This data is then interpolated at the positions where test equipment is to be mounted and extra stations are added at these points. The polar inertia is estimated by treating the blade as a hollow elliptical prism, and the inertia of the blade sections about their ends is found by treating them as a rod.

5.2.2 Beam elements

The linear 3-D Timoshenko beam element defined by Przemieniecki was used as the basis for the blade simulation [110]. Although more complex beam elements have been developed that allow the effects of tapering of the beam section, material anisotropy and so forth to be taken into account their use was not possible because they require knowledge of the full blade design. Manufacturers are unwilling to provide sufficient data for them to be used to a third-party test house such as Narec. The Timoshenko beam element requires much less information; all that is required is simple data about the cross sectional properties of the blade. The beam element (local) coordinate system is shown in Figure 5.1.

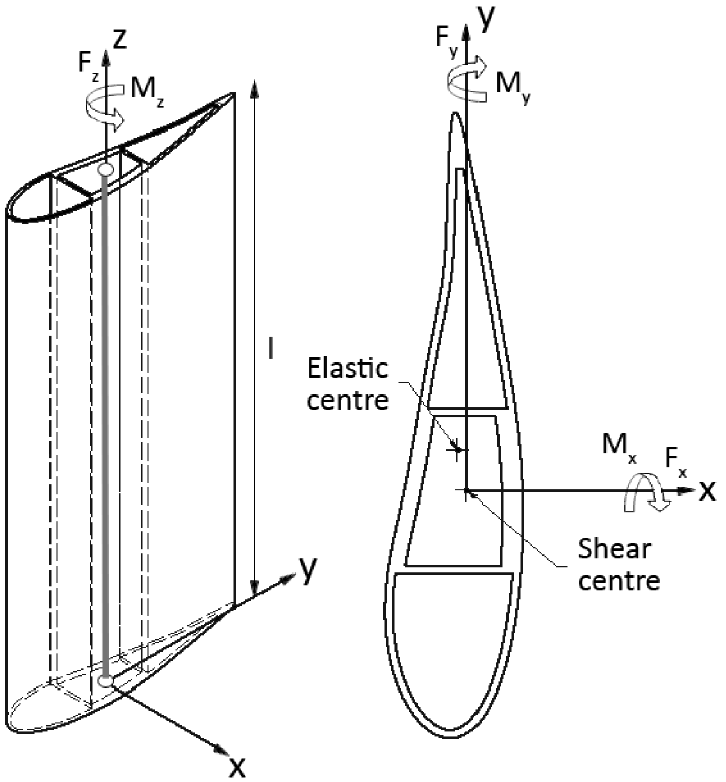

Figure 5.1- Beam element coordinate system

The element stiffness and mass matrices are shown in appendix C as they are rather large. The shear centre of the blade is chosen as the origin for each section, which means that the shear forces do not induce a torsional moment. This simplifies the stiffness matrix considerably.

Wind turbine blades tend to have complex asymmetrical cross sections so the influence of the coupling bending stiffness cannot be neglected if it is present. The structural twist angle (the angle the principle axes relative to the reference axes, not to be confused with the aerodynamic twist angle) is used so that the coupling bending stiffness can be ignored.

The value of the structural twist which will make the coupling stiffness vanish is found from equation (5.1), where EI_{xx} is the bending stiffness about the x-axis, EI_{yy} is the bending stiffness about the y-axis and EI_{xy} is the product bending stiffness.

$$\phi = -\frac{1}{2}\tan^{-1}\left(\frac{2EI_{xy}}{EI_{xx} - EI_{yy}}\right) \tag{5.1}$$

The new values for the bending stiffness about the principle axes at this value of structural twist are then found from equations (5.2) and (5.3) respectively [100].

$$EI'_{xx} = \left(\frac{EI_{xx} + EI_{yy}}{2}\right) + \left(\frac{EI_{xx} - EI_{yy}}{2}\right)\cos(2\phi) - EI_{xy}\sin(2\phi) \tag{5.2}$$

$$EI'_{xx} = \left(\frac{EI_{xx} + EI_{yy}}{2}\right) - \left(\frac{EI_{xx} - EI_{yy}}{2}\right)\cos(2\phi) + EI_{xy}\sin(2\phi) \tag{5.3}$$

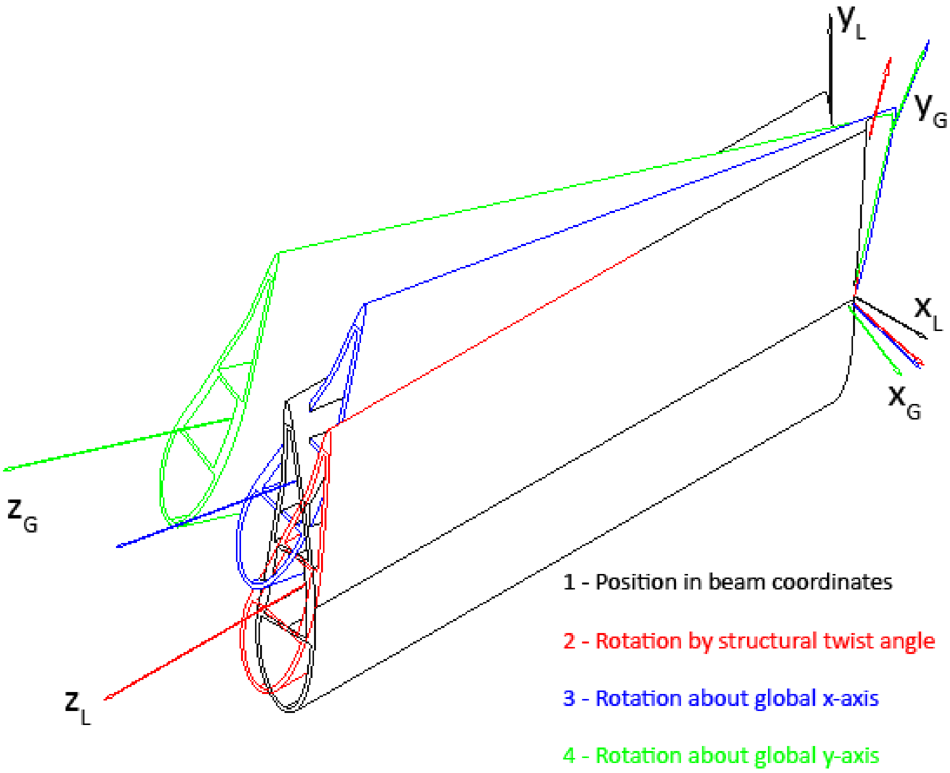

Figure 5.2 - Rotation from beam coordinate system to global coordinate system

Each element must then be transformed from the element (local) coordinate system into the global coordinate system. The first step of this transformation is a rotation about the local z-axis by the structural twist angle. A rotation is then performed about the x-axis and then the y-axis (if it is required because of pre-bend, blade sweep or the position of the shear centre). This process is shown in Figure 5.2.

The global stiffness and mass matrices are then obtained by adding the element matrices to the appropriate parts of the global matrices. This is very straightforward as the nodes and elements are simply numbered sequentially from root to tip.

5.2.3 Boundary conditions

The boundary conditions are also simple. Previous work on blade testing has shown that the influence of the test stand stiffness is negligible [111], so all displacements at the root attachment node are set to zero. In practical terms this means that the rows and columns related to this node are simply deleted from the mass and stiffness matrices.

5.2.4 Structural damping

The structural damping matrix was obtained using Rayleigh damping. This approach is straightforward, and as the response of the blade is mainly due to the first flapwise and edgewise modes it is a reasonable approach.

When using Rayleigh damping, the damping matrix $[\boldsymbol{C}]$ is assumed to be a linear combination of the mass, $[\boldsymbol{M}]$ and stiffness matrices, $[\boldsymbol{K}]$ as shown in equation (5.4) [104].

$$[\boldsymbol{C}] = \alpha[\boldsymbol{M}] + \beta[\boldsymbol{K}] \tag{5.4}$$

The coefficients α and β are found using equations (5.5) and (5.6) in which ζ is the damping ratio and ω is the natural circular frequency. The subscripts F and E refer to the flap and edge directions respectively. The natural frequencies are found from the mass and stiffness matrices by performing a modal analysis.

$$\alpha = \frac{2\omega_F\omega_E}{\omega_E^2 - \omega_F^2}(\omega_E\zeta_F - \omega_F\zeta_E) \tag{5.5}$$

$$\beta = \frac{2}{\omega_E^2 - \omega_F^2}(\omega_E\zeta_F - \omega_F\zeta_E) \tag{5.6}$$

If these equations are rearranged to give the damping ratio as a function of frequency as shown in equation (5.7) then we can see how the damping ratio will change with frequency in Figure 5.3.

$$\zeta = \frac{\alpha}{2\omega} + \frac{\beta\omega}{2} \tag{5.7}$$

When the flapwise and edgewise natural frequencies are used to define the damping ratio, the higher frequencies are much more heavily damped. This is not a problem, as the blade is being excited at the flapwise and edgewise natural frequencies rather than the higher frequencies.

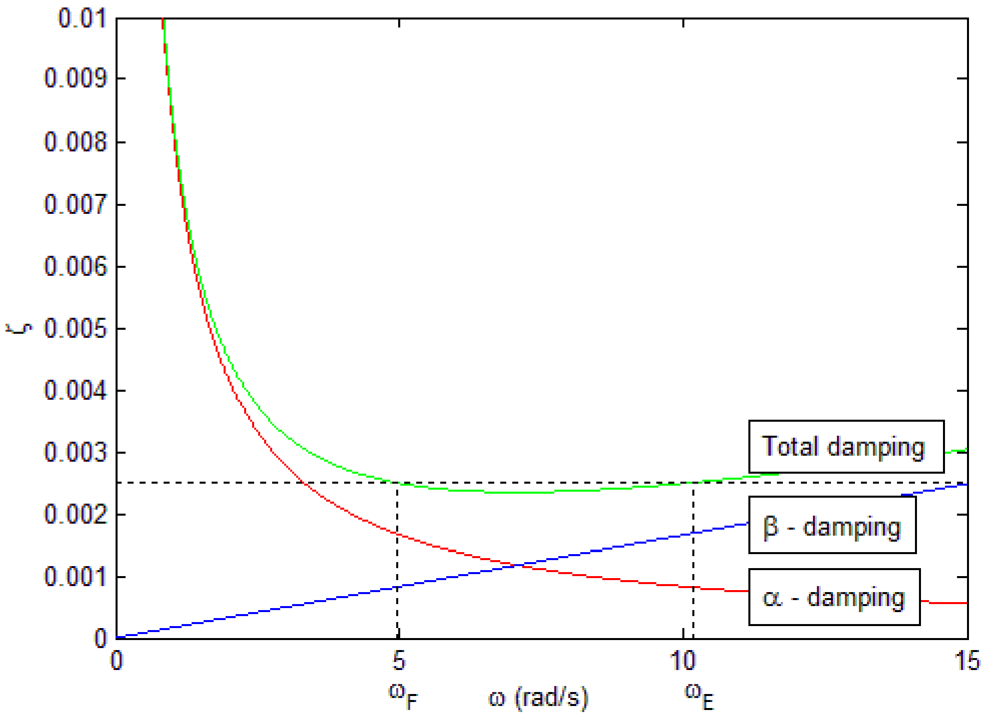

Figure 5.3 - Rayleigh damping

The structural damping is generally very small compared to the aerodynamic drag so it is not necessary to obtain a damping matrix that is based on the material behaviour. The experimental approach detailed here and in section 4.3.6 is readily achievable using the information and equipment available to a third-party test house such as Narec.

5.2.5 Numerical Integration

The choice of integration method was important. Wind turbine blades are so lightly damped that any integration scheme that introduces significant numerical damping will not be viable. The length of simulation required in order to provide representative results means that explicit integration schemes such as the central difference method are not useful either. This is because they require very small time steps in order to remain stable [104]. The Houbolt method was eventually chosen as it introduces almost no numerical damping and is much less computationally expensive (per time step) than higher order alternatives such as the Runge-Kutta method [104].

Despite the fact that Newmark-β method introduced unacceptable amounts of numerical damping it was still used (with a high damping ratio) in order to find the equilibrium position of the blade due to its own weight. The Newmark method is based on the assumption that the acceleration varies linearly between two points in time [104], and the normal process for using this scheme is outlined below [104].

- Choose suitable time step, Δt and α and β (these are the Newmark coefficients, not the Rayleigh damping coefficients).
- Calculate the initial acceleration using equation (5.8) in which $\ddot{\boldsymbol{x}}$, $\dot{\boldsymbol{x}}$, $\boldsymbol{x}$ and $\boldsymbol{F}$ are the acceleration vector, velocity vector, displacement vector and force vector respectively. The velocity vector and displacement vector are both known from the initial conditions.

$$\ddot{\boldsymbol{x}}_0 = [\boldsymbol{M}]^{-\mathbf{1}}(\boldsymbol{F}_0 - [\boldsymbol{C}]\dot{\boldsymbol{x}}_{\mathbf{0}} - [\boldsymbol{K}]\boldsymbol{x}_{\mathbf{0}}) \tag{5.8}$$

- Calculate the value of the inverted term $[\boldsymbol{A}]$ using equation (5.9) to avoid matrix inversions during the time stepping routine.

$$[\boldsymbol{A}] = \left[\frac{1}{\alpha(\Delta t)^2}[\boldsymbol{M}] + \frac{\beta}{\alpha \Delta t}[\boldsymbol{C}] + [\boldsymbol{K}]\right]^{-1} \tag{5.9}$$

- Step through the time history until the stop time is reached. The next value of the displacement vector is found using equation (5.10). This result is then used in equations (5.11) and (5.12) to calculate the next values of the acceleration and velocity vectors. As this routine is only used to find the equilibrium position, the force vector contains only the gravity force and does not change.

$$\begin{aligned}\boldsymbol{x}_{\boldsymbol{i}+\mathbf{1}} = [\boldsymbol{A}]\Bigg\{\boldsymbol{F}_{\boldsymbol{i}+\mathbf{1}} + [\boldsymbol{M}]\left(\frac{1}{\alpha(\Delta t)^2}\boldsymbol{x}_{\boldsymbol{i}} + \frac{1}{\alpha \Delta t}\dot{\boldsymbol{x}}_{\boldsymbol{i}} + \left(\frac{1}{2\alpha} - 1\right)\ddot{\boldsymbol{x}}_{\boldsymbol{i}}\right) \\ + [\boldsymbol{C}]\left(\frac{\beta}{\alpha \Delta t}\boldsymbol{x}_{\boldsymbol{i}} + \left(\frac{\beta}{\alpha} - 1\right)\dot{\boldsymbol{x}}_{\boldsymbol{i}} + \left(\frac{\beta}{\alpha} - 2\right)\frac{\Delta t}{2}\ddot{\boldsymbol{x}}_{\boldsymbol{i}}\right)\Bigg\}\end{aligned} \tag{5.10}$$

$$\ddot{\boldsymbol{x}}_{\boldsymbol{i}+\mathbf{1}} = \frac{1}{\alpha(\Delta t)^2}(\boldsymbol{x}_{\boldsymbol{i}+\mathbf{1}} - \boldsymbol{x}_{\boldsymbol{i}}) - \frac{1}{\alpha \Delta t}\dot{\boldsymbol{x}}_{\boldsymbol{i}} - \left(\frac{1}{2\alpha} - 1\right)\ddot{\boldsymbol{x}}_{\boldsymbol{i}} \tag{5.11}$$

$$\dot{\boldsymbol{x}}_{\boldsymbol{i}+\mathbf{1}} = \dot{\boldsymbol{x}}_{\boldsymbol{i}} + (1-\beta)\Delta t \ddot{\boldsymbol{x}}_{\boldsymbol{i}} + \beta \Delta t \ddot{\boldsymbol{x}}_{\boldsymbol{i}+\mathbf{1}} \tag{5.12}$$

The Houbolt method approximates the function $\boldsymbol{x}(t)$ as the first three terms of its Taylor series expansion with a backward step [104]. This makes the method non self-starting, but as the position is available at previous time steps from finding the equilibrium position this is not a problem. Again, the terms involving matrix inversions are calculated before the time stepping scheme starts using equation (5.13) to decrease the computation time. The displacement at the next time step is then found using equation (5.14). Although the velocity vector is not required for the time integration scheme, it is necessary to calculate the aerodynamic drag force on the blade so it is calculated using equation (5.15).

$$[\boldsymbol{A}] = \left[\frac{2}{(\Delta t)^2}[\boldsymbol{M}] + \frac{11}{6\Delta t}[\boldsymbol{C}] + [\boldsymbol{K}]\right]^{-\mathbf{1}} \tag{5.13}$$

$$\begin{aligned}\boldsymbol{x}_{\boldsymbol{i}+\mathbf{1}} = [\boldsymbol{A}]\Bigg\{\boldsymbol{F}_{\boldsymbol{i}+\mathbf{1}} + \left(\frac{5}{(\Delta t)^2}[\boldsymbol{M}] + \frac{3}{\Delta t}[\boldsymbol{C}]\right)\boldsymbol{x}_{\boldsymbol{i}} - \left(\frac{4}{(\Delta t)^2}[\boldsymbol{M}] + \frac{3}{2\Delta t}[\boldsymbol{C}]\right)\boldsymbol{x}_{\boldsymbol{i}-\mathbf{1}} \\ + \left(\frac{1}{(\Delta t)^2}[\boldsymbol{M}] + \frac{1}{3\Delta t}[\boldsymbol{C}]\right)\boldsymbol{x}_{\boldsymbol{i}-\mathbf{2}}\Bigg\}\end{aligned} \tag{5.14}$$

$$\dot{\boldsymbol{x}}_{i+1} = \frac{1}{6\Delta t}(11\boldsymbol{x}_{i+1} - 18\boldsymbol{x}_i + 9\boldsymbol{x}_{i-1} - 2\boldsymbol{x}_{i-2}) \tag{5.15}$$

The Houbolt integration method was found to be very reliable, and it is also relatively quick. The time step size was chosen so that there were 100 steps per edgewise cycle which is rather a large number. This helps to further decrease numerical damping and cycle elongation [104].

5.2.6 Forces

The force vector is composed of the gravitational force, aerodynamic forces and the forces from the excitation equipment.

The gravitational force is very straightforward; it is simply dependent on the mass lumped at each node. The gravitational force in the z-direction at the ith node is found from equation (5.16). As it is invariant throughout the process it is calculated before the time stepping scheme starts.

$$F_{\boldsymbol{z}\,\boldsymbol{i}} = gm_i \tag{5.16}$$

The force from the excitation equipment is calculated using the equations of simple harmonic motion. In equation (5.17), F_{CRM} is the magnitude of the force developed by a pair of CRMs, m_d is the dynamic mass of the pair of CRMs, a is the amplitude of the CRM motion, ω is the circular frequency of the CRM motion and t is the amount of time that has elapsed since the time integration process started.

$$F_{CRM} = -m_d a\omega^2 cos(\omega t) \tag{5.17}$$

As the inclination of the point on the blade at which the excitation equipment is mounted changes as it is cycled, the unit vector that is normal to a point on the blade is calculated from the node initial position and its displacement from the previous time step. The contribution of a pair of CRMs to the force vector can then be calculated from the unit vector defining the orientation of the CRM at the current time and the CRM force magnitude at the current time step. Currently, the fact that the CRMs are not equally spaced about the shear centre and will therefore also induce a torsional moment is not taken into account.

The aerodynamic forces were discussed in detail in section 4.3.5. The assumption that the unsteady effects can be accounted for by increasing the drag coefficient and calculating the quasi-steady force is made again here. This is assumption is not completely valid and future work will address this issue.

The magnitude of the aerodynamic drag force at each node is calculated using equation (5.18).

$$F_{D\,i} = -\frac{1}{2}\rho A_i C_{D\,i}\dot{x}_i|\dot{x}_i| \tag{5.18}$$

In equation (5.18), ρ is the density of air, A_i is the area around the node in m^2 (see Figure 4.7 in section 4.3.5), $C_{D\,i}$ is the drag coefficient for the section (which takes account of whether the force is being calculated for the flapwise direction or the edgewise direction) and $\dot{x}_i$ is the node velocity at the previous time step resolved into the flapwise or edgewise direction. As there are at least 100 time steps per cycle it is not thought that using the velocity from the last time step will have a significant effect on the results. Aerodynamic forces in the spanwise direction are ignored.

A unit vector is calculated for the flapwise and edgewise directions at each node and time step that describes the direction in which the aerodynamic force will be applied, as was the case for the CRM forces. For the flapwise direction this unit vector is normal to the plane described by the blade chord and the blade centerline, and for the edgewise direction it is parallel to the blade chord.

The force vector can therefore be found at each time step by summing the contributions from the gravitational force, the aerodynamic force and the forces from the excitation equipment.

5.2.7 Element loads

Once the displacements in the global coordinate system have been calculated, they are transformed back into the element coordinate system using the inverse of the local to global transformation. The internal element loads for the ith element are then found using equation (5.19).

$$\boldsymbol{f_i} = [\boldsymbol{K_e}]_i \boldsymbol{x_i} \tag{5.19}$$

5.2.8 Visualisation

A visualisation of the blade test was created so that any mistakes could easily be seen. The visualisation allows the user to view the air resistance forces and forces from the CRMs in order to make sure that they are in the correct direction. The blade can be coloured according to the magnitude of the flapwise or edgewise bending moment.

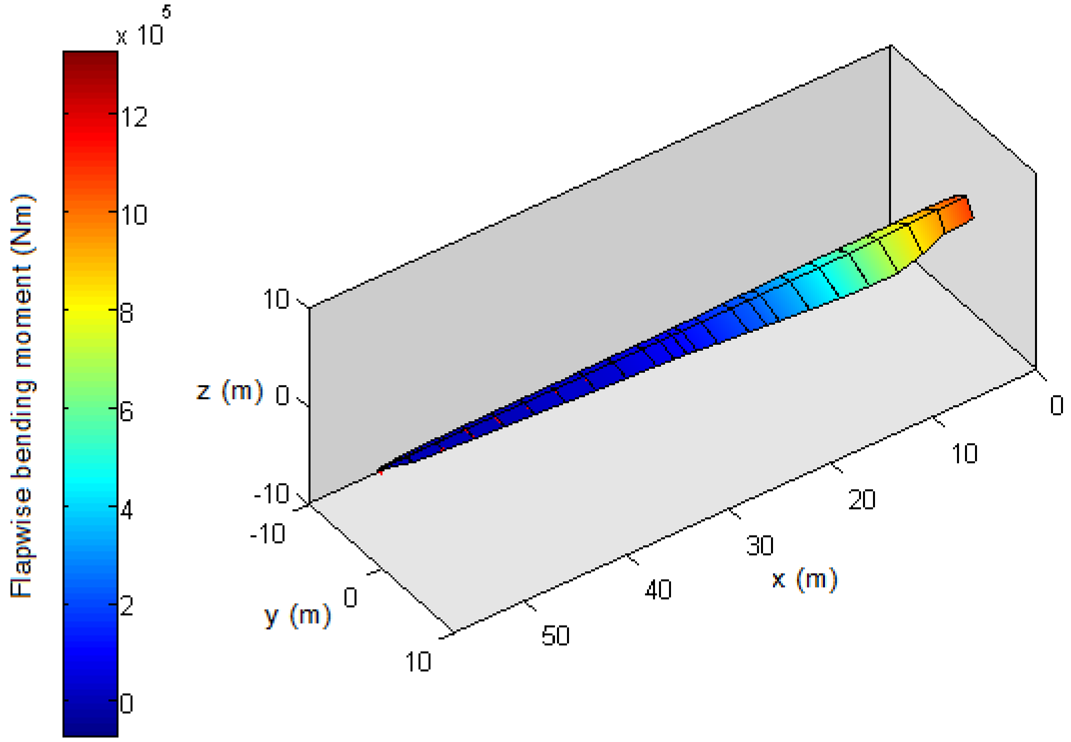

Figure 5.4 – Typical fatigue test simulation visualisation (flapwise bending moment)

5.2.9 Static test simulation

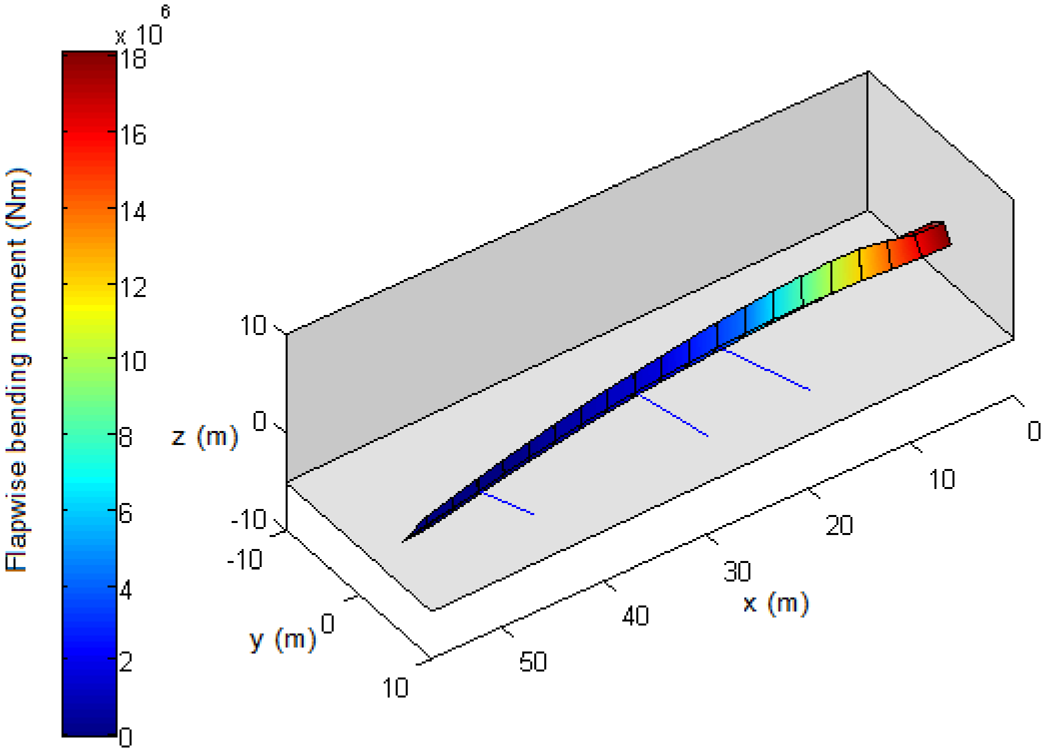

Figure 5.5 – Typical static blade test visualisation (flapwise bending moment)

Static blade testing is relatively simple compared to fatigue testing. The effect of air resistance can be neglected, and the structural damping can be increased to stop the blade vibrating as the load is applied. The effect of the winches changing their angle to the blade as the load is applied can also easily be accounted for due to the transient nature of the simulation. Figure 5.5 shows a visualisation of a static test, with the winch cables shown as blue lines.

5.2.10 Edgewise frequency reduction feasibility study

As part of the frequency alteration feasibility study discussed in section 4.3.16 a test configuration based on this method was modelled. The proposed test configuration is shown in Figure 5.6. The push rods are modelled as beam elements with very high axial stiffness and bending stiffness. The connections at each end of the push rod are modelled as very short beams with almost no bending stiffness but a high axial stiffness, which allows them to act as pivots. The tuning mass itself is lumped at the end node of this joint element. The boundary conditions for the tuning mass node are defined in such a way that it is only free to move along the rails. The best position and size for the masses was found using the optimisation routine described in section 4.3.9.

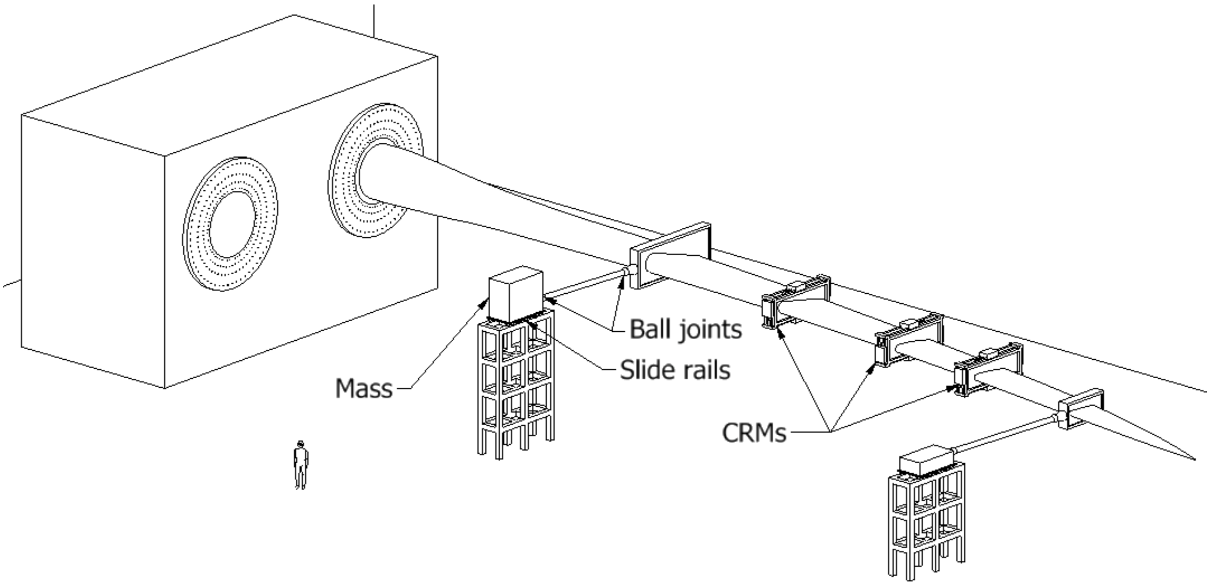

Figure 5.6 - Edgewise frequency reduction method

5.2.11 Small scale test rig

As part of the validation of the simulation model a small scale test rig was developed. The purpose of this rig was to allow the simulation model to be validated in a way that did not rely on having access to full scale blade test data. A schematic of the test rig is shown in Figure 5.7, and the assembled rig is shown in Figure 5.8.

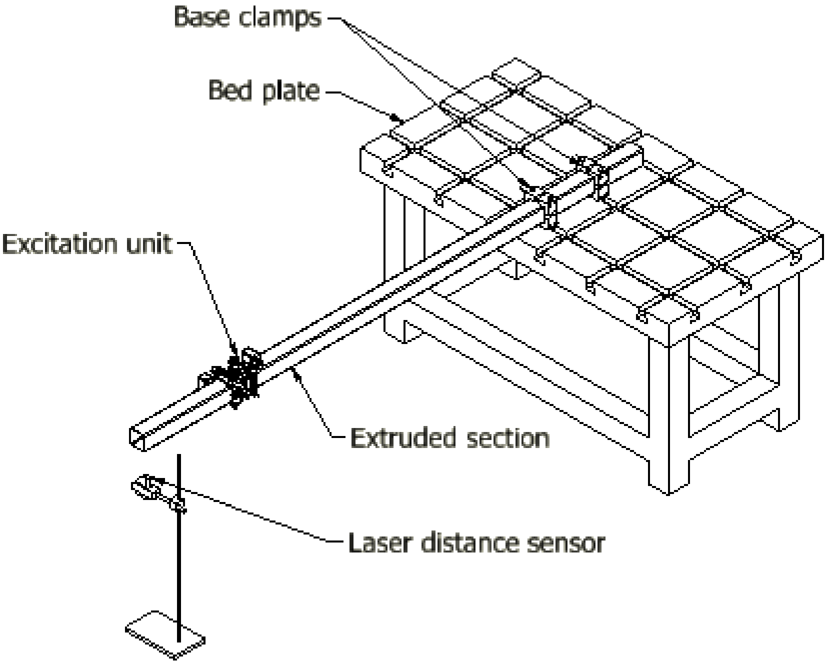

Figure 5.7 – Small scale test rig

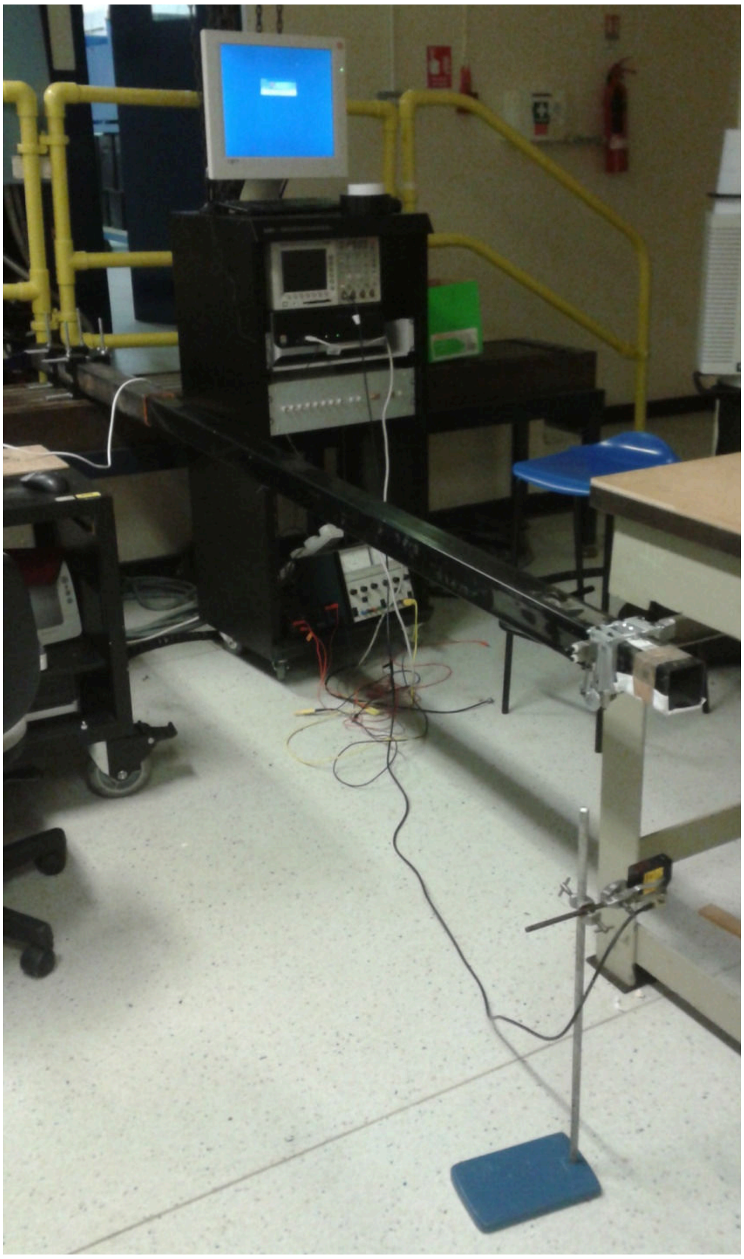

Figure 5.8 - Test rig

The displacement of the tip is measured using a laser distance sensor. The excitation frequency is measured using an optical sensor mounted on the excitation unit, so the frequency can either be inferred from the tip displacement time history or logged directly.

The exciter is driven by a small 5W DC motor, the speed of which can be controlled by changing the voltage. The amplitude of the excitation can be coarsely adjusted by altering the radius at which the link arm is attached to the driving wheel. The mass can be altered by bolting different numbers of the small weights onto the slider. A schematic of the excitation equipment is shown in Figure 5.9, and the exciter mounted on the test rig is shown in Figure 5.10.

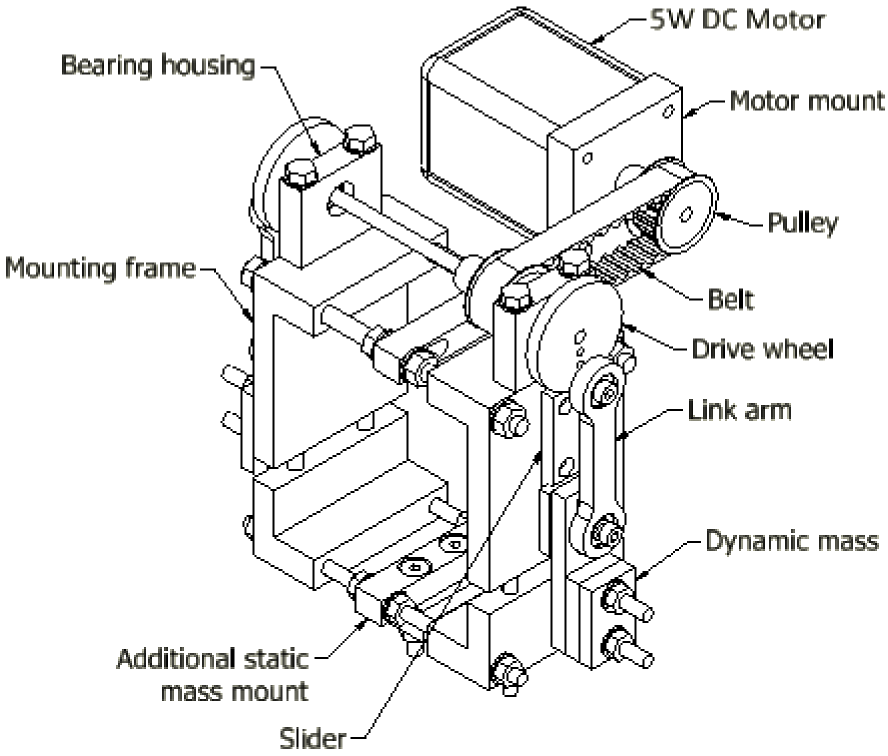

Figure 5.9 - Small scale model excitation unit

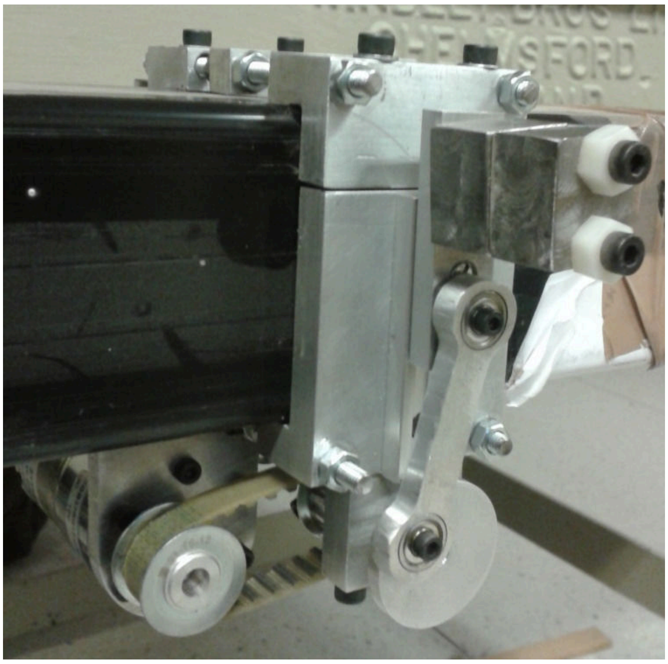

Figure 5.10 - Exciter in place on test rig

Experiments were also performed to obtain the Young's modulus of the plastic extruded section material which represents the test piece. The shear modulus was inferred from the Young's modulus using a typical Poisson's ratio for PVC. This data, along with the dimensions of the section, allows all cross sectional properties required to model the test piece to be obtained.

5.3 Results and Discussion

The model was validated using data from full scale blade tests performed by LM Wind Power, and against data obtained on the small scale test rig discussed in section 5.2.11. It was also used to simulate tests on the benchmark blade discussed in chapter 3.

5.3.1 Model test rig simulation

Single axis excitation of the of the small scale test rig was performed and the predicted results were compared against the experiment. The variables of interest were the tip displacement and the frequency. Section data for the box section is given in Table 5.1. The static mass of the exciter was 0.7069kg, and the dynamic mass was 0.266kg, moving with a fixed amplitude of 1.5cm. The frequency was measured and calculated for the bare beam and four different exciter positions with a beam length of 2m. The beam could not be considered to be built in to the bed plate so an effective length was used to account for the non rigid support. The effective length was found by measuring the frequency of the beam under free vibration without any mass mounted on it. The length of the beam that would result in this frequency is then calculated assuming that all other parameters that affect the frequency are the same.

The comparison is shown in Table 5.2. The model predicts the frequency very well, and the results are inside the confidence bounds.

Variable	Value	Bounds
E (GPa)	3.7	±0.1
Area (m^2)	4.78-4	±35e-5
I (m^4)	3.16e-7	±2.2e-8
Mass per unit length (Kg/m)	0.71	±0.01
Effective length (m)	2.05	±0.05

Table 5.1 - Box section data

Exciter distance from root (m)	Nominal predicted frequency (Hz)	Minimum predicted frequency (Hz)	Maximum predicted frequency (Hz)	Experiment frequency (Hz)
No exciter	5.2622	4.7679	5.9221	5.27
0.5	5.1792	4.7499	5.8147	5.18
1	4.5596	4.2181	5.0428	4.53
1.5	3.5895	3.3530	3.9042	3.47
1.85	2.9831	2.7998	3.2178	2.92

Table 5.2 – Frequency comparison

The mean tip displacement was measured using a laser mounted at the root. Again, the model predicts the experimental results well (the nominal values in Table 5.1 are used), although it is under-predicting the displacement when the exciter is mounted at the very tip. This could be due to erroneous values for the cross sectional properties, as the frequencies are also slightly higher than the experiment (meaning that either the stiffness or area properties are incorrect). The stiffness was measured at a strain rate different to that experienced in the test, and the wall thickness varies significantly around the cross section so either of these scenarios is a possibility.

Exciter distance from root (m)	Predicted tip displacement Shear and bending (cm)	Predicted tip displacement Bending only (cm)	Experiment tip displacement (cm)	Error (%)
No exciter	1.27	1.26	1.2	5.8
0.5	1.5	1.45	1.5	0.0
1	2.07	2.06	2.1	1.4
1.5	2.82	2.8	3	6.0
1.85	3.38	3.37	3.9	13.3

Table 5.3- Mean tip displacement

It is difficult to draw conclusions about tip displacement as the excitation frequency could not be monitored ‘on the fly’ with the available equipment. Furthermore, the exciters were not always able to maintain their speed if the accelerations experienced were too high. The only way to ascertain if the beam was at its resonant frequency was to vary the frequency of the excitation slowly and judge from the amplitude of the oscillations. As the tip displacement was greater than the range of the laser distance measure, the displacement at 0.7m from the root was recorded.

The structural damping was determined both by logarithmic decrement and curve fitting as described in section 4.3.6, and was estimated to be around 0.01. The drag coefficient is more complex. The rounded edge square section would be expected to have a slightly lower drag coefficient than a blade (for which CFD was performed as described in section 4.3.5) under steady state conditions, but the high frequency means that interaction with the wake will have more of an effect. As the structural damping is much higher than for a real blade the influence of the air resistance is less in this case. For example, for the scenario when the exciter is mounted at the tip the amplitude is 15.7cm if no air resistance is included. If a ‘best estimate’ drag coefficient of 3.6 is used then the amplitude is 12.7cm, and if an unrealistically high value of 10 is used then the predicted amplitude is 10.27cm. This illustrates that the air resistance plays a much smaller role than it does for a full sized blade.

Furthermore, the logarithmic decrement method of finding the structural damping (which results in the largest variation of the damping) results in a value of between 0.008 and 0.02, depending on the time that has elapsed since excitation of the blade ceased. It is more likely to be towards the lower end of this range as some of the damping shortly after excitation has stopped will be due to air resistance.

Results were obtained and a comparison of the predicted and measured response is shown in Table 5.4.

Exciter distance from root (m)	Predicted displacement at 0.7m from root (cm)	Experiment displacement at 0.7m from root (cm)
0.5	0.6208	0.87
1.0	1.83	0.95
1.5	2.1522	0.83
1.85	2.0799	1.18

Table 5.4 – Amplitude comparison

Apart from the case where the exciter is mounted 0.5m from the root, the simulation model over-predicts the tip displacement by a large margin. This is due to the test rig being unable to maintain resonant conditions for enough time for a stable state to be attained. At the 0.5m mounting point the acceleration due to the beam movement is much less and so resonance can be attained and the results at this point are more realistic. The simulation model excites the blade at the correct frequency, so resonance is always maintained which could not be achieved with the exciter mounted at 1m, 1.5m or 1.85m.

The small scale test rig results show that the model can accurately predict natural frequencies for simple models. The amplitude comparison was hindered by incomplete knowledge of the test conditions.

5.3.2 Full-scale test simulation

The beam element model discussed in the previous sections was used to predict the response of the LM 40.3 P2 blade during a flapwise fatigue test. LM Wind Power utilise a rotating eccentric mass to excite their blades during fatigue tests, which means that an axial force and a moment are induced in addition to the vertical force. A schematic of the test set-up is shown in Figure 5.11.

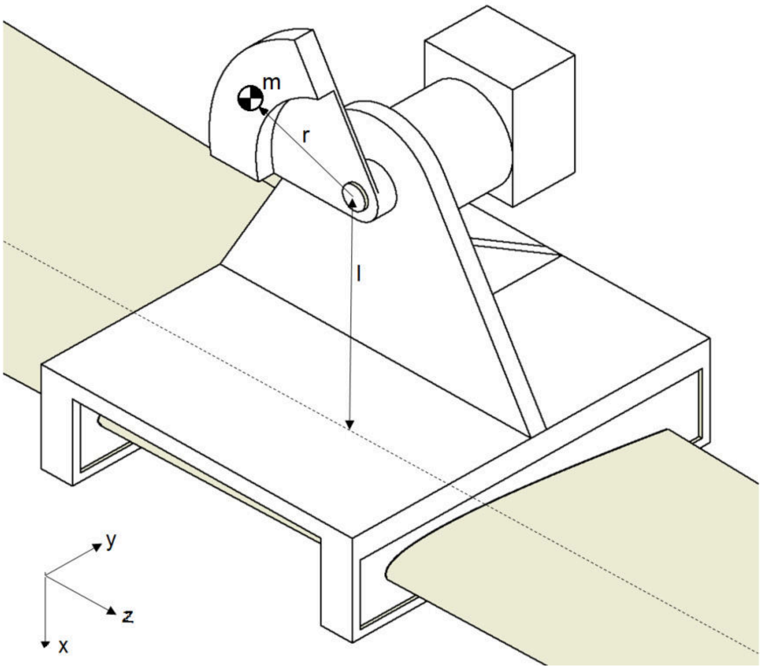

Figure 5.11 - Rotating eccentric mass excitation

The induced forces and moments at the reference node can be calculated as shown in equations (5.20) to (5.22). These forces are calculated at each time step and added to the relevant position in the force vector.

$$F_x = mr\omega^2 \sin(\omega t) \tag{5.20}$$

$$F_z = mr\omega^2 \cos(\omega t) \tag{5.21}$$

$$M_y = mrl\omega^2 \sin(\omega t) \tag{5.22}$$

As the data provided by LM Wind Power pertains to a commercial blade, the comparison has been normalized for presentation here. The data provided includes:

- Flapwise natural frequency of the test set-up
- Position and mass of exciter and static masses
- Target and achieved bending moment distribution
- Calibration data which shows how the stiffness changes as the test progresses
- Design data for the blade

The flapwise drag coefficient was chosen to be 4, which is based on the CFD simulations in section 4.3.5. The structural damping is impossible to calculate from the data provided by LM Wind Power as the eccentric mass continues to spin after the blade test stops, so the blade continues to be excited. For this reason the damping for the first two modes was chosen to be 0.0025, which is based on a blade of a similar size tested at Narec.

The structural damping coefficient has relatively little effect compared to the aerodynamic damping, as shown in Figure 5.12, in which the y axis has been normalised by the average root bending moment of the full scale test. The non-linear nature of the aerodynamic damping means that it has a much greater effect on the results than the linear structural damping. The model predicts the root bending moment achieved well when the best estimate values of ζ (0.0025) and C_D (4) are used.

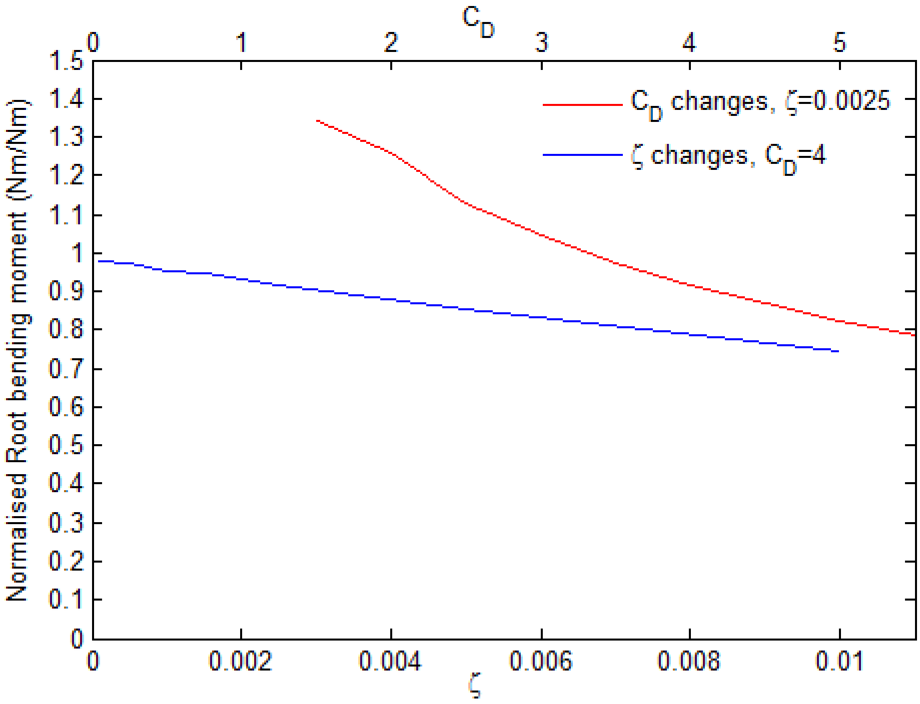

Figure 5.12 - Effect of varying damping and drag coefficient

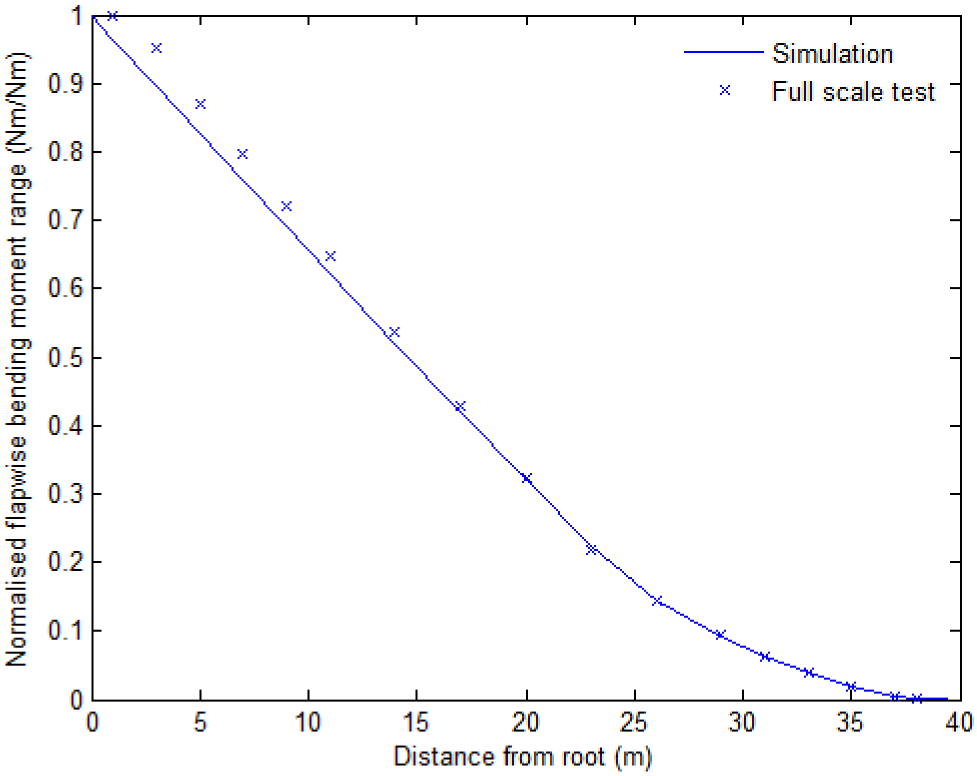

Figure 5.13 - Comparison of simulation and full scale test results for LM 40.3 P2 blade

The flapwise natural frequency was predicted with an accuracy of within 1% and the bending moment distribution prediction was also very close to the physical test as shown in Figure 5.13. Again, as this information is commercially sensitive the data cannot be given without being normalised.

The simulation tool has been shown to be capable of predicting the response of a blade during a full scale test, and as such it will be very useful for reducing set-up times and designing test equipment.

5.3.3 Simulation and fatigue results of 2MW blade tests

The service life damage distributions around 8 cross sections of the 38.75m blade described in section 3.2.2 were obtained in chapter 3. Synthesised test loads were developed that matched the target flapwise and edgewise bending moments exactly and the effects of various different types of fatigue test were compared. It is not possible to obtain the target bending moment amplitude along the whole blade length, so in order to assess the quality of the results which can be achieved in practice with resonant testing it is necessary to simulate the tests.

The blade test simulation software described in this chapter has been used to analyse the test configurations found using the optimisation routine in the previous chapter. The resulting load time histories have then been analysed using the fatigue analysis method described in chapter 3. This allows us to compare how well dual axis testing and single axis testing perform by juxtaposing the fatigue damage sums obtained during testing with those resulting from the service life.

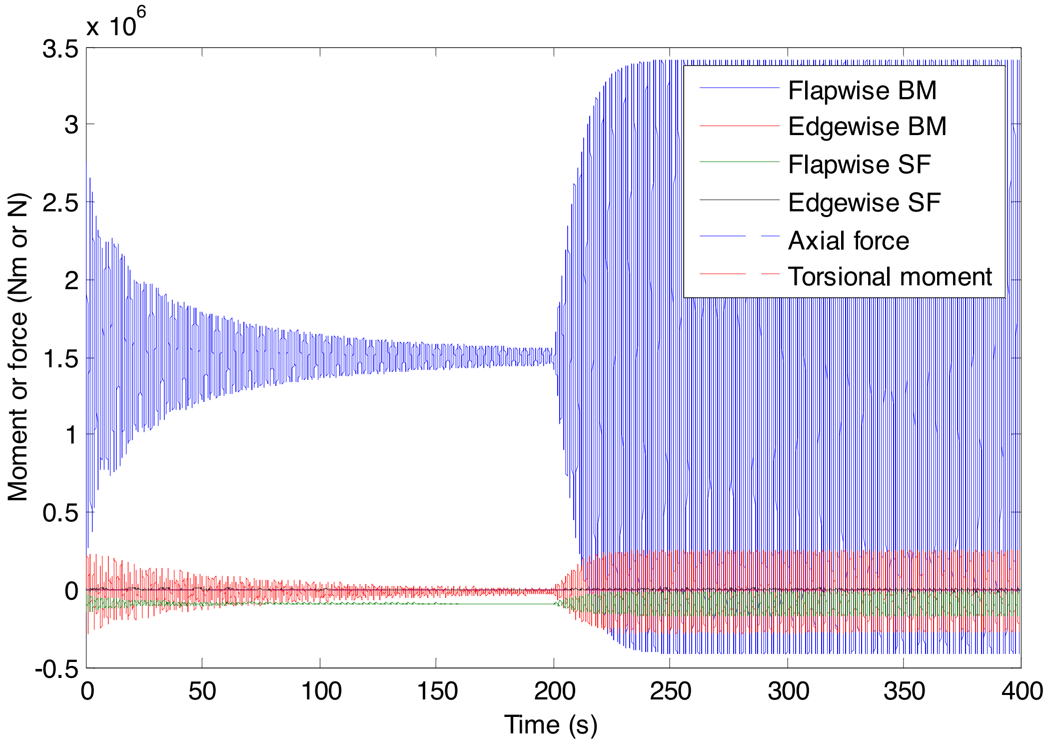

Figure 5.14 - Flapwise test load time histories at 1.15m station

Figure 5.14 shows time histories of the forces and moments acting on the 1.15m station during a flapwise test. The first point to note is that the amplitude of the flapwise bending moment is larger than was predicted by the optimisation routine. The reason for this is that the optimisation routine treats the aerodynamic damping force as sinusoidal with the amplitude equal to the peak velocity of the node, when in actual fact it is proportional to the square of the instantaneous velocity of the node. This means that less work is done by the aerodynamic drag over the course of a cycle in the transient simulation so the predicted amplitude is higher. This is not a problem, as it means the optimisation code is slightly conservative. In a real test the amplitude of the excitation equipment is controlled to match the target strains, and in the transient simulation code this issue can be addressed in the same way. Another point of interest is that the edgewise bending moment is not zero, because the blade twist results in the flapwise loading exciting the edgewise direction. This unwanted moment occurs at the same frequency and is in phase with the flapwise moment, but it is sufficiently small that it will not affect the fatigue analysis if the power law relationship is used. The other loads acting on this cross section are small in comparison (the axial force and moment are both zero at all times as the stiffness and mass matrices are constant throughout the simulation). The flapwise shear force is very small and its mean value is the same as would be predicted by a static analysis. Both the edgewise and flapwise frequencies are within 2% of the values predicted by the optimisation code. The reason for this difference is that the blade twist is accounted for in the transient simulation.

Because the edgewise direction is much less susceptible to air resistance, when a similar analysis is performed for the test configuration shown in Table 3.8 the results were almost exactly the same as in the optimisation model. As in the case of the flapwise study, the direction not being tested (in this case the flapwise direction) was excited at low amplitudes as a result of the blade twist. This is unavoidable, but as a result of the low slope of composite fatigue curves low amplitude cycles cause very little damage. Also, the edgewise frequency is higher so more time steps are needed per cycle in order to match up with the results found using modal superposition.

The flapwise excitation was adjusted so that the bending moment amplitude at the root was the same as in the optimisation routine, and all of the test configurations shown in Table 3.8 were simulated.

The simulation length was chosen so that if the flapwise and edgewise cycle periods are rounded to the nearest one-hundredth of a second then the analysis section of the load history will repeat once (in Figure 5.14 the analysis section would be any time after 250 seconds when the blade has stabilised). This was achieved using the least common multiple function in MatLab. The time step was chosen so that there were at least one hundred steps per cycle at the highest frequency being excited. This could be reduced by using a variable time step with more steps when the blade is moving slowly, but this was not considered necessary as the simulation is not very CPU intensive (it runs faster than real time using the parameters described above).

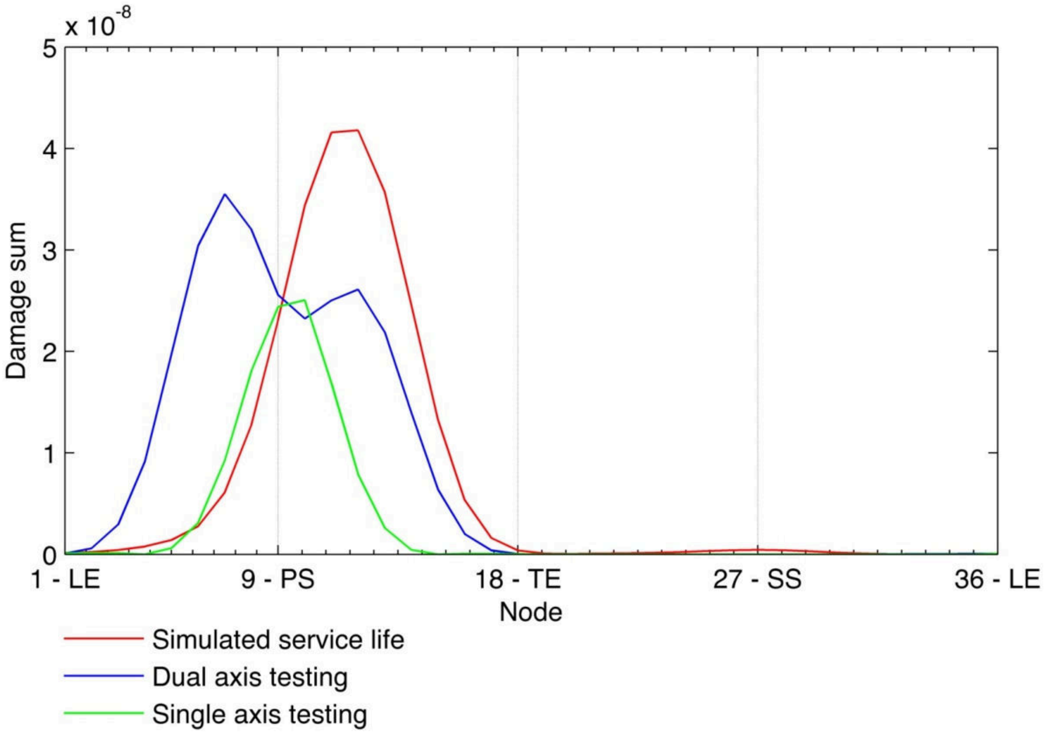

Figure 5.15 - Comparison of damage sums around section 1.25m from the root

In Figure 5.15 to Figure 5.20, the node numbering scheme shown in Figure 3.13 is used. Cross sections of the blade are shown in Figure 3.3, Figure 3.4 and Figure 3.5.

In Figure 5.15 we can see that at the blade root it is difficult to match the edgewise target loads without over testing the rest of the blade. The effect of this can be studied by comparing Figure 3.34 in chapter 3, which shows the results if the loads are exactly correct. Dual axis is shown to test more of the blade cross-section than single axis testing, at the expense of increased damage to the leading edge pressure side. The position of the peaks on the dual axis graph can be shifted by pitching the blade on the test stand; this can have implications for the rest of the blade, as it will alter the edgewise target loads because the mean stress at the trailing edge is higher. Pitching is only really beneficial at the blade root, as the blade is thicker there so the effect of the combination of the edgewise and flapwise loads is more significant.

It should also be noted that the safety factors have not been added to the test loads; if this was the case then the service life damage would be considerably smaller than the test damage. They have not been included here to allow a more informative comparison between the damage caused by testing and the service life damage.

In Figure 5.16 the damage at the start of the transition from the root section to the airfoil profile is compared. The thickness is 64% of the chord at this point, and it is possible to see that the damage at the trailing edge is starting to become more significant as we move along the blade. Again, dual axis is testing the blade more realistically than single axis testing and the over testing towards the leading edge is less pronounced.

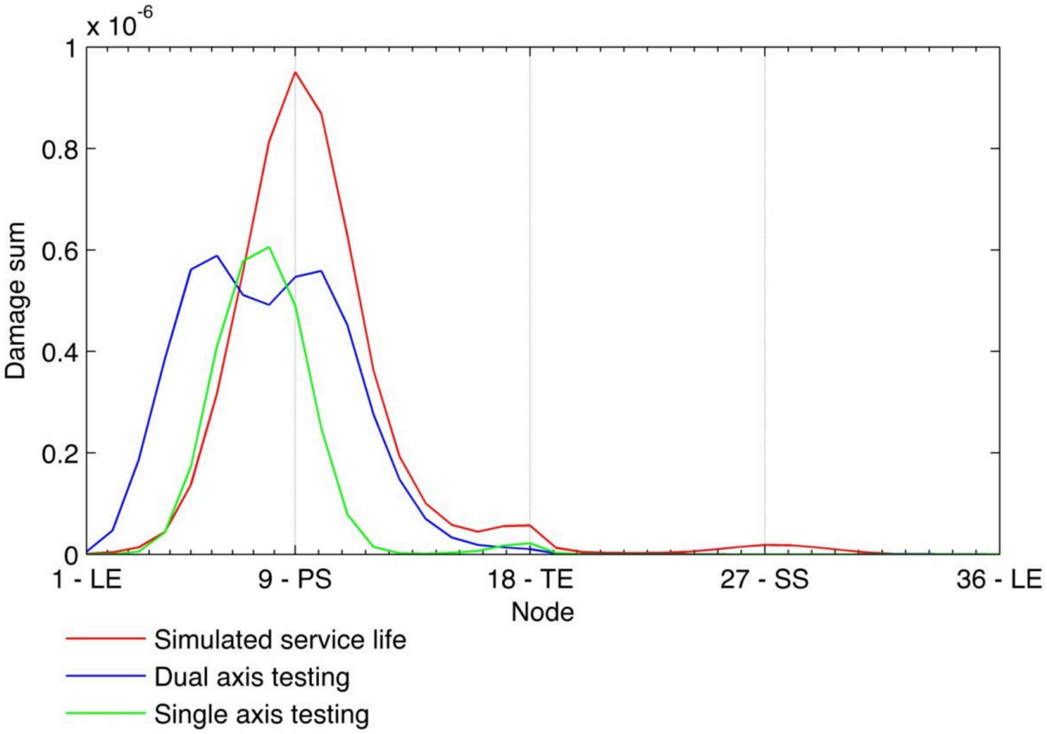

Figure 5.16 - Comparison of damage sums around section 3.44m from the root

Figure 5.17 shows the damage sums around the blade cross section towards the end of the transition section. The trailing edge is now the most damaged part of the blade, and the fact that the edgewise loads are not perfect is now more significant. This issue can be addressed by continuing the test for a longer time edgewise only. Although dual axis is not testing the trailing edge as well as single axis testing, it is much more realistic for the rest of the blade.

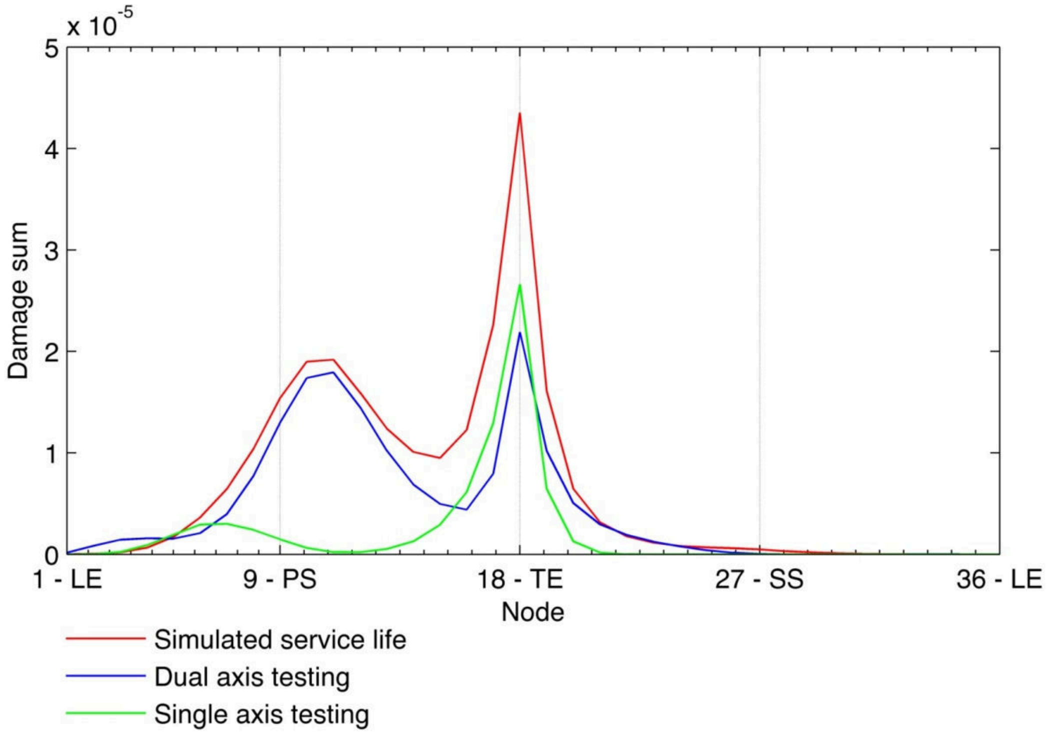

Figure 5.17 - Comparison of damage sums around section 5.75m from the root

Both single axis tests and dual axis tests are obtaining approximately the correct loads at the section 9.20m from the root, as shown in Figure 5.18. At this point dual axis is testing the blade much more realistically than single axis testing.

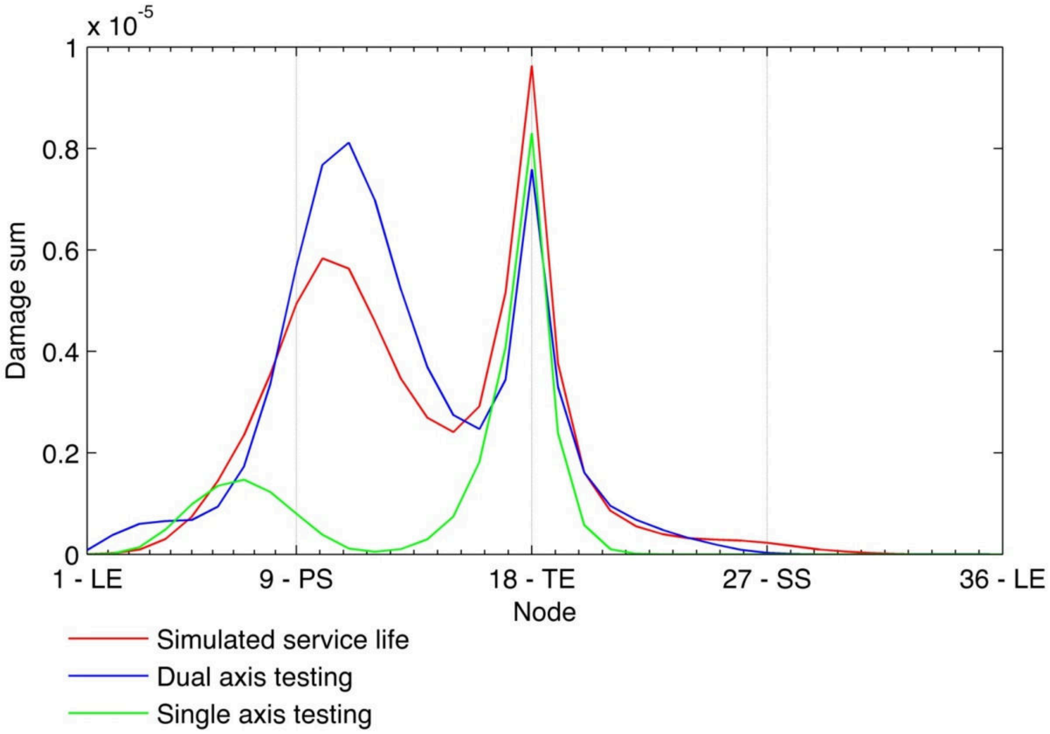

Figure 5.18 - Comparison of damage sums around section 9.20m from the root

Figure 5.19 shows that at 16.05m from the root the edgewise loads for both dual axis and single axis testing are too high. This has resulted in fairly severe over testing on the pressure side for the dual axis test.

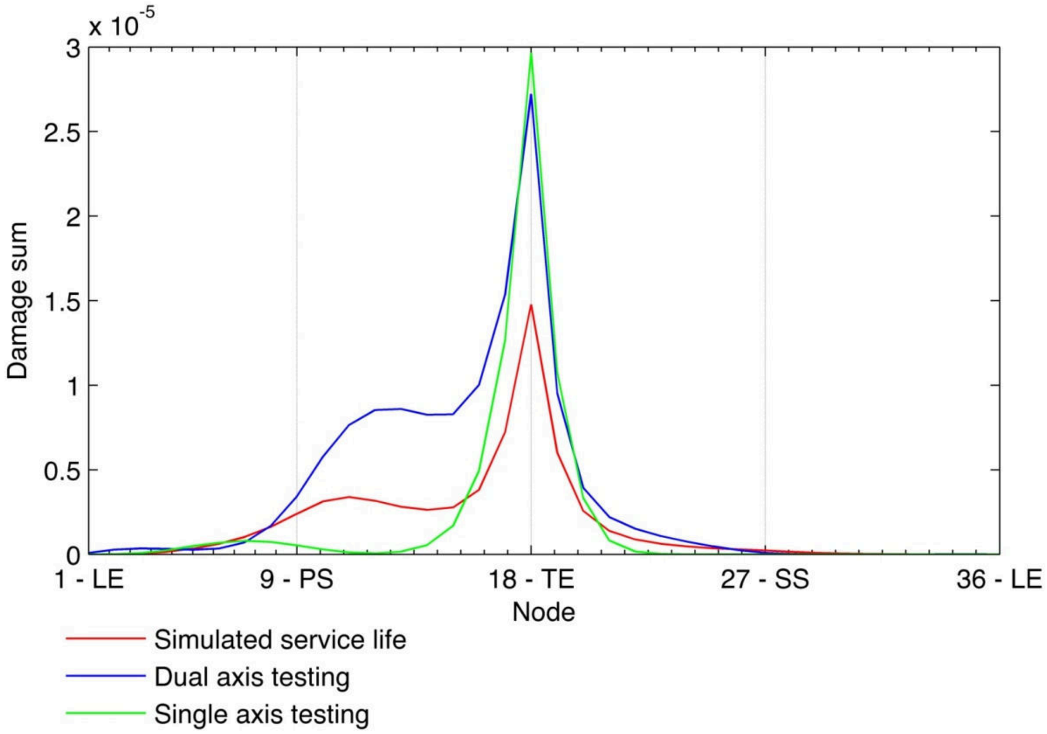

Figure 5.19 - Comparison of damage sums around section 16.05m from the root

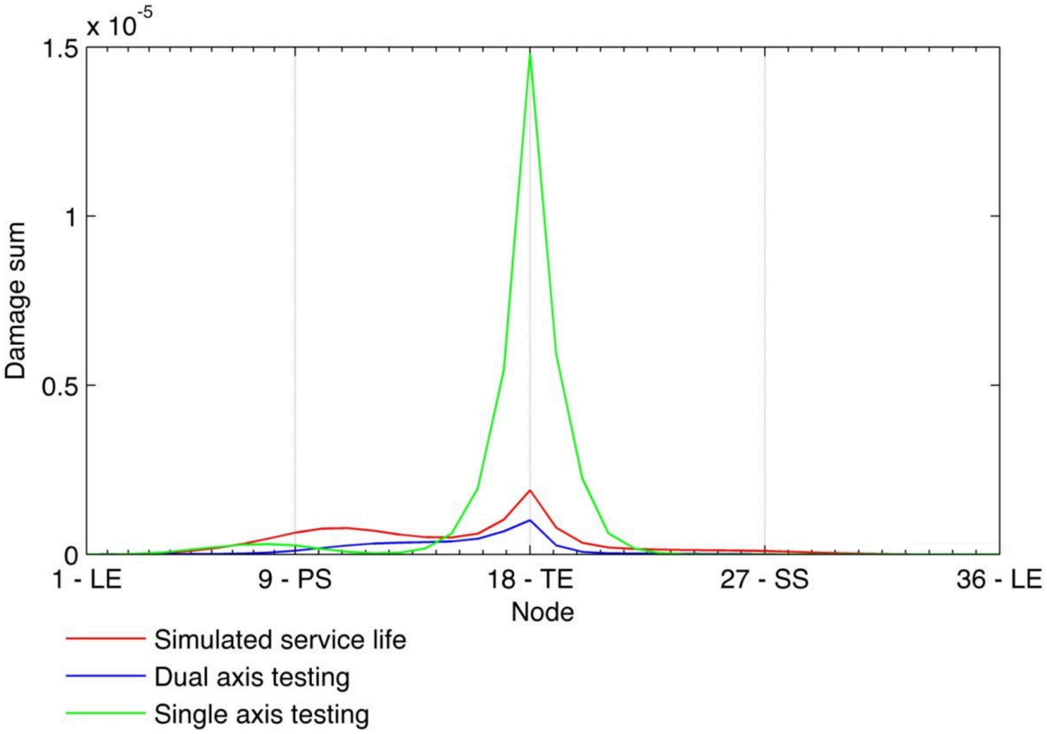

Figure 5.20 - Comparison of damage sums around section 26.40m from the root

Figure 5.20 shows that at 26.40m from the root, the single axis test loads are far too high. This is a result of better performance closer to the root for matching the edgewise optimisation. Dual axis testing is under testing much of the blade, and yet it still causes a more conservative and realistic amount of damage between nodes 10 and 15.

Whilst both dual axis testing and single axis testing are failing to match the service life damage sums realistically at several points along the blade, it is clear that dual axis testing is much more conservative across the whole of the blade span. Apart from at the root where the blade is very thick, the over testing associated with dual axis testing is not particularly severe if the loads can be matched, and the over testing is much less than that caused by including the safety factors in the test loads.

To put the results into perspective, although the damage sums obtained through testing differ from those resulting from the service life considerably (in Figure 5.20, the difference is almost an order of magnitude), the fact that the highest service life damage found anywhere on the blade is 5×10^{-5} means that theoretically the blade could survive 20,000 lifetimes. Much of the damage results from very low stress amplitudes occurring at higher frequencies, and the damage sums are calculated by extrapolating to considerably lower stresses than those for which test data are available, so there is already great uncertainty in the quality of fatigue results.

5.3.4 Edgewise frequency reduction feasibility

The test configuration found using the optimisation routine described in 4.3.16 was analysed using the 3-D transient model described in section 5.2. The flapwise excitation given in Table 4.13 was used and additional edgewise masses, isolated from the flapwise direction by means of push rods as shown in Figure 5.6, were added at 11.3m from the root and 28.9m from the root. The sizes of the masses were 29.5t and 1.9t respectively. As a first approximation, the push rods were given an extremely high stiffness and very low mass so that the effects of the isolated masses could be distinguished from the elastic and inertial effects induced by the push rods.

It was quickly apparent that the 1-D optimisation model was not capable of predicting the approximate response, which is not the case when the edgewise and flapwise natural frequencies are significantly different as in a standard dual axis test. The fact that the two modes have very similar frequencies means that they excite each other, and because movement in the flapwise direction necessitates movement in the edgewise direction (as a result of the push rod constraining vertical motion) it is impossible to control the motion of the edgewise and flapwise modes individually. The blade twist also effects the phase angle and natural frequency in the flapwise and edgewise directions, and is the third barrier to this technique being useful.

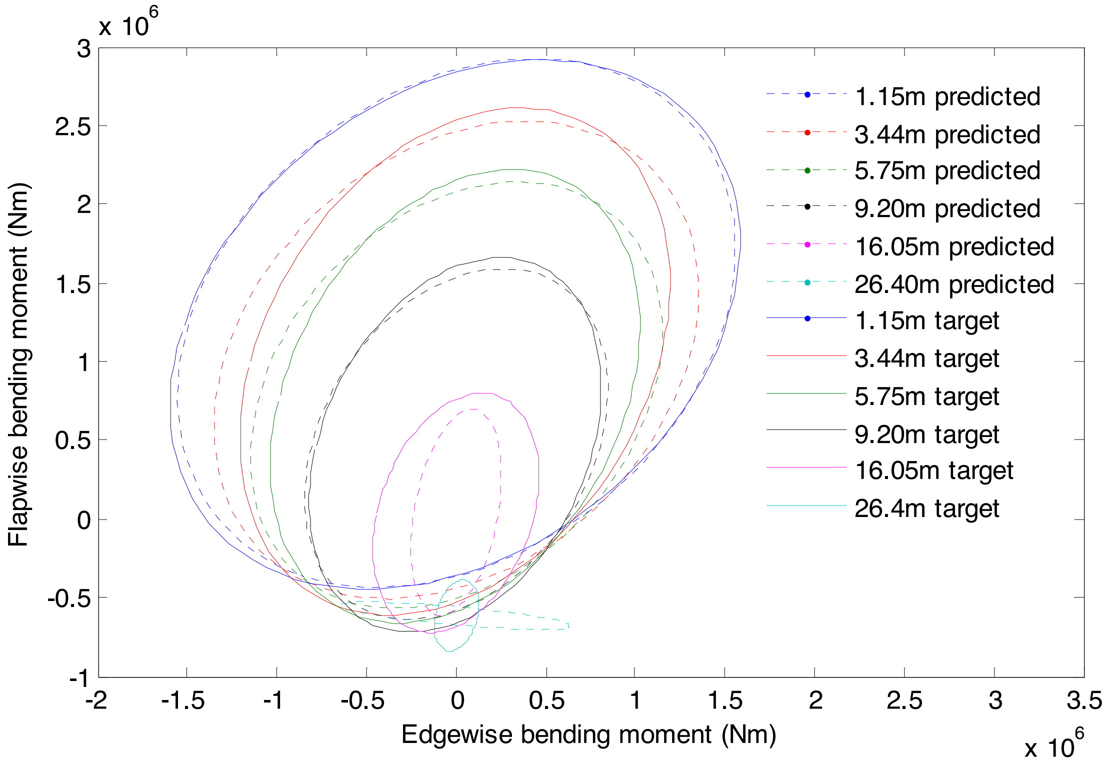

Figure 5.21 - Comparison of target and predicted bending moment loci for an untwisted blade

Figure 5.21 shows predicted results for an untwisted blade, which is as close to the problem studied with the optimisation routine as possible. As the blade is not twisted, it is possible to control the flapwise and edgewise directions independently if the push rod is long enough (in this case 10m) and get good results for the first four sections studied. The difference between the predicted and target results at the 26.4m section can be attributed to the presence of the push rods, which cause motion in the flapwise direction to induce motion in the edgewise direction. This issue could be solved by dynamically positioning the isolated masses so that they are always level with the blade, but the masses involved mean that this solution would be very costly, particularly for large blades where the masses and displacements involved are greater. The natural frequency for this test configuration is 1.01Hz and the phase angle between the two loads could be controlled under these conditions, as the flapwise and edgewise mode shapes are completely independent.

If the blade is twisted along its length in a realistic manner then the results are very different. The loads can no longer be controlled independently, and altering the excitation phase angle has very little effect on the phase angle between the flapwise and edgewise bending moment. The mode shapes are also coupled (so excitation in the flapwise direction results in bending moments of comparable or greater magnitude in the edgewise direction). A typical plot is shown in Figure 5.22. The force magnitude has been kept constant from the untwisted blade for both the flap and edge directions, and a range of different excitation frequencies produce similar results; the edgewise behaviour dominates, and increasing the flapwise excitation only increases the edgewise loads further.

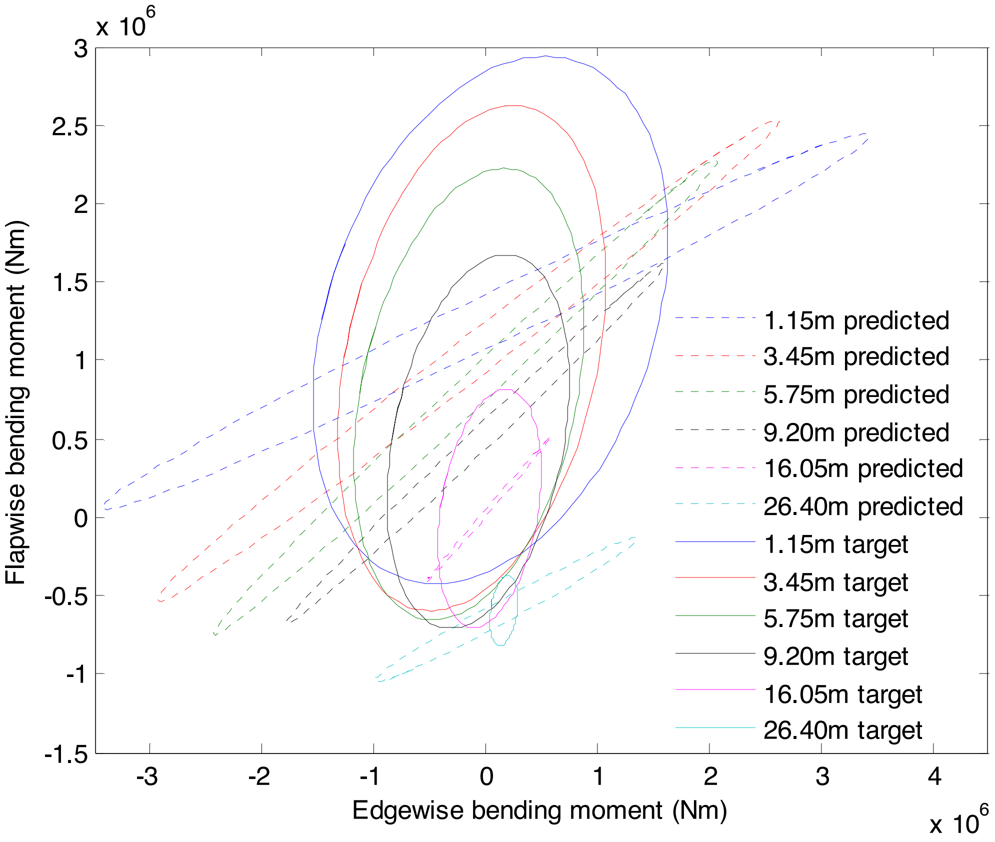

Figure 5.22 - Comparison of target and predicted bending moment loci for benchmark 2MW blade

The solution for this is to greatly increase the length of the push rods to reduce the coupling between the two directions, but this will be limited by the size of the test facility and buckling of the push rods.

In the simple simulation where the blade is untwisted, the peak axial force in the push rod was 44kN. Assuming the stress in the push rods must be kept below the fatigue limit of a typical engineering steel (150MPa), it is possible to ascertain if it is feasible to manufacture the push rods from affordable materials. The maximum bending moment in a beam loaded laterally by its own self weight and axially by a compressive force can be found using equation (5.23), in which w is the distributed gravitational load due to the rod's self weight, P is the axial load, EI is the bending stiffness of the steel rod and L is the length of the rod [112]. The maximum bending stress can be found from equation (5.24), where y is the distance from the neutral axis and I is the second moment of area.

$$M_{max} = \frac{wEI}{F_z}\left[\sec\left(\frac{1}{2}L\sqrt{F_z/EI}\right) - 1\right] \tag{5.23}$$

$$\sigma_{max} = \frac{M_{max}y}{I} \tag{5.24}$$

Using these equations, it was found that a steel tube with an outside diameter of 130mm and an inside diameter of 120mm would satisfy the design requirements. It would weigh around 150kg and so would be easy enough to handle with the test facility equipment, and the natural frequency would be 3.58Hz, which is sufficiently far from the excitation frequency of 1.01Hz. The study was also performed for a 20m tube, but at this length steel is no longer feasible because the natural frequency of the beam is too close to that of the blade. For this reason a carbon fibre reinforced plastic tube was chosen. Assuming a CFRP lay-up with a Young's modulus of 100GPa and a density of 1600kg/m^3, a design with an outside diameter of 500mm and an inside diameter of 480mm would satisfy the requirements. In practice, this would be very expensive to manufacture so a 10m tube would realistically be towards the limit of what is feasible.

It has already been shown that a 10m tube is not sufficient to prevent excessive edgewise loads at the 26.4m station on an untwisted blade. If blade twist is accounted for then cycling the blade at a single frequency has been found to be impossible at all points along the blade; interaction between the two modes means it is impossible to control the load magnitude of the flapwise and edgewise directions independently. Finally, the blade which has been studied here is rather small by modern standards, so the challenges involved in testing a larger blade would be even greater.

Several test houses around the world [113, 114] employ near resonant tests, in which the edgewise frequency is reduced by adding mass. The objective of this technique is to reduce the energy requirements for forced displacement dual axis blade testing somewhat whilst still allowing the blade to be cycled in the edgewise direction at the flapwise natural frequency. Although it has some advantages over conventional forced displacement testing, it is still only possible to achieve a linear bending moment distribution in the edgewise direction and its use on large blades would pose a challenge because of the high cylinder strokes required.

5.4 Summary and conclusions

The development of a 3-D beam element model that allows transient analyses of full scale static and fatigue tests of wind turbine blades to be performed has been described. The model accounts for forces due to the excitation equipment mounted on the blade, gravity and air resistance. This last is calculated using the drag equation with modifications to the drag coefficient to account for unsteady effects resulting from the blade re-entering its own wake. Visualisation tools have also been developed to allow the user to check that the results in a more intuitive manner.

The model has been validated against test data from a full scale fatigue test and it performs well. It has also been validated against a scale model. This model is to be used in the future for further investigation of the unsteady aerodynamic effects.

The model has been used to produce load time histories for several blade cross sections for single axis and dual axis tests. These load time histories have been used to perform fatigue analysis on the blade cross sections, and it was found that dual axis testing is consistently more rigorous than single axis testing. The effect of adding the test safety factors and pitching the blade on the test stand was also studied. It was shown that dual axis testing allows faster, more representative tests to be performed than single axis testing, so dual axis testing is the recommended method of fatigue testing.

A possible alternative to dual axis testing in which the edgewise natural frequency was altered by adding masses that were isolated to some extent from the flapwise direction was investigated further. The work that was performed in the previous chapter showed that the method could possibly improve the edgewise bending moment distribution, and results presented in chapter 3 showed that if the edgewise and flapwise loads are cycled at the same frequency with a set phase angle between them then a better damage distribution can be obtained. The method was found to pose problems that are not apparent when the flapwise and edgewise directions are analysed independently as they are in the 1-D optimisation model. These problems mean that the method is not worth pursuing.

The main conclusions that can be drawn from the work presented in this chapter are that dual axis testing can be successfully modeled and that it definitely represents an improvement over single axis testing.

6 Alternative Fatigue Analysis Methodology

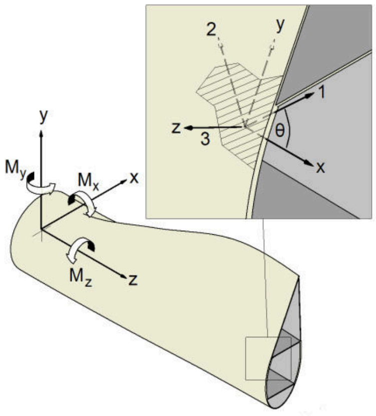

6.1 Introduction

The fatigue analysis methodology based on the Palmgren-Miner [53, 54] linear damage assumption that is suggested in the design standards [10, 11] has several drawbacks. Nijssen [41] performed a thorough review on the effects of several variables, including the load order, test frequency, creep and temperature. He concluded that if the stress amplitude was not so high that failure occurred due to temperature rise from hysteretic energy dissipation then the effect of increasing frequency was to increase the number of cycles to failure [41]. He also suggested that rather than having the constant life diagram converge at the ultimate tensile stress and ultimate compressive stress, the creep strength should be used [41]. Sutherland found that the WISPER wind turbine spectrum was much more damaging than its truncated counterpart WISPERX in which all of the cycles below a certain amplitude are removed [98]. This suggests that creep or 'time at load' effects could well be reducing the lifetime.

The effect of load order is well documented; references [41, 45] provide extensive details of research related to this phenomenon. If large loads occur early on in a metal's life then the material will work harden, leading to an increase in the life for low loads later on [49]. In composites the reverse is true; if high loads occur early on then they are more damaging than if they occur at the end of the life [58].

Fertig and Kenik [71] proposed an alternative fatigue analysis methodology based on the kinetic theory of fracture. Although the kinetic theory of fracture had been applied to composites before by Mishnaevsky and Brøndsted [84], the approach treated the composite as a whole, whereas Fertig and Kenik used multi-continuum theory to obtain the volume averaged stress in the matrix [71]. Fatigue of composites occurs predominantly due to the development of matrix cracks, so this approach is sensible. The kinetic theory of fracture approach proposed by Fertig and Kenik [71] addresses several of the issues with composite fatigue analysis that the standard approach neglects. Temperature, frequency and 'time at load' effects are accounted for, as are multi-axial stress states and load order effects.

6.2 Method

The fatigue analysis method developed by Fertig and Kenik [70] has been implemented in the Helius:Fatigue plug-in [115] for the FE-Safe/Composites software [101]. The method used in this software has been further developed in the present work to allow its use for wind turbine blade fatigue analysis.

The design standards dictate that 10 minute simulations of wind turbine behaviour are used at a range of wind speeds [10, 11] as well as other fatigue simulations of, for instance, start up and shut down or fault load cases. For a class 1A turbine this would require a minimum of 13 operational load cases and 6 start-up/ shut-down load cases. These long simulations are potentially possible in the full shell element models that would typically be used in the software developed in [70], but they would be very time consuming and a progressive failure analysis would not be feasible. For this reason a beam stress analysis was used in the present work to reduce the computational effort and a model was developed which allows block loading to be applied, which is not currently possible in Helius:Fatigue. The modeling of temperature rise due to hysteretic heating was improved to allow its use for long simulations and a correction for the behavior at low stresses was implemented also.

Time histories of the normal and shear flows at any given point on a blade cross section are calculated using thin walled beam theory. Classical laminate theory is then used to convert these flows into a composite stress in the material coordinate system.

The multi-continuum theory originally proposed by Hansen and Garnisch [116] is then used to break the composite stress down into a volume averaged stress state in the fibre and matrix.

The method used by Fertig and Kenik [71] which is based on the kinetic theory of fracture was then used to perform a fatigue analysis. The kinetic theory of fracture was originally developed by Zhurkov and co-workers [73]. A small modification to the theory was required in order to facilitate its application to wind turbine blade analysis.

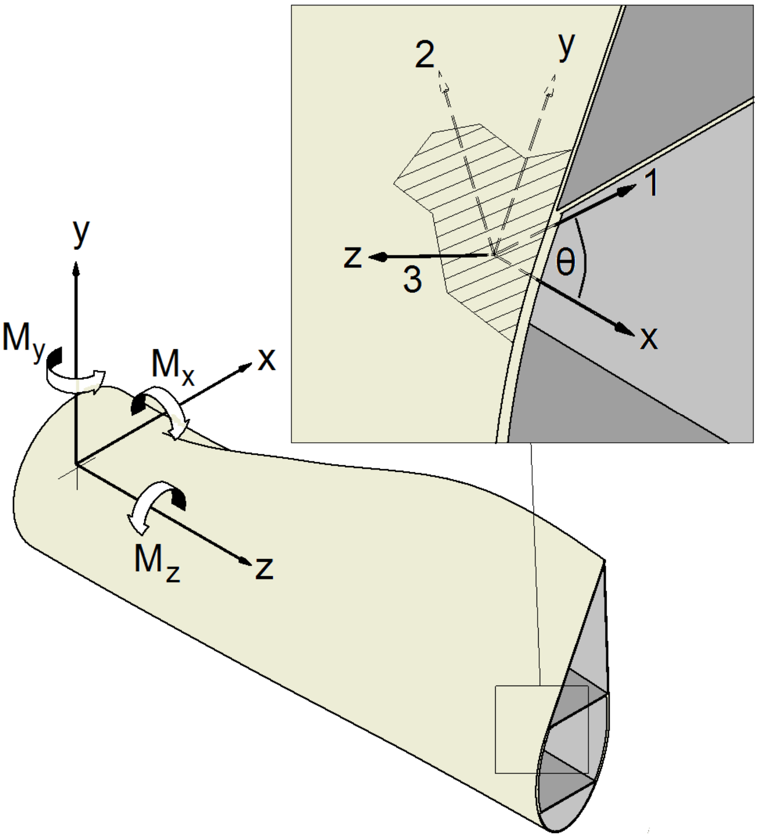

Figure 6.1 – Blade, laminate and ply coordinate systems

The process of performing a fatigue analysis on a blade cross section begins at the ply level. The laminate properties are obtained using classical laminate theory and then the blade properties are obtained using thin walled beam theory. The coordinate systems for the blade, laminate (x,y,z) and ply (1,2,3) are defined in Figure 6.1.

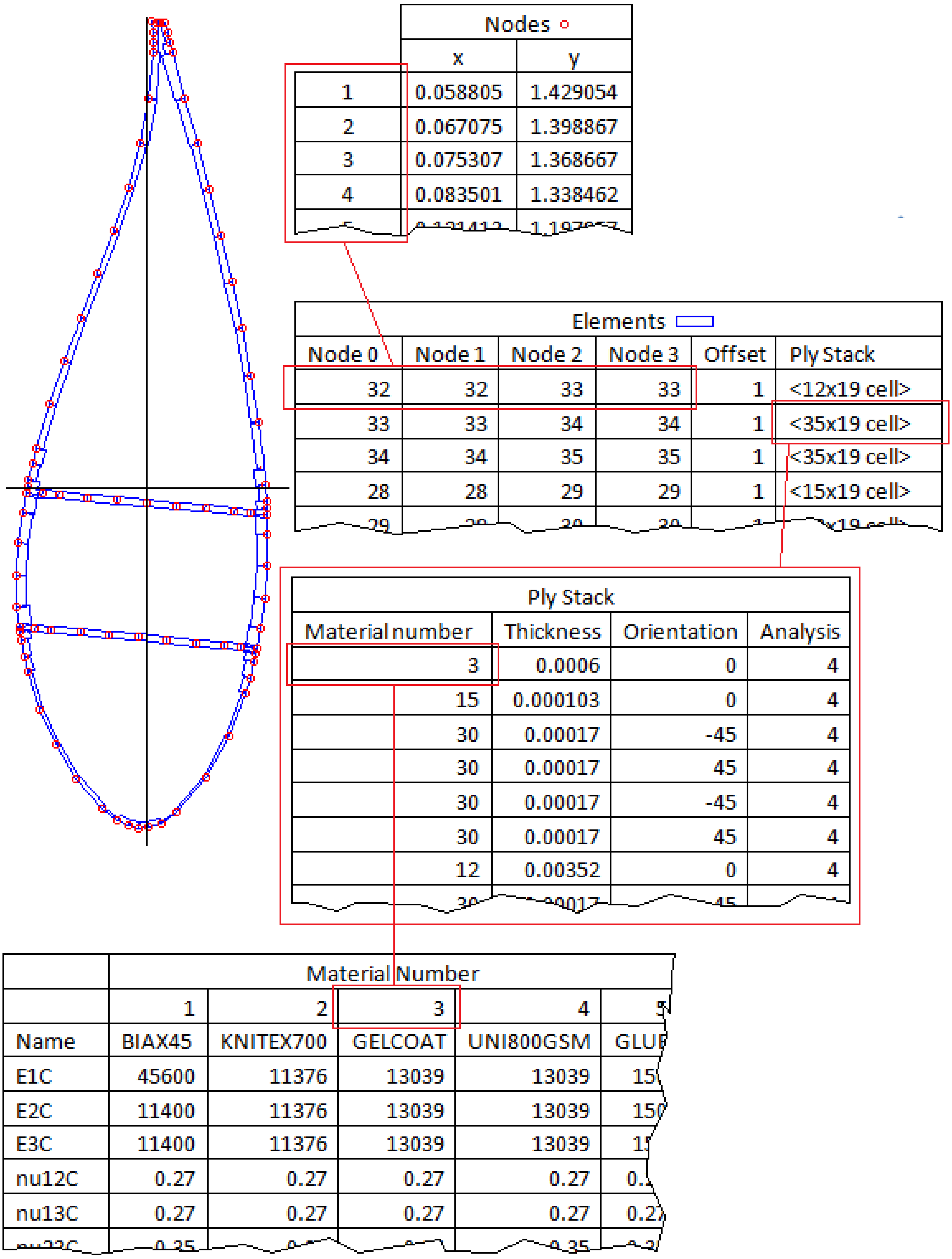

Nodes ○		
	x	y
1	0.058805	1.429054
2	0.067075	1.398867
3	0.075307	1.368667
4	0.083501	1.338462

Elements ▭					
Node 0	Node 1	Node 2	Node 3	Offset	Ply Stack
32	32	33	33	1	<12x19 cell>
33	33	34	34	1	<35x19 cell>
34	34	35	35	1	<35x19 cell>
28	28	29	29	1	<15x19 cell>

Ply Stack			
Material number	Thickness	Orientation	Analysis
3	0.0006	0	4
15	0.000103	0	4
30	0.00017	-45	4
30	0.00017	45	4
30	0.00017	-45	4
30	0.00017	45	4
12	0.00352	0	4

	Material Number				
	1	2	3	4	5
Name	BIAX45	KNITEX700	GELCOAT	UNI800GSM	GLU
E1C	45600	11376	13039	13039	15
E2C	11400	11376	13039	13039	15
E3C	11400	11376	13039	13039	1
nu12C	0.27	0.27	0.27	0.27	0.
nu13C	0.27	0.27	0.27	0.27	0.2

Figure 6.2 - Blade definition hierarchy

The structure of the blade cross-section must be fully defined. As the blade is treated as a thin-walled beam, the location of the walls must be given. A series of points representing the inner surface, outer surface or middle of the walls are defined; these will be referred to hereafter as ‘nodes’. The properties of the blade wall between any two nodes are contained in ‘elements’. These elements are defined by the nodes that they link, the adjacent nodes to those which they link (this allows a considerably more accurate description of the shape of the element to be developed than if just the endpoints are known), whether the nodes describe the midpoint or a surface of the element, and the ply stack. It should be noted that although the terms ‘nodes’ and ‘elements’ are used, the cross sectional properties are not calculated using a finite element approach, and the terminology is borrowed simply because it is a convenient way of defining the blade cross section. The ply stack is described by a table containing the ply thickness, the ply orientation angle, a number identifying which material the ply is made out of, and a number that specifies whether the ply should be analysed or not. This hierarchy is illustrated in Figure 6.2.

The following sections detail how the analysis approach used in the present work allows fatigue failure due to the rupture of atomic bonds at a microscopic level to be calculated from loads that are based on the behaviour of the whole wind turbine, a structure which is typically over 100m tall.

6.2.1 Laminate property calculation

Before a beam stress calculation can be performed, it is first necessary to calculate the cross-sectional properties of the blade at the point of interest. The first step in this process is to calculate equivalent material properties for each element. In the present work this has been achieved by using classical laminate theory.

Every material used in the blade cross-section must be defined. The amount of information required about a material depends on the level of analysis; if the stress in a ply is the quantity of interest then only information about the stiffness of the composite is necessary. If the stress in the matrix must be found then stiffness information about the composite, matrix and fibre must be provided and if a fatigue analysis is to be performed then still further information must be given.

All materials used in the blade are assumed to be transversely isotropic and planar. The compliance matrix for an orthotropic material is given in equation (6.1) [117].

$$[\boldsymbol{S}] = \begin{bmatrix} \frac{1}{E_1} & -\frac{\upsilon_{21}}{E_2} & -\frac{\upsilon_{31}}{E_3} & 0 & 0 & 0 \\ -\frac{\upsilon_{12}}{E_1} & \frac{1}{E_2} & -\frac{\upsilon_{32}}{E_3} & 0 & 0 & 0 \\ -\frac{\upsilon_{13}}{E_1} & -\frac{\upsilon_{23}}{E_2} & \frac{1}{E_3} & 0 & 0 & 0 \\ 0 & 0 & 0 & \frac{1}{G_{23}} & 0 & 0 \\ 0 & 0 & 0 & 0 & \frac{1}{G_{13}} & 0 \\ 0 & 0 & 0 & 0 & 0 & \frac{1}{G_{12}} \end{bmatrix} \tag{6.1}$$

If transverse isotropy is assumed then several simplifying assumptions can be made [117]. These are summarised in equation (6.2). Also, if plane stress is assumed then the compliance matrix can be simplified to a 3 x 3 matrix.

$$E_2 = E_3$$

$$G_{12} = G_{13}, G_{23} = \frac{E_2}{2(1+\nu_{23})} \tag{6.2}$$

$$\nu_{13} = \nu_{12}$$

In a progressive failure analysis, it may be necessary to degrade the stiffness of a ply after the material has failed. Fertig and Kenik distinguished between a longitudinal failure mode and a transverse failure mode [71], and in the present work these two failure mechanisms are represented by using the rule of mixtures to calculate the composite stiffness properties after a failure (if an anisotropic failure is being modelled) or simply reducing all of the stiffness properties to a much lower value if the failure is considered to be isotropic. Equation (6.3) shows how the reduced stiffness properties are calculated in the event of a failure [118]. The subscripts F and M refer to properties of the fibre and matrix respectively and ϕ_F is the fibre volume fraction. For a transverse failure, the matrix properties are reduced by a user specified proportion. Similarly, in the event of a longitudinal failure the fibre properties are reduced.

$$E_{1C} = \phi_F E_{1F} + (1-\phi_F)E_{1M}$$

$$E_{2C} = \frac{E_{2F}E_{2M}}{E_{2M}\phi_F + (1-\phi_F)E_{2F}} \tag{6.3}$$

$$G_{12C} = \frac{\phi_F}{G_{12F}} + \frac{(1-\phi_F)}{G_{12M}}$$

$$\upsilon_{12C} = \phi_F \upsilon_{12F} + (1-\phi_F)\upsilon_{12M}$$

In order to increase the speed at which the code can run, the compliance matrices for every material in the intact, longitudinal failure and transverse failure state are calculated before the analysis begins. For each ply, they are rotated from the ply coordinate system $[\boldsymbol{S}]$ into the laminate coordinate system $[\bar{\boldsymbol{S}}]$ using equations (6.4) and (6.5) [117].

$$[\mathbf{T}] = \begin{bmatrix} cos^2\theta & sin^2\theta & 2sin\theta cos\theta \\ sin^2\theta & cos^2\theta & -2sin\theta cos\theta \\ -sin\theta cos\theta & sin\theta cos\theta & cos^2\theta - sin^2\theta \end{bmatrix} \tag{6.4}$$

$$[\bar{\boldsymbol{S}}] = [\boldsymbol{T}][\boldsymbol{S}][\boldsymbol{T}]^{\boldsymbol{T}} \tag{6.5}$$

The overall properties of the laminate can then be calculated using classical laminate theory [117]. The laminate load-strain response can be found using equation (6.6) in which $\boldsymbol{N}$ and $\boldsymbol{M}$ are the force and moment vectors, $[\boldsymbol{A}]$, $[\boldsymbol{B}]$ and $[\boldsymbol{D}]$ are the laminate extensional, coupling and bending stiffness matrices and $\boldsymbol{\varepsilon_0}$ and $\boldsymbol{k}$ are the laminate mid-plane strains and curvatures.

$$\begin{Bmatrix} \boldsymbol{N} \\ \boldsymbol{M} \end{Bmatrix} = \begin{bmatrix} \boldsymbol{A} & \boldsymbol{B} \\ \boldsymbol{B} & \boldsymbol{D} \end{bmatrix} \begin{Bmatrix} \boldsymbol{\varepsilon_0} \\ \boldsymbol{k} \end{Bmatrix} \tag{6.6}$$

The $[\boldsymbol{A}]$, $[\boldsymbol{B}]$ and $[\boldsymbol{D}]$ matrices are calculated by integrating through the laminate as shown in equation (6.7) in which $\bar{C}_{ij}$ are the components of the ply stiffness matrix (the inverse of the compliance matrix which was calculated using equation (6.1)), k is the layer number (starting from the outermost ply) and z_k is the distance from the laminate mid-plane to the top of the k^{th} layer, as shown in Figure 6.3 [117].

$$\begin{aligned} A_{ij} &= \sum_{k=1}^{N} \left(\bar{C}_{ij}\right)_k (z_k - z_{k-1}) \\ B_{ij} &= \frac{1}{2}\sum_{k=1}^{N} \left(\bar{C}_{ij}\right)_k \left(z_k^2 - z_{k-1}^2\right) \\ D_{ij} &= \frac{1}{3}\sum_{k=1}^{N} \left(\bar{C}_{ij}\right)_k \left(z_k^3 - z_{k-1}^3\right) \end{aligned} \tag{6.7}$$

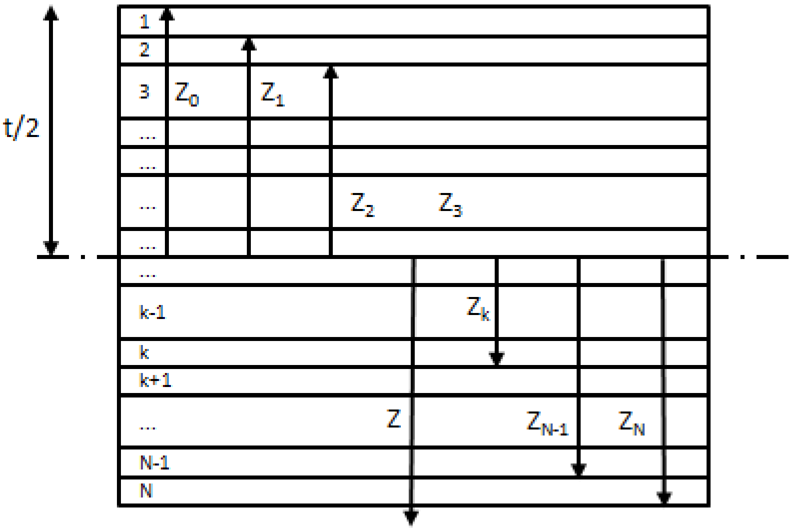

Figure 6.3 - Classical laminate theory notation

The equivalent Young's modulus, $\hat{E}_x$, and shear modulus, $\hat{G}_{xy}$, for the laminate are calculated using equation (6.8) in which A^*_{ij} are components of the laminate compliance matrix, which is found by inverting the matrix in equation (6.6) [117].

$$\begin{aligned} \hat{E}_x &= \frac{1}{h}\frac{1}{A^*_{11}} \\ \hat{G}_{xy} &= \frac{1}{h}\frac{1}{A^*_{33}} \end{aligned} \tag{6.8}$$

If a ply fails during an analysis, the laminate properties are recalculated using the appropriate stiffness matrix for the failed layer. This ensures that stress redistribution is properly accounted for.

6.2.2 Beam cross sectional properties calculation

With the equivalent stiffness properties of the blade elements known it is possible to calculate the overall beam properties at a given cross-section on the blade.

The first step in this process is to find the neutral axis of the blade, as all other calculations rely on the origin of the blade being taken to be the neutral axis of the blade. The process begins by finding the centroid of each element around the blade cross section. This is calculated using the coordinates of the ends of the element, its thickness and whether the end nodes define the element mid-plane or its top or bottom.

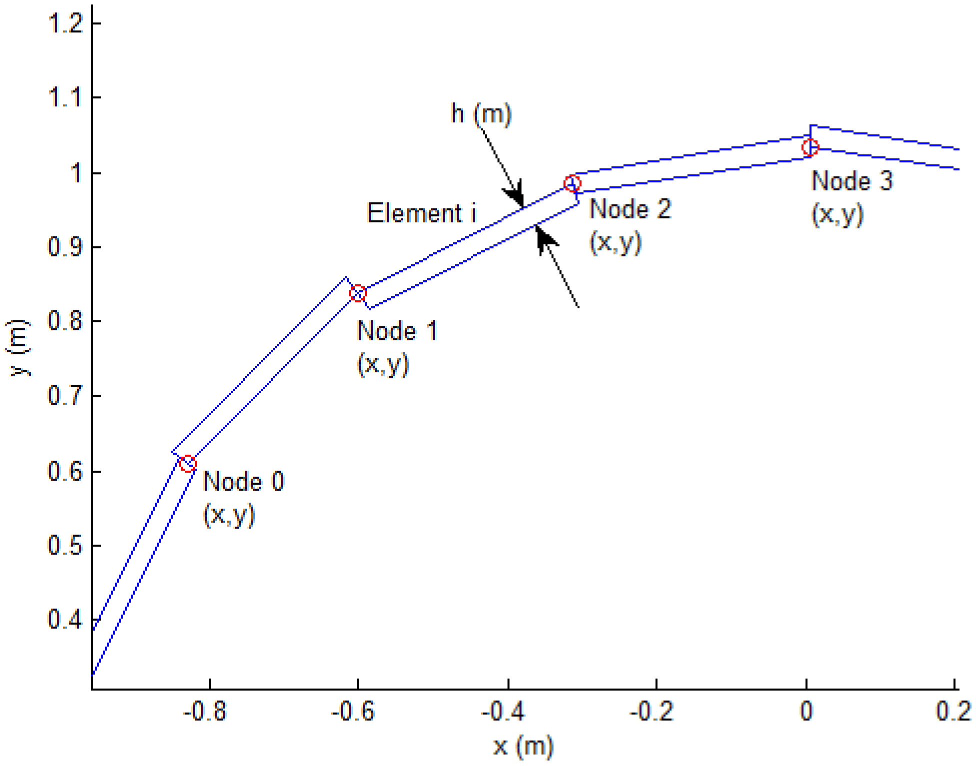

Figure 6.4 - Element detail

Figure 6.4 shows a detail of an element, including the nodes which define it. In element i the nodes define the outer surface, while in the previous and next element the nodes define the inner surface and mid-plane of the element respectively.

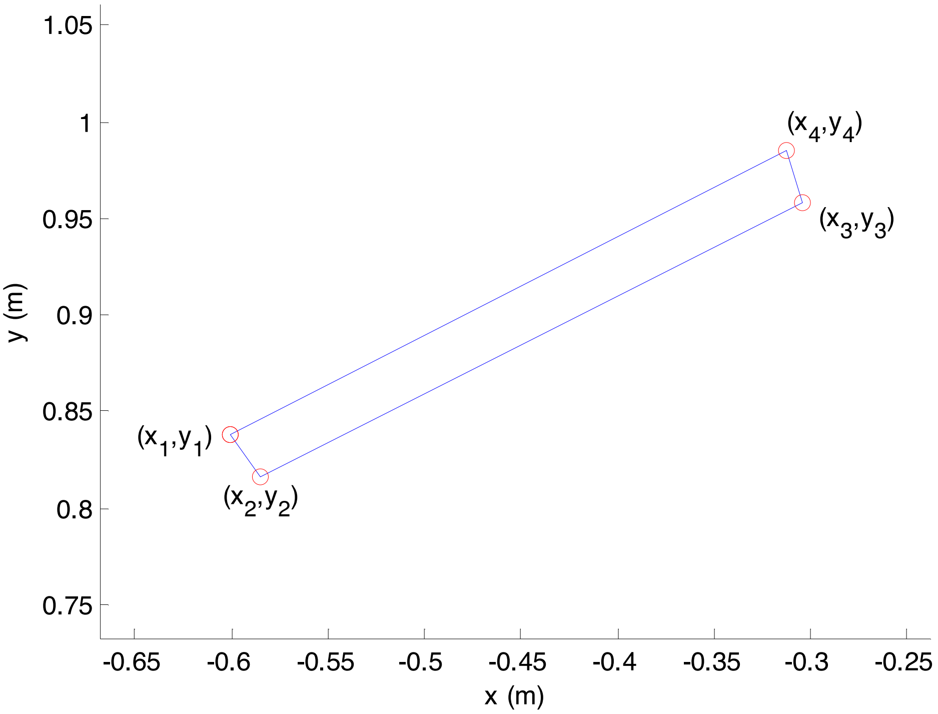

Figure 6.5 - Element corner coordinates

In order to minimise the error caused by increasing the wall thickness, the element shape is trapezoidal rather than rectangular. The coordinates of the corners of each element are calculated by taking the normal to a tangent drawn to the blade surface at the element end. The angle of the tangent is calculated from the coordinates of the adjacent nodes. Using simple trigonometry it is possible to calculate the coordinates of the corners of each trapezoidal element as shown in Figure 6.5. The area and centroid are found using a form of the 'Surveyor's formula' [119]. By following a closed anti-clockwise path around the trapezium vertices, it is possible to use equation (6.9) to calculate the area and equation (6.10) and (6.11) to calculate the x and y coordinates of the centroid of each element from the coordinates of the n vertices.

$$A = \frac{1}{2} \sum_{i=1}^{i=n-1} (x_i y_{i+1} - x_{i+1} y_i) \tag{6.9}$$

$$C_x = \frac{1}{6A} \sum_{i=1}^{i=n-1} (x_i + x_{i+1})(x_i y_{i+1} - x_{i+1} y_i) \tag{6.10}$$

$$C_y = \frac{1}{6A} \sum_{i=1}^{i=n-1} (y_i + y_{i+1})(x_i y_{i+1} - x_{i+1} y_i) \tag{6.11}$$

It is then possible to find the x-y coordinates of the centre of mass and the neutral axis of the whole blade cross section using equations (6.12), (6.13), (6.14) and (6.15) respectively. In these equations, n is the number of elements, $\hat{\rho}_i$ is the equivalent density of the i^{th} element (calculated by integrating through the ply stack) and $\hat{E}_i$ is the equivalent extensional modulus of the laminate found using the process described in section 6.2.1.

$$C_{mx} = \frac{\sum_{i=1}^{i=n} \hat{\rho}_i A_i C_{ix}}{\sum_{i=1}^{i=n} \hat{\rho}_i A_i} \tag{6.12}$$

$$C_{my} = \frac{\sum_{i=1}^{i=n} \hat{\rho}_i A_i C_{iy}}{\sum_{i=1}^{i=n} \hat{\rho}_i A_i} \tag{6.13}$$

$$C_{ex} = \frac{\sum_{i=1}^{i=n} \hat{E}_i A_i C_{ix}}{\sum_{i=1}^{i=n} \hat{E}_i A_i} \tag{6.14}$$

$$C_{ey} = \frac{\sum_{i=1}^{i=n} \hat{E}_i A_i C_{iy}}{\sum_{i=1}^{i=n} \hat{E}_i A_i} \tag{6.15}$$

The nodes describing the cross section are then translated so that the neutral axis is at the origin. The calculation of the first moments of area of each element (necessary for the calculation of shear flow) is trivial, as is the calculation of the extensional stiffness. The bending stiffness of each element can be easily calculated using equations (6.16), (6.17) and (6.18) [119]. As in the calculation of the element areas, the calculation assumes n vertices ordered in an anti-clockwise manner, with $i = 1$ equal to $i = n$.

$$EI_{xx} = \frac{\hat{E}_x}{12} \sum_{i=1}^{i=n-1} \left(y_i^2 + y_i y_{i+1} + y_{i+1}^2\right)\left(x_i y_{i+1} - x_{i+1} y_i\right) \tag{6.16}$$

$$EI_{yy} = \frac{\hat{E}_x}{12} \sum_{i=1}^{i=n-1} \left(x_i^2 + x_i x_{i+1} + x_{i+1}^2\right)\left(x_i y_{i+1} - x_{i+1} y_i\right) \tag{6.17}$$

$$EI_{xy} = \frac{\hat{E}_x}{24} \sum_{i=1}^{i=n-1} \left(x_i y_{i+1} + 2x_i y_i + 2x_{i+1} y_{i+1} + x_{i+1} y_i\right)\left(x_i y_{i+1} - x_{i+1} y_i\right) \tag{6.18}$$

These results are stored for every element within the blade cross-section, and are used in the calculation of the normal and shear flows. Although this approach is more computationally intensive than the thin-walled bending stiffness calculation in, for example, [100], it yields more accurate section properties than would be obtained by considering the blade elements as lines.

6.2.3 Calculation of normal and shear flows

The calculation of the normal and shear flows within the blade cross-section was performed using the thin-walled beam theory described in [100] and [120]. The normal flow can be calculated at a point in the cross section using equation (6.19) [100]. The value of $\hat{E}_i$ for an element is recalculated whenever a ply fails within it using the method described in section 6.2.1.

$$N_{zi} = \hat{E}_i t_i \left[\frac{F_z}{EA} + \frac{1}{k_{xy}}\left[\left(-M_y \sum_{i=1}^{i=n} \hat{E}_i I_{xxi} + M_x \sum_{i=1}^{i=n} \hat{E}_i I_{xyi}\right) x_i + \left(M_x \sum_{i=1}^{i=n} \hat{E}_i I_{yyi} + M_y \sum_{i=1}^{i=n} E_i I_{xyi}\right) y_i\right]\right]$$

where (6.19)

$$EA = \sum_{i=1}^{n} \hat{E}_i A_i$$

$$k_{xy} = \sum_{i=1}^{n} \hat{E}_i I_{xxi} \sum_{i=1}^{n} \hat{E}_i I_{yyi} - \left(\sum_{i=1}^{n} \hat{E}_i I_{xyi}\right)^2$$

The shear flow calculation is more complex. It has components from the shear forces acting on the blade and the torsional moment acting on the section. The full derivation of the formulae for the shear flow is very involved, and will not be presented here. The interested reader can refer to any text on the analysis of aerospace structures, such as [100, 121]. The method has been applied to composite wind turbine blades by Fernandez de Silva [120]. In the present work the user of the developed computer program has the option to neglect the shear flow for comparison purposes.

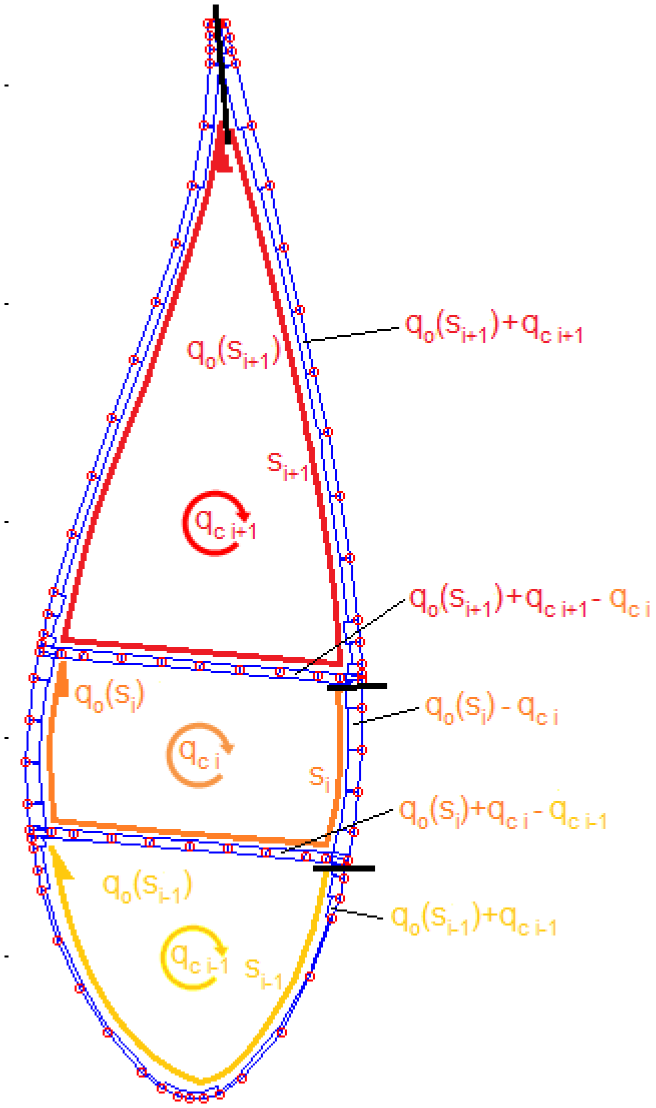

Figure 6.6 - Shear flow components due to transverse forces

The shear flow due to transverse forces is composed of an open section component and a closed section component, as shown in Figure 6.6. As wind turbine blades are closed sections, there are no free edges at which it is known that the shear flow is zero, so each cell of the blade must be 'cut' to make it into an open section (the thick black lines in Figure 6.6). The open section shear flow is then evaluated, and a closing shear flow is then calculated for each cell.

$$
\begin{aligned}
q_o(s) = \frac{1}{k_{xy}} \Bigg[& F_y \left[\sum_{i=1}^{n^*} \hat{E}_i M_{yyi} \sum_{i=1}^{n} \hat{E}_i I_{xyi} - \sum_{i=1}^{n^*} \hat{E}_i M_{xxi} \sum_{i=1}^{n} \hat{E}_i I_{yyi} \right] \\
& - F_x \left[\sum_{i=1}^{n^*} \hat{E}_i M_{yyi} \sum_{i=1}^{n} \hat{E}_i I_{xxi} - \sum_{i=1}^{n^*} \hat{E}_i M_{xxi} \sum_{i=1}^{n} \hat{E}_i I_{xyi} \right] \Bigg]
\end{aligned}
\tag{6.20}
$$

The blade discretisation scheme used previously is employed. The first and second moments of area are known for every element from the calculation of the blade cross-sectional properties. The curvilinear variable s is used to describe the distance from the cut made in each cell as shown in Figure 6.6. The open section shear flow q_o after n^* elements from the cut along s can be calculated from equation (6.20) [120].

The closing shear flow can then be calculated for each cell. The requirement for a single value displacement for the whole cross section of total length S along the variable s can be defined as shown in equation (6.21) [120].

$$\int_0^S \gamma_{zs} ds = 0 \tag{6.21}$$

For an anisotropic cross-section made from laminates that can be considered symmetric, this can be represented in terms of shear flow as shown in equation (6.22) [120].

$$\int_0^S \frac{q(s)}{G_{zs}(s)t(s)} ds = 0 \tag{6.22}$$

For a multi-cell discretised cross-section such as that shown in Figure 6.6, equation (6.22) can be evaluated as shown in equation (6.23). The summations over $n_i n_{i-1}$ and $n_i n_{i+1}$ refers to elements that are common to cell i and $i-1$ and those that are common to cell i and $i+1$ respectively.

$$q_{ci} \sum_{n_i} \frac{l_j}{\hat{G}_{zsj} t_j} - q_{ci-1} \sum_{n_i n_{i-1}} \frac{l_j}{\hat{G}_{zsj} t_j} - q_{ci+1} \sum_{n_i n_{i+1}} \frac{l_j}{\hat{G}_{zsj} t_j} = -\sum_{n_j} \frac{q_{oj} l_j}{\hat{G}_{zsj} t_j} \tag{6.23}$$

By using a system of simultaneous equations it is possible to solve for the unknown closing shear flow q_c in each cell.

The shear flow due to torsion can then be calculated in each cell by assuming uniform torsion along the blade. The requirement for a single value displacement for the whole cross section of total length S along the variable s can be defined as shown in equation (6.24), in which θ is the angle of twist and Ω is the area enclosed by the median line of the section.

$$\int_0^S \gamma_{zs} ds - 2\Omega\theta = 0 \tag{6.24}$$

For an anisotropic cross-section made from laminates that can be considered symmetric, this can be represented in terms of shear flow due to torsion as shown in equation (6.25) [120].

$$\int_0^S \frac{q_t(s)}{G_{zs}(s)t(s)} ds = 2\Omega\theta \tag{6.25}$$

For a multi-cell discretised cross-section such as that shown in Figure 6.6, equation (6.25) can be evaluated as shown in equation (6.26). Again, the summations over $n_i n_{i-1}$ and $n_i n_{i+1}$ refers to elements that are common to cell i and $i-1$ and those that are common to cell i and $i+1$ respectively.

$$q_{ti} \sum_{n_i} \frac{l_j}{\hat{G}_{zsj} t_j} - q_{ti-1} \sum_{n_i n_{i-1}} \frac{l_j}{\hat{G}_{zsj} t_j} - q_{ti+1} \sum_{n_i n_{i+1}} \frac{l_j}{\hat{G}_{zsj} t_j} = 2\Omega_{\mathrm{i}}\theta \tag{6.26}$$

There are now as many equations as there are cells in the cross section, but there is an extra unknown, θ, the twist angle. A final equation is needed in order to solve for q_t in each cell. The equilibrium of moments can be used to form equation (6.27), meaning there are now n+1 simultaneous equations, where n is the number of cells in the blade cross-section [120].

$$M_z = 2(\Omega_1 q_{t1} + \Omega_2 q_{t2} + \cdots \Omega_i q_{ti} + \cdots \Omega_n q_{tn}) \tag{6.27}$$

The shear flow is found for unit loads in the x and y directions and a unit torsional moment. The distribution of shear flow around the blade elements due to these unit loads is stored, and the shear flow due to arbitrary loading can then be found by scaling and superposition.

The location of the shear centre can be easily found by calculating the moment about the origin caused by the shear flows within the blade wall using equation (6.28). By applying unit loads in the x and y direction individually the shear centre can be found using equation (6.29) [100].

$$M_0 = \sum_{i=1}^{n} q_i (x_{1i} y_{2i} - x_{2i} y_{1i}) \tag{6.28}$$

$$\begin{aligned} SC_y &= 0 - M_{0x} \\ SC_x &= 0 + M_{0y} \end{aligned} \tag{6.29}$$

The shear flow distribution relies on the equivalent shear modulus of each element being known, so it is recalculated whenever a ply fails.

In the present work, time histories of the loads M_x, M_y, M_z, F_x, F_y and F_z (see Figure 6.1) were calculated by LM Wind Power using the wind turbine simulation tool FLEX 5. However, these loads could be obtained from any other wind turbine simulation tool.

6.2.4 Calculation of composite stress

The normal and shear flow in a given blade element are used to calculate the stress state in every ply within that element. Although laminates within the blade cross-section will be bent, this effect has been neglected in the present work to simplify the stress calculations. Ignoring the bending moment means that only the normal and shear flows are required to calculate the mid-plane strains as shown in equation (6.30). The extensional compliance matrix $[\boldsymbol{A}^*]$ is simply the inverse of the extensional stiffness matrix found for each laminate using equation (6.7). The normal flow, N_x, is calculated using equation (6.9) (the change in notation is because of the move from the blade to the laminate coordinate system) and the shear flow, q_{xy}, is calculated using equations (6.20) to (6.27). The assumption that plane sections remain plane after bending means that N_y is assumed to be 0. Classical laminate theory as described by Kollar and Springer is used to calculate the stress state in each ply [117].

$$\begin{Bmatrix} \varepsilon_x^0 \\ \varepsilon_y^0 \\ \gamma_{xy}^0 \end{Bmatrix} = [\boldsymbol{A}^*] \begin{Bmatrix} N_x \\ N_y \\ q_{xy} \end{Bmatrix} \tag{6.30}$$

The plane stress in the laminate coordinate system for an individual ply can then be calculated using equation (6.31). The components of $\bar{C}$ for ply k are found by inverting the plane stress form of the compliance matrix shown in equation (6.1).

$$\begin{Bmatrix} \sigma_{cx} \\ \sigma_{cy} \\ \tau_{cxy} \end{Bmatrix} = \begin{bmatrix} \bar{C}_{11}^{k} & \bar{C}_{12}^{k} & \bar{C}_{16}^{k} \\ \bar{C}_{21}^{k} & \bar{C}_{22}^{k} & \bar{C}_{26}^{k} \\ \bar{C}_{61}^{k} & \bar{C}_{62}^{k} & \bar{C}_{66}^{k} \end{bmatrix} \begin{Bmatrix} \varepsilon_{x}^{0} \\ \varepsilon_{y}^{0} \\ \gamma_{xy}^{0} \end{Bmatrix} \tag{6.31}$$

This stress state can then be rotated into the ply coordinate system using equation (6.32).

$$\begin{Bmatrix} \sigma_{c1} \\ \sigma_{c2} \\ \tau_{c12} \end{Bmatrix} = [\boldsymbol{T}]_{\boldsymbol{k}}^{\boldsymbol{-1}} \begin{Bmatrix} \sigma_{cx} \\ \sigma_{cy} \\ \tau_{cxy} \end{Bmatrix} \tag{6.32}$$

This process allows the stress in any ply at any point in the blade cross-section to be found from the normal flow and shear flow at that point, which in turn can be calculated from the loads applied to the section. Time histories of σ_1, σ_2, and τ_{12} in every ply of every element can be obtained from section loads. These composite stress states can then be broken down into a stress in the matrix and a stress in the fibre using multi-continuum theory.

6.2.5 Calculation of matrix stress using multi-continuum theory

The method used in the Helius:Fatigue plug-in developed by Firehole Composites has been extended to facilitate its use for wind turbine blade analysis. A high level representation of the process is shown in Figure 6.7 [122].

A finite element model with reference loads is used to find the composite strains and stresses due to these loads in each layer of each element. Multi-continuum theory is then used to break these stresses down into an average fibre stress and an average matrix stress in each element. A time history of the scaling factor for each reference load is then used to calculate time histories of the matrix stress using superposition. The material longitudinal and transverse axis fatigue properties are then used to calculate the amount of damage caused by the load history. There are several aspects of the process used in Helius:Fatigue that make it unsuitable for wind turbine blade analysis in its current implementation. Some of these issues have been addressed in the present work, and where the approach used differs to that used in Helius:Fatigue it will be highlighted.

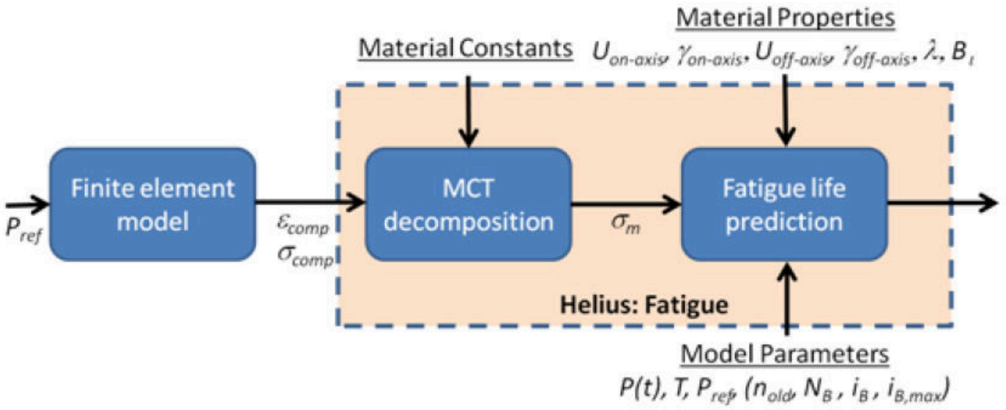

Figure 6.7 - Schematic showing the process used to predict composite fatigue failure in Helius:Fatigue [122]

Clearly, the first difference is that in the present work the composite stresses and strains are found using beam theory rather than the finite element method. However, this is not a requirement for wind turbine blade analysis; it simply speeds the process up at the expense of a less realistic model.

The multi-continuum theory (hereafter MCT) decomposition process is performed exactly as it is in Helius:Fatigue. For this reason, the complete derivation of the equations developed by Hansen and Garnich [116, 123] is not shown. Again, the process used to obtain the matrix and fibre elastic properties from the properties of the composite is described elsewhere by Mayes and Hansen [124, 125] and will not be described in depth here.

Multi-continuum theory was originally developed by Hansen and Garnich in 1995 [116]. They later extended the theory to account for thermal stresses [123] and developed an optimisation routine to obtain the elastic properties of the constituents (matrix and fibres) from those of the composite [125].

The basis of the theory is that failure of composites is dependent on the processes occurring in the individual constituents of the composite rather than those which can be obtained by treating the composite as a homogeneous entity. For instance, under uni-axial tension applied along the fibre axis failure initiates when the matrix cracks and loses its ability to share the load between the fibres. Ultimate failure then occurs when the fibres break.

The theory is micromechanics based, insofar as the initial calculation of the matrix and fibre stiffness properties for a given material are performed using a micromechanical model. The following assumptions are made [124]:

- Linear elastic behaviour of the fibres and matrix (nonlinear matrix behavior has been modeled using multi-continuum theory [126] but linear behavior is assumed in the present work).
- Perfect bonding between the fibres and matrix.
- Stress concentrations at the fibre boundaries are accounted for only as an increase in the volume averaged matrix stress.
- The effect of fibre distribution on the composite stiffness and strength is accounted for in the finite element modelling of a representative volume of microstructure.
- The ability to fail one constituent while leaving the other intact results in a piecewise continuous composite stress–strain curve.

Even in materials that are considered to be isotropic and homogeneous the stress distribution is not uniform if viewed on a microscale. It is useful to describe the stress-state by taking a volume average of all of the stresses in a region as shown in equation (6.33) [124].

$$\boldsymbol{\sigma_C} = \frac{1}{V_C}\int_D \boldsymbol{\sigma_C}(\boldsymbol{x})dV \tag{6.33}$$

In a composite with two clearly identifiable constituents (namely the fibre and matrix phases) [124]:

$$\boldsymbol{\sigma_F} = \frac{1}{V_F}\int_{D_F} \boldsymbol{\sigma_F}(\boldsymbol{x})dV \tag{6.34}$$

$$\boldsymbol{\sigma_M} = \frac{1}{V_M}\int_{D_M} \boldsymbol{\sigma_M}(\boldsymbol{x})dV \tag{6.35}$$

where

$$D = D_F \bigcup D_M \tag{6.36}$$

Combining equations (6.33) to (6.36) it is possible to obtain the following expressions for the composite stresses and strains [124], where ϕ_F and ϕ_M are the fibre and matrix volume fractions respectively:

$$\boldsymbol{\sigma_C} = \phi_F \boldsymbol{\sigma_F} + \phi_M \boldsymbol{\sigma_M} \tag{6.37}$$

$$\boldsymbol{\varepsilon_C} = \phi_F \boldsymbol{\varepsilon_F} + \phi_M \boldsymbol{\varepsilon_M} \tag{6.38}$$

The elastic constitutive laws for the composite and its constituents are given by equations (6.39) to (6.41) [124] where the subscript 0 refers to thermally induced strains.

$$\boldsymbol{\sigma_C} = [\boldsymbol{C_C}](\boldsymbol{\varepsilon_C} - \boldsymbol{\varepsilon_{C0}}) \tag{6.39}$$

$$\boldsymbol{\sigma_F} = [\boldsymbol{C_F}](\boldsymbol{\varepsilon_F} - \boldsymbol{\varepsilon_{F0}}) \tag{6.40}$$

$$\boldsymbol{\sigma_M} = [\boldsymbol{C_M}](\boldsymbol{\varepsilon_M} - \boldsymbol{\varepsilon_{M0}}) \tag{6.41}$$

By combining equations (6.37) to (6.41) it is possible to derive fibre and matrix strain fields from equations (6.43) and (6.42).

$$\boldsymbol{\varepsilon_M} = \left[\phi_M[\mathbf{1}] + \phi_F[\boldsymbol{A}]\right]^{-\mathbf{1}} \{\boldsymbol{\varepsilon_C} - \Delta T \boldsymbol{a}\} \tag{6.42}$$

$$\boldsymbol{\varepsilon_F} = \frac{1}{\phi_F}\{\boldsymbol{\varepsilon_C} - \phi_M \boldsymbol{\varepsilon_M}\} \tag{6.43}$$

where

$$[\boldsymbol{A}] = \frac{\phi_M}{\phi_F}\left[[\boldsymbol{C_C}] - [\boldsymbol{C_F}]\right]^{-1}\left[[\boldsymbol{C_C}] - [\boldsymbol{C_M}]\right] \tag{6.44}$$

and

$$\boldsymbol{a} = \left[[\boldsymbol{C_C}] - [\boldsymbol{C_F}]\right]^{-1}\{[\boldsymbol{C_C}]\boldsymbol{\alpha_C} - \phi_F[\boldsymbol{C_F}]\boldsymbol{\alpha_F} - \phi_M[\boldsymbol{C_M}]\boldsymbol{\alpha_M}\} \tag{6.45}$$

The variable $\boldsymbol{\alpha}$ is the coefficient of thermal expansion for the relevant phase. The major advantage of this approach is that it allows representative matrix and fibre stress states to be obtained in each layer of every element without recourse to micromechanical modelling [124].

The micromechanical aspect of the approach is performed before the structural analysis to obtain the stiffness properties of the fibre and matrix which result in composite properties matching those obtained during physical testing [124]. An optimisation routine is used with the model to find the matrix and fibre elastic properties that result in the homogenised composite properties that match those obtained during physical testing.

The model currently used in Helius:Fatigue assumes unidirectional laminae with hexagonal packing as shown in Figure 6.8. The model mesh is calculated using the fibre volume fraction.

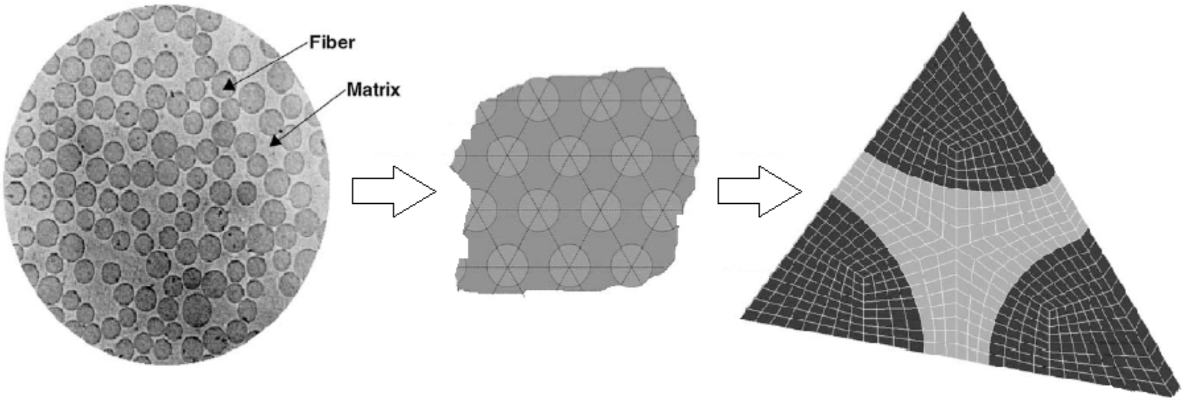

Figure 6.8 - Micromechanical model used in Helius:Fatigue, adapted from [124]

This approach accounts for several issues which can be encountered when using micromechanical models. Generally speaking, it is rare that the composite properties predicted from measured bulk constituent properties will agree with measured composite properties. There are several reasons for this [122]:

- The micromechanical model represents an idealised microstructure, not the true microstructure. The fibre spacing will be random, not even, as illustrated in Figure 6.8. Also, defects which occur during curing are not accounted for.
- Knowledge of the bonding between fibre and matrix is not available.
- It is unlikely that the material used to obtain the measured constituent properties will have been subjected to identical cure conditions to those for the materials used in the composite.
- Knowledge of the bulk constituent thermal and elastic properties is typically incomplete.

By using in-situ constituent properties calculated using an optimisation routine it is possible to account for these unknowns by tuning the material elastic properties.

6.2.6 Application of the kinetic theory of fracture

The nature of polymers means that the kinetic theory of fracture can be applied to model their breakdown. There is a large amount of published literature on the theory. Tobolsky and Eyring [76] first proposed a form of the kinetic theory equation based on the theory of absolute reaction rates in 1943. Coleman investigated the time dependence of polymer breakdown [127, 128], and Zhurkov and co-workers [73, 77-80] developed a huge body of work on the kinetic theory of fracture in the period between the 1950s and the end of the Soviet Union.

The following sections detail the application of the kinetic theory of fracture to the problem of composite fatigue. Where the approach used in the present work differs from that used in Helius:Fatigue it will be highlighted.

6.2.6.1 Overview of the kinetic theory of fracture

Assuming the temperature is greater than absolute zero, atoms and molecules vibrate at a frequency that is proportional to ν_0 given by equation (6.46), in which T is the absolute temperature, k is the Boltzmann constant (1.38 x 10^{-23} J/K) and h is the Planck constant (6.62 x 10^{-34} Js).

$$\nu_0 = \frac{kT}{h} \tag{6.46}$$

The numbers in equation (6.46) are more manageable if the per-mol values are used for k (8.3145 J/K-mol) and h (3.99 x 10^{-10} Js/mol).

The thermal energy associated with each oscillation is a distribution rather than a single number [122]. The probability that any given oscillation will have sufficient energy to overcome the energy barrier is given by equation (6.47) in which U is an energy barrier with the units of J/mol [81]. This equation also applies for bond recombination [129].

$$P = exp\left(-\frac{U}{kT}\right) \tag{6.47}$$

An applied stress σ increases the probability that an oscillation will have sufficient energy to break its bonds and reduces the probability that bonds will heal as shown in equation (6.48) and (6.49) [129]. Usually bond healing is neglected as it is negligible unless the stresses are very low. The energy barrier for moving from state 1 (intact bond) to state 2 (broken bond) is illustrated in Figure 6.9 in the absence (left) and presence (right) of an applied stress. Bond healing is currently neglected in Helius:Fatigue [122].

$$P_B = \exp\left(-\frac{U - \gamma\sigma}{kT}\right) \tag{6.48}$$

$$P_H = \exp\left(-\frac{U + \gamma\sigma}{kT}\right) \tag{6.49}$$

The constant γ is called an activation volume, and is related to the volume over which the process is taking place [81, 130].

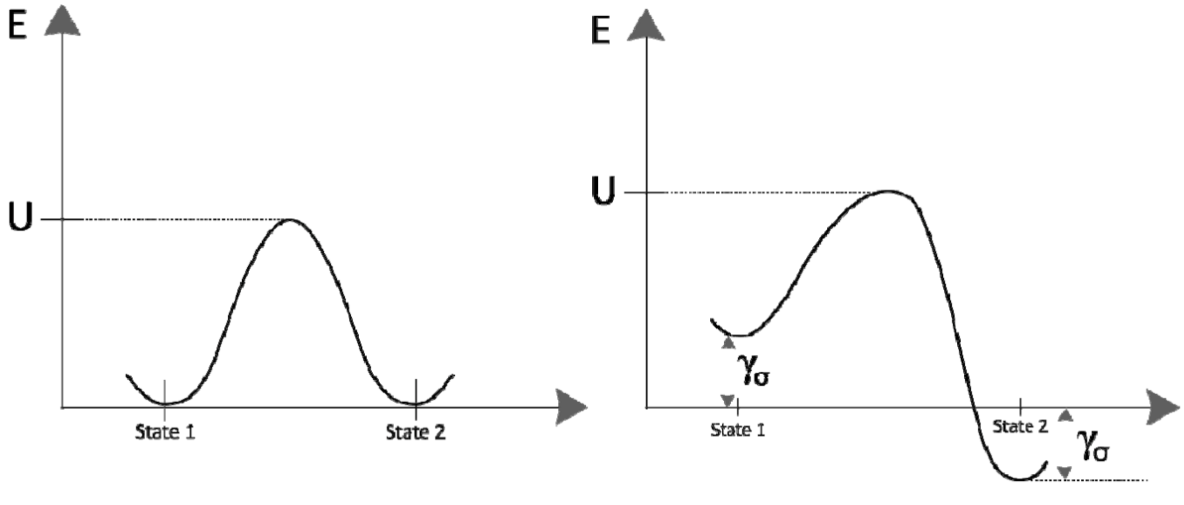

Figure 6.9 - Energy barrier with activation energy U for transition from state 1 to state 2 [122]

By combining equations (6.46) and (6.48) it is possible to arrive at equation (6.50) for the bond rupture rate, K_B which is used in Helius:Fatigue [122].

$$K_B = \frac{kT}{h}\exp\left(-\frac{U-\gamma\sigma}{kT}\right) \tag{6.50}$$

Equation (6.51) is the inverse of equation (6.50) and gives the time to failure under a constant applied stress. This is the form of the equation which is usually quoted [73].

$$\tau = \tau_0 \exp\left(\frac{U-\gamma\sigma}{kT}\right) \tag{6.51}$$

Zhurkov and co-workers performed thousands of tests on huge variety of materials, including polycrystalline metals, single crystals, non-metallic compounds, polymers, alloys and composites and recorded the time to failure. The results of these tests were summarised in [77], from which Figure 6.10 was obtained. The plots show the logarithm of time to failure in seconds against the applied stress for different materials. It is extremely clear that there is a linear relationship between the applied stress and the log of the time to failure, and that this relationship persists over a very broad range of materials.

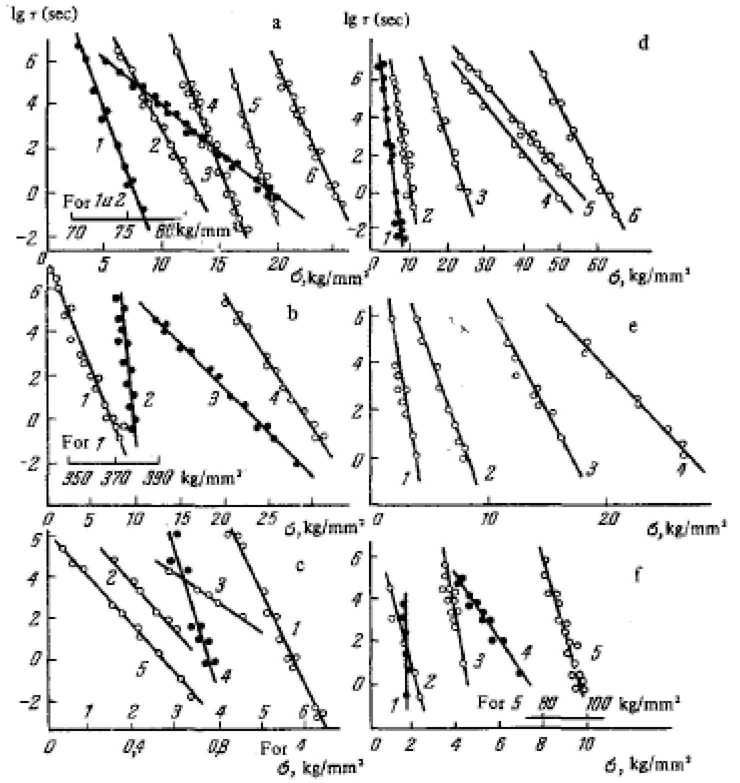

a) Polycrystalline metals: 1—niobium, 2—vanadium, 3—aluminum, 4—zince, 6—silver (1—4 and 6, room temperature); 5—platinum (300°C). b) Alloys: 1—molybdenum-rhenium (18°C); 2—aluminum with 0.75% copper (70°C); 3—silver with 2.5% aluminum (300°C); 4—aluminum with 4% copper (100°C). c) Single crystals: 1—aluminum (18°C); 2 and 3—zinc with varying orientations of the stress with respect to the basal plane (2—35°C; 3—20°C); 4—rock salt (18°C); 5—aluminum (300°C). d) Polymers (room temperature): 1—plexiglas (polymethylmethacrylate); 2—polystyrene; 3—polyvinylchloride (fiber); 4—viscose (fiber); 5—capron (polycaproamide, fiber); 6—polypropylene (fiber). 3) Heterogeneous (composite) materials (room temperature): 1—paper; 2—wood (stressed along the fiber axis); 3—cement, 4—fiberglas. f) Endurance in vacuo (10^{-7} Torr): 1—silver chloride (18°C); 2—aluminum (300°C); 3—aluminum (18°C); 4—polymethylmethacrylate (18°C); 5—oriented capron (18°C).

Figure 6.10 - Time to failure of different solids under the load σ [77]

The effect of temperature was also shown by Zhurkov, as shown by Figure 6.11 which is taken from the kinetic theory review paper by Regel et al [81]. Notice that the lines of tests at different temperatures converge at the characteristic period τ_0.

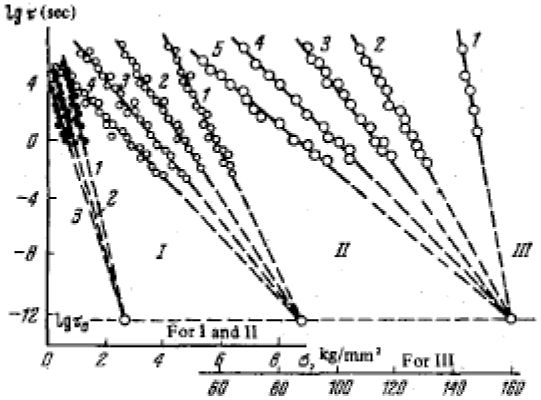

I—rock salt: 1—400°C; 2—500°C; 3—600°C. II—aluminum (polycrystalline): 1—18°C; 2—100°C; 3—200°C; 4—300°C. III—capron (oriented fiber): 1—(−180°C); 2—(−120°C); 3—(−75°C); 4—(20°C); 5—(80°C).

Figure 6.11 - Endurance temperature relation [81]

Zhurkov also showed that unlike the activation energy, U, the activation volume, γ, is altered by the initial state of the material [81]. The y-axis intercept is controlled by U, whereas the gradient is controlled by γ. This can be seen in Figure 6.12, again taken from the review paper by Regel et al [81]. This data is for aluminium, so the results will differ for fibre reinforced plastics.

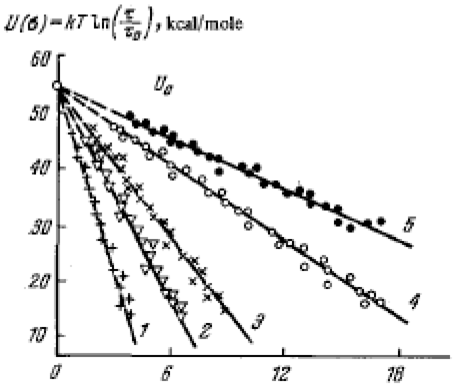

1—annealed at 550°C; 2—annealed at 420°C; 3—annealed at 290°C; 4—rolled; 5—alloyed (2% Mg).

Figure 6.12 - Relation of the activation energy to stress for different initial states [81]

Although there is overwhelming evidence that kinetic theory can successfully describe polymer fracture, there are some limitations. These are discussed in the review paper by Regel et al [81].

One of the major issues that is encountered when applying the theory to wind turbine blades is the behaviour at low stresses. Figure 6.13 shows that at low stresses the material deviates from the linear relationship between the logarithm of the time to failure and the applied stress. Zhurkov [73] attributed this behaviour to recombination processes and material instability.

Wind turbine blades are designed to survive gusts of wind that are predicted to occur once in 50 years, and have long lives. This means that the stresses in everyday operation are very low, so if equation (6.50) is used then it is clear that a significant amount of damage will still accrue even if the stress is 0.

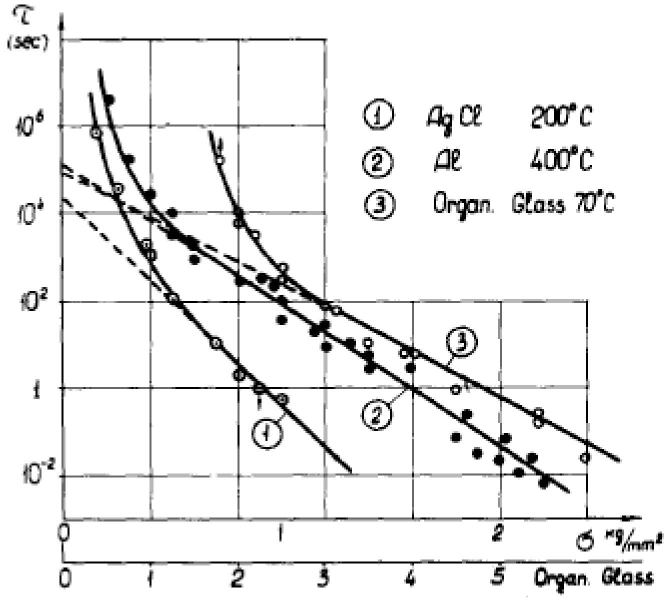

Figure 6.13 - Variations in the lifetime of solids at low stresses and high temperatures [73]

One of the major changes to kinetic theory as it is usually applied that has been made in the present work is to modify the bond rupture rate to account for this.

6.2.6.2 Effective stress

Several failure modes are observable in composites undergoing fatigue loading. The failure mode varies depending on the magnitude, direction and nature of the applied load. Under tensile loading, unidirectional composites can fail due to cracks developing in the matrix that are either parallel to the fibres (transverse cracks) or at a right angle to them (longitudinal cracks).

Before the effective stress is calculated, the time histories of the matrix stress tensor elements are interpolated and zero crossings are calculated for σ_{11m}, σ_{22m} and τ_{12m}. This feature is not present in Helius:Fatigue, and it increases the accuracy of the calculation of the time integral of the bond rupture rate, particularly for stress time histories where the loading is both tensile and compressive. It also permits different values of the activation energy and volume to be used for compressive loading and tensile loading. In order to increase the calculation speed in Helius:Fatigue, certain checks are made on the time history of stresses to determine if the failure mode is certain to be longitudinal or transverse. In the present work, the use of beam theory means that this is not necessary and the failure mode is simply assumed to be whichever of the two modes will result in the shortest life.

Hashin and Rotem found that in order for longitudinal cracks to occur, the load must be tensile and within 2° of the fibre direction [131], and this is the assumption used in Helius:Fatigue [122]. Equation (6.52) is used to calculate the effective stress in the longitudinal direction, where the curly brackets indicate that the encompassed quantity is 0 if it is negative.

$$\sigma_{eff} = \{\sigma_{11m}\} \tag{6.52}$$

Transverse cracks can occur due to either tensile stresses in the 2-direction or the in-plane shear stress [132]. In Helius:Fatigue, the effective stress in the transverse direction is found from a criterion developed for static failure [122]. The form of the failure criterion is shown in equation (6.53), in which values inside curly brackets are again zero if they are negative [122].

$$B_t\{I_t\}^2 + [B_{s1}I_{s1} + B_{s2}I_{s2}] = 1 \tag{6.53}$$

where

$$I_t = \frac{\sigma_{22m} + \sigma_{33m} + \sqrt{(\sigma_{22m} + \sigma_{33m})^2 - 4(\sigma_{22m}\sigma_{33m} + {\tau_{23m}}^2)}}{2} \tag{6.54}$$

$$I_{s1} = {\tau_{12m}}^2 + {\tau_{13m}}^2$$

$$I_{s2} = \frac{1}{4}(\sigma_{22m} + \sigma_{33m})^2 + {\tau_{23m}}^2$$

The values of B_i are determined by performing transverse tension, transverse compression and in-plane shear static tests [122]. Equation (6.53) can then be used to solve for B_{s1}, and then solved simultaneously for B_{s2} and B_t. The effective stress in the transverse direction is then found by dividing equation (6.53) through by B_{s1} and taking the square root as shown in equation (6.55) [122].

$$\sigma_{eff} = \sqrt{\frac{B_t}{B_{s1}}\{I_t\}^2 + \left[I_{s1} + \frac{B_{s2}}{B_{s1}}I_{s2}\right]} \tag{6.55}$$

This form of the effective stress has not been modified in the present work. A final form of failure that has not been addressed in either Helius:Fatigue or the present work is delamination. This caused by out of plane stresses at the free edges of the laminate, or in the case of multidirectional laminates the inter-laminar stresses. In coupon testing delamination followed by buckling is the observed failure mode for laminates loaded compressively in line with the fibres. If the compressive load is not in line with the fibres, then failure would be expected to occur in the transverse direction due to the in-plane shear stresses.

6.2.6.3 *Effect of temperature*

The bond rupture rate K_B is dependent on the temperature. When stress cycles are applied to a polymer, the viscoelastic response causes energy to be dissipated due to hysteresis which results in an increase in the temperature.

The energy dissipated during a cycle can be calculated from equation (6.56) [133]. The parameter J'' is the loss compliance of the polymer, f is the frequency and σ_a is the amplitude of the stress. The temperature rise can be assumed to be proportional to the energy dissipated.

$$E = \pi f J'' \sigma_a^2 \tag{6.56}$$

This explains the fact that at low stress amplitudes (when the temperature rise is not significant) an increase in frequency increases the number of cycles to failure [41]. However, if the stress amplitude is higher the number of cycles to failure will be lower at high frequencies because the higher temperature increases the bond rupture rate.

Figure 6.14 shows a plot of the bond rupture rate for a high amplitude cycle and a lower amplitude cycle. The time integral of the K_B curve is clearly larger for the R=0.5 history than the R=0 history, meaning that it is more damaging. In practice, because the R=0 cycle has a higher amplitude it will have a higher temperature than the R=0.5 cycle so it will be more damaging, as shown by the dashed line.

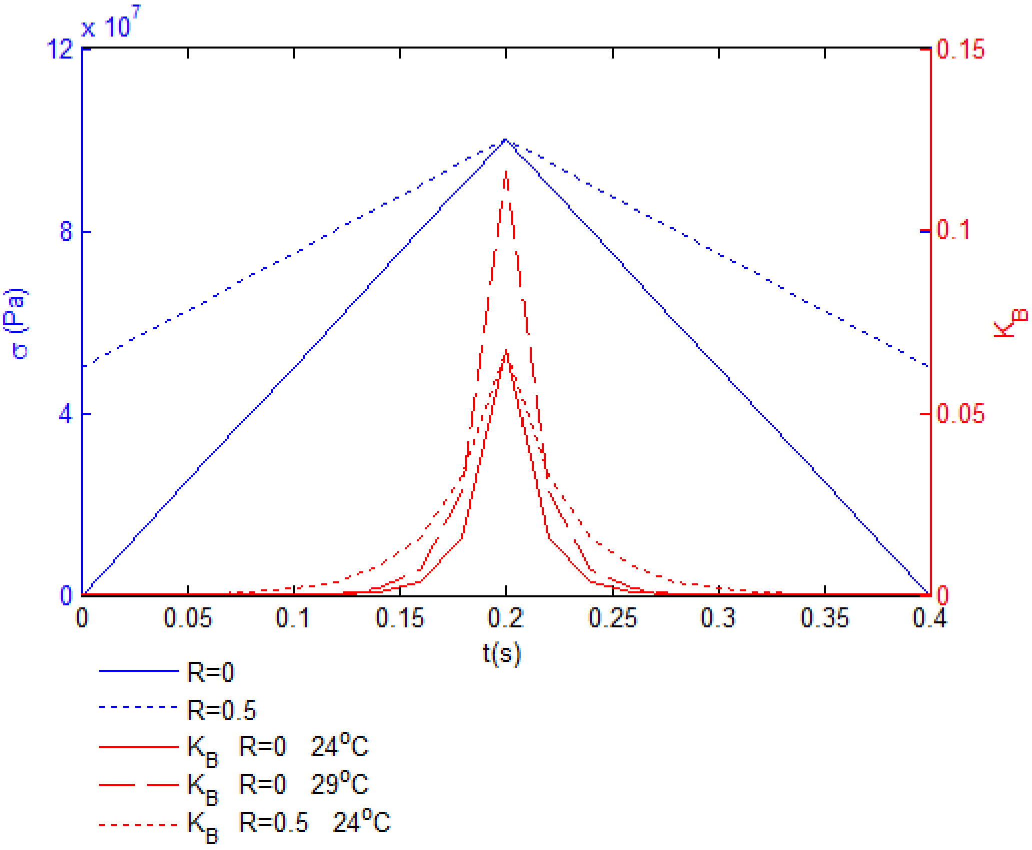

Figure 6.14 - Stress and bond rupture rate at R=0 and R=0.5

This correction allows the effect of test frequency and mean stress to be properly accounted for. In Helius:Fatigue, the temperature is assumed to be proportional to the total energy dissipated during the time history and the temperature is calculated using equation (6.57) [122].

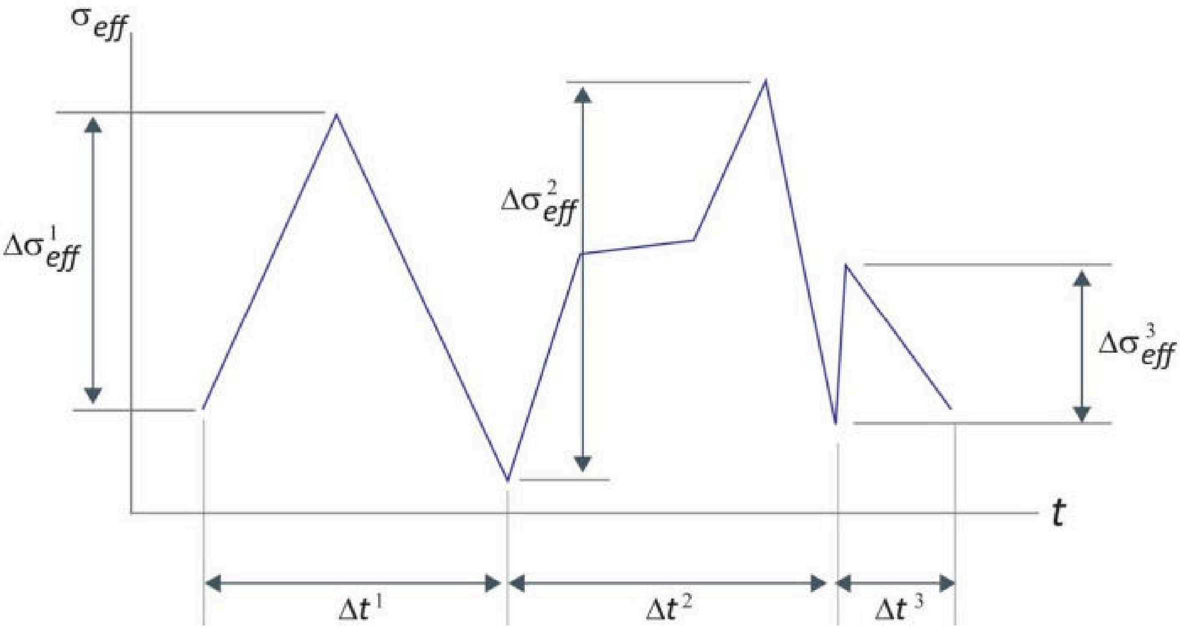

Figure 6.15 - Helius:Fatigue temperature calculation [122]

The value of ψ is found by calibrating against physical test data, T_{amb} is the ambient temperature, and the meaning of $\Delta\sigma_{eff}$ and Δt are shown in Figure 6.15.

$$T = T_{amb} + \psi \sum_{i=1}^{n} \frac{\Delta\sigma_{eff\,i}^{2}}{\Delta t_i^2} \tag{6.57}$$

This equation is effective for short time histories, but for long time histories the temperature increases indefinitely. For this reason, the equation has been modified in the present work to account for the fact that the temperature will eventually stabilise as the rate of heat flow to the surrounding area increases [134].

The stress used to calculate the temperature has also been changed from the effective stress used in the kinetic theory (as in Helius:Fatigue) to the signed Von Mises matrix stress at each point in the time history. This is more representative of what will happen in reality; it is easy to imagine a biaxial stress state where the fibre axis stresses are high (and thus are heating the matrix up) and failure occurs in the transverse direction due to this temperature increase. The sign for the Von Mises stress is taken from the principal stress component with the largest absolute value.

By adding zero crossings to the time history the temperature calculation can be improved further, as shown in Figure 6.16. This has the additional effect of making the integral of the bond rupture rate more realistic, the importance of which can be seen in Figure 6.14.

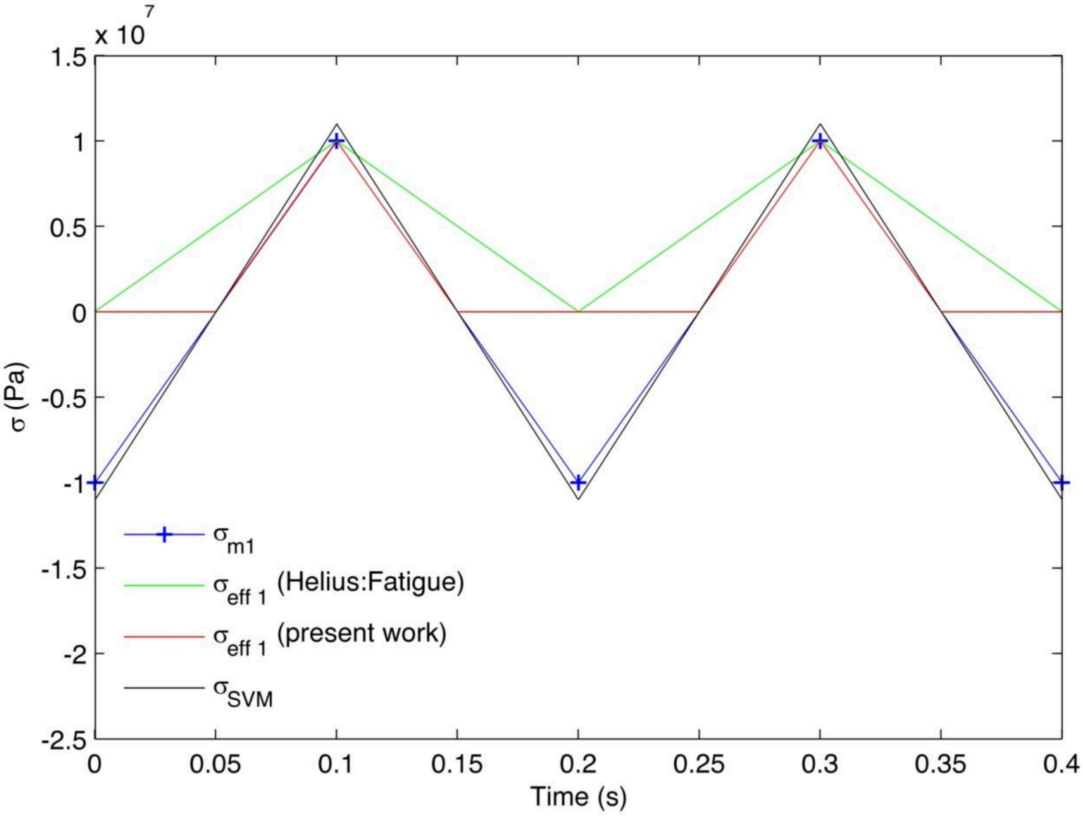

Figure 6.16 - Effect of adding zero crossings for longitudinal effective stress

Newton's law of cooling is used to calculate the final temperature of the laminate by looping through the stress history as shown in equation (6.58), where k is the Newton cooling constant,

σ_{SVM} is the signed Von Mises stress and t is time in seconds. The subscript i refers to the point in the time history.

$$T_{i+1} = \left(T_i - T_{amb} - \psi \frac{\Delta\sigma_{SVM\,i}{}^2}{\Delta t_i^2}\right) e^{-k\Delta t_i} + T_{amb} + \psi \frac{\Delta\sigma_{SVM\,i}{}^2}{\Delta t_i^2 k} \tag{6.58}$$

As ψ is found by calibrating against physical test data, the choice of the cooling constant k is arbitrary and for the calibration case where the amplitude and frequency are constant the stable temperature is found from the last two terms of equation (6.58).

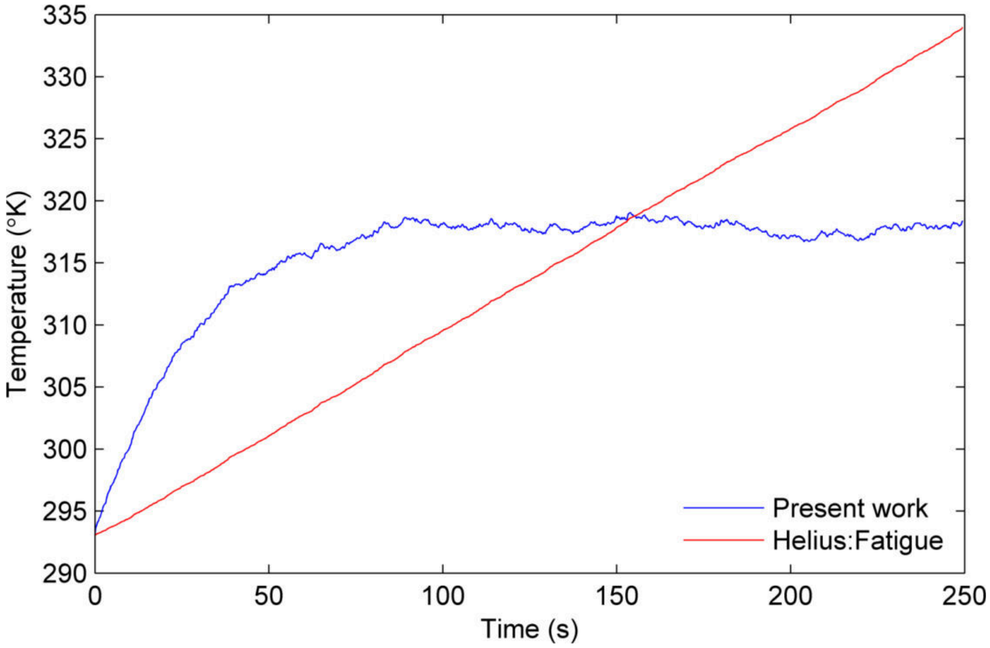

Figure 6.17 - Temperature calculation comparison

When using this equation, the temperature will eventually stabilize as shown in Figure 6.17, just as in reality. The user can choose to use the temperature at the end of the time history or the stable temperature that would eventually be reached if the time history was repeated indefinitely.

6.2.6.4 Low stress behaviour

As mentioned earlier, the behaviour at low stresses is very important for wind turbine blade design. If the kinetic theory of fracture is applied in the form usually described then damage will still accumulate at zero stress, which is clearly not acceptable. This has been accounted for in the present work by allowing for the effect of bond recombination as shown in equation (6.59).

$$K_B = \frac{kT}{h}\left[\mathrm{e}^{\left(-\frac{U-\gamma\sigma}{kT}\right)} - \mathrm{e}^{\left(-\frac{U+\gamma\sigma}{kT}\right)}\right] \tag{6.59}$$

At low stresses various studies have shown that the bond rupture rate is lower than that which is calculated by accounting for recombination alone [73]. By digitising Figure 6.13 it is possible to study the effect of bond recombination.

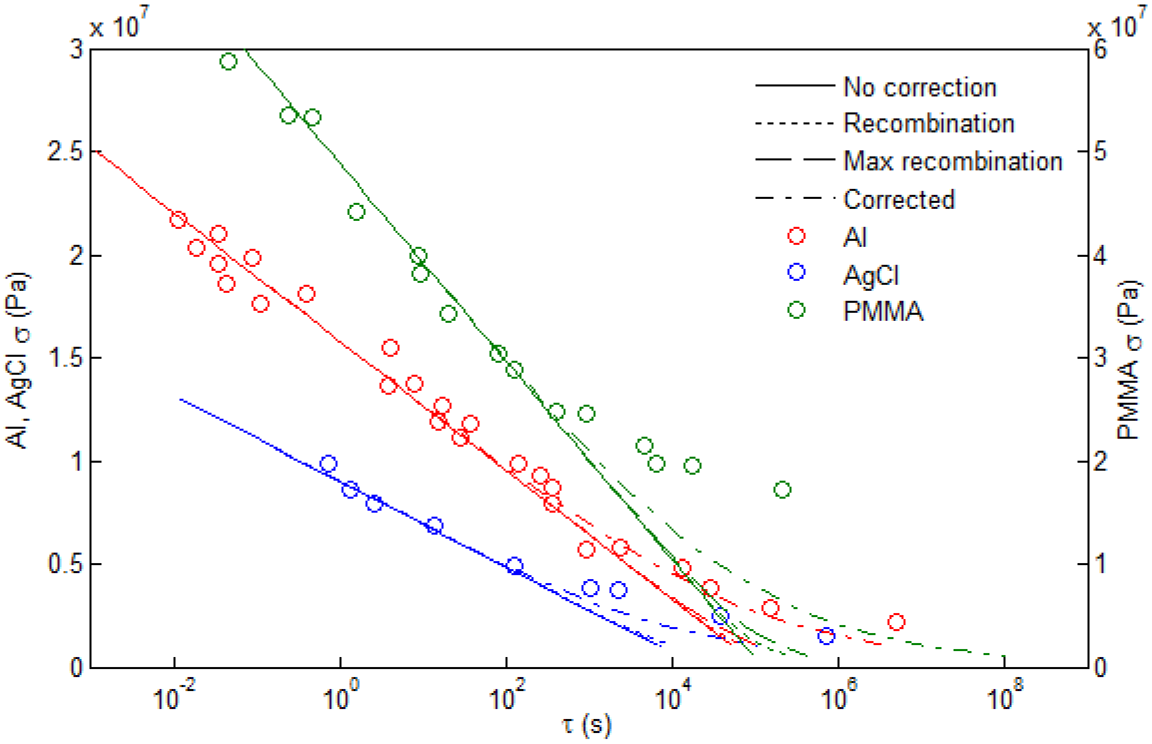

Figure 6.18 - Effect of accounting for recombination

Even at very low stresses, recombination alone is not sufficient to match up to the data. We can see from the dotted lines in Figure 6.18 that it makes very little difference even at the lowest stresses, although it will mean that the material does not have a finite life at zero stress. The dashed lines, which are calculated using equation (6.59) with a value of 0 for γ in the recombination term, show a very slight improvement. However, it is still not sufficient to come close to approximating the test data. This means that material instability (in the case of polymers this is assumed to result from molecular chains straightening before bonds rupture) must be accounted for also. Zhurkov [73] states that if the material is prepared in a stable state before testing then recombination alone is sufficient to account for the discrepancy at low stresses, but in the case of wind turbine blades this is not feasible.

It was necessary to account for this effect. It was noted that for all three of the materials in Figure 6.18 and Figure 6.13, the divergence from the log-linear behaviour occurred at a similar proportion of the time axis (when it is considered to extend from the atomic vibration period, which is approximately 10^{-13} seconds, to the calculated intersection of the log-linear line with the time axis). This proportion is calculated from equation (6.60), in which d is the proportion of the life at which divergence occurs and τ_d is the time at which divergence occurs. The value of d is found to be between 0.82 and 0.85 for all three materials in Figure 6.18.

$$d = \frac{\left(\log_{10}(\tau_d) - \log_{10}\left(\frac{h}{Tk}\right)\right)}{\left(\log_{10}\left(\frac{h}{Tk}\exp\left(\frac{U}{kT}\right)\right) - \log_{10}\left(\frac{h}{Tk}\right)\right)} \tag{6.60}$$

If d is chosen to take a value between 0 and 1 (0.9 was used in the present work) then the divergence time can be calculated from equation (6.61).

$$\tau_d = 10^{d\left(\log_{10}\left(\frac{h}{Tk}\exp\left(\frac{U}{kT}\right)\right)-\log_{10}\left(\frac{h}{Tk}\right)\right)+\log_{10}\left(\frac{h}{Tk}\right)} \tag{6.61}$$

To correct for material instability, a power law version of the equation for bond rupture was created that comes into effect if the stress is low enough to result in a life longer than the calculated point of divergence from log linear behaviour. Unfortunately, this is not based on physics, but it is necessary in order that the lifetimes predicted at low stresses are not unrealistically short. The function does not require any additional characterisation data, and is shown in equation (6.62). The power law curve fit is commonly used in composite fatigue analysis.

$$K_B = \left(\frac{\sigma_{eff}}{\sigma_{Ref}}\right)^B \tag{6.62}$$

The constant B is the slope factor for a power law curve fit to the fatigue data (typically 9 -12), and σ_{Ref} is the stress axis intercept of power law curve with slope B that intersects the line described by the kinetic theory at τ_d. The calculation of these constants is described in Figure 6.19. The principle of time-temperature superposition has been applied to composite strength before [135], and accelerating tests by increasing the temperature could be a good way to obtain useful data in the low stress regime without the tests being inordinately long, allowing realistic values for the parameters B and d to be chosen.

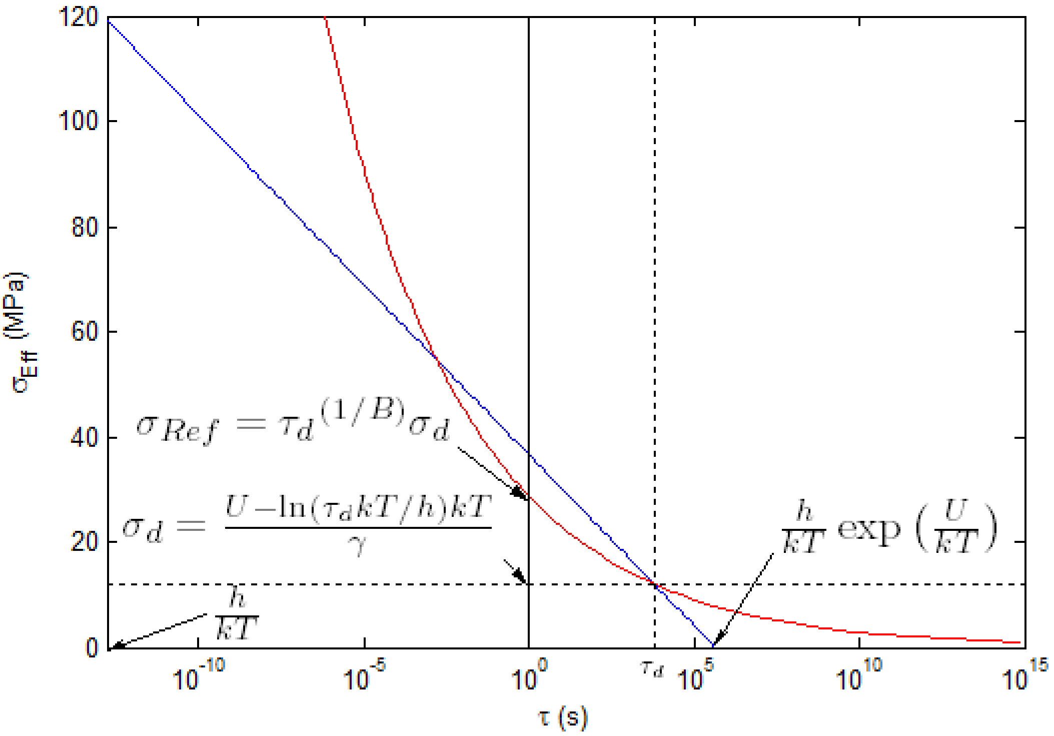

Figure 6.19 - Calculation of power law constants

Equation (6.62) is effectively a representation of the power law curve fit usually used in fatigue analyses that has been rearranged to work in terms of the bond rupture rate instead of the number of cycles to failure. Although there is very little data available to quantify the behaviour at low stresses due to the test times involved, this method is inherently conservative in terms of conventional fatigue analysis. This is because when curve fits are made to fatigue data using linear regression, the power law curve fit will always have a greater y-intercept than the exponential fit. The effect of temperature is included in the calculation of τ_d.

For each segment of the effective stress time history, the method which results in the least damage is chosen. This means that at high stresses where kinetic theory works effectively it is used, but at low stresses the bond rupture rate is reduced by using the power law relationship.

The chained line in Figure 6.18 shows the predicted lifetimes with material instability accounted for. Accounting for material instability in polymers using a method with a physical basis should be an area of research in the future.

6.2.6.5 Damage accumulation

The microscopic process of bond rupture is linked to the macroscopic process of crack accumulation using the differential equation developed by Hansen and Baker-Jarvis [129]. They created a damage parameter n that is zero initially and 1 at failure, which is linked to the bond rupture rate using a differential equation (6.63).

$$\frac{dn}{dt} = (n_0 - n)K_B \tag{6.63}$$

The parameter n_0 can be considered to be representative of how resistant the material is to crack formation. Its value is found by enforcing the condition given in equation (6.64). The result is consistent with experimental observations based on the measurement of free radicals formed as materials rupture made by Zhurkov and Kuksenko [80].

$$\int_0^1 \frac{dn}{(n_0 - n)} = 1 \tag{6.64}$$

This approach has been extended by Fertig and Kenik [71], who altered equation (6.63) to the form shown in equation (6.65). This approach was not used in the present work, as preliminary studies showed that unless the load blocks had very different magnitudes, the variable λ had little effect on the final time to failure. Wind turbine blades are assumed to have a repeating duty cycle year to year [10, 11], although in practice this is not true.

$$\frac{dn}{dt} = (n_0 - n)^{\lambda} K_B \tag{6.65}$$

The effect of different values of λ is shown in Figure 6.20. Although the damage evolves very differently, if K_B remains relatively constant (which can be assumed over the life of a wind turbine) then failure occurs at around the same time regardless of the value of λ. For this reason λ has been set to the value of 1 in the present work, as in equation (6.63).

Fertig and Kenik [71] presented a solution to equation (6.63) for the case when n changes from 0 to 1 over a single load block. This is the equation implemented in Helius:Fatigue at the time of writing.

The wind turbine design standards require that fatigue analysis is performed at a range of average wind speeds [10, 11], so an analysis method based on a single load block is not acceptable. For this reason, equation (6.63) is solved in the present work as shown in equation (6.66).

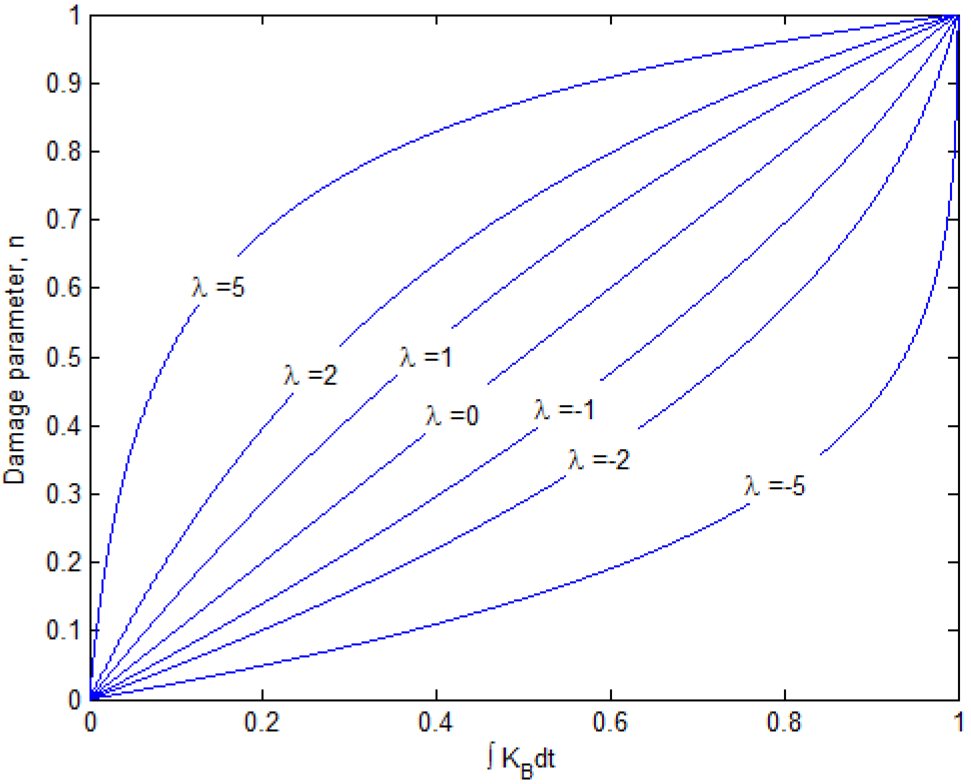

Figure 6.20 - Effect of changing the variable λ

$$n(t_i) = (n(t_{i-1}) - n_0)\exp\left(-N\int_{t_{i-1}}^{t_i} K_B(t)\right) + n_0 \tag{6.66}$$

This approach allows block loading and progressive failure analyses to be performed. In Helius:Fatigue, the time integral of K_B is calculated using the trapezium rule. In the present work the effective stress history is assumed to be piecewise linear, and the time integral of K_B is calculated mathematically between adjacent time points. From Figure 6.14 we can see that the variation of K_B with stress is highly nonlinear, and so the trapezium rule can greatly overestimate the area under the K_B curve. The time integral of equation (6.59) for a linearly varying stress is given in equation (6.67), and the total is calculated by summing the contribution from every segment of the effective stress time history.

$$\int_0^{t_1} K_B dt = \frac{(kT)^2\left[\exp\left(\frac{2\gamma c}{kT}\right)\exp\left(\frac{\gamma m t_1}{kT}\right) - 1\right]\left[\exp\left(\frac{\gamma m t_1}{kT}\right) - 1\right]}{\gamma h m \exp\left(\frac{U}{kT}\right)\exp\left(\frac{\gamma c}{kT}\right)\exp\left(\frac{\gamma m t_1}{kT}\right)} \tag{6.67}$$

where

$$m = \frac{\sigma_{eff}(t_{i+1}) - \sigma_{eff}(t_i)}{\mathrm{t_{i+1}} - \mathrm{t_i}}$$

$$c = \sigma_{eff}(t_i)$$

$$t_1 = t_{i+1} - t_i$$

The temperature and activation energy/ volume are assumed to be invariant across the time step.

As described in section 6.2.6.4, it is necessary to account for changes in the behaviour at low stresses. The time integral of a linearly changing stress for the power law version of the bond rupture equation (6.62) is given by equation (6.68), where m, c and t_1 are given above and σ_{Ref} and B are described in section 6.2.6.4. As discussed previously, the smaller of the two values given by equations (6.67) and (6.68) is used for each linear segment of the effective stress time history.

$$\int_0^{t_1} K_{Bp} dt = \frac{\sigma_{Ref}}{m(B+1)} \left[\left(\frac{mt_1}{\sigma_{Ref}} + \frac{c}{\sigma_{Ref}} \right)^{(B+1)} - \left(\frac{c}{\sigma_{Ref}} \right)^{(B+1)} \right] \tag{6.68}$$

The number of repeats of a given block which will cause failure to occur can be calculated by setting $n = 1$ and rearranging equation (6.66) for N, the number of repeats of the block.

6.2.7 Computational implementation

The composite fatigue algorithm has been implemented as a MatLab code. The software flowchart is shown in Figure 6.21.

There are several features of the software which are designed to reduce the computational effort.

Firstly, the program does not recalculate the stiffness properties every time a ply fails, as this would mean it would run very slowly. Rather, the ply with the smallest number of cycles to failure is found at each iteration and any plies for which this number of cycles causes the damage parameter to be greater than a predefined value are also failed. This predefined value is very close to unity (eg. 0.99), so this will not have a significant effect on the accuracy of the results.

Secondly, the calculation of the composite stress, matrix stress, effective stress, temperature and the time integral of K_B are all vectorised. This is a feature of MatLab which means that it is not necessary to loop through the time histories.

Thirdly, the choice of a beam stress analysis rather than a shell finite element model is probably the main reason that analyses can be performed quickly.

Finally, because the analysis assumes that only extensional deformation of each element occurs (and not bending or twisting), a further feature to speed up the analysis is possible. The user has the option to consolidate all of the plies which are made from the same material and have the same angle in each element into one ‘super ply’. There is no reduction in simulation quality when this option is chosen, but it greatly speeds up the analysis.

The software takes around 30 minutes to analyse a root section of a blade (36 elements and around 50 plies in each layer, with 34 load cases, each of which is 10 minutes long) on a PC with a dual core 2.1GHz processor and 8GB of RAM. A full analysis of the blade would therefore be expected to take around 10 hours if the blade is sectioned at 20 points.

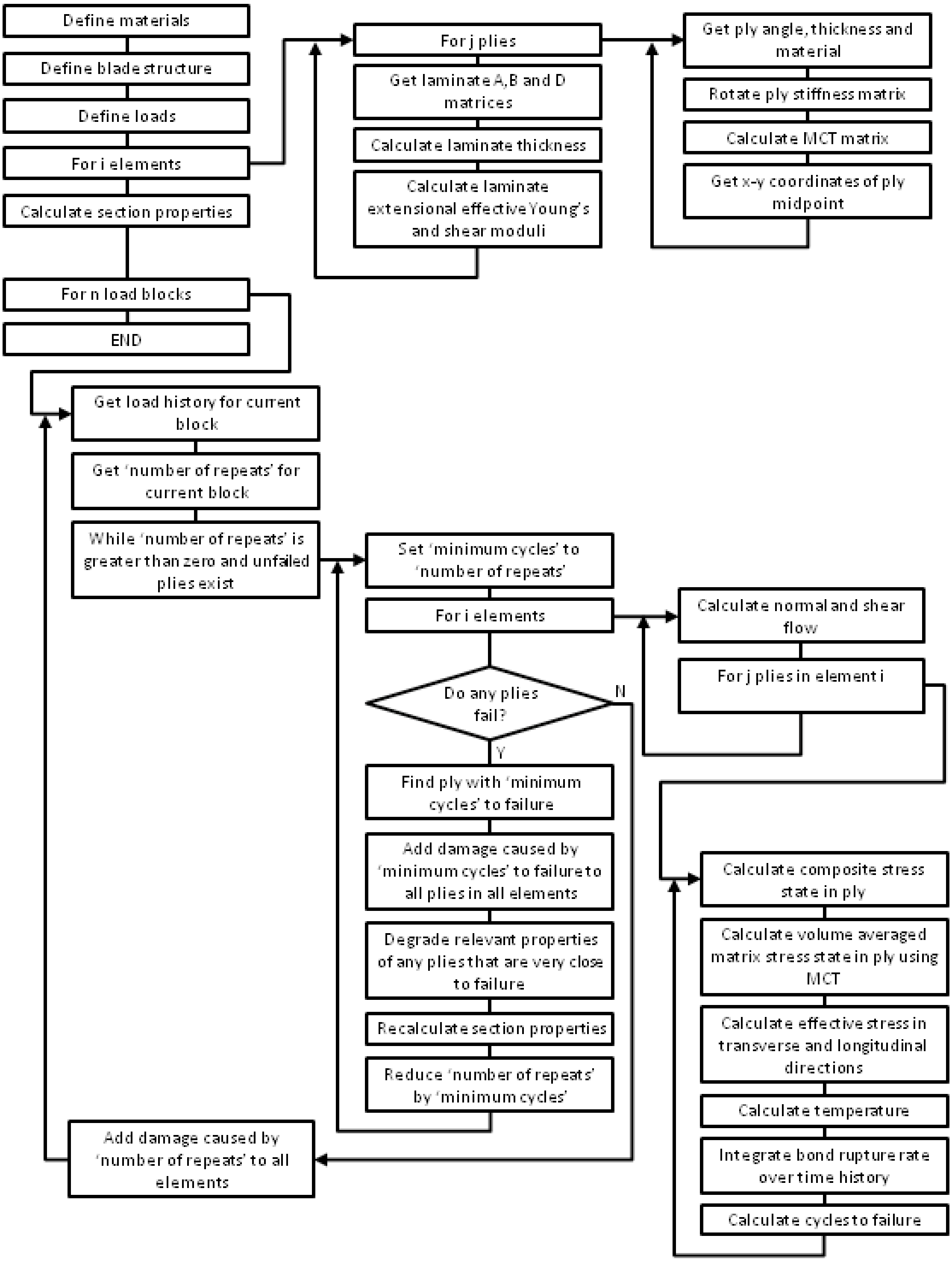

Figure 6.21 - Block loading with progressive failure analysis flowchart

6.2.8 Calibration of kinetic theory variables

The variables U and γ in the kinetic theory equation and the hysteretic heating variable ψ were found in the present work using a 'brute force' method. A search space is defined by the user, with maximum and minimum bounds on each variable and the number of increments between these bounds. The increments are logarithmic; for example, if the user specifies 100 increments between 100 and 10000 then there would be 10 values between 100 and 1000 and 10 between 1000 and 10000.

Physical test data for constant amplitude coupon testing is entered, defined by its maximum stress, number of cycles to failure, test frequency and R-value. When optimising for the variables for failure in the transverse direction, the ply angle is also required.

The first step is to obtain the stress in the material coordinate system. For the longitudinal direction, this is simply the applied stress but for the transverse direction the stress state may need to be rotated. Multi-continuum theory is then used to obtain the matrix stress, and the effective stress is calculated at each point in a 'saw tooth' representation of a single load cycle. The temperature rise of the specimen due to hysteretic heating is also calculated as described previously.

The integral of the bond rupture rate over a single cycle is then calculated, and this is used to calculate the number of cycles to failure. This process is repeated at each point in the search space, and the variables which result in the smallest difference between the measured data and the predicted values are chosen.

The method is identical to that used in the Helius:Fatigue algorithm used in FE-Safe/Composites [122], except for the use of 'brute force' optimisation algorithm in the present work. This has the advantage that a solution close to the global minimum is found, and the time penalty is insignificant; if 50 increments are used for each of the three variables, then the optimum is found in less than 10 seconds. This is slightly dependent on how many physical test specimens are being analysed, but as the calculation is vectorised the slowdown is not significant for larger datasets.

6.2.9 Full scale fatigue testing

The nature of the analysis method presented here lends itself to a different method of full scale fatigue testing to that described in earlier chapters. In the present method it is the time integral of the bond rupture rate that determines how much damage is caused, not the amplitude of the stress cycles. Over the life of the blade the flapwise direction experiences loading in one direction, whilst the edgewise direction experiences full load reversals as a result of the self weight of the blade. This means that the flapwise loading can be constant over a long period of time (instead of the cycling load applied during a typical fatigue test) whilst the edgewise cycling can be achieved in the normal manner by resonating the blade. Two possible ways to test the blade in this manner have been considered, both of which have advantages and disadvantages. Using winches normally used to perform static tests as shown in Figure 6.22 allows the mass of the equipment attached to the blade to be minimised, so the edgewise frequency will be much higher and the test can be performed more quickly. The applied load could also be adjusted to keep the bond rupture rate constant as the ambient temperature changes. However, the winches may be damaged by fatigue unless the cable is locked in position, and the winch cable would have to be long near the blade tip where the edgewise displacements are higher in order to keep unwanted loads at an acceptable level. The main problem with this configuration is that the mean edgewise bending moment is dictated by the self weight of the blade, which will be significantly different from the service life edgewise bending moment distribution.

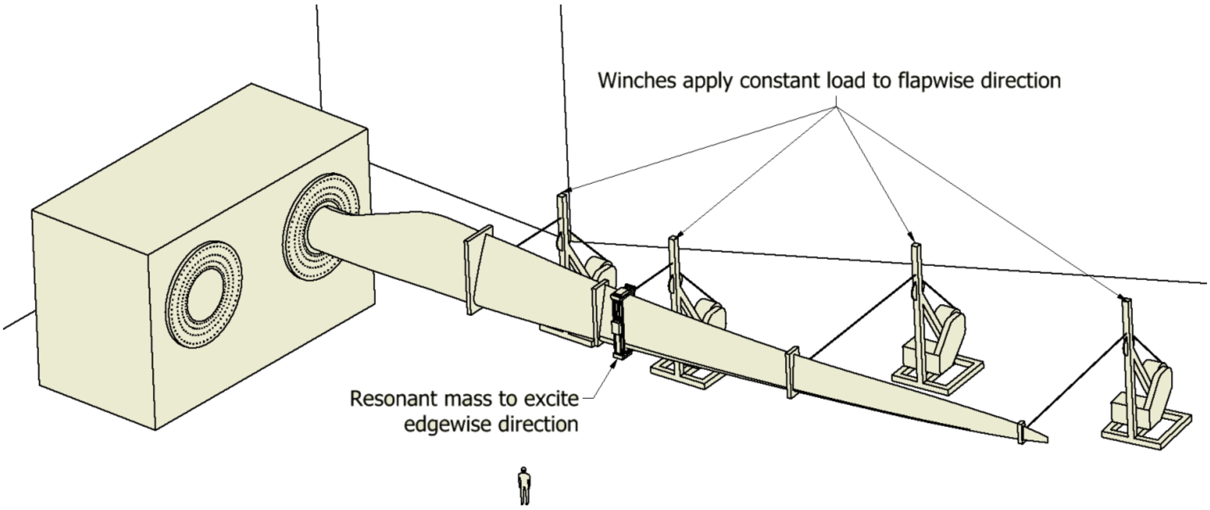

Figure 6.22 - Possible kinetic theory of fractures based test configuration 1

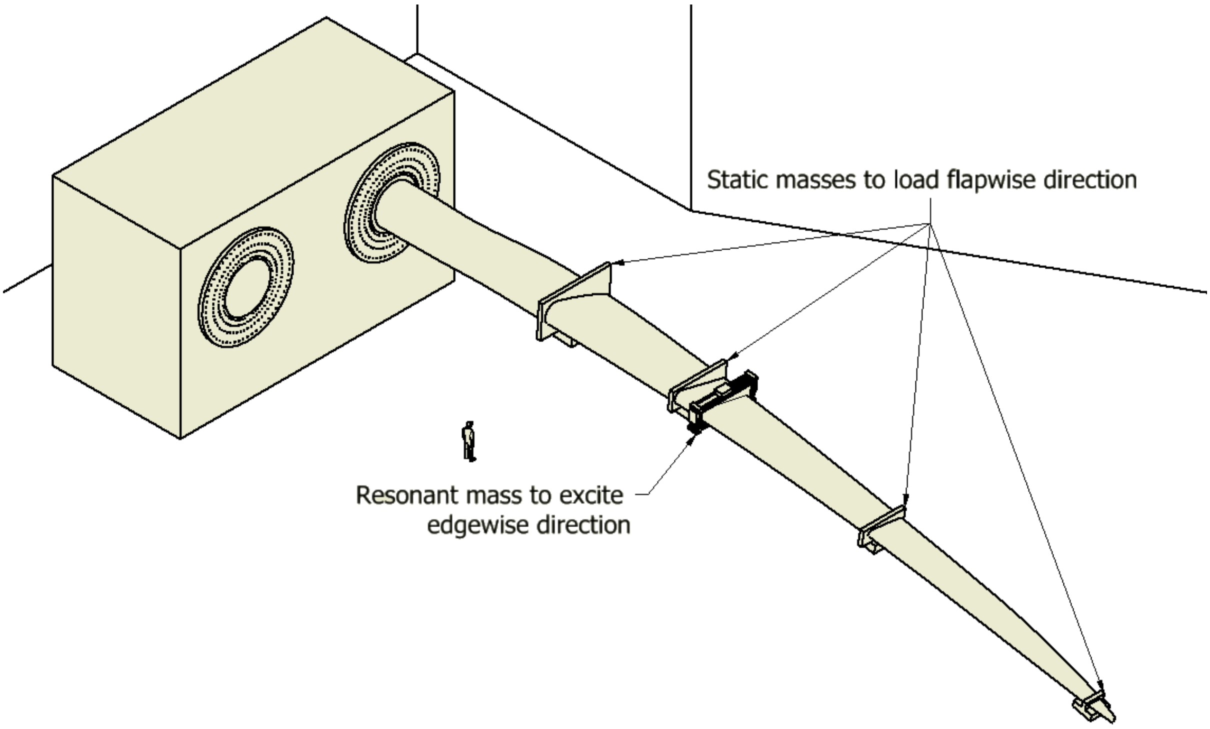

Figure 6.23 - Possible kinetic theory of fracture based test configuration 2

Another possible test configuration is shown in Figure 6.23. This method has the advantage that the edgewise mean bending moment distribution is close to zero, which is more realistic. However, the static masses which load the flapwise direction will have to be very large, which will affect the edgewise mode shape. It will also cause the edgewise natural frequency to be much lower, extending the duration of the test.

The test loads can be calculated in a similar manner to that used in chapter 3. The situation is more complex because the stress states which caused the damage are not uni-axial and the effective stress is dependent on both the shear and the transverse stress, which will be affected by the ply angle. For this reason the test loads were calculated from the longitudinal damage and effective stress in the 0° plies of the elements closest to the neutral axis in both the flapwise and edgewise directions. This is also the most important damage parameter, as the 0° plies provide most of the blade's resistance to bending.

The test loads are calculated by applying a unit flapwise and edgewise bending moment to the blade cross-section and finding the effective longitudinal stress in the 0° plies of the closest element to edgewise and flapwise neutral axes. The time integral of the bond rupture rate K_B required in order to cause the same amount of damage as the service life after a given test length is then found using equation (6.69). The parameter t_{test} is the test length in seconds, n_s is the longitudinal damage parameter in the reference ply after the service life and n_0 was described in section 6.2.6.5.

$$\int_0^{t_{test}} K_B dt = -\ln\left(\frac{n_s - n_0}{-n_0}\right) \tag{6.69}$$

The flapwise loads are assumed to be invariant, so the effective stress that will result in the correct bond rupture rate can be calculated directly using equation (6.70). This is a simplification as the blade twist will cause the edgewise loads to affect the flapwise direction, and the fact that the winch cables have finite length will also cause coupling between the flapwise and edgewise directions.

$$\sigma_{eff} = \frac{U + \ln\left(\frac{h\int_0^{t_{test}} K_B dt}{kTt_{test}}\right)kT}{\gamma} \tag{6.70}$$

Even accounting for the fact that the test is accelerated so the stress is larger than in the field, the test may still be in the low stress regime described in section 6.2.6.4. For this reason the effective stress is also calculated using equation (6.71), in which σ_{Ref} and B are described in section 6.2.6.4.

$$\sigma_{eff} = \sigma_{Ref}\left(\frac{\int_0^{t_{test}} K_B dt}{t_{test}}\right)^{\frac{1}{B}} \tag{6.71}$$

The lowest value of σ_{eff} from equations (6.70) and (6.71) is used, and the flapwise bending moment corresponding to this stress is calculated using equation dividing σ_{eff} by the value of σ_{eff} for a unit flapwise bending moment in the reference ply.

The edgewise loads are more complicated because they are cyclical which means that the bond rupture rate varies. The mean effective stress was calculated from the blade bending moment due to its self weight, and the amplitude was iterated by 1kNm until the integral of the bond rupture rate over one cycle (calculated using either equation (6.67) or (6.68), depending on which resulted in the lowest bending moment) had the required value, calculated using equation (6.69). Zero crossings were added to the stress time history if necessary. With the target loads calculated, the test can be optimised in the way described in chapter 4 and simulated using the model described in chapter 5.

6.3 Results and Discussion

The fatigue analysis method described above was applied to two problems during the course of the present work. The first problem was a benchmarking exercise in which the results obtained were compared to physical test data from the OPTIDAT wind turbine blade materials database [17]. The results are compared for a range of constant amplitude R-value tests, variable amplitude spectrum loading, residual strength tests and static tests. The second problem was a full fatigue analysis performed according to the design standards for a commercial blade, the LM 40.3 P2. The load data, blade design data and material data were all provided by LM Wind Power. The purpose of this test was to show that the analysis method could be extended to a full scale blade.

6.3.1 OPTIDAT benchmarking exercise

The OPTIDAT database [17] was suitable for the benchmarking exercise performed in the present work for several reasons. The fibre and matrix materials and test coupon manufacturing methods used are consistent for most of the physical tests, and all of the information required to use the fatigue analysis method described above is readily available. Unidirectional and multidirectional laminates are available, so the unidirectional test results can be used to characterise the ply behaviour for the multidirectional analysis. Three of the thirteen different laminates available in the database were used in this study, with the remaining ten being ruled out due to insufficient data.

In order to perform the analysis, the following information about each ply material is required:

- Ply Young’s modulus in 1 and 2 directions (3 direction is assumed to be the same as 2 direction) for the multi-continuum breakdown described in section 6.2.5.
- Ply shear modulus and Poisson’s ratio in the 1-2 direction and 2-3 direction (1-3 direction is assumed to be equal to 1-2 direction) for the multi-continuum breakdown described in section 6.2.5.
- Ply ultimate strength data in the 1 and 2 directions for tension and compression and ultimate shear strength in 1-2 direction. This is used to find the effective transverse matrix stress using the method described in section 6.2.6.2.
- Ply fatigue test data in the 1 direction, ideally at several R-values. This is used to calculate the activation energy U, the activation volume γ and the hysteretic heating constant ψ for longitudinal failure of the material as described in section 6.2.6.
- Ply fatigue test data for off 1-axis directions, ideally at several R-values. This is used to calculate the activation energy U, the activation volume γ and the hysteretic heating constant ψ for transverse failure of the material as described in section 6.2.6.

The unidirectional laminate for which most of this data was available was material UD3. Only the ultimate shear strength was not available, for which data from material UD2 was used. The only difference between the two laminates was the number of layers, so this was not considered to be a problem. Laminate UD3 consists of 7 layers of PPG2002 fabric with a Prime 20 epoxy matrix and slow hardener [17]. It was manufactured using vacuum infusion [17]. Strength and stiffness data for UD3 is given in Table 6.1 and Table 6.2 respectively [17].

Strength	Value	Units
$\sigma_{1\,UT}$	800	MPa
$\sigma_{1\,UC}$	530	MPa
$\sigma_{2\,UT}$	53	MPa
$\sigma_{2\,UC}$	165	MPa
$\sigma_{12\,US}$	65	MPa

Table 6.1- UD3 strength data (from [17])

Stiffness	Value	Units
E_1	39.105	GPa
E_2=E_3	14.165	GPa
$G_{12} = G_{13}$	4.659	GPa
G_{23}	5.238	GPa
$\upsilon_{12} = \upsilon_{13}$	0.279	
υ_{23}	0.352	

Table 6.2 - UD3 stiffness data (from [17])

Helius Material Manager, which is supplied with FE-Safe/Composites, was used to perform the finite element optimisation to find the material properties of the fibre and matrix which result in a composite with stiffness properties that most closely match the measured values. The fibre and matrix stiffness properties found for UD3 are given in appendix D.

Fatigue data for the longitudinal and transverse directions are shown in Figure 6.24 and Figure 6.25 respectively. The constants in the kinetic theory equation and the hysteretic heating equation found using the optimisation routine are given in Table 6.3. It is noteworthy that the hysteretic heating constant for the longitudinal direction takes the lowest value allowed by the optimisation routine, effectively resulting in no increase in temperature. Unfortunately, this is thought to be because the input fatigue data has some specimens that are cooled by a fan and some that are not. This has resulted in lower quality results for the R=-1 data.

For the transverse data in Figure 6.25, the heating constant takes a more typical value and the influence of test frequency can be seen at high stress levels for the R=0.1 data. The sharp kink in the theoretical line is due to a test with a high frequency and effective stress amplitude, resulting in a high temperature and reduced life.

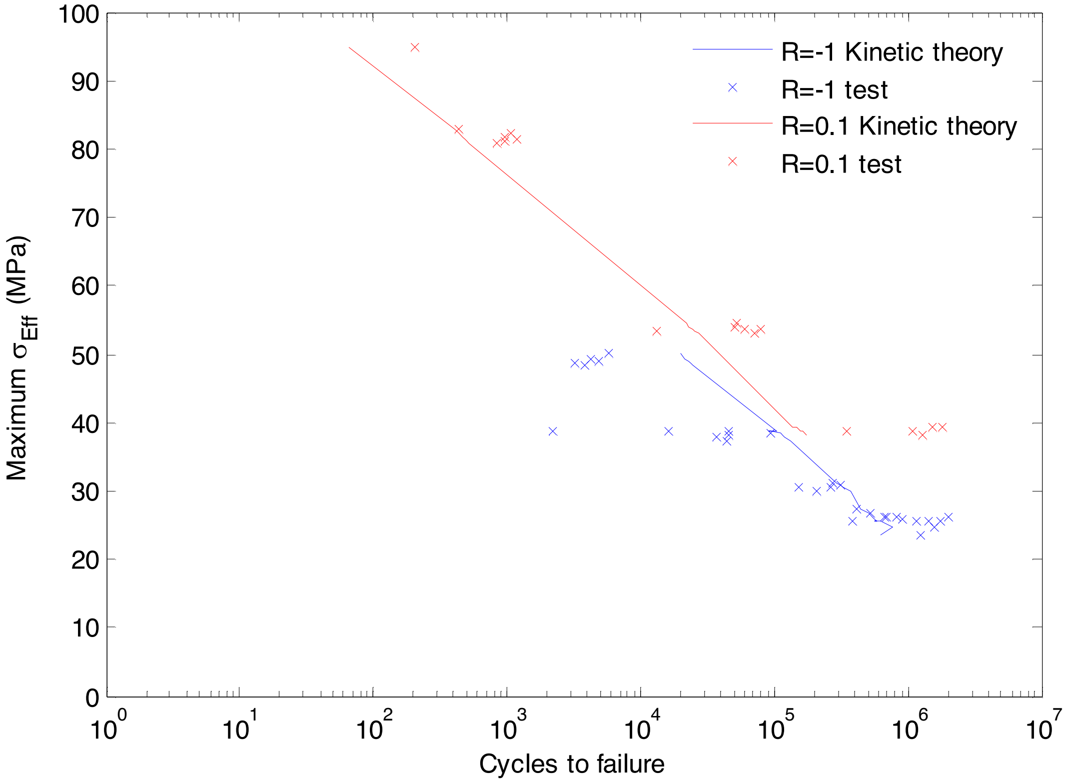

Figure 6.24 - Longitudinal fatigue test characterisation data

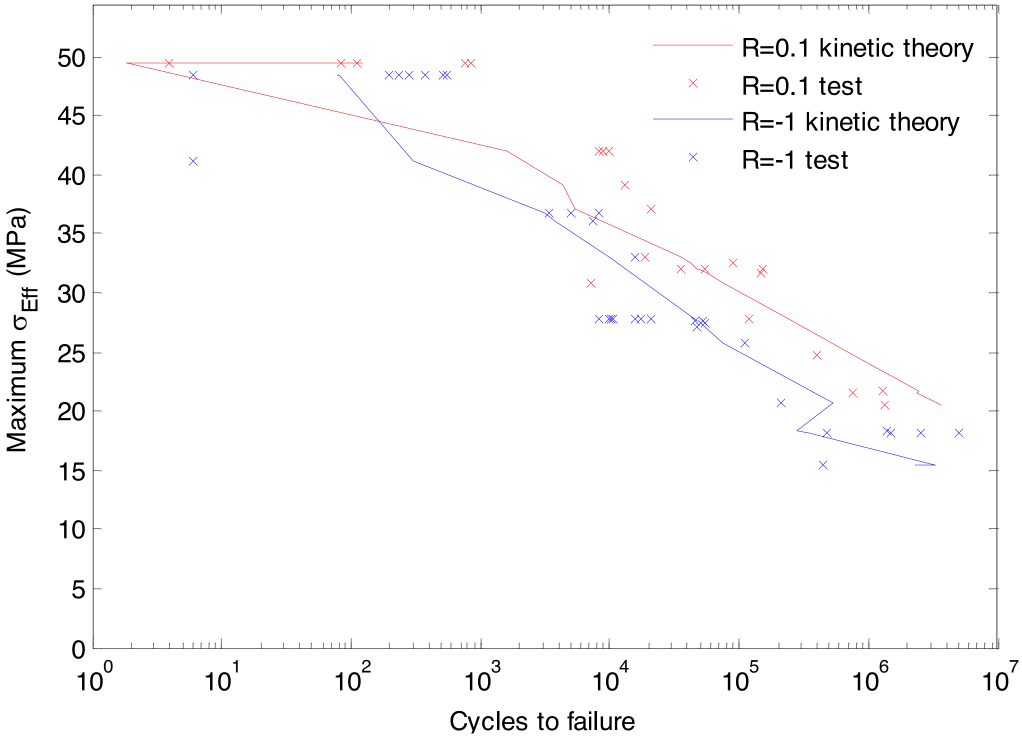

Figure 6.25 – Transverse fatigue test characterisation data

Constant	Description	Value	Units
U_1	Longitudinal activation energy	1.0570e5	J/mol
γ_1	Longitudinal activation volume	2.8840e-4	m^3/mol
ψ_1	Longitudinal hysteretic heating constant	1e-18	Ks^2/Pa^2
U_2	Transverse activation energy	1.1810e5	J/mol
γ_2	Transverse activation volume	8.3176e-4	m^3/mol
ψ_2	Transverse hysteretic heating constant	3.6308e-17	Ks^2/Pa^2

Table 6.3- Constants in kinetic theory equation

This data is used in all subsequent analyses of the laminates from the OPTIDAT database. An attempt was made to improve on the method developed by Fertig and Kenik [71] by allowing the activation volume and energy to vary linearly with mean stress or temperature, but it was found that this rarely improved the results. The changes to their method which did yield improvements without requiring extra characterisation data were mainly due to improving the treatment of data that changed from compressive to tensile loading, and they are listed below.

- Interpolating the matrix stress tensor time history whenever the stress in the 1 direction, 2 direction or 1-2 direction underwent a zero crossing.
- Using the signed Von Mises matrix stress as the stress used to calculate the temperature instead of the effective stress in the kinetic theory equation. This means that reversing tests heat up in a more realistic manner, because the effective stress is never negative in the longitudinal direction.

The multidirectional laminates analysed were laminates MD2 and MD3. Both of these laminates used the same constituent materials as UD3, and their lay-ups are $[[\pm45°, 0°]_4;\pm45°]$ and $[\pm45°]_5$ respectively. The 45° layers are nominally 0.305mm thick and the 0° layers are nominally 0.88mm thick. The 45° layers are not properly characterised as no data is available for laminates consisting solely of 45° layers, but the fibre volume fraction is the same so the data can still be used to analyse 45° layers.

6.3.1.1 UD3 constant amplitude fatigue

In order to demonstrate that the fatigue analysis method described here can be used to perform fatigue analysis at ply angles different to those for which the material was characterised (and thus reduce the amount of fatigue testing required), it has been used to predict failure of a test coupon loaded at 60° from the fibres from data for tests at 0° and 90° from the fibres. The 60° data is the only load angle available for material UD3 in the OPTIDAT database for which sufficient data is available to draw conclusions. It can be seen that the use of multi-continuum theory allows the kinetic theory to accurately predict failure at other ply angles than those for which the material has been characterised, as shown in Figure 6.26. This is consistent with the work of Fertig [136], who obtained excellent results for T800H/2500EP carbon-epoxy composites using this method.

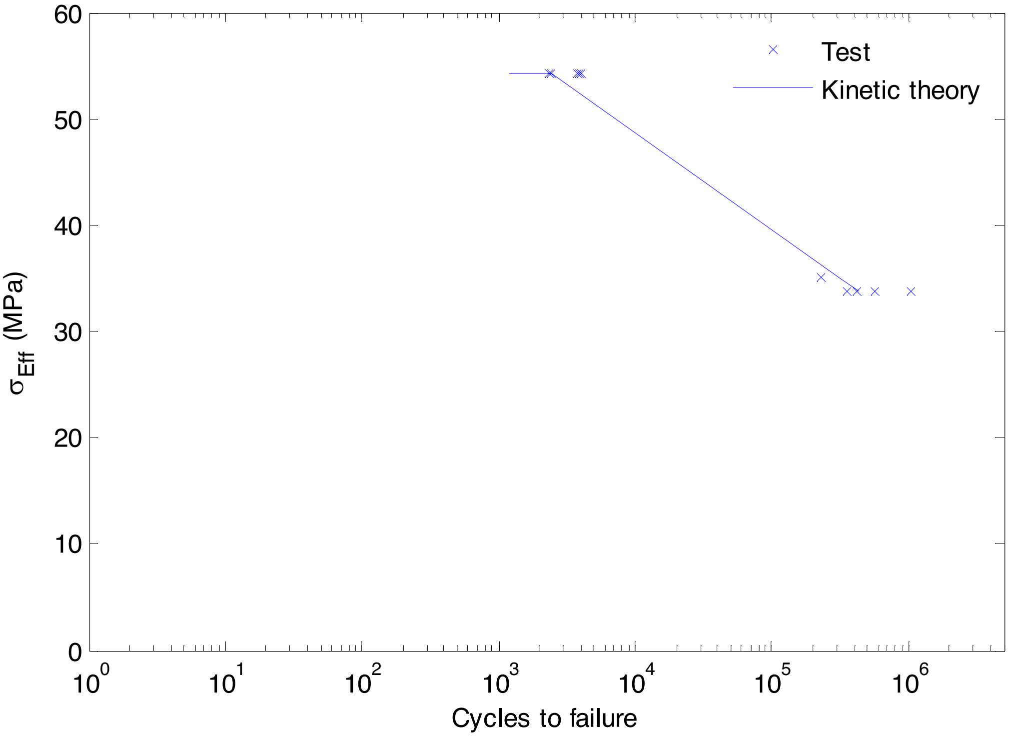

Figure 6.26 - Comparison of test and theory for 60° load angle at R=0.1

As the method has been shown to be suitable for the analysis of unidirectional laminates at a range of loading angles, it will now be applied to the modelling of multi-directional laminates.

6.3.1.2 MD2 progressive failure analysis

The analysis of multidirectional laminates is considerably more complex than unidirectional laminates because the layers will fail at different times, and the load will redistribute across the different plies as the stiffness of the failed plies reduces. Fertig and Kenik presented a damage evolution equation which could be used to analyse single load blocks [71]. This has been modified in the present work to a form that allows multiple load blocks and progressive failure to be analysed, given by equation (6.66). When a layer has failed its stiffness is reduced as described in section 6.2.1. In order to compare how the results differ when progressive failure is implemented, fatigue analysis was performed with and without progressive failure on the MD2 laminate. The results are shown in Figure 6.27. Note that the y-axis shows the composite maximum stress rather than the effective matrix stress, as there are multiple layers. It is clear that the progressive failure analysis is more conservative than the simple analysis, and also that 45° layers fail very early in the composites life compared to the 0° layers. This is consistent with the ‘critical element’ approach adopted by Reifsnider et al [65]. In this case the critical element is the 0° layer.

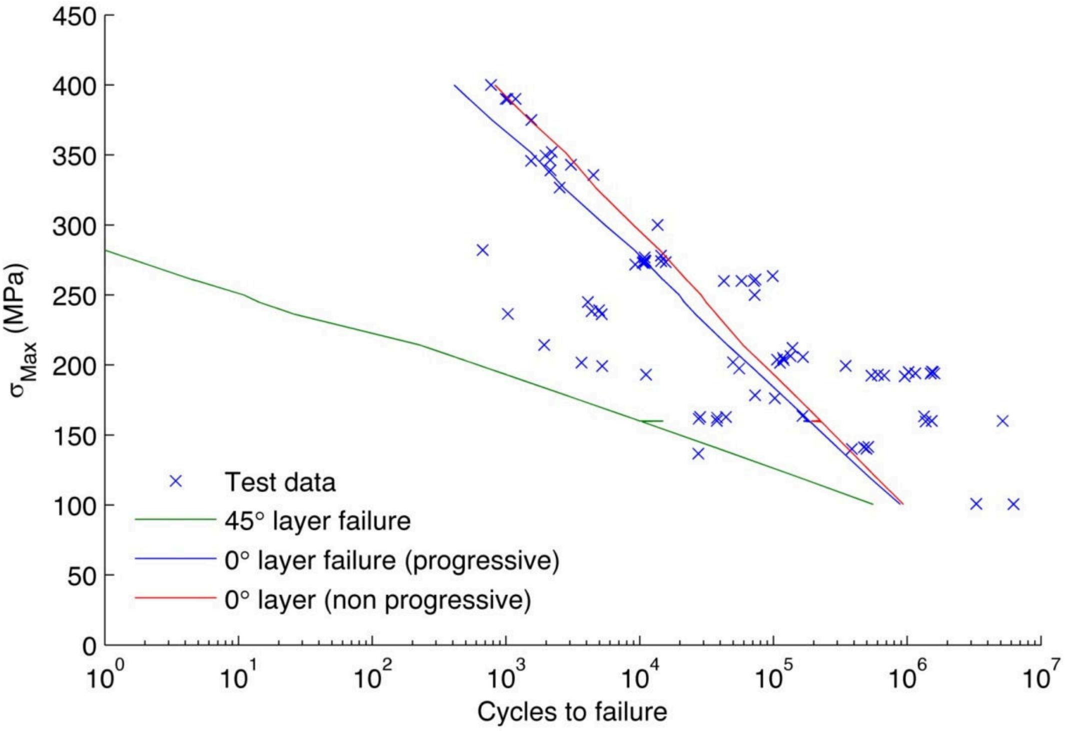

Figure 6.27 - Comparison of progressive failure with simple analysis for MD2 laminate under R=0.1 loading

The progressive failure algorithm described in section 6.2.7 has been shown to work for a multidirectional laminate.

6.3.1.3 MD2 constant amplitude fatigue

With the progressive failure algorithm proven to work for multidirectional laminates, the analysis was performed for all of the constant amplitude R-values for which data was available in the OPTIDAT database [17]. Figure 6.28 show a comparison of theoretical results and physical test results for the MD2 laminate when it is subjected to purely tensile loading. There is rather a lot of scatter in the R=0.1 test data that is not due to temperature or frequency effects (the scatter may be due to the fact that the tests were performed at several different labs) so it is difficult to draw conclusions but it seems overall that the theory is predicting the results well. Insufficient data was available to properly characterise the laminates response to hysteretic heating effects, so the R=0.5 theoretical predictions are conservative. Temperature information was not available for much of the data from the OPTIDAT database, and ambient temperature data is completely unavailable. For this reason, a physical test program which is designed around the fatigue analysis method presented here would be very beneficial.

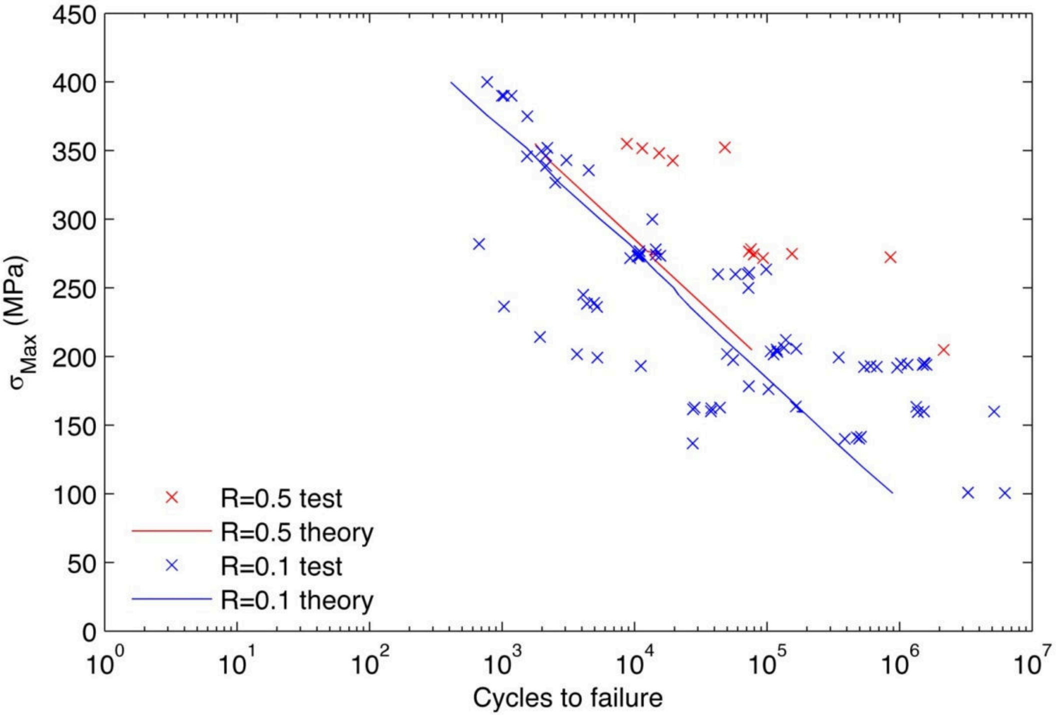

Figure 6.28 - Tensile constant amplitude loading of MD2 laminate

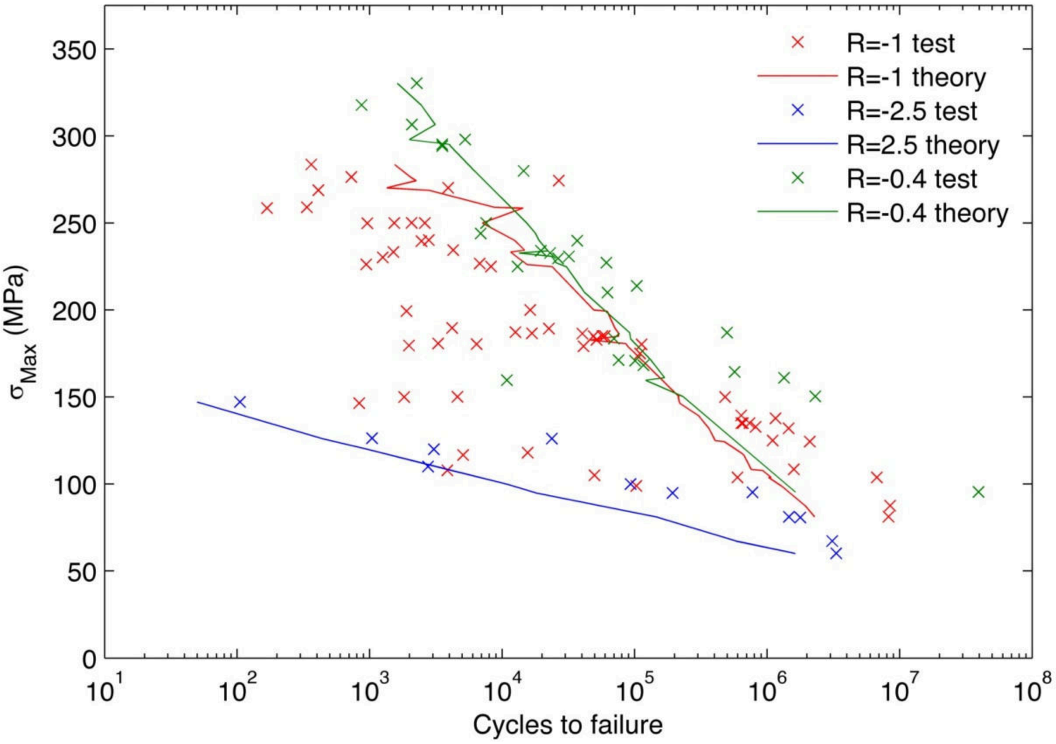

Figure 6.29 - Reversing constant amplitude loading of MD2 laminate

Under combined tensile and compressive (reversing) loading the predictions are still good, as seen in Figure 6.29. There is a huge quantity of R=-1 data in the OPTIDAT database (perhaps because the linear Goodman diagram given in the design standards [11] requires R=-1 data), from many different labs, so it is unsurprising that there is a lot of scatter. Again, a test program focused around the present work would be beneficial so that issues such as ambient temperature which affect the theory can be recorded. The R=-0.4 (tensile dominated) and R=-2.5 (compression dominated) results are better, as they come from only two different labs so there is less scatter in the test data.

The compressive results are very poor, as shown in Figure 6.30. The 45° layer failure predictions may well be correct, but unfortunately the 0° layers are not predicted well. The reason for this is the failure mode of unidirectional plies loaded parallel to the fibres is not accounted for. The anisotropic predictions (in which the 45° layers retain more stiffness, because the fibre direction is still almost as stiff as it was before failure) are too low, because in reality the fibres in the post failure 45° layers will not be able to transmit significant tensile transverse loads into the 0° layers. The isotropic predictions (in which the stiffness of the failed layers is reduced to 1% of its original value in all directions) are too high, as the small transverse loads which are still allowed through are insufficient to do any damage. The true failure mode in compression is likely to be delamination (due to free edge out of plane stresses and inter-laminar shear stresses) followed by buckling [45].

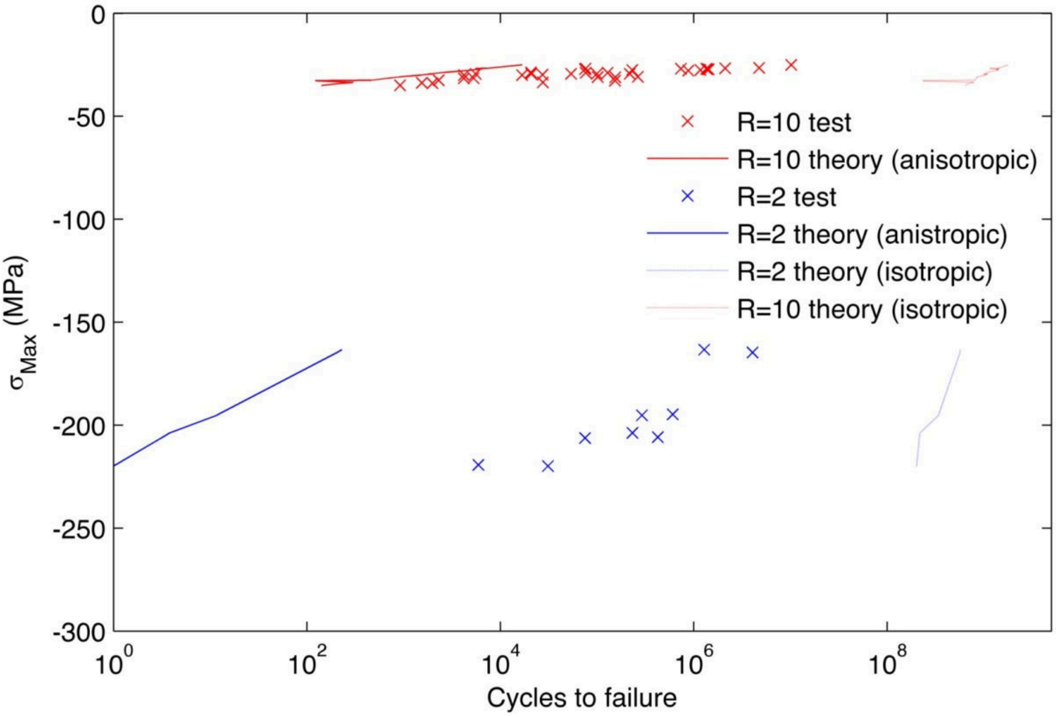

Figure 6.30 – Compressive constant amplitude loading of MD2 laminate

This failure mode is impossible to model using the present plane-stress composite stress analysis method. Several authors have developed finite elements for modelling free-edge stresses [137] and inter-laminar shear, and the compressive behaviour of the laminates is something that will be investigated in future work. The compressive test specimens shown in Figure 6.31 have failed in this manner, and those shown in Figure 6.32 would have failed in this way had the loading continued. In Figure 6.32 it is clear that the delaminations initiated at the free edges.

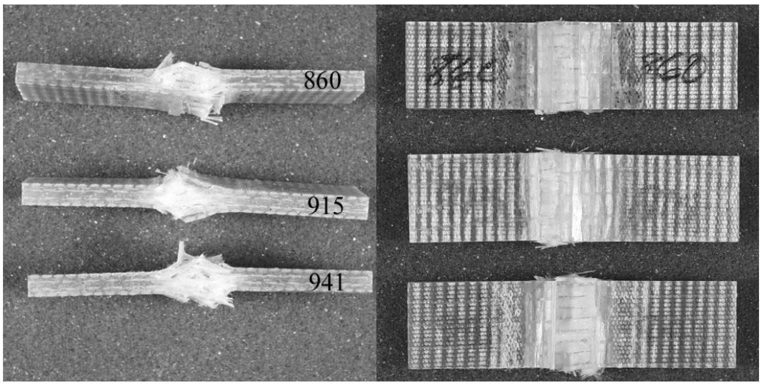

Figure 6.31 - Multidirectional laminate failure resulting from compressive loading [49]

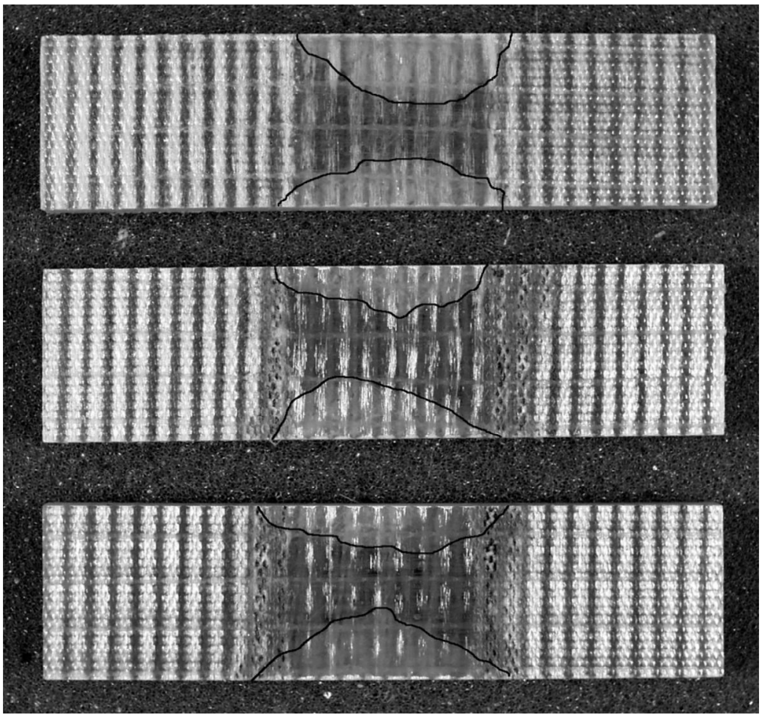

Figure 6.32 - Run out multidirectional compressive test laminates [49]

The compressive failure is not necessarily a problem for full scale blade analysis; the suction side of the blade is often not analysed for fatigue anyway and if isotropic degradation is chosen as the failure mode then the blade will continue to survive after any 45° layers have failed. The behaviour under tensile and reversing loading is acceptable (considering the uncertainty resulting from incomplete knowledge of the physical testing), so the method can be used to analyse wind turbine fatigue spectra such as WISPER and WISPERX.

6.3.1.4 Wind turbine spectra

The WISPER (Wind SPEctrum Reference) and WISPERX spectra were developed in 1992 to provide the wind turbine industry with a standard variable amplitude load time history for fatigue testing [138, 139]. They were synthesised from measured flapwise root bending loads on 9 different turbines of vastly different sizes. More recently, the NEW WISPER spectrum was created as part of the OPTIMAT project [140]. This spectrum is more representative of the variable speed/ variable pitch turbines which are prevalent today, but there is very little NEW WISPER data for laminate MD2 in the OPTIDAT database. The scaling values for the WISPER and WISPERX spectra are shown in Figure 6.33 and Figure 6.34 respectively.

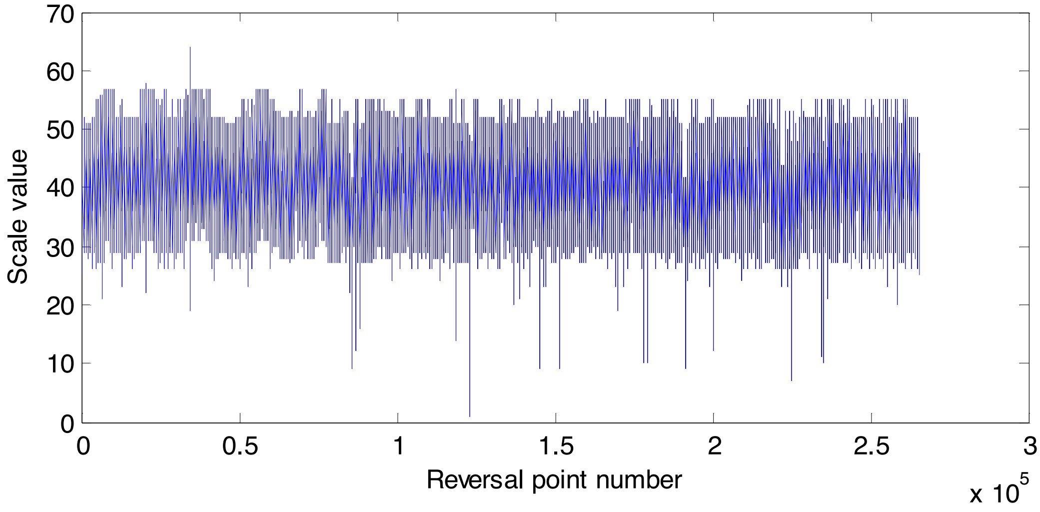

Figure 6.33 - WISPER spectrum

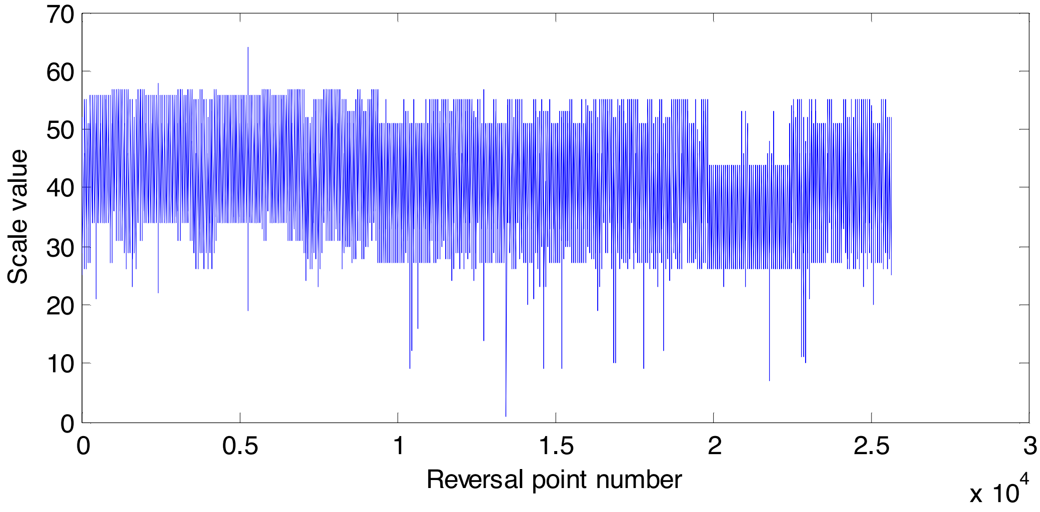

Figure 6.34 - WISPERX spectrum

The WISPER spectrum consists of around 265000 load reversal points, and the WISPERX has around 26500 points. The OPTIDAT database has fatigue results for the two spectra defined by the maximum stress, the load rate, the number of spectrum repeats, and the total number of cycles. The fatigue testing machines used in the OPTIMAT project are controlled so that the load follows a ‘haversine’ (half sine wave) between adjacent reversal points. The load rate given in the OPTIDAT project is therefore the peak rate, so in order for the piecewise linear approximation used in the present work to be more accurate the calculated time between load reversals must be extended by a factor of $\pi/2$.

The results for the WISPER spectrum are shown in Figure 6.35. The present analysis method gives conservative results, sometimes by a factor of a decade. This is consistent with other analyses of the spectrum, but in the present case it could be due to the limited data available to characterise the longitudinal direction hysteretic heating response for the longitudinal failure mode. A further issue which could cause shorter lifetimes is the temperature prediction; many of the WISPER tests only have a few repeats, so the temperature could be much lower than the temperature used in the analysis for much of the specimen life. Again, it would be very beneficial to perform tests focused around the kinetic theory of fracture so that the specimen temperature could be recorded throughout the process.

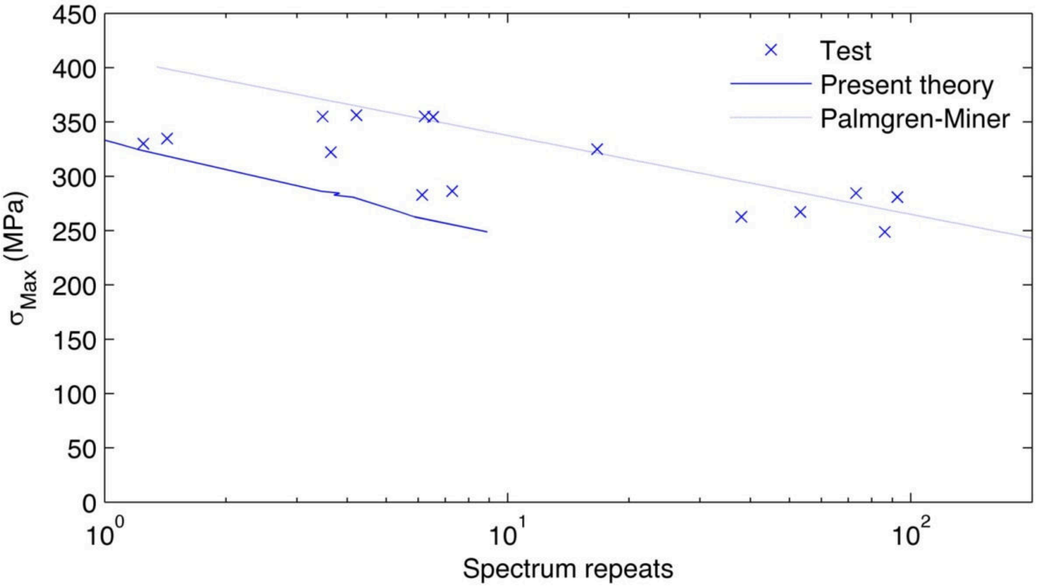

Figure 6.35 - Comparison of theory and test results for WISPER spectrum

The results for the WISPERX spectrum, shown in Figure 6.36, are better. This could be because the shorter time history means more repeats are performed, so the temperatures predicted in the analysis are more representative of those occurring in practice. Of particular note are the three specimens tested at maximum stresses of between 277 and 287 MPa. These three specimens were tested with load rates that were nearly double those in the specimens immediately above and below on the graph, and because the 0° ply failure dictates the life and the hysteretic heating constant for this direction is low (because of insufficient data) the specimens last much longer in terms of number of cycles.

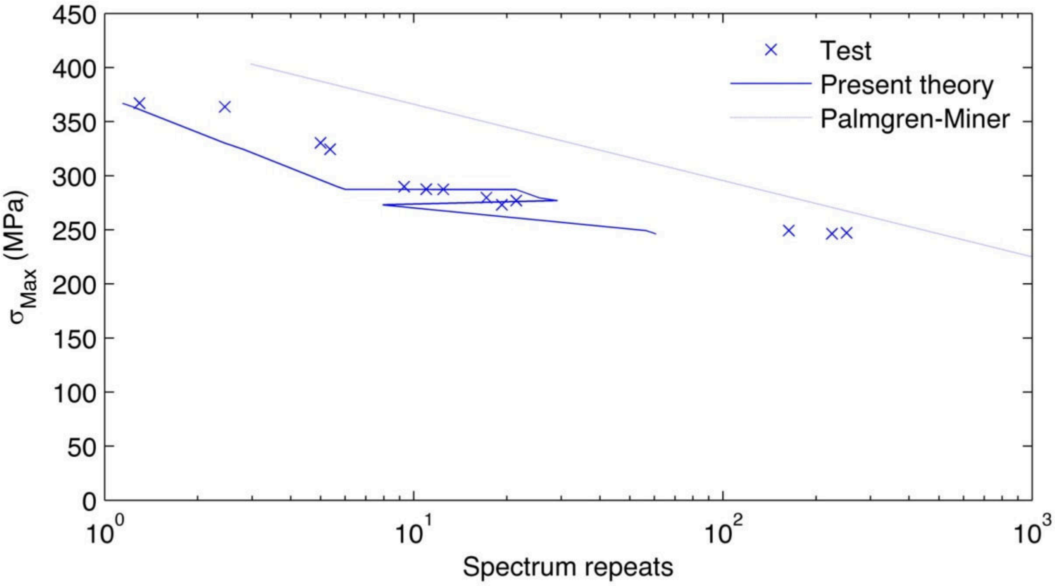

Figure 6.36 - Comparison of theory and test results for WISPERX spectrum

Although the OPTIDAT database is an excellent composite fatigue resource, there are limitations when it is to be used for a kinetic theory based validation. However, the quality of the predictions made using the WISPER and WISPERX spectra are typical of other published work such as [46, 48, 69]. Crucially, the results are conservative; many other methods are non conservative when applied to variable amplitude loading. The line marked ‘Palmgren-Miner’ on Figure 6.35 and Figure 6.36 was obtained from work by Nijssen [41] on spectrum fatigue. It is for the same laminate and the predictions were produced using a ‘best practice’ conventional fatigue analysis, and are clearly considerably less conservative. A possible cause for the more conservative nature of the present results is that the WISPER spectrum is tensile dominated, so ‘time at load’ effects will play a part in the number of cycles that can be tolerated. Other methods do not account for this, whereas the kinetic theory approach presented here does.

6.3.1.5 Residual strength simulations of MD2

The physics based method applied in the present work has certain advantages because the damage parameter that evolves as bonds are ruptured tracks a physical characteristic of the material (the proportion of microcracks compared to the proportion at failure). This means that the method should be able to predict residual strength degradation test results. Residual strength based methods were described in detail in chapter 2, and their basis is that the strength of the material is tracked, and when a load is applied that results in a greater stress than the residual strength of the material failure occurs.

Residual strength tests were performed as part of the OPTIDAT project, and consisted of fatigue cycling followed by a tensile or compressive static test. The compressive tests were not studied in this work as it had already been established that the model was incapable of simulating compressive failure of plies loaded in line with the fibres.

Furthermore, there are some barriers to the use of this method for the prediction of residual strength. In the context of fatigue, the time to failure is mostly made up from cracks developing in the matrix, with the fibres failing at the end of the life when the matrix can no longer distribute the load between them. This assumption may not hold under the faster load conditions of static testing. In order to establish if this was the case, the theoretical value of the damage parameter n (see equation (6.66)) in the 0° plies after the fatigue test of MD2 coupons was plotted against the laminates static tensile strength after fatigue testing. Only laminates tested at the same displacement rate (0.25mm/min) are shown, as increased strain rate has been shown to increase the ultimate strength [41] (which is predicted by the kinetic theory of fracture). The static portion of the test was implemented as a series of load blocks, with the stress increasing linearly across each block by 1 MPa and the length in seconds of the block calculated from the rate of change of the applied stress. The stress rate σ_C was calculated from the displacement rate using equation (6.72), where x is the testing machine grip displacement, E_C is the composite Young’s modulus in the load direction and L is the gauge length of the test specimen.

$$\frac{d\sigma_C}{dt} = \frac{dx}{dt}\frac{E_C}{L} \tag{6.72}$$

The results are shown in Figure 6.37 for the actual test specimens.

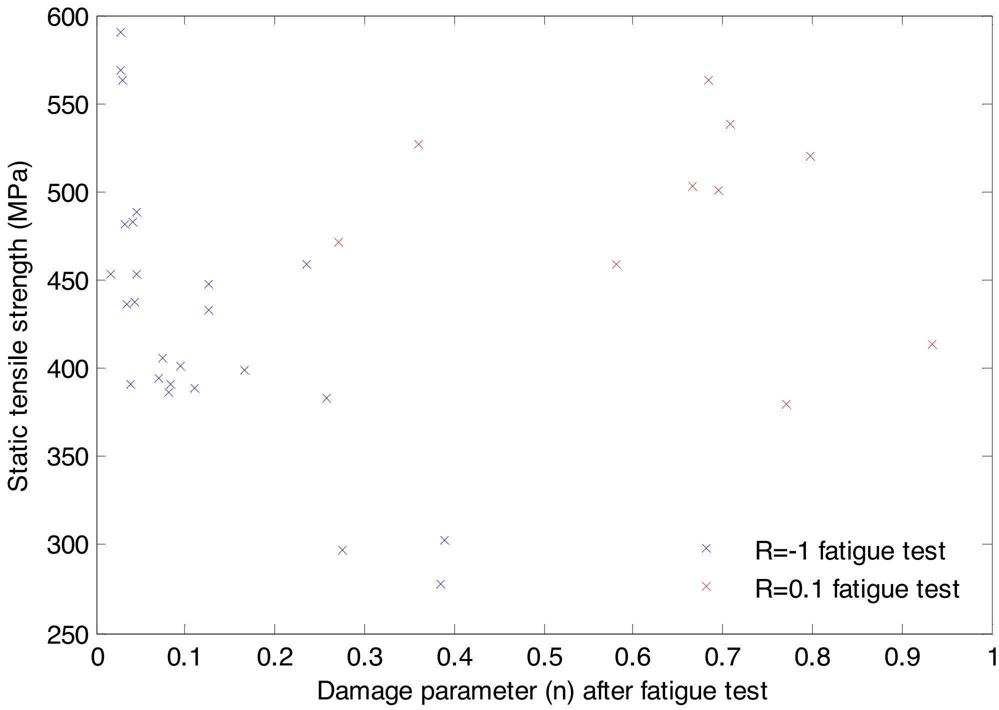

Figure 6.37 - Relationship of damage parameter to ultimate tensile strength

There is a general trend towards higher static strength for the specimens that are theoretically less damaged by the fatigue test, but there is a great deal of scatter, particularly for the R=-1 specimens with a low initial damage parameter. There are many factors which are not accounted for in the present work that may have a greater influence under static test conditions than they would in a fatigue test. These include fibre-matrix debonding, fibre breakage and damage outside of the gauge length of the specimens.

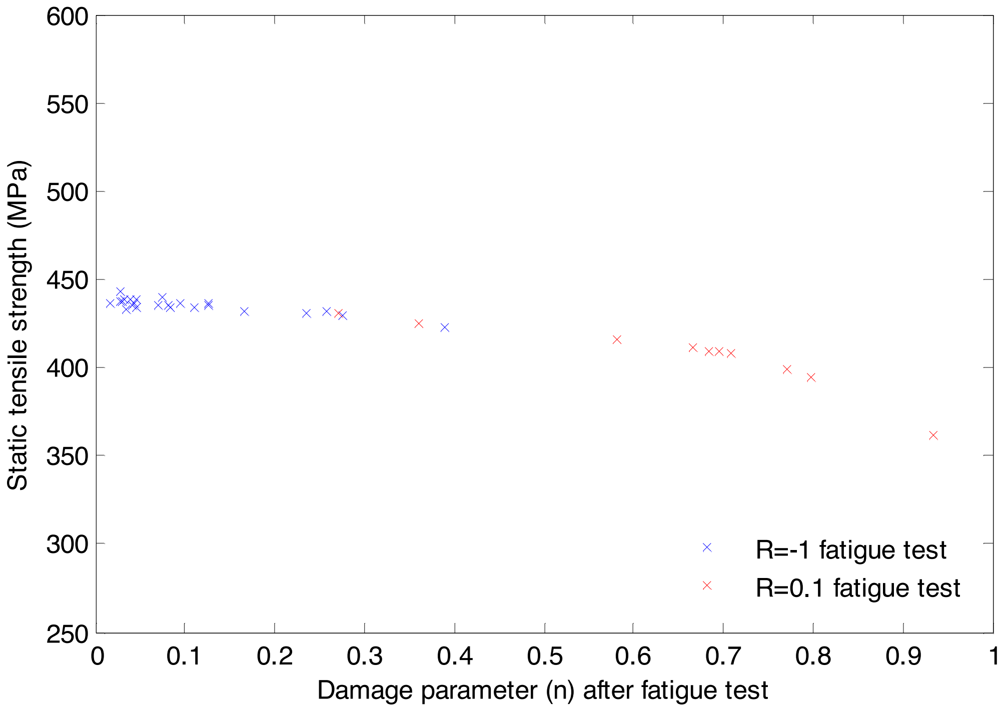

Figure 6.38 – Relationship of damage parameter to predicted ultimate tensile strength

If the same comparison is made as above for the theoretical predictions of ultimate tensile strength from kinetic theory it can be seen that there is much less variation in the final strengths. The results are shown in Figure 6.38.

The prediction of the ultimate strength is very reasonable when compared to the physical results shown in Figure 6.37, but the ultimate strength is not greatly affected by the initial fatigue damage until n approaches unity. This is consistent with many residual strength models [42], but in reality it seems there are other factors to consider with static testing that are not accounted for with the present model.

6.3.1.6 *Prediction of static failure*

As discussed above, the static strength of composites is affected by the rate at which they are tested. In order to ascertain if the model could usefully predict static failure, it was used to model the tensile static failure of several different laminates. The results for the unidirectional laminate UD2 loaded parallel to the fibres are shown in Figure 6.39.

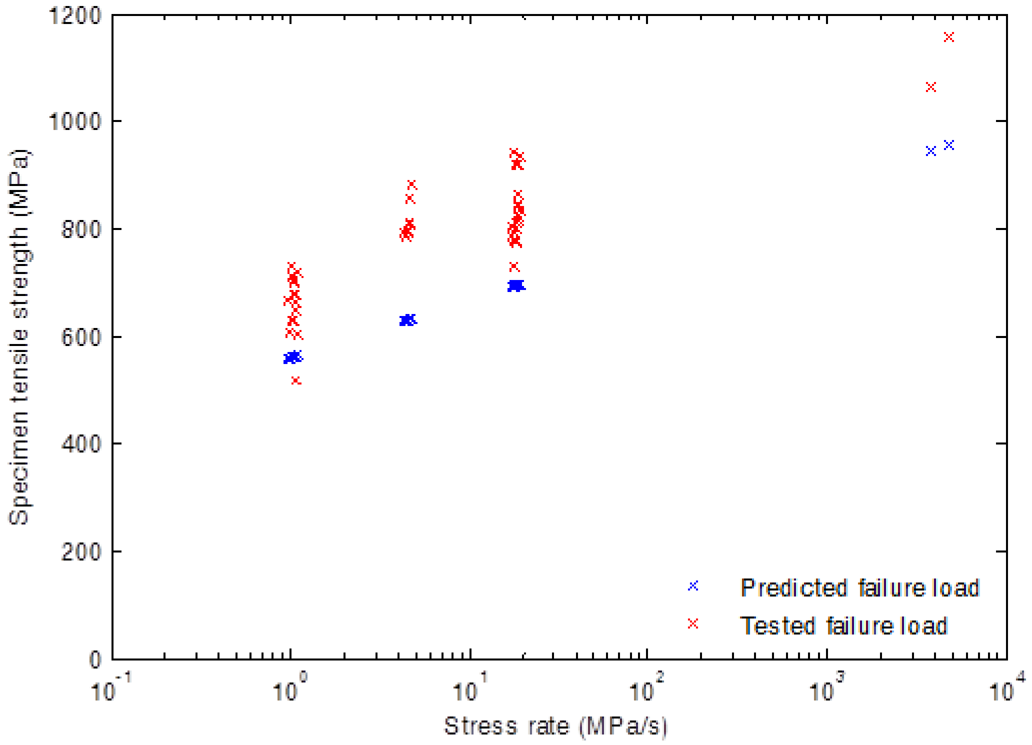

Figure 6.39 - Comparison of predicted and tested ultimate tensile strength for UD2 specimens loaded at 0° to fibres

It can clearly be seen that is a trend towards increased strength for increasing stress rate in both the predictions and the physical test results. In the predictions there is a linear relationship between increasing stress rate and ultimate tensile strength, as predicted by kinetic theory. The predicted ultimate failure stress is consistently lower than that for the physical tests, most probably because the method used in the present work predicts failure of the matrix rather than the composite as a whole. In order to increase the accuracy of the predictions it would be necessary to extend the present theory to the fibres as well as the matrix, and account for stress redistribution across the fibres as the load increases. As the present work focuses on fatigue, this has not been done but it could be a future area for research.

The results improve greatly when failure of the fibres is no longer an issue. Figure 6.40 shows a comparison between predicted results and physical test results for a unidirectional laminate loaded perpendicular to the fibres. The mean error in the results is around 5% and the predictions are slightly conservative, so the method can predict failures which occur exclusively due to processes occurring in the matrix very well.

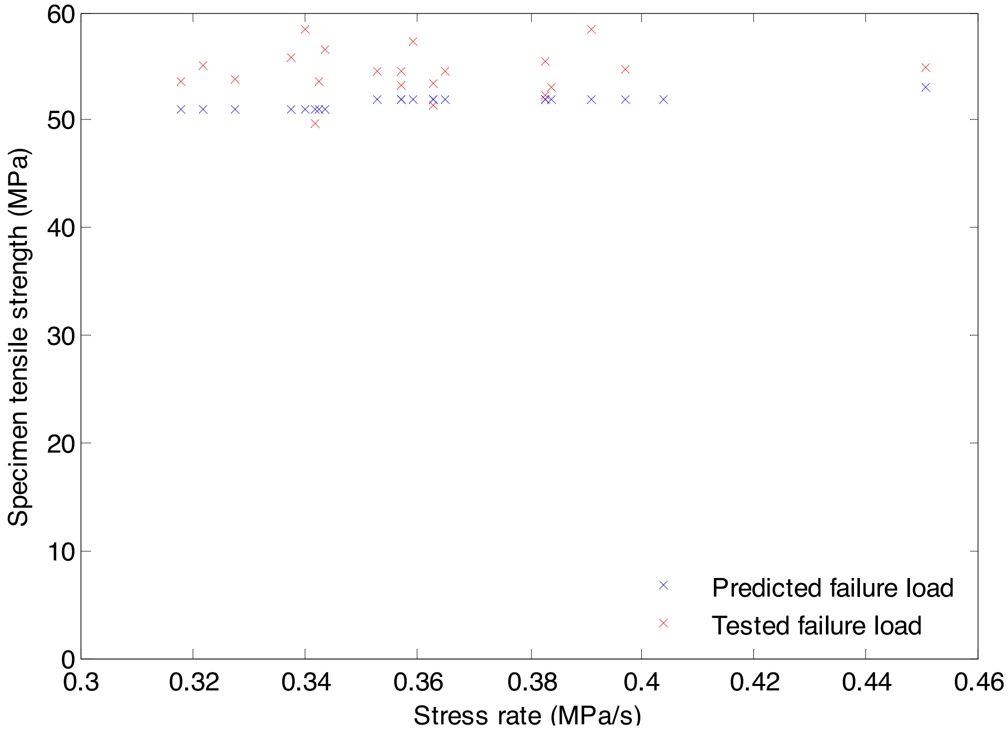

Figure 6.40 - Comparison of predicted and tested ultimate tensile strength for UD2 specimens loaded at 90° to fibres

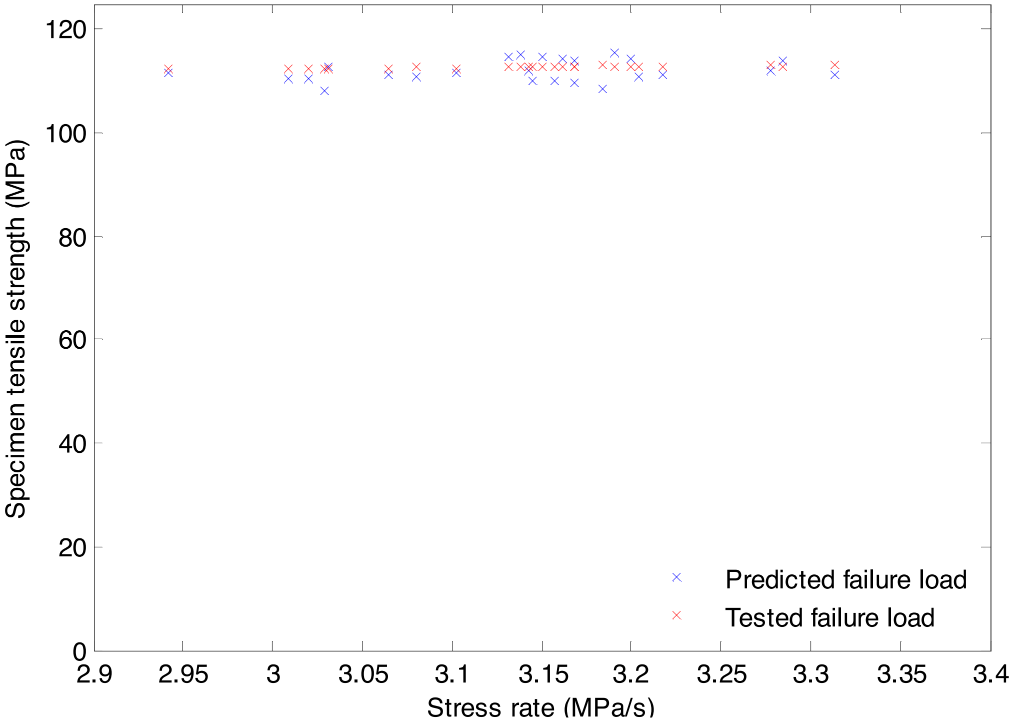

Figure 6.41 - Comparison of predicted and tested ultimate tensile strength for MD3 specimens

When the analysis is performed for laminate MD3 (which is composed of 5 layers of bi-axial fabric orientated at ±45° from the direction of the applied load) the results are again very good. Figure 6.41 shows a comparison of the predicted and actual failure stresses for this laminate.

Again, the predictions agree very favourably with physical test data. In this case the mean discrepancy between the predicted ultimate tensile strength and the actual values is less than 2%. Failure of this laminate is again dictated by the matrix behaviour, and it is encouraging that the method achieves good agreement for this type of laminate as bi-axial fabrics are very frequently used in wind turbine blades for the shear webs and aerodynamic faces.

The final laminate analysed for static failure is the MD2 type which was used for most of the previous fatigue analysis work. This laminate combines load bearing 0° layers with ±45° layers, and the effect of the 0°layers can be seen in Figure 6.42.

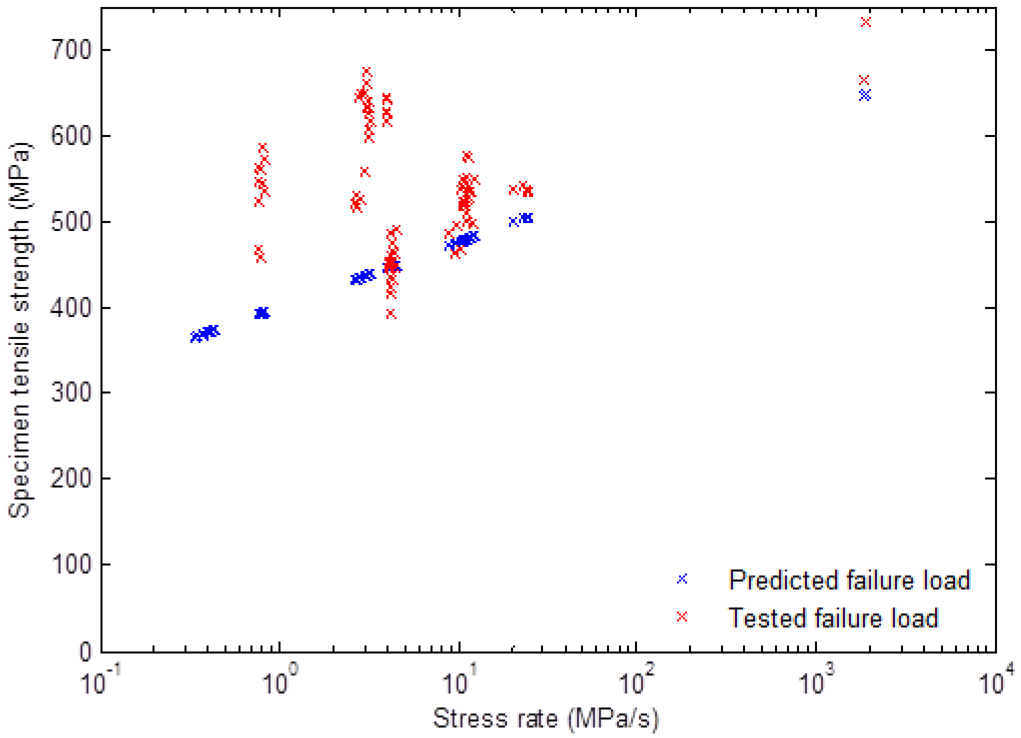

Figure 6.42 - Comparison of predicted and tested ultimate tensile strength for MD2 specimens

Just as in the case of the unidirectional test specimen loaded in line with the fibres, the effect of the stress redistributing across the fibres can be seen again both in the increased amount of scatter for the physical test specimen strengths and the overly conservative predicted failure stresses from kinetic theory. It is interesting to note that at higher strain rates (when there is less time for the stress to redistribute across the fibres) the predicted results are more accurate as failure tends to be more of a matrix dominated event. Again, the method appears to account for the effects of stress rate well.

It is worth reiterating that the predicted ultimate tensile strengths here were derived solely from on and off axis fatigue data for a single ply, and that the relationship between static failure and fatigue failure has been much discussed in the literature (Nijssen's review can be found in [41]).

The present method allows the fatigue behaviour and static behaviour to be considered together (particularly if it were extended to cover failure of the fibres).

6.3.2 Fatigue analysis of the LM 40.3 P2 blade

As the analysis method has been proven to be effective for tensile and reversing loading, it can be applied to the fatigue analysis of a complete blade. The slope of the SN curve for compressive loading tends to be flat, so fatigue in compression is not a design driver for wind turbine blades. This was demonstrated in chapter 3.

Blade design data has been provided by LM Wind Power in the form of a shell finite element model of the LM 40.3 P2 blade. The model includes information on the geometry, materials and lay-up used across the whole blade. Material strength and stiffness data was also provided, and cross sectional loads were given for 20 points along the blade length for all of the load cases required by the design standards [10, 11].

Much of the information is commercially sensitive, and where this is the case data has been normalised. Information about the blade is given in Table 6.4.

Designation	LM 40.3 P2
Length (m)	40.00
Blade mass (kg)	6022
Bolt circle diameter (m)	1.80
Wind class	IEC IIIA
Annual average wind speed (m/s)	7.5
Weibull shape parameter	2

Table 6.4 - LM 40.3 P2 data

A MATLAB program to read information from the finite element model input file and convert it into the data structure given in Figure 6.2 was written. Using this program, it is possible to ‘slice’ the blade at each of the 20 cross sections at which load data is available, and obtain a beam model of the blade. There are over 30 different materials used in the blade FE model, but most of them have stiffness properties reasonably close to those given in the supplied material data. Only those plies which are made from fibre reinforced plastic are analysed, so core materials, glue and gelcoat are ignored (except for in the calculation of the blade stiffness and shear flow distribution).

Almost all of the required information discussed in section 6.3.1 was supplied for the unidirectional material that forms most of the blade. The only information that was not supplied was the strength in tension and compression in the 2 direction and the shear strength, which was either estimated from the fatigue data or obtained from similar materials in the DOE/MSU database [62]. As the strength and stiffness values are commercially sensitive, only the normalised fatigue curves for the 1-direction and 2-direction will be shown here.

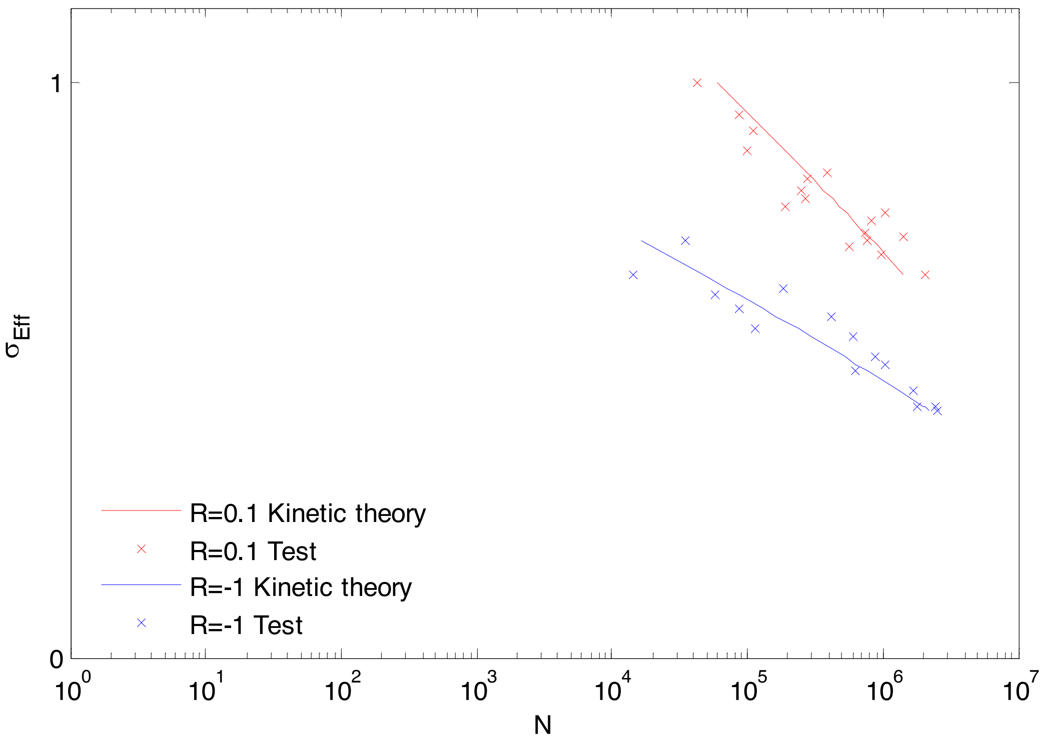

Figure 6.43 - LM 1-axis fatigue data (normalised)

Figure 6.43 shows fatigue data for the 1-axis (longitudinal) direction along with the predictions obtained using the kinetic theory of fracture. There is much less scatter in the characterisation data, as all coupons were tested at the same frequency, in the same lab and under the same cooling conditions. This has enabled a much better fit than was possible when characterising the longitudinal variables for material UD3 from the OPTIDAT database.

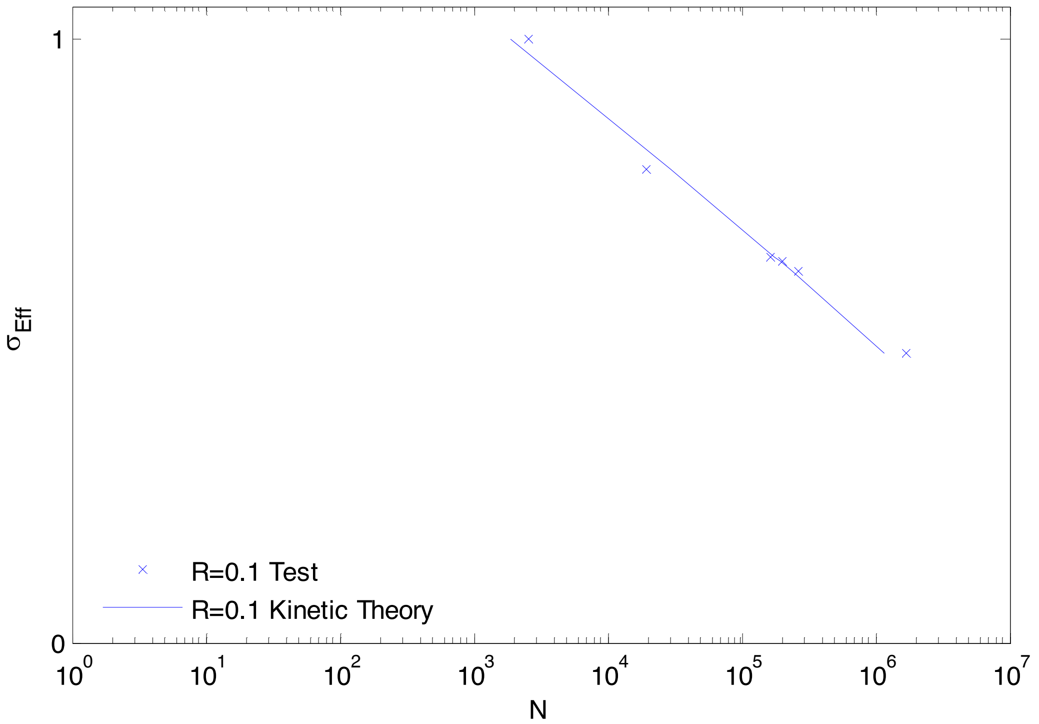

Figure 6.44 - LM 2-axis fatigue data (normalised)

An interesting feature of the fatigue data provided by LM Wind Power is that the activation energy, U, has the same value for the longitudinal and transverse directions. In Figure 6.12 it was seen that the activation energy is usually a material constant, and the activation volume γ varies depending on the state of a material. Again, this could be because all coupons were tested under similar circumstances.

There is limited data available for the 2-axis (transverse) direction, but the fit is very good to the available data, as shown in Figure 6.44. The temperature on a full wind turbine blade in operation is very unlikely to be significantly different from ambient as there is a constant cooling flow of air over the blades, so the hysteretic temperature constant is less important than when trying to validate coupon data. However, during full scale fatigue testing the temperature can rise because the cooling airflow is slower and the frequency and applied stresses are higher.

There are several variables in the fatigue algorithm developed in the present work that will have a significant effect on the fatigue life. These are the sequence of the load cases, whether shear flow is included in the calculations, the life proportion at which the low stress correction described in section 6.2.6.4 comes into effect, and the method used to degrade the stiffness of the blade. It is impossible to study the effect of every single combination of these factors, but by taking them in turn it is possible to arrive at an analysis method that is conservative without being unrealistically harsh. The combinations of simulation parameters used here are shown in Table 6.5, with the values that are used when studying the effects of other variables highlighted.

	Shear flow	Stiffness degradation factor	Kinetic theory cut off	Load case order
Value	On	Anisotropic – 0.01	d=0.85	Random
		Anisotropic – 0. 5	d=0.9	Ascending
	Off	Isotropic – 0.01	d=0.95	Descending
		Isotropic - 0. 5	d=1	20 year repeat

Table 6.5 - Simulation configuration parameters

Furthermore, the effects can be studied without analysing every blade section for which data is available; for the purposes of finding the best simulation configuration we can restrict the analysis to the blade root and a mid-span section.

There are several criteria that can be used to judge how harsh a simulation configuration is on the blade. These include:

- Number of years of operation until a transverse and longitudinal ply failure occurs.
- Blade stiffness at end of life compared to stiffness at start of life.
- Percentage of plies that have failed in the transverse and longitudinal direction at the end of the life. This is useful because it gives an idea of how harsh a simulation configuration is on the blade.
- Maximum normal and shear strain in any element during the course of a simulation. This is of interest when comparing stiffness degradation models.
- Maximum effective stress during a simulation. This is useful when assessing when the transition from kinetic theory to power law behaviour should begin.
- Maximum transverse and longitudinal damage
- Average transverse and longitudinal damage

Using these metrics, and visual comparisons of the damage distribution around the blade, it is possible to choose appropriate simulation parameters.

6.3.2.1 Effect of load order

The damage accumulation equation discussed in section 6.2.6.5 will cause different amounts of damage depending on whether the high loads occur early on in the life of the blade or towards the end. In Figure 6.20 it can be seen that for the $\lambda = 1$ line the integral of K_B between 0 and 0.2 causes the damage parameter n to increase by around 0.3 whereas between 0.8 and 1 n only increases by approximately 0.15. This implies that harsher load cases occurring at the start of the load case sequence will cause more damage than if they occurred at the end of the load case sequence.

The results for the blade root section are shown in Table 6.6.

	Low-High		**High-Low**		**Random**		**20 year repeat**	
	Flap	Edge	Flap	Edge	Flap	Edge	Flap	Edge
End of life stiffness (% start)	99.9	99.9	99.9	99.9	99.9	99.9	99.9	99.9
	Normal	Shear	Normal	Shear	Normal	Shear	Normal	Shear
Maximum strain – (με)	491.74	270.99	491.21	270.56	491.74	270.99	491.74	270.99
	1-axis	2-axis	1-axis	2-axis	1-axis	2-axis	1-axis	2-axis
First failure (years)	-	17.67	-	4.49	-	15.81	-	12.64
Percentage failed (%)	0	2.96	0	2.96	0	2.96	0	2.96
Maximum effective stress (MPa)	4.32	11.86	4.29	1.21e7	4.32	11.86	4.33e6	1.21e7
Maximum damage	8.65e-6	1	8.66e-6	1	8.65e-6	1	8.65e-6	1
Average damage	2.80e-7	0.0589	2.81e-7	0.059	2.80e-7	0.0589	2.80e-7	0.0588

Table 6.6 - Effect of load case sequence on blade root section damage signifiers

The effect of the load order on the root section is not significant. The only damage signifier which changes much between the four load case sequences is the time to the first failure. As predicted, the sequence with the most harsh load cases first (‘High-Low’) is the most damaging, and the sequence with the most harsh cases at the end (‘Low-High’) is the least damaging. The ‘Random’ and ’20 year repeat’ scenarios give very similar results. This is significant because the ’20 year repeat’ scenario is the most realistic. This block sequence is comprised of 20 year-long repeats of the sequence, whereas the random sequence is composed of one 20 year set of load cases. The disadvantage with the 20 year repeat scenario is that it takes 20 times as long to run, so it is good that randomly ordered load blocks summing to 20 years produce similar results.

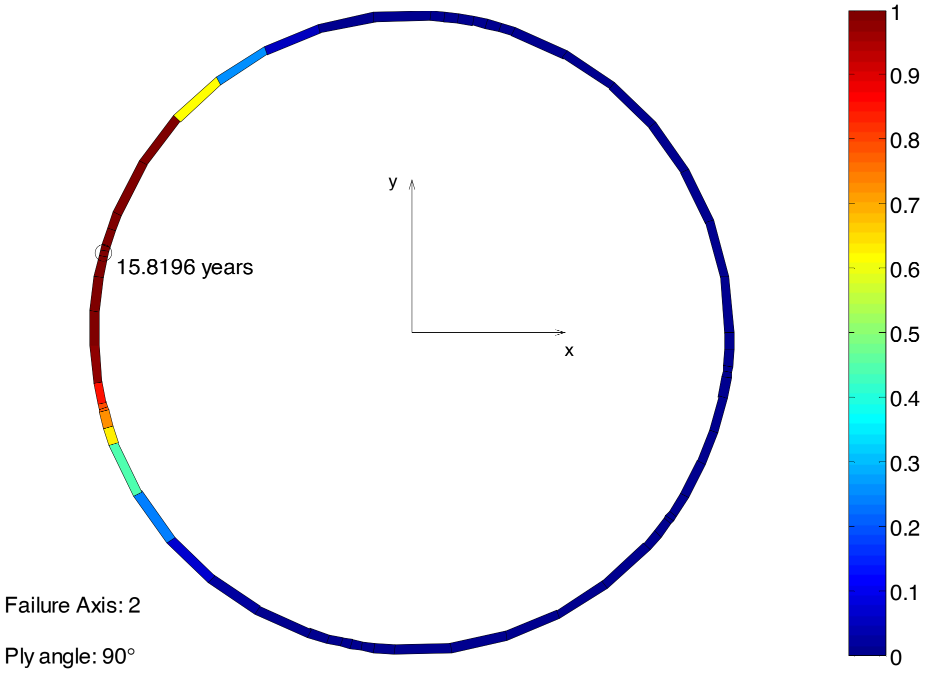

Figure 6.45 - Transverse damage parameter in 90° plies of blade root section

The only plies which failed in the root analysis for any load order were plies orientated at 90° to the spanwise direction, as shown in Figure 6.45. The damaged area is consistent with the conventional fatigue analysis performed in chapter 3 (blade dimensions are not shown as they are commercially sensitive, and the thickness of each element is shown as the average element thickness).

The same number of plies fail in all scenarios, and as such the maximum strain does not change. The low number of failures means that the blade stiffness does not degrade much during the analysis.

The results for the blade mid-span section are shown in Table 6.7. The percentage of plies which fail is much higher, although there are still no longitudinal failures. However, it is important to note that the maximum longitudinal damage is much closer to 1.

Again, the same number of plies fail in all scenarios so the maximum strain does not vary much. The variation which is present is due to the sequence of the load cases changing.

	Low-High		**High-Low**		**Random**		**20 year repeat**	
	Flap	Edge	Flap	Edge	Flap	Edge	Flap	Edge
End of life stiffness - Flap/Edge - (% start)	98.5	99.4	98.5	99.4	98.5	99.4	98.5	99.4
	Normal	Shear	Normal	Shear	Normal	Shear	Normal	Shear
Maximum strain - Normal/Shear – (με)	712	1675	723	1672	723	1674	726	1679
	1-axis	2-axis	1-axis	2-axis	1-axis	2-axis	1-axis	2-axis
First failure (years)	-	8.85	-	0.038	-	3.51	-	0.36
Percentage failed (%)	0	22.8	0	22.8	0	22.8	0	22.8
Maximum effective stress (MPa)	7.70	20.03	7.64	24.66	7.67	26.44	7.70	26.44
Maximum damage	0.0028	1	0.0028	1	0.0028	1	0.0028	1
Average damage	8.2e-5	0.262	8.2e-5	0.262	8.2e-5	0.262	8.2e-5	0.262

Table 6.7 - Effect of load case sequence on blade mid-span section damage signifiers

The anisotropic stiffness degradation model used means that 45° layers retain their stiffness in the fibre direction, so the effective Young's modulus does not reduce significantly. This is reflected in the fact that the bending stiffness does not degrade much.

The most appropriate load case order is a random sequence of the load cases. This is because it is not unduly harsh and is more realistic than ascending or descending load case sequences. It is also much quicker to perform analyses with than a repeating sequence of load cases. The load cases were randomly ordered once, and the same random sequence will be used for all subsequent analyses.

6.3.2.2 *Effect of kinetic theory cut-off point*

As discussed in section 6.2.6.4, the log-linear relationship between the bond-rupture rate and applied stress does not persist into the low stress regime. In the present work, this has been accounted for by transitioning from the kinetic theory approach at higher stresses to a power law approach at lower stresses. The stress at which this transition occurs is dependent on the factor d in equation (6.61). The value of this variable for the three materials in Figure 6.13 was calculated to be between 0.82 and 0.86.

	d=0.85		**d=0.9**		**d=0.95**		**d=1**	
	Flap	Edge	Flap	Edge	Flap	Edge	Flap	Edge
End of life stiffness (% start)	100	100	99.7	99.9	98.3	99.8	17.2	25.8
	Normal	Shear	Normal	Shear	Normal	Shear	Normal	Shear
Maximum strain (με)	491.21	270.56	491.74	270.99	492.37	270.97	5787.5	453.2
	1-axis	2-axis	1-axis	2-axis	1-axis	2-axis	1-axis	2-axis
First failure (years)	-	-	-	15.8	-	3.64	2.03	0.35
Percentage failed (%)	0	0	0	3.33	0	14.81	15.5	83.3
Maximum effective stress (MPa)	4.29	12.11	4.29	12.11	4.34	12.11	12.8	25.4
Maximum damage	1.54e-6	0.3887	8.66e-6	1	0.0010	1	1	1
Average damage	4.93e-8	0.0175	2.82e-7	0.0592	3.13e-5	0.0010	0.19	0.89

Table 6.8 - Effect of low stress correction parameter on blade root section damage signifiers

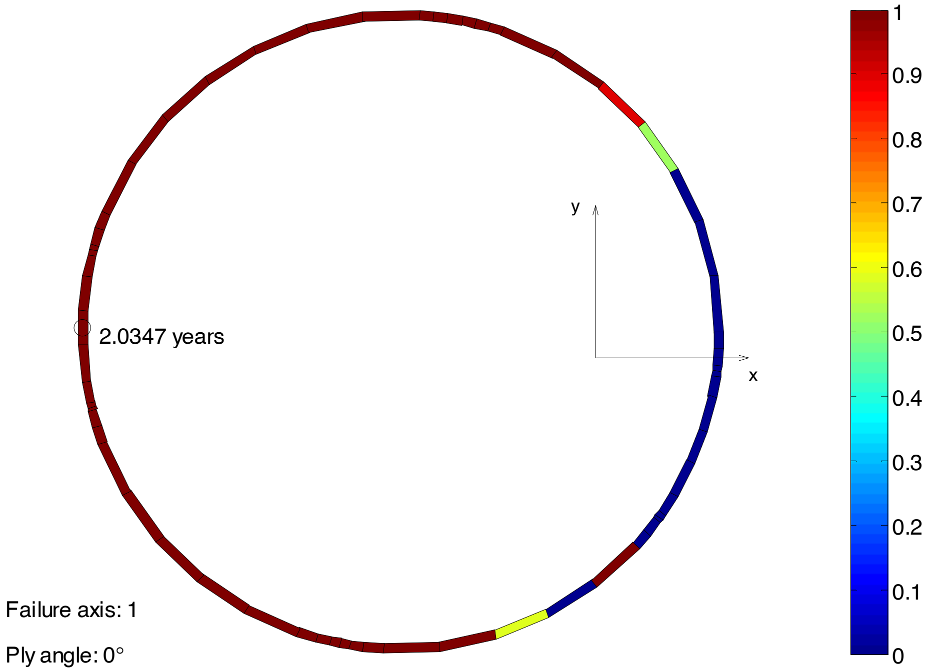

Figure 6.46 – Longitudinal damage in 0° plies at root section (no low stress correction)

The results for the blade root section are shown in Table 6.8. It is clear that the low stress correction is necessary, as when the value of d is equal to 1 (no low stress correction) even the root, which experiences relatively low stresses, fails early in the blade life. The blade bending stiffness degrades a great deal as a result of the longitudinal failures of the 0° layers, and as a result the normal strains are very high. The value of d=0.95 produces effective results at the root, which are fairly similar to those for d=0.9. A value of d=0.85 (which is thought to be more realistic) produces no failures at all.

There is no data available for the polyester matrix material used in the present work, so the effect of varying d was studied to enable an appropriate value to be chosen. Future work will aim to find a physical basis for the deviation from the log-linear behaviour at low stresses.

Figure 6.46 shows the effect of the huge quantity of failures on the stiffness of the blade when no low stress correction is used (d=1). The neutral axis has moved as a result of the stiffness degradation.

The same is true of the mid-span section, the results for which are shown in Table 6.9; all plies fail when a value of d=1 is used (this was the only scenario in which a 'failure cascade' was seen, although evidently it was very close to happening at the root for d=1). The maximum normal and shear strains are again very high.

	d=0.85		**d=0.9**		**d=0.95**		**d=1**	
	Flap	Edge	Flap	Edge	Flap	Edge	Flap	Edge
End of life stiffness (% start)	98.7	99.8	98.5	99.4	98.5	99.4	11.9	13.1
	Normal	Shear	Normal	Shear	Normal	Shear	Normal	Shear
Maximum strain (με)	725	1671	723	1675	712	1685	9867	2654
	1-axis	2-axis	1-axis	2-axis	1-axis	2-axis	1-axis	2-axis
First failure (years)	-	3.53	-	3.51	-	0.097	1.13	0.11
Percentage failed (%)	0	10.0	0	22.8	0	46.8	15.6	84.4
Maximum effective stress (MPa)	7.65	26.44	7.67	26.44	7.75	23.02	27.2	33.5
Maximum damage	4.9e-4	1	0.0028	1	0.28	1	1	1
Average damage	1.41e-5	0.18	8.2e-5	0.262	0.0082	0.52	0.19	0.90

Table 6.9 - Effect of low stress correction parameter on blade mid-span section damage signifiers

Although a value of d=0.85 appears to be correct for the materials in Figure 6.13, the sensitivity analysis showed that d=0.9 was not significantly harsher than d=0.85, so d=0.9 was used for the full blade analysis in order to keep the analysis reasonably conservative.

6.3.2.3 Effect of shear flow

The method usually used to perform fatigue analysis is based on the assumption that there is a uni-axial stress state in the blade at all times. This method was described in detail in chapter 3. In order to assess whether this assumption is reasonable, the analysis was performed with and without shear flow and the results were compared.

Stiffness degradation affects the shear flow as well as the normal flow around the blade cross section. The calculation of the shear flow was discussed in section 6.2.3. The shear flow due to torsion is dependent on the effective shear modulus of each element, and the shear flow due to transverse forces is dependent on the effective extensional modulus for the element (for the open section calculation) and the effective shear modulus of each element (for the calculation of the closing shear flows).

	Root				Mid-span			
	No shear flow		**Shear flow**		**No shear flow**		**Shear flow**	
	Flap	Edge	Flap	Edge	Flap	Edge	Flap	Edge
End of life stiffness (% start)	99.8	99.9	99.8	99.9	99.2	99.8	98.5	99.4
	Normal	Shear	Normal	Shear	Normal	Shear	Normal	Shear
Maximum strain (με)	491.21	0	491.21	270.56	726	0	723	1675
	1-axis	2-axis	1-axis	2-axis	1-axis	2-axis	1-axis	2-axis
First failure (years)	-	15.81	-	15.81	-	4.83	-	3.51
Percentage failed (%)	0	2.96	0	3.33	0	15.2	0	22.8
Maximum effective stress (MPa)	4.29	12.11	4.29	12.11	7.66	12.73	7.67	26.44
Maximum damage	5.14e-6	1	8.66e-6	1	0.0027	1	0.0028	1
Average damage	2.19e-7	0.0593	2.82e-7	0.0593	7.2e-5	0.19	8.2e-5	0.262

Table 6.10 - Effect of accounting for shear flow on damage signifiers

Table 6.10 shows the effect of the shear flow on the blade root section and a mid-span section. The inclusion of shear flow does not appear to have a significant effect at the root, as it only causes one more element to fail. The time to first failure is also the same. The mid-span section shows a great increase in damage when shear flow is included, with the first failure occurring much sooner and a 35% increase in the average transverse damage. The highest effective stress encountered in any ply during the simulation almost doubles in the transverse direction. The longitudinal damage is not greatly affected by the shear flow, which is not surprising as there is no coupling in the classical laminate theory model between shear and longitudinal stress for a balanced symmetric laminate of the type allowed by this analysis method. The longitudinal damage will be affected when transverse failure of plies which occurs sooner due to a higher shear stress on the laminate causes stress redistribution to the 0° plies. Figure 6.47 and Figure 6.48 show the transverse damage distribution around the blade without shear flow and with shear flow respectively. It is clear that the shear webs are considerably more damaged when shear flow is accounted for.

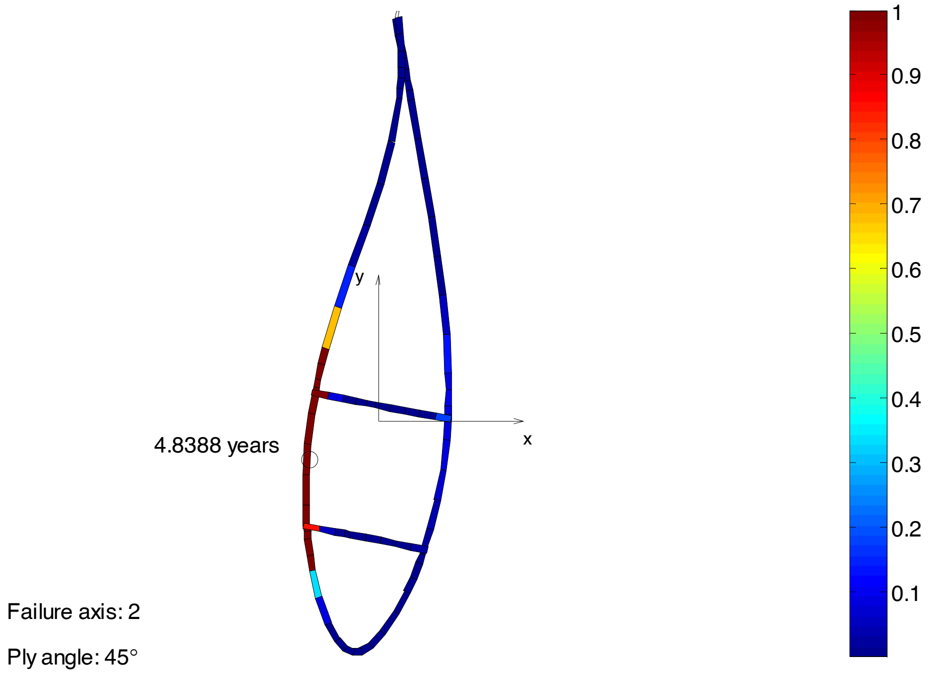

Figure 6.47- Transverse failure of 45° plies with no shear flow

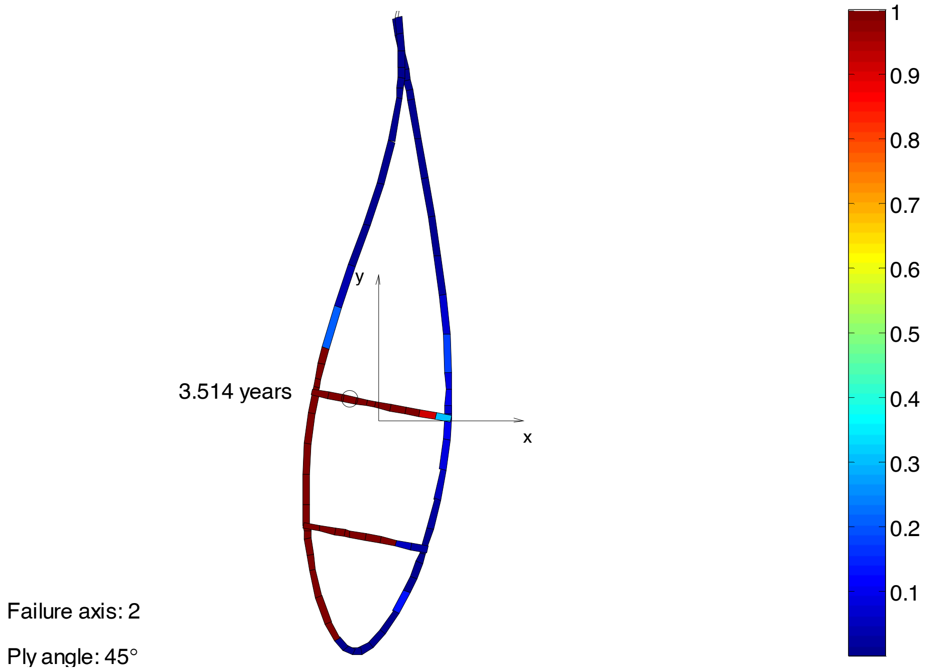

Figure 6.48 - Transverse failure of 45° plies with shear flow

Including the effects of shear flow results in more conservative and accurate predictions of blade failure, so it will be used in all subsequent analyses. Although conventional fatigue analysis methods do not account for multi-axial stress states, this work shows that using the present assumptions shear flow does not significantly affect the life of the 0° plies which dictate the life of the blade. The linear model used here does not account for failure occurring due to stability issues which could arise from inability to sustain the shear loads.

6.3.2.4 Effect of stiffness degradation parameters

The choice of stiffness degradation model is critical as it effects how the stress redistributes around the blade cross section after a failure occurs. The model can either be anisotropic or isotropic. In the anisotropic model, the stiffness of the composite after a failure is calculated using the rule of mixtures. This means that a transverse matrix failure will result in greatly reduced stiffness perpendicular to the fibres but most of the stiffness is retained in the direction of the fibres. An isotropic model degrades the composite properties equally in both directions after a failure has occurred. In practice, if transverse cracks are very prevalent then the fibres are free to slide relative to each other, so an isotropic model may be more realistic. However, the development of cracks is a continuous process so the stiffness is not lost immediately, and this approach may be over conservative. In this section, the results with different models are compared to establish which model is the most effective.

The results for the blade root are compared in Table 6.11. The low number of ply failures means there is very little damage to the blade, so there is very little difference between the 5 scenarios. However, even with this small number of failures, the models where the stiffness is degraded to 1% of its original value either anisotropically or isotropically result in more ply failures.

	Anisotropic				**Isotropic**				**None**	
Stiffness reduction	**0.01**		**0.5**		**0.01**		**0.5**		**1**	
	Flap	Edge	Flap	Edge	Flap	Edge	Flap	Edge	Flap	Edge
End stiffness (% start)	99.6	99.9	99.9	99.9	99.6	99.9	99.9	99.9	100	100
	Normal	Shear	Normal	Shear	Normal	Shear	Normal	Shear	Normal	Shear
Maximum strain (με)	491.2	270.5	491.2	270.5	491.2	270.5	491.2	270.5	491	270.5
	1-axis	2-axis	1-axis	2-axis	1-axis	2-axis	1-axis	2-axis	1-axis	2-axis
First failure (years)	-	15.8	-	15.8	-	15.8	-	15.8	-	15.8
Percentage failed (%)	0	3.33	0	2.96	0	3.33	0	2.96	0	2.96
Maximum effective stress (MPa)	4.29	12.11	4.29	12.11	4.29	12.11	4.29	12.11	4.29	12.11
Maximum damage	9e-6	1	9e-6	1	9e-6	1	9e-6	1	9e-6	1
Average damage	3e-7	0.059	3e-7	0.058	3e-7	0.059	3e-7	0.058	3e-7	0.058

Table 6.11 - Effect of stiffness degradation model on blade root damage signifiers

The mid-span section sees many more ply failures, as shown in Table 6.12. This means that the effect of the degradation model is much more apparent. The isotropic model in which the stiffness is reduced to 1% of its original value is the most conservative, and results in several more plies failing. The maximum shear strain is much higher because of the low effective shear modulus, and more importantly the maximum longitudinal damage is higher. When 0° plies start to fail the blade will quickly degrade, as they increase the bending stiffness significantly. The anisotropic model in which the transverse stiffness is reduced to 1% of its original value after a failure appears to yield similar results to both the anisotropic model with less stiffness degradation and the isotropic degradation model with 50% stiffness degradation.

	Anisotropic				**Isotropic**				**None**	
Stiffness reduction	**0.01**		**0.5**		**0.01**		**0.5**		**1**	
	Flap	Edge	Flap	Edge	Flap	Edge	Flap	Edge	Flap	Edge
End stiffness - Flap/Edge - (% start)	99.1	99.4	99.2	99.4	99.0	96.3	99.4	99.6	100	100
	Normal	Shear	Normal	Shear	Normal	Shear	Normal	Shear	Normal	Shear
Maximum strain - Normal/Shear –	723	1675	723	1658	721	2207	724	1801	726	1634
	1-axis	2-	1-axis	2-	1-axis	2-	1-axis	2-	1-axis	2-
First failure - 1/2 - (years)	-	3.51	-	3.51	-	3.51	-	3.51	-	3.51
Percentage failed - 1/2 - (%)	0	22.8	0	22.8	0	29.2	0	23.2	0	23.2
Maximum effective stress -1/2 -	7.67	26.44	7.64	26.44	7.91	26.67	8.59	26.44	7.63	26.4
Maximum damage - 1/2	0.0028	1	0.0027	1	0.0037	1	0.0031	1	0.0027	1
Average damage – 1/2	8.2e-5	0.262	7.5e-5	0.263	1.0e-4	0.334	8.3e-5	0.267	7.2e-5	0.260

Table 6.12 - Effect of stiffness degradation model on blade mid-span damage signifiers

As shown in section 6.3.1.3, the isotropic model is less conservative for compression loading because the 45° layers do not produce such high tensile transverse forces in the 0° layers. For this reason, the anisotropic model with a stiffness reduction to 1% of its original value has been chosen. This means that in the event of a longitudinal failure the fibre stiffness is reduced, and in the event of a transverse failure the matrix stiffness is reduced.

6.3.2.5 Fatigue analysis of all blade sections

LM Wind Power provided load data for 21 cross-sections along the length of the blade. The first section has not been analysed as it contains the root bolting arrangement so the present analysis method is not suitable. As the chord length is very small for the last two sections there are not enough elements to build a useful cross section model, but this is not an issue as the blade tip is not fatigue critical. The remaining 18 sections have been analysed using the simulation parameters chosen previously. To recap, the chosen parameters are as follows:

- Stresses due to shear forces are included
- The load cases are randomly ordered

- The stiffness of the matrix is degraded to 1% of its original value in the event of a transverse failure, and the stiffness of the fibres is degraded to 1% of its original value in the event of a longitudinal failure
- The parameter d which controls when the low stress correction to the bond rupture rate begins to take effect was chosen to be 0.9.

The distribution of damage around the blade cross section is presented for longitudinal and transverse failures at each section. If any elements have failed then the first element to fail is highlighted, otherwise the most damaged element is highlighted.

Generally the blade is composed of 0° layers and ±45° layers. The 0° layers tend to be more damaged in the longitudinal direction and the ±45° layers tend to be more damaged in the transverse direction. For this reason, results for most sections of the blade are presented for longitudinal damage in the 0° plies and transverse damage in the ±45° plies.

As seen in the previous section, 0° plies do not accumulate significant damage in the transverse direction so no results are shown for this case (unless significant damage has occurred, for example due to ply failure in other layers). The requirement for the principal stress to be within 2° of the fibres in order for longitudinal damage to occur means that the 45° layers are not damaged in the longitudinal direction. Again, this assumption is checked for each section and results are shown if significant damage has occurred. Accounting for the shear stress in the blade means that the effective stress can be significantly different in the +45 layers to the -45 layers, so the more damaged of these two ply angles is shown.

The distance from the root of each section is not given as this information is commercially sensitive.

Results are shown in appendix E for the analysis neglecting the effects of shear flow.

The first section analysed is from near the blade root and has no shear webs. This is the only section with 90° plies in it, and these are the only plies which fail, as shown in Figure 6.49. The damage is concentrated in the same area as it was for the traditional fatigue analysis performed in chapter 3.

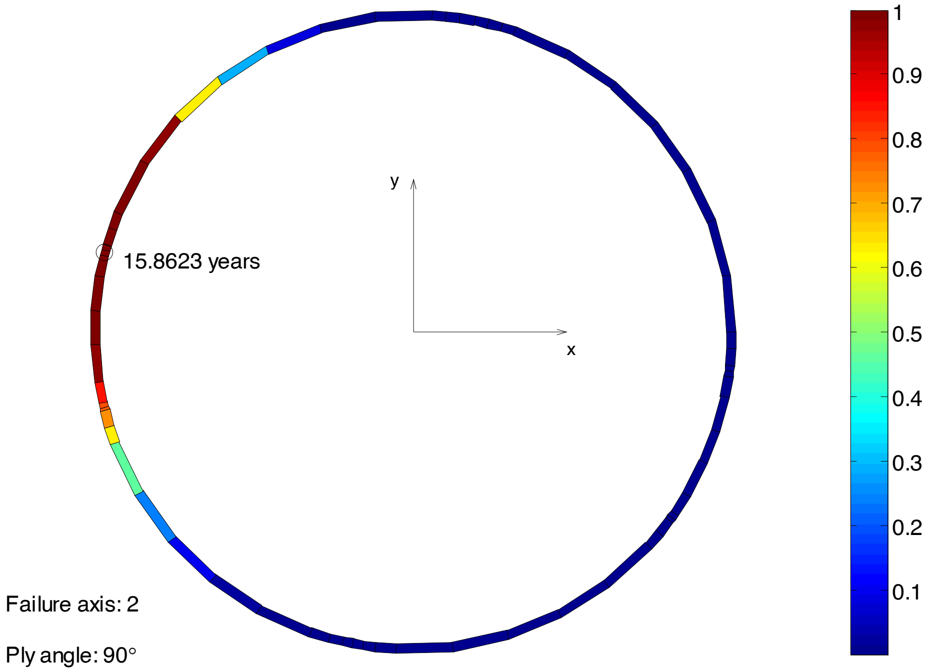

Figure 6.49 - Transverse damage of 90° plies of section 1

The longitudinal damage is very low, and it is interesting to note that the element in which it peaks is not the same as for the transverse damage. This is because shear flow has been included in the calculation. Figure 6.50 shows the damage in the 45° layers of section 1. The damage distribution is similar to that in the 90° layers but no plies fail in this case. The damage distribution for the 0° plies of section 1 is shown in Figure 6.51. None of these plies are approaching failure, and it is interesting to note that including the shear flow has shifted the damage around the blade.

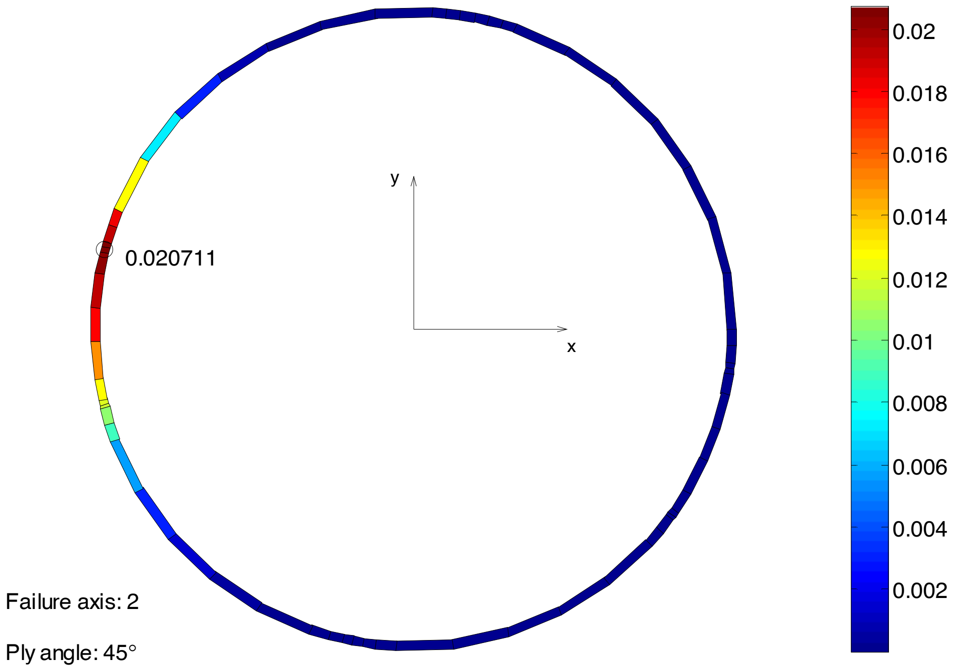

Figure 6.50 - Transverse damage of 45° plies of section 1

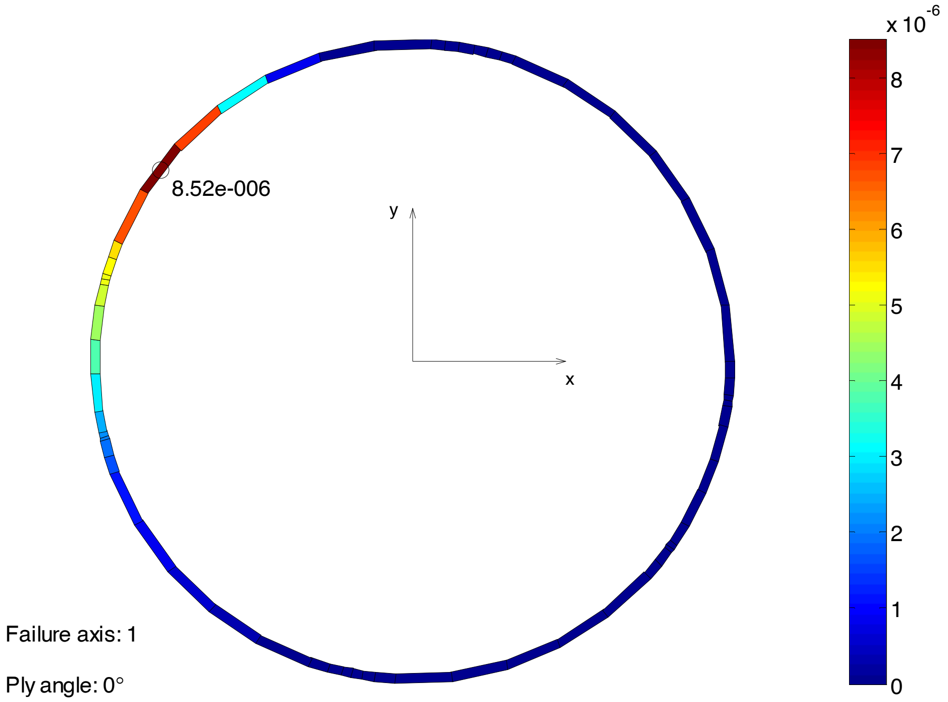

Figure 6.51 - Longitudinal damage of 0 plies of section 1

Section 2 is a transition section from the circular profile used at the root to the aerofoil shape used for the rest of the blade. The damage is concentrated on the pressure side, as shown in Figure 6.52. No elements had failures in this section, although the transverse damage in the 45° plies is approaching unity.

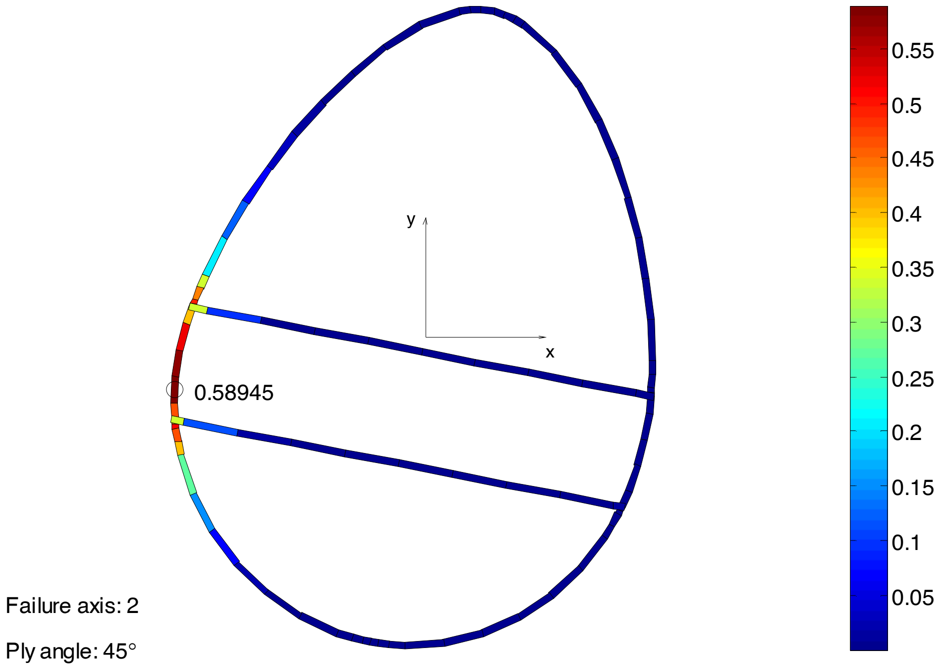

Figure 6.52 - Transverse damage in 45° plies of section 2

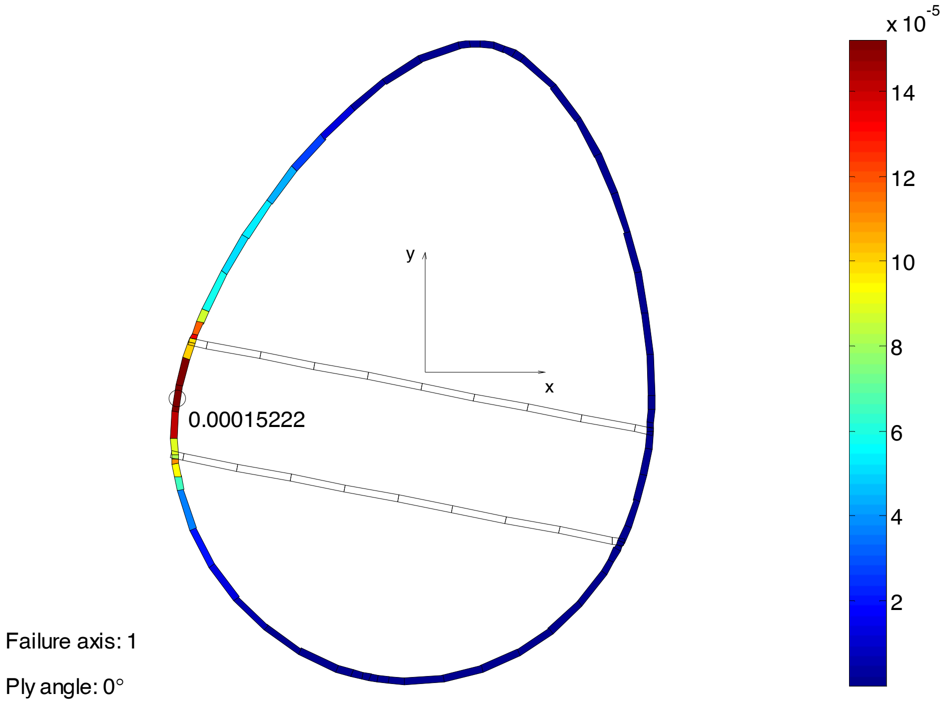

Figure 6.53 - Longitudinal damage in 0° plies of section 2

By comparing Figure 6.52 and Figure 6.53 it can be seen that the most damaged elements in the transverse and longitudinal direction do not coincide in section 2 either. Although the longitudinal damage is still very low in this part of the blade, its value is higher than it was at section 1.

In section 3 transverse failures occur in the seventh year, as shown in Figure 6.54. The distribution of damage around the blade cross-section obtained using the present method is now beginning to differ from that found using a traditional fatigue analysis of the kind described in chapter 3. At a similar section on the blade, the traditional fatigue analysis predicts that the trailing edge will be the most damaged part. This is because the traditional analysis is based on fatigue data generated at much higher strain amplitudes than those seen in service, so the temperature increases and as a result the higher amplitude cycles appear more damaging. As the trailing edge sees the highest stress amplitudes (because of reversing edgewise loading), it is the area that appears most damaged in a traditional fatigue analysis. In operation the temperature of the blade is unlikely to be significantly different from the ambient temperature because the stress amplitude and frequency is much lower than during coupon testing and the blade has a continual cooling airflow over its surface. This means that failure is caused predominantly by sustained high stresses, instead of the combined effect of temperature and stress that is seen when testing coupons. As the kinetic theory approach used here accounts for this fact, the most damaged part of the blade is the pressure side because this part experiences the highest sustained tensile stresses.

Also of note is the fact that the 45° layers on the suction side are beginning to be slightly damaged in compression.

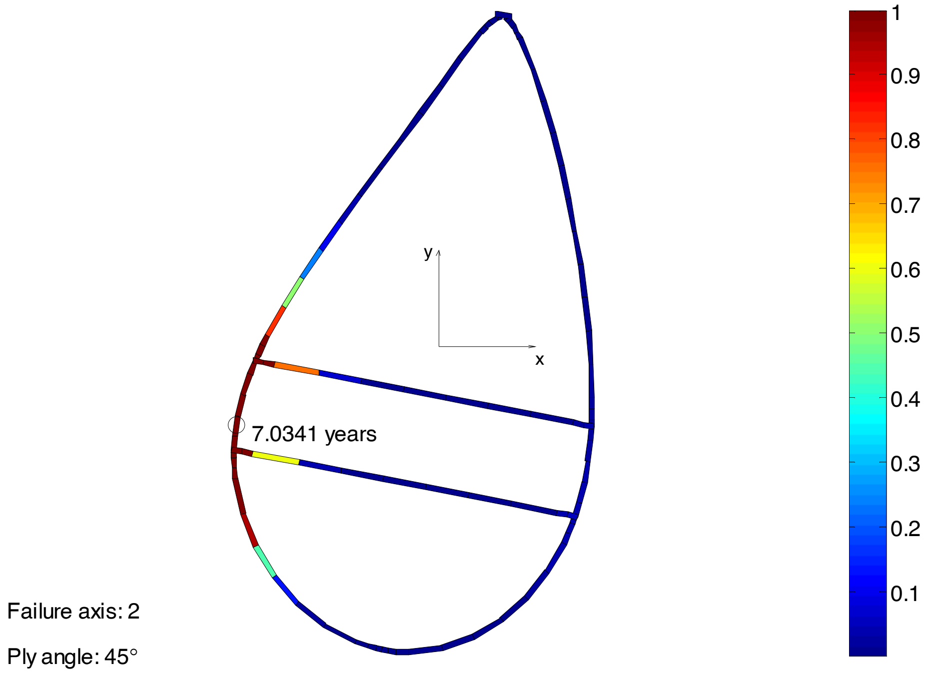

Figure 6.54 - Transverse damage in 45° plies of section 3

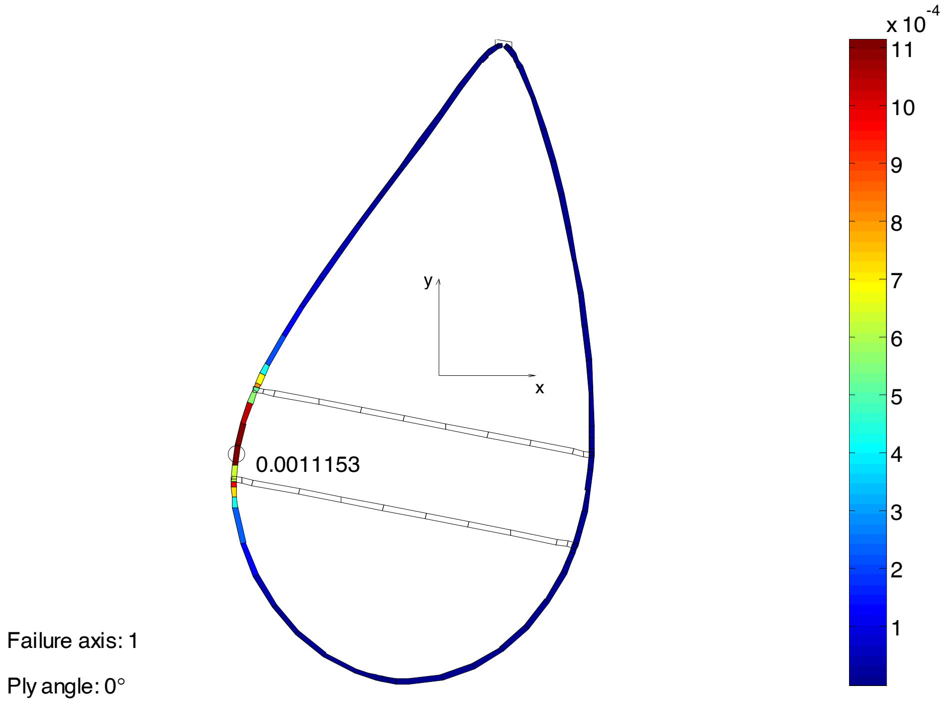

Figure 6.55 - Longitudinal damage of 0° plies in section 3

The longitudinal damage is again concentrated on the pressure side, and for section 3 the maximum longitudinal and transverse damage occur in the same element, as can be seen by comparing Figure 6.54 and Figure 6.55.

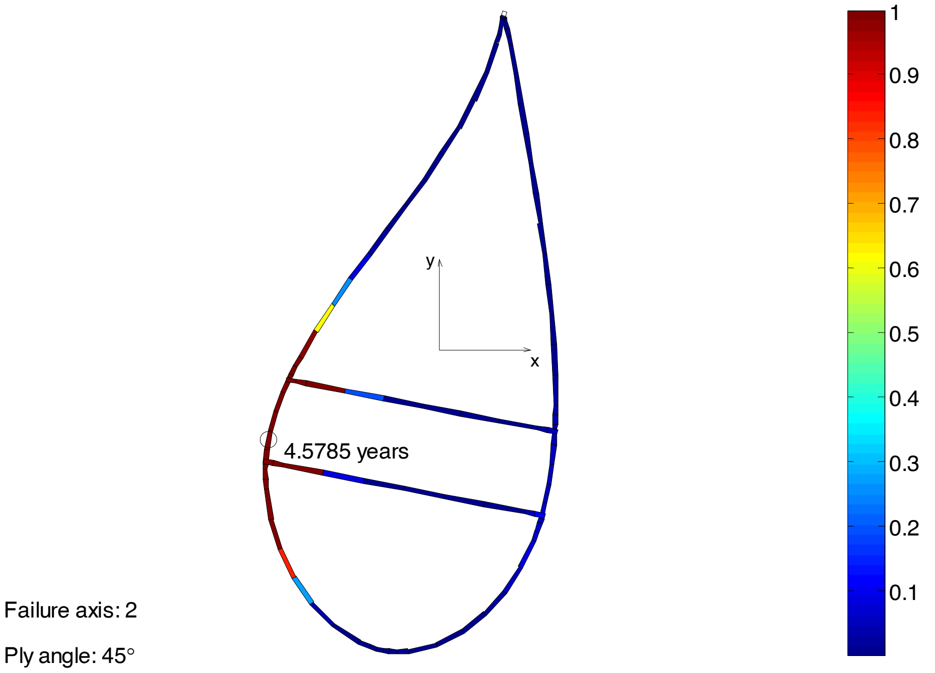

Figure 6.56 - Transverse failure of 45° plies in section 4

In section 4, there are widespread transverse failures in the ±45° layers. It is localised on the pressure side and in the shear webs, as shown in Figure 6.56.

The longitudinal damage in the 0° plies of section 4 is shown in Figure 6.57. Longitudinal damage is the most important, as these plies are the 'critical elements' which dictate when catastrophic failure will occur. The blade is still a long way from experiencing longitudinal failures at this section of the blade.

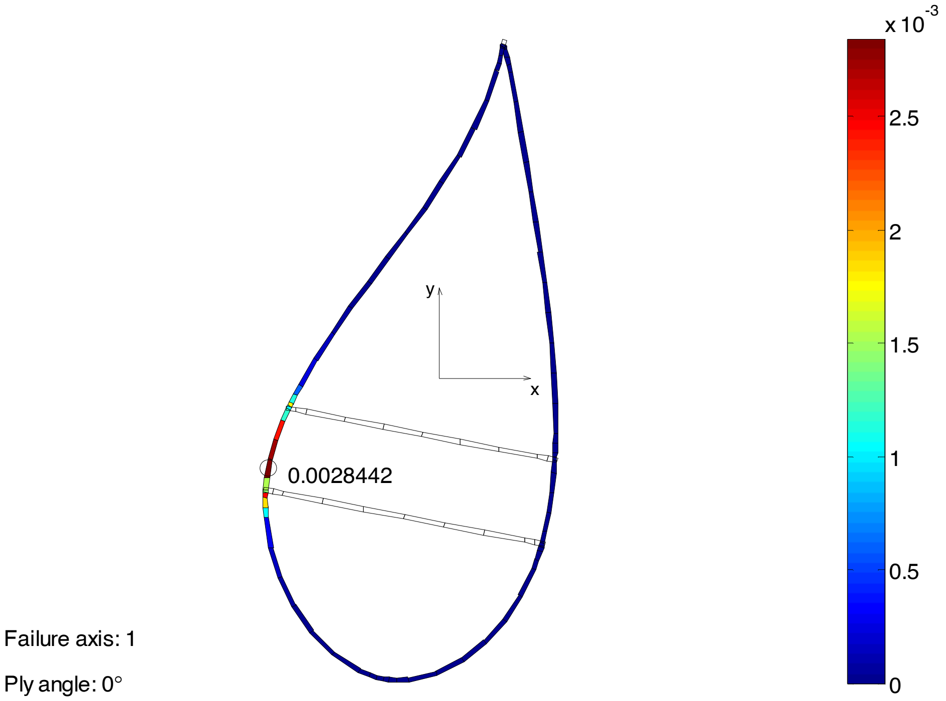

Figure 6.57 - Longitudinal damage in 0° plies of section 4

The transverse damage in the 45° layers of section 5 is shown in Figure 6.58. The most damaged area is again the pressure side.

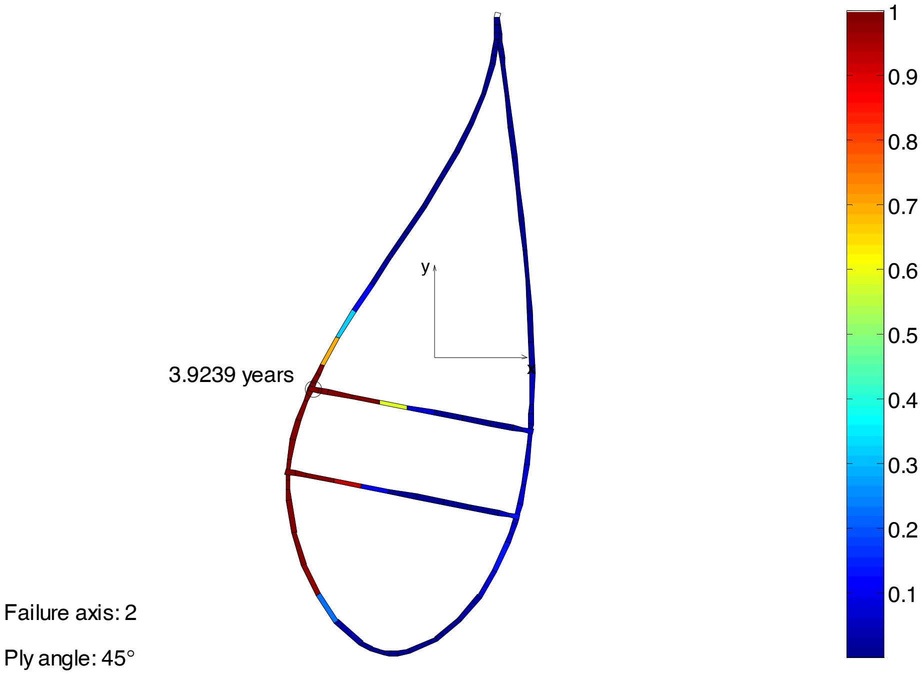

Figure 6.58 - Transverse damage in 45° plies of section 5

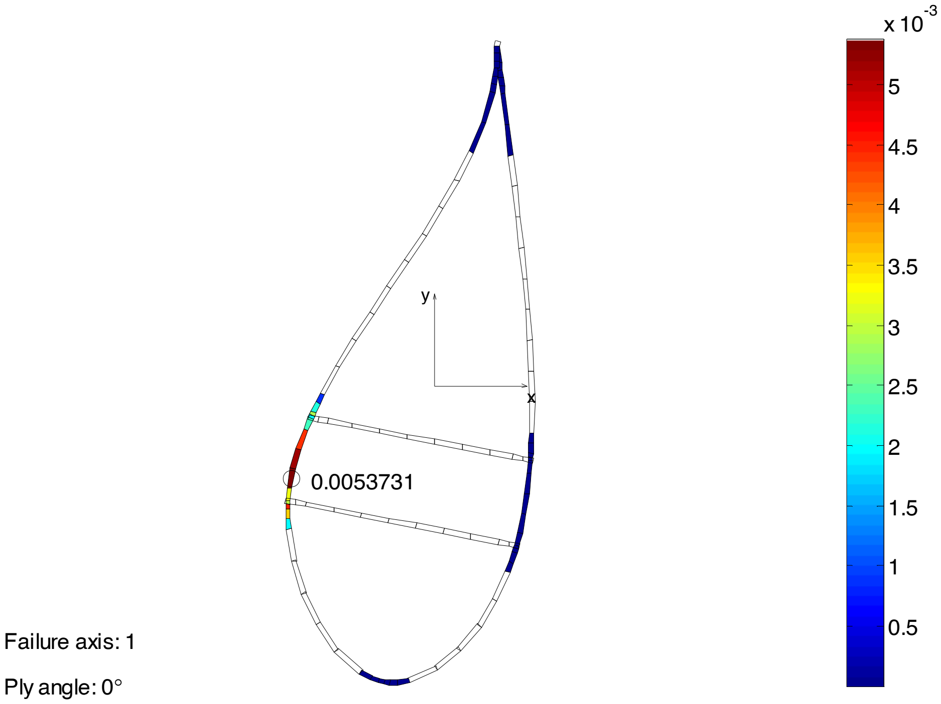

Figure 6.59 - Longitudinal damage in 0° plies of section 5

At section 5, the use of 0° plies is now limited to the spar caps and local reinforcement of the leading and trailing edges. The longitudinal damage in the 0° plies is relatively high in this region of the blade although it would still be expected to survive a lot longer than its design life unless further transverse failures increase the stress very rapidly.

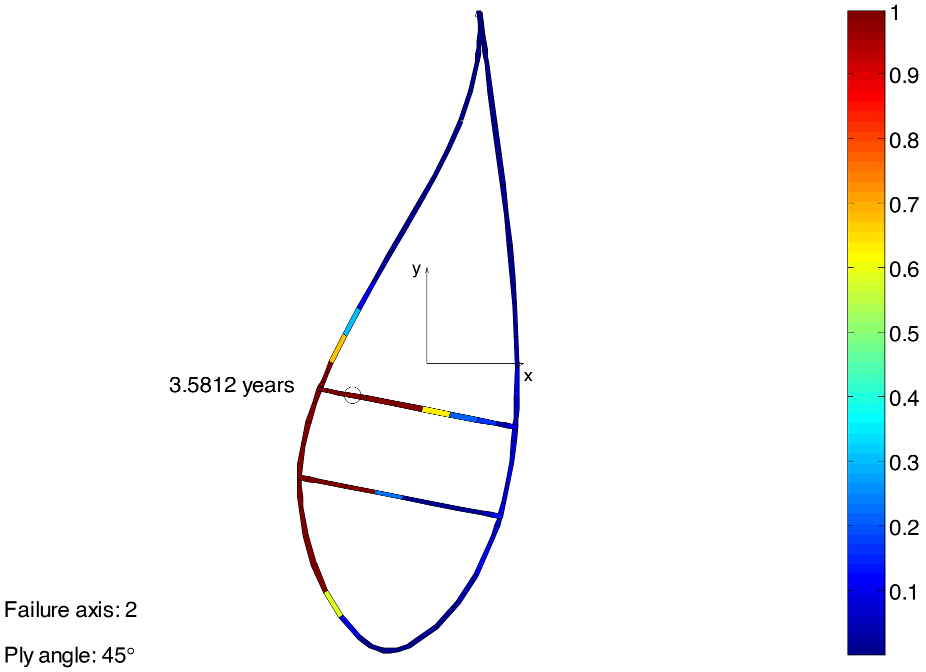

Figure 6.60 - Transverse damage of 45° plies of section 6

Figure 6.60 shows transverse damage in the 45° layers of section 6. The shear webs are now the first part of the blade to fail, which is significant because the webs have a specific structural role and their failure will cause the shear flow to redistribute around the blade cross section, accelerating failures elsewhere.

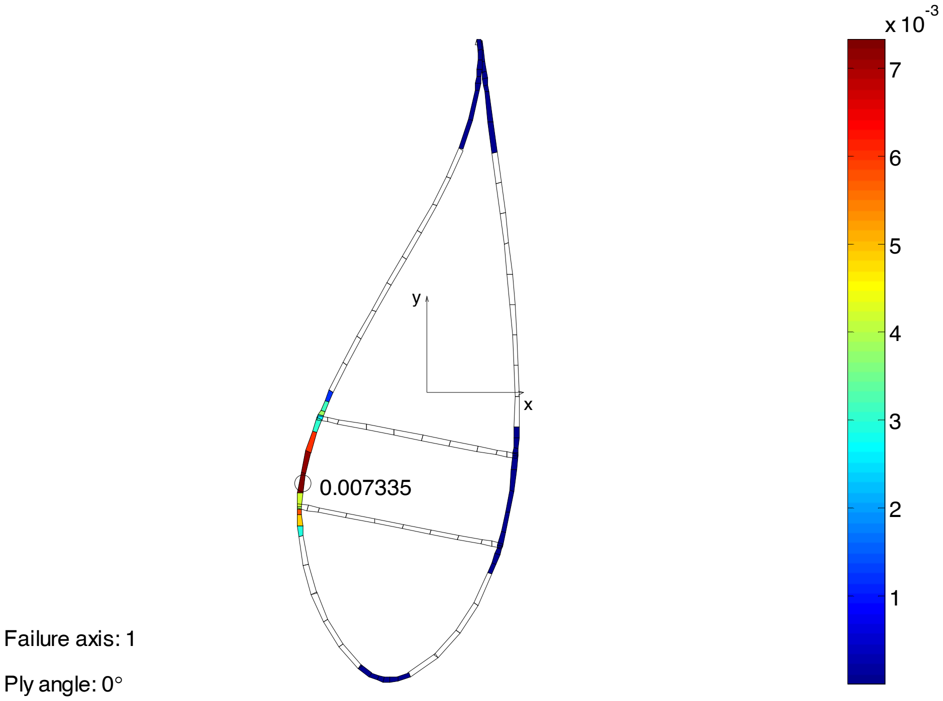

Figure 6.61 - Longitudinal damage of 0° plies of section 6

Figure 6.61 shows the longitudinal damage in the 0° plies of section 6. The damage is concentrated around the pressure side spar cap, and this section is the most damaged on the blade (although the 0° plies are still a long way from experiencing a longitudinal failure).

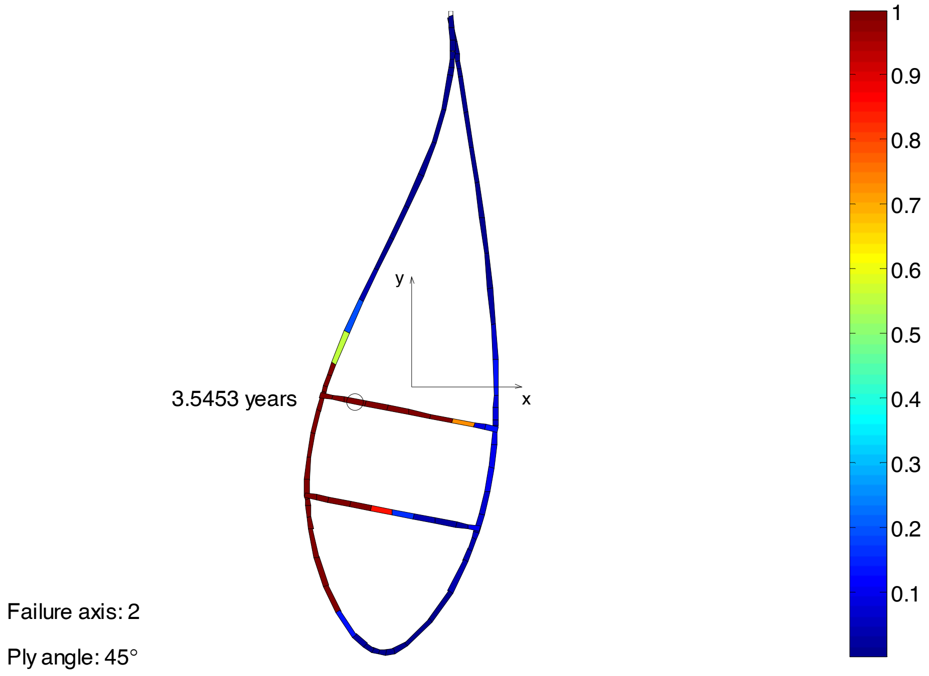

Figure 6.62 - Transverse damage of 45° plies of section 7

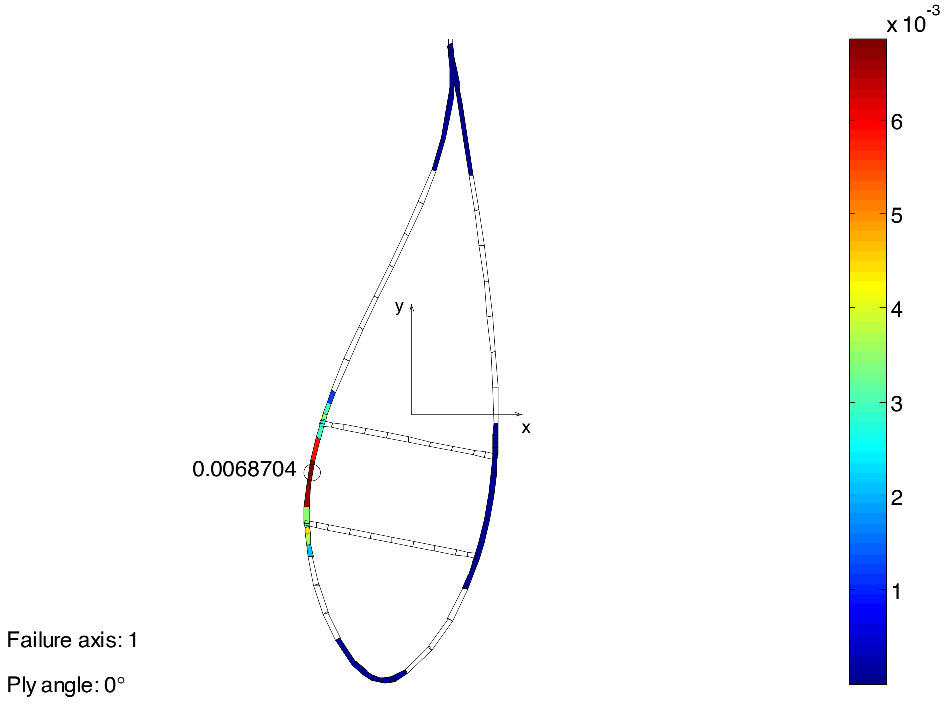

Figure 6.63 - Longitudinal damage of 0° plies of section 7

In Figure 6.62 and Figure 6.63 the damage distribution is similar to that seen at section 6, although the damage values are lower.

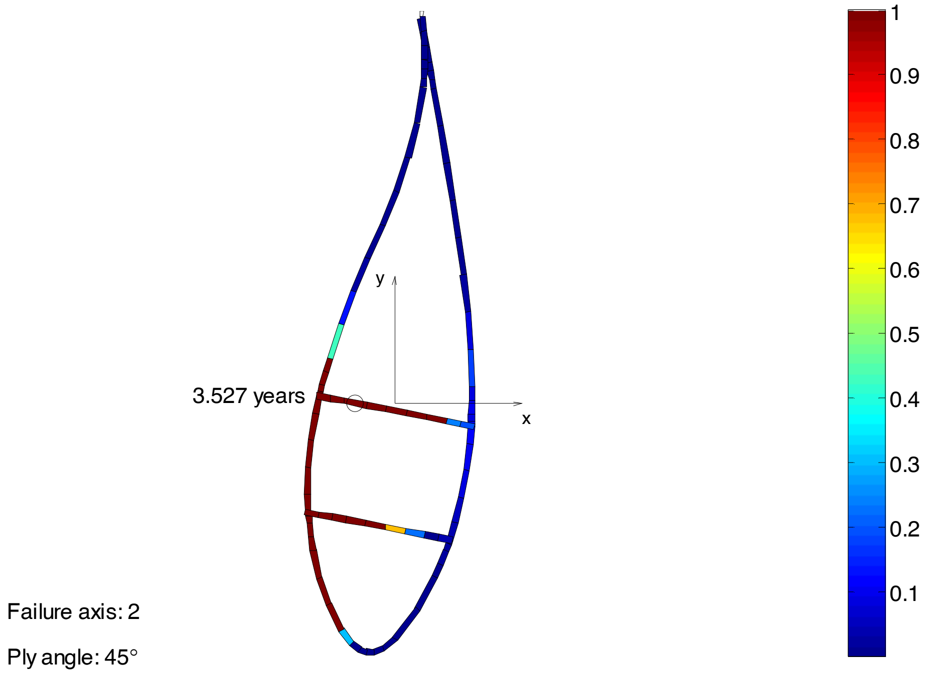

Figure 6.64 - Transverse damage of 45° plies of section 8

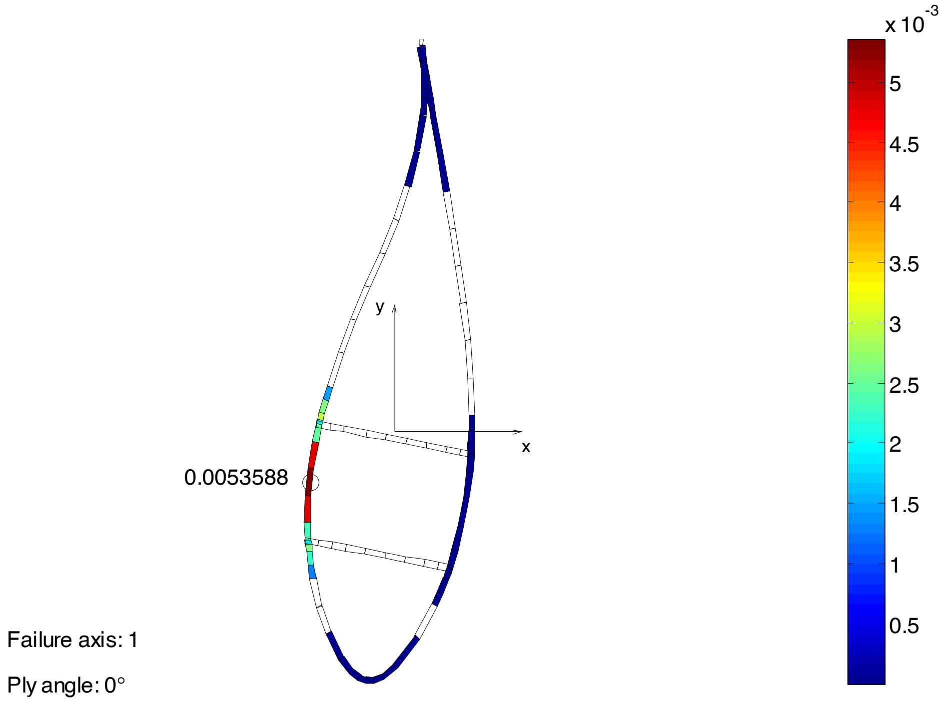

Figure 6.65 - Longitudinal damage of 0° plies of section 8

Figure 6.64 and Figure 6.65 show the transverse and longitudinal damage distributions respectively at section 8. The longitudinal damage is decreasing along the length of the blade, and the transverse damage to the shear webs no longer penetrates all the way to the suction side.

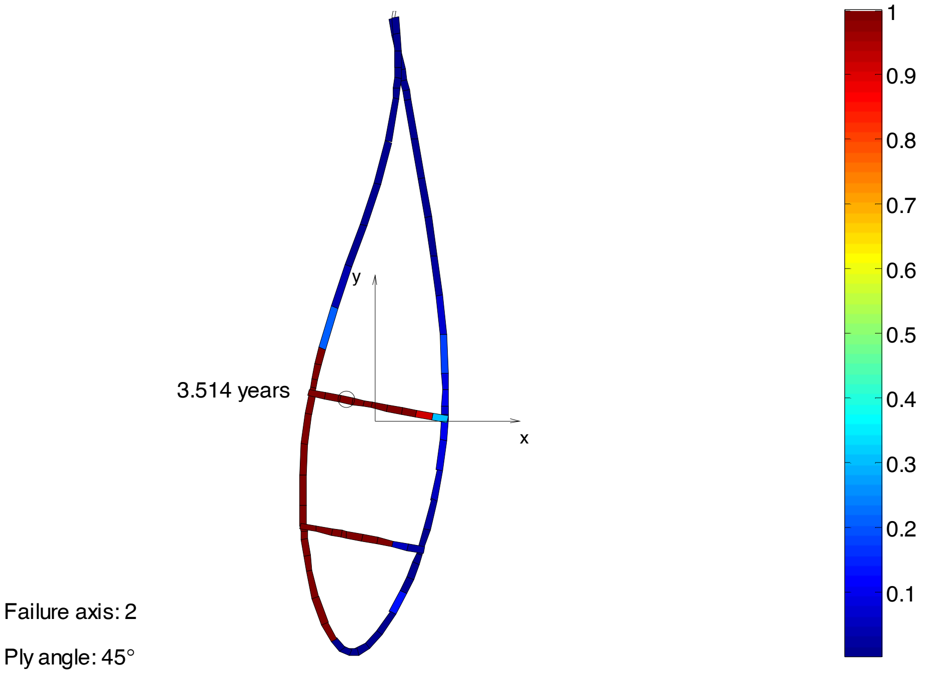

Figure 6.66 - Transverse damage to 45° plies of section 9

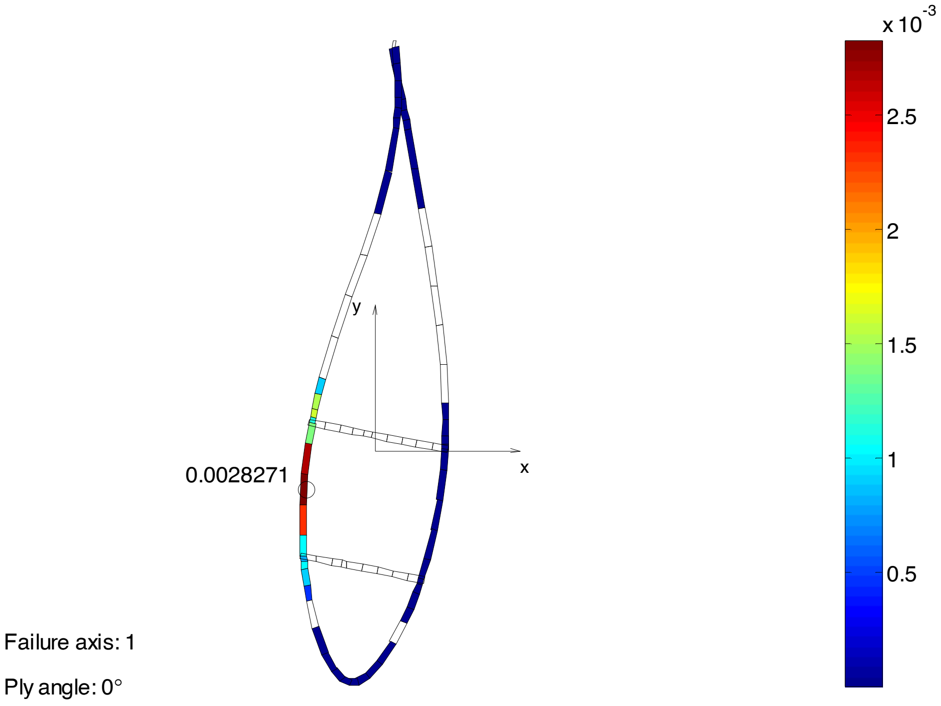

Figure 6.67 - Longitudinal damage to 0° plies in section 9

Figure 6.66 shows the transverse damage to the 45° in section 9. This section is mid-span, and it is interesting to note that the shear webs are more damaged at this point than they were earlier in the blade. Although the thickness of the composite layers is the same at this point, the thickness of the core has been reduced and so the composite plies experience higher stress. In Figure 6.67 it can be seen that the maximum longitudinal damage is starting to reduce compared to its value nearer to the root of the blade.

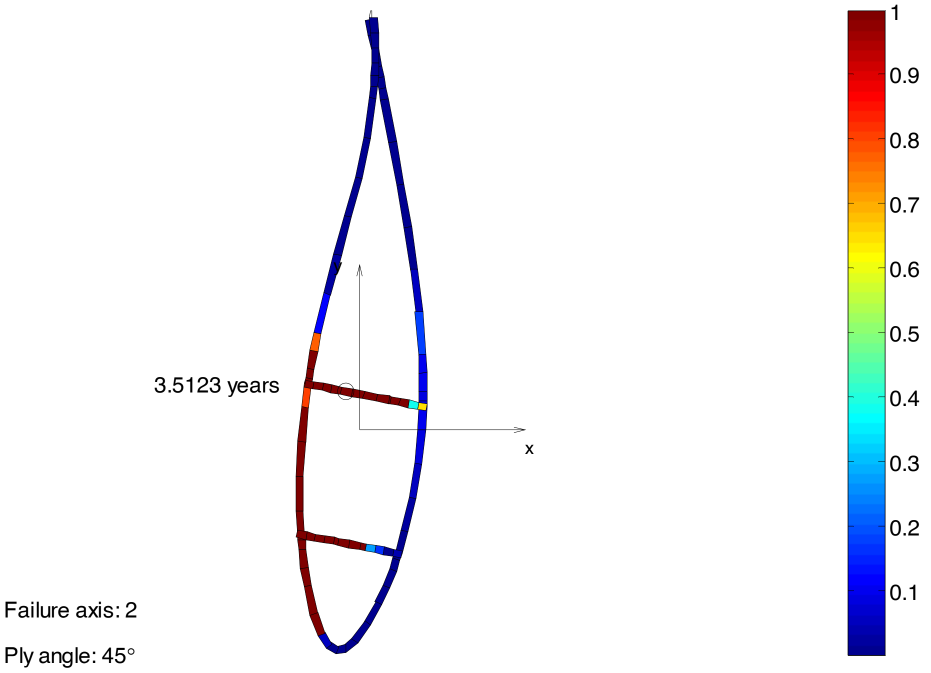

Figure 6.68 - Transverse damage of 45° plies of section 10

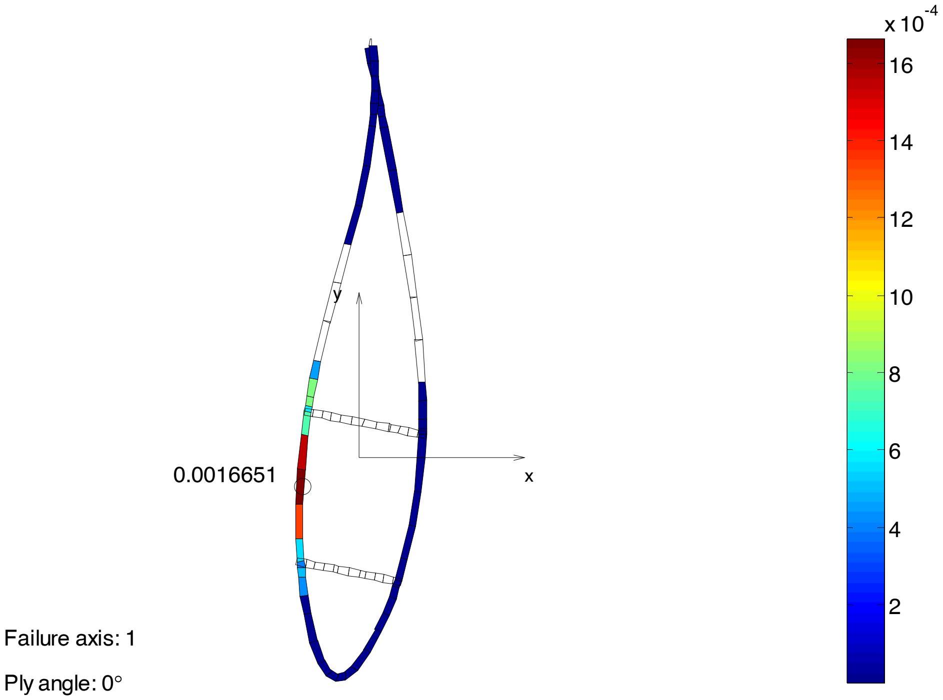

Figure 6.69 - Longitudinal damage of 0° plies of section 10

Figure 6.68 and Figure 6.69 show the transverse and longitudinal damage respectively of plies in section 10. The same patterns of damage are observable as for previous sections but the damage in both the transverse and longitudinal directions has reduced further when compared to the inboard portions of the blade.

In Figure 6.70 it can be seen that the transverse damage in section 11 has decreased once again compared to its value closer to the centre of the rotor. A similar trend can be seen in Figure 6.71 for the longitudinal damage in the 0° reinforcement layers of section 11.

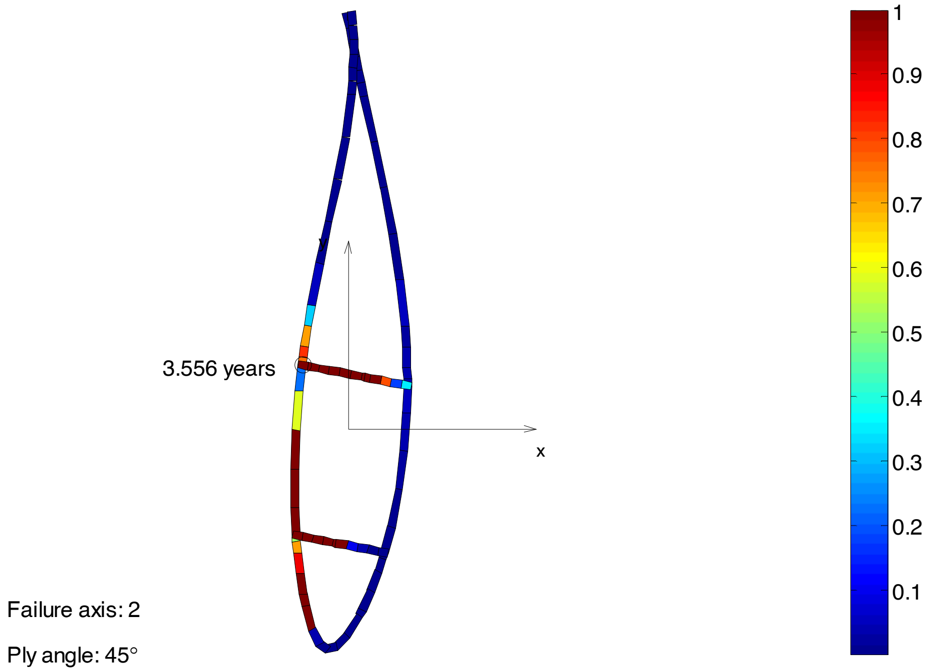

Figure 6.70 - Transverse damage of 45° plies of section 11

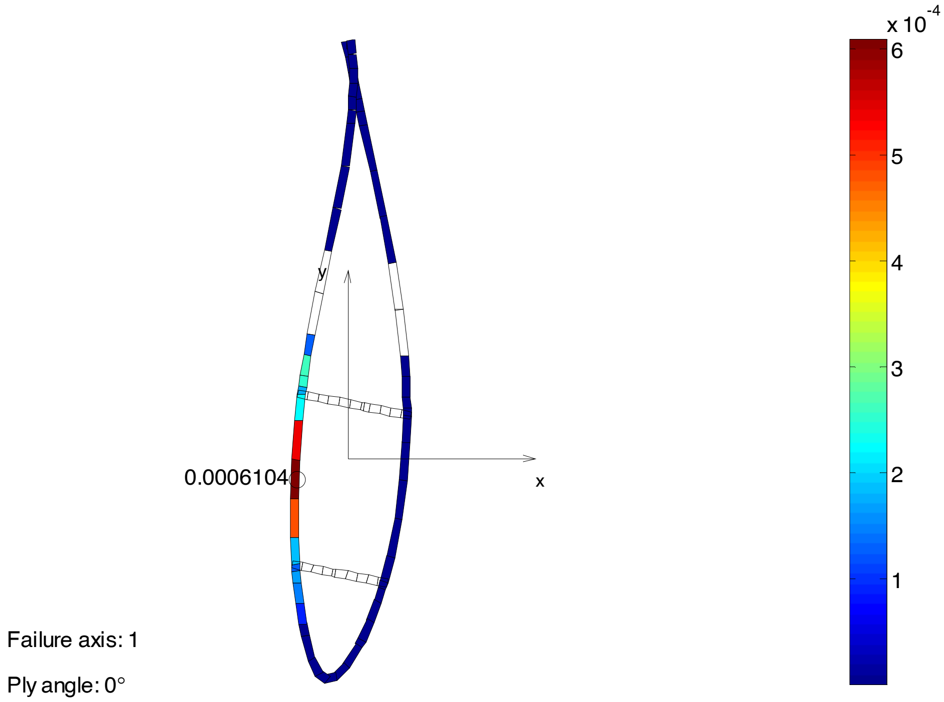

Figure 6.71 - Longitudinal damage to 0° plies of section 11

The transverse ply failures in section 12 are located entirely in the shear webs, as shown in Figure 6.72. In Figure 6.73 it can be seen that the longitudinal damage is again lower than at the previous section.

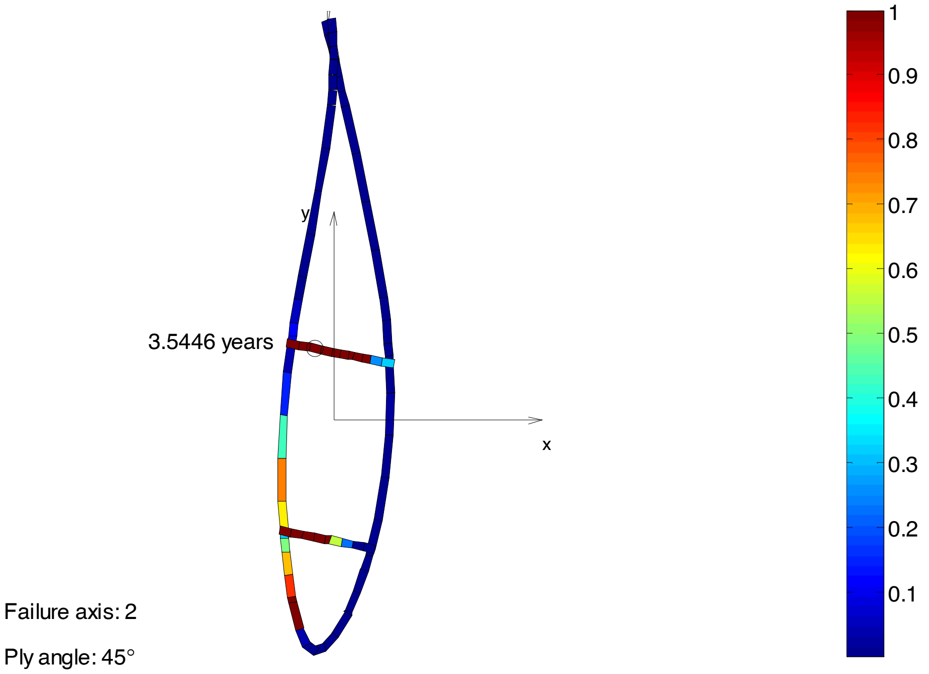

Figure 6.72 - Transverse damage in 45° plies of section 12

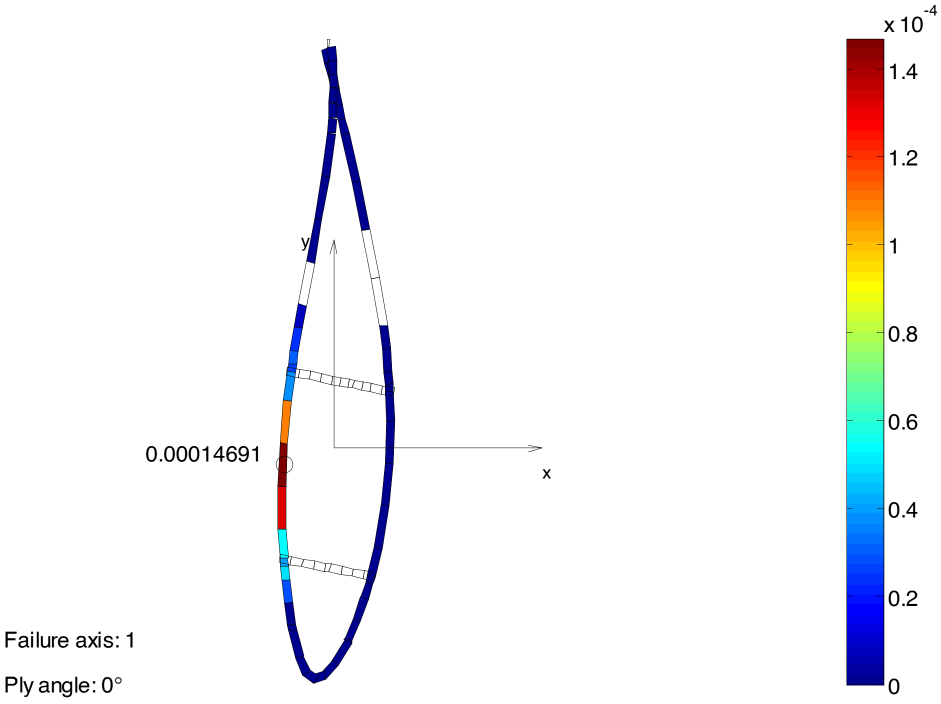

Figure 6.73 - Longitudinal damage in 0° plies of section 12

The damage continues to reduce along the remainder of the blade. Figure 6.74, Figure 6.76, Figure 6.78, Figure 6.80, Figure 6.82 and Figure 6.84 show the transverse damage in sections 13, 14, 15, 16, 17 and 18 respectively. From section 15 onwards there are no transverse ply failures at all, and the maximum value of the transverse damage parameters reduces.

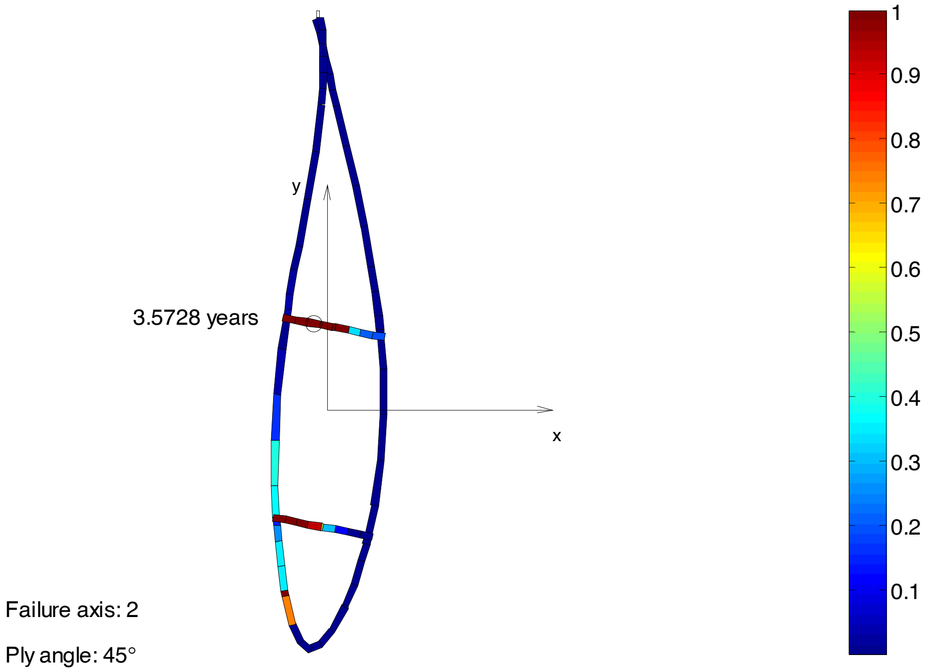

Figure 6.74 - Transverse damage to 45° plies of section 13

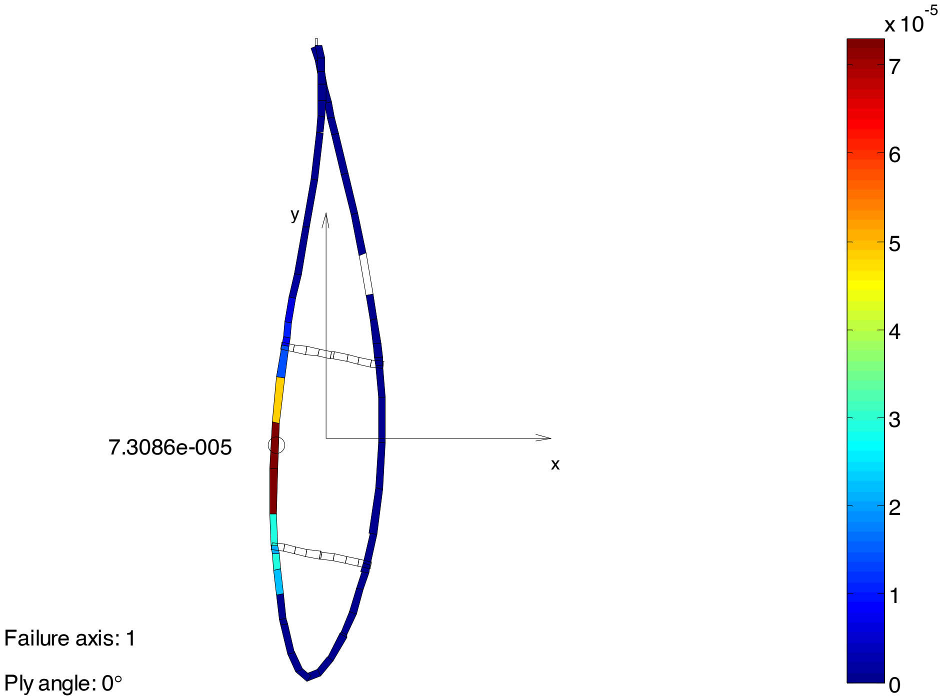

Figure 6.75 - Longitudinal damage to 0° plies of section 13

Figure 6.75, Figure 6.77, Figure 6.79, Figure 6.81, Figure 6.83 and Figure 6.85 show the longitudinal damage in sections 13, 14, 15, 16, 17 and 18 respectively.

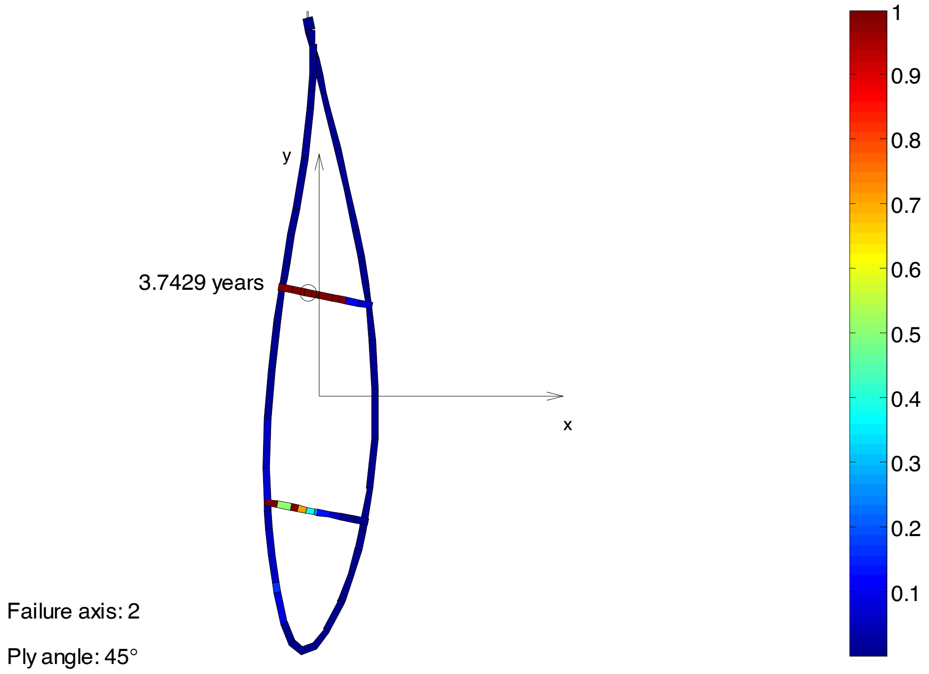

Figure 6.76 - Transverse damage of 45° plies of section 14

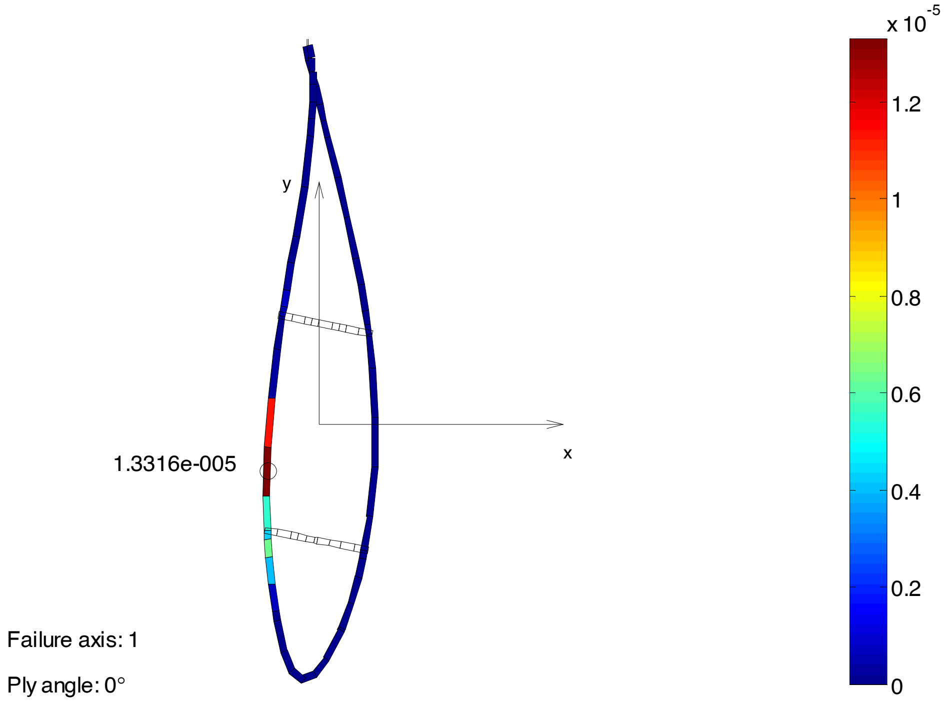

Figure 6.77 - Longitudinal damage of 0° plies of section 14

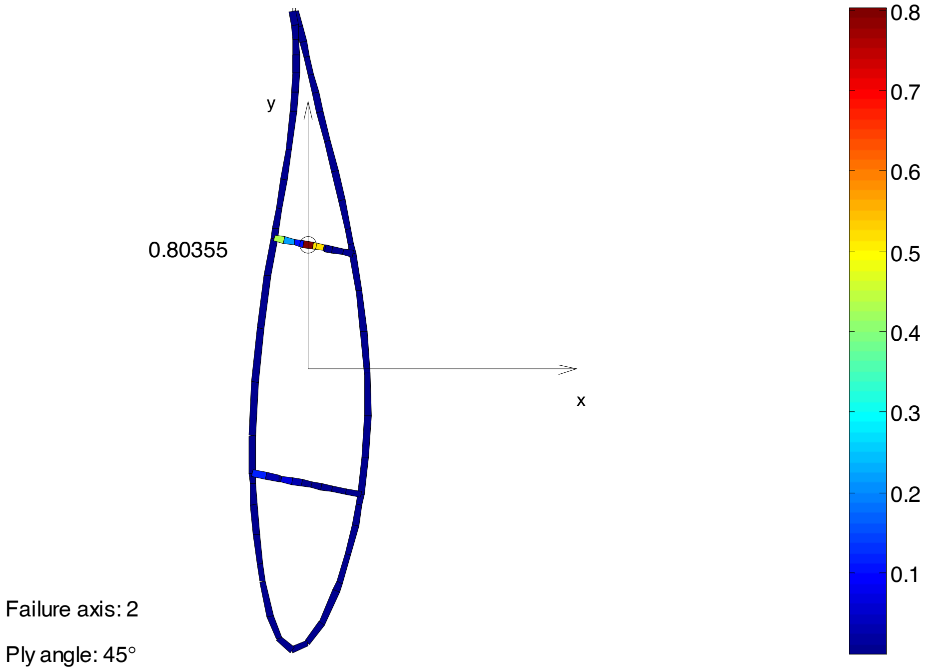

Figure 6.78 - Transverse damage of 45° plies of section 15

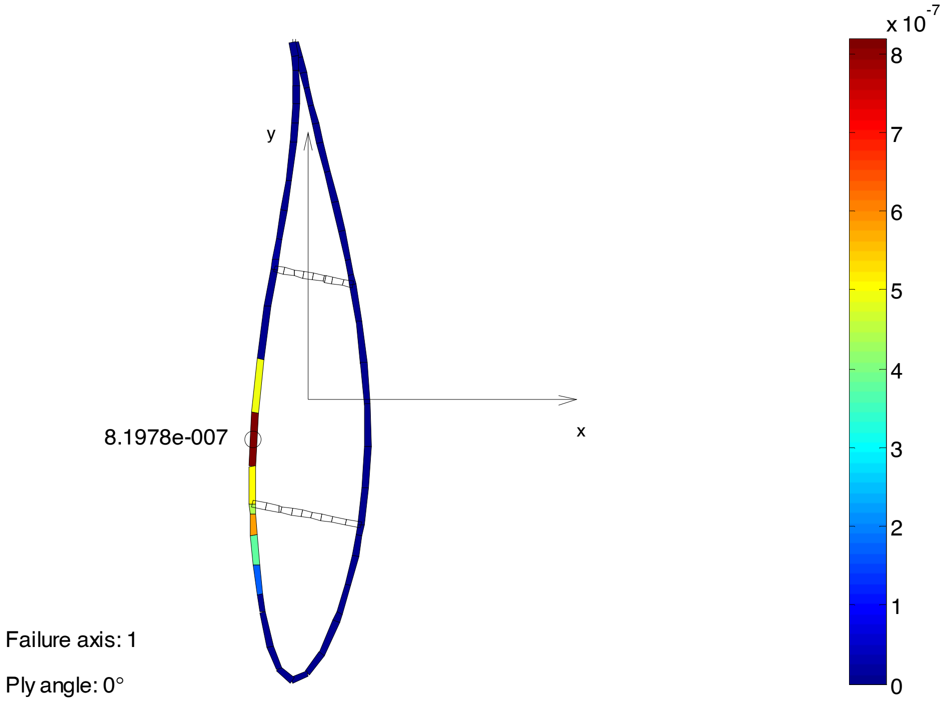

Figure 6.79 - Longitudinal failure of 0° plies of section 15

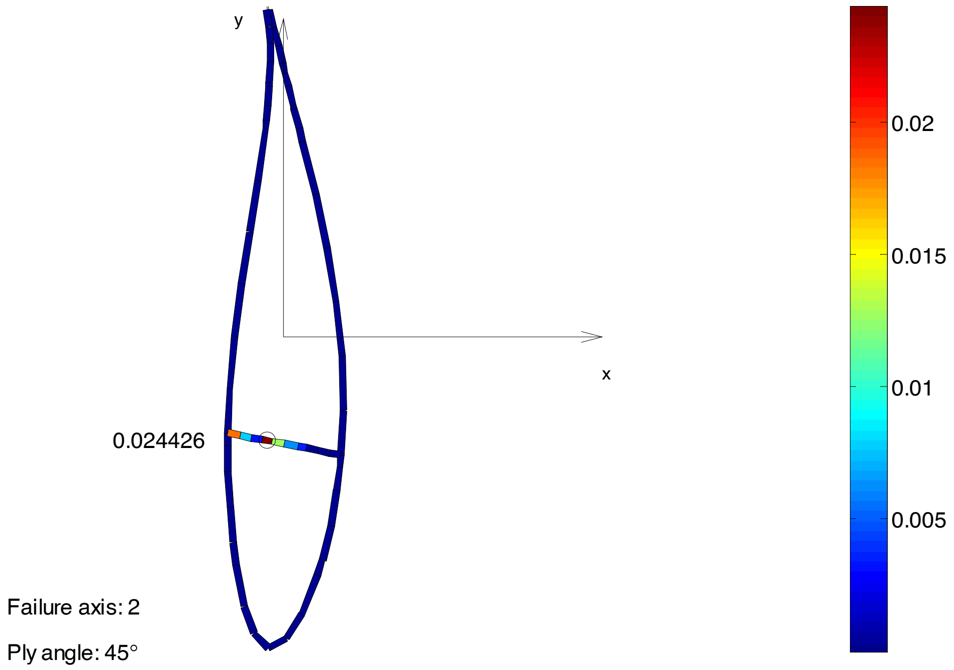

Figure 6.80 - Transverse damage of 45° plies of section 16

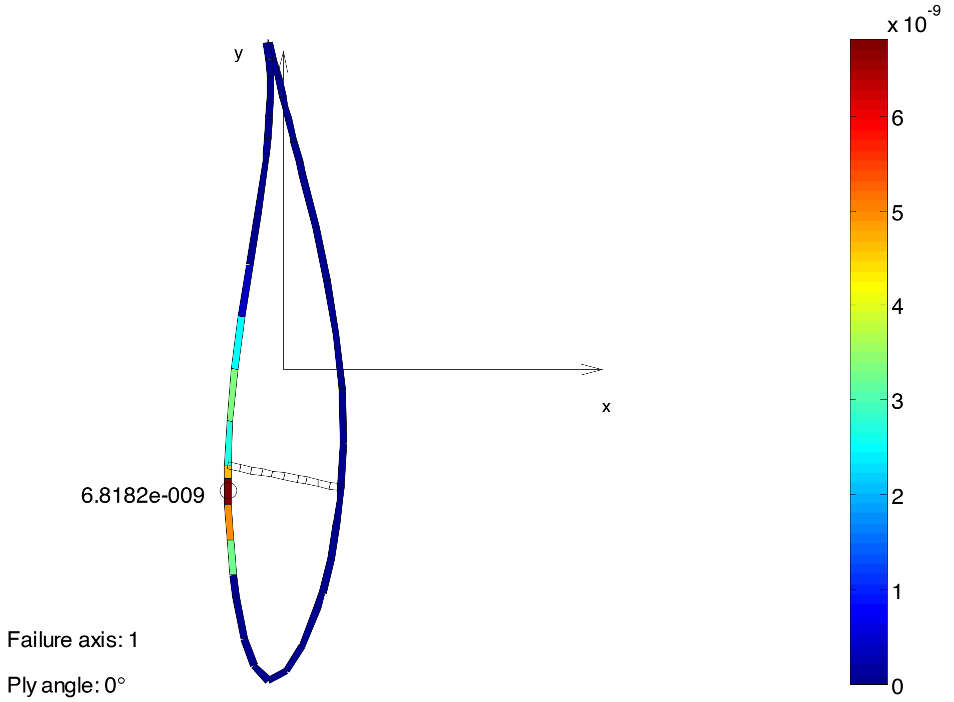

Figure 6.81 - Longitudinal damage of 0° plies of section 16

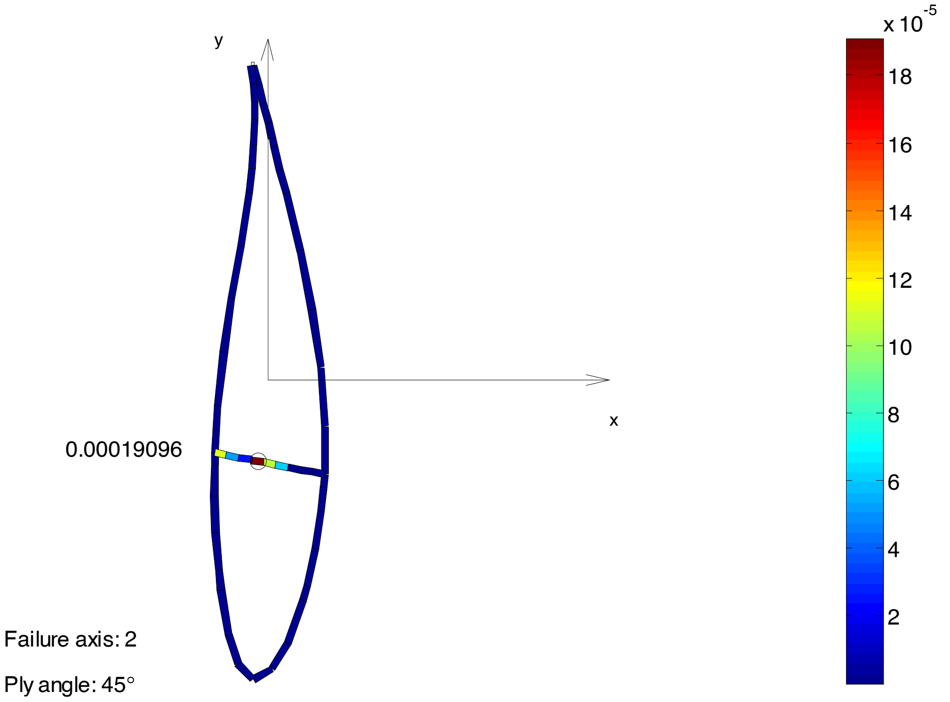

Figure 6.82 - Transverse damage to 45° plies in section 17

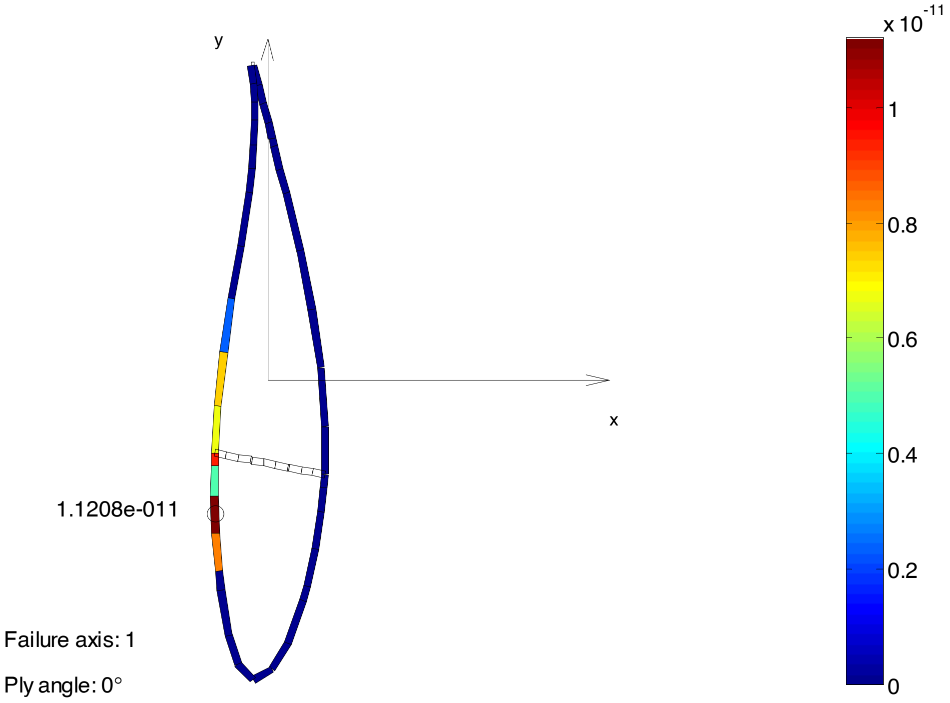

Figure 6.83 - Longitudinal damage to 0° plies in section 17

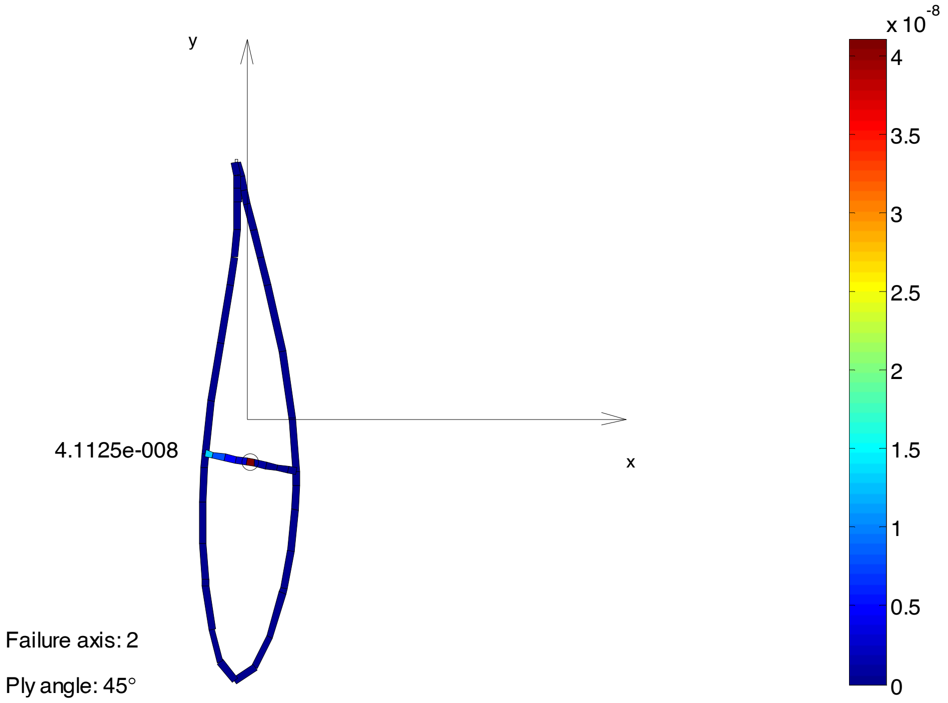

Figure 6.84 - Transverse failure of 45° plies of section 18

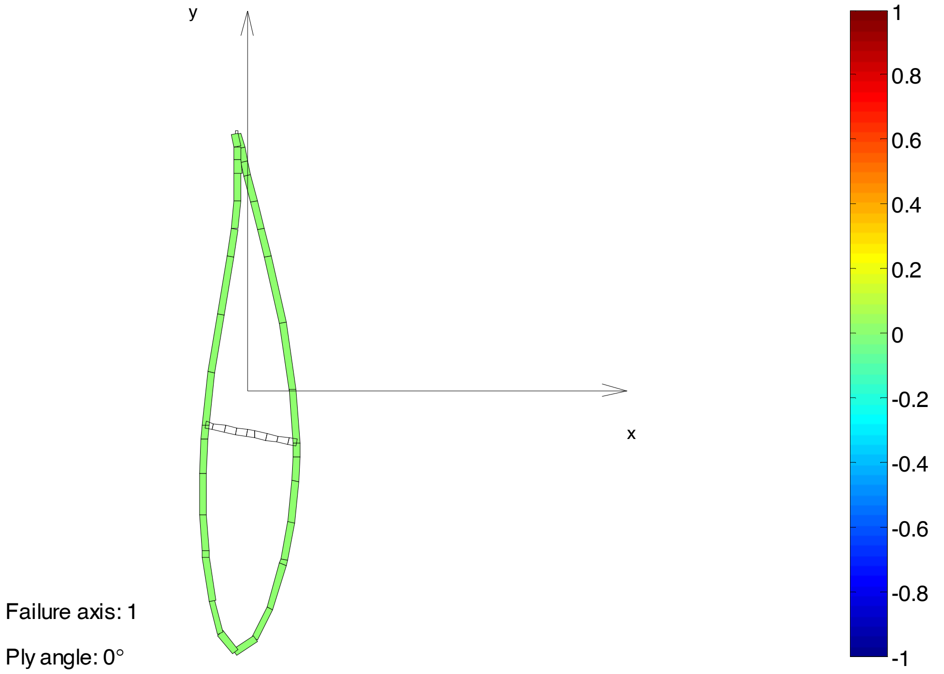

Figure 6.85 - Longitudinal damage to 0° plies of section 18

The damage decreases steadily along the final section of the blade, until at the final section studied the damage is zero due to the floating point precision.

6.3.3 Summary of blade fatigue analysis results

The alternative method of fatigue analysis described in the present work has been shown to be applicable to the analysis of a full wind turbine blade. The damage distribution around the blade cross section differs from that obtained using a conventional fatigue analysis, with the trailing edge no longer being a fatigue critical area. This is a result of the fact that the present method accounts for the differences between coupon testing and operational conditions better by allowing for the effect of temperature.

6.3.4 Results of fatigue test analysis

Using the method described in section 6.2.9, a test was designed for the LM 40.3 P2 blade for which results have already been obtained. Both of the test configurations described in section 6.2.9 were analysed by simulating a test.

The first test configuration involves using winches normally used for static testing to load the blade in the flapwise direction at a constant level to simulate the wind loads, while exciting the edgewise direction with a resonant mass to simulate the gravity loads. This test configuration has the advantage that the edgewise frequency is kept at a higher level because the mass of equipment attached to the blade is minimised. However, the edgewise mean bending moment is much higher than it would be in practice, which means the leading edge damage is unlikely to be realistic.

The test design process started by performing a screening optimisation to find the best position of the winches used to load the flapwise direction. Using the saddle locations obtained from this process the edgewise frequency and bending moment distribution were found and the target flapwise bending moment and edgewise bending moment amplitude were recalculated. The edgewise direction was then excited using a pair of resonant masses attached to the nearest saddle to the root. The true test loads were then obtained using the optimisation routine described in chapter 4 and the blade test simulation tool described in chapter 5. The target and achieved bending moment distributions are shown in Figure 6.86.

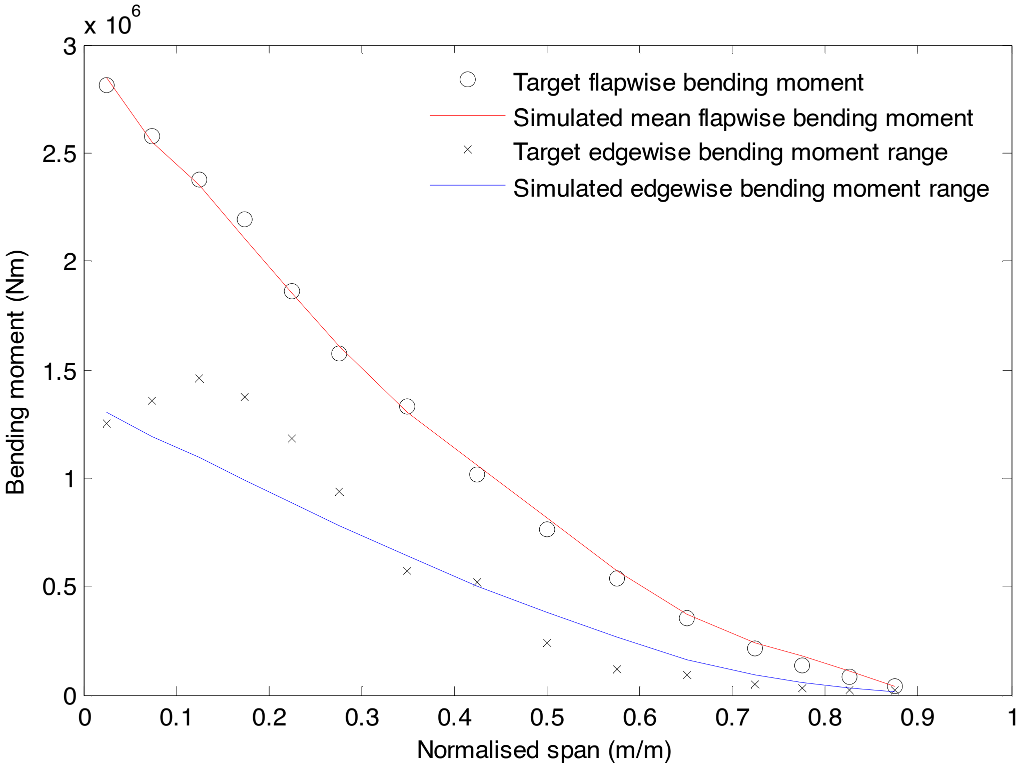

Figure 6.86 - Comparison of target and simulated bending moment distributions for test configuration 1

It can be seen that because the flapwise bending moment is applied by winches it is very close to the target. However, the weight of the saddles affects the edgewise test target loads, resulting in a bending moment distribution that does not decrease monotonically from root to tip. This means that it is impossible to achieve using resonant mass excitation. The edgewise natural frequency dictates the length of the test, and with this test configuration it is 1.33Hz so the test would take 43 days to complete 5 million cycles. Saddle data is given in Table 6.13.

	1	2	3	4	5
Distance from root (m)	12.3	27.2	28.8	36.2	24.7
Saddle mass (kg)	1370	230.8	207.3	129.9	278.2
Winch force (kN)	4.29	8.06	7.60	33.40	32.90

Table 6.13 - Kinetic theory based test configuration 1

The second test configuration involves mounting the blade so that the chord is horizontal with the pressure side facing upwards and applying the flapwise loading using heavy saddles, as shown in Figure 6.23. This is slightly more realistic because the mean bending moment is closer to zero, but the extra mass means the test will take much longer to complete as the frequency will be lower. Another potential issue with this test configuration is that the large masses added to the blade alter the edgewise mode shape considerably, meaning it is again difficult to achieve the correct bending moment distribution as shown in Figure 6.87. Some test facilities around the world have the winches mounted on the floor and pull the blade downwards which would solve this issue, and saddles designed to be lighter than the standard saddles considered here would also help.

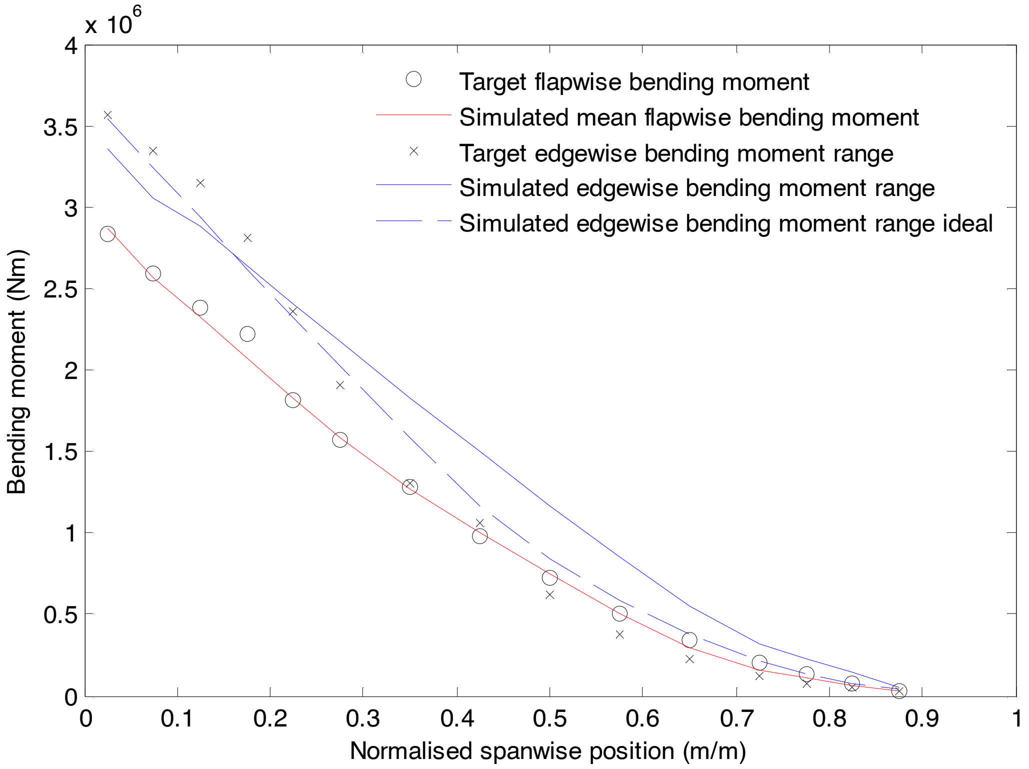

Figure 6.87 - Comparison of target and simulated bending moment distributions for test configuration 2

These improvements are shown in Figure 6.87 by the ‘ideal’ line. The heavy saddles used to load the blade result in a low edgewise frequency of 0.67Hz, so a 5 million cycle test will take 86 days. The saddle configuration used to analyse this test method is shown in Table 6.14. The edgewise dynamic mass forms part of the saddle mass so its size is arbitrary and can be chosen to take the value that gives optimum results.

	1	2	3	4	5
Distance from root (m)	12.3	27.2	28.8	36.2	24.7
Saddle mass (kg)	2215	609	2115	1859	1978

Table 6.14 -Kinetic theory based test configuration 2

The way in which the blade is damaged by this loading is shown in the following figures. The labels LE, PS, TE, SS, ASW and FSW correspond to the leading edge, pressure side, trailing edge, suction side, aft shear web and fore shear web respectively.

The damage caused to the 90° plies at the root by the different test methods is shown in Figure 6.88. The service life damage is shown in red. The damage distributions due to the target loading would be expected to cause less damage in the off-axis plies because the target distribution does not account for shear flow, whereas the simulation does. However, as was seen earlier the shear flow does not greatly affect the damage at the root. The shortcomings of the test methods are apparent; as compressive loading is less damaging, the mass loaded test over-tests the blade at the leading edge, whereas the winch loaded test under-tests the blade between the leading edge. The results on the pressure side trailing edge are better because this is the area for which the test loads were calculated.

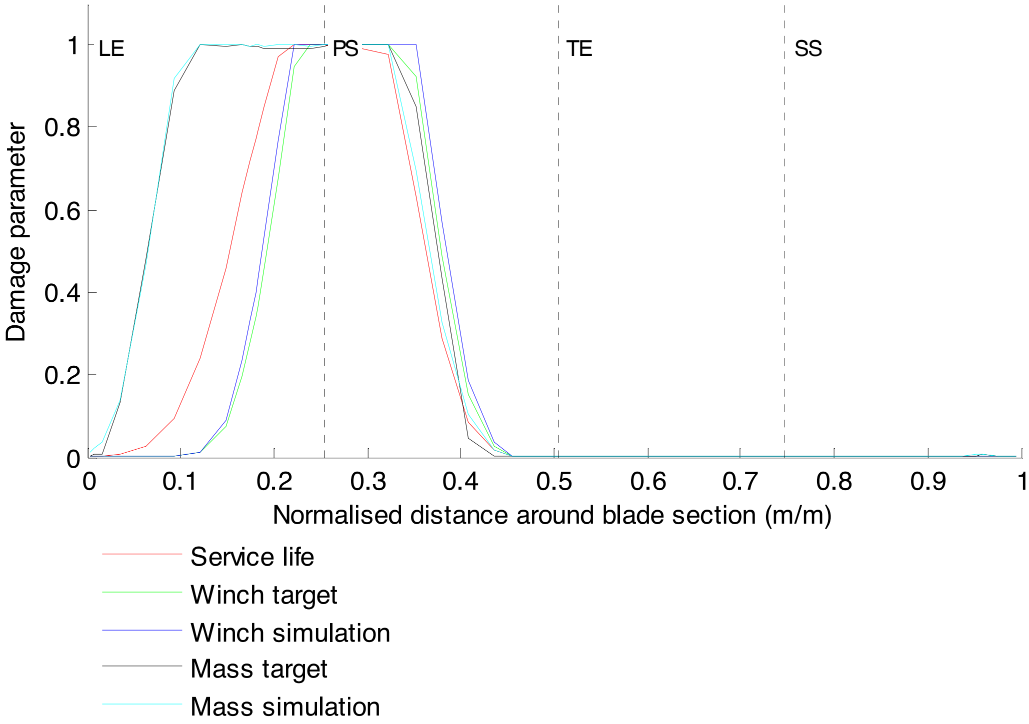

Figure 6.88 - Transverse damage in 90° plies of section 1

The transverse damage in the 45° plies is shown in Figure 6.89. It can be seen that the target loading for the mass direction thoroughly tests the whole blade, but the simulated mass loading results in over-testing because of the difficulties in attaining the correct mode shape in the edgewise direction discussed earlier. Similarly, the winch loading method over-tests the area on the pressure side towards the trailing edge, because of the mean edgewise bending moment with this method is too high.

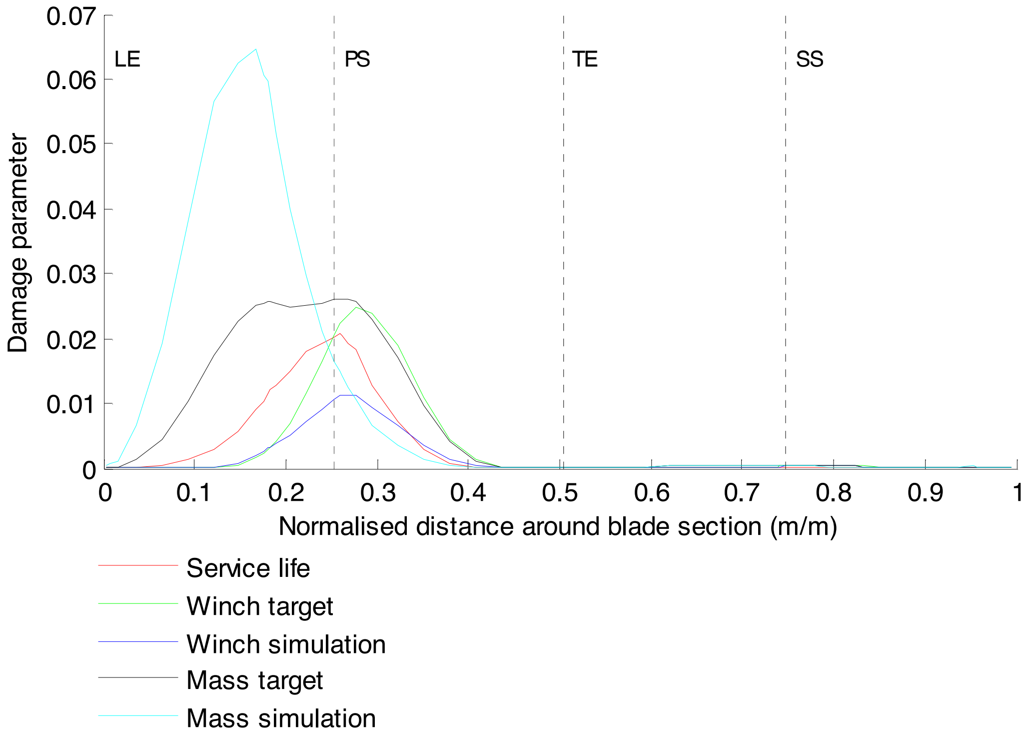

Figure 6.89 - Transverse damage in 45° plies of section 1

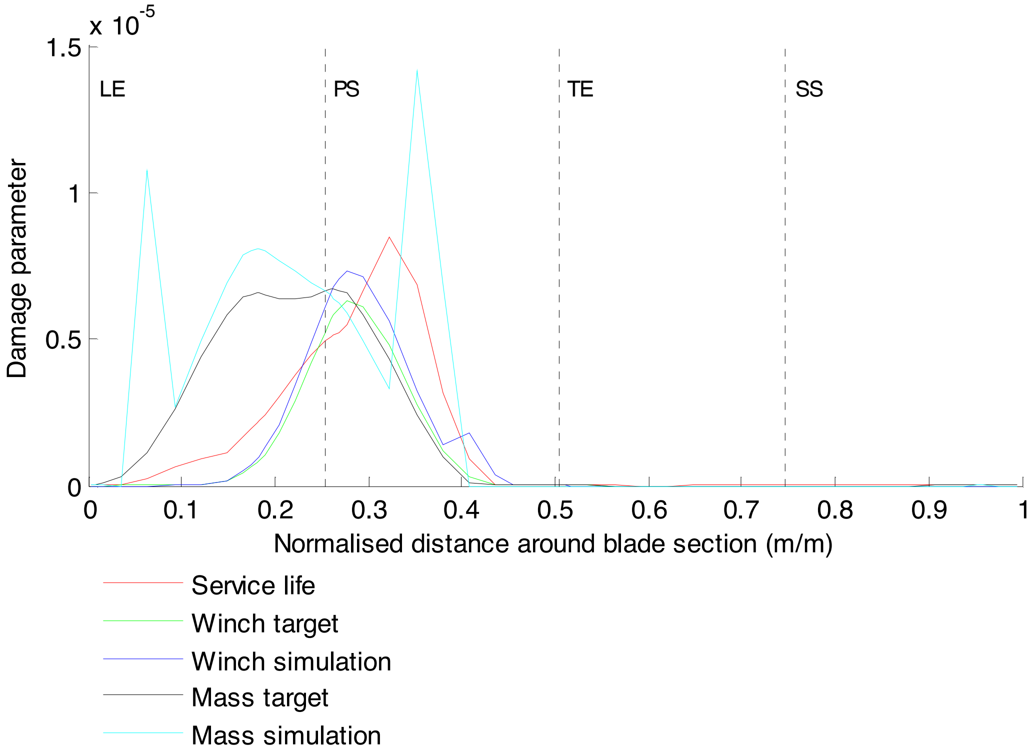

Figure 6.90 - Longitudinal damage in the 0° plies of section 1

The longitudinal damage in the 0° plies at the root is shown in Figure 6.90. It can clearly be seen at this point that the edgewise bending moment amplitude is too high, resulting in the damage spikes towards the leading and trailing edge.

The transverse damage distribution in the 45° plies of section 2 is shown in Figure 6.91 for the different test configurations. The target mass loaded test is conservative over most of the blade, but the simulated loads are again over harsh as a result of the poor edgewise mode shape. The target winch loading is under conservative but perhaps more realistic, while the actual results of the winch loaded test are very non conservative because the edgewise bending moment amplitude is much less than the target at this point.

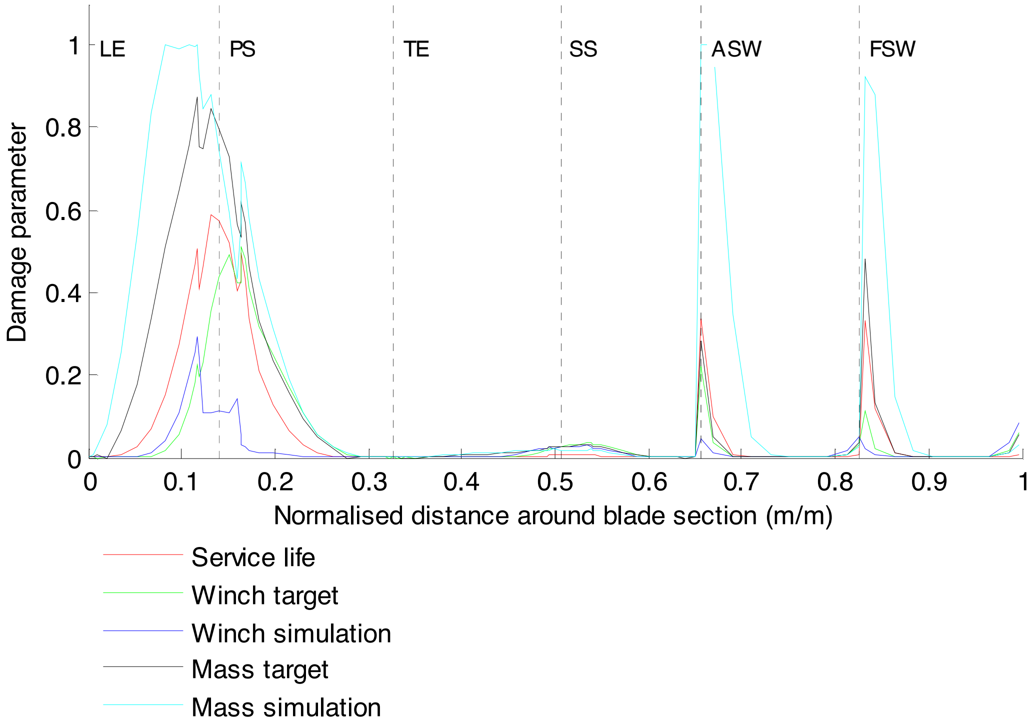

Figure 6.91 - Transverse damage of 45° plies at section 2

The longitudinal damage in the 0° plies of section 2 is shown in Figure 6.92 for the different test configurations. Again, the mass loaded test is conservative whilst the winch loaded test results are more realistic but non-conservative for the target loads and highly unrealistic for the simulated winch test loads, owing to the required edgewise mode shape being impossible to achieve, as shown in Figure 6.86.

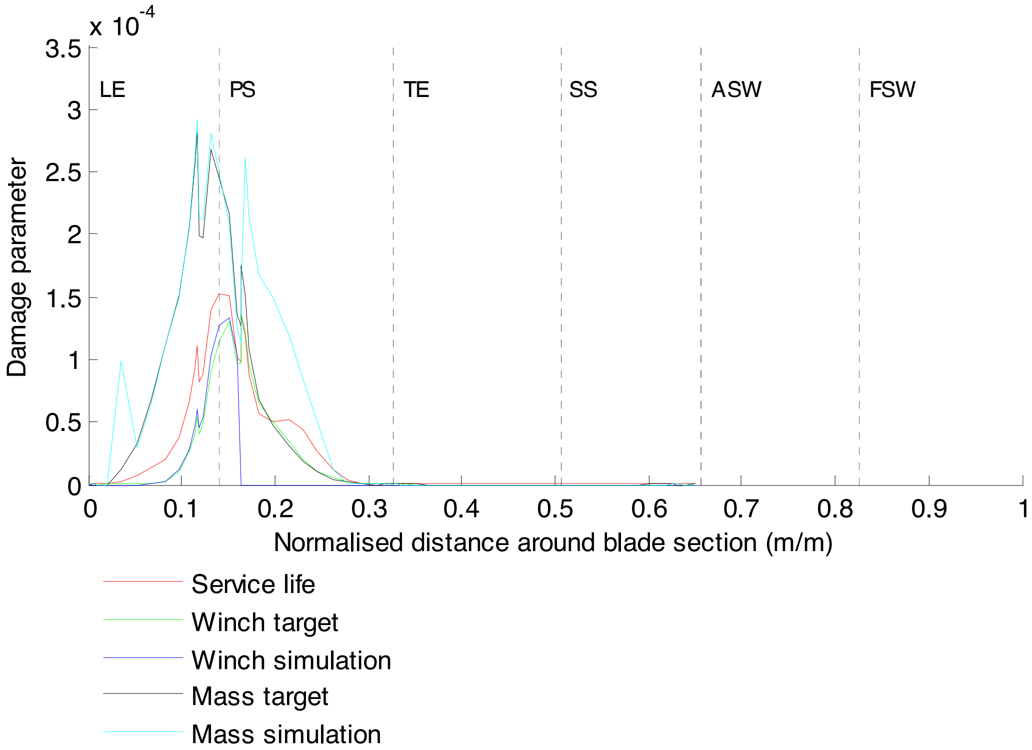

Figure 6.92 - Longitudinal damage in 0° plies of section 2

The trend for the rest of the blade follows a similar pattern; the mass loaded test configuration is conservative, whilst the winch loaded test configuration is non-conservative but more realistic. As shown in Figure 6.86 and Figure 6.87, the achieved edgewise bending moment amplitude can be very different to the target bending moment amplitude for both test configurations, so the achievable damage distributions can be rather poor. Full results for the every blade section are given in appendix F, but for the sake of brevity only sections of interest are shown here.

At section 9 the edgewise bending moment amplitude is almost exactly correct for the winch loaded test, whilst the edgewise amplitude for the mass loaded test is much too high. The transverse damage distribution in the 45° plies is shown in Figure 6.93. The mass test simulation damage distribution is overly harsh, and the large spikes on the suction side are a result of the edgewise bending moment amplitude being too high.

Figure 6.94 shows the longitudinal damage in the 0° plies of section 9, which are limited to local reinforcement of the leading and trailing edge and the spar cap. The pressure side spar cap is greatly over-tested by the mass loaded test as a result of the edgewise bending moment amplitude being far too high there. The other test types are all reasonably effective.

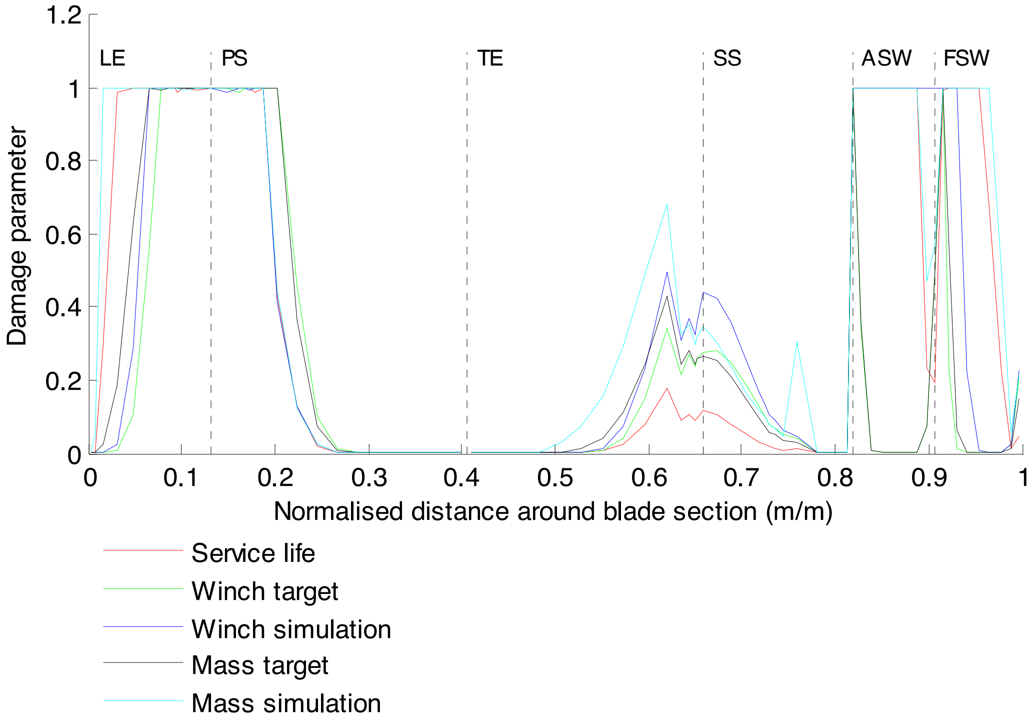

Figure 6.93 - Transverse damage in 45° plies of section 9

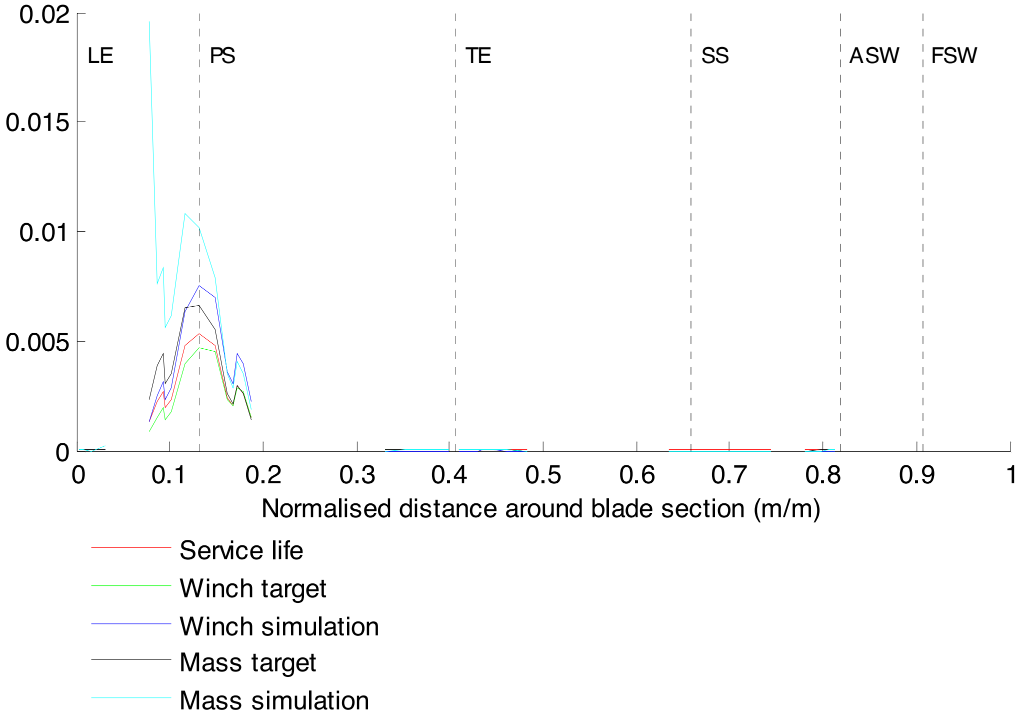

Figure 6.94 - Longitudinal damage in 0° plies of section 9

The test methods discussed here could represent a significant improvement over current methods in terms of test speed, as effectively the edgewise test is the only test performed. The flapwise test generally takes the longest and requires the highest loading, so this test method could reduce energy consumption as well. If a test configuration designed expressly around the method described here were used, the mean edgewise bending moment could be improved by pitching the blade on the test stand. Winches mounted at floor level could then be used to load the blade in the flapwise direction perpendicular to the chord, keeping the mass of equipment mounted on the blade lower and thereby increasing the test frequency. Saddles designed to be as light as possible could allow the edgewise bending moment distribution to be as close to the true distribution as possible, as shown in Figure 6.87.

6.4 Summary and Conclusions

6.4.1 Summary

A novel method of performing fatigue analysis on thin walled beam structures has been described. The blade cross section is discretised into elements, which are composed of laminates. Thin walled beam theory is used to find time histories of the normal and shear flows in each element and classical laminate theory is used to calculate the composite stress state in each ply.

Multi-continuum theory [123] is then used to calculate a time history of the stress state in the matrix, and the failure criteria described by Fertig and Kenik is used [71] to calculate a scalar effective stress in the matrix from the matrix stress tensor for transverse and longitudinal cracks.

The kinetic theory of fracture is then used to calculate the bond rupture rate. This allows the prediction of transverse and longitudinal crack evolution in the matrix. The differential equation described by Hansen and Baker-Jarvis [129] is then used to calculate the evolution of a damage parameter with time in the longitudinal and transverse directions for each ply.

The present work builds on the method described by Fertig and Kenik [71] to allow it to be used for the analysis of wind turbine blades. The modifications made include:

- Use of beam theory to allow the long load cases required by wind turbine design standards [10, 11] to be analysed.
- Addition of zero crossing points to the stress time history to improve results for reversing loading.
- Improvements to the method used to calculate the temperature rise due to hysteretic heating.
- Calculating the time integral of the bond rupture rate mathematically instead of using the trapezium rule, which leads to a large over-estimation of the damage if the stress changes significantly across a time step.
- Changes to the damage evolution equation to allow it to be used for multiple load cases (required by the design standards [10, 11]) and to allow progressive failure simulation.
- Modification to the bond rupture rate to allow the kinetic theory to be applied into the low stress regime described by Zhurkov [73] in which wind turbines operate for much of their lives.

The fatigue analysis model has been benchmarked against coupon test data from the OPTIDAT database [17] and shown to perform well under constant amplitude tensile and reversing loading and spectrum loading. The predictions for compressive loading are poor because the failure mode in compression is not accounted for. Future work should address the predictions obtained under compressive loading by adding a delamination failure mode.

The model has also been applied to the analysis of a full turbine blade. The results are thought to be more realistic than those found using conventional fatigue analysis methods.

Finally, a novel fatigue test method that exploits the fact that kinetic theory of fracture can describe failure in terms of 'time at load' rather than stress or strain amplitude has been described. This test method would be considerably quicker than a typical resonant test, but modifications to the test facilities available at Narec would be necessary in order to get the best from the method. These modifications include mounting winches at floor level and using lighter saddles to speed up the test and allow a more realistic edgewise mode shape to be obtained.

6.4.2 Conclusions

The fatigue analysis method described by Fertig and Kenik [71] has several advantages over the empirical approach suggested by the design standards [10, 11] which is based on the Palmgren-Miner rule [53, 54]. The method eliminates the need for characterisation of every laminate used in the blade, as laminate results can be inferred from the failure of individual plies. This greatly reduces the amount of material testing required, whilst simultaneously allowing multi-axial stress states to be analysed. Allowing for multi-axial stress states has conventionally required a huge amount of material testing.

The present work builds on that performed by Fertig and Kenik [71] to allow the analysis method to be used for wind turbine blades. The progressive failure algorithm allows multi-directional laminates to be analysed, and it has been shown that the method can predict a wide range of coupon level fatigue behaviour whilst requiring less fatigue testing than conventional methods.

It has been shown convincingly that the method can be used to analyse a full blade, which would certainly not be possible with the method described in [71].

The method described here also allows full scale testing to be undertaken in a manner which can account for temperature variation during the test whilst simultaneously allowing the tests to be performed more quickly.

As described previously several of the shortcomings of the approach were addressed, but there are still issues that require further work.

For the analysis of full blades, the principal problem is that the low stress correction has no physical basis. Although the energy barrier to bond rupture is constant for a wide range of applied stresses, it is known to vary in the low stress regime and there are 'first principles' software products available that allow predictions of how the energy barrier varies with applied stress [141] based on the atomic composition of the material. This could be a good starting point for correcting the low stress behaviour whilst maintaining the physical basis of the analysis which is an attractive feature of the kinetic theory. Time temperature superposition has been used to predict the creep failure of composites over long time frames by Reeder [135], and this approach could be used with the power law correction described in the present work to improve the results.

For laminate level analysis, the main issue is the inaccurate predictions of compressive failure. This results from the inability of the model to predict delamination, which could be corrected by a more sophisticated stress analysis method such as the variational asymptotic beam method described by Yu [142]. This method allows out of plane stresses to be calculated, and the inter-laminar shear stresses can also be found.

A coupon testing program designed around the present method would be very beneficial for proving the method and future work should address this issue.

In conclusion, the presented method builds upon previous work by other authors to provide a novel method of fatigue analysis which has several attractive features compared to the conventional method of performing fatigue analysis of wind turbine blades.

7 Conclusions

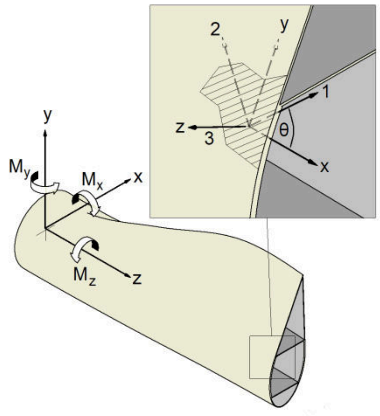

7.1 Summary and Conclusions

In this thesis fatigue analysis and testing of large wind turbine blades has been investigated. During the course of the literature review, it became apparent that there are several factors affecting the accumulation of fatigue damage that are not captured by the standard fatigue analysis methodology which is described in chapter 3.

Nevertheless, in order to evaluate different methods of fatigue testing it is necessary to have an understanding of the damage caused by the service life. For this reason, the fatigue behaviour of a typical 2MW blade was calculated using standard fatigue analysis methods that go beyond what is required by the design guidelines [11]. The results were compared to those obtained when using the fatigue analysis method prescribed by the design guidelines [11], and it was found that the method described in the design guidelines results in unrealistic damage distributions around the blade cross section. Analysis of the loading which causes the greatest amount of damage showed that much of the damage is due to the low amplitude cycles which occur frequently. The loading in this regime is more akin to creep than fatigue cycling, and this was identified as a possible area for later research.

Another important result from the initial analysis of the blade is that a power law curve fit is much less conservative than an exponential fit, and results in very different damage distributions around the blade because the low amplitude cycles are much more damaging when an exponential fit is used.

When test loads were calculated for a ‘bare blade’ with no test equipment mounted on it they were significantly different to the loads obtained when there is equipment mounted on the blade because the higher mean strain means that a lower amplitude oscillation can be used. Test design should therefore be an iterative process.

When the calculated test loads were applied as single axis tests and dual axis tests it was found that a dual axis test in which the edgewise and flapwise frequencies were different tested the blade much more thoroughly than single axis tests, which under-test large areas of the blade. A dual axis test in which the edgewise frequency was the same as the flapwise frequency and the loads cycle with a realistic phase angle between them was found to be the most realistic test, but this is more difficult to achieve in practice for very large blades.

Unfortunately, it is not possible to test every section of the blade with the exact target bending moment. However, if the position and mass of the test equipment is correctly chosen then it is possible to achieve a bending moment distribution close to that which is required over a large part of the span. Prior to the present work, optimisation of dual axis resonant tests had not been performed. The genetic algorithm used in this work was shown to be capable of optimising single and dual axis tests, and it is designed to provide only feasible test configurations. It was found that the air resistance plays a very significant role in the amount of force required to achieve the target bending moment amplitudes. As a result of the blade interacting with its own wake the effective drag coefficient can be much higher than under steady conditions, and this has recently been verified using vortex model developed for modelling insect flight.

Whilst the optimisation tool allows feasible test configurations to be found it does not permit modelling the blade’s structural behaviour in great detail. For this reason a transient 3-D beam element model of a blade test was developed which can account for the non-linear effects of air resistance and the structural twist of the blade. The model was shown to be capable of simulating a small scale test rig and a full scale blade test, using data provided by LM Wind Power. Further analysis of the blade sections for which fatigue damage distributions were obtained in chapter 3 showed that the dual axis test method still outperforms single axis testing even when complicating factors such as imperfect bending moment distributions and blade twist were accounted for.

A model of a test configuration designed to allow the edgewise frequency to be reduced so that it is the same as the flapwise frequency was found to be unfeasible even for a blade that is not large by today’s standards. Other authors have also attempted to alter the either the edgewise or flapwise frequencies, and it seems that the only possibility is to either force the edgewise direction at the flapwise frequency (which requires higher actuator forces) or perform ‘near resonant’ dual axis testing which reduces actuator forces by adding extra mass to the edgewise direction (without making the frequencies the same). Wind turbine blades are very lightly damped and the range of frequencies over which significant force amplification can be achieved is quite small, so near resonant testing still requires large actuator forces.

The shortcomings in the fatigue analysis methods prescribed by the design guidelines [11] became apparent during the work in chapter 3. If a blade uses many different laminates then a huge quantity of physical testing is required in order to characterise the behaviour of each laminate under a range of loading conditions. Even after performing this quantity of testing, multi-axial stress states, creep, temperature and test frequency are not accounted for, all of which can have significant effects.

During the course of this research, a plug-in for the popular fatigue analysis software FE-Safe made by Firehole Composites became available. This software uses multi-continuum theory to obtain the stress state in each ply of a composite structure, and the kinetic theory of fracture is then used to calculate the number of repeats of given load case that can be tolerated before failure. The software requires fatigue testing only on a ply level, so much less testing is required, and it is based on physical rather than empirical laws so loading frequency and temperature effects are accounted for implicitly.

However, it cannot be used reliably for wind turbine blade analysis in its standard form. At the time of writing, multiple load blocks cannot be analysed, long time histories cause the temperature to increase indefinitely, the change in behaviour at low stresses is not accounted for and the requirement to use full finite element models of the blade means that analyses are very time consuming. As the method used in this software is described by Fertig and Kenik [71], it was possible to implement the approach as a stand-alone program and develop solutions to allow the method to be used for wind turbine blade analysis.

These improvements included adding zero crossings to the stress time history to improve the modelling of reversing loading, developing an improved time integration method, adding a cooling model to stop the temperature increasing indefinitely during the analysis of long time histories and changing the damage accumulation equation to allow progressive failure analyses and multi-block loading to be analysed.

The program developed was benchmarked against a wide range of fatigue test data from the OPTIDAT database and was found to perform well for tensile and reversing loading. Compressive failure of unidirectional coupons loaded in line with the fibres could not be modelled because the delamination failure mode was not accounted for. It is thought that compressive failure in laminates with no layers orientated parallel to the load can still be modelled, although no data was available to validate this.

The beam element model was used to analyse 18 cross sections from a real wind turbine blade, the LM 40.3 P2. It was shown that accounting for multi-axial stress states results in a significant increase in damage around the blade, particularly to the shear webs. The effect of stiffness degradation was studied, and it was found that anisotropic failure was more conservative as it resulted in earlier compressive failure to the 0° plies than would be seen in practice. Compressive failures were not seen on the blade however. It was also shown that it is essential to include a correction for the change in the behaviour at low stresses in order to use the approach in the stress regimes in which wind turbines operate, although there is limited data available to decide when this low stress correction should begin to come into effect.

A full scale fatigue test method based on the kinetic theory of fracture was described which could provide benefits over current methods including more accurate testing, reduced energy input and faster test times. Winches are used to load the flap direction to simulate the wind loads, while the edgewise direction is loaded using resonant excitation. However, the effect of fatigue on the winches was not investigated.

7.2 Suggestions for further work

As blades grow in size, the air resistance will continue to dictate the capabilities of test equipment, particularly for flapwise testing. The model used in the present work is based on simply increasing the drag coefficient to account for unsteady effects, which will not give accurate results across a particularly wide range of scenarios. The insect wing model described by Ansari in [143, 144] could be used to give predictions of the unsteady effects for a range of different chord lengths, frequencies and amplitudes of motion, allowing the drag coefficient for a given scenario to be ‘looked up’. There is also no knowledge of the effect of the proximity of the floor and walls in a test facility on the air resistance, or the effect of 3-D spanwise flow, so research into these phenomena would be useful.

The Rayleigh damping model used in the present work, although typical of similar models, requires the structural damping of the blade to be known a priori. It is possible to develop a damping matrix from the properties of the ply, thus allowing the blade damping to be estimated using the techniques described in, for example [105]. This could save time when configuring a test by calculating a test set-up before the blade is attached to the test stand.

The beam element used for modelling the fatigue test is rather simple, with no accounting for the twist or taper of the blade, except by discrete steps. A more complex beam element could improve the results at the expense of the simplicity of the program.

Multi-continuum theory coupled with the kinetic theory of fracture has been shown to have great potential for composite fatigue analysis. However, there is more work needed before the theory can offer a comprehensive solution to composite fatigue. A test program based around the fatigue analysis method described in chapter 6 would be very beneficial, as current fatigue databases are missing crucial information which would allow judgments to be made on the quality of the results. Any program would need to provide complete information on the temperature of all specimens and the ambient temperature as well. It would also be useful to have more off axis data to validate the failure criterion for the transverse direction.

A major issue when validating against compressive data is the lack of a representative failure mode. The present method could be greatly improved by the addition of a model which predicts delamination growth to allow compressive failure of plies loaded in line with the fibres to be investigated.

The most important issue relating to the application of the model to a full blade analysis is the lack of data to fit the low stress correction model. As these tests are very time consuming, they could be accelerated by using the time-temperature superposition method as described by Reeder [135]. The results could then be fit using the physics based model developed by Kausch von Schmeling [85].

The ideal improvement would be a function describing the activation energy U and the activation volume γ that is based on the molecular physics, as the present method is at higher stresses. These could be derived using physics based simulation tools such as dmol^3 [141].

The blade test optimisation and simulation tools are complete and function well, but the kinetic theory method offers great benefits for fatigue analysis if the problems described above can be resolved.

References

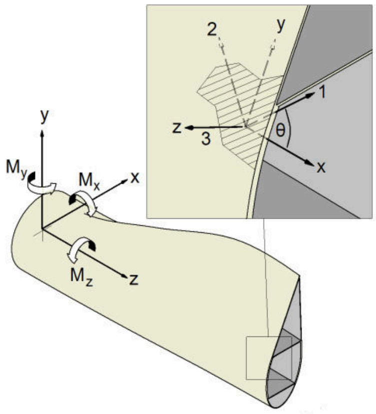

1. Manwell, J.F., J.G. McGowan, and A.L. Rogers, *Wind energy explained theory, design and application*. 2002, Chichester; New York: Wiley.
2. Cowie, J., *Climate change : biological and human aspects*. 2007, Cambridge; New York: Cambridge University Press.
3. Pilkey, O.H., K.C. Pilkey, and M.E. Fraser, *Global climate change: A primer*. 2011: Duke University Press.
4. IPCC, *Intergovernmental Panel on Climate Change - Fourth Assessment Review Summary for Policymakers*. 2007.
5. Metz, B., *Climate change 2007 : mitigation of climate change : contribution of Working Group III to the Fourth Assessment Report of the Intergovernmental Panel on Climate Change*. 2007, Cambridge; New York: Cambridge University Press.
6. European Parliment, *Road map for renewable energy in Europe* 2007.
7. MacKay, D.J.C., *Sustainable energy--without the hot air*. 2009, Cambridge, England: UIT.
8. Junginger, M., A. Faaij, and W. Turkenburg, *Cost reduction prospects for offshore wind farms.* Wind Engineering, 2004. **28**(1): p. 97-118.
9. Burton, T., et al., *Wind energy handbook*. 2001, Chichester: John Wiley and Sons Ltd.
10. BSI, *BS EN 61400-1 Wind Turbines - Design requirements*. 2005.
11. Germanischer Lloyd, *Guideline for the certification of wind turbines*. 2003, Germanischer Lloyd Industrial Services.
12. Söker, H., et al., *A guide to design load validation*, in *DEWEK 2006 Deutsche Windenergie-Konferenz*. 2006, DEWI: Bremen, Germany.
13. Hau, E., *Wind turbines: Fundamentals, technologies, application, economics*. 2nd Revised edition ed. 2005, Berlin: Springer.
14. Brøndsted, P., H. Lilholt, and A. Lystrup, *Composite materials for wind power turbine blades* Annual Review of Materials Research, 2005. **35**: p. 505-538.
15. Passon, P., et al., *OC3—Benchmark Exercise of Aero-elastic Offshore Wind Turbine Codes.* Journal of Physics: Conference Series, 2007. **75**(1): p. 12-71.
16. Vassilopoulos, A.P. and T. Keller, *Fatigue of fiber-reinforced composites*. 2011, London: Springer.
17. Knowledge Centre WMC. *OPTIDAT database*. 2009 [cited 2010 12/03]; Available from: http://www.wmc.eu/optimatblades_optidat.php.
18. BSI, *BS EN61400-23 Wind turbine generator systems - Full scale structural testing of rotor blades*. 2005.
19. Van Delft, D.R.V. and J.L. Van Leeuwen, *Full-scale testing of wind turbine rotor blades*, in *EWEC*. 1994: Thessaloniki, Greece
20. White, D., *New method for dual-axis fatigue testing of large wind turbine blades using resonance excitation and spectral loading*. 2004, University of Boulder, Colorado.
21. Narec. *Wind energy overview*. 2009 [cited 2010 11/03]; Available from: http://www.narec.co.uk/sectors/wind_energy/.

22. Desmond Jr, M., D. White, and W. Barott. *Finite element modeling of a dual axis resonant test system for wind turbine blades*. in *ASME 2009 3rd International Conference on Energy Sustainability*. 2009. San Francisco, California
23. Desmond Jr, M. and D. White. *Predictions of structural testing characteristics for wind turbine blades*. in *ASME International Mechanical Engineering Congress and Exposition*. 2010. Lake Buena Vista, Florida
24. GL Garrad Hassan. *Bladed - GL Garrad Hassan - Software*. 2011 [cited 2011 20/05]; Available from: http://www.gl-garradhassan.com/en/software/GHBladed.php.
25. Petersen, J.T., *Kinematically nonlinear finite element model of a horizontal axis wind turbine*, in *Department of Meteorology and Wind Energy*. 1990, Risø National Laboratory: Roskilde.
26. DTU Wind Energy. *HAWC2*. 2012 [cited 2012 10/12]; Available from: http:/www.hawc2.dk.
27. MSC Software. *ADAMS Multibody dynamics simulation*. 2012 [cited 2012 10/12]; Available from: http://www.adams.com.
28. Jonkman, J.M. and M.L. Buhl, *FAST user's guide*. 2005, NREL.
29. Quarton, D.C., *The evolution of wind turbine design analysis: a twenty year progress review.* Wind Energy, 1998. **1**(S1): p. 5-24.
30. Hansen, M.O.L., et al., *State of the art in wind turbine aerodynamics and aeroelasticity.* Progress in Aerospace Sciences, 2006. **42**(4): p. 285-330.
31. Heege, A., et al., *Fatigue damage computation of a composite material blade using a "Mixed non-linear FEM and super element approach"*, in *EWEA 2011*. 2011: Brussels.
32. Court, R.S., et al., *Fatigue testing of wind turbine blades with computational verification*, in *ICCM*. 2009: Edinburgh.
33. Grujicic, M., et al., *Multidisciplinary design optimization for glass-fiber epoxy-matrix composite 5 MW horizontal-axis wind-turbine blades.* Journal of Materials Engineering and Performance, 2010. **19**(8): p. 1116-1127.
34. Kong, C., J. Bang, and Y. Sugiyama, *Structural investigation of composite wind turbine blade considering various load cases and fatigue life.* Energy, 2004. **30**(11-12): p. 2101-2114.
35. Kong, C., et al., *Investigation of fatigue life for a medium scale composite wind turbine blade.* International Journal of Fatigue, 2006. **28**(10): p. 1382-1388.
36. Sandia National Laboratories. *Wind Energy Technology*. 2009 [cited 2010 20/04]; Available from: http://www.sandia.gov/wind/NuMAD.htm.
37. Bonnet, P. and G. Dutton, *Parametric Modelling Of Large Wind Turbine Blades*, in *2007 Abaqus UK Regional User Meeting*. 2007.
38. Knowledge Centre WMC. *Knowledge Centre WMC - FOCUS 6 - The Integrated Wind Turbine Design Tool*. 2009 [cited 2010 20/04]; Available from: http://www.wmc.eu/focus6.php.
39. NSE Composites. *NSE Composites - Services - Finite Element Analysis*. 2008 [cited 2010 20/04]; Available from: http://www.nsecomposites.com/services/finite-element-analysis.html.
40. LM Windpower. *LM Blades*. 2010 [cited 2010 20/04]; Available from: http://www.lmwindpower.com/Blades/Technology/Design/LM%20Blades.aspx.
41. Nijssen, R., *Fatigue life prediction and strength degradation of wind turbine rotor blade composites*. 2006, Technische Universiteit Delft: Delft.
42. Post, N.L., S.W. Case, and J.J. Lesko, *Modeling the variable amplitude fatigue of composite materials: A review and evaluation of the state of the art for spectrum loading.* International Journal of Fatigue, 2008. **30**(12): p. 2064-2086.
43. ASM International, *Characterization and failure analysis of plastics*. 2003, Materials Park, OH: ASM International.
44. Mandell, J.F., et al., *New fatigue data for wind turbine blade materials.* Journal of Solar Energy Engineering, Transactions of the ASME, 2003. **125**(4): p. 506-514.

45. Post, N., *Reliability based design methodology incorporating residual strength prediction of structural fiber reinforced polymer composites under stochastic variable amplitude fatigue loading*. 2008, Virginia Polytechnic Institute and State University: Blacksburg.

46. Sutherland, H. and J. Mandell, *Updated Goodman diagrams for fiberglass composite materials using the DOE/MSU fatigue database*, in *Global Windpower 2004*. 2004: Chigago, Illinois. p. 12.

47. Sutherland, H.J. and J.F. Mandell. *Optimized Goodman diagram for the analysis of fiberglass composites used in wind turbine blades*. in *ASME Wind Energy Symposium*. 2005. Reno, Nevada

48. Sutherland, H.J. and J.F. Mandell, *The effect of mean stress on damage predictions for spectral loading of fibreglass composite coupons.* Wind Energy, 2005. **8**(1): p. 93-108.

49. Wahl, N., *Spectrum fatigue lifetime and residual strength for fiberglass laminates*, in *School of Mines & Engineering*. 2002, Montana State University: Bozeman, Montana, US.

50. Matsuiski, M. and T. Endo, *Fatigue of metals subjected to varying stress*, in *Japan Society of Mechanical Engineers*. 1969: Kyushu, Japan.

51. Downing, S.D. and D.F. Socie, *Simple rainflow counting algorithms.* International Journal of Fatigue, 1982. **4**(1): p. 31-40.

52. Fatemi, A. and L. Yang, *Cumulative fatigue damage and life prediction theories: a survey of the state of the art for homogeneous materials.* International Journal of Fatigue, 1998. **20**(1): p. 9-34.

53. Miner, M.A., *Cumulative damage in fatigue.* Journal of Applied Mechanics, 1945. **12**(3): p. A159-A164.

54. Palmgren, A., *Die lebensdauer von kugellagern.* VDI-Zeitschrift, 1924. **68**(14): p. 339-341.

55. Marco, S.M. and W.L. Starkey, *A concept of fatigue damage.* Trans. ASME, 1954. **76**(4): p. 627-632.

56. Owen, M.J. and R.J. Howe, *The accumulation of damage in a glass-reinforced plastic under tensile and fatigue loading.* Journal of Physics D: Applied Physics, 1972. **5**: p. 1637–1649.

57. Bond, I.P., *Fatigue life prediction for GRP subjected to variable amplitude loading.* Composites Part A: Applied Science and Manufacturing, 1999. **30**(8): p. 961-970.

58. Broutman, L.J. and S. Sahu. *A new theory to predict cumulative fatigue damage in fiberglass reinforced plastics*. in *Composite materials: testing and design (second conference) ASTP 497*. 1972. Anaheim, California: American Society for Testing and Materials.

59. Hahn, H.T. and R.Y. Kim, *Proof testing of composite materials.* Journal of Composite Materials, 1975. **9**(3): p. 297-311.

60. Chou, P.C. and R. Croman, *Residual strength in fatigue based on the strength-life equal rank assumption.* Journal of Composite Materials, 1978. **12**(2): p. 177-194.

61. Sarkani, S., et al., *Comparative study of nonlinear damage accumulation models in stochastic fatigue of FRP laminates.* Journal of Structural Engineering, 2001. **127**(3): p. 314-322.

62. Montana State University. *DOE/MSU Composite material fatigue database*. 2009 [cited 2010 12/03]; Available from: http://www.coe.montana.edu/composites/.

63. Schaff, J.R. and B.D. Davidson, *Life prediction methodology for composite structures. Part I—Constant amplitude and two-stress level fatigue.* Journal of Composite Materials, 1997. **31**(2): p. 128-157.

64. Reifsnider, K., *Fatigue behavior of composite materials.* International Journal of Fracture, 1980. **16**(6): p. 563-583.

65. Reifsnider, K.L. and W.W. Stinchcomb, *A critical-element model of the residual strength and life of fatigue-loaded composite coupons*. 1986, Philadelphia, PA: American Society for Testing and Materials. 16.

66. Subramanian, S., K.L. Reifsnider, and W.W. Stinchcomb, *Cumulative damage model to predict the fatigue life of composite laminates including the effect of a fibre-matrix interphase.* International Journal of Fatigue, 1995. **17**(5): p. 343-351.

67. Song, D.-Y. and N. Otani, *Fatigue life prediction of cross-ply composite laminates.* Materials Science and Engineering: A, 1997. **238**(2): p. 329-335.
68. Philippidis, T.P. and V.A. Passipoularidis, *Residual strength after fatigue in composites: Theory vs. experiment.* International Journal of Fatigue, 2007. **29**(12): p. 2104-2116.
69. Passipoularidis, V.A., T.P. Philippidis, and P. Brondsted, *Fatigue life prediction in composites using progressive damage modelling under block and spectrum loading.* International Journal of Fatigue, 2011. **33**(2): p. 132-144.
70. Fertig, R. and D. Kenik, *Physics-Based Fatigue Life Prediction of Composite Structures*, in *NAFEMS World Congress*. 2011: Boston, MA.
71. Fertig, R. and D. Kenik, *Physics-based fatigue life prediction of composite structures*, in *NAFEMS World Congress 2011*. 2011: Boston, MA.
72. Griffith, A.A., *The phenomena of rupture and flow in solids.* Philosophical Transactions of the Royal Society of London. Series A, Containing Papers of a Mathematical or Physical Character, 1921. **221**: p. 163-198.
73. Zhurkov, S.N., *Kinetic concept of the strength of solids.* International Journal of Fracture Mechanics, 1965. **1**: p. 311-323.
74. Aleksandrov, A.P. and Y.S. Lazurkin, *A study of polymers. I. Highly elastic deformation of polymers.* Rubber Chemistry and Technology Rubber Chemistry and Technology, 1940. **13**(4): p. 886-898.
75. Gurevich, G.I., *On the strain laws for solids and fluids.* Zhurnal Tekhnicheskoi Fiziki, 1947. **17**(2): p. 1491–1502.
76. Tobolsky, A. and H. Eyring, *Mechanical properties of polymeric materials.* Journal of Chemical Physics, 1943. **11**(3): p. 125-134.
77. Zhurkov, S.N., *The kinetic view of the tensile strength of solids.* Neorganicheskie Materialy 1967. **3**(10): p. 1767-1776
78. Zhurkov, S.N., Betekhti.Vi, and A.I. Petrov, *Temperature-time dependence of strength of metals and alloys in state of disequilibrium.* Physics of Metals and Metallography-Ussr, 1967. **24**(1): p. 156-&.
79. Zhurkov, S.N., et al., *Block disorientation and low-temperature strength of aluminium.* Physics of Metals and Metallography, 1966. **21**(2): p. 87-90.
80. Zhurkov, S.N. and V.S. Kuksenko, *The micromechanics of polymer fracture.* International Journal of Fracture, 1975. **11**(4): p. 629-639.
81. Regel, V.R., A.I. Slutsker, and É.E. Tomashevskiĭ, *The kinetic nature of the strength of solids.* Soviet Physics Uspekhi, 1972. **15**(1): p. 45.
82. Emanuel', N.M. and A.L. Buchachenko, *Chemical physics of polymer degradation and stabilization*. 1987, Utrecht, The Netherlands: VNU Science Press.
83. Regel, V.R. and A.M. Leksovsky, *A study of fatigue within the framework of the kinetic concept of fracture.* International Journal of Fracture, 1967. **3**(2): p. 99-109.
84. Mishnaevsky, L. and P. Brøndsted, *Modeling of fatigue damage evolution on the basis of the kinetic concept of strength.* International Journal of Fracture, 2007. **144**(3): p. 149-158.
85. Kausch von Schmeling, H.H., *Recent developments in the kinetic theory of fracture of polymers.* Colloid & Polymer Science, 1970. **236**(1): p. 48-58.
86. Musial, W. and J. Allread, *Test methodology and control of full-scale fatigue tests on wind turbine blades*, in *Wind Energy*. 1993: Houston, Texas.
87. Musial, W.D., M.E. Clark, and T. Stensland, *Application of BSTRAIN software for wind turbine blade testing*, in *AWEA Windpower '96*. 1996: Denver, Colorado.
88. RISØ. *Fatigue tests of wind turbine blades*. 2001 [cited 2010 11/03]; Available from: http://130.226.56.153/rispubl/VEA/sparkaer/fatigue_test.pdf.
89. Grove-Nielsen, E. *Winds of change - Stories of a dawning wind power industry*. 2006 [cited 2012 31/05]; Available from: http://www.windsofchange.dk/WOC-bladestory.php.
90. Jensen, P.H., et al., *Fatigue testing of wind turbine blades*, in *European Wind Energy Association Conference and Exhibition*. 1986: Rome, Italy.

91. Hughes, S., W. Musial, and T. Stensland, *Implementation of two axis servo-hydraulic system for full-scale testing of wind turbine blades*, in *Windpower '99*. 1999, NREL: Burlington, Vermont.
92. Larwood, S., et al., *NedWind 25 blade testing at NREL for the European standards measurement and testing program*. 2001, NREL.
93. Kristensen, O.J.D. and E.R. Jørgensen, *Accelerated fatigue testing of LM 19.1 blades*. 2003, RISØ-R-1358(EN).
94. White, D.L. and W.D. Musial, *The effect of load phase angle on wind turbine blade fatigue damage.* Journal of Solar Energy Engineering, Transactions of the ASME, 2004. **126**(4): p. 1050-1059.
95. Ridley, S., *Simulation of a 40m wind turbine blade during a fatigue test*, in *School of Computing, Engineering and Information Sciences*. 2009, Northumbria University: Newcastle.
96. Malhotra, P., et al., *A review and design study of blade testing systems for utility-scale wind turbines.* Renewable and Sustainable Energy Reviews, 2012. **16**(1): p. 284-292.
97. White, D., et al., *Development of a dual-axis phase-locked resonant excitation test method for fatigue testing of wind turbine blades*, in *ASME 2011 International Mechanical Engineering Congress & Exposition*. 2011: Denver, Colorado.
98. Surtherland, H.J., *On the fatigue analysis of wind turbines*. 1999, Sandia National Laboratories.
99. UIUC Applied Aerodynamics Group. *UIUC Airfoil data site*. 2010 [cited 2010 10/8]; Available from: http://www.ae.illinois.edu/m-selig/ads/coord_database.html.
100. Bauchau, O.A. and J.I. Craig, *Structural analysis: With applications to aerospace structures*. 2009, London: Springer.
101. Safe Technology. *FE-Safe/Composites*. 2012 [cited 2012 02/04]; Available from: http://www.safetechnology.com/fe-safe_Composites.html.
102. Nieslony, A., *MatLab Rainflow Counting Algorithm*. 2010.
103. Chapra, S.C. and R.P. Canale, *Numerical methods for engineers*. 2002, Boston: McGraw-Hill Higher Education.
104. Rao, S.S., *Mechanical vibrations*. 4th ed. 2004, Upper Saddle River: Pearson Education.
105. Chortis, D.I., N.A. Chrysochoidis, and D.A. Saravanos, *Damped structural dynamics models of large wind-turbine blades including material and structural damping.* Journal of Physics: Conference Series, 2007. **75**(1).
106. Du, L., *Flow structure behind fatigue testing for wind turbine blades*. 2012, Durham University, Durham.
107. Mitchell, M., *An introduction to genetic algorithms*. 1998, Boston, Massachusetts: MIT Press.
108. Griffith, D.T. and B.R. Resor, *Description of model data for SNL100-00: The Sandia 100-meter all-glass baseline wind turbine blade*. 2011, Sandia National Laboratory: Albuquerque, New Mexico.
109. Griffith, D.T. and T.D. Ashwill, *The Sandia 100-meter all-glass baseline wind turbine blade: SNL100-00*. 2011, Sandia National Laboratories: Albuquerque, New Mexico.
110. Przemieniecki, J.S., *Theory of matrix structural analysis*. 1985, Mineola, New York: Dover Publications.
111. Baumgart, A., *A mathmatical model for wind turbine blades.* Journal of Sound and Vibration, 2002. **251**(1): p. 1-12.
112. Case, J., H.C. Chilver, and C.T.F. Ross. *Strength of materials and structures*. 1999; Available from: http://www.knovel.com/knovel2/Toc.jsp?BookID=496.
113. Blade Test Centre Gujarat. *Fatigue testing*. 2009; Available from: http://www.btcgujarat.com/fatigue_test.html.
114. Knowledge Centre WMC. *Facilities*. 2008 [cited 2010 11/03]; Available from: http://www.wmc.eu/facility.php.

115. Firehole Composites. *Helius:Fatigue*. 2012 [cited 2012 02/04]; Available from: http://www.firehole.com/products/fatigue/.

116. Hansen, A.C. and M.R. Garnich, *A multicontinuum theory for structural analysis of composite material systems.* Composites Engineering, 1995. **5**(9): p. 1091-1103.

117. Kollar, L.P. and G.S. Springer, *Mechanics of composite structures*. 2003, Cambridge; New York: Cambridge University Press.

118. Halpin, J.E., *Revised primer on composite materials : analysis*. 1984, Lancaster, PA.: Technomic Pub. Co.

119. Zienkiewicz, O.C., *The finite element method*. 1977, London; New York: McGraw-Hill.

120. Fernandes da Silva, G., J.C. Marín, and A. Barroso, *Evaluation of shear flow in composite wind turbine blades.* Composite Structures, 2011. **93**(7): p. 1832-1841.

121. Megson, T.H.G., *An introduction to aircraft structural analysis*. 2010, Amsterdam: Elsevier.

122. Kenik, D., *FE-Safe/Composites theory manual*. 2010: Laramie, Wyoming.

123. Garnich, M.R. and A.C. Hansen, *A multicontinuum theory for thermal-elastic finite element analysis of composite materials.* Journal of Composite Materials, 1997. **31**(1): p. 71-86.

124. Mayes, J.S. and A.C. Hansen, *Composite laminate failure analysis using multicontinuum theory.* Composites Science and Technology, 2004. **64**(3–4): p. 379-394.

125. Mayes, S. and A.C. Hansen, *Multicontinuum failure analysis of composite structural laminates.* Mechanics of Composite Materials and Structures, 2001. **8**(4): p. 249-262.

126. Mayes, J.S. and A.C. Hansen, *A comparison of multicontinuum theory based failure simulation with experimental results.* Composites Science and Technology, 2004. **64**(3–4): p. 517-527.

127. Coleman, B.D., *Time dependence of mechanical breakdown phenomena.* Journal of Applied Physics, 1956. **27**(8): p. 862-866.

128. Coleman, B.D., *Application of the theory of absolute reaction rates to the creep failure of polymeric filaments.* Journal of Polymer Science, 1956. **20**(96): p. 447-455.

129. Hansen, A. and J. Baker-Jarvis, *A rate dependent kinetic theory of fracture for polymers.* International Journal of Fracture, 1990. **44**(3): p. 221-231.

130. Andrews, E. and P. Reed, *Failure in polymers*. Vol. 27. 1978, Berlin Springer / Heidelberg.

131. Hashin, Z. and A. Rotem, *A fatigue failure criterion for fiber reinforced materials.* Journal of Composite Materials, 1973. **7**(4): p. 448-464.

132. Reifsnider, K., *Damage tolerance and durability of material systems* 2002, New York: Wiley.

133. Sauer, J.A. and G.C. Richardson, *Fatigue of polymers.* International Journal of Fracture, 1980. **16**(6): p. 499-532.

134. Burmeister, L.C., *Convective heat transfer*. 1983, New York: Wiley.

135. Reeder, J.R., D.H. Allen, and W.L. Bradley, *Accelerated strength testing of thermoplastic composites.* ASTM special technical publication, 2000. **1357**: p. 318-337.

136. Fertig, R.S., *Bridging the gap between physics and large-scale structural analysis: A novel method for fatigue life prediction of composites*, in *SAMPE Fall Technical Conference*. 2009: Wichita, KS.

137. Raju, I.S., et al., *A new look at numerical analyses of free-edge stresses in composite laminates*. 1980, Washington, D.C.; Springfield, Va.: National Aeronautics and Space Administration, Scientific and Technical Information Branch ; For sale by the National Technical Information Service].

138. Have, A.A.T., *WISPER and WISPERX : Final definition of two standardised fatigue loading sequences for wind turbine blades*. 1992, Amsterdam: Nationaal Lucht- en Ruimtevaartlaboratorium.

139. Have, A.A.T., *WISPER and WISPERX : A summary paper describing their background, derivation and statistics*. 1994, Amsterdam: NLR.

140. Bulder, B., et al., *NEW WISPER - Creating a New Standard Load Sequence From Modern Wind Turbine Data*. 2005, OPTIMAT Project.

141. Accelrys. *Use Accelrys Materials Studio for materials modelling and simulation*. 2012 [cited 2012 16/10]; Available from: http://accelrys.com/products/materials-studio/index.html.

142. Yu, W., D.H. Hodges, and J.C. Ho, *Variational asymptotic beam sectional analysis – An updated version.* International Journal of Engineering Science, 2012. **59**(0): p. 40-64.

143. Ansari, S.A., R. Åbikowski, and K. Knowles, *Non-linear unsteady aerodynamic model for insect-like flapping wings in the hover. Part 1: methodology and analysis.* Proceedings of the Institution of Mechanical Engineers, Part G: Journal of Aerospace Engineering, 2006. **220**(2): p. 61-83.

144. Ansari, S.A., R. Åbikowski, and K. Knowles, *Non-linear unsteady aerodynamic model for insect-like flapping wings in the hover. Part 2: implementation and validation.* Proceedings of the Institution of Mechanical Engineers, Part G: Journal of Aerospace Engineering, 2006. **220**(3): p. 169-186.

Appendix A – Demonstration Turbine Model

Hub vertical offset (m)	1.5
Tilt angle (°)	4
Overhang (m)	3.7
Cut-in windspeed (m/s)	4
Cut-out windspeed (m/s)	25
Rotor position	Upwind
Variable speed	Yes
Variable pitch	Yes
Transmission	Gearbox
Hub mass (kg)	14000
Inertia about shaft (kg m^2)	12000
Blade root length (m)	1.25
Blade root diameter (m)	1.9
Blade root drag coefficent	0.8
Spinner diameter (m)	2.5

Table A 1 - Turbine properties

Height above surface (m)	-15	15	35	50	60
Diameter (m)	3.5	3.19231	2.88462	2.73077	2.6
Mass/m (kg/m)	2935.71	2214.09	1492.47	1131.66	824.972
Bending stiffness Nm^2	2.46e11	1.43e11	7.81e10	5.65e10	4.22e10

Table A 2 - Tower properties

Distance from root (m)	0	1.15	3.44	5.74	9.19	16.07	26.41	35.59	38.23	38.75
Chord length (m)	2.07	2.07	2.76	3.44	3.44	2.76	1.84	1.15	0.69	0.03
Aerodynamic twist (°)	0	0	9	13	11	7.8	3.3	0.3	2.75	4
Thickness (% chord)	100	100	64	40	30	22	15	13	13	13
Pitch axis (% chord)	50	50	38	29	29	29	29	29	29	29
Neutral axis (% chord)	50	50	38	29	29	29	29	29	29	29
Mass/unit length (kg/m)	1084.77	369.81	277.36	234.21	209.56	172.58	103.55	55.47	40.68	24.65
Flapwise EI (Nm^2)	7.47e9	2.61e9	2.09e9	1.43e9	1.29e9	5.65e8	1.22e8	2.43e7	4.52e6	8.17e3
Edgewise EI (Nm^2)	7.47e9	2.43e9	1.41e9	8.34e8	5.56e8	2.09e8	2.95e7	2.26e6	1.14e5	3.13e3

Table A 3 - Blade properties

Length (m)	6
Height (m)	2.5
Width (m)	2.5
Drag coefficient	1.6
Mass (kg)	72000
Position of mass centre to side of tower (m)	0
Position of mass centre above tower top (m)	1.3
Position of mass centre in front of tower (m)	-0.6
Yaw inertia (kg m^2)	215000

Table A 4 - Nacelle properties

Gearbox ratio	83.3
Generator inertia (kg m^2)	60
Low speed shaft stiffness (Nm/rad)	1.6e8
Low speed shaft damping (Nms/rad)	250000
Max demanded generator torque (Nm)	14400
Min demanded generator torque (Nm)	0
Speed control	Optimal below rated speed
Pitch control	Pitch regulated above rated speed

Table A 5 - Drivetrain properties

Appendix B – SNL 100m Blade Data

Station	Radius (m)	Flapwise EI (Nm^2)	Edgewise EI (Nm^2)	Torsional GJ (Nm^2)	Axial EA (N)	Mass/m (kg/m)	Flap inertia (kgm^2)	Edge inertia (kgm^2)
1	0	3.22e11	3.22e11	1.68e11	8.46e10	5.74e3	2.18e4	2.18e4
2	0.5	2.88e11	2.88e11	1.50e11	7.51e10	5.09e3	1.95e4	1.95e4
3	0.7	2.50e11	2.52e11	1.29e11	6.54e10	4.44e3	1.69e4	1.71e4
4	0.9	2.12e11	2.15e11	1.09e11	5.57e10	3.78e3	1.43e4	1.46e4
5	1.1	1.75e11	1.80e11	8.97e10	4.65e10	3.15e3	1.19e4	1.22e4
6	1.3	1.62e11	1.63e11	7.98e10	4.28e10	2.88e3	1.08e4	1.11e4
7	2.4	1.45e11	1.54e11	7.22e10	4.01e10	2.91e3	1.02e4	1.06e4
8	2.6	1.31e11	1.41e11	6.47e10	3.65e10	2.68e3	9.29e3	9.74e3
9	4.7	1.04e11	1.24e11	5.01e10	3.08e10	2.33e3	7.58e3	8.75e3
10	6.8	7.99e10	1.04e11	3.53e10	2.55e10	1.98e3	5.85e3	7.65e3
11	8.9	7.05e10	9.37e10	2.54e10	2.40e10	1.84e3	4.93e3	7.13e3
12	11.4	5.58e10	8.34e10	1.50e10	2.21e10	1.63e3	3.72e3	6.32e3
13	14.6	4.97e10	8.76e10	9.27e9	2.34e10	1.68e3	3.14e3	6.60e3
14	16.3	4.76e10	9.85e10	7.66e9	2.59e10	1.74e3	2.82e3	7.00e3
15	17.9	4.17e10	1.05e11	5.89e9	2.68e10	1.76e3	2.42e3	7.24e3
16	19.5	3.88e10	1.05e11	4.41e9	2.85e10	1.81e3	2.17e3	7.14e3
17	22.2	3.36e10	1.03e11	3.85e9	2.84e10	1.79e3	1.87e3	6.95e3
18	24.9	2.85e10	9.91e10	3.22e9	2.81e10	1.76e3	1.58e3	6.62e3
19	27.6	2.31e10	6.65e10	2.67e9	2.45e10	1.58e3	1.28e3	4.96e3
20	35.8	1.45e10	5.48e10	1.72e9	2.26e10	1.43e3	7.97e2	3.97e3
21	43.9	8.96e9	3.37e10	1.10e9	2.00e10	1.26e3	4.87e2	2.61e3
22	52	5.38e9	2.18e10	6.90e8	1.77e10	1.11e3	2.92e2	1.78e3
23	60.2	3.11e9	1.44e10	4.32e8	1.47e10	9.35e2	1.69e2	1.25e3
24	66.7	1.80e9	1.14e10	2.94e8	1.22e10	7.79e2	9.94e1	9.61e2
25	68.3	1.55e9	1.07e10	2.64e8	1.16e10	7.40e2	8.57e1	8.92e2
26	73.2	1.01e9	8.72e9	2.10e8	9.29e9	6.07e2	5.73e1	7.09e2
27	76.4	7.36e8	7.41e9	1.86e8	7.53e9	5.04e2	4.28e1	5.90e2
28	84.6	3.55e8	4.90e9	1.29e8	5.02e9	3.59e2	2.22e1	3.86e2
29	89.4	2.08e8	3.66e9	9.78e7	3.82e9	2.90e2	1.41e1	2.93e2
30	94.3	8.10e7	1.74e9	4.51e7	2.72e9	2.10e2	5.72e0	1.39e2
31	95.7	4.29e7	9.07e8	2.58e7	2.11e9	1.56e2	3.07e0	7.16e1
32	97.2	1.92e7	4.19e8	1.15e7	1.63e9	1.20e2	1.37e0	3.30e1
33	98.6	5.13e6	1.19e8	3.03e6	1.07e9	7.91e1	3.62E-01	9.38e0
34	100	5.84e3	6.22e4	2.57e3	8.87e7	6.55e0	6.33E-04	4.83E-03

Table B 1 - SNL 100m all glass fibre blade data

Appendix C – Beam Element Matrices

Stiffness Matrix

$$[\boldsymbol{K_E}] = \begin{bmatrix} K_{11} & K_{12} \\ K_{21} & K_{22} \end{bmatrix}$$

where

$$[\boldsymbol{K_{11}}] = \begin{bmatrix} \frac{EA}{l} & 0 & 0 & 0 & 0 & 0 \\ 0 & \frac{12EI_{yy'}}{l^3} & 0 & 0 & 0 & \frac{6EI_{yy'}}{l^2} \\ 0 & 0 & \frac{12EI_{xx'}}{l^3} & 0 & -\frac{6EI_{xx'}}{l^2} & 0 \\ 0 & 0 & 0 & \frac{GJ}{l} & 0 & 0 \\ 0 & 0 & -\frac{6EI_{xx'}}{l^2} & 0 & \frac{4EI_{xx'}}{l} & 0 \\ 0 & \frac{6EI_{yy'}}{l^2} & 0 & 0 & 0 & \frac{4EI_{yy'}}{l} \end{bmatrix}$$

$$[\boldsymbol{K_{12}}] = \begin{bmatrix} -\frac{EA}{l} & 0 & 0 & 0 & 0 & 0 \\ 0 & -\frac{12EI_{yy'}}{l^3} & 0 & 0 & 0 & -\frac{6EI_{yy'}}{l^2} \\ 0 & 0 & -\frac{12EI_{xx'}}{l^3} & 0 & \frac{6EI_{xx'}}{l^2} & 0 \\ 0 & 0 & 0 & \frac{GJ}{l} & 0 & 0 \\ 0 & 0 & \frac{6EI_{xx'}}{l^2} & 0 & \frac{2EI_{xx'}}{l} & 0 \\ 0 & -\frac{6EI_{yy'}}{l^2} & 0 & 0 & 0 & \frac{2EI_{yy'}}{l} \end{bmatrix}$$

$$[\boldsymbol{K_{21}}] = \begin{bmatrix} -\frac{EA}{l} & 0 & 0 & 0 & 0 & 0 \\ 0 & -\frac{12EI_{yy'}}{l^3} & 0 & 0 & 0 & -\frac{6EI_{yy'}}{l^2} \\ 0 & 0 & -\frac{12EI_{xx'}}{l^3} & 0 & \frac{6EI_{xx'}}{l^2} & 0 \\ 0 & 0 & 0 & -\frac{GJ}{l} & 0 & 0 \\ 0 & 0 & -\frac{6EI_{xx'}}{l^2} & 0 & \frac{2EI_{xx'}}{l} & 0 \\ 0 & \frac{6EI_{yy'}}{l^2} & 0 & 0 & 0 & \frac{2EI_{yy'}}{l} \end{bmatrix}$$

$$[\boldsymbol{K_{22}}] = \begin{bmatrix} \frac{EA}{l} & 0 & 0 & 0 & 0 & 0 \\ 0 & \frac{12EI_{yy'}}{l^3} & 0 & 0 & 0 & -\frac{6EI_{yy'}}{l^2} \\ 0 & 0 & \frac{12EI_{xx'}}{l^3} & 0 & \frac{6EI_{xx'}}{l^2} & 0 \\ 0 & 0 & 0 & \frac{GJ}{l} & 0 & 0 \\ 0 & 0 & \frac{6EI_{xx'}}{l^2} & 0 & \frac{4EI_{xx'}}{l} & 0 \\ 0 & -\frac{6EI_{yy'}}{l^2} & 0 & 0 & 0 & \frac{4EI_{yy'}}{l} \end{bmatrix}$$

where

$EI_{xx'}$	Bending stiffness about local x-axis
$EI_{yy'}$	Bending stiffness about local y-axis
GJ	Torsional stiffness
EA	Axial stiffness
l	Element length

Mass matrix

$$[\boldsymbol{M_E}] = \begin{bmatrix} M_{11} & M_{12} \\ M_{21} & M_{22} \end{bmatrix}$$

where

$$[\boldsymbol{M_{11}}] = \begin{bmatrix} M_1 & 0 & 0 & 0 & 0 & 0 \\ 0 & M_1 & 0 & 0 & 0 & 0 \\ 0 & 0 & M_1 & 0 & 0 & 0 \\ 0 & 0 & 0 & M_1 r_{1zz}^2 & 0 & 0 \\ 0 & 0 & 0 & 0 & M_1 r_{1xx}^2 & 0 \\ 0 & 0 & 0 & 0 & 0 & M_1 r_{1yy}^2 \end{bmatrix}$$

$$[\boldsymbol{M_{22}}] = \begin{bmatrix} M_2 & 0 & 0 & 0 & 0 & 0 \\ 0 & M_2 & 0 & 0 & 0 & 0 \\ 0 & 0 & M_2 & 0 & 0 & 0 \\ 0 & 0 & 0 & M_2 r_{2zz}^2 & 0 & 0 \\ 0 & 0 & 0 & 0 & M_2 r_{2xx}^2 & 0 \\ 0 & 0 & 0 & 0 & 0 & M_2 r_{2yy}^2 \end{bmatrix}$$

$$[\boldsymbol{M_{12}}] = [\boldsymbol{M_{21}}] = \begin{bmatrix} 0 & \dots & 0 \\ \vdots & \ddots & \vdots \\ 0 & \dots & 0 \end{bmatrix}$$

M_1	Mass lumped at node 1
M_2	Mass lumped at node 2
$r_{1xx}, r_{1yy}, r_{1zz}$	Radius of gyration about x, y and z axes at node 1
$r_{2xx}, r_{2yy}, r_{2zz}$	Radius of gyration about x, y and z axes at node 2

Appendix D – OPTIMAT Material UD3 Properties

Symbol	Value			Units	Description
ϕ_F	0.52				Fibre volume fraction
E_{1C}, E_{2C}, E_{3C}	39105	14165	14165	MPa	Composite Young's modulus
$\upsilon_{12C}, \upsilon_{13C}, \upsilon_{23C}$	0.279	0.279	0.352		Composite Poisson's ratio
$G_{12C}, G_{13C}, G_{23C}$	4659	4659	5238	MPa	Composite shear modulus
$\alpha_{1C}, \alpha_{2C}, \alpha_{3C}$	7.27E-6	3.82E-5	3.82E-5	1/K	Composite thermal expansion coefficient
E_{1F}, E_{2F}, E_{3F}	70375	70375	70375	MPa	Fibre Young's modulus
$\upsilon_{12F}, \upsilon_{13F}, \upsilon_{23F}$	0.254	0.254	0.186		Fibre Poisson's ratio
$G_{12F}, G_{13F}, G_{23F}$	13130	13130	29649	MPa	Fibre shear modulus
$\alpha_{1F}, \alpha_{2F}, \alpha_{3F}$	2.59E-6	5.63E-6	5.63E-6	1/K	Fibre thermal expansion coefficient
E_{1M}, E_{2M}, E_{3M}	5572	5572	5572	MPa	Matrix Young's modulus
$\upsilon_{12M}, \upsilon_{13M}, \upsilon_{23M}$	0.315	0.315	0.315		Matrix Poisson's ratio
$G_{12M}, G_{13M}, G_{23M}$	2118	2118	2118	MPa	Matrix shear modulus
$\alpha_{1M}, \alpha_{2M}, \alpha_{3M}$	6.73E-5	6.73E-5	6.73E-5	1/K	Matrix thermal expansion coefficient

Table D 1 - Ply stiffness properties

Symbol	Value	Units	Description
S_{11T}	800	MPa	Ply longitudinal tensile ultimate strength
S_{11T}	530	MPa	Ply longitudinal compressive ultimate strength
S_{22T}	53	MPa	Ply transverse tensile ultimate strength
S_{22C}	165	MPa	Ply transverse compressive ultimate strength
S_{33T}	53	MPa	Ply out of plane tensile ultimate strength
S_{33C}	165	MPa	Ply out of plane compressive ultimate strength
S_{12}	75	MPa	Ply in-plane tensile ultimate shear strength
S_{13}	75	MPa	Ply out of plane ultimate shear strength
S_{23}	70	MPa	Ply transverse ultimate shear strength

Table D 2 - Ply strength properties

Appendix E –LM 40.3 P2 Fatigue Analysis Neglecting Shear Flow

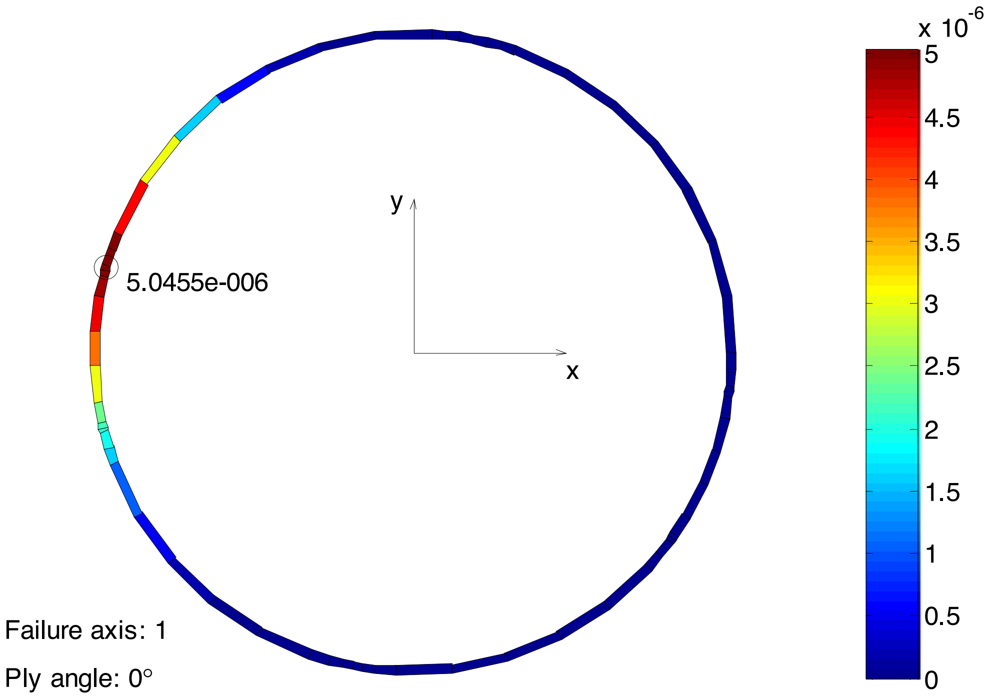

Figure E 1 – Longitudinal damage to 0° plies in section 1

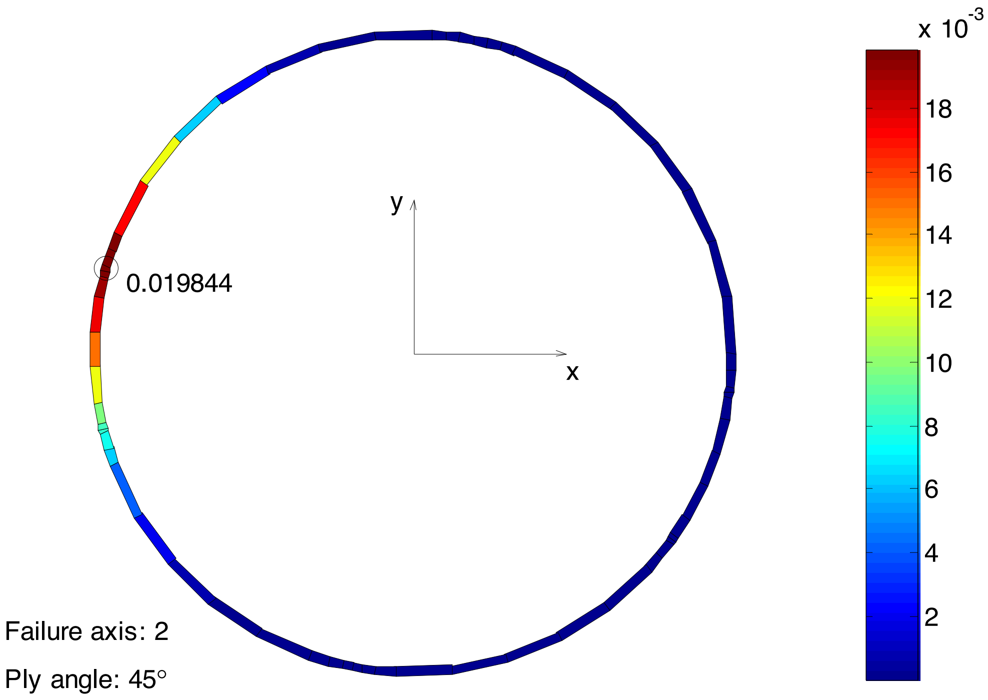

Figure E 2- Transverse damage to 45° plies in section 1

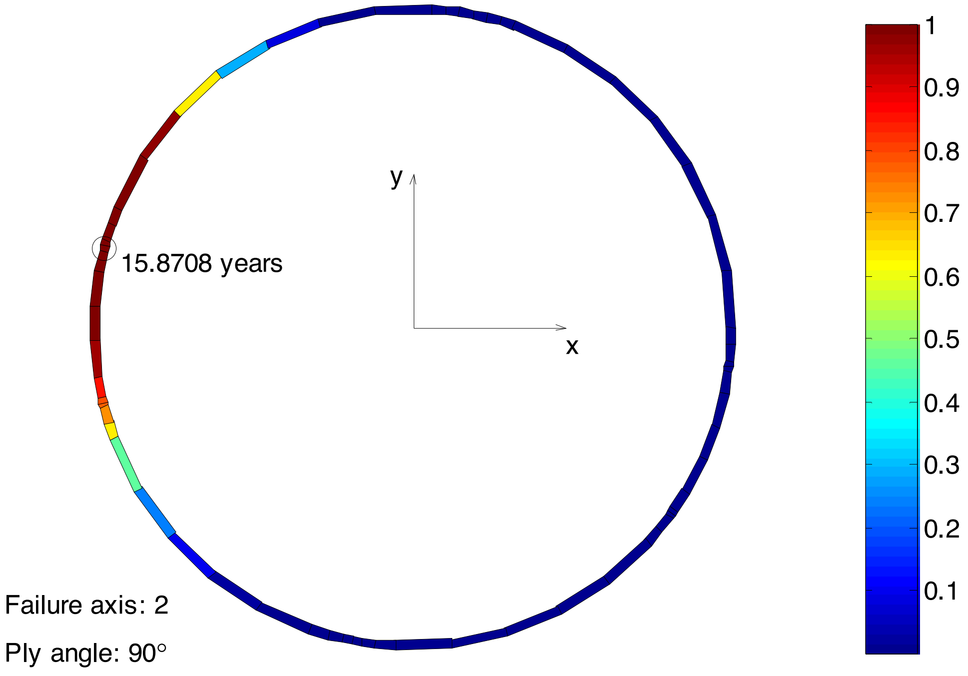

Figure E 3 - Transverse damage to 90° plies in section 1

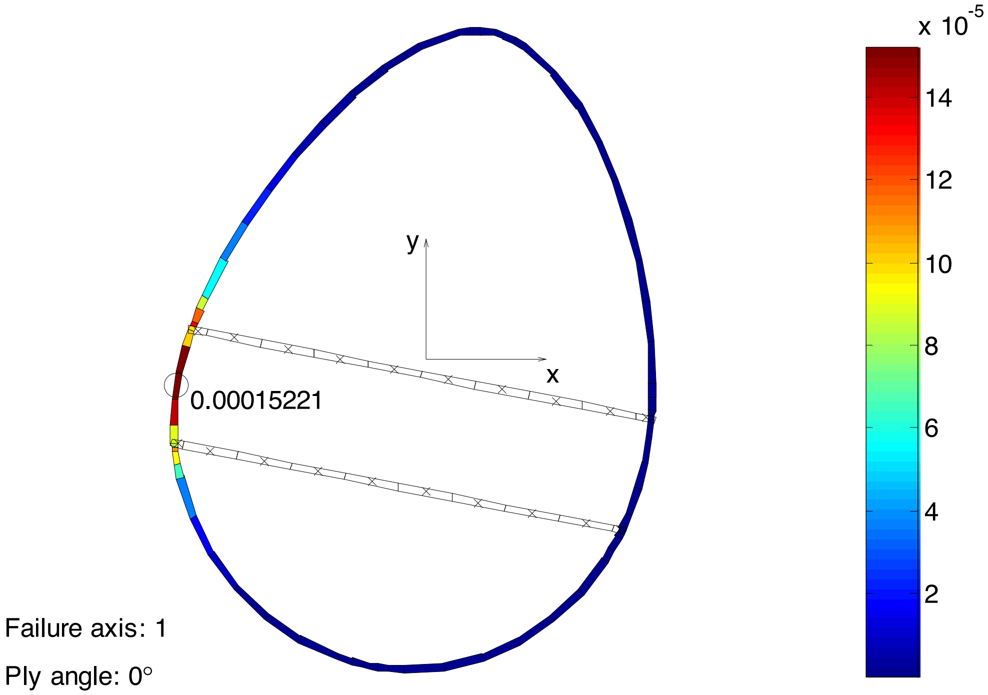

Figure E 4 - Longitudinal damage to 0° plies in section 2

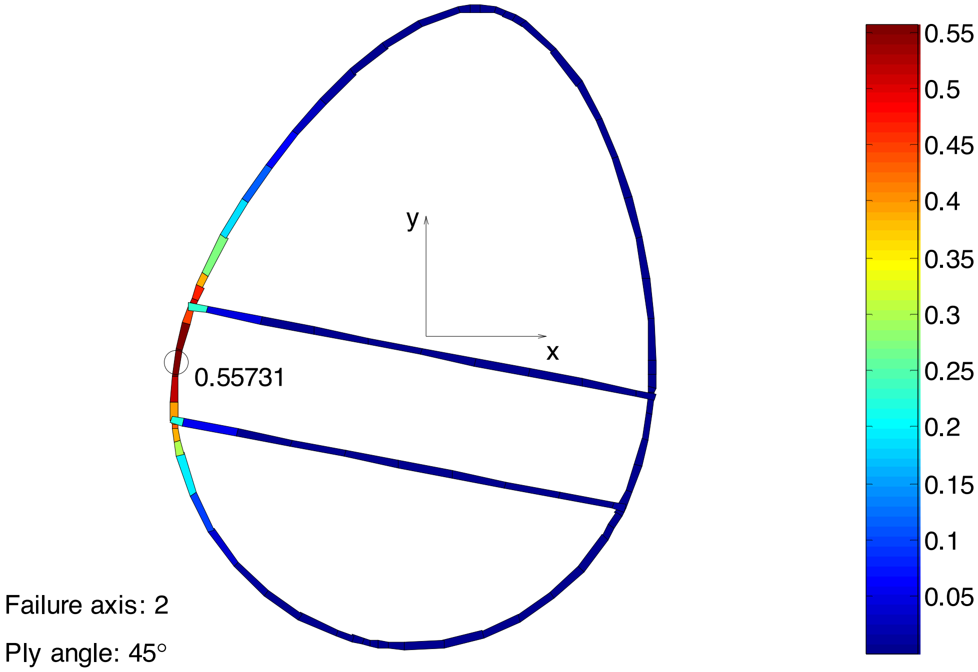

Figure E 5 - Transverse damage to 45° plies in section 2

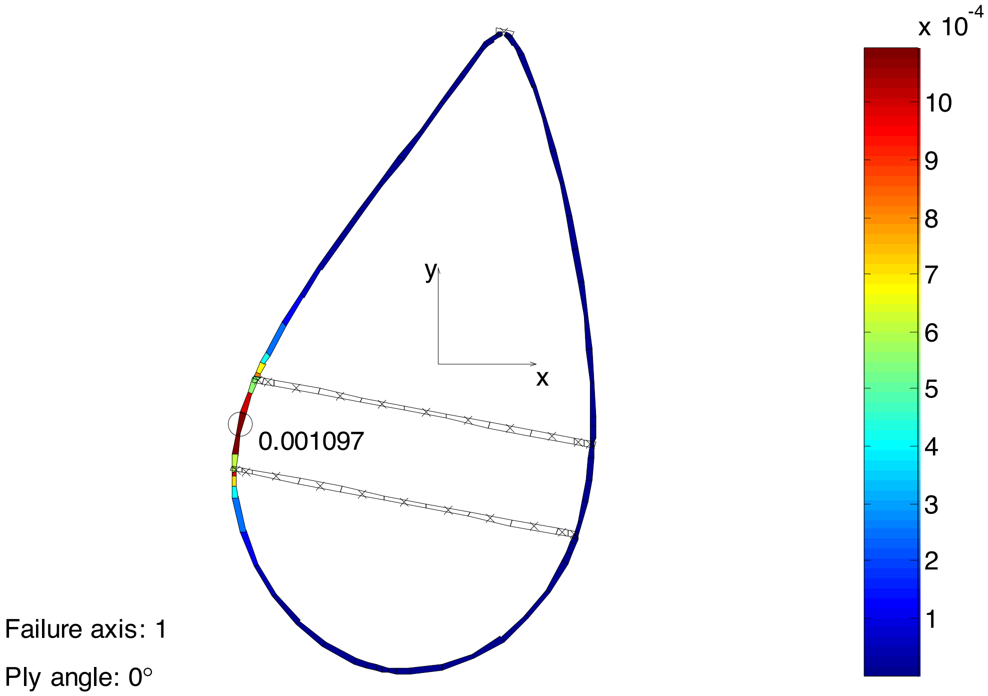

Figure E 6 - Longitudinal damage to 0° plies in section 3

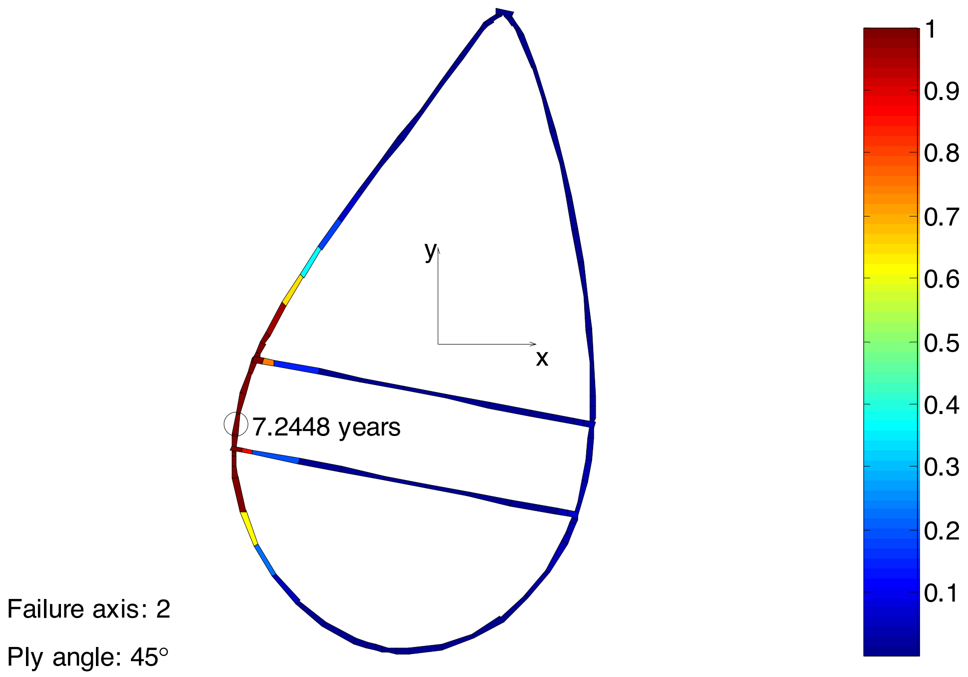

Figure E 7 - Transverse damage to 45° plies in section 3

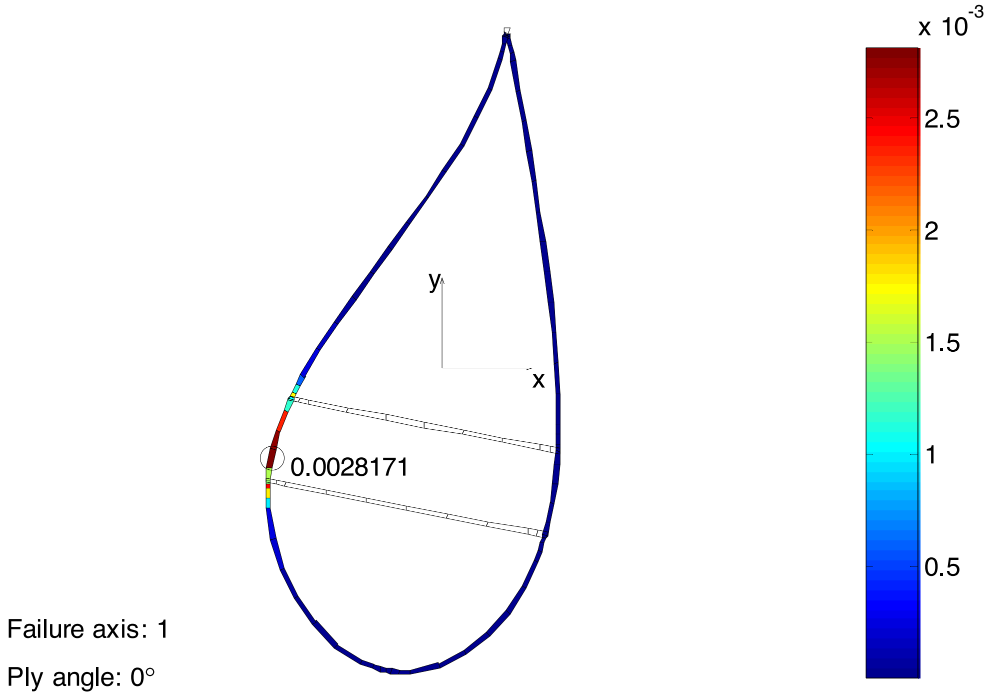

Figure E 8 - Longitudinal damage to 0° plies in section 4

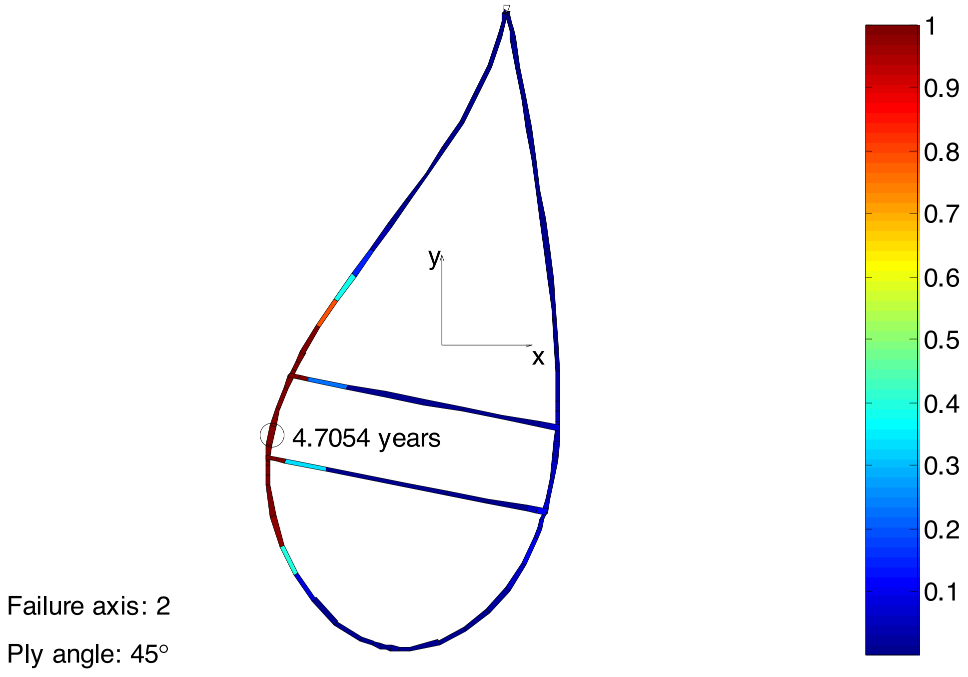

Figure E 9 - Transverse damage to 45° plies in section 4

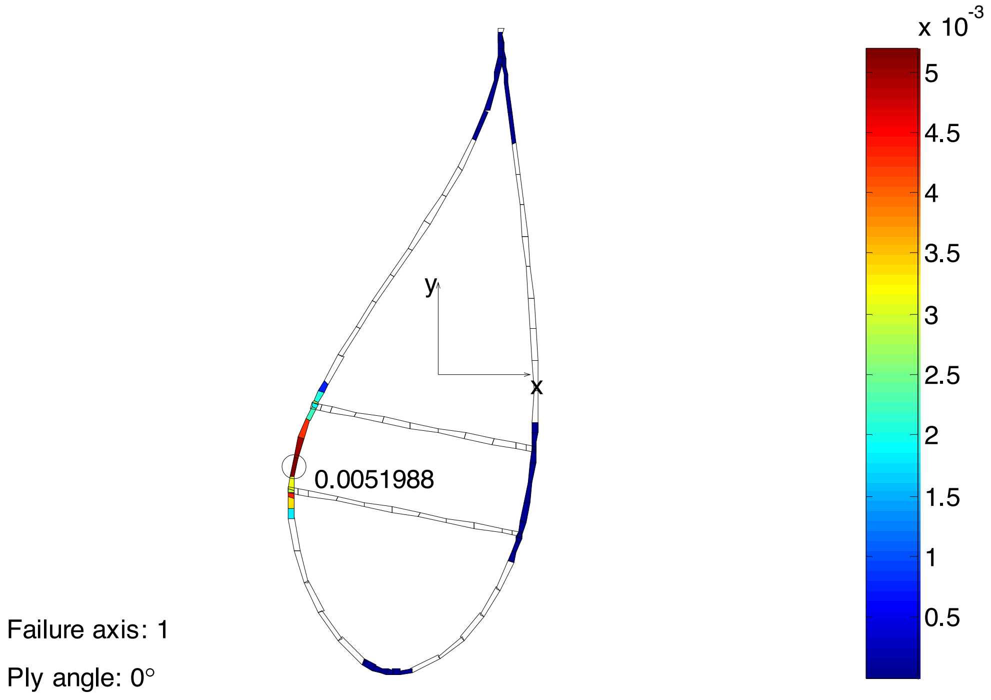

Figure E 10 - Longitudinal damage to 0° plies in section 5

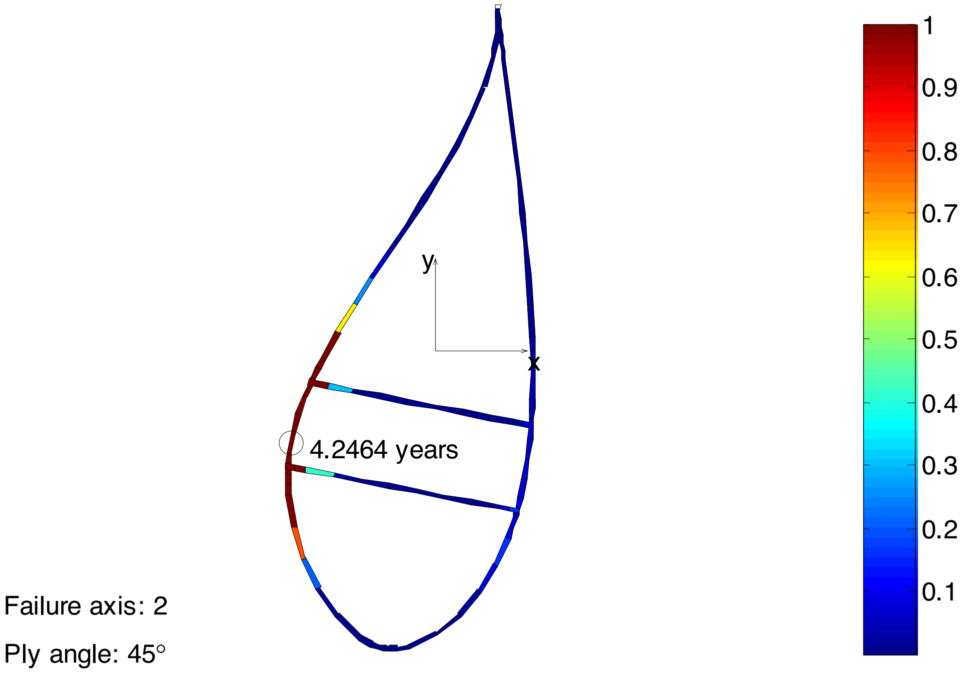

Figure E 11 - Transverse damage to 45° plies in section 5

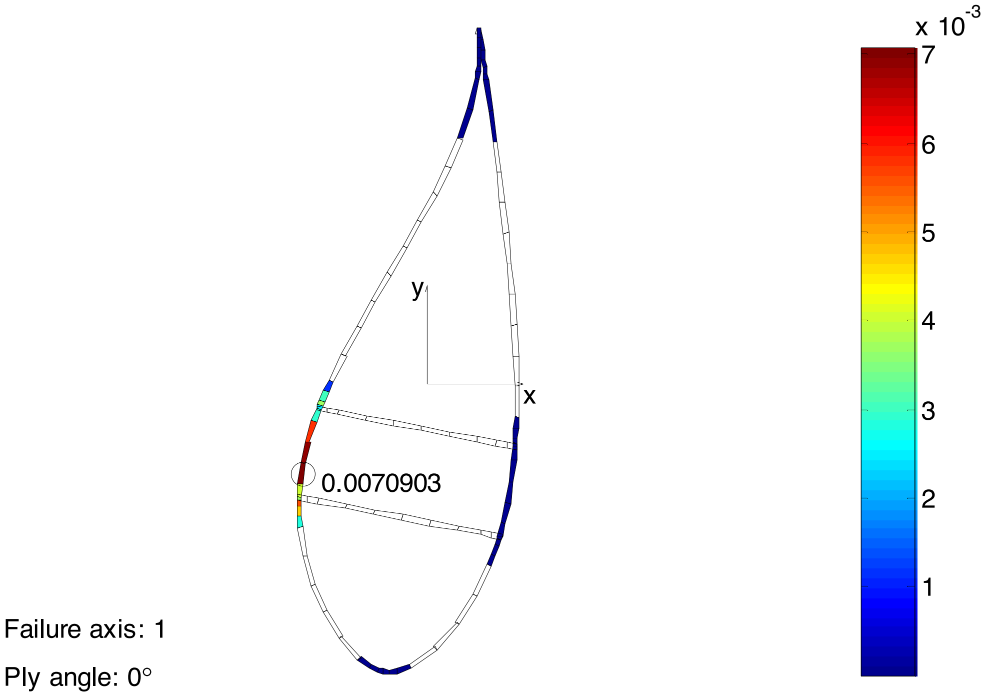

Figure E 12 - Longitudinal damage to 0° plies in section 6

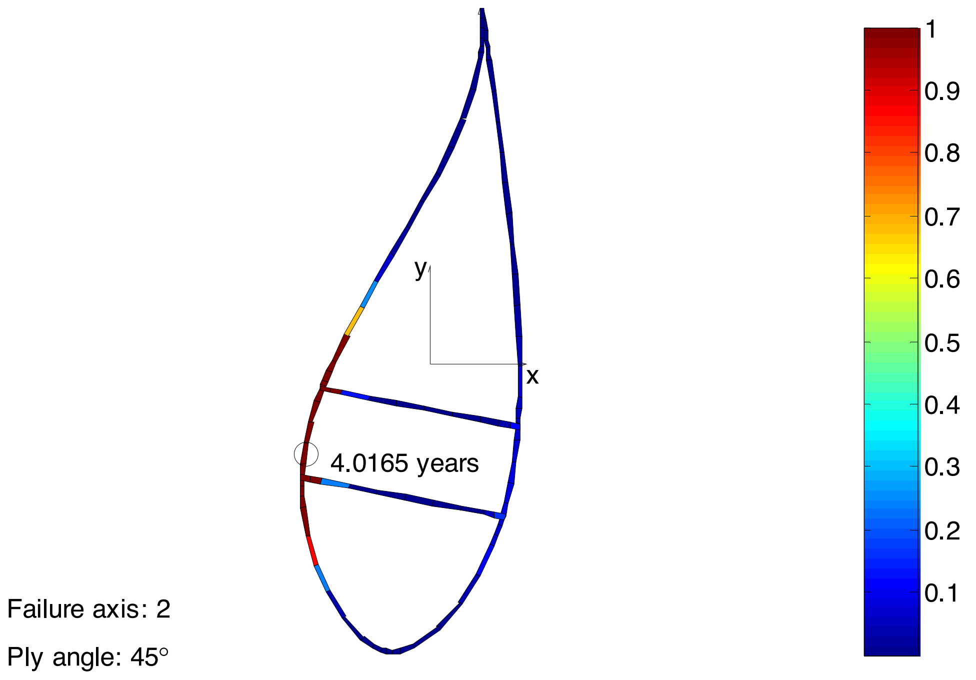

Figure E 13 - Transverse damage to 45° plies in section 6

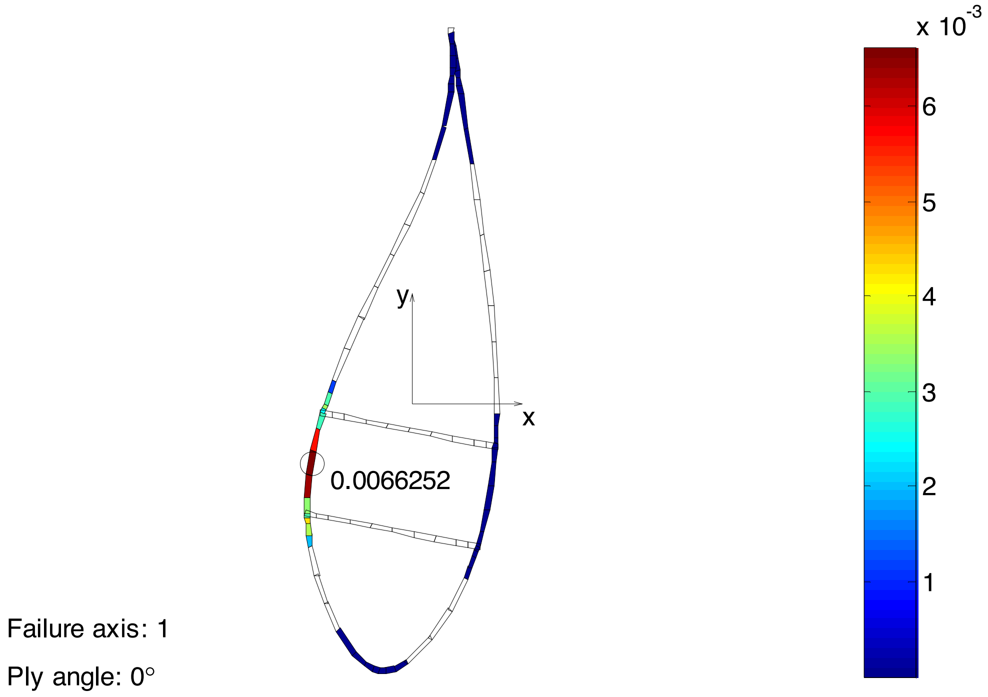

Figure E 14 -Longitudinal damage to 0° plies in section 7

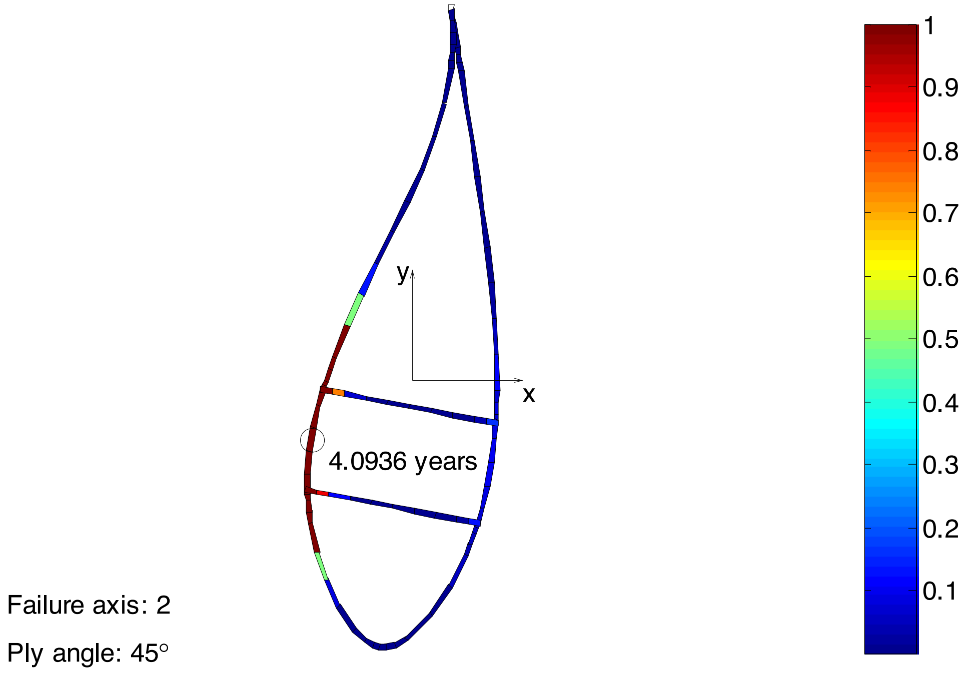

Figure E 15 - Transverse damage to 45° plies in section 7

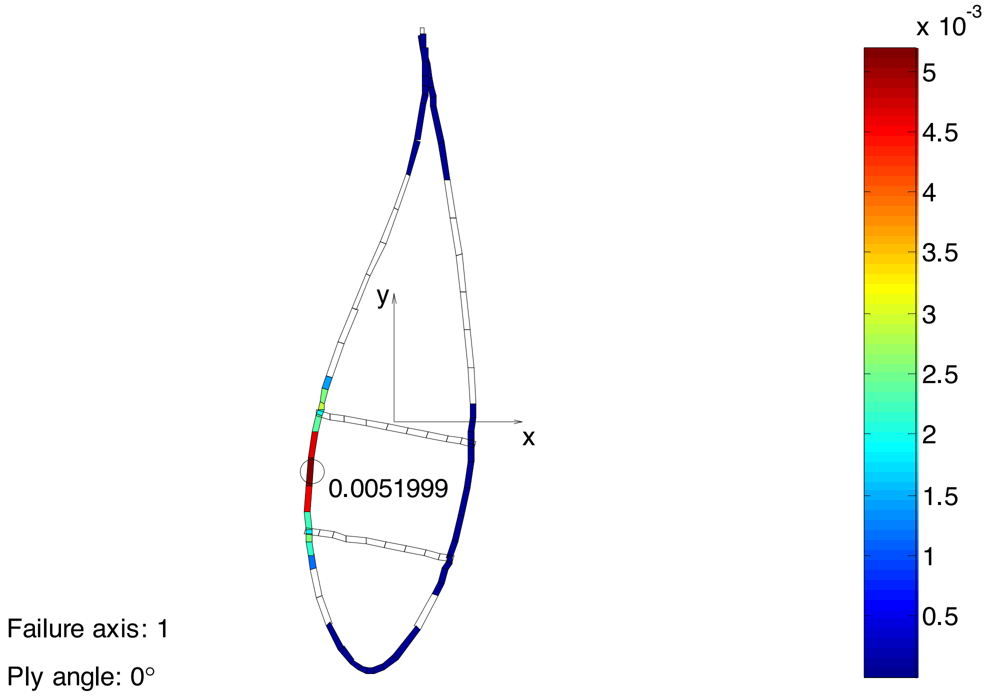

Figure E 16 - Longitudinal damage to 0° plies in section 8

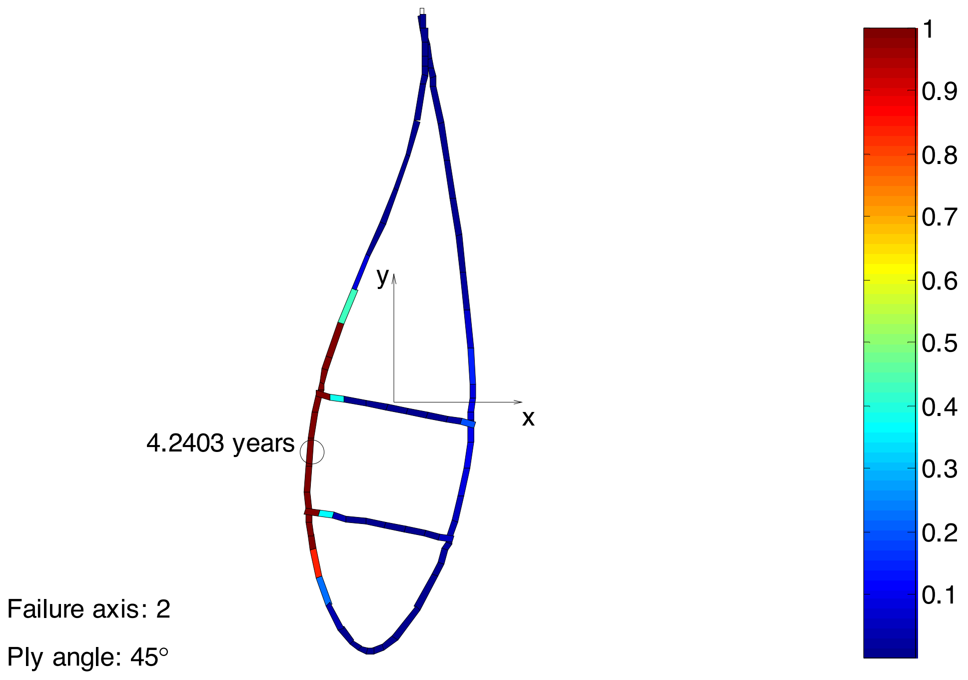

Figure E 17 – Transverse damage to 45° plies in section 8

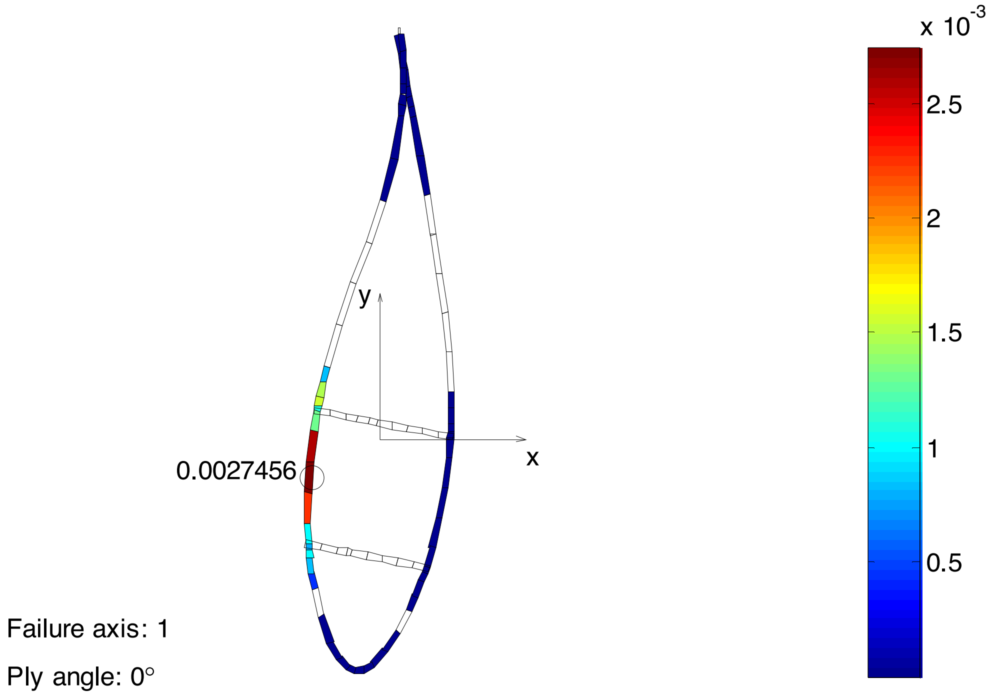

Figure E 18 - Longitudinal damage to 0° plies in section 9

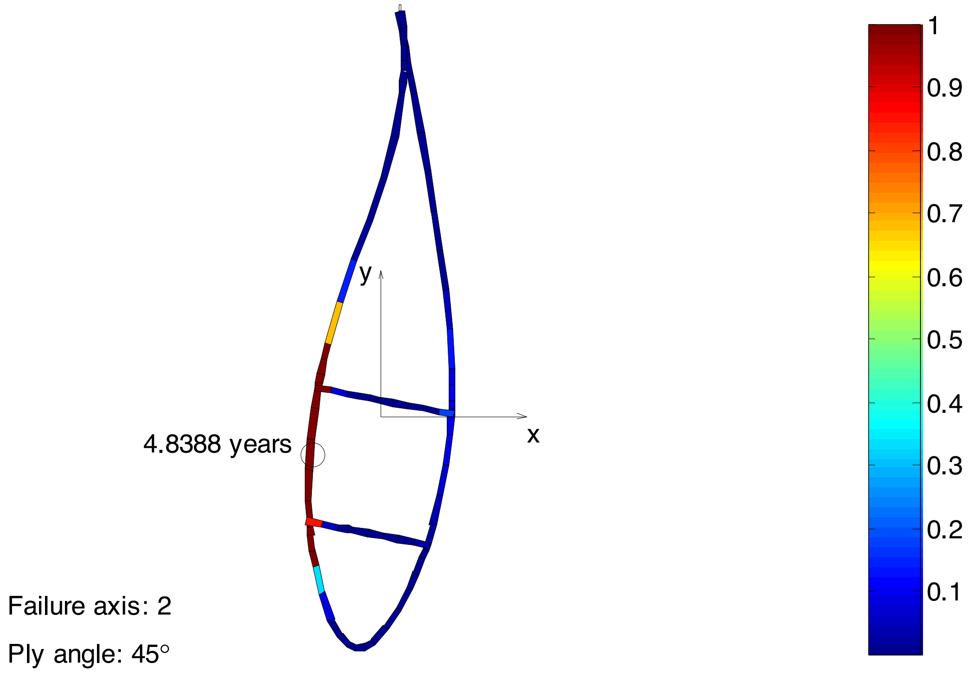

Figure E 19 - Transverse damage to 45° plies in section 9

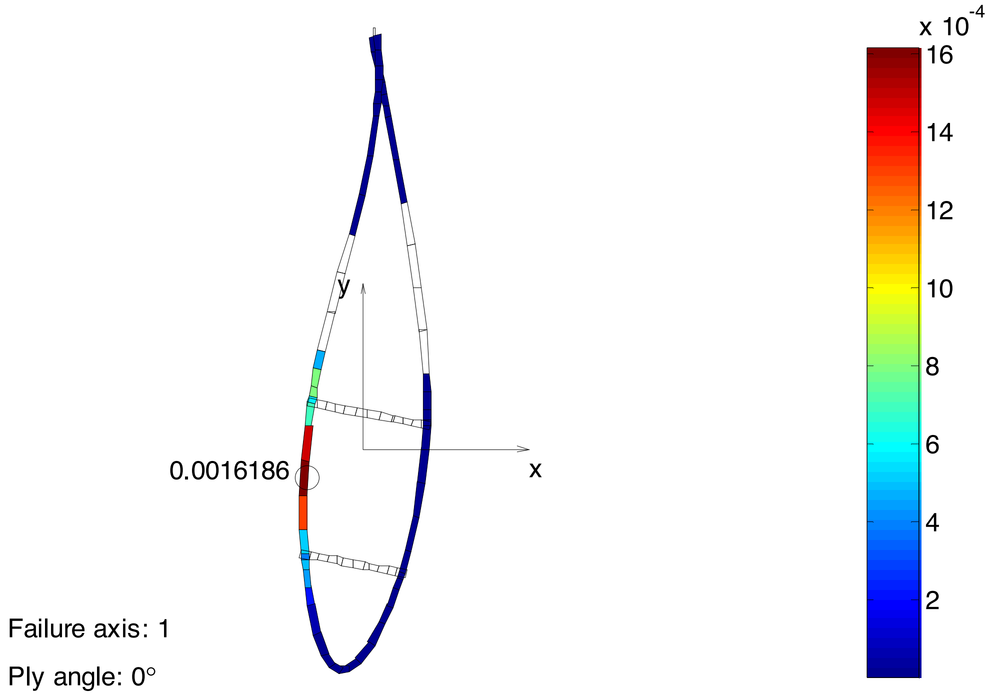

Figure E 20 - Longitudinal damage to 0° plies in section 10

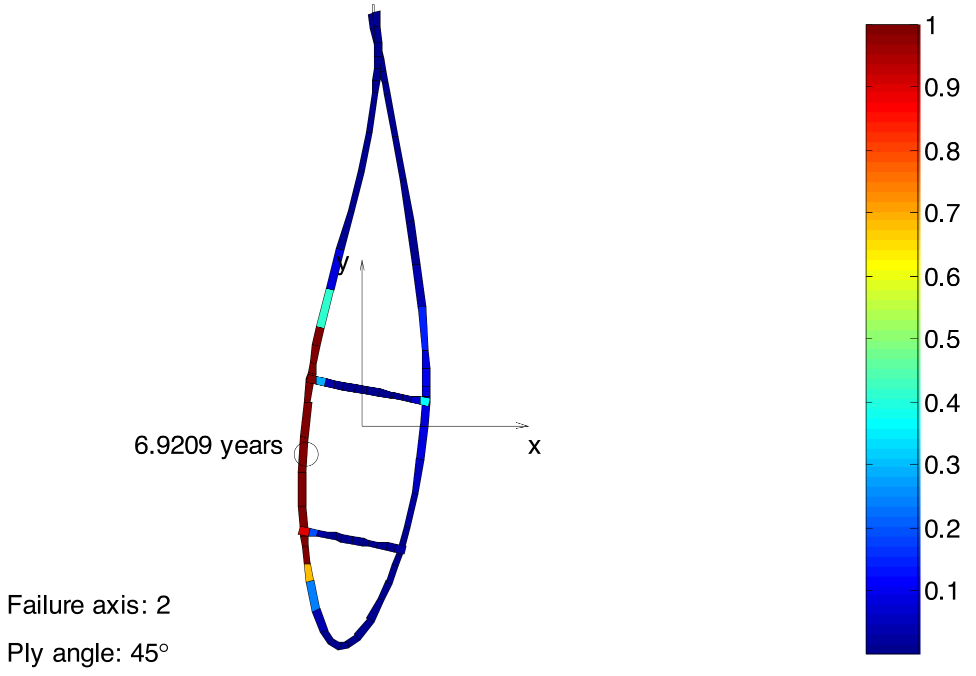

Figure E 21 - Transverse damage to 45° plies in section 10

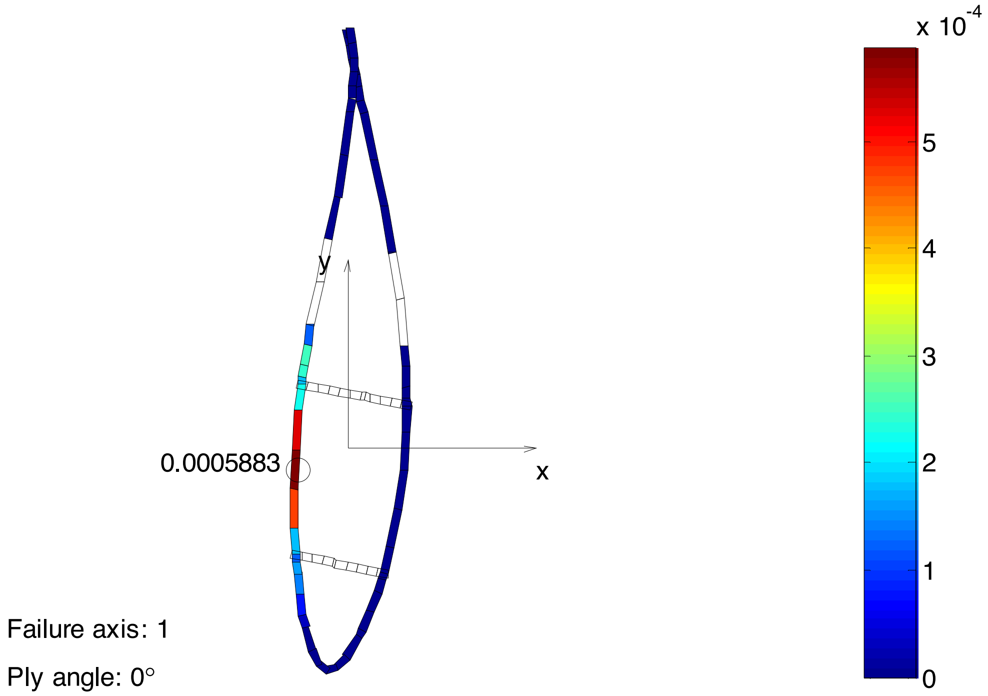

Figure E 22 - Longitudinal damage to 0° plies in section 11

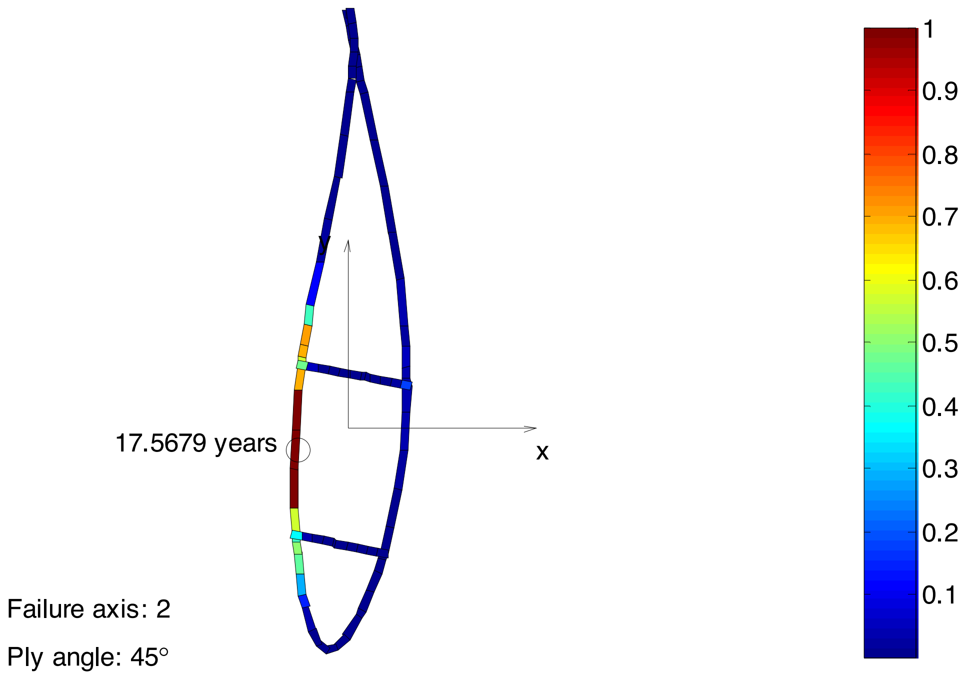

Figure E 23 - Transverse damage to 45° plies in section 11

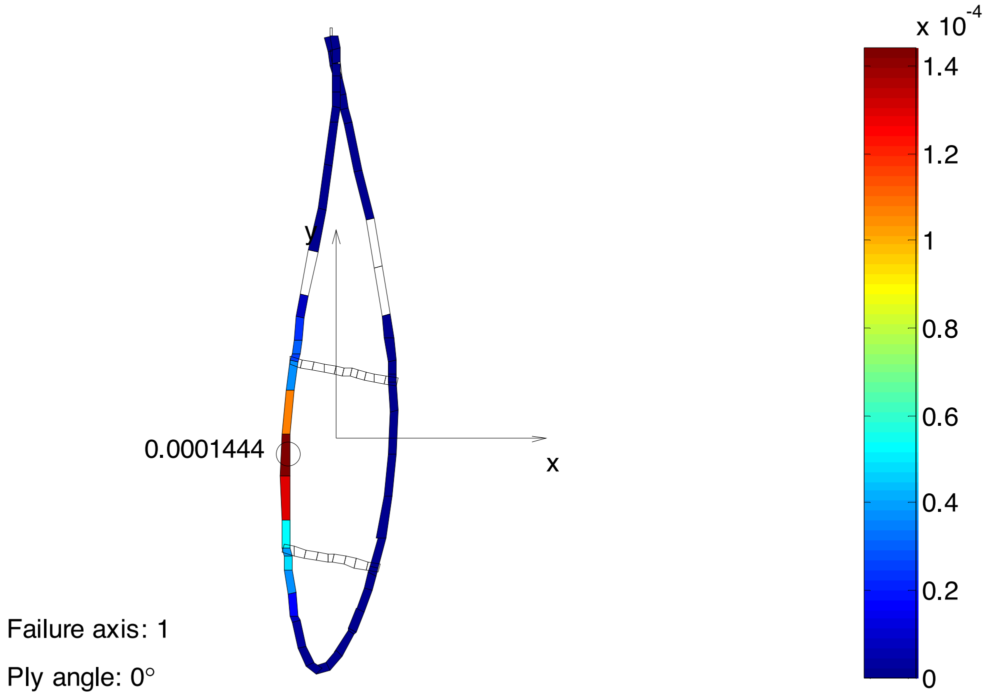

Figure E 24 - Longitudinal damage to 0° plies in section 12

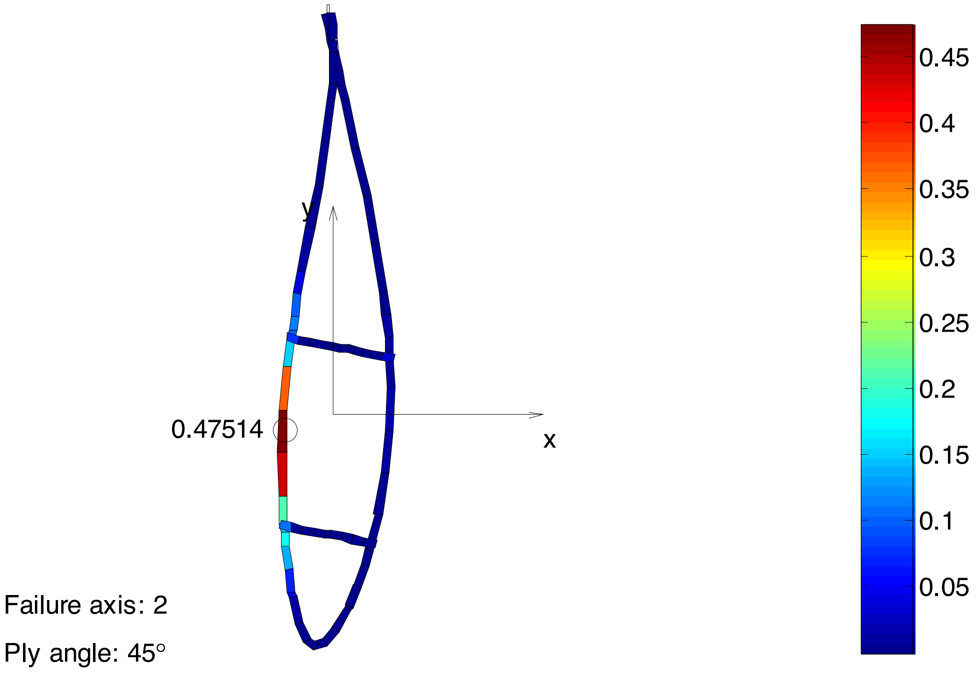

Figure E 25 - Transverse damage to 45° plies in section 12

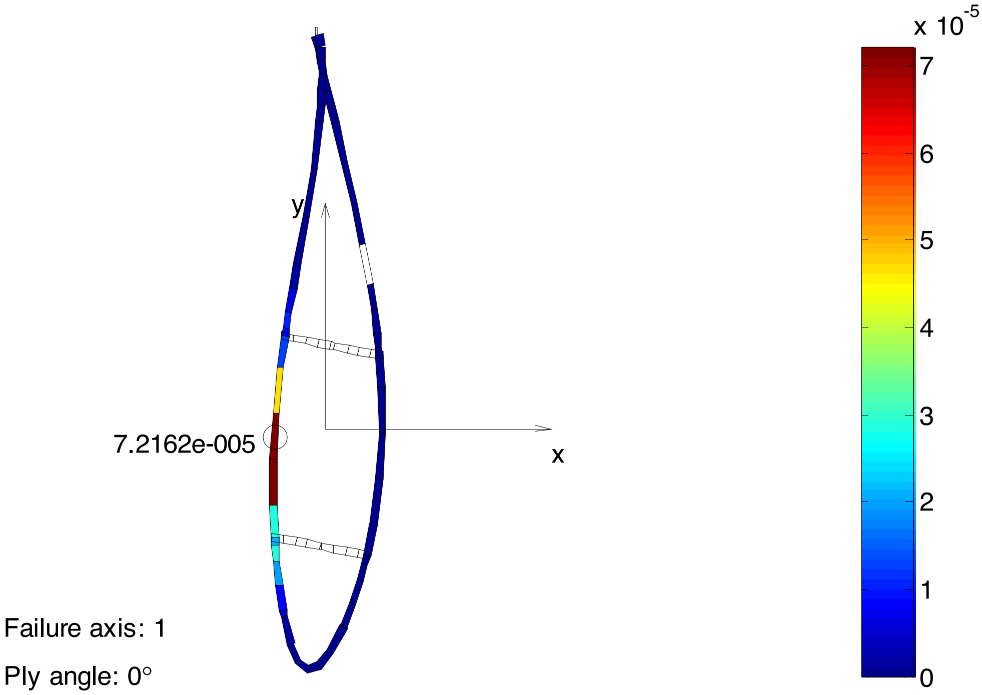

Figure E 26 - Longitudinal damage to 0° plies in section 13

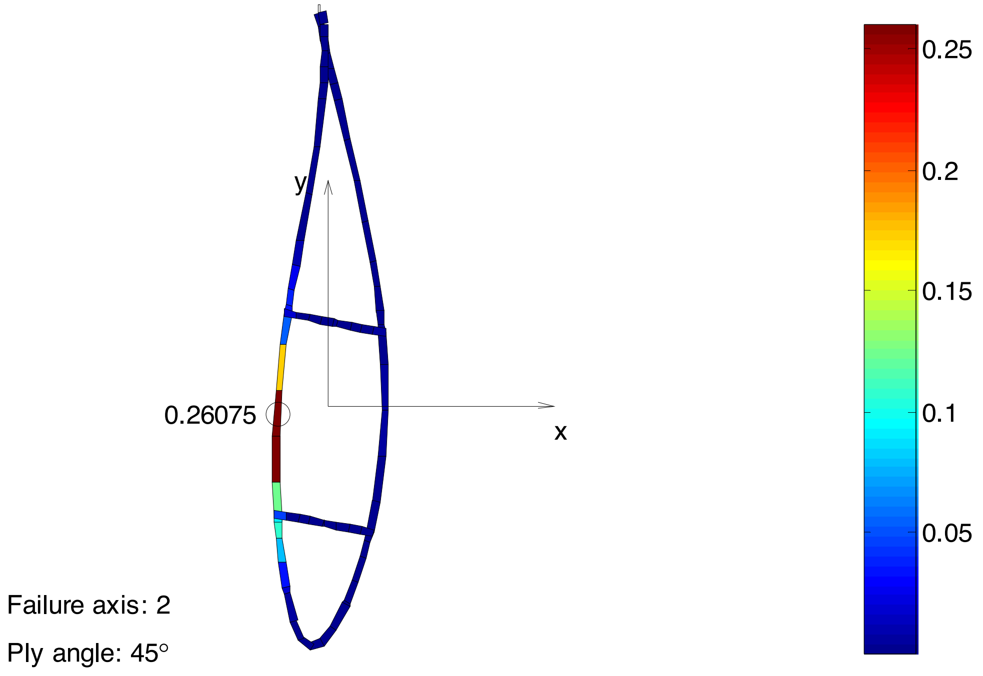

Figure E 27 - Transverse damage to 45° plies in section 13

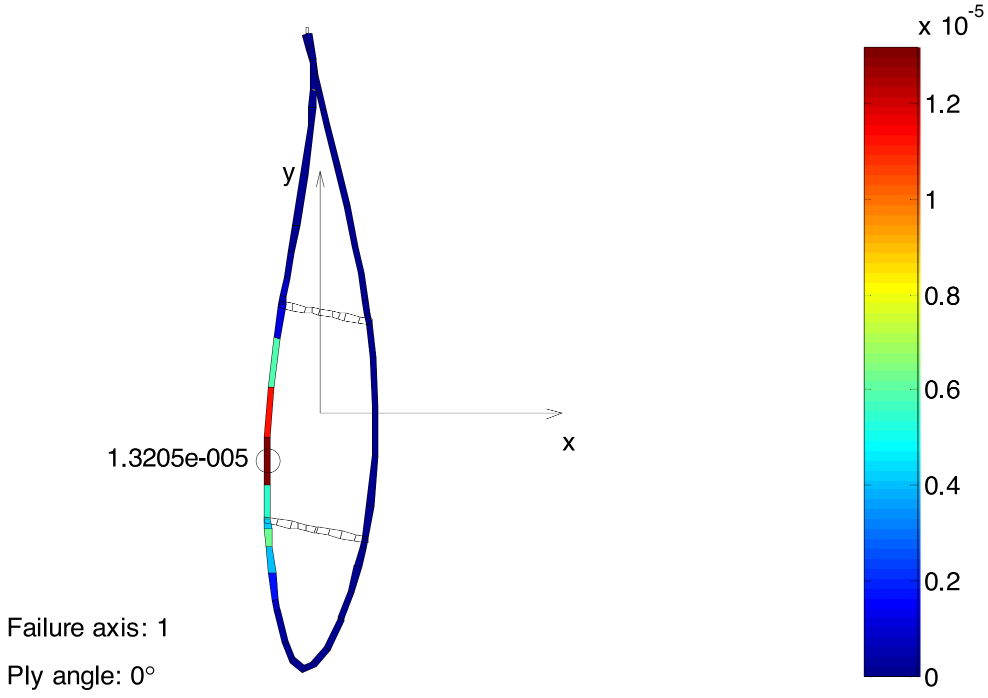

Figure E 28 - Longitudinal damage to 0° plies in section 14

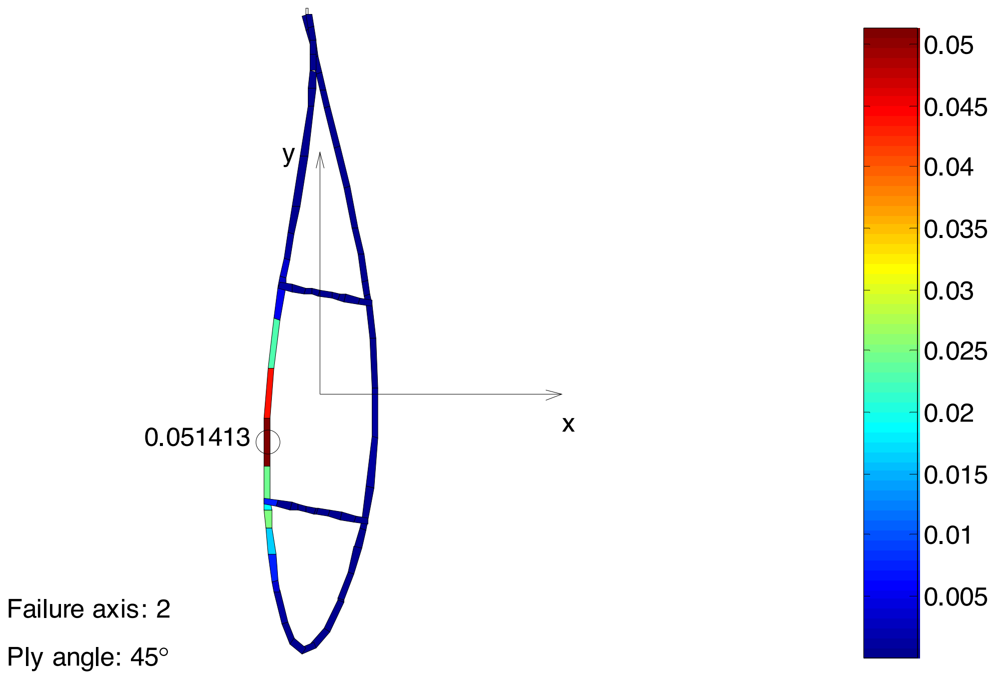

Figure E 29 - Transverse damage to 45° plies in section 14

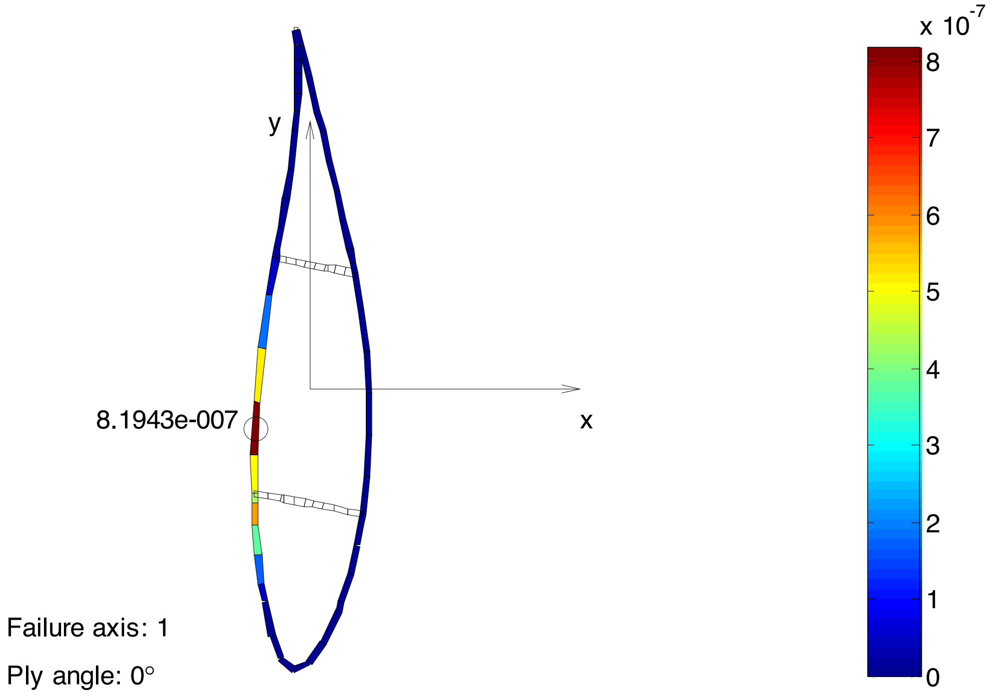

Figure E 30 - Longitudinal damage to 0° plies in section 15

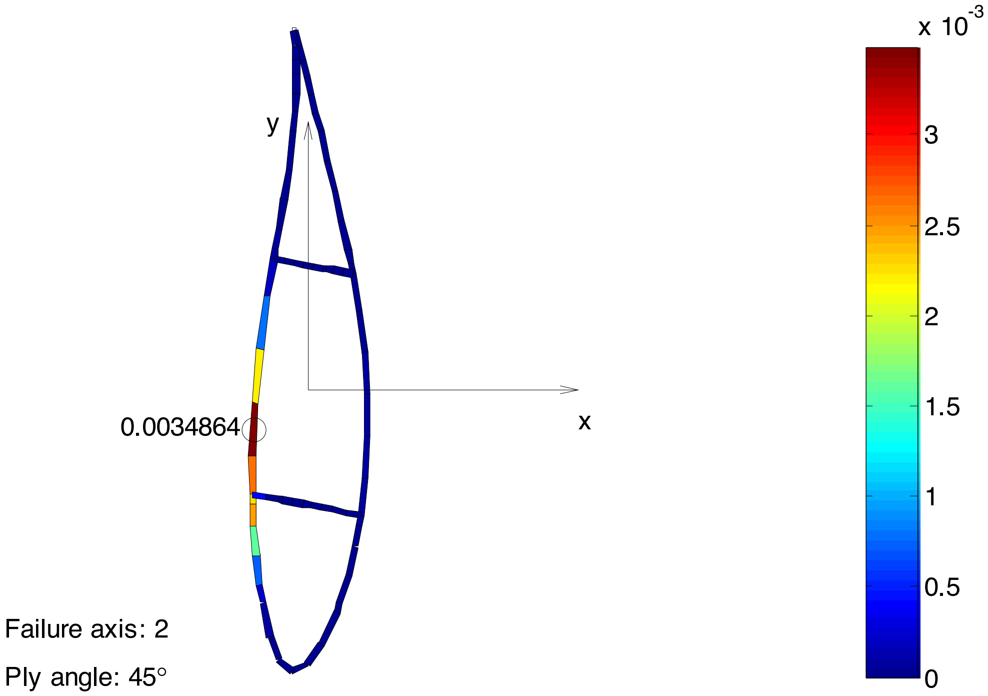

Figure E 31 - Transverse damage to 45° plies in section 15

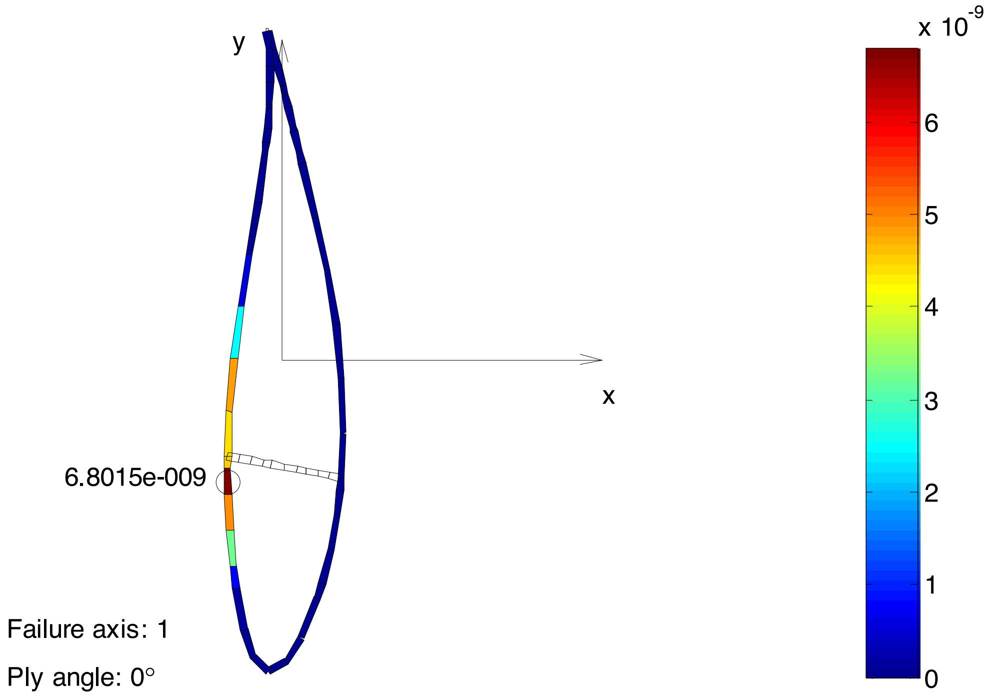

Figure E 32 - Longitudinal damage to 0° plies in section 16

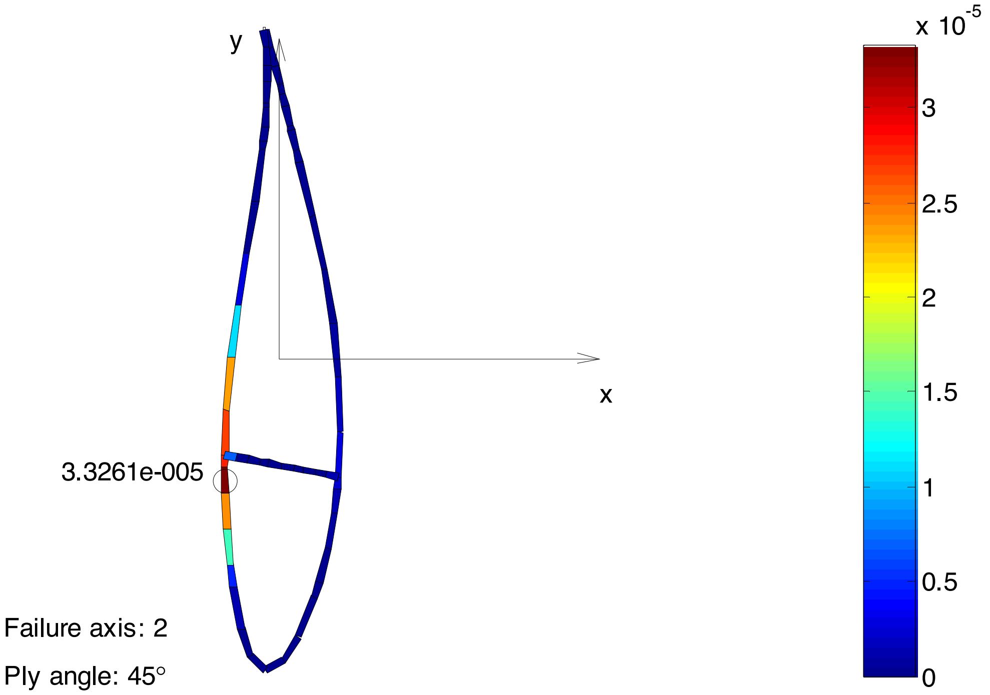

Figure E 33 - Transverse damage to 45° plies in section 16

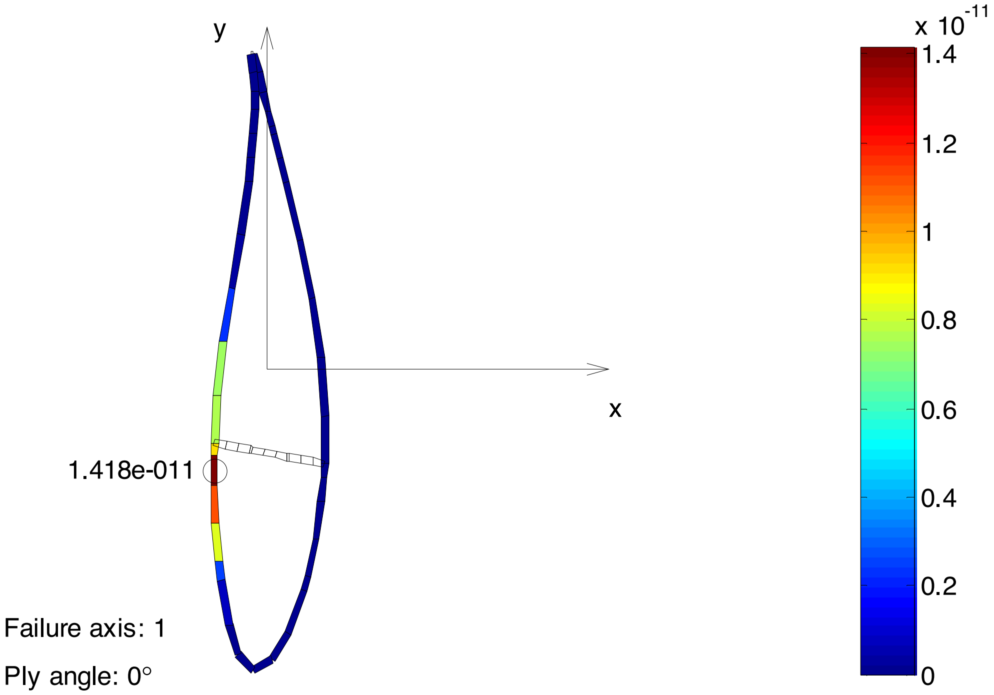

Figure E 34 - Longitudinal damage to 0° plies in section 17

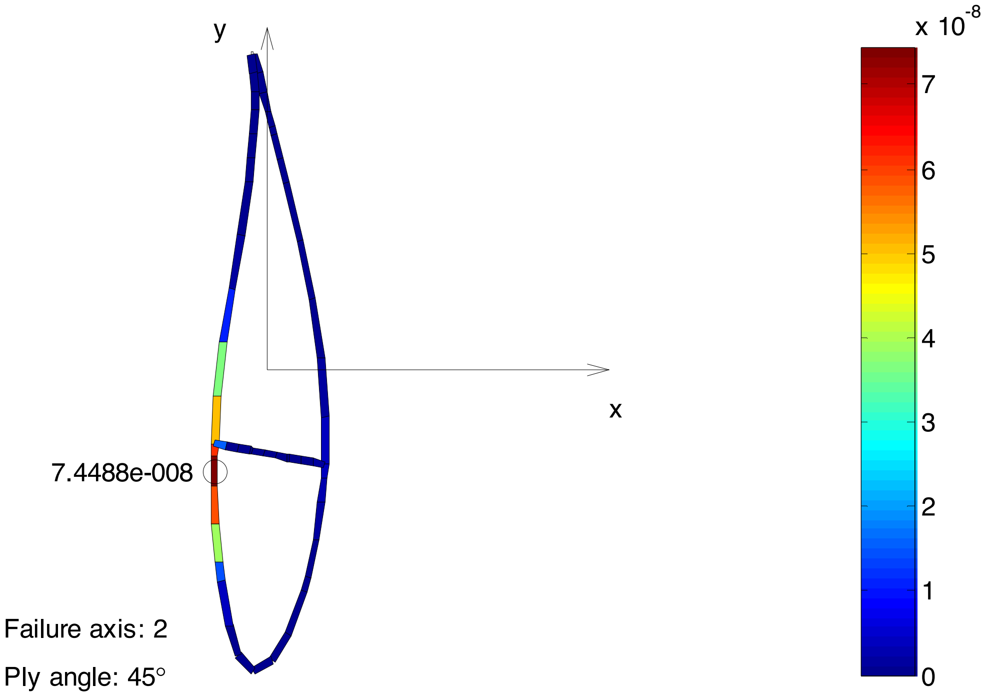

Figure E 35 - Transverse damage to 45° plies in section 17

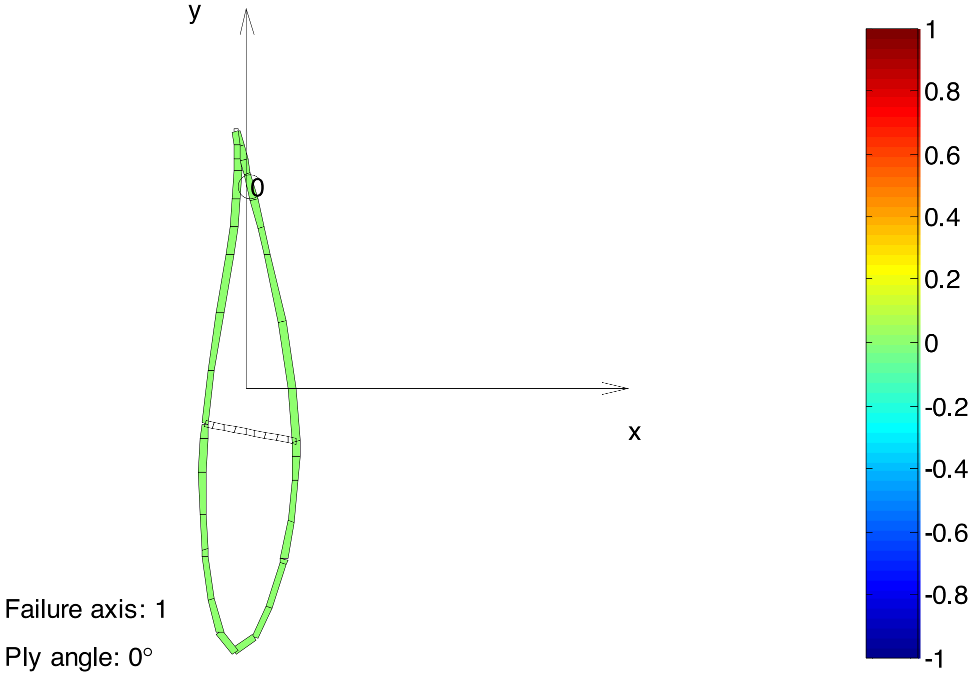

Figure E 36 - Longitudinal damage to 0° plies in section 18

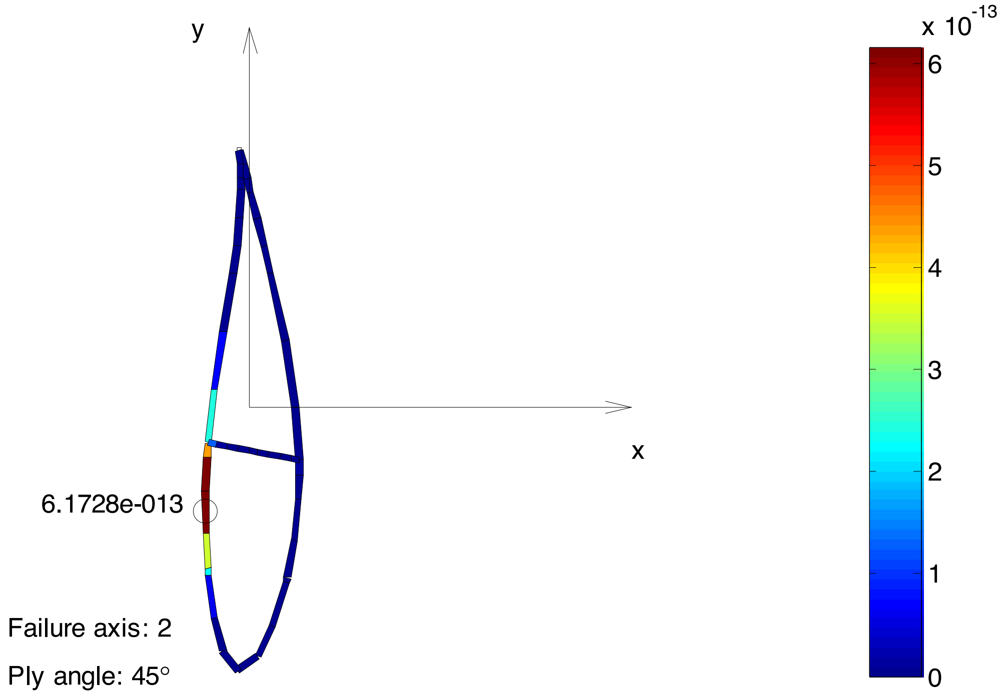

Figure E 37 - Transverse damage to 45° plies in section 18

Appendix F –Kinetic Theory Based Fatigue Test

Complete Results

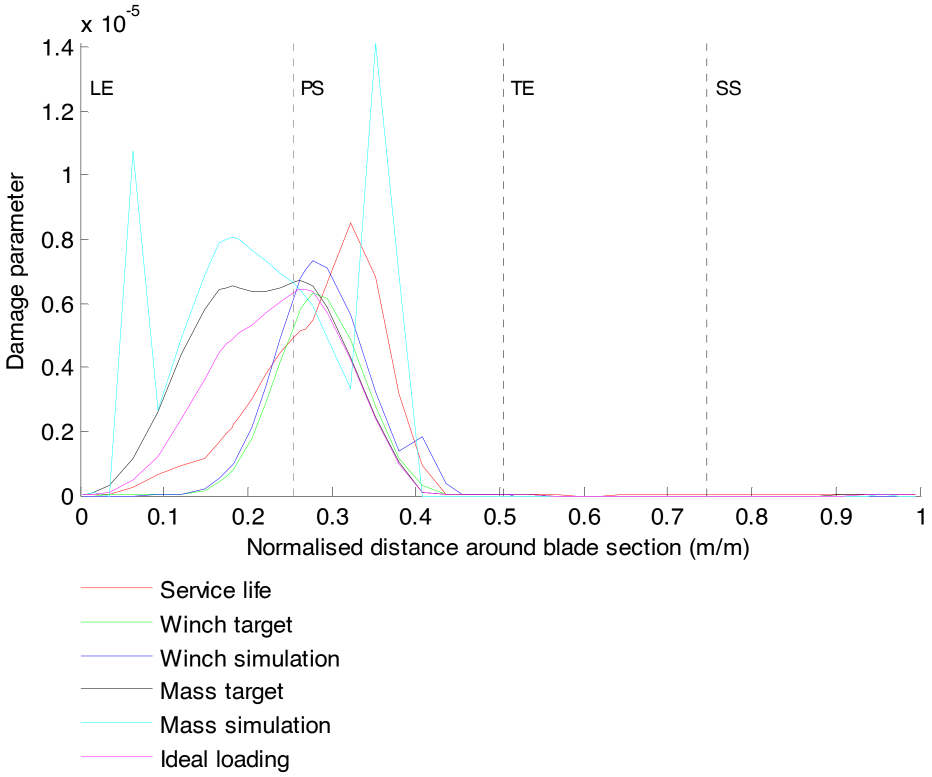

Figure F 1 - Longitudinal damage to 0° plies of section 1 due to various test types

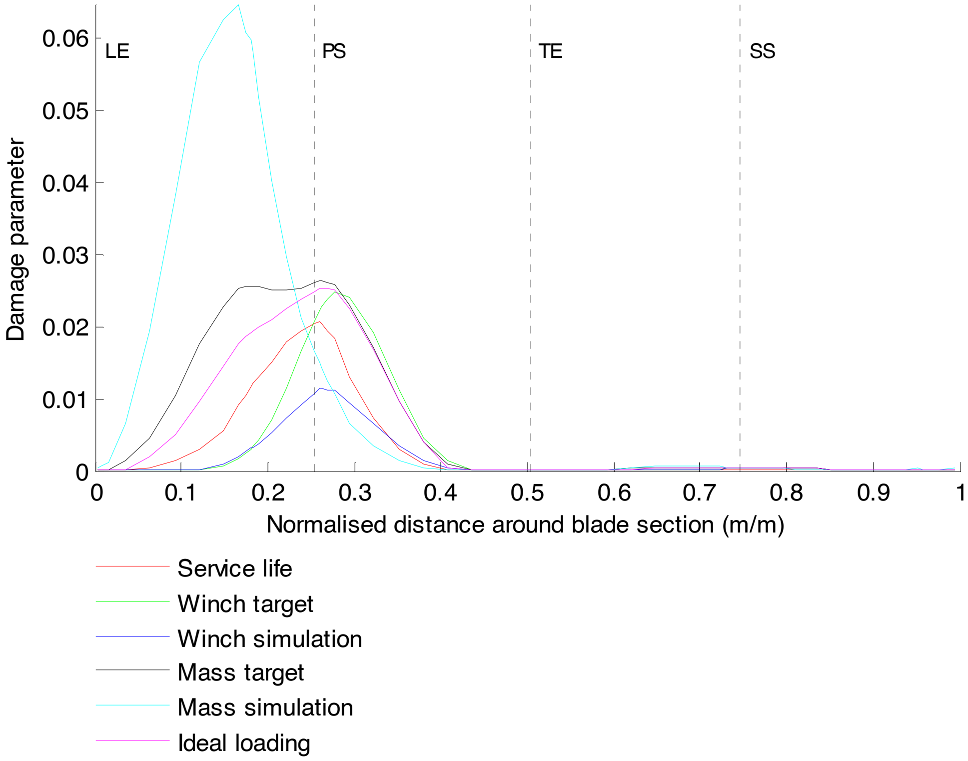

Figure F 2 - Transverse damage to 45° plies of section 1 due to various test types

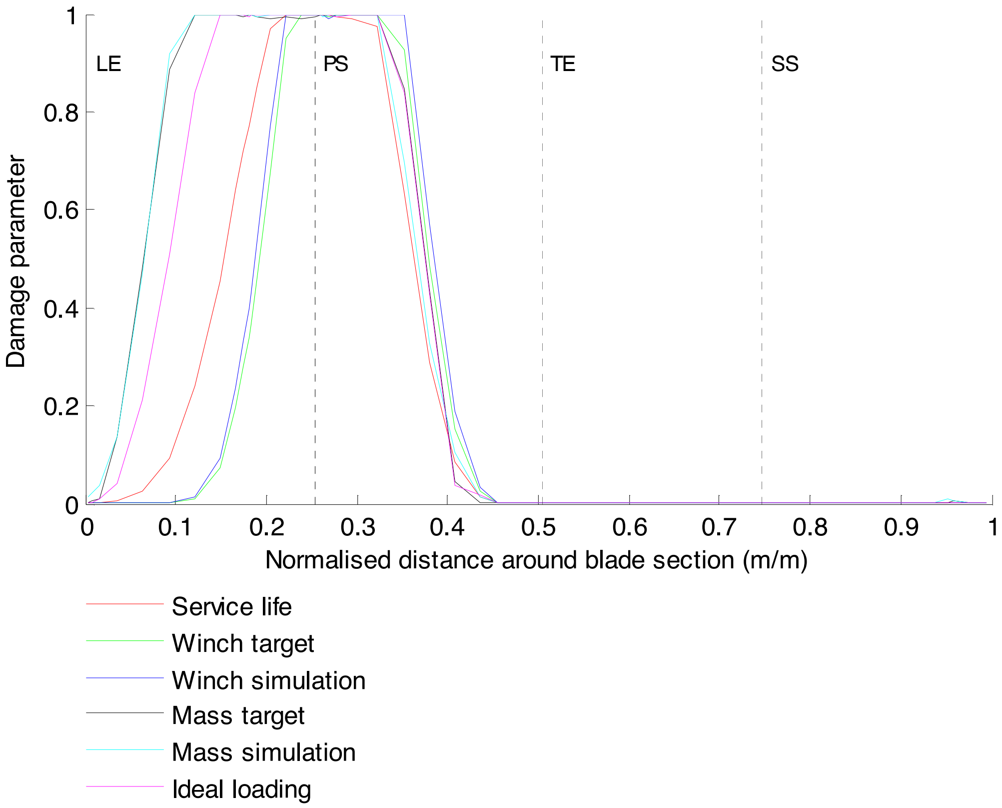

Figure F 3 - Transverse damage to 90° plies of section 1 due to various test types

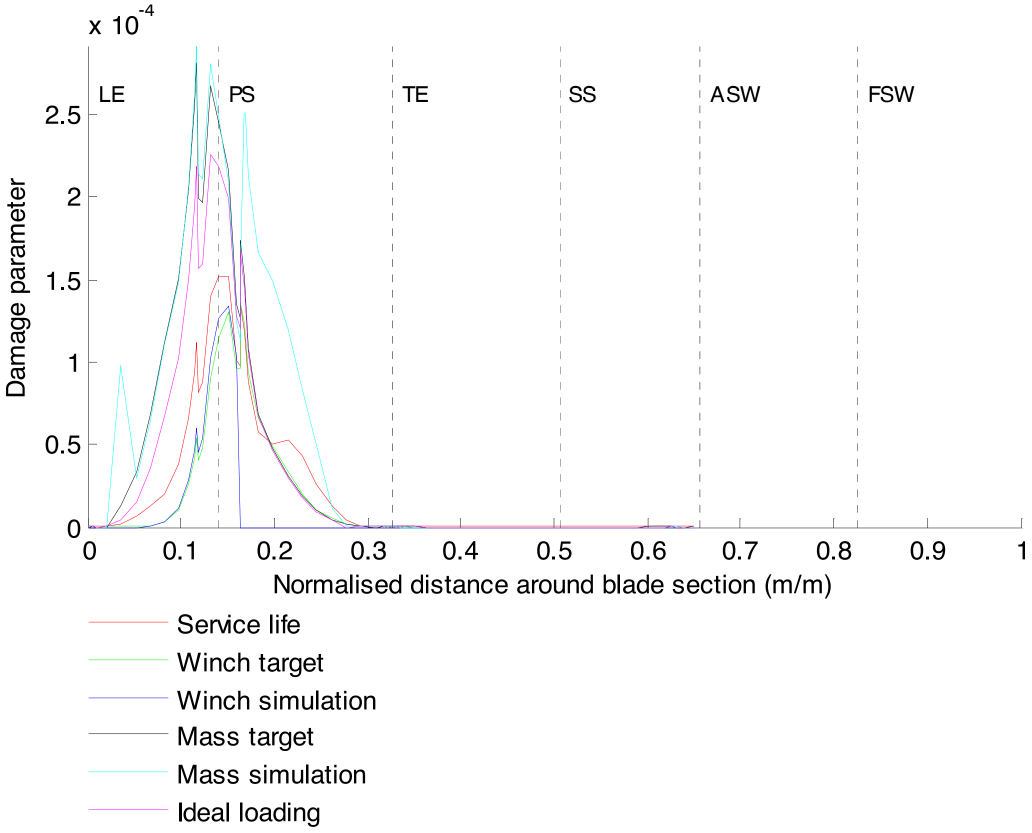

Figure F 4 - Longitudinal damage to 0° plies of section 2 due to various test types

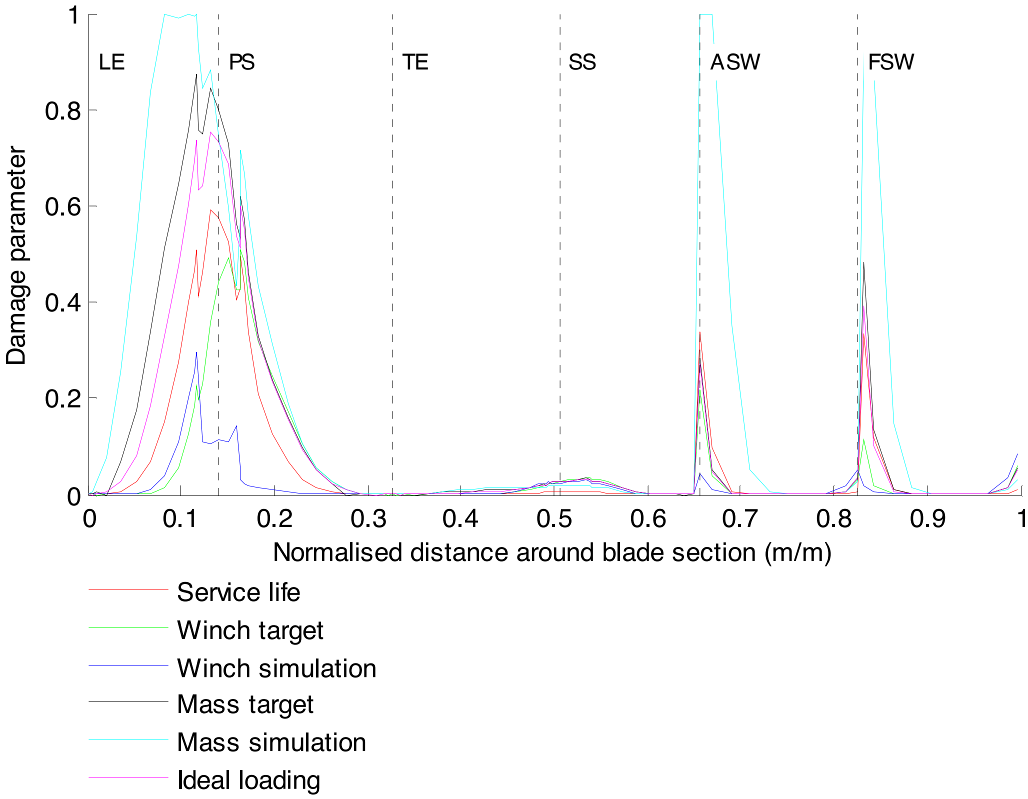

Figure F 5 - Transverse damage to 45° plies of section 2 due to various test types

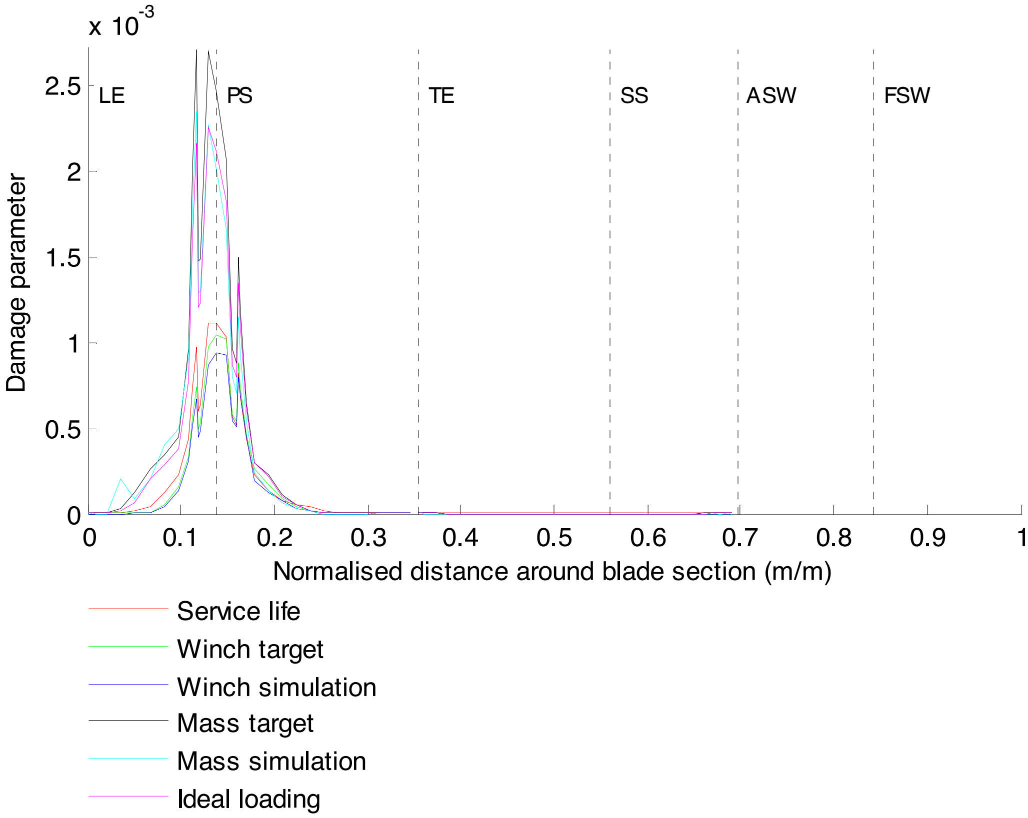

Figure F 6 - Longitudinal damage to 0° plies of section 3 due to various test types

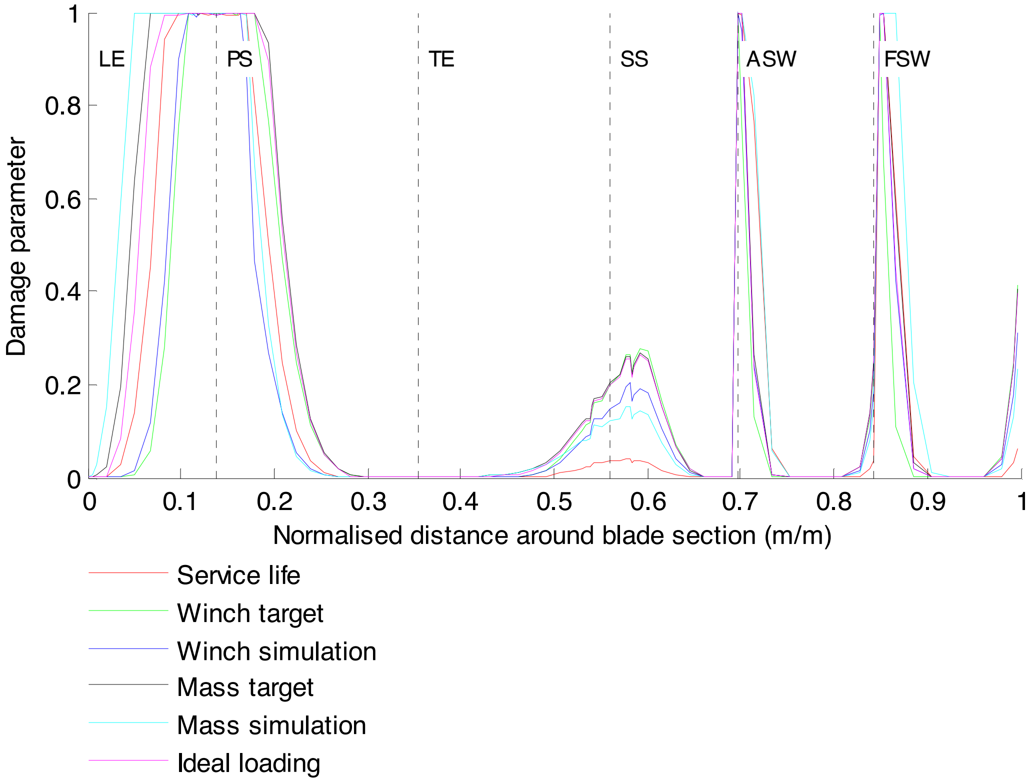

Figure F 7 - Transverse damage to 45° plies of section 3 due to various test types

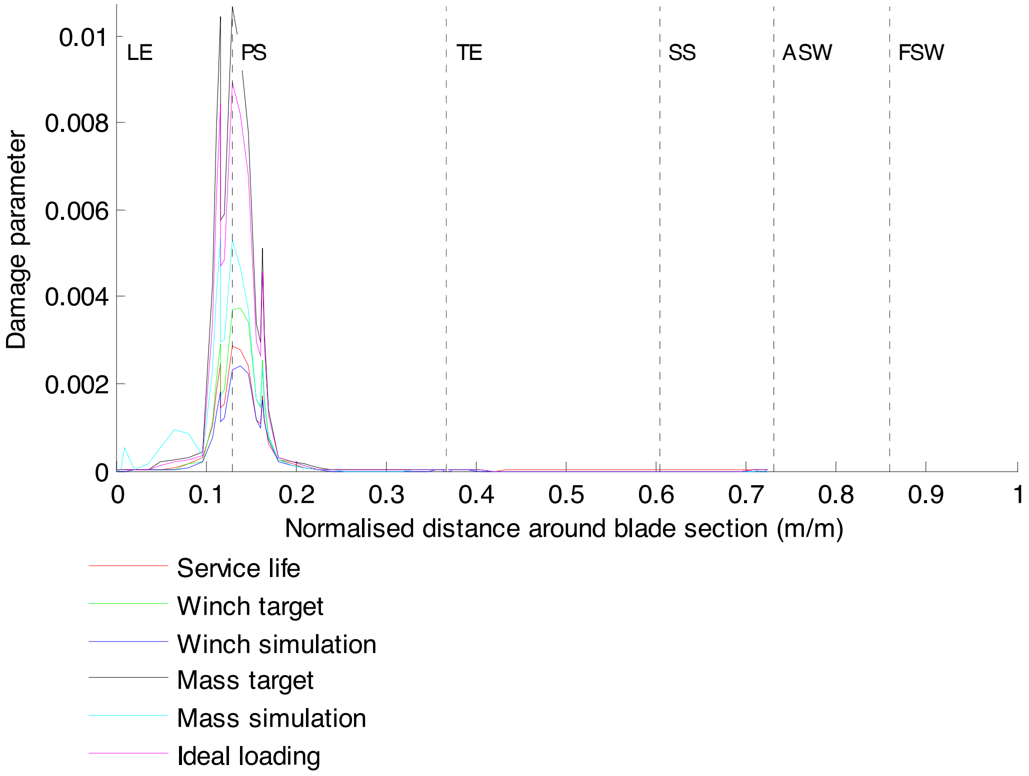

Figure F 8 - Longitudinal damage to 0° plies of section 4 due to various test types

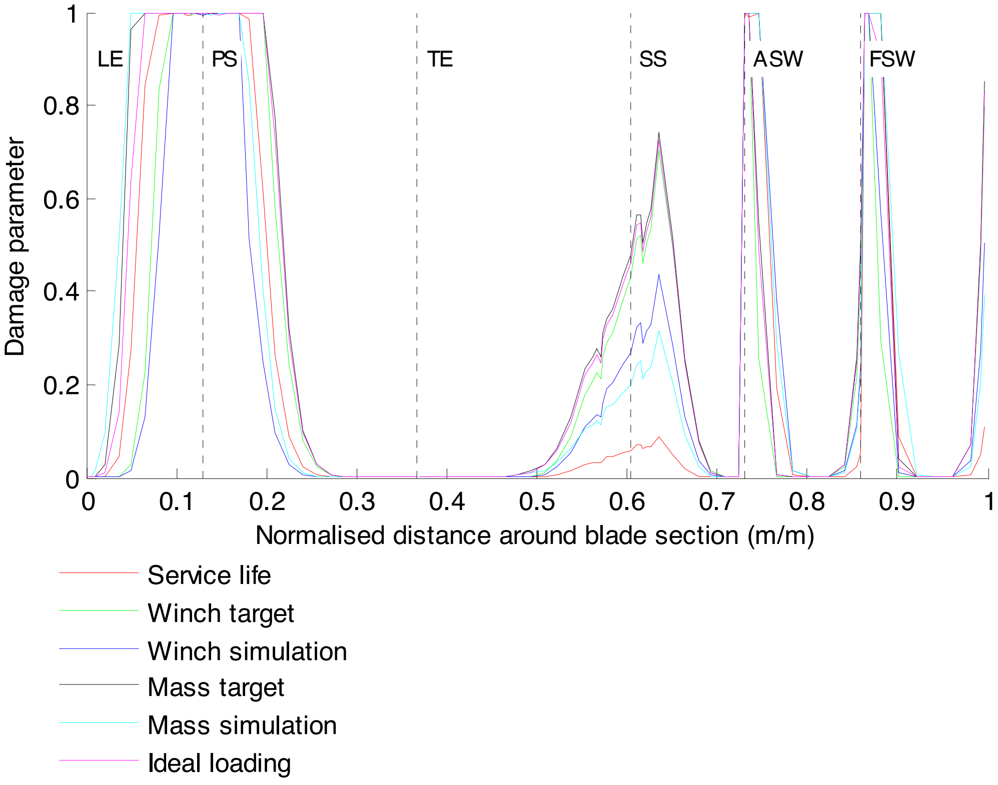

Figure F 9 - Transverse damage to 45° plies of section 4 due to various test types

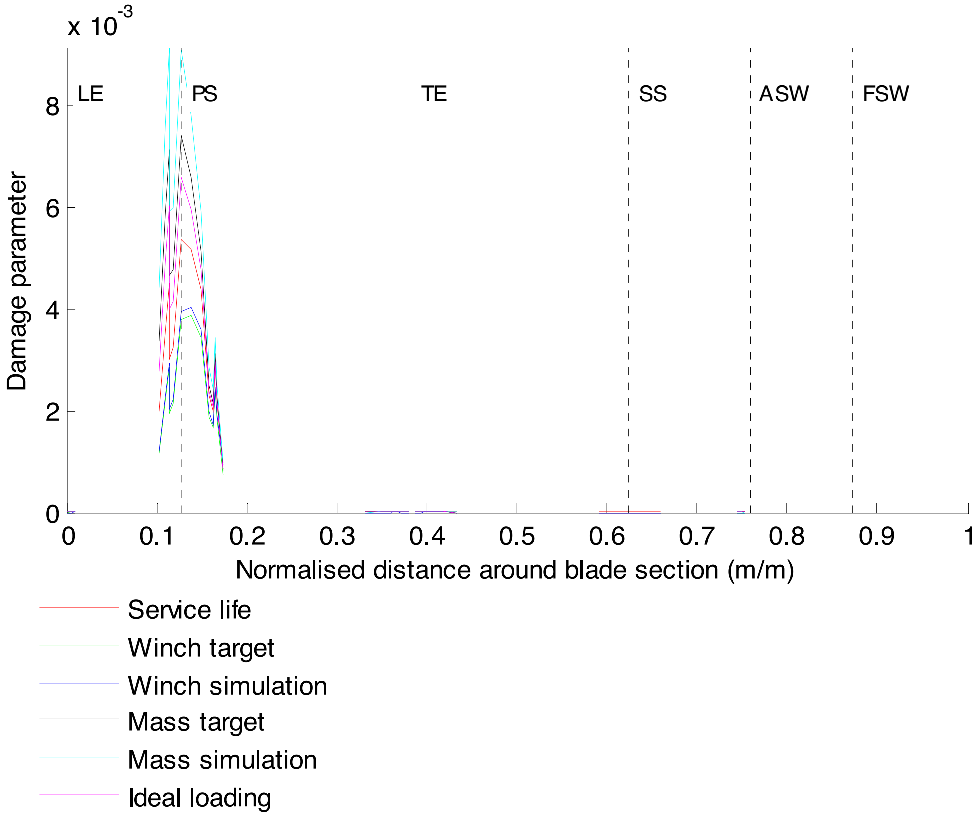

Figure F 10 - Longitudinal damage to 0° plies of section 5 due to various test types

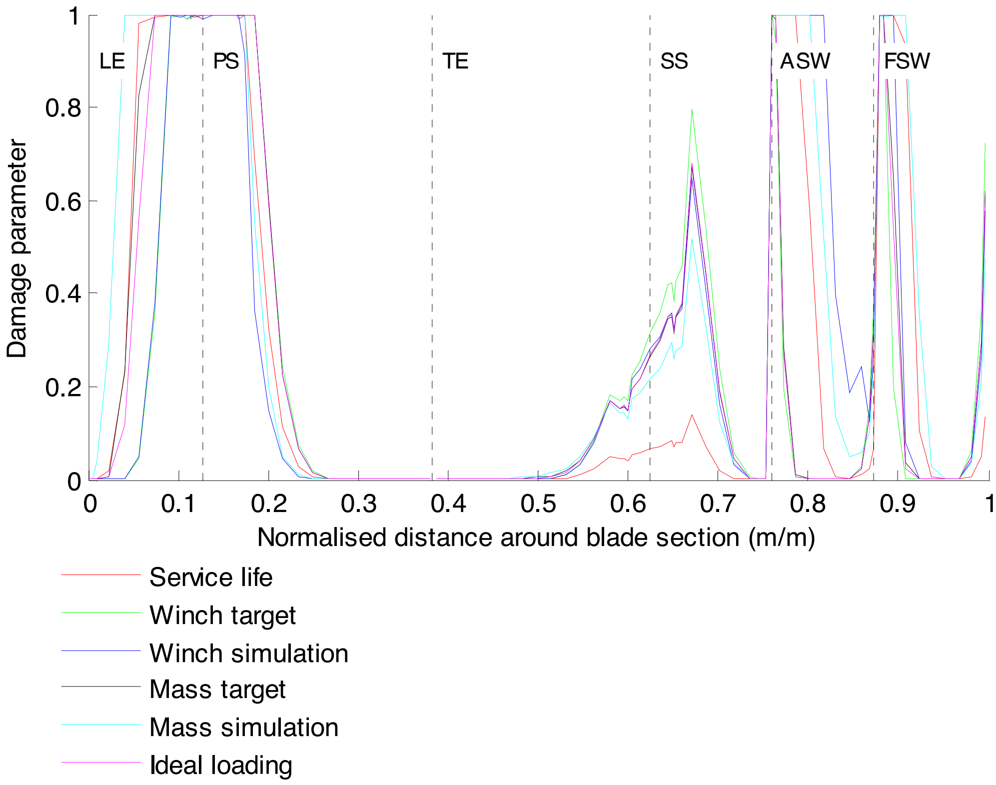

Figure F 11 - Transverse damage to 45° plies of section 5 due to various test types

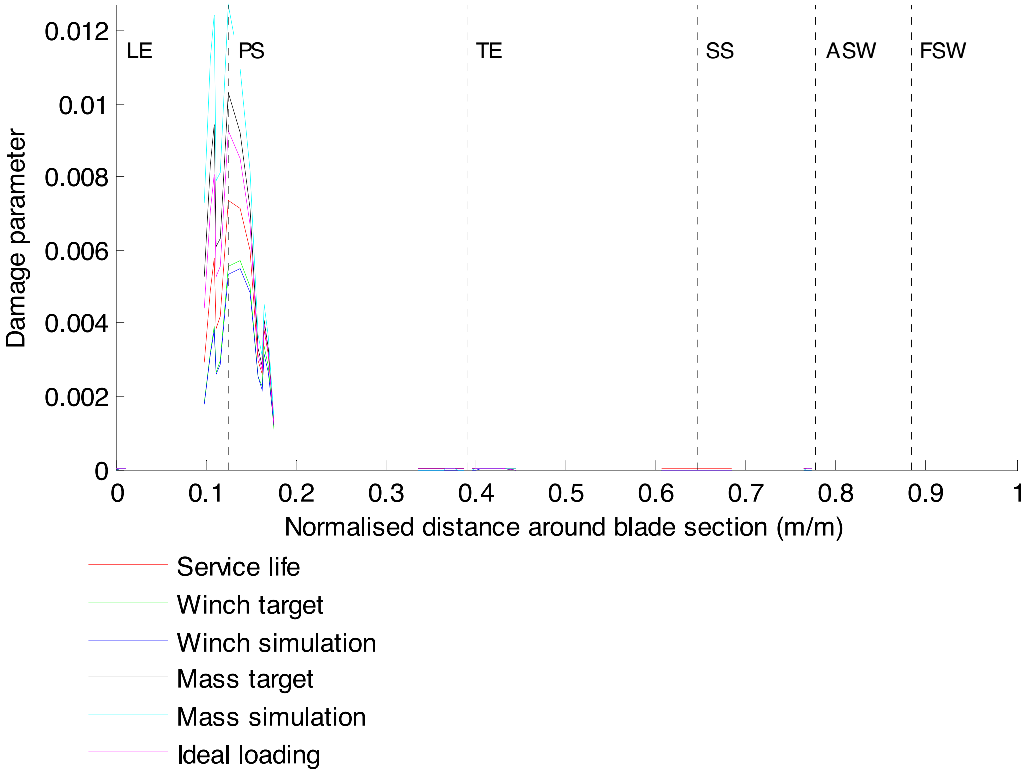

Figure F 12 - Longitudinal damage to 0° plies of section 6 due to various test types

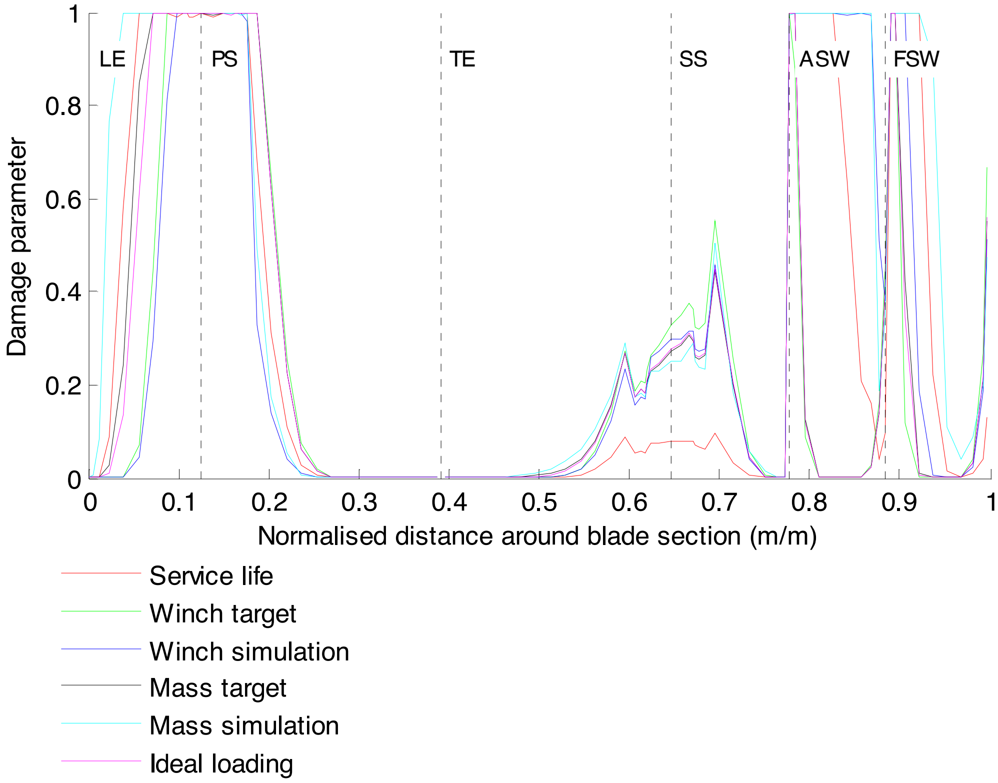

Figure F 13 - Transverse damage to 45° plies of section 6 due to various test types

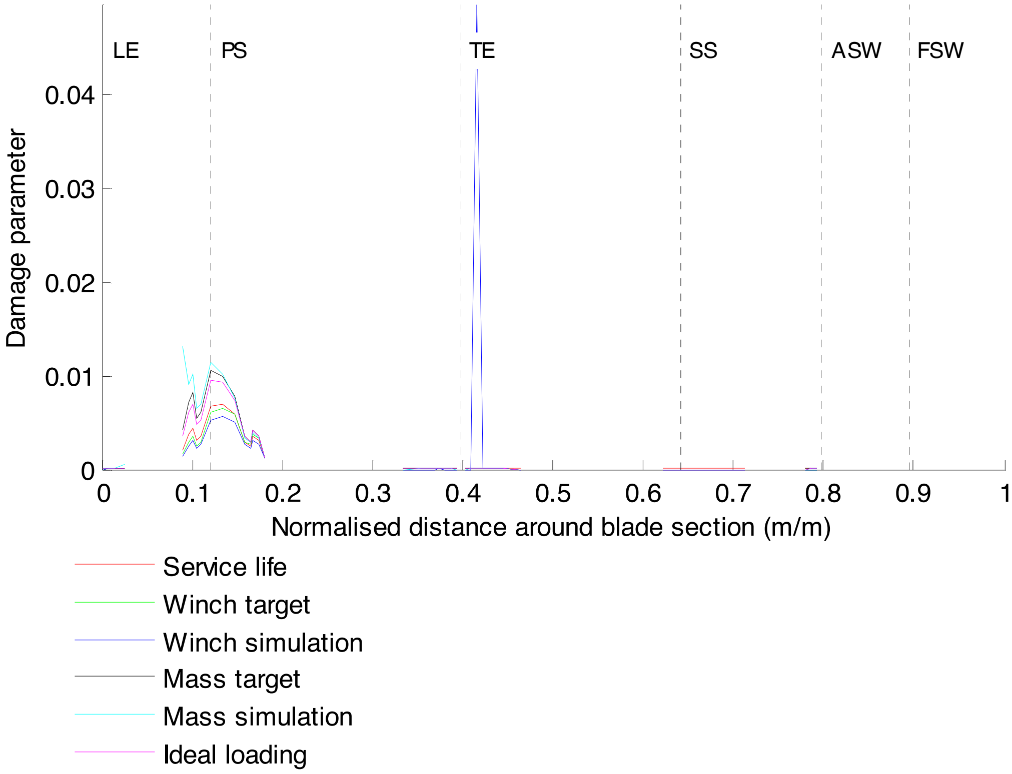

Figure F 14 - Longitudinal damage to 0° plies of section 7 due to various test types

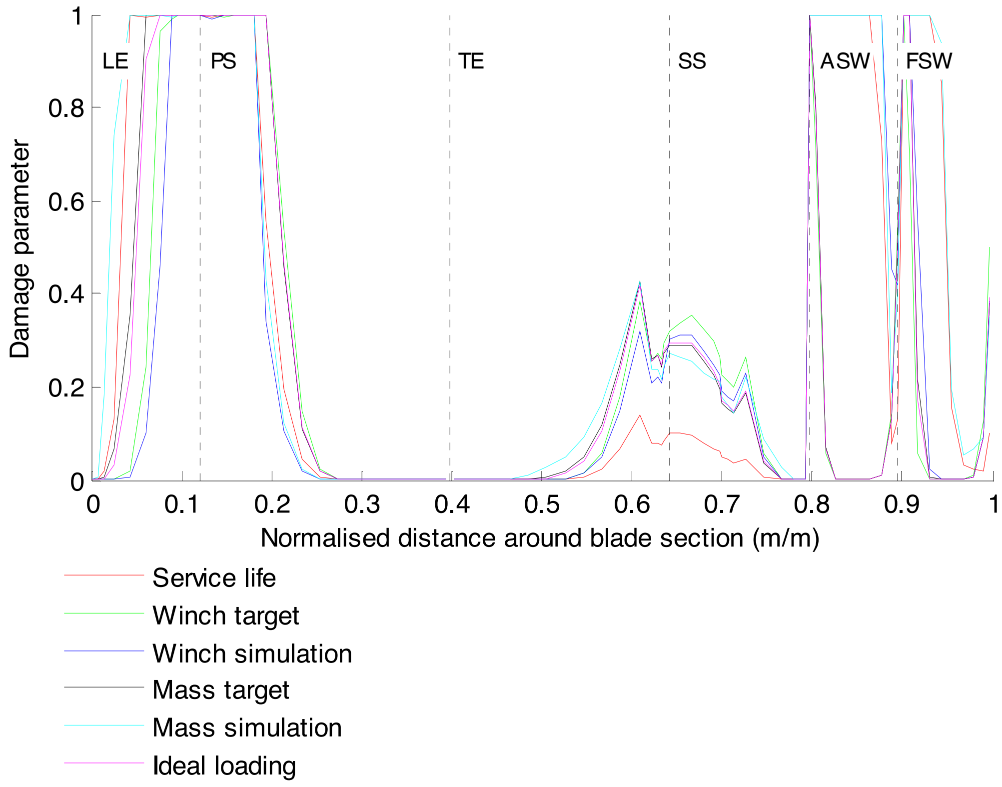

Figure F 15 - Transverse damage to 45° plies of section 7 due to various test types

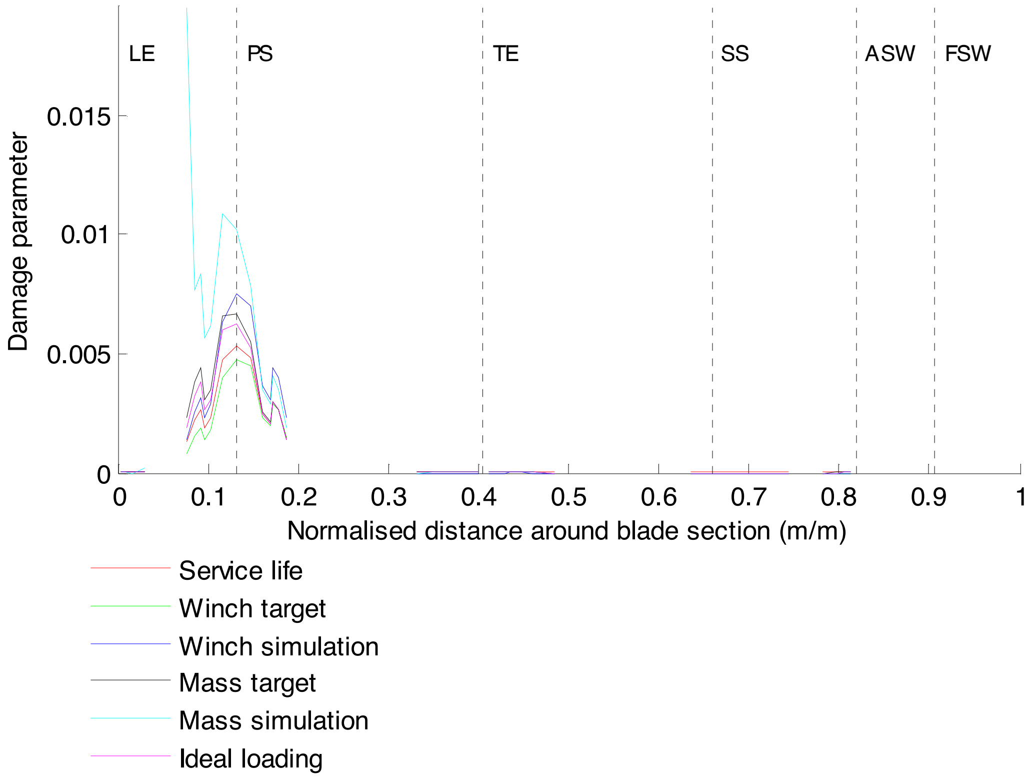

Figure F 16 - Longitudinal damage to 0° plies of section 8 due to various test types

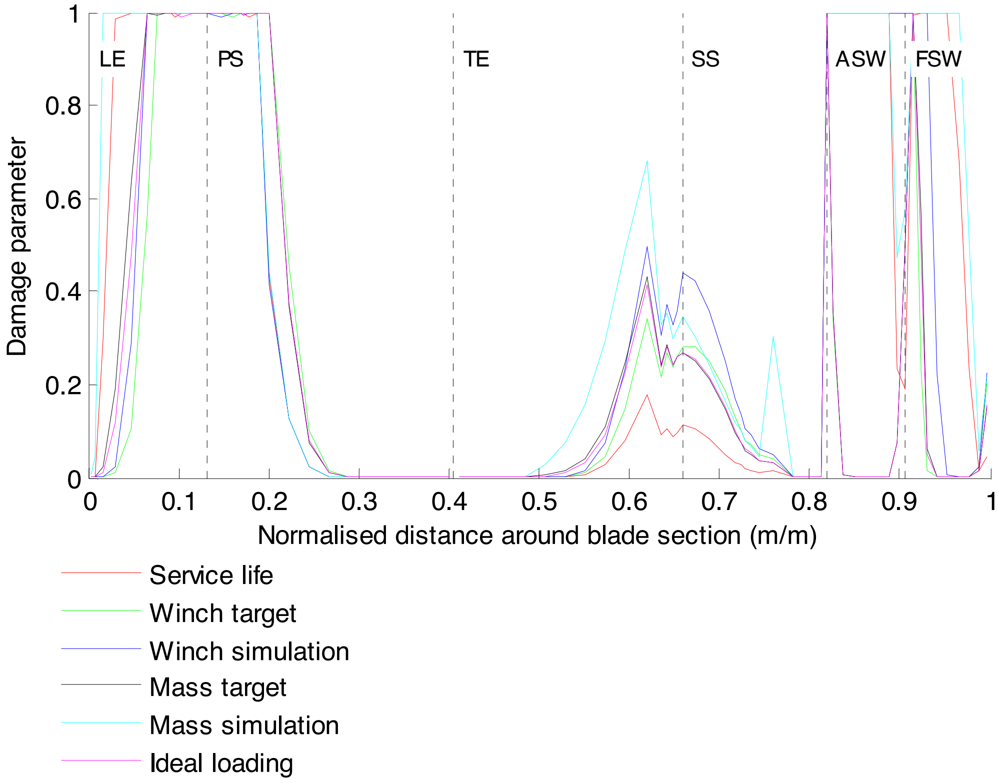

Figure F 17 - Transverse damage to 45° plies of section 8 due to various test types

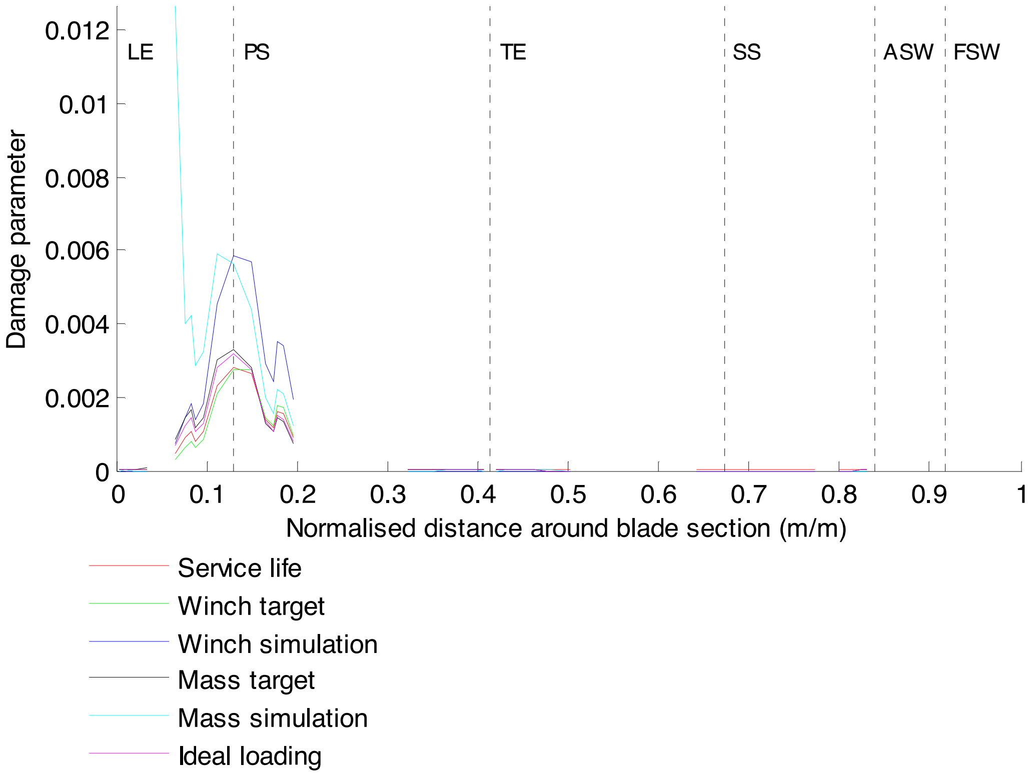

Figure F 18 - Longitudinal damage to 0° plies of section 9 due to various test types

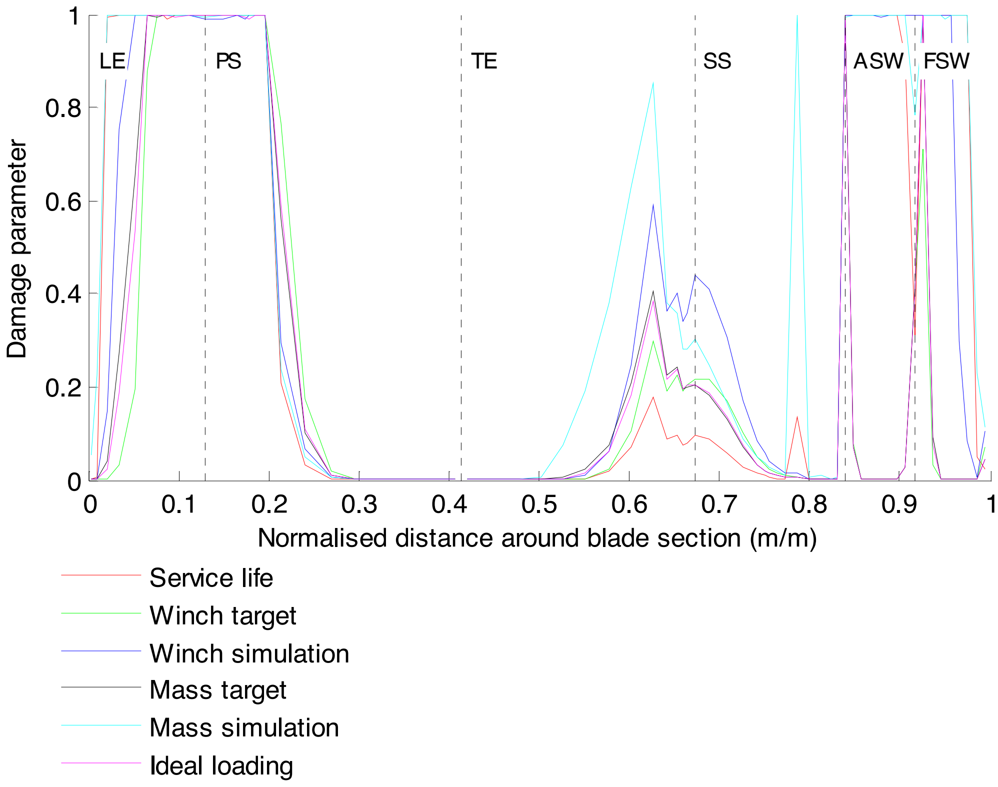

Figure F 19 - Transverse damage to 45° plies of section 9 due to various test types

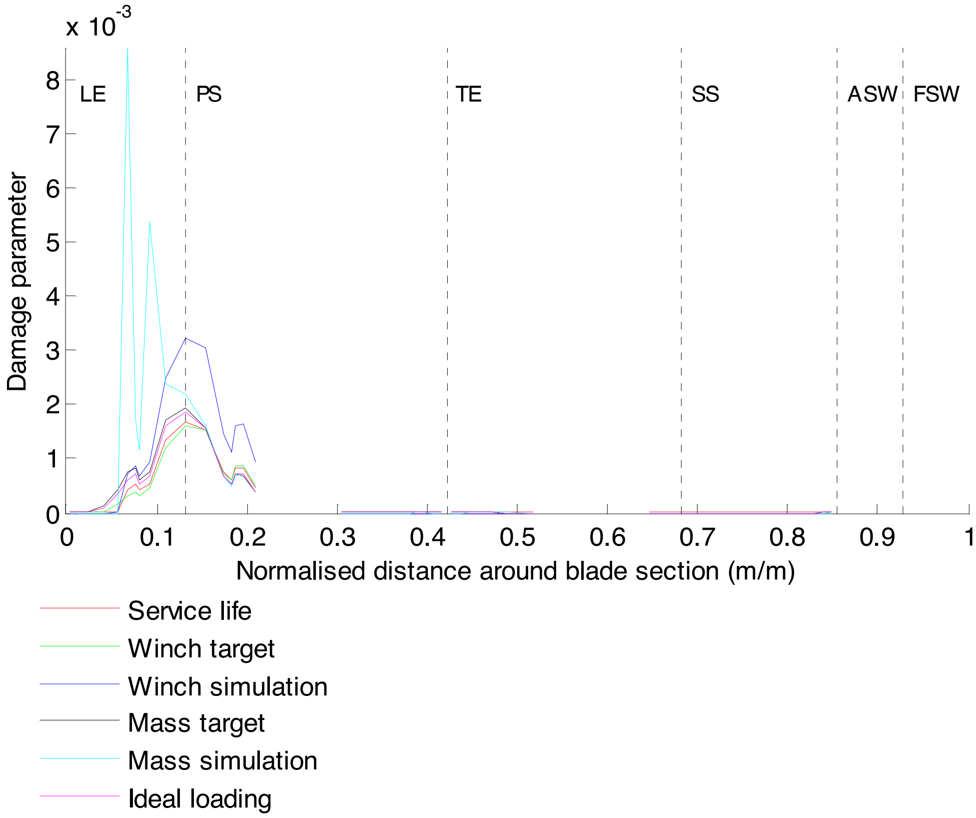

Figure F 20 - Longitudinal damage to 0° plies of section 10 due to various test types

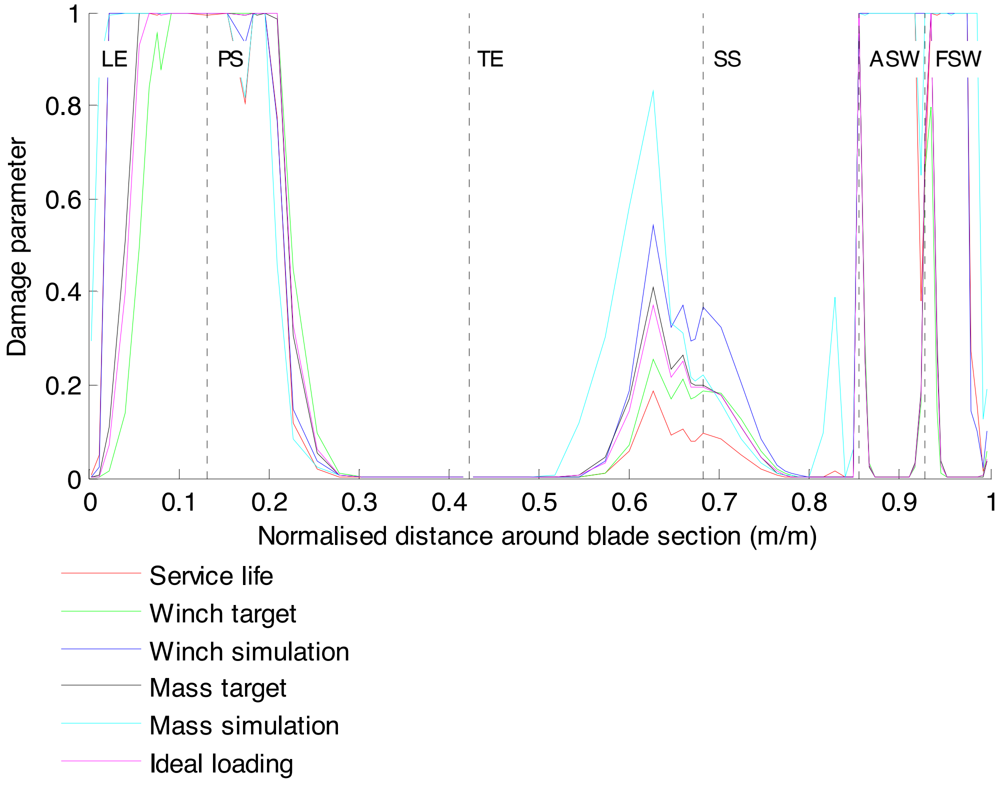

Figure F 21 - Transverse damage to 45° plies of section 10 due to various test types

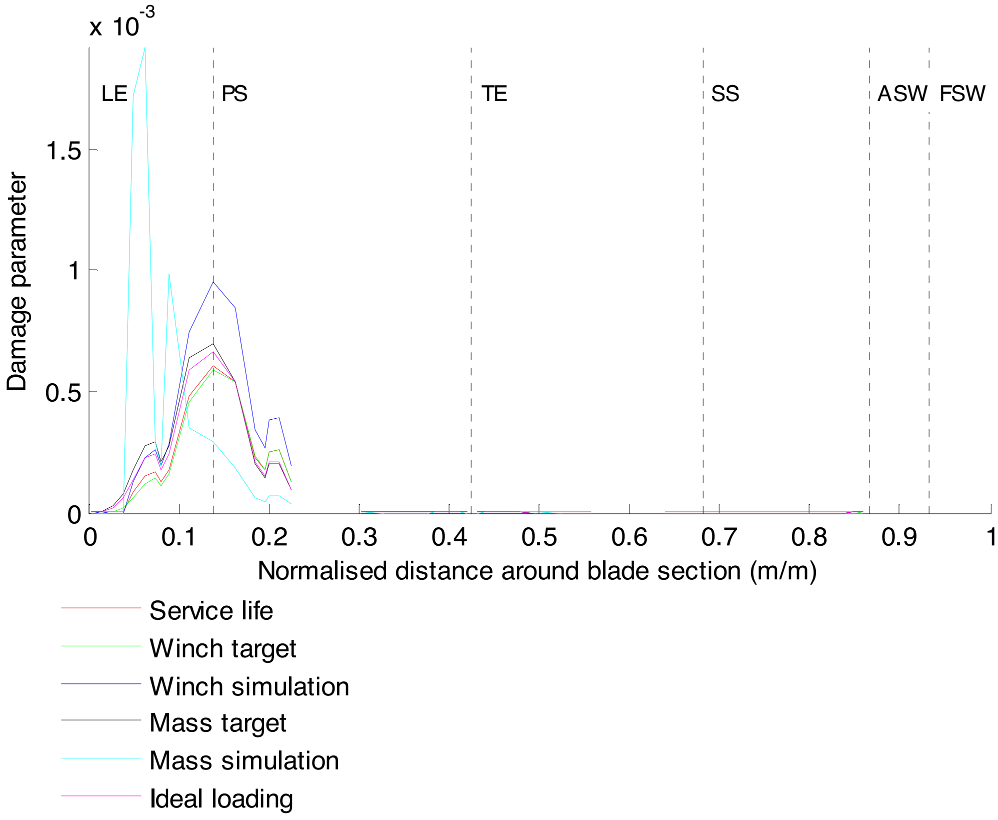

Figure F 22 - Longitudinal damage to 0° plies of section 11 due to various test types

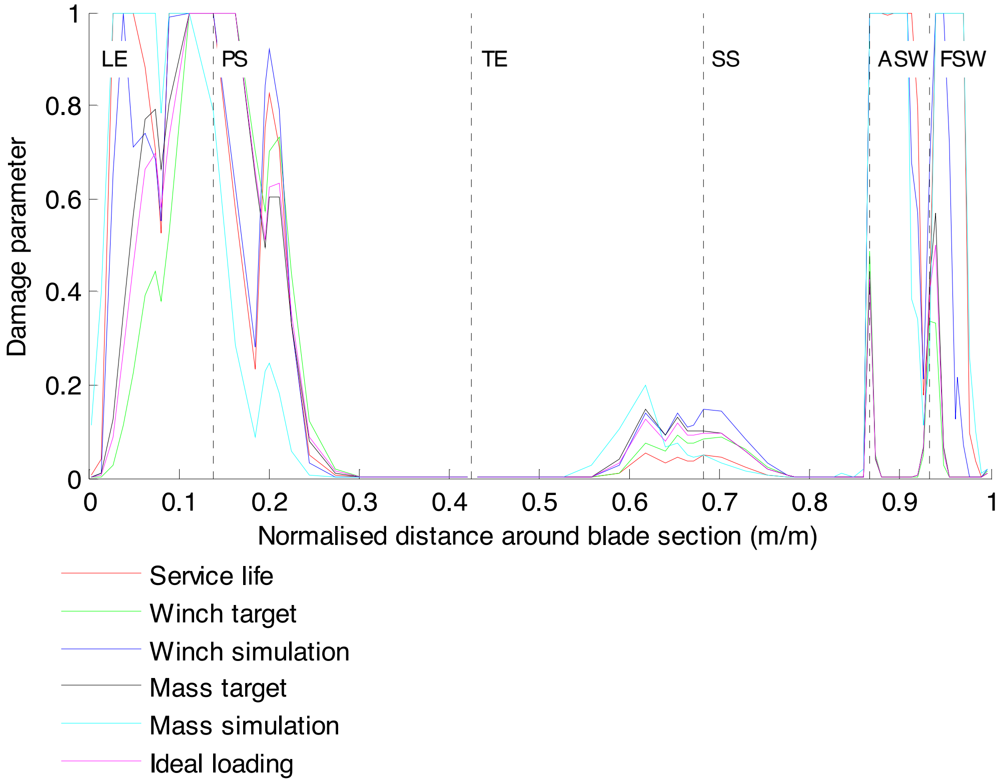

Figure F 23 - Transverse damage to 45° plies of section 11 due to various test types

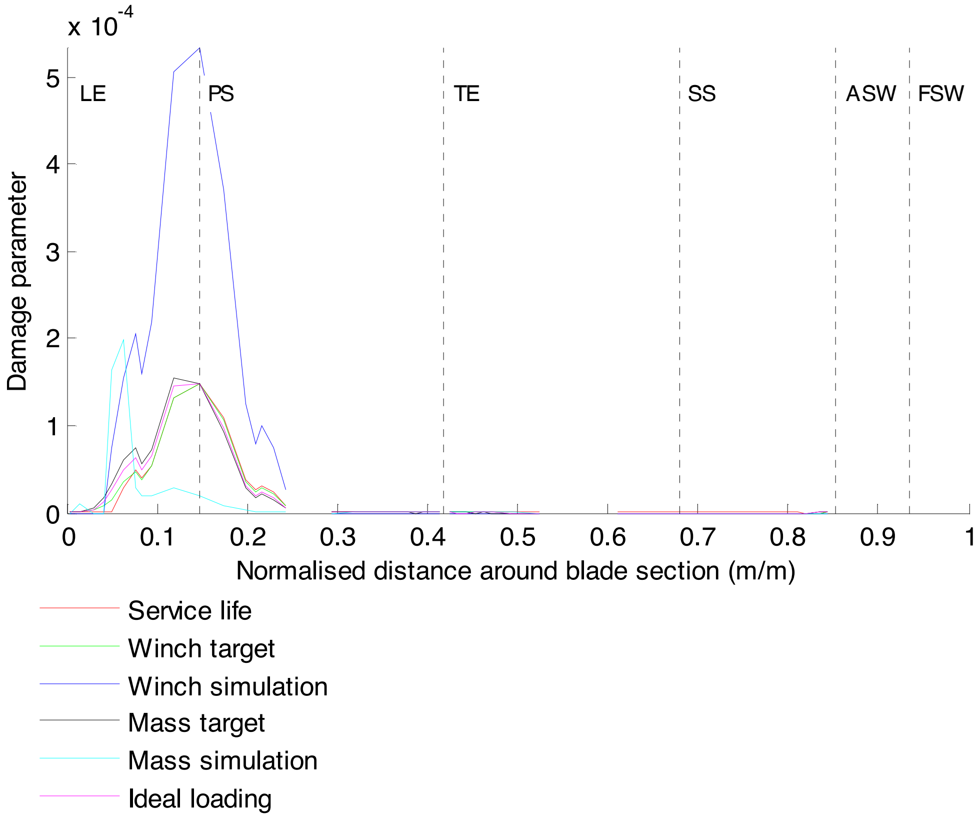

Figure F 24 - Longitudinal damage to 0° plies of section 12 due to various test types

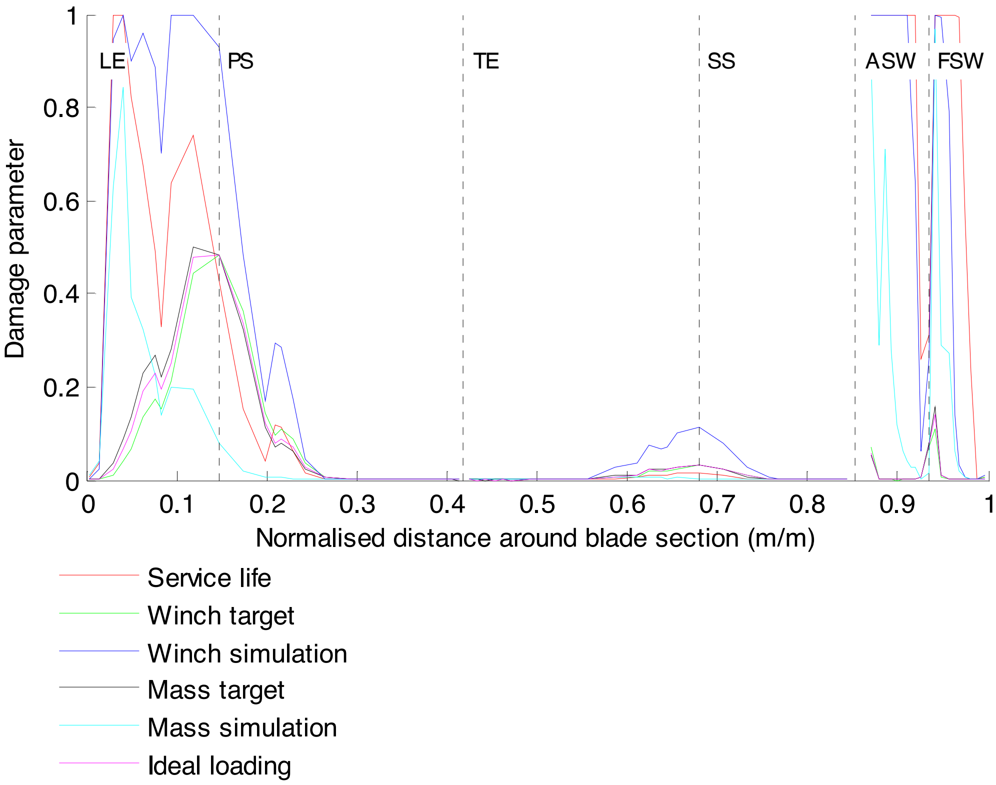

Figure F 25 - Transverse damage to 45° plies of section 12 due to various test types

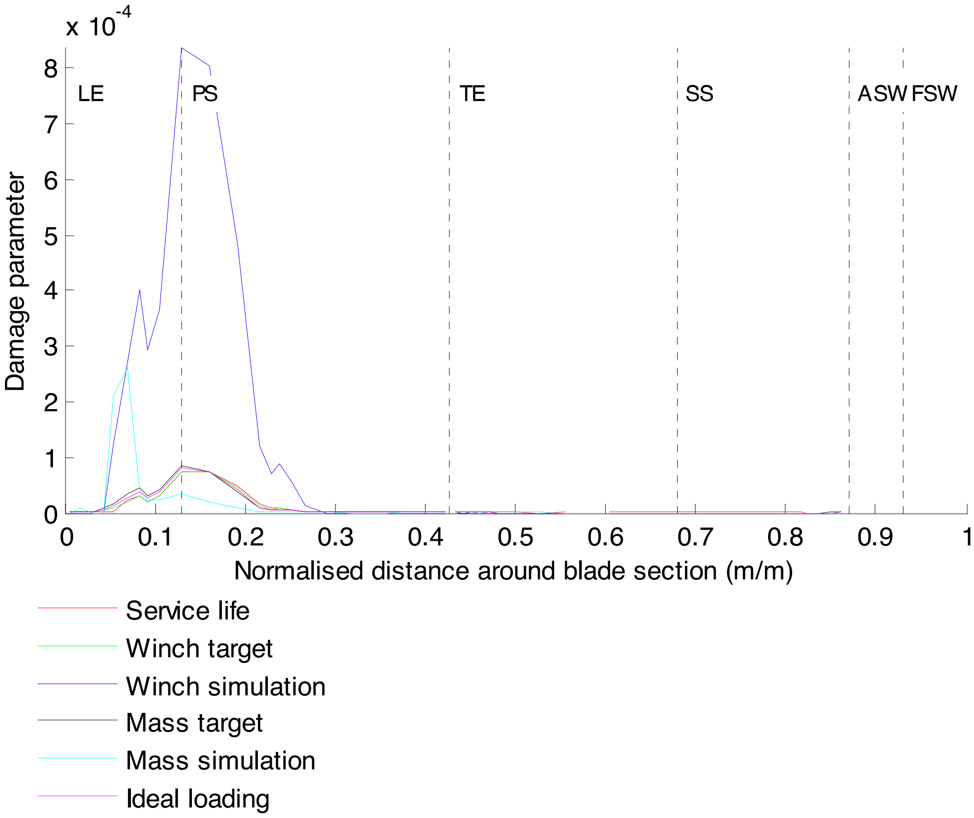

Figure F 26 - Longitudinal damage to 0° plies of section 13 due to various test types

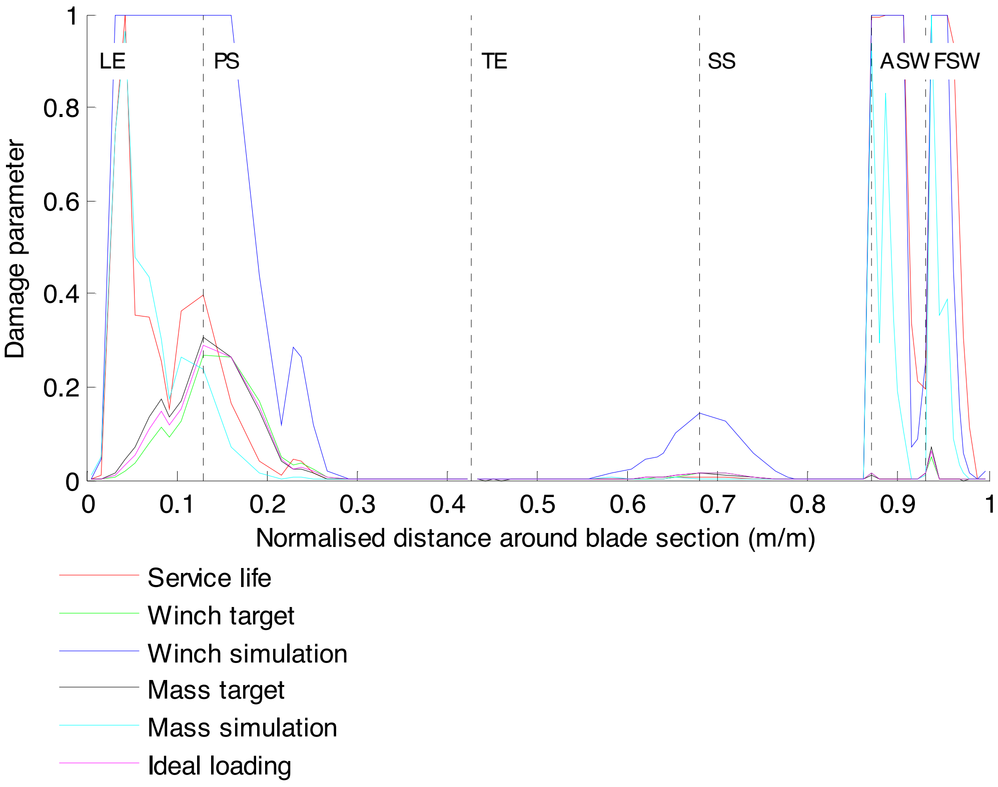

Figure F 27 - Transverse damage to 45° plies of section 13 due to various test types

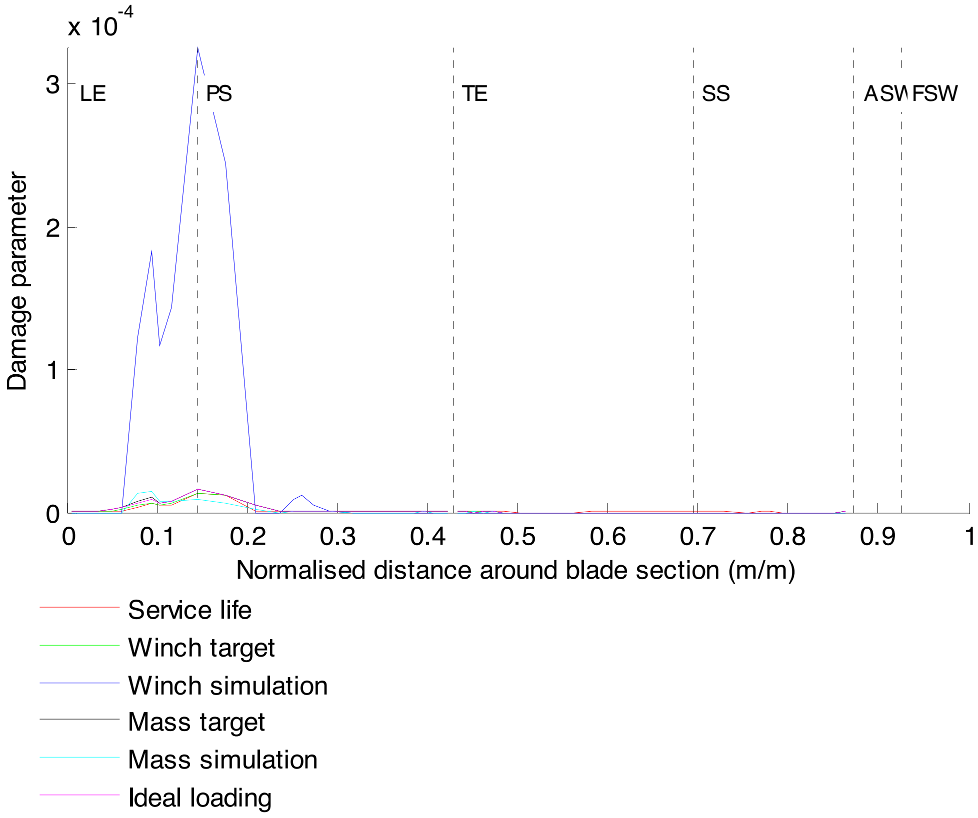

Figure F 28 - Longitudinal damage to 0° plies of section 14 due to various test types

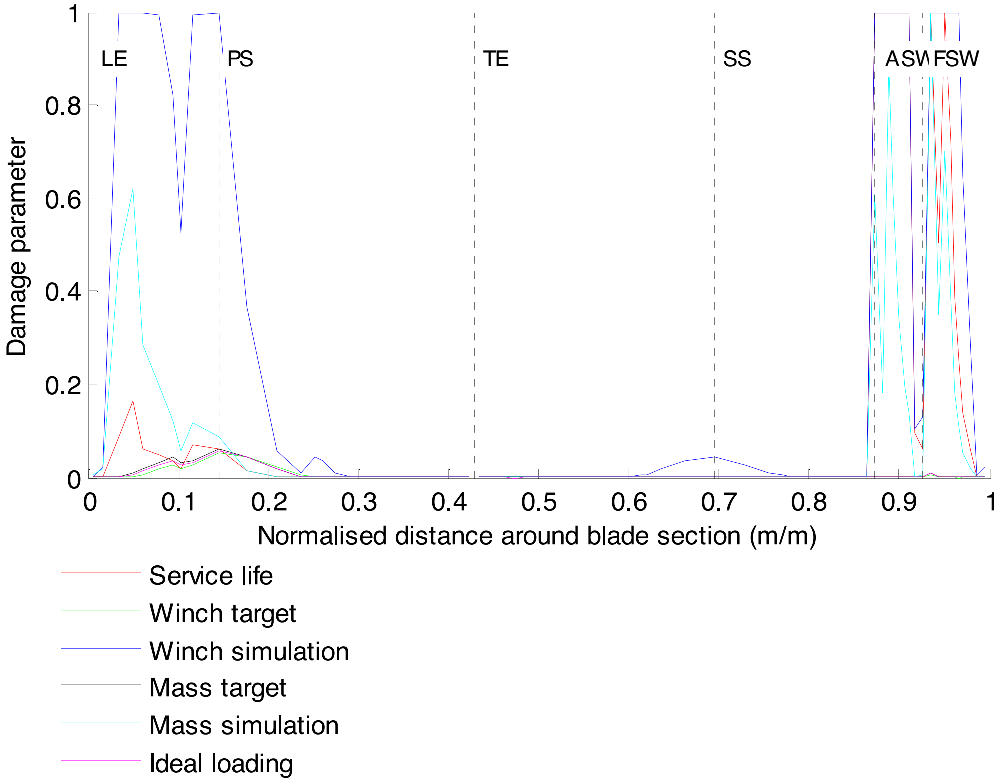

Figure F 29 - Transverse damage to 45° plies of section 14 due to various test types

Appendix G –Published Journal and Conference Papers

1. Greaves, P.R., et al., *Evaluation of Dual Axis Resonant Fatigue Testing of Large Wind Turbine Blades*, in *EWEA 2011*. 2011: Brussels, Belgium.
2. Greaves, P.R., *Birds and bees (letter).* New Scientist, 2012. **216**(2895): p. 36-37.
3. Greaves, P.R., et al., *Evaluation of dual-axis fatigue testing of large wind turbine blades.* Proceedings of the Institution of Mechanical Engineers, Part C: Journal of Mechanical Engineering Science, 2012. **226**(7): p. 1693-1704.
4. Greaves, P.R., et al., *Fatigue Analysis of Wind Turbine Blades using Multi-Continuum Theory and the Kinetic Theory of Fracture*, in *EWEA 2013*. 2013: Vienna, Austria.